UNIVERSITAT DE BARCELONA

Understanding the measurements and variability of aerosol optical properties in NE Spain

Jesús Yus Díez

Aquesta tesi doctoral està subjecta a la llicència ***Reconeixement 4.0. Espanya de Creative Commons***.

Esta tesis doctoral está sujeta a la licencia ***Reconocimiento 4.0. España de Creative Commons***.

This doctoral thesis is licensed under the ***Creative Commons Attribution 4.0. Spain License***.

UNIVERSITAT DE BARCELONA

Understanding the Measurements and Variability of Aerosol Optical Properties in NE Spain

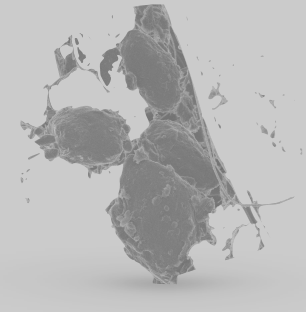

Jesús Yus Díez
PhD Thesis
Universitat de Barcelona

UNDERSTANDING THE MEASUREMENTS AND VARIABILITY OF AEROSOL OPTICAL PROPERTIES IN NE SPAIN

MEMÒRIA PRESENTADA PER OPTAR AL GRAU DE DOCTOR PER LA UNIVERSITAT DE BARCELONA.

PROGRAMA DE DOCTORAT EN FÍSICA

Autor

Jesús Yus Díez

Directors

Dr. Andrés Alastuey Urós
Dr. Marco Pandolfi

Tutor

Dr. Joan Bech Rustullet

UNIVERSITAT DE BARCELONA

Jesús Yus Díez
Understanding the measurements and variability of aerosol optical properties in NE Spain

Instituto de Diagnóstico Ambiental y Estudios del Agua - Consejo Superior de Investigaciones Científicas (IDAEA-CSIC)
Grupo de Geoquímica Ambiental e Investigación Atmosférica (EGAR)
C. Jordi Girona 18-26
08008 and Barcelona

Universitat de Barcelona
Grup de meteorologia
Departament de Fisica Aplicada
C. Martí i Franquès n2
08008 and Barcelona

This thesis has been possible thanks to the funding from the Ciencia e Innovación (HOUSE, grant no. CGL2016-78594-R and grant no. PID2019- 108990PB-100)); the Generalitat de Catalunya, Agència de Gestió d'Ajuts Univer- sitaris i de Recerca (grant nos. AGAUR 2014 SGR33 and AGAUR 2017 SGR41); the Spanish Scientific Council, CSIC (project Geoquimica de aerosoles atmosféricos: implicaciones en salud y clima, program Proyecto Intramural Especial, project no. 202030E261) and the European Comission's ERC grants (Fragment project (no. 773051)).

Copyright: Physical and online reproduction of the total and/or part of this publication must include the appropriate bibliographic citation, i.e. author, title, etc.

Cover photos: dust devil in L'Bour, Morocco, during the Sahara 2019 FRAGMENT (front cover top; own source), AE33 filter tape spot (front cover middle; own source), Helium Ion Microscrope from a AE33 filter tape during a Saharan dust event over the Mediterranean (front cover bottom and back cover main; Rok Podlipec from Helmholtz-Zentrum Dresden-Rossendorf and Jožef Stefan Institute), and Scanning Electron Microscope of a nuclepore of black carbon and mineral dust particles (spine; Rok Podlipec from Helmholtz-Zentrum Dresden-Rossendorf and Jožef Stefan Institute).

Al Angelico y la María,
la Choneta y Jesús,
como espurnicas
de esta tierra
dura y sincera.

AGRADECIMIENTOS

Este trabajo nunca hubiera sido posible sin la presencia de muchas personas que me rodean, es por ello que me gustaría dedicarles mi más sincero agradecimiento:

En primer lugar a mis directores de tesis: Marco y Andrés, gracias. A Marco por la paciencia para ayudarme y guiarme con todas las vicisitudes de la investigación, por enseñarme tanto, pero sobretodo por confiar en mi desde el primer momento. A Andrés, gracias por tus espurnas de sapienza, tu humildad, tu humanidad y tu saber hacer, por tu visión de conjunto, por enseñarme todo lo que no eran propiedades ópticas, que es mucho. Gracias por toda vuestra ayuda y empenta durante lo que han sido unos intensos cuatro años, grazie per tutto.

La investigación realizada durante esta tesis no existiría sin una sólida base humana, es por eso que me gustaría agradecer a todos los investigadores y técnicos del grupo EGAR (IDAEA-CSIC), sin cuyo esfuerzo y trabajo no hubiera sido posible, gracias a todos. Al equipo de *les cabines de mesura de qualitat de l'aire*, sin vosotros no habría datos que analizar: Cristina Reche en Palau Reial; Noemí, Marco y Andrés en Montseny y Montsec, los viajes a las estaciones en coche, los pinchos de tortilla del Lanau y los marinerets en Àger han sido parte una parte integral de esta tesis. En concreto, quisiera hacer mención aparte a Noemí: gracias por tu paciencia para explicarme como funcionaban los instrumentos y como arreglaros, por arrimar el hombro cuando hacía falta.

Muchas gracias a todos mis compañeros de grupo y oficina por los *coffee breaks*, por las charradetas en el pasillo, por ayudarme a desconectar y hacer que los días pasarán de forma más amena. A los "atletas" del IDAEA lunch run por descubrirme el paraíso natural que es Collserola. A todos los estudiantes de doctorado que han pasado por la 1518 y 1543 con los que compartir el camino: a Amaia y Alessia, por llenar de vida y alegría el despacho, por los buenos momentos que pasamos; a Marta y Adolfo por invadirnos un poco más tarde y ayudarme tanto; a Carla, Tolis, Pedro y Cristina C. por ser una estela a la que seguir. Gracias, grazie mille, milla esker, gràcies de tot cor.

Vull agrair a la professora Maria Rosa Soler Duffour, la Dra. Mireia Udina i tot el grup de Meteorologia de la Univesitat de Barcelona per acollirme i donarme suport amb els meus primers passos a l'investigació. Gràcies per l'oportunitat.

I would like to acknowledge the best dust measurement campaigns colleagues one could ask for amid dust storms and dust-devils, under the 45 °C Saharan sun or inside the frigid Vatnajökull melted glacier waters: Adolfo, Cris, Agnesh, Hannah, Alex, Claudia, and the whole FRAGMEMT & HILDA people. *Shukran*, *takk fyrir*.

I would like also to acknowledge all the collaborators and co-authors with whom I have been able to participate with and learn from, too many to list. Especially to Aerosol, Clouds and Trace Gases Research Infrastructure (ACTRIS) and Chemical On-Line cOmpoSition and Source Apportionment of fine aerosoL (COLOSSAL) Cost Action for providing me with the opportunity of attending the Hyytiälä summer camp as well as multiple workshops. I would also like to acknowledge the help provided by Matic Ivancic and all the Aerosol d.o.o. staff for all the help regarding the AE33 aethalometer.

En una nota más personal, me gustaría agradecer a mis compañeros Adolfo, Cristina, Marta, Pedro y Amaia por las reuniones presenciales y online, por los viajes y las risas, que no decaigan. Especialmente quiero agradecer a l'Adolfo, y a l'Anna, por ser dos bellísimas personas, me habéis escuchado, hecho reír y acogido con las manos abiertas siempre que lo he necesitado, para vosotros mi cariño incondicional y deuda eterna. A Anabel, Jaume y Marina, por compartir tantas horas, tantos juegos de mesa, tantos momentos felices, unos años únicos, el piso de Cardenal Reig. A Nachet, Javier, Mónica y el pequeño Guille, amigos que son familia, grasias per compartí chuegos y excursions per ixa vall nuestra, per ixas tucas, ixas selvas, sigue hivert o estíu. Agradecimiento es poco el que tengo a David, Julia, Marina y Ricardo, no hubiera podido pedir gente más bonica. Gracias, Ricardo, por las masterclass de tenis y remo, las dominadas, las charradetas y reflexiones, el sentimiento de gratitud y fortuna por la vida, y sin saberlo, ayudarme a terminar esta tesis. Gracias a todos los amigos y compañeros que desde la infancia me han acompañado y dejado su impronta: Lucía, Nico, Marcos, Javier M., los Danieles, Kike, Igna... Gracias a las profesoras que me formaron desde pequeño, en especial a Asun. Mención especial requiere Irene, gracias por toda tu ayuda y apoyo, por haber sido mi compañera de vida durante tantos años, por ayudarme en los momentos más difíciles y disfrutar las alegrías.

Por último, quisiera agradecer a mi familia, pilar vital sin la cual esta tesis hubiera sido una quimera. A mis padres y mi hermana, a quienes les debo ser quien soy, y por siempre estar ahí cuando es más necesario, os quiero. Mi máximo respeto y más sincero agradecimiento a mis abuelos, a quienes está dedicada esta tesis: Ángel y María, Choneta y Jesús. Gracias por dármelo todo.

“We come spinning out of nothingness,
scattering dust like stars.”
Yalāl ad-Dīn Muhammad Rūmī.

“Poco basta cada día,
si cada día logramos ese poco.”
Santiago Ramón y Cajal

Abstract

Atmospheric aerosol particles are key for regulating Earth's atmosphere processes, and are estimated to present an overall cooling effect on the Earth's climate. Given the current climate change crisis and the need for precise mitigation measures on anthropogenic emissions, it is paramount to reduce the uncertainties related to the actual degree of this cooling effect and the impact that the reduction on the aerosol particles emissions will have on the Earth's radiative forcing and global temperature. The main sources of uncertainty of the contribution of aerosol particles to the radiative balance are associated to their highly variable and heterogeneous spatial and temporal distribution, to the large array of aerosol species with varying physico-chemical properties, and to the measurement errors. In particular, the most important aerosol species with regards to their absorption properties and effect on climate as warming agents are black carbon (BC), the organic aerosols (OA) absorbing fraction, referred to as brown carbon (BrC), and, potentially, mineral dust.

The Mediterranean basin is a region in Southern Europe heavily affected by anthropogenic emission sources, as well as from natural sources such as wildfires, Saharan dust mineral outbreaks and other biogenic processes. The multiple sources coupled with the meteorological conditions and the abrupt topography favour the accumulation and recirculation of air masses, especially during summer, which onsets the ageing of particles at several layers above ground, giving place to a complex mixture of aerosol particles.

In this context, this PhD thesis main focus is on the characterization of the optical properties of the BC, BrC and mineral dust particles, and its variations under different meteorological scenarios over an area on the Western Mediterranean Basin (NE of Spain). More specifically, this thesis addresses improvements in i) the determination of the absorption coefficients from a highly deployed instrument, the dual-spot multi-wavelength AE33 aethalometer, via a novel approach; ii) the characterization of the horizontal and vertical distribution of the aerosol particles physico-chemical properties at a regional recirculation event and a Saharan dust event; and iii) the analysis of the effects on the absorption enhancement of the BC particles by its mixing with BrC and other non-absorbing organic and inorganic aerosols. Finally, this thesis describes the optical properties of mineral dust at an emission source in a Saharan arid region and introduces the variations related to the types of events and the strength of the emission processes.

With this aim, this thesis combines datasets from monitoring stations at three different backgrounds and an intensive measurement campaign with instrumented flights in NE Spain,

in addition to an intensive campaign in a mineral dust emission area in the Saharan outskirts. The monitoring stations in the NE of Spain are operated by the EGAR group (IDAEA-CSIC) at an urban background in Barcelona (BCN), a regional background in Montseny natural park (MSY), and a remote mountain-top station in Montsec d'Ares mountain range (MSA).

A multi-instrumental analysis of the multiple scattering of the sampled particles deposited in the filter from which the aethalometer AE33 derives the absorption enabled an in-depth analysis of the parameter introduced by the aethaloemter, the *C parameter*. It was found that the multiple scattering has a very rapid increase for highly efficient scattering particles. Indeed, at the regional station of MSY and the mountain-top site of MSA, it was measured up to a 3-fold increase when the single-scattering albedo (SSA) was above 0.92-0.95, which implies that for highly scattering particles, the absorption provided by the AE33 can potentially be overestimated by a factor of 3. At MSA station, this sharp increase is associated to the influence of the Saharan dust particles, whereas at MSY it is linked to the presence of very efficient scattering OA particles. Conversely, at BCN urban background station, the C parameter did not show this sharp increase since the sampled particles SSA do not usually present values above the 0.92-0.95 threshold. Moreover, the C parameter showed an statistically significant increase with the wavelength at the mountain-top station, MSA, which was mainly linked to the presence of very high SSA values and mineral dust particles. As a consequence of this increase towards the longer wavelengths, the wavelength dependence of the absorption coefficient derived from the multi-wavelength AE33 showed a 13% increase when using a wavelength dependent parameter instead of a constant one.

Summer regional recirculation and Saharan dust events are highly frequent during the summer months, with a high impact on the atmospheric aerosol particles concentrations over NE Spain. Aerosol measurements from the monitoring stations and via instrumented flights during this events enabled the characterization of the horizontal and vertical spatial distribution of their physico-chemical properties over the main area of study. During the recirculation patterns the layer below 1.5 km a.s.l., i.e. the planetary boundary layer (PBL), presented very homogeneous values both in the vertical profiles and between the measurement stations, albeit with a slightly larger influence of the fine particles from the anthropogenic and biogenic sources at MSY compared to MSA. The vertical profiles showed a highly stratified atmosphere above the PBL, with multiple aerosol layers, mostly with aerosol particles similar to those closer to the surface, although some of these layers contain BrC particles from wildfires. During the Saharan dust event, due to its higher exposure to the long-transport of aerosol particles, the mountain-top station showed a higher impact of the mineral dust particles. The vertical profiles show an impact over the whole atmosphere with an increase in the relative contribution with height. Moreover there were several layers where the relative contribution from mineral dust particles was higher.

The highly absorbing BC particles are not usually sampled in a pure state in the atmosphere, rather they are typically mixed with other organic and inorganic aerosols which have the potential to alter their absorption properties. This mixing produces an enhancement of the absorption efficiency of the BC particles which, as a result of the high spatial and temporal

variability of the mixing material, has been found to be highly region dependent. Indeed, higher absorption enhancement values were found at the regional station (MSY) than at the urban station (BCN) as a consequence of the higher amount of OA, with an average absorption enhancement of 1.42 and 1.87 at a wavelength of 637 nm at BCN and MSY, respectively. The absorption enhancement showed an exponential increase with the amount of material available for mixing, with values up to 2 at BCN and 3 at MSY. The seasonal and trend evolution of the absorption enhancement presented a high dependency with the evolution of secondary OA at the MSY station, with higher values during summer, when the SOA to OA ratio increases, and an s.s. increase over the last decade, also due to the s.s. increase in the SO to OA ratio. At BCN station, no trend was found and the highest values were recorded during the winter period, where the accumulation of highly absorbing OA particles, i.e. BrC particles, both from primary and secondary organic aerosols from traffic, cooking, biomass burning and the oxidation of OA particles, produced the largest BC absorption enhancement.

Finally, the optical properties of Saharan mineral dust particles were characterized through an intensive measurement campaign at an emission area in SE Morocco, at the outskirts of the Sahara desert. The campaign was characterized by overall low particle number concentration, with frequent sharp increases in the particle number concentration and the extensive optical properties. These increments are due to the local saltation processes emitting dust particles into the atmosphere, as well as some sporadic larger number and mass concentration values as a combination of the advection of dust and local saltation during Haboob storms. The results showed similar overall behaviour to other similar campaigns, with average values of SSA around 0.97 and a MAC of around 0.04 $\mathrm{m^2 g^{-1}}$, at 525 nm, an absorption Ångström exponent (AAE) of 2.2, and an asymmetry parameter of 0.65. Moreover, the optical properties converged towards those measured at laboratory chambers using soil samples as the strength of the dust emission processes increased, with AAE reaching values up to 2.5, SSA significantly decreasing for the short-UV wavelengths as a consequence of the larger relative proportion of iron-oxides particles, and the asymmetry parameter increasing as a consequence of the larger fraction of coarse particles.

In conclusion, this thesis provides an advance in the characterization and study on the most relevant optical properties of the BC particles and its interaction with other organic, absorbing (BrC) and non-absorbing, and inorganic aerosols, and of the mineral dust particles. This thesis focuses on measurements performed over the NE of Spain, yet the results can be extrapolated and applied to other areas with similar aerosol backgrounds, both in the Mediterranean and other regions on Earth.

Resumen

Los aerosoles y partículas atmosféricas son elementos clave en la regulación los procesos climáticos de la Tierra, con una estimación neta sobre su efecto sobre el clima a nivel global de enfriamiento. Dada la actual situación de urgencia climática debido al calentamiento global y la necesidad de tomar medidas adecuadas de mitigación de las emisiones antropogénicas, es necesario reducir las incertidumbres sobre el nivel de enfriamiento de los aerosoles atmosféricos y sobre el impacto que tiene la reducción de sus emisiones en el forzamiento radiativo y, por tanto, en la temperatura global de la Tierra. Las principales fuentes de incertidumbre de la contribución de los aerosoles al balance radiativo están asociadas a la alta variabilidad y heterogeneidad de su distribución espacial y temporal, la gran cantidad de especies de aerosoles con diferentes propiedades físico-químicas, y los errores de medida. En particular, las especies de aerosoles más relevantes debido a sus propiedades de absorción de radiación y su efecto en el calentamiento del clima son el carbono negro (BC), la fracción absorbente de los aerosoles orgánicos (OA), conocida como carbono marrón (BrC), y, potencialmente, el polvo mineral.

La cuenca mediterránea es una región del sur de Europa con un alto impacto de fuentes antropogénicas y naturales de aerosoles, tales como incendios forestales, intrusiones de polvo mineral del Sahara, y procesos biogénicos. La combinación de las múltiples fuentes, las condiciones meteorológicas y la abrupta topografía favorece la acumulación y recirculación de las masas de aire, especialmente durante el verano, que promueven el envejecimiento y oxidación de las partículas a diferentes alturas sobre la superficie, dando lugar a una mezcla compleja de partículas atmosféricas.

En dicho contexto, el principal objetivo de esta tesis es la caracterización de las propiedades ópticas de las partículas de BC, BrC y polvo mineral, y sus variaciones bajo diferentes escenarios meteorológicos sobre una región en la cuenca occidental del Mediterráneo (noreste de España). En concreto, esta tesis presenta avances en: i) la determinación de los coeficientes de absorción utilizando el aethalometro AE33, el instrumento más extendido en las redes de monitoreo, mediante la implementación de una nueva metodología; ii) la caracterización de la distribución horizontal y vertical de las propiedades físico-químicas de los aerosoles durante eventos de recirculación e intrusiones de polvo mineral saharianas; y iii) la estimación del efecto en la absorción de las partículas de BC como consecuencia de su interacción con con partículas de BrC y otras aerosoles orgánicos no absorbentes e inorgánicos. Por último, esta tesis describe las propiedades ópticas del polvo mineral en una fuente de emisión del Sahara y sus variaciones según los tipos de eventos y según la intensidad de los procesos de emisión.

Para lograr estos objetivos, en esta tesis se combinan las medidas realizadas en continuo en estaciones de monitoreo atmosférico y durante una campaña intensiva de medidas en el noreste de España, y las realizadas en una campaña de medida en un área de emisión de polvo mineral en el Sahara. Las estaciones de monitoreo en el noreste de España, integradas en la red de investigación atmosférica del grupo EGAR (IDAEA-CSIC), registran medidas de aerosoles atmosféricos en diferentes entornos: fondo urbano en Barcelona (BCN), fondo regional en el parque natural del Montseny (MSY), y en lo alto de la sierra del Montsec d'Ares (MSA).

Se ha realizado un análisis exhaustivo del parámetro de dispersión múltiple, *el parámetro C*, utilizado por el aethalometro AE33 para derivar la absorción a partir de las medidas de atenuación. Dicho parámetro corrige la difracción múltiple de la radiación producida por las partículas depositadas en el filtro del AE33. Con el fin de mejorar la caracterización del parámetro C y su dependencia con la difracción de la luz, se ha llevado a cabo un un análisis multi-instrumental mediante medidas de referencia de la absorción y la dispersión de la luz. Se ha demostrado que el parámetro C presenta un notable incremento para partículas con una alta eficiencia de dispersión. De hecho, en las estaciones de fondo regional y de montaña, MSY y MSA, el incremento es de hasta 3 veces el valor promedio para albedos (SSA) por encima de 0.92-0.95, lo que implica que para partículas con un alto nivel de dispersión la absorción proporcionada por el instrumento puede ser hasta 3 veces mayor que la real. En la estación de MSA, este rápido incremento se asocia a la influencia de las intrusiones de polvo sahariana, mientras que en el MSY se debe a la presencia de OA con alto nivel de dispersión. Por contra, en la estación de fondo urbano, BCN, el parámetro de dispersión múltiple no presenta dicho aumento, lo cual se debe a la ausencia de medidas con valores de SSA por encima del umbral de 0.92-0.95. Por tanto, el análisis de la variación de la C con el SSA resulta de gran relevancia en estaciones de medida con altos valores de SSA, como son aquellas ubicadas en fondos regionales, de alta montaña o estaciones Árticas. Además, se ha obtenido una dependencia espectral para el parámetro C en la estación de montaña, MSA, donde se ha encontrado un aumento estadísticamente significativo con la longitud de onda debido principalmente a la presencia de altos valores de SSA y de partículas de polvo mineral. Como consecuencia de este aumento con la longitud de onda de la C, la dependencia espectral de la absorción mostró un incremento del 13% al usar un parámetro dependiente de la longitud de onda en vez de uno constante. Dicho incremento es de gran relevancia, ya que supone que dicho parámetro, ampliamente utilizado en la literatura para determinar el incremento hacia las longitudes más cortas de la absorción, estaría infraestimado para medidas de polvo mineral.

Los eventos de de recirculación regional e intrusión de polvo sahariano son altamente frecuentes durante el verano en el noreste de España, con una gran relevancia en los niveles de aerosoles atmosféricos. Se ha realizado la caracterización de la distribución horizontal y vertical de las propiedades físico-químicas de los aerosoles atmosféricos sobre el área de estudio durante estos eventos a partir de las medidas realizadas de manera continua en las estaciones de medida de la red EGAR y de los vuelos instrumentalizados. La variación

de la concentración de los diferentes tipos de partículas en las múltiples capas a lo largo de la atmósfera, la altura a la que se encuentran, y el grosor de las capas de aerosoles, tiene un gran impacto en el efecto de los aerosoles en el clima. Durante los periodos de recirculación la capa por debajo de 1.5 km s.n.m., i.e. la capa límite (PBL), presenta un alto grado de homogeneidad entre las estaciones de medida y los perfiles verticales, si bien con una mayor influencia de partículas altamente absorbentes en la moda fina, asociadas a fuentes antropogénicas y biogénicas, en MSY en comparación con MSA. Los perfiles verticales muestran una atmósfera altamente estratificada por encima de la PBL, con múltiples capas de aerosoles compuestas en su mayoría de partículas similares a las medidas cerca de la superficie, es decir de partículas finas con un gran impacto de BC y otros OAs, con la excepción de algunas capas con partículas de BrC procedentes de incendios forestales y OAs envejecidos. Durante las intrusiones de polvo sahariano la estación situada en lo alto de la montaña, MSA, registra una mayor incidencia del polvo mineral dada su mayor exposición a las advecciones de aerosoles en capas medias de la troposfera. Los perfiles verticales muestran la presencia del polvo mineral en toda la atmósfera, con una alta homogeneidad de los valores de las propiedades ópticas típicos para dichos eventos. Además, se midió un aumento en la contribución con la altura así como la presencia de capas con una mayor contribución relativa de polvo.

Las partículas de BC no suelen estar presentes en un estado puro en la atmósfera, sino que suelen estar agregadas con otros aerosoles orgánicos e inorgánicos que pueden modificar su elevada capacidad de absorción. Esta mezcla produce un incremento de la absorción, que presenta una alta dependencia regional como consecuencia de la alta variabilidad temporal y espacial de los materiales con los que se mezcla el BC. Así, la estación de fondo regional (MSY) presenta un mayor incremento de la absorción que la urbana (BCN), con valores promedios de 1.87 y 1.42 para una longitud de onda de 637 nm en MSY y BCN, respectivamente, debido a la mayor cantidad de OA disponible en MSY. El incremento de la absorción presenta un aumento exponencial con la concentración de aerosoles con los que mezclarse, llegando a valores de hasta 2 en BCN y 3 en MSY. La evolución estacional y la tendencia del incremento de la absorción muestra una gran dependencia con la evolución de los aerosoles orgánicos secundarios (SOA) en MSY, con valores más elevados durante el verano y un aumento estadísticamente significativo durante este periodo del año. En BCN, los valores más altos fueron registrados durante el invierno, cuando la acumulación de partículas de BrC procedentes de fuentes primarias y secundarias de las emisiones del tráfico, la quema de biomasa y la oxidación de OA produjo el mayor incremento de la absorción de las partículas de BC.

Finalmente, se han caracterizado las propiedades del polvo mineral sahariano mediante una campaña intensiva de medidas en una región de emisión en el sureste de Marruecos, en la periferia del desierto del Sahara. Durante la campaña se registraron valores de fondo de concentración del número de partículas muy bajos, con frecuentes y súbitos incrementos, reflejados también en las medidas ópticas extensivas. Dichos incrementos son consecuencia de los procesos de emisión de polvo locales, y en menor medida de advección de polvo

procedentes de Haboobs. Los resultados muestran valores similares a otras campañas de medidas en el norte de África, con valores promedio de SSA en torno a 0.97 y eficiencias de absorción por masa de a 0.04 $\mathrm{m^2 g^{-1}}$, para longitudes de onda de 525 nm, así como un AAE de 2.2 y un parámetro de asimetría de 0.65. Conforme los procesos de emisión se intensifican, las propiedades ópticas convergen hacia las medidas obtenidas en cámaras de laboratorio que usan muestras de suelos, alcanzando valores de AAE de 2.5, el SSA reduciéndose para las longitudes de onda cercanas al UV debido a la presencia de partículas con óxidos de hierro, y un parámetro de asimetría en aumento como consecuencia de la mayor fracción de partículas gruesas.

En conclusión, esta tesis presenta un avance en la caracterización y estudio de las propiedades ópticas más relevantes de las partículas de BC y su interacción con otras partículas orgánicas, absorbentes (BrC) o no, e inorgánicas, y de las partículas de polvo mineral. Esta tesis se centra en las medidas realizas sobre el noreste de España, si bien sus resultados pueden ser extrapolados y aplicados en otras regiones con fondos de partículas y aerosoles atmosféricos similares, tanto en el Mediterráneo como en otras regiones de la Tierra.

CONTENTS

II Methodology

III Results

IV Discussion and conclusion

LIST OF FIGURES

LIST OF TABLES

ACRONYMS

2-D	2-Dimensional.
3-D	3-Dimensional.
a.g.l.	Above ground level.
a.s.l.	Above sea level.
AAE	Absorption Ångström Exponent.
ACTRIS	Aerosols, Clouds and Trace gases Research InfraStucture.
AE33	Dual-spot Aethalometer.
AERONET	AErosol RObotic NETwork.
BC	Black Carbon.
BCN	Barcelona measurement site.
BF	Backscattering Fraction.
BrC	Brown Carbon.
CAMS	Copernicus Atmosphere Monitoring Service.
CCN	Cloud Condensation Nuclei.
CSIC	Consejo Superior de Investigaciones Científicas.
DNAAP	Detection of Non-Anthropogenic Air Pollution.
DRE	Direct Radiative Effect.
eBC	Equivalent Black Carbon.
EC	Elemental Carbon.
EGAR	Environmental Geochemistry and Atmospheric Research group (Grupo de Geoquímica Ambiental e Investigación Atmosférica).
ERF	Effective Radiative Forcing.
ESA	European Space Agency.

FRAGMENT	FRontiers in dust minerAloGical coMposition and its Effects upoN climaTe.
GAW	Global Atmospheric Watch.
GRASP	Generalized Retrieval of Aerosol and Surface Properties.
HYSPLIT	HYbrid Single-Particle Lagrangian Integrated Trajectory.
IDAEA	Institute of Environmental Assessment and Water Research (Insituto de diagnóstico ambiental y estudios del agua).
IN	Ice Nuclei.
IP	Iberian Peninsula.
IPCC	Intergovernmental Panel on Climate Change.
IR	Infrared electromagnetic radiation.
LIDAR	LIght Detection and Ranging or Laser Imaging Detection and Ranging.
MAAP	Multi-Angle Absorption Photometer.
MAC	Mass absorption cross-section.
MAE	Mass absorption efficiency.
MSA	Montsec d'Ares measurement site.
MSE	Mass scattering efficiency.
MSY	Montseny measurement site.
NASA	National Aeronautics and Space Administration.
NOAA	National Oceanic and Atmospheric Administration.
OA	Organic Aerosols.
OC	Organic Carbon.
ONA	Optimized Noise-reduction Algorithm.
OPC	Optical Particle Counter.
PBL	Planetary Boundary Layer.
PNSD	Particle Number Size Distribution.
POA	Primary Organic Aerosols.
Q-ACSM	Quadrupole Aerosol Chemical Speciation Monitor.
SAE	Scattering Ångström Exponent.
SIA	Secondary Inorganic Aerosols.

SOA Secondary Organic Aerosols.

SSA Single-Scattering Albedo.

SSAAE Single-Scattering Ångström Exponent.

UV Ultraviolet electromagnetic radiation.

VOCs Volatile Organic Compounds.

WCPC Water-based Condensation Particle Counter.

WHO World Health Organization.

WMB Western Mediterranean Basin.

WMO World Meteorological Organization.

Part I
Introduction

1

Introduction

The Earth's atmosphere is a complex dynamic fluid that is retained by Earth's gravity over its surface and that interacts with the rest of the Earth's system, playing a key role in regulating life as well as the processes that modulate the Earth evolution. The atmosphere is composed of a mixture of molecules and aerosol particles either in a gaseous, liquid or solid state, that together with Earth's surface are the main systems responsible for energy transfer from solar and terrestrial electromagnetic radiation into the atmospheric system. Therefore, to correctly characterize an evolving climate, it is crucial to provide an accurate estimation of the contribution to the Earth's radiative balance from the different components of the atmosphere., i.e. the amount of energy transferred into the atmosphere from the interaction of radiation with these components.

The gaseous composition of the atmosphere is well known and highly stable, with a 78% of nitrogen, a 21% of oxygen, and a 1% of Argon, with the remaining fraction composed of a miscellaneous of water vapour and other trace gases. Some of these trace gases (cf. Fig. 1.1) can efficiently absorb solar (e.g. ozone) and terrestrial radiation (e.g. water vapour and carbon dioxide), and as such are key for the analysis of Earth's radiative balance (Seinfeld et al., 1998). Given their absorbing efficiency and their long lifetime in the atmosphere, gaseous compounds as carbon dioxide, methane, nitrous oxide, and stratospheric ozone are the most relevant with regards to the Earth climate warming (Szopa et al., 2021). Indeed, the residence time of greenhouse gases in the atmosphere is of utter importance for climate. In fact, water vapor is the most abundant greenhouse gas responsible for about half of Earth's greenhouse effect due to its high absorption efficiency of infrared, i.e. thermal, radiation (Schmidt et al., 2010). However, its contribution remains fairly stable over time since it is self-regulated through rainfall. Conversely, carbon dioxide, which is highly dependent on anthropogenic emission, has a much longer residence time in the atmosphere, with estimates of an adjustment time over 100 years (Lord et al., 2015; Köhler et al., 2018). The overall influence on climate of these gases is well parametrized in the climate models due to the accurate characterization of their absorption capacity, concentration and lifetime in the atmosphere, and impact on the radiative balance (cf. Fig. 1.1).

Atmospheric aerosol particles, distributed over the entire Earth's troposphere, although with a highly heterogeneous temporal and spatial distribution, present multiple mechanisms

through which they can affect the radiative effect, which impairs an accurate determination of the influence of these aerosol particles on the radiative balance. Overall, aerosols particles are considered to act as coolers in the climate system (cf. Fig. 1.1), with the most recent estimate of the net contribution to the radiative balance of -1.23 [-2.0 to -0.6] Wm^{-2}, with a contribution from the aerosol-radiation interaction of -0.3 Wm^{-2} and from aerosol-cloud interaction of -1.0 Wm^{-2} (Forster et al., 2021). As a consequence, anthropogenic aerosols present to some degree an offset of the warming caused from anthropogenic greenhouse gases. The most important aerosol particles with regards to the cooling effects are sea salt particles, sulphates and nitrates. The most relevant aerosol particles species, given their absorbing properties and potential impact on a warming climate, are carbonaceous aerosols, especially Black Carbon (BC), and a large array of organic compounds with high absorption efficiencies at the ultraviolet-visible range, also known as brown carbon, BrC (Myhre et al., 2013; Szopa et al., 2021). However, given the complexity for accurately assessing the sign and magnitude of the contribution of each aerosol species, the aerosols could potentially have a lesser cooling effect than what is currently assumed. This proves crucial, since Lund et al. (2018) recently found a weaker immediate cooling effect of aerosol particles on radiative forcing, with an estimate around -0.17 Wm^{-2}, as a consequence of an improved parametrization of BC absorption, an increase in the absorption produced by the BrC, and a decrease in the concentration of sulphates, and consequently on their cooling effect. Moreover, the effect of mineral dust particles— that represent the second most abundant aerosol specie by mass in the atmosphere at a global scale— on the radiative balance still presents large uncertainties. Indeed, although up to this point it has been considered to act as a cooler, recent studies have shown that mineral dust particles could potentially act as a warming agent on the atmosphere. This thesis focuses on the study of the optical properties of atmospheric aerosol particles with special attention on the potentially warming aerosol species, i.e. BC, BrC and mineral dust.

Atmospheric aerosol particles are defined as **suspended fine liquid or solid particles in the atmosphere**, although it is usually restricted to the particulate matter, hence aerosol and aerosol particles are indistinctly used (Seinfeld et al., 1998). A single aerosol particle is an aerosol unit with a dimension above 1 nanometer (nm) made of multiple molecules bonded by intermolecular forces, or as two or more of such units held together by adhesive forces so that its behaviour is analogue to a unit. The aerosol particles sizes range from 1 nm to tens of micrometers (μm) in diameter, and the aerosol particles usual concentration in number ranges between 10^2 and 10^6 cm^{-3} depending on the background characteristics of the measurement site.
The complexity of the characterization of the atmospheric aerosol particles and its interaction with radiation is mainly associated to the large range of particle sizes, shape, chemical and physical properties from numerous aerosol sources and emission processes. These particles remain suspended the atmosphere with varying lifetimes, where they undergo a large array of physico-chemical processes before being deposited on the surface.

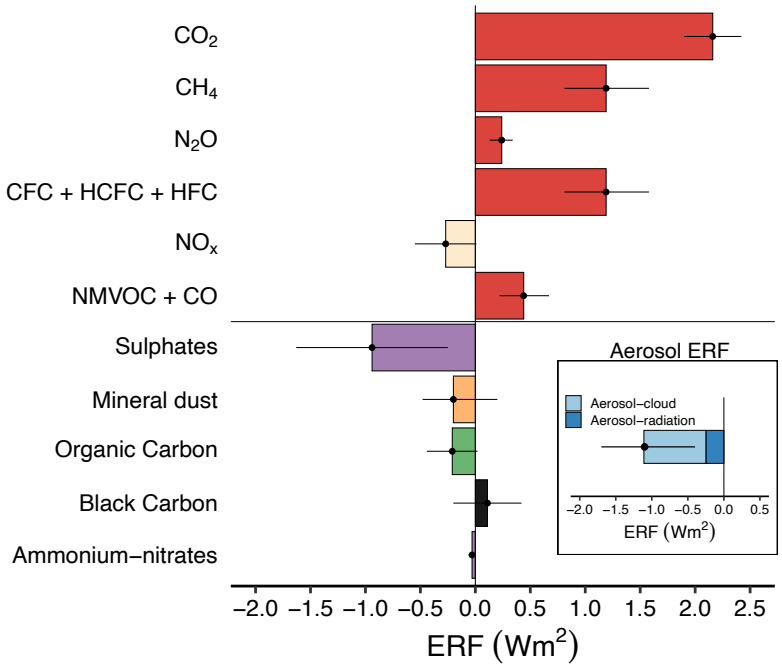

Figure 1.1: Contribution to the effective radiative forcing (ERF) by the main anthropogenic greenhouse gases and aerosol particles. Estimations from emissions from pre-industrial levels (ca. 1750) to 2019 are based on CMIP6 model (Coupled Model Intercomparison Project Phase 6). *Adapted from Szopa et al. (2021) and Forster et al. (2021), and from Kok et al. (2017) for mineral dust particles*

1.1 Aerosol particle size distribution

Atmospheric aerosol particles present a large range of sizes, from a few nanometers (nm) up to 30-40 micrometers (μm). These particles can be classified upon their size diameter (d): nanometric for particles with $d < 25$ nm, ultrafine if $d < 100$ nm, fine ($d < 1-2$ μm), and coarse for particles with d above $> 1-2$ μm (Fig. 1.2). The mechanisms that regulate the formation, transformation and removal of atmospheric particles change with the particle size, therefore creating different peaks in the particle size distribution, which are referred to as particle size distribution modes. The need for the analysis of each mode and the variations on the chemical composition, and the particle number and mass concentration is based on the need for correctly assessing their impact on the optical properties and consequently on climate.

The particle size mode ranges vary between studies, but are generally defined as: a nucleation mode for particles with a diameter below 25 nm, an Aitken mode for particles diameters ranging between 25 to 100 nm, an accumulation mode for particles with diameters between 100 nm and 1 μm, and a coarse mode for particles ranging between 1 μm and 30-40 μm in diameter (cf. Fig. 1.2).

The nucleation mode contains particles with diameters below 25 nm. The formation pathways for the particles within this mode is a major topic of research within the scientific

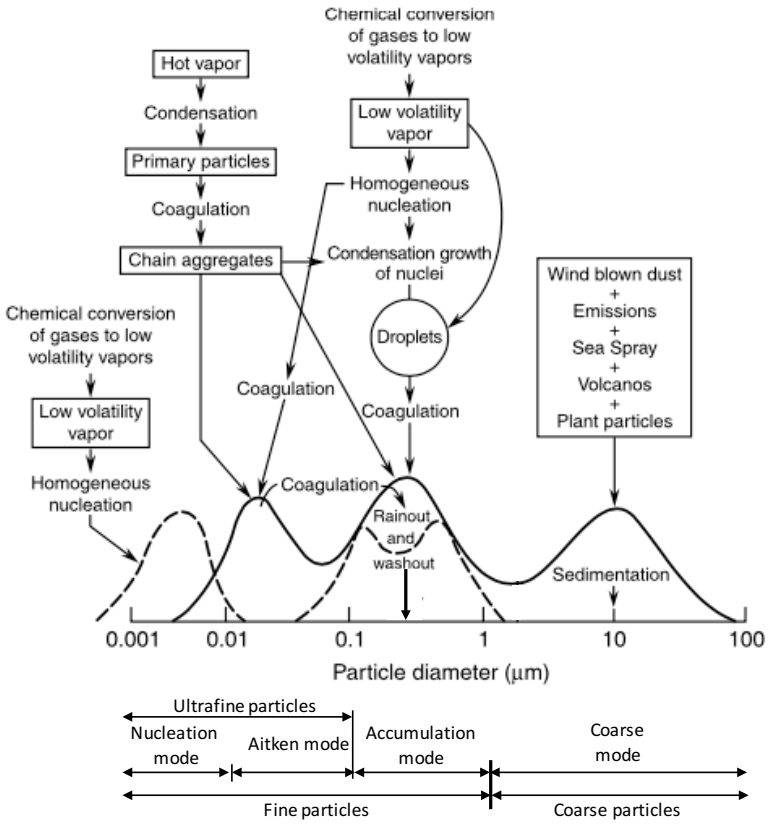

Figure 1.2: Schematic of the atmospheric aerosol particle size distribution modes, sources, formation and transformation pathways. The solid lines represent the Aitken, accumulation and coarse mode, and the dashed line represent the ultrafine particles nucleation mode and the two peaks within the accumulation that are sometimes observed due to the deposition processes. *Adapted from Finlayson-Pitts and Pitts Jr (1999), originally adapted from Whitby and Cantrell (1976)*

community, with major recent advances (e.g. Lee et al., 2019). A simplified model divides the particle formation pathways into 3 regimes: i) gas-phase reactions where the net cluster growth is limited due to the continuous chemical reactions, and vapour uptake and evaporation that creates/destroys small clusters and molecules; ii) a key process where the clusters are stabilized by ammonia and other amines, and the size growth is promoted by sulfuric acid condensation; and iii) enhanced growth rate that takes place by the activation of oxidized organic vapors that enhance the vapor uptake (Seinfeld et al., 1998; Finlayson-Pitts and Pitts Jr, 1999; Kulmala et al., 2004; Kulmala et al., 2013).

The atmospheric aerosol particles in the Aitken mode ($25 < \mathrm{d} < 100$ nm) are produced by gas-to-particle conversion, by condensation of low-vapor-pressure products of gas-phase reactions, and by coagulation of smaller particles in the nucleation mode (Finlayson-Pitts and Pitts Jr, 1999).

The accumulation mode ($100\ \mathrm{nm} < \mathrm{d} < 1\mu\mathrm{m}$) is formed by aerosol particles that predominantly result from semi and low-volatility compounds condensation on the surface of smaller

particles, and from coagulation of particles in the nucleation and Aitken mode, either by coagulation with other smaller nuclei range particles or with accumulation mode particles, as well as from self-coagulation of particles in the accumulation mode that promote further growth (Seinfeld et al., 1998; Finlayson-Pitts and Pitts Jr, 1999).

The coarse mode ($\mathrm{d} > 1\mu\mathrm{m}$) aerosol particles are mainly emitted into the atmosphere by mechanical processes such as wind erosion and emission of mineral dust, sea spray, volcano eruptions and biogenic emissions, among others (Seinfeld et al., 1998; Finlayson-Pitts and Pitts Jr, 1999).

The nucleation and Aitken modes are the major contributors to particle number concentration, with over 70-90 $\%$ (Charron and Harrison, 2003), yet do not represent more than a few percent of the contribution to the mass concentration given the small size of particles in these modes (Fig. 1.2). Conversely, the accumulation mode, albeit only making up just $\sim 5\%$ of the particle number concentration, represents around 50% of the total aerosol mass concentration (Finlayson-Pitts and Pitts Jr, 1999). Similarly, the coarse mode particles, which represent a small fraction of the total number concentration, contribute largely to the surface, and the mass and volume concentration, as the surface is proportional to the square particle radius and the mass and volume to the cube of the particle radius. The ultrafine particles have a lifetime of hours in the atmosphere, whereas the fine mode particles within the accumulation mode remain in the atmosphere for long periods of time, with the ability of reaching remote and isolated locations, with the main mechanism of deposition for the finer particles being Brownian diffusion and in-cloud and below cloud scavenging. As the particles increase in size and become coarse, which are also effectively deposited by below cloud scavenging and gravitational forces, they tend to have a larger sedimentation velocity and a shorter lifespan in the atmosphere (Seinfeld et al., 1998).

1.2 Aerosol particle sources and composition

The influence that the aerosol particles exert on the atmospheric radiative balance, i.e. their optical properties, largely depends on their emission origin, the formation processes that they undergo in the atmosphere, and their chemical and mineralogical composition. Atmospheric aerosols can be classified upon their formation processes, as primary aerosols and secondary aerosols, and also based on their origin, either originated by natural or anthropogenic sources.

Primary aerosols particles are directly emitted as particles into the atmosphere from the source, whereas secondary aerosols refers to the particulate matter that is formed in the atmosphere as a consequence of gas-to-particle conversion processes or by coagulation and condensation processes between gases and atmospheric particles. The major sources of primary aerosols are those produced by combustion processes in the nucleation and Aitken modes and those emitted through mechanical processes in the coarse mode, such as mineral dust and sea salt. Secondary aerosols particles are mainly formed from gaseous precursors (e.g. sulphur dioxide, nitrogen oxides, ammonia, amines, VOCs, etc.) reacting with already

formed particles or particle clusters. The formation of secondary aerosol particles mainly takes place in the fine mode through: i) uptake of precursor gases that result from the combustion emissions and their photo-chemically transformations, also known as particle ageing, as well as from condensation or adsorption processes in the nucleation mode, ii) coagulation and agglomeration of particles in the Aitken and accumulation modes as a consequence of the Brownian motion of the aerosol particles, and iii) through volatilization of freshly emitted nucleated particles, that increase the coagulation rate after being volatilize, and therefore increase the particle growth (Meszaros, 1999; Jacobson et al., 2005).

Natural aerosol emission sources represent the largest contribution to the global load of aerosol particles in the atmosphere (Gieré and Querol, 2010). The biggest natural sources of aerosols are of primary origin, mainly sea salt and spray, mineral dust emission from deserts and drylands, volcanic emissions, wild forest fires and biological emissions, although some secondary aerosols also contribute to the global load, mostly triggered by natural gaseous precursors emitted from volcanoes, storms, and the oxidation of biogenic emissions, etc. (Fig. 1.3). Anthropogenic aerosol emission sources do not represent such a large contribution to the mass concentration of aerosol particles at a global scale (Fig. 1.3), yet, close to the more populated areas with a higher density of emissions from human-driven sources, they can account for the majority of the measured aerosols near the surface (Reche et al., 2011; Pandolfi et al., 2020). The main sources of anthropogenic aerosols are related to industrial emissions, combustion and non-exhaust processes associated to transportation (road, maritime and air-flights), domestic use, biomass burning, construction and demolition emissions, farming and agriculture, among others. Unlike for natural emissions, secondary aerosols account for an important fraction of the total anthropogenic emissions, mostly from the oxidation of the inorganics (mostly SO_2 and NO_x) and organic gaseous precursors (VOCs), mainly by combustion processes.

The most relevant aerosol particles compounds in the atmosphere according both to their large contribution to the total aerosol mass load, and to the impact on the radiative balance of the atmosphere by scattering or absorbing radiation are: mineral dust particles emitted from arid and semi-arid regions, marine aerosols, particles linked to combustion processes that result in the emission of black carbon (BC) particles, and/or in highly absorbing organic aerosols, also referred to as brown carbon (BrC), as well as secondary inorganic aerosols formed from precursor gaseous species.

1.2.1 Mineral dust particles

Mineral dust particles are one of the largest contributors of atmospheric aerosols by mass on Earth, with an estimated emission of $5.1 \cdot 10^3$ Tg yr^{-1} (Gieré and Querol, 2010; Kok et al., 2021a), accounting for a 32 $\%$ of the global aerosol emission load (Fig. 1.3). Of these, most of the emissions come from natural sources, mainly from arid and semi-arid regions around the globe (Kok et al., 2021a; Kok et al., 2021b), although a not negligible fraction is of anthropogenic origin (2%), mainly from agricultural processes, the increase in the aridity of the soils due to land use changes, construction and demolition processes, and tyre and

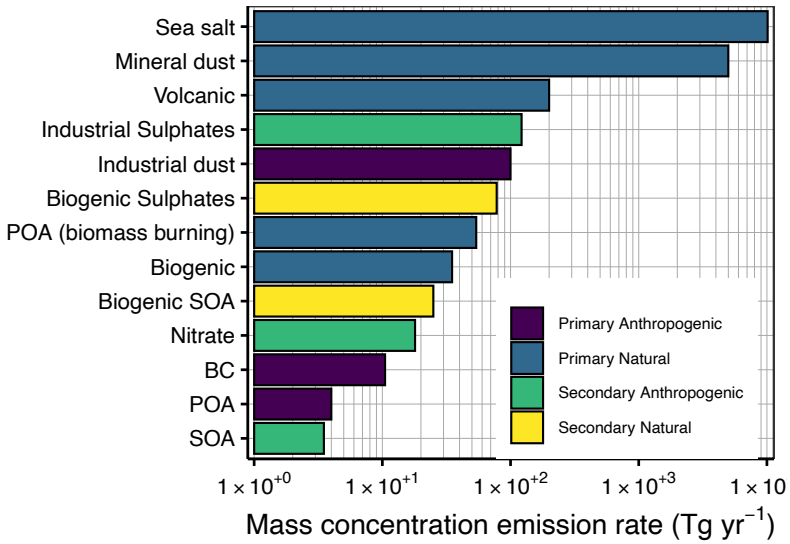

Figure 1.3: Relative contribution to the total mass concentration emission rate (in Tg per year) from the main aerosol species differentiating upon formation and origin processes. The x-axis is in a logarithmic scale for visual purposes. *Adapted from Gieré and Querol (2010), with mineral dust mass concentration emission rates from Kok et al. (2021a)*

non-exhaust emissions from road traffic at urban level (e.g. breaks and tyre wear; Amato et al., 2009).

Mineral dust particles are emitted from arid and semi-arid regions under conditions of high wind-speeds and wind friction velocities. The wind friction velocity is a parameter that describes the strength of the turbulence of the wind near the surface. Higher wind friction velocities imply stronger turbulent processes which favour the emission of mineral dust particles from the surface into the atmosphere (Shao, 2008). The main mechanisms for the emission of mineral dust particles are: i) direct aerodynamic entrainment if the dust particles are loose enough over the surface so that a strong enough wind force can directly lift them from the surface, ii) saltation bombardment from coarser sand particles and/or aggregates of dust particles that are displaced by the strong wind forces and strike the surface, thus emitting finer dust particles, and iii) disaggregation of mineral particles from either soil aggregates and/or dust coated sand particles when this grains impact the soil as a consequence of the strong wind forces scattering them along the surface.

The mineralogical composition of the dust particles ultimately depends on the mineralogical composition of the parent soil of the emission area and on the physico-chemical processes that the mineral particles undergo after being emitted. However, the overall mineralogical composition for all soil samples presents oxides and hydroxides, feldspars, clay minerals and other silicates, Ca-rich particles, sulphates, and an array of mixtures and others minerals (Glaccum and Prospero, 1980; Kandler et al., 2009). With regards to their positive direct radiative effect, i.e. warming effect, on climate, the most important minerals are those with a higher degree of iron content (e.g. Claquin et al., 1999; Lafon et al., 2006; Li et al., 2021). In addition to the impact on the direct radiative effect, mineral dust also influences the

atmosphere indirectly and semi-indirectly by i) influencing the pathways for cloud formation, ii) acting as source for ice nuclei (indirectly), and iii) evaporating cloud droplets by absorbing light radiation adjacent to the dust particles (semi-directly).

The Saharan and Sahel emission areas in North Africa are the major sources of atmospheric mineral dust particles, with an estimated 50 $\%$ of the global dust emission load and an average yearly emission of around $2.1 \cdot 10^3$ Tg yr^{-1}, and a dust loading of 13 Tg (Kok et al., 2021b). The importance of Saharan dust particles, in addition to the effects that these produce over the areas of emission, is that they can be transported over large distances, from North Africa to the Mediterranean and the European continent, and over the Atlantic to the Caribbean and south America (Engelstaedter et al., 2006). Other important emission areas are the arid and semi-arid regions over the Middle East and the Arabian peninsula, Australia, and the Gobi desert in Asia, with studies showing the possibility of mineral dust transport over the Pacific Ocean into North America for the latter source area (Biscaye et al., 1997; Sassen et al., 2003). This ability for long-range transport over large portions of the atmosphere and the variations in the particle size distribution and mineralogical composition depending on the source emission areas, states the importance of mineral dust particles in the radiative balance at a global scale.

1.2.2 Sea salt aerosols

Sea salt and spray aerosols are a form of primary emissions emitted over the ocean surfaces and by the coastal areas as a result of two processes: i) by the breaking of the waves and the following emission of aerosols into the atmosphere, and ii) the most important process, which is the bursting of micro-bubbles at the air-water interface (Vitols and Stipendiat, 1976; Seinfeld et al., 1998).

Sea salt aerosols represent the second largest contribution to the total global mass concentration of aerosol particulate matter in the atmosphere, with an estimated 64$\%$ of the total emissions (Fig. 1.3). The particle size distribution of sea salt aerosol particles is biased towards the coarse mode, with a mineralogical composition similar to the composition of sea water. The main species that form sea salt aerosol is NaCl, $MgCl_2$, magnesium and sodium sulphates.

1.2.3 Carbonaceous aerosols

Carbonaceous aerosol, i.e. aerosol particles that have some amount of carbon content, excluding carbonates, represent between 2 and 5$\%$ of the total emission load of aerosols into the atmosphere (Fig. 1.3), and can account for up to a 20-40$\%$ of the total particle load concentration at a regional scale close to the emission areas (Putaud et al., 2004). These aerosols, albeit with a small contribution to the global mass concentration load, are considered to be the main source of light absorption by aerosol particles in the atmosphere (Szopa et al., 2021).

The light absorbing subgroup of the carbonaceous aerosols, known as light absorbing carbonaceous (LAC) aerosol particles, are subject to many different nomenclature in the bibliography. These differences are mainly associated to the methodology used for obtaining the measurements, with different classification depending on whether thermochemical or optical methods are used (Andreae and Gelencsér, 2006; Moosmüller et al., 2009). The most common subgroups of LAC according to their measuring method are: elemental carbon (EC) and organic carbon (OC) from its thermal refractory standpoint, and black carbon (BC) and brown carbon (BrC) from its optical absorption capacity.

Black carbon (BC) and elemental carbon (EC) denominations refer to the particles formed by incomplete combustion of gaseous hydrocarbons in high-temperature combustion processes ("soot") made-up by a large fraction of graphene layers, formed by graphite structures of carbon atoms arranged in a 2-D lattice. The thermo-chemical term EC showcases how refractive the carbon particles are, and is used for carbon that is oxidized by volatilizing the aerosol sample above a certain temperature threshold, based on the stability of carbon at high temperatures (Andreae and Gelencsér, 2006). Instead, the optical term BC is defined by the black colour appearance of the aerosol particles when collected with filter-based instruments, and is the most widely used therm for the measurements of highly absorbing carbonaceous aerosols. Given that the optical properties are the focus of this thesis, the latter term, BC, is the term chosen here, along with equivalent BC (eBC), which stands for the BC inferred via filter-based optical instruments. Given that these instruments do not directly measure BC concentration, but the attenuation of light, theoretical mass absorption cross-sections (MAC) are used to derive the BC concentration from these filter-based instruments (e.g. Petzold and Schönlinner, 2004).

The formation processes of BC particles from the incomplete combustion of fossil fuel and, although not as efficiently, from the most efficient combustion stages from biomass burning processes, follow a multi-step mechanism: i) generation of precursor species and particle inception, and ii) particle surface growth and agglomeration. First, the combustion of the fuel undergoes a pyrolysis process, from which poly-cyclic aromatic hydrocarbons (PAHs) are formed and increase in size to the point where they can act as particle nuclei. Then, a gaseous-to-solid state phase transition takes place forming solid particle nuclei, that grows their surface by absorbing adjacent gas molecules, adding disordered and non-smooth graphite layers over the amorphous carbonaceous core to form larger spherules. Finally, particles undergo Brownian motion which results in collisions that bond particles together, creating BC agglomerates. The BC particles growth and agglomeration processes end as the particles cool down as they exit the combustion flame, resulting in a fractal-like morphology with typical particle diameter sizes in the Aitken mode, between 20 and 40 nm (Bond and Bergstrom, 2006; Andreae and Gelencsér, 2006). In addition, upon cooling, organic compounds such as PAHs can get adsorbed or condensed over the BC spherules, creating a mixing of BC and OC particles that influence the absorption properties of BC.

Organic aerosols (OA) are the mixture of carbon-containing aerosols that can have bonds with hydrogen and oxygen, whereas organic carbon refers (OC) refers to the carbon mass

of OA without the hydrogen and oxygen compounds. OC includes both refractory and non-refractory aerosol particles formed by anthropogenic or natural combustion processes and by biogenic sources. The OC aerosol particles are a combination of PAH, humic-like substances (HULIS), water-soluble organic carbon (WSOC), and biopolymers, among others, and are emitted either as primary organic aerosols (POA) or as secondary organic aerosols (SOA) as a consequence of the condensation of volatile organic compounds (VOCs) (Seinfeld et al., 1998; Andreae and Gelencsér, 2006; Moosmüller et al., 2009). Brown carbon (BrC) aerosol particles represent the absorbing fraction of OC and have recently attracted the interest of the scientific community due to their potential of absorbing radiation in the ultraviolet-visible range. The most used term in this thesis when referring to the absorbing OA particles is the optical term BrC, with the exception of the analysis performed with thermal refractory based instrumentation. In the latter case, OC is used.

BrC aerosol particles can be formed either from primary emissions from combustion processes from both fossil fuel and biofuel, or in the atmosphere through multi-phase reactions involving organic and inorganic gaseous precursors, gas-to-phase particles reactions that can form brown SOA, and cloud micro-droplet compounds (Andreae and Gelencsér, 2006; Laskin et al., 2015). With regards to primary BrC, during the pyrolysis processes, the emitted aromatics products can elude further processes within the flame and cool down and condensate in the plume. Additionally, BrC can also be formed when the combustion process is associated to smouldering, i.e. a low-temperature flameless oxidation of the solid fuel. Poly-cyclic aromatic hydrocarbons (PAHs) produced in the initial steps of the combustion processes are emitted and undergo thermal processing to the point where the particles acquire some level of graphitization (Patterson and McMahon, 1984). With regards to the generation of secondary BrC particles, it has been mainly associated to natural HULIS and WSOC associated to biogenic sources, such as isoprene emissions, polymeric substance formation from plant and soil degradation, and reaction of POA with different acid particles resulting into brown SOA (Andreae and Gelencsér, 2006), although more recent studies suggest pathways for secondary BrC formation from anthropogenic and biogenic volatile organic compounds (VOCs) reactions with nitrogen oxides and ammonia (Updyke et al., 2012; Lu et al., 2015; Laskin et al., 2015).

The contribution to the total LAC's emissions load to the atmosphere is of around 8 Tg yr^{-1} for BC particles, with 3.3-5.0 Tg yr^{-1} from biomass burning and around 3.0-4.6 Tg yr^{-1} from fossil fuel combustion (Bond et al., 2004; Moosmüller et al., 2009). OC is estimated to make up between 20 and 90% of the fine mode (sub-micron) particulate mater mass concentration (Jimenez et al., 2009), with POA yearly emission rate $\sim$ 46.9 Tg yr^{-1}, and secondary organic aerosols (SOA) estimates of $\sim$ 388 Tg yr^{-1} (Bond et al., 2004). The SOA concentration present considerable variations due to the vastness of pathways for its formation and the difficulty to constrain which processes prevail and to which extent they contribute to the formation of SOA particles.

1.2.4 Secondary inorganic aerosols (SIA)

Secondary inorganic aerosols (SIA) represent around a 5% of the global emissions, yet can account up to 30-40% of the particulate matter concentration below the 10 μm fraction at a regional scale (e.g. Putaud et al., 2004; Querol et al., 2004; Szopa et al., 2021). Secondary inorganic aerosols, i.e. sulphate (SO_4^{2-}), nitrate (NO_3^-) and ammonium (NH_4^+), are formed in the atmosphere as precursor gaseous species following a gas-to-particle pathway.

The precursor gas for the formation of sulphates is sulphur dioxide (SO_2) emitted from anthropogenic sources, mainly from industrial and energy generation process, and traffic and domestic emissions. Sulphur dioxide gas is oxidized in the atmosphere, forming sulphuric acid aerosol particles, which after reacting with ammonia, sodium chloride and calcium carbonate results in ammonium sulphate particles $[(NH_4)_2SO_4]$, sodium sulphates (Na_2SO_4), and calcium sulphates ($CaSO_4$), respectively. Moreover, volcanic eruptions can directly emit sulphate particles into the atmosphere (e.g. Pinatubo volcanic eruption). Nitrate and ammonium precursor gases are nitrogen oxides (NO_x) and ammonia (NH_3), respectively. NO_x is emitted primarily by combustion processes (traffic in urban areas, industrial activity, etc.) and acts as precursors of acid nitrate, which trough several oxidation pathways and reactions can be transformed into ammonium, sodium and calcium nitrate (Meszaros, 1999; Putaud et al., 2004).

The sizes of the neutralizing agent of sulphuric and nitrate acid for the sulphates and nitrates, respectively, determine the size of the resulting secondary inorganic aerosols. Therefore, ammonium sulphates and nitrates are within the fine mode, whereas calcium and sodium sulphates and nitrates fall within the coarse mode. The largest fraction of nitrates are fine, yet under warm temperatures, ammonium nitrate becomes unstable and can react with other compounds which can be coarse (such as sea salt) and result in the formation of coarse ammonium nitrate particles.

1.3 Aerosol particle-radiation interaction

A beam of radiation travelling through the atmosphere is attenuated by its interaction with atmospheric aerosol particles and molecules. This attenuation in the intensity radiation produced by the interaction with the gaseous molecules and aerosol particles in the atmosphere is known as extinction. There are two physical processes that combined are responsible for the extinction of electromagnetic radiation, namely scattering and absorption .

The attenuation of the intensity of the radiation when traversing an atmospheric layer is described by the Bouguer-Lambert-Beer law, where it is assumed that the medium is homogeneous and multiple scattering processes are neglected. The Bouguer-Lambert-Beer law can be expressed by

$$I_\lambda(s_f) = I_\lambda(s_0) \cdot e^{-k_\lambda \tau}, \tag{1.1}$$

where for a given wavelength (λ), $I_\lambda(s_f)$ and $I_\lambda(s_0)$ are the radiation intensities at the final and initial points of the traversed atmospheric layer, τ is the optical path length, and k_λ is the mass extinction cross-section of the medium. The mass extinction cross-section denotes the energy removed from the incident radiation wave by the particle normalized to its mass, and its units are typically given in $[\mathrm{m}^2\ \mathrm{g}^{-1}]$. The mass extinction cross-section depends on the physico-chemical and micro-physical properties of the aerosol particles, such as its particle size distribution, shape, chemical composition, and ageing state, among others. Similarly, the mass absorption cross-section and the mass scattering cross-section represent the energy absorbed and scattered, respectively, by the particle normalized by its mass. If the extinction cross-section is multiplied by the volumetric mass concentration, it then becomes the extinction coefficient (b_{ext}), with units of length $[\mathrm{m}^{-1}]$. As a result, the extinction coefficient is the sum of the absorption (b_{abs}) and scattering (b_{scat}) coefficients,

$$b_{ext} = b_{abs} + b_{scat}. \tag{1.2}$$

The extinction coefficient, and therefore also the absorption and scattering coefficient (cf. eq. 1.2), are magnitudes that are often referred to as *extensive optical properties*. The term extensive indicates the dependence of these optical properties with the amount of aerosol particles, since the larger amount of aerosol particles per volume unit, the larger the values of these parameters. Hereafter, it is introduced a brief description of the main scattering and absorption processes in the atmosphere by gaseous molecules and aerosol particles, and its dependencies with other variables, such as the wavelength and the particle size, among others.

1.3.1 Atmospheric light scattering

Light scattering is the process by which the particle (either aerosol or molecule) extracts energy from the incident radiation beam through scattering process. There are three mechanism by which particles scatter the radiation: i) quasi-elastic, where the radiation scattered by the molecules has a shift in the wavelength due to Doppler effects and diffusion broadening, ii) inelastic scattering by molecules, where received and emitted radiation wavelengths differ as a consequence the of Raman scattering and fluorescence processes, and iii) the elastic scattering, which is the interaction of interest for analyzing the scattering of solar radiation with the atmospheric particles and gaseous molecules, where the wavelength of the scattered radiation remains unchanged upon the particle-radiation interaction. The size range of the particles that scatter radiation in the atmosphere goes from $\sim 10^{-4}\ \mu\mathrm{m}$ for gas molecules, $\sim 1 - 10\ \mu\mathrm{m}$ for aerosol particles, $\sim 10 - 100\ \mu\mathrm{m}$ for water droplets and ice crystals and even up to $\sim 10^4\ \mu\mathrm{m}$ for large water droplets and hail. A largely used parameter to study the effect of the particle size on the scattering of radiation is the so-called size parameter, x, which for spherical particles is defined as the ratio of the particle circumference to the incident radiation wavelength, $x = 2\pi r/\lambda$. Usually, atmospheric aerosol particles are far enough from each other so that the scattering by each particle is assumed to be independent. However if the scattering volume contains many particles, a phenomena called multiple scattering can take

place, where the scattered light from a particle can be subsequently scattered by another one, which can substantially complicate the study of atmospheric scattering by aerosol particles, such is the case within clouds and fog.

The scattering produced by small particles is described by Rayleigh scattering (see Fig. 1.4a), and was first introduced by Lord Rayleigh for describing the color and polarization of skylight as a consequence of the scattering of light by the atmospheric molecules ("On the light from the sky, its polarization and colour" 1871). For the Rayleigh scattering to occur the particle has to be much smaller than both the incident radiation wavelength and the wavelength of the radiation after it enters the particle, i.e.:

$$x \ll 1, \tag{1.3}$$

and

$$x \ll 1/|m|, \tag{1.4}$$

where x is the size parameter, and $m = n - i \cdot k$, is the refractive index, which is the parameter that describes the variation undergone by the light-radiation upon its interaction with the particles. The real part, n describes the particles scattering properties, and the imaginary part, k, describes their absorption properties. As a consequence of these conditions, Rayleigh scattering is mainly dominated by gaseous molecules in the atmosphere. For unpolarized solar radiation, the Rayleigh scattering equation can be expressed as

$$I \propto \lambda^{-4}. \tag{1.5}$$

A visual example of Rayleigh scattering is the scattering of solar radiation in the visible spectra, around $0.4 - 0.7\ \mu\mathrm{m}$, which given the relationship with the wavelength of the intensity (eq. 1.5), produces scattered intensity for the blue colour about 5 times more intense than red, and causes the sky to be viewed as blue.

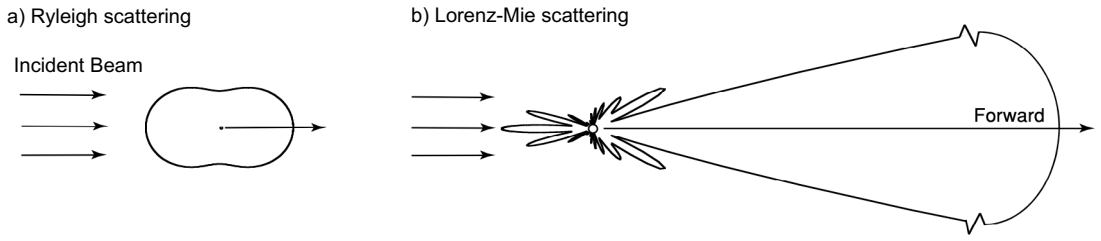

Figure 1.4: Schematic of the scattered intensity angular patterns from two spherical particles illuminated with a radiation beam that undergo: a) Rayleigh scattering, and b) Lorenz-Mie scattering. *Adapted from Liou (2002)*

Lorenz-Mie scattering theory was independently proposed by Lorentz (Lorenz, 1890) and Mie (Mie, 1908), and describes the scattering of radiation by isotropic homogeneous spherical

particles which have a size similar or larger than the radiation wavelength, $x \gtrsim 1$ (see Fig. 1.4b). It is based on Maxwell's equations, and describes the scattered intensity such as

$$I(\theta) = I_0 \left(\frac{\sigma_s}{r^2}\right) \frac{P(\theta)}{4\pi}, \tag{1.6}$$

where I_0 is the incident radiation intensity, σ_s is the scattering cross-section coefficient, r is the distance between the observer and the particle, and $P(\Theta)$ is the normalized phase function, which describes the angular distribution of the scattered radiation,

$$P(\theta) = \frac{4\pi}{\sigma_{scat}} \frac{d\sigma_{scat}}{d\Omega}, \tag{1.7}$$

where Ω is the solid angle.

The scattering cross-section, σ_{scat} can be derived following Lorenz-Mie theory by expanding the incident radiation wave into a vector of spherical harmonics, and then solving Maxwell's equations. It yields the internal and scattered field in therms of vector spherical harmonics, i.e. the phase function, and is expressed per particle volume (V) as

$$\sigma_{scat}/V = \frac{1}{4\mathrm{a}} c_1 x^4 \left(1 + c_2 x^2 + c_3 x^3 + \dots\right), \tag{1.8}$$

where $c_1 = \left(\frac{\mathrm{m}^2-1}{\mathrm{m}^2+2}\right)^2$ is the first order coefficient. If the particles are very small and satisfy $x \ll 1$, then eq. (1.8) becomes the Rayleigh scattering cross-section. As the particles increase in diameter, the second and higher orders become more relevant, and the size prevails over λ and determines the amount of scattered radiation intensity (Liou, 2002).

The angular distribution of scattered light is determined by the phase function which can be obtained from Lorenz-Mie computation for spherical aerosol particles (cf. Mishchenko et al., 2002). For the case of Rayleigh scattering for small particles, the angular distribution of scattered light tends to be symmetrical in the forward (0°) and backward (180°) directions, with a minimum in the plane perpendicular to the incident beam of radiation, i.e. at an scattering angle of 90° (Figure 1.5). For coarse particles, the scattering pattern has an absolute maximum in the forward direction, a minimum at an scattering angle of $\sim 120°$, and a second relative maximum between $120 - 150°$ (Figure 1.5).

The atmospheric scattering by aerosol particles as a function of particle size parameter (x) shows a maximum when the particle effective radius is close to the length of the considered wavelength. Subsequent maxima ripples for the scattering coefficient decrease in magnitude with increasing size parameter, getting smoother as the effective variance of the particle size number distribution and the imaginary refractive index of the particle, i.e. the absorption, increases (cf. Figure 1.6). Fine mode particles are associated with higher scattering coefficients values, with increasing values with decreasing wavelengths as a consequence of the larger particle number concentration at the fine modes and the higher intensity levels of solar electromagnetic radiation at wavelengths close to x. This is specially relevant when the largest particle number concentration falls within the fine mode (e.g. in heavily

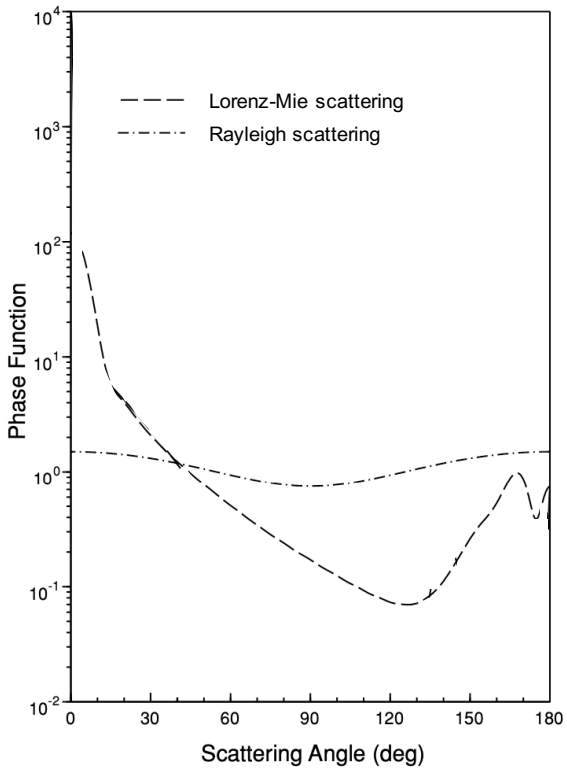

Figure 1.5: Normalized phase function for Rayleigh scattering (dashed-dot line), and Lorenz-Mie scattering (dashed line). *Adapted from Liou (2002)*

aerosol-loaded atmospheres in urban backgrounds). However, under the special case that the particle number size distribution is skewed toward the coarse mode, such as for mineral dust particles in an atmosphere with a relatively low impact of anthropogenic emissions, then the larger number concentration of coarse particles implies large scattering coefficients for this mode. For the latter case, if the scattering coefficients are obtained with instruments that use wavelengths in the visible range, then the scattering coefficients will show an increasing trend with increasing wavelength, since the wavelengths used for measuring the scattering are smaller than the effective radius of the particles at which the scattering efficiency has its maximum.

1.3.2 Atmospheric light absorption

The absorption of radiation is the physical process by which the energy is transferred from the radiation beam into the particle, which then will jump into an excited state. The absorption by the molecular gases in the atmosphere represents a large fraction of the total absorption of the electromagnetic radiation into the atmosphere.

The electromagnetic spectrum range and intensity at which molecular gases absorb radiation is determined by the coupling of their electric dipole moment with the incoming radiation field. The possible wavelengths at which molecules can undergo energy transitions and absorb radiation is determined by their quantum structure of the energy levels of the

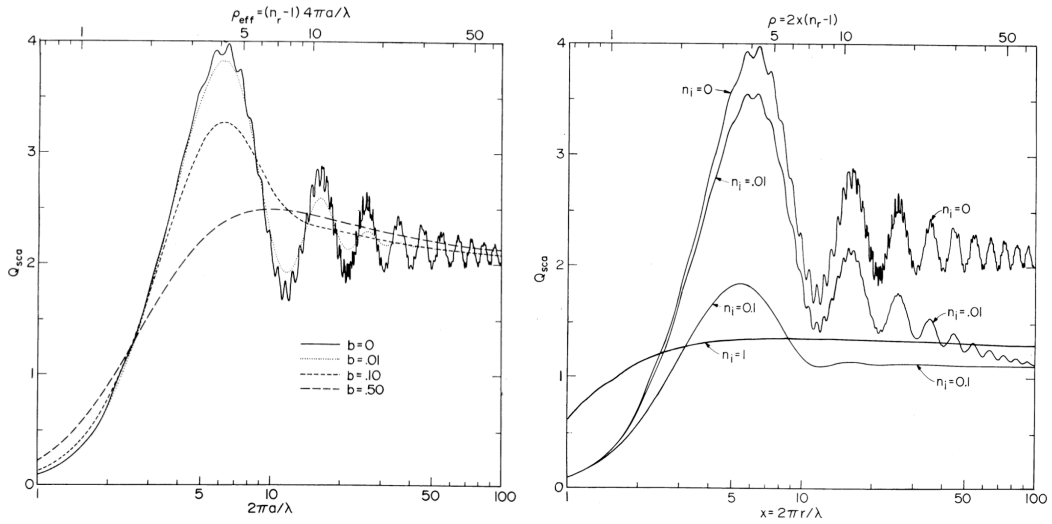

Figure 1.6: Scattering efficiency factor, $\mathrm{Q_{scat}}$, as a function of the effective size parameter, $x = 2\pi a/\lambda$, with variation in the particle size distribution variance, b, for particles with a refractive index of n =1.33, and k=0 (left panel); and the size parameter $x = 2\pi r/\lambda$ with a real refractive index of 1.33, and a varying imaginary refractive index, $n_i = k$ (right panel). *Adapted from Figs. 8 and 9 from Hansen and Travis (1974)*

molecular gases, specifically by their translational, vibrational and rotational energy transitions. In particular, O_2 and O_3 are responsible for the absorption of most of the incident solar radiation for wavelengths shorter than 290 nm, and water vapour (H_2O) and carbon dioxide (CO_2) present an absorption spectrum with several high absorbing bands in the infrared spectrum of radiation, i.e. wavelengths longer than 800 nm (Seinfeld and Pandis, 1998). H_2O and CO_2 only absorb radiation at the near-IR and IR spectral range and are transparent to shorter wavelengths in the visible range of the spectrum, thus the reason why they are referred to as *greenhouse gases*.

Atmospheric aerosol particles also have the potential to absorb radiation, with their size and chemical composition determining the amount of radiation that can be absorbed. As for the scattering, the absorption cross-section coefficient (σ_{abs}) for very small particles is described by the Rayleigh absorption theory, which presents an inverse relationship with the wavelength, $\sigma_{abs} \propto \lambda^{-1}$ (Moosmüller et al., 2009).

The absorption cross-section for homogeneous, linear, isotropic, spherical particles is obtained by solving Maxwell's equations, and as for the scattering, it is described through the Lorenz-Mie theory (Liou, 2002). This approach yields the internal and scattered field in therms of vector spherical harmonics, which for the smaller particles converges to Rayleigh absorption,

$$\sigma_{abs}/V = \frac{6\pi}{\lambda}\mathrm{Im}\left(\frac{\mathrm{m}^2-1}{\mathrm{m}^2+2}\right), \tag{1.9}$$

where σ_{abs} is normalized by the particle volume (V), and in addition to the λ^{-1} wavelength-dependence, it also showcases its dependence with the imaginary part of the refractive index.

The complex refractive index (m) depends on the physico-chemical properties of the aerosol particle, and its determination has been subject of many studies. The complex refractive index is usually obtained either by computational processes from predicted density of electrons, or as a mix of a theoretical approach and empirical data. The main theoretical approaches are: i) the linear oscillators approach, where electrons act as linear oscillators that interact with radiation, and the refractive index is obtained adding the interactions of all the electrons that the particle contains (Stull and Plass, 1960); ii) the band-gap theory, which follows from the oscillator theory, and establishes that the band-gap is the energy needed for an electron to reach an excited state (roto-vibrational excitation), so that only the photons with an energy greater than the band-gap can cause electron transitions (Tauc et al., 1966).

As aforementioned, the most relevant aerosol species that absorb radiation are carbonaceous aerosols, such as BC and BrC, and potentially, mineral dust. However, due to their different composition and formation processes, the absorption properties of these species differ.

Mineral dust particles are made of a mixture of different minerals, among which the main absorbing compounds are those iron-related, especially the iron-oxides. Of these iron-oxides, the more important ones given their high absorption efficiency are goethite, hematite and magnetite. These iron compounds present a progressive increase of the imaginary refractive index towards the shorter UV wavelengths, which is associated to the larger energy-gap that characterize the electronic structure of these iron oxides found in the dust particles. Although the absorption efficiency of these minerals towards the near-IR and IR is not null, it is highly reduced, since the photons do not that much energy to enable the valence electron transitions into an excited state [1].

The high absorption efficiency of BC is due to the disposition of the carbon atoms. Despite its amorphous structure at a macroscopic level, BC has a 2-D graphite-like structure at a microscopic level. Carbon atoms present three of the valence electrons in the sp^2 orbitals in a plane with a 120° angle between them, and a fourth valence free electron in a π-orbital perpendicular to the aforementioned plane that does not participate in the carbon-carbon bonds (Bond and Bergstrom, 2006). This fourth free valence π-electron makes the energy-gap to be fairly small, and thus making BC particles highly absorbing of electromagnetic radiation independently of the wavelength over a broad spectral range. This high absorbing capacity in the whole spectrum range states the importance of correctly measuring the concentration and optical properties of BC particles for accurately deriving their influence on climate.

BrC is composed of a large array of organic compounds that can absorb radiation as a consequence of the presence of atoms, such as carbon and nitrogen, that can jump into an excited state (Laskin et al., 2015). Although BrC particles present a lower imaginary refractive index than BC particles through the electromagnetic spectrum, the imaginary refractive index of BrC increases from relatively low absorption at the visible wavelengths

[1] The energy carried by a photon is described by the Planck-Einstein relation and is inversely proportional to the wavelength, $E = hc/\lambda$, where h is the Planck's constant and c is the speed of light

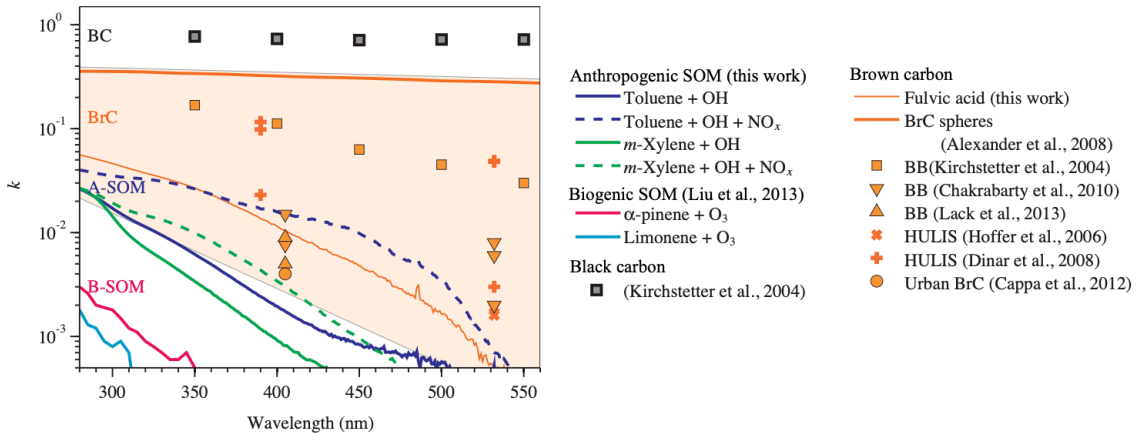

Figure 1.7: Imaginary refractive index spectral variations for different light-absorbing atmospheric aerosols from both anthropogenic and biogenic secondary organic aerosols (A-SOM and B-SOM), black carbon (BC) and brown carbon (BrC). *Source: Liu et al. (2015a)*

towards the short-UV spectral range (Fig. 1.7), in contrast with BC, for which the imaginary refractive index presents a weak wavelength dependency (Kirchstetter et al., 2004). Unlike mineral dust particles, which do absorb at the near-IR and IR, BrC particles do not absorb at these longer near-IR and IR wavelengths.

The value of the imaginary refractive index of BrC aerosol particles, which defines the absorption properties of the aerosol particles, highly depends on the formation pathways, since they determine the level of sp^2 hybridization of the carbon atoms and the presence of nitrogen compounds and their level of sp^2 and sp^3 hybridization (Laskin et al., 2015). Indeed, it has been found that as the carbon sp^2 hybridization of BrC increases, the particles become more BC-like (Hopkins et al., 2007; Saleh et al., 2018; Lu et al., 2015; Laskin et al., 2015), with a higher absorption and a lower wavelength dependency (Fig. 1.8). In addition, the presence of nitrogen-containing compounds during the formation of SOA has been linked with an increase in the overall absorbance and the mass absorption efficiency of these SOAs in the short-UV, and especially in the visible wavelengths (Updyke et al., 2012; Laskin et al., 2015). Therefore, as seen in Figure 1.7, particles formed via secondary aromatics, such as nitroaromatics and HULIS, are expected to have lower imaginary refractive index than the BC-like compounds formed through more efficient combustion processes, such as those resulting from benzene and toluene combustion (Liu et al., 2015a; Saleh et al., 2018).

BC particles can get mixed with surrounding organic and inorganic aerosols, either during the formation process of BC (cf. Sect. 1.2), when organic compounds can get adsorbed or condensed over the BC particles upon cooling, or in the atmosphere through ageing and photo-chemical processes. Depending on the absorbing properties of these mixing materials, these can either enhance or decrease the absorbing efficiency of the BC cores. The mixing of BC particles with these compounds is classified depending on the mixing state: internal and external mixing. External mixing is the heterogeneous mixture of homogeneous particles, and internal mixing is the homogeneous mixture either of internally homogeneous particles,

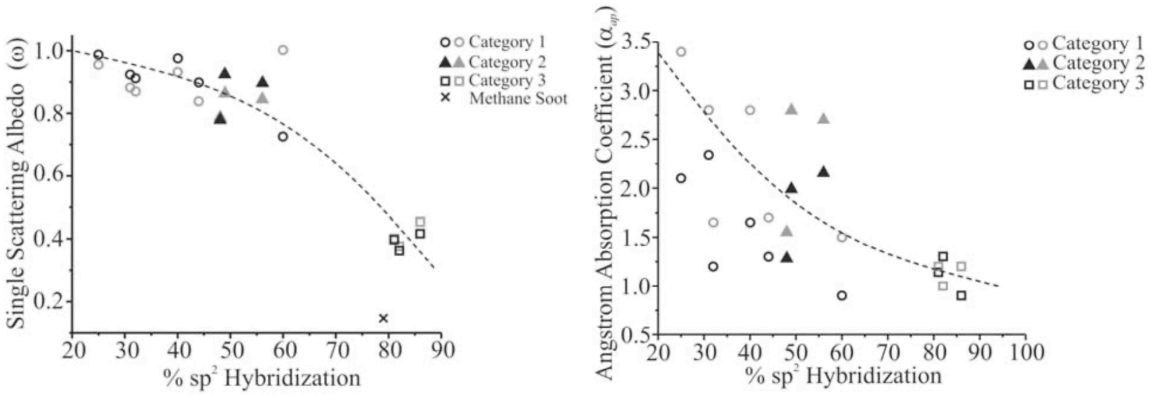

Figure 1.8: Dependence of a) the single scattering albedo (SSA), and b)the Absorption Ångström Exponent (AAE) with the percentage of the particles sp^2 hybridization. AAE describes the wavelength dependence of the absorption, with higher AAE values showing an increasing dependence. SSA reflects the fraction of radiation that is scattered back into the medium, a SSA of 0/1 implies the total absorption/scattering of the radiation. Both SSA and AAE are explained in further detailed in Sect. 4.4.1 from **Chapter 4**. *Source: Hopkins et al. (2007)*

or of a heterogeneous mixture of particles (Bond and Bergstrom, 2006). Overall, the mixing of BC particles with these compounds is estimated to produced an absorption enhancement, E_{abs}, which is treated as constant around 1.5 by some climate models, i.e. absorption from the BC particles is enhanced by around 50% (Flanner et al., 2007; Wang et al., 2014; Liu et al., 2015b). The contribution to the absorption enhancement by the external mixing of BC is produced as a consequence of the addition of the absorption by BrC particles to the overall absorption, whereas internal mixing can increase the absorption of BC particles due to the modification of the path length that the radiation follows through the mixture to reach the BC core. The internal mixing absorption enhancement is usually studied through a core-shell theory, which assumes a BC core with an outer shell of organic and inorganic materials that either enhances the absorption cross-section of the BC particles by focusing the radiation beam into the BC core if the shell material is transparent (i.e. the so called "lensing effect"), or reduces the BC absorption cross-section if the shell material absorbs radiation itself, thus reducing the amount of light reaching the BC core (Lack and Cappa, 2010).

In order to obtain the refractive index for carbonaceous aerosols, two different models are used: a simple model based on the hydrogen-to-carbon ratio for carbonaceous particles as a proxy for the absorption capacity of the particles, and the medium-range order approach, where, for amorphous carbon, the band-gap is controlled by the adjacent sp^2-bonded rings of the amorphous carbons, and as the number of adjacent rings increases, the energy gap decreases, eventually reaching 0 for materials with many adjacent aromatic rings (Bond and Bergstrom, 2006).

The absorption and scattering of particles by the Rayleigh theory usually can be formulated for ultrafine particles in the nucleation and Aitken mode, especially for those BC cores generated in combustion processes. However, for particles in the accumulation and coarse mode,

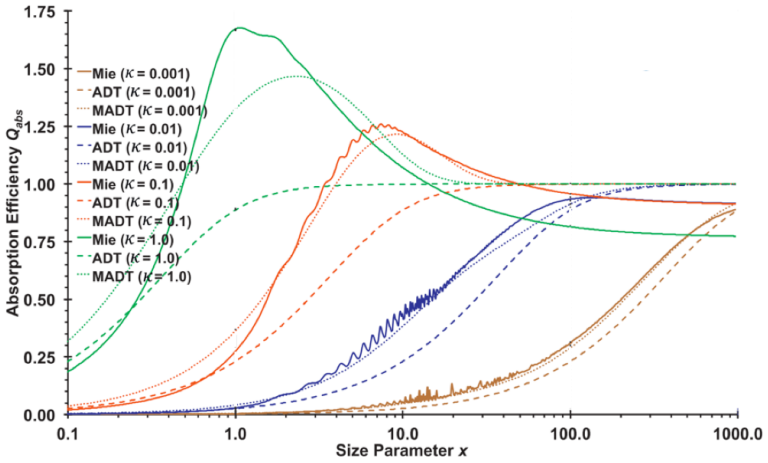

Figure 1.9: Absorption efficiency, Q_{abs}, variation with the size parameter, x, for varying imaginary refractive index, k, obtained by applying Mie theory, Anomalous Diffraction Theory (ADT), and Modified Anomalous Diffraction Theory (MADT). *Source: Moosmüller et al. (2009)*

such as mineral dust particles and BC and BrC aggregates, Lorenz-Mie theory calculations are needed to correctly compute the absorption and scattering properties. In the latter case, calculations are usually performed assuming a given density and particle size distribution (Lack and Cappa, 2010; Virkkula, 2021). In addition, if the particles are not spherical, more complicated computations are needed, for which the T-Matrix theory is used in order to resolve the Maxwell equations (e.g. Mishchenko et al., 2002).

The absorption dependence with the size parameter (x) differs from the scattering in that the maximum absorption is not found at wavelengths similar to the particle effective radius, but it changes with the imaginary part of the refractive index, k, and decreases at a slower rate towards higher x values instead of presenting ripples from the maximum onward (Moosmüller and Sorensen, 2018). As k decreases, the absorption efficiency maximum decreases and increases from x values in the Rayleigh regime towards x values in the Mie regime (Fig. 1.9. This dependency of the absorption coefficient with the size parameter, and more importantly with the imaginary part of the refractive index, is reflected in a higher absorption coefficients for the fine mode of the aerosol particles since at these modes there are both a higher amount of particles and also the particles tend to be more absorbing, as black carbon (BC, cf. Sect. 1.2), therefore dominating the overall absorption (Moosmüller et al., 2009).

1.4 Aerosol particles effect on climate and the environment

Atmospheric aerosol particles have a myriad of effects on the Earth's atmospheric systems, climate, and ecosystems, and are responsible for many processes crucial for life on Earth, such as cloud formation, modulation of the hydrological cycle and soil and ocean fertilization,

among others (e.g. Szopa et al., 2021; Forster et al., 2021). Moreover, aerosol particles, and especially fine anthropogenic particles, are airborne, and therefore can be introduced into the respiratory and cardiovascular system, harming human health (WHO, 2016).

The study of the atmospheric aerosol particles effects on climate at a local, regional and global scale is paramount to better understand the Earth's climate. The interaction of the atmospheric radiative active gases and aerosol particles with the Sun's and Earth's radiation modifies the black-body thermodynamic equilibrium reached between the Sun and the Earth (Kirchhoff, 1860). The presence of this gaseous molecules and particles alters the Earth's radiative balance, i.e. its thermodynamic equilibrium, and as a consequence, without anthropogenic emissions, the Earth's average temperature reaches values that enable the presence of life on Earth (Liou, 2002). This change in the radiative balance is referred to as radiative forcing, and its sign depends on the coupling of the radiative effects of all atmospheric constituents and the resulting radiative feedbacks that can be either positive if the induced change forces the atmosphere to absorb more energy, or negative if the induced changed forces the atmosphere to scatters back to space a larger fraction of the incoming radiation, hence inducing a cooling effect. The characterization of the radiative forcing by gaseous molecules, especially of the most relevant species (e.g. CO_2, CH_4), and its effect on climate and on climate change is rather well constrained. This better identifications of the interactions and influence of these gases on climate is mainly due to a larger and more detailed emission inventory, the better characterization of their absorption properties, and the longer lifetime and, consequently, higher homogeneity around the globe, albeit with hotspots at the main emission source areas. Conversely, the determination of the aerosol particles influence on Earth's climate still presents large uncertainties to date, mainly due to the large spatial and temporal variability of both their concentrations in the atmosphere and their physico-chemical properties. Aerosol particle are originated by a vast variety of both natural and anthropogenic sources and, consequently, these are present in the atmosphere with very different size distributions, chemical composition and optical (scattering and absorption) properties that ultimately determine their radiative forcing properties. The latest reports from the Intergovernmental Panel on Climate Change (IPCC; Myhre et al., 2013; IPCC, 2021) highlight the need for a better understanding and characterization of the climate effects of atmospheric aerosol particles, especially in the current context of climate change, and the urgency for a phase-out from fossil fuel energy and a rapid shift towards energy sources that do not emit greenhouse gases. The urgency of this shift is also relevant considering that the measures to improve air quality have drastically reduced the anthropogenic emissions of both aerosol particles and precursors in large areas of the northern hemisphere, thus altering the radiative balance of the aerosol particles on climate (Shindell et al., 2012; Szopa et al., 2021). In fact, certain types of aerosol particles with high mass scattering efficiencies that act as net coolers of the atmosphere, as sulphate and nitrates, actually cool the climate, contrasting the warming effects from anthropogenic greenhouse gases. As an example, Navarro et al. (2016) found that up to 0.5 ° C of the warming that has been observed in the Arctic (the most rapidly warming region on the planet) since 1980 has been caused by atmospheric particle reductions in Europe.

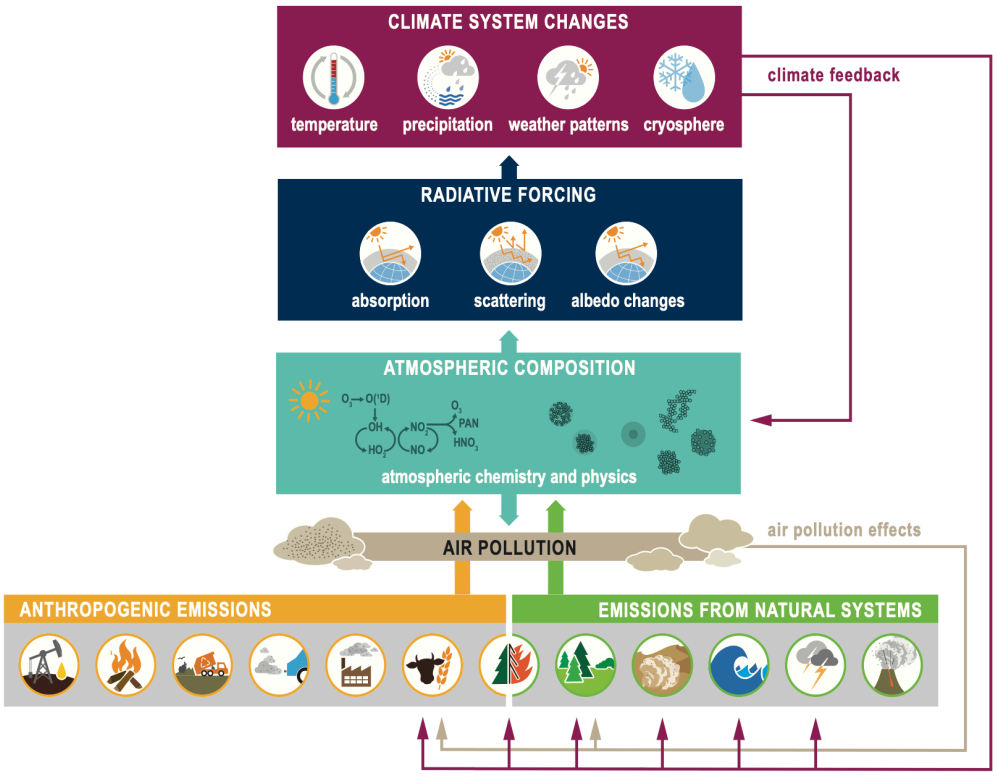

Figure 1.10: Overview of the climate interactions and feedbacks from the main aerosol particles and short-lived climate forcers emitted by the principal anthropogenic and biogenic sources. The sources are: fossil fuel, biofuel, waste, transportation, industry, agricultural sources, open biomass burning, natural biomass burning from wildfires, vegetation, soil and ocean emissions, lightning, and volcanic eruptions. *Source: Szopa et al. (2021)*

Figure 1.10 shows the main sources of short-lived climate forcers, both aerosol particles and gaseous molecules, the way that they influence the radiative forcing and their impact on different climate systems. Briefly, the main pathways through which aerosol particles induce variations in the radiative balance are: i) direct interaction with both the solar and terrestrial radiation, ii) semi-directly through the absorption of radiation inside clouds systems which heats the air parcels around the particles and increases the evaporation of cloud droplets surrounding the aerosol particles, and iii) indirectly through its impacts on aerosol-cloud formation, the cryosphere, and the atmospheric and biological chemistry (Engelstaedter et al., 2006; Choobari et al., 2014).

The aerosol particles direct radiative effect (DRE), accounts for the direct radiative forcing of the aerosol particle-radiation interaction for the whole solar and terrestrial radiation spectrum (Forster et al., 2021). The aerosols DRE on the Earth's radiative balance depends on their capacity to absorb and scatter radiation (Sect. 1.3) both at the short wavelengths, mostly solar radiation from UV to the near-infrared, and the long wavelengths, mostly from the terrestrial infrared radiation (Liou, 2002). One of the most important parameters to

characterize the scattering and absorbing properties of the aerosols particles species is the complex refractive index (m). In addition to the refractive index, other parameters commonly used to determine the scattering and absorbing properties of aerosols are the mass scattering and absorption efficiencies, MSE and MAE, respectively (cf. Sect. 4.4.1), which are of special interest for climate estimations, since global emissions of aerosols are reported by mass concentration (e.g. Szopa et al., 2021).

The indirect radiative effects of aerosol particles is achieved as a consequence of their ability to transform the optical properties of clouds by changing their albedo, and to act as both cloud condensation nuclei (CCN) and ice nuclei (IN). An increase of the number of aerosol particles promotes the creation of more CCN and IN, which leads to an increase in the number of smaller cloud droplets for the same water content. This increase can increment the particles reflectance (known as the first indirect effect, or the cloud albedo effect (Twomey, 1974; Twomey, 1977; Twomey et al., 1984) and can suppress collision and coalescence processes, and hence precipitation formation (Rosenfeld, 1999; Rosenfeld, 2000), thus increasing cloud lifetime and therefore its reflectivity over time (known as the second indirect or Albrecht effect; Albrecht, 1989). Precipitation suppression promotes an increase in latent heat and mix-phase cloud freezing processes, which enhances the cloud top heights and delays the onset of precipitation (known as the aerosol invigoration effect; Andreae et al., 2004). However, these indirect effects can be overturned if, for example, the aerosol layer is dominated by BC, which reduces the reflectivity of the cloud, or if the aerosol particles are coarse enough to form a less amount of CCN, thus promoting precipitation instead of suppressing it (e.g. Tao et al., 2012). Additionally, the semi-direct radiative effect of aerosol particles is achieved through the absorption of radiation by aerosol particles within clouds, which reduces relative humidity and increases the cloud evaporation, leading to a reduction in cloud cover and therefore an increase in surface warming (Ackerman et al., 2000). Moreover, the relative position of the aerosol particles respect to the cloud cover is crucial since if the absorption of the aerosol layer takes place below the cloud layer the convection is enhanced, favoring cloud formation. Conversely, if the aerosol layer is above the cloud layer it promotes stability, thus inhibiting the cloud development (Bond et al., 2013; Choobari et al., 2014).

As commented above, aerosol particles are net coolers of the atmosphere, with an estimated global DRE of -0.3 [-0.6 to $+0.0$] Wm^{-2}, mostly due to the high scattering efficiencies of sea salt, sulphates and nitrates, but also some OAs (Forster et al., 2021). Moreover, the semi-direct and indirect of particles as cloud condensation and ice nuclei to the radiative forcing is of -1.0 [-1.7 to -0.3] Wm^{-2} (Forster et al., 2021). However, these estimations present a large uncertainty, therefore the increasing need for correctly assessing the radiative effects of the aerosol particles and especially of those particles with high absorption efficiencies and those that can act as CCN and IN.

The aerosols responsible for most of the cooling are sea salt aerosols and secondary inorganic aerosols which present high single scattering albedo values, hence reflecting most of the incoming light radiation (Myhre et al., 2013; Szopa et al., 2021). Indeed, SIAs, and in

particular ammonium sulphates and nitrates, present very high mass scattering efficiencies and SSA — with a high similarity between diverse regions — mainly associated to the bias towards the fine mode of their particle size distribution where particles are more efficient scatterers (Seinfeld et al., 1998; Hand and Malm, 2007). Finally, Hand and Malm (2007) review of various aerosol particles mass scattering efficiencies showed that sea salt, which represents a large contribution of the total global load of aerosols in the atmosphere, showed one of the highest mass scattering efficiencies, followed by ammonium sulfate and nitrates.

As shown by the latest studies from the literature and the IPCC reports (IPCC; Myhre et al., 2013; Szopa et al., 2021), the most important aerosol particles with regards to their effects in the warming of the atmosphere are black carbon (BC), the absorbing fraction of the organic aerosols (OA), and potentially mineral dust particles. The biggest warming agents are BC and specific OA compounds, called BrC for their ability to absorb radiation, even if less efficiently compared to BC particles. However, their climate effects are important because these OA particles have the ability to enhance the absorption produced by the BC particles and also present a higher global concentration load compared to BC. The most important source globally of BrC particles into the atmosphere is biomass burning both from anthropogenic use and from wildfires. The role of mineral dust on the climate radiative balance presents one of the largest uncertainties. Although previous studies and the newest IPCC report have described mineral dust particles as net cooling agents (Myhre et al., 2013; Szopa et al., 2021), recent studies (e.g. Di Biagio et al., 2019; Huang et al., 2020; Li et al., 2021) have demonstrated that mineral dust particles can potentially act as net warming agents (cf. Fig. 1.11). The latter result was mainly due to improvements in dust particles characterization and in modelling assumptions that resulted in: i) a better representation of the mineralogical composition of the emitted dust particles in climate models depending on the emission source region, and ii) a better coupling of surface and satellite measurements for improving the mineral dust particle size distribution and load in the atmosphere. In fact, recent studies have demonstrated that the application of these improvements resulted in a reduction of the cooling effect of dust particles in the shortwave spectral range and an increase in the magnitude of the warming effect in the longwave spectral range (Kok et al., 2017; Di Biagio et al., 2019; Li et al., 2021). Since mineral dust particles account for the second highest global mass concentration emission source of aerosol particles, it is paramount to correctly quantify their effects on climate. An additional effect that aerosols particles exert on climate is trough the deposition of absorbing particles, such as BC or mineral dust, on snow and ice covered surfaces, which reduces the Earth's surface albedo and increases the surface absorption and the warming of the boundary layer (Forster et al., 2021).

The interaction of aerosol particles with the Earth's systems is not limited to the atmosphere and presents multiple interactions with the environment. In fact, aerosol particles play a key role in numerous terrestrial and oceanic ecosystems, as fertilization of soils with mineral nutrients from other regions, like Saharan mineral dust outbreaks over the Amazon (Engelstaedter et al., 2006), enhancement of algae production in the oceans by wildfires (Tang et al., 2021), modulation of the cryosphere cycle (Kaspari et al., 2015; McCutcheon

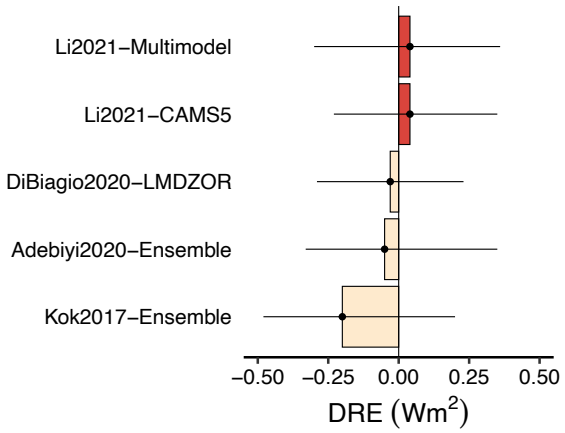

Figure 1.11: Contribution to the direct radiative effect (DRE) by mineral dust particles from multiple studies assessing the potential warming effect of dust on climate through different models and parametrizations of mineral dust particles on the atmosphere. In Li et al. (2021), Li2021-Multimodel used multiple models (CAM5, CAM6, ModelE2, GFDL, MONARCH) upon their soil scheme, and psd assumptions, whereas LI2021-CAMS5 only uses CAMS5. DiBiagio2020-LMDZOR, from Di Biagio et al. (2020), uses the LMDZOR-INCA model, which coupes the LMDZ global circulation model, the ORCHIDEE land surface, and the INCA aerosol model. Adebiyi2020-Ensemble, from Adebiyi and Kok (2020), uses a model ensemble from GISS. WRF-Chem, CESM, GEOS-Chem, Arpege-Climate and IMPACT) and presents new constrains in the global concentration of coarse mineral dust. Kok2017-Ensemble, from Kok et al. (2017), is the study providing the ERF of dust in Fig. 1.1, uses a statistical model based on multiple models (WRF-Che, GEOS-Chem and HadGEM) and constrains the amount of coarse mineral dust particles.

et al., 2021), and regulation of the hydrological cycle (Ramanathan et al., 2020), among others. Moreover, aerosol particles also influence human activity by, for example, producing visibility reduction under intense haze or sand storm scenarios or by degrading buildings and infrastructures (Malm et al., 1994).

This thesis is focused on the optical properties of atmospheric aerosol particles and their effects on climate. However, for the sake of completeness, this paragraph briefly summarizes another important consequence of the presence of particles in the atmosphere, i.e. their effects on human health. The human health effects from exposure to atmospheric aerosol particles, both mid and long-term, have been subject to research by multiple epidemiological and toxicological studies, from which strong evidences of the increase of morbidity and mortality, as well as an increased risk of developing cancer have been found (WHO, 2016; WHO, 2021). The chemical composition and physical properties (e.g. number concentration, size, shape) of the aerosol particles is associated with varying effects on human health. Overall, smaller particles are more hazardous since they can penetrate deeper into the respiratory system, and ultimately reach the alveolars (submicron particles) and be introduced into the bloodstream (ultrafine particles) from where they can be spread into other organs (WHO, 2016). The most hazardous particles are those associated with anthropogenic sources such as combustion processes, where BC, emitted along with other organic particles with reactive potential that can carry carcinogenic compounds, is associated with an increase risk in diseases (WHO,

2012; Shiraiwa et al., 2012). Coarse particles, although do not reach that far into the respiratory system, also present adverse effects, as they have a high potential inflammatory effect, specially those related to mechanical wear and traffic non-exhaust emission, which can be linked to metals toxicity (Perez et al., 2009).

1.5 Atmospheric aerosol particles: Europe and the Mediterranean

The atmospheric aerosol particles and its multiple effects presents substantial spatial and temporal variability that, as aforementioned, are mainly due to the multiple emission sources, and the large differences in the particle size distribution, the lifespan on the atmosphere, and the physico-chemical and mineral composition. The majority of the aerosol particle load in the atmosphere is concentrated in the northern hemisphere as a consequence of the larger proportion of emission sources, both natural and anthropogenic (Szopa et al., 2021). In particular, Europe is subject to large aerosol particles heterogeneities as a consequence of the different climates, meteorologic patterns, complex topography, densely populated and industrial areas, and long-transport aerosols contributions from external emission areas (Putaud et al., 2004; Putaud et al., 2010; Zanatta et al., 2016; Pandolfi et al., 2018; Bressi et al., 2021).

The analysis of the atmospheric aerosol particles characteristics in Europe has been subject to numerous studies, with the main focus on urban and regional backgrounds and, despite their lower amount on the continent, remote stations (Laj et al., 2020). These studies show that the main sources of aerosol particles are traffic and industrial processes over urban and sub-urban areas, energy production, shipping over coastal areas with large sea-ports, agriculture and biomass burning on rural areas, especially on central, eastern and northern Europe where wood-stove heating is common, and mineral dust transport, especially in southern Europe, near the Mediterranean basin (Colette and Ineris, 2020; Colette et al., 2021). Thanks to the implementation of measures that restrict the emission of aerosol particles into the atmosphere (see `https://www.eea.europa.eu/themes/air/air-quality-management/improving-europe-s-air-quality/policy-context`), the air quality has greatly improved over Europe over the last decades (Szopa et al., 2021). However, despite these regulations, more than 70 % of the european population are exposed to values that exceed the World Health Organization (WHO) limits. In southern Europe, and in particular in the Mediterranean basin, the aerosol particles differ from central and northern Europe, and present a larger variability in their sources and chemical composition (Lelieveld et al., 2002). The main differences arise from the abrupt topography enclosing the basin altogether with a lower number of precipitation and venting episodes, hence leading to higher concentrations and accumulations of aerosol particles over time, especially during summer. In fact, during the warm season, when high pressure systems coupled with the onset of recirculation patterns (Pérez et al., 2004), the high insolation levels and recycling of aerosols in the troposphere favours photo-chemical processes that increase the formation of secondary aerosols and

the ageing of the particles. In addition to the anthropogenic sources (e.g. emission from densely-populated areas, shipping vessels, industrial processes, etc.), the Mediterranean basin is also heavily impacted by aerosols from natural sources, such as mineral dust advections from North Africa, a larger rate of wildfires than other parts of Europe, sea spray, and biogenic processes (e.g. Lelieveld et al., 2002; Pey et al., 2013).

Remote measurement sites, such as those located at the top of mountain ranges and in the Arctic, are of special interests since they showcase the background characteristics of the atmospheric aerosol particles that are less influenced by nearby sources, either because they are above the planetary boundary layer (PBL) and/or due to their remote location. These sites are of great interest since they enable a more accurate characterization of i) natural origin sources emitted in these pristine areas without masking from anthropogenic origin sources, ii) long-range transport sources, such as mineral dust from North Africa, especially in the Mediterranean basin and the Alps, volcanic aerosol plumes and mineral dust from Iceland at central and northern Europe, and wildfire smoke plumes from North America, iii) aerosol particles ageing over time on the atmosphere, as well as iv) deriving pseudo-vertical profiles of the characteristics of aerosol particles if multiple measurements are performed at several heights along the mountain.

1.5.1 Global measurements and monitoring networks

With the aim of mapping global atmospheric aerosol particles concentrations, distributions, optical properties, and ultimately their influence on the radiative balance of the Earth's atmosphere, measurements are performed both around the globe and at the most important emission source areas. This is accomplished through a combination of monitoring networks and intensive measurement campaigns on the Earth's surface, either in-situ or remote sensing, airborne vertical profiles measurements, and specific satellite-borne instrumentation (Laj et al., 2020).

Continuous aerosol particles measurements are performed through an array of monitoring networks that measure multiple variables such as the aerosol concentrations, particle size distributions, chemical composition, and optical properties, among others. These networks are linked to different levels of governmental and inter-governmental administrations, such as the Global Atmosphere Watch (GAW) from the WMO (GAW, 2016), the Global Monitoring Laboratory from the NOAA, and the Aerosols, Clouds, Traces gases Research Infrastructure (ACTRIS) and the Copernicus Atmosphere Monitoring Service (CAMS) from the European Commission.

In-situ surface based measurements are performed through a combination of techniques and instruments deployed at sites located in different background scenarios, mostly urban, regional and mountain-top. The instrumentation deployed at these measurement sites, and in particular the optical instruments used for measuring the absorption and scattering coefficients are the base of this thesis. The instruments for measuring the absorption coefficients were filter-based photometers, whereas the scattering coefficients were measured

through integrating nephelometers. These surface-based measurements allow for a complete characterization of atmospheric aerosol particles physico-chemical properties due to the large array of instruments that can be deployed, however their spatial distribution is not homogeneous around the globe due to their maintenance costs, with a much more dense network of measurements in wealthier countries in the northern hemisphere, mainly in Europe and North-America, with a lower cover in less wealthy countries (Laj et al., 2020). Their representativeness is limited to the area nearby the measurement site and only close to the surface. Complementary, remote sensing optical measurements can provide the vertical profiles of specific aerosol properties, however the amount of variables that can be retrieved is more limited than in-situ surface measurements.

A more complete characterization of aerosol particles vertical profiles is often performed through airborne measurements, carried out with customized air-crafts that are able to measure the physico-chemical aerosol properties with high vertical and horizontal spatial resolution. Yet, instrumented flights are only used during intensive measurement campaigns and are not suited for routine long-term measurements. Finally, satellite-based measurements, conversely to the in-situ surface and remote measurements, provide a global estimation of atmospheric aerosol concentrations, optical properties as well as composition to a certain degree (Kaufman et al., 2002). The satellite measurements provide both integrated vertical column variables, such as the aerosol optical depth, and are able to obtain the vertical structure of different atmospheric aerosol layers by applying some retrieval algorithms (Sekiyama et al., 2010). However, they cover large areas and the resolution and detail provided by their measurements is lower than the surface-based measurements.

2

Optical properties analysis and monitoring: State of the art review

As stated in **Chapter 1**, the measurement of the aerosol particles optical properties, and especially of the absorption properties of key species as BC, BrC and mineral dust, is crucial for a better understanding of the effects that aerosol particles have on climate radiative forcing. In order to reduce the uncertainties associated to the complexity related to the climate effects of aerosol particles, numerous measurements and studies are performed around the globe. Given the high horizontal, vertical and temporal variability of aerosol particles, special attention is focused on characterizing the aerosol properties in the atmosphere as a whole and not only at the surface level. However a full long-term characterization of the physico-chemical properties of particles is possible only at the surface, and for this reason many networks at a regional, national and international level have been set worldwide. The measurement sites operated by the EGAR group at the NE of Spain are part of the two most important international networks, GAW and ACTRIS (e.g. Laj et al., 2020; Collaud Coen et al., 2020). Moreover, the increase in the availability of new measuring techniques has enabled to better characterize important aspects related to the aerosol particles, such as the absorption efficiency of different BrC compounds and their influence on the BC absorption properties when mixed with BC, as well as of mineral dust particles and its impact on climate.

2.1 Measurement of the aerosol particles optical properties

The aerosol particles optical properties, i.e. the absorption and scattering coefficients, are obtained through a variety of different techniques based on the mechanisms through which light radiation interacts with the sampled particles. The measurement and monitoring of the optical properties of the aerosol particles is subject to multiple sources of uncertainties associated to the measurement errors itself, instrumentation differences and biases, and aerosol sampling artifacts. Measuring guidelines are established by national and inter-governmental panels (e.g. WMO, 2016; ECAC-CAIS, 2022), with the aim to harmonize

instrumentation differences, and resolve the sampling artifacts and errors. These guidelines are proposed as a combination of reports and recommendations from intercomparisons workshops and from the instruments manufacturers. The most relevant guidelines for the sampling and measurements of the aerosol particle properties are related to maintaining a constant flow with a tubing and inlet system with minimal diffusion and inertial losses, minimizing the evaporation of volatile organic compounds, and keeping a dry aerosol sample with a relative humidity low enough so that water vapour is not condensed onto the aerosol particles, thus impairing the size, mass and optical properties of the measured particles (e.g. WMO, 2016). Moreover, these guidelines provide information about procedures to control the measurement flow and avoid particle loss through the inlet and tubing system so that the sample accurately describes the aerosol composition and particle size distribution.

The scattering coefficients are obtained by measuring the intensity of the radiation after the scattering of the light source (typically emitted with a LED source at a specific wavelength) with the particles. The most common instruments used for in-situ measurements are the cavity attenuated phase shift (CAPS) spectroscopy, and the integrating nephelometers which allow for online continuous measurements of the scattering coefficients. The CAPS also measures the extinction coefficient, and therefore, the absorption coefficient can be derived following eq. (1.2). This instrument, however, presents high values of noise and a large measurement error if highly absorbing particles are measured, around 10 % for scattering coefficients, whereas the integrating nephelometer error is between 3 and 5 % depending on the model and manufacturer (Müller et al., 2011a). These uncertainties are mostly attributed to the instrument measurement stability. As a consequence, the integrating nephelometer is the reference method for measuring the scattering coefficients (WMO, 2016), and as such it is the most widely used instrument for measuring the scattering coefficients both at in-situ surface measurement sites and in instrumented flights. The integrating nephelometer main artifact is the truncation error, which consists in the inability to measure the light radiation scattered near the forward (0-10°) and the backward (170-180°) direction due to the geometric structure of the instrument. The truncation error is resolved through a dynamic parametrization depending on the size of the particles (Müller et al., 2011a). Moreover, the vertically resolved and column-integrated scattering coefficients can also be retrieved through a set of remote sensing instrumentation. LIDARs instruments in elastic-Raman configuration measures the extinction and backscattering of light in the atmosphere with high vertical resolution (e.g. Ansmann et al., 1992). In addition, by applying sophisticated inversion techniques, such as GRASP, that involve co-located LIDARs or ceilometers and sun-photometers measurements, the vertical profiles of extinction, scattering, backscattering, absorption and volume particle concentrations can also be derived (e.g. Titos et al., 2019). Column integrated variables such as the aerosol optical depth (AOD) can be retrieved directly from the sun photometer measurements, and specific inversion techniques are applied to the AERONET AOD to obtain the absorption, scattering and SSA AOD (Dubovik and King, 2000; Dubovik et al., 2000). Although the state of these methods is continuously improving with better algorithms able to provide more accurate measurements, they still present large uncertainties: 21 % for the backscattering and 31 % for the backscattering (e.g. Román et al.,

2018; Titos et al., 2019). Nevertheless, they are a great tool to retrieve vertical profiles of the scattering coefficients, which is crucial for assessing the impact of these particles for all the layers in the atmosphere and not just on the surface. Additional remote sensing measurements are performed via satellite based lidar systems, such as the ones mounted in CALIPSO and AEOLUS, from the NASA and the ESA, respectively.

The measurement of the absorption coefficients presents more difficulties than the scattering coefficients, mainly due to the fact the radiation is retained by the aerosol particles and not directly scattered into a photodetector. To solve this difficulties there are multiple approaches, described with more details below, with the most established at monitoring networks and aerosol chamber experiments being: the aforementioned subtraction method, the direct measurements of the absorption coefficients of suspended particles in a enclosed cell, with either photo-thermal interferometry or photoacoustic techniques (Ajtai et al., 2010; Drinovec et al., 2022), and the filter-based photometers, either on-line or off-line, that derive the absorption coefficient from the attenuation of light through a particle-loaded filter tape (e.g. Lin et al., 1973; Terhune and Anderson, 1977; Hansen et al., 1984; Stephens et al., 2003; Moosmüller et al., 2009; Drinovec et al., 2015; Vecchi et al., 2014).

The subtraction method, which calculates the absorption from the difference between extinction and scattering by suspended particles, can present large errors at high single scattering albedo (SSA) values since the extinction is dominated by scattering, and therefore the absorption values are low and small variations can present large errors, between 10 and 100 % (Modini et al., 2021). The application of this method is not recommended by the ACTRIS guidelines for continuous measurements (WHO, 2016), since the error is very high due to the high measured average SSA values (Laj et al., 2020), and is more frequently used at laboratory measurements and experimental set-ups (Singh et al., 2014; Onasch et al., 2015), where the particles introduced into the system can be precisely controlled to have low SSA values (e.g. soot, nigrosin).

The photoacoustic approach, such as the online multi-wavelength photoacoustic spectroscopy (PAS; Ajtai et al., 2010), obtains directly the absorption coefficients of the sampled particles as a result of the conversion of the absorbed energy by the particle into heat, and then into an acoustic wave due to the density change of the air in the cell, which has a wave amplitude proportional to the amount of absorbed energy. However, this technique presents some artifacts, since the heating of the sample and the evaporation of coating materials on the sample can potentially increase the detection limit and impair the measurement accuracy, specially for environments with a high amount of high and semi volatile organic compounds (Lack et al., 2006; Linke et al., 2016). Moreover, photo-thermal interferometry (PTI) was originally developed for measurements of trace gases, either at one wavelength (e.g. Lee and Moosmüller, 2020; Visser et al., 2020), or at multiple wavelengths (e.g. PTAAM-2λ; Drinovec et al., 2022). The working principle of the PTI is such that an energy beam is focused onto the particles, which absorb energy and heat the surrounding air thus causing a reduction of its refractive index, which is measured with a set of interferometer laser. This variation of the refractive index measured by the interferometers is linearly proportional

to the absorption coefficient (Campillo et al., 1981). Given the lack of a filter artifact, the absence of a pre-heating of the sample, and the possibility of measuring very highly accurate multi-wavelength absorption coefficients, the PTI could potentially be a reference technique for absorption measurements. However, at the moment the use of this technique remains focus at experimental sites and chambers due to its need for continuous supervision and larger experimental set-up, with a more compact and autonomous instrumentation needed for its implementation at measurement sites.

Filter-based instruments sample aerosol particles into a filter matrix and then measure the light intensity variation with a photometer, either by measuring the attenuation of the transmitted light radiation (Hansen et al., 1984; Bond et al., 1999; Drinovec et al., 2015), or by measuring both transmittance and reflectance (Petzold and Schönlinner, 2004). The main artifacts affecting this approach are due to the presence of a filter tape and its interaction with radiation, namely, multiple light scattering within the filter, the filter loading effect, and the particle scattering correction (Liousse et al., 1993; Bond et al., 1999; Weingartner et al., 2003; Schmid et al., 2006; Collaud Coen et al., 2010; Lack et al., 2014). Numerous algorithms have been developed and tested for correcting these artifacts, yet there are corrections and dependencies that still need to be tackled, such as the cross-sensitivity to scattering of the filter tape, which can highly influence the absorption coefficient measurements, especially under high single scattering albedo scenarios (Weingartner et al., 2003; Arnott et al., 2005; Schmid et al., 2006; Virkkula et al., 2007; Collaud Coen et al., 2010; Virkkula et al., 2015). Off-line in-house made filter based polar photometers, which measure both transmittance and reflectance, provide much more accurate measurements than on-line photometers, mainly as a result of the improved correction schemes that can be used and the lower measurement error, but can not be used for continuous monitoring due to its off-line based working principle. These off-line polar photometers are deployed at specialized research centers, such as the MWAA (multi-wavelength absorption analyzer) deployed at University of Genoa (Massabò et al., 2013) and the PP_UniMI polar photometer deployed at University of Milan (Vecchi et al., 2014; Bernardoni et al., 2017). Additionally, on-line instruments, given their relatively low unattended operation and possibility of providing real-time data, are deployed in international networks such as GAW and ACTRIS. The most common on-line filter-based instruments are the particle soot absorption Photometer (PSAP; Bond et al., 1999), the continuous light absorption photometer (CLAP; Ogren et al., 2017), the multi-angle absorption photometer (MAAP, Model 5012, Thermo, Inc., USA; Petzold and Schönlinner, 2004), and the aethalometer (Hansen et al., 1984), in particular the dual-spot multi-wavelength Aethalometer (AE33; Drinovec et al., 2015).

Currently, due to the limitations and assumptions described above, no reference technique for measuring in-situ near-real time aerosol particles light absorption is yet available in international networks (Petzold et al., 2013; Lack et al., 2014). As aforementioned, from remote sensing measurements with LIDARs and ceilometers, in combination with sun-sky photometers the vertical profiles of the absorption coefficient and absorption-related variables such as the absorption ångström exponent and single scattering albedo could be retrieved

(Schuster et al., 2016; Andrews et al., 2017) However, these retrieved properties still present a large uncertainty associated to the multiple assumptions used by the algorithms.

2.2 Aerosol particles distribution and optical properties

The major current topics of analysis with regards to the influence of the aerosol particles on the radiative forcing are: i) the accurate characterization of both the horizontal and vertical distribution of aerosol particles and their evolution and transformation processes through the atmosphere, and ii) the assessment of the absorption properties and concentrations of the most absorbing aerosol species, i.e. BC, BrC and mineral dust.

As described in **Chapter 1**, the aerosol particles concentration and distribution on the atmosphere depends on the location of the emission sources, the meteorological dynamics, and their life-spam before being transformed or deposited back on the surface. The higher aerosol concentrations are expected to take place close to the emission sources, such as in urban and industrial areas for anthropogenic aerosols like BC, or the arid and semi-arid areas for mineral dust particles, as well as in regions where the local orography and meteorological patterns favour their accumulation over time. The freshly emitted particles tend to be deposited back into the surface, either through dry-deposition, mainly by Brownian deposition for the finer mode and by gravitational forces for the coarse mode particles, or through wet-deposition processes, such as wet-scavenging. The remaining aerosol particles get mixed in the atmosphere and follow the local meteorological patterns, which enables for local and regional transport. During this transport, aerosol particles undergo transformation processes associated to the interaction with other aerosol species and reactive gaseous species as well as photo-oxidation processes, that ultimately can act as sources or sinks for new particle formation, thus highly modulating the aerosol particle composition and concentration values. Furthermore, under favouring meteorological dynamic conditions, and if the particles life-spam is large enough, this particles can be transported for long distances. Indeed, the average life-spam of fine particles is estimated to be around 1 week, and consequently aerosol particles from anthropogenic emissions are also measured in remote sites, such as the Arctic and the Antarctic (Shaw, 1980; Asmi et al., 2010; Virkkula et al., 2022). The aerosol particles vertical distribution in the atmosphere mainly depends on the emission pathways and the meteorological dynamics, since the emission at a given height can favour the transport of aerosols over different atmospheric layers. For example: volcanic eruptions can emit aerosol particles up to the stratosphere, strong mineral dust emission episodes lift the particles high above ground up to heights of around 5 km or more a.g.l. (Su et al., 2015), especially under convective episodes when particles can be lifted at higher layers (Bukowski and Heever, 2021; Roberts and Knippertz, 2012), and certain recirculation patterns create stratified polluted layers in the atmosphere, affecting the vertical structure of the aerosol particle distribution at a more regional scale (Pérez et al., 2004; Gangoiti et al., 2001).

Currently, the main objective of the scientific community is to improve the quality of spatial, both horizontally and vertically, and temporal measurements of the aerosol particles, and study the transformation processes and their ultimate influence on the optical properties. Thus, providing an extensive analysis of these subjects is crucial for better integrating the aerosol particles on climate models and therefore obtaining a more accurate output about their role on the radiative forcing. In particular, as already stated, it is of utter relevance a better characterization of the aerosol particles that are associated with a greater effect on warming the atmosphere, namely BC, BrC and mineral dust (cf. Sect. 1.4).

A comprehensive review of BC particles can be found in the literature (e.g. Moosmüller et al., 2009; Bond et al., 2013), where the BC formation processes, its physico-chemical properties as well as the effects and pathways through which they influence the Earth's climate are described in great detail. It is of particular interest the mass absorption cross-section (MAC) of pure BC particles, which has been estimated to have a theoretical value of 7.5 $\mathrm{m^2 g^{-1}}$ at 550 nm (Bond and Bergstrom, 2006). However, this value does not correspond with experimental measurements of MAC for ambient BC. In fact, ambient BC MAC presents a great variability with an average value in Europe of around 10 $\mathrm{m^2 g^{-1}}$ at 637 nm, i.e. $\sim$ 11.58 $\mathrm{m^2 g^{-1}}$ at 550 nm assuming an absorption ångström exponent of 1, higher than the theoretical value (Zanatta et al., 2016). This discrepancy is mainly due to the low probability of measuring pure BC particles in the atmosphere, where it is typically mixed with other aerosol particles that have the ability to modify the BC absorption cross-section. The pathways by which the BC can be modified upon mixing are: i) an external mixing with other less absorbing carbonaceous aerosols that also absorb light radiation, i.e. BrC, causing an apparent enhance of the BC absorption, and ii) BC is internally mixed with either absorbing or non-absorbing particles that can reduce/increase the path length of the radiation interacting with the BC particles, thus reducing/increasing the absorption by the BC cores (Bond and Bergstrom, 2006; Lack and Cappa, 2010). Overall, the absorption enhancement produced by the mixing of BC with other aerosol particles assumed in climate models is around 1.5. However, experimental studies have shown it varies from almost no enhancement to increasing the absorption by a factor of 2 or even 3 (Cappa et al., 2019). Given the importance of the absorption of BC, the study of this enhancement and the reasons for its large variation is of great interest. The increase of this parameter is mainly due to increases in the amount of mixing material available, the relative proportion of different organic aerosol species, and their mass absorption efficiencies, as well as the ageing state of the aerosol particles (e.g. Liu et al., 2015b; Zhang et al., 2018; Cappa et al., 2019; Zhang et al., 2020).

Among the aerosol particles that can be externally and internally mixed with BC, the BrC compounds are currently the focus of many studies due to the high absorption efficiencies they can present at the visible and short-UV wavelengths, thus potentially producing a positive effect on the radiative forcing of the OA. The main uncertainties associated to the radiative effect of BrC are mainly associated to the numerous formation pathways, which result in: i) a large variety of compounds with different chemical composition and structures, in contrast

to the more simple chemical structure of BC particles, therefore presenting a larger range of absorption efficiencies, and ii) a larger uncertainty in correctly assessing the BrC global concentration. An extensive review is presented in Laskin et al. (2015), which shows that the absorption efficiency of BrC is highly correlated to the carbon sp^2 hybridization, with increasing absorption with increasing hybridization. Moreover, it also shows that if SOA particles are formed in the presence of nitrogen compounds, higher absorption efficiencies are measured, especially at the visible range of the electromagnetic spectrum compared to BrC and SOA particles not formed in nitrogen-rich conditions (Updyke et al., 2012).

The radiative forcing of mineral dust particles has historically been estimated to be negative, i.e. to cool the atmosphere, however, recent studies have shown the potential for mineral dust to warm the atmosphere (e.g. Kok et al., 2017; Di Biagio et al., 2020; Li et al., 2021). This potential shift in the sign of the radiative forcing is mainly due to underestimation in the models of the coarse mode of the particle size distribution of the atmospheric mineral dust, and to an improved characterization of the refractive index of the mineralogical composition for each source emitting areas. By constraining the aerosol particle size distribution of the mineral dust particles by coupling experimental measurements from instrumented flights and the total load of mineral dust concentration from satellite measurements, it has been shown that the total mass and the coarse mode of mineral dust particles was higher than expected, mainly due to an underestimation of both the emission of coarse particles in the source areas and the ability of these coarser particles to remain in the atmosphere for longer periods of time. The main effect of this underestimation is to decrease the cooling effect of mineral dust in the shortwave spectrum and increase the warming effect in the longwave part of the spectrum, which makes the overall effect to be substantially less cooling than expected, with the possibility of being a net warmer (e.g. Kok et al., 2017; Ryder et al., 2018; Di Biagio et al., 2020; Adebiyi and Kok, 2020; Kok et al., 2021a; Kok et al., 2021b; Li et al., 2021). In addition to the coarse mode underestimation, there are also other aspects limiting the correct representation of the mineral dust cycle by the models, mainly associated to the particle shape, and to the refractive index assumed in the models for mineral dust (Di Biagio et al., 2020; Huang et al., 2020). Indeed, Li et al. (2021) shows that by assuming variations in the shape of the particles and the mineral dust mineralogical composition, i.e. its asphericity shape and the ratio of iron oxides that they contain, there is a variation in the complex refractive index which heavily influences the direct radiative effect of mineral particles at the top of the atmosphere. This demonstrates the relevance for an accurate determination of the optical properties of freshly emitted mineral dust particles, and of their variations among the source regions, and in distant regions after being transported, mixed and transformed over time. With this aim, there are multiple studies that have studied the optical properties on laboratory chambers resuspending mineral dust particles from soil samples collected from different source regions (e.g. Sokolik and Toon, 1999; Lafon et al., 2006). However, in-situ measurements of mineral dust particles freshly emitted in the source regions, despite the importance of accurately measuring the optical properties of the emitted dust particles, are more scarce (e.g. SAMUUM-1; Müller et al., 2009), and therefore more measuring campaigns are required. In this context, numerous campaigns are currently being

performed throughout several mineral dust particle source regions around the globe, such as the Sahara, Iceland, Mojave and Jordan under the FRAGMENT project (see `https://cordis.europa.eu/project/rcn/214076/factsheet/en`). Mineral dust particles after long-range transport are commonly measured, as done by Caribbean measuring stations and European monitoring networks, therefore allowing for the measurement of the optical properties at the receptor sites when mineral dust outbreaks reach these areas (e.g. Engelstaedter et al., 2006; Collaud Coen et al., 2010; Ealo et al., 2016).

2.2.1 Previous studies in the NE of Spain

There are multiple studies describing the aerosol particle composition and properties over the Iberian Peninsula and over the NE of Spain (e.g. Querol et al., 1998; Querol et al., 2001; Rodrıguez et al., 2002; Pey et al., 2009; Pandolfi et al., 2011; Pandolfi et al., 2016; Via et al., 2021; Veld et al., 2021). This thorough analysis has been performed both via intensive measurement campaigns in regions of high interest and through continuous monitoring of the aerosol particles at three measurement sites in NE Spain, representing different backgrounds over more than a decade (more info in **Chapter 4**).

The area of the NE of Spain in this thesis is located in the western side of the Mediterranean sea, and therefore the aerosols particles patterns follows those typically from this area, namely high pressure systems promoting stagnant conditions during the winter months and sea-breezes and local/regional recirculation patterns during the summer months with sparse precipitation events (cf. **Chapter 4**). With regards to the optical properties of the aerosol particles over this area, previous studies have provided an analysis of the evolution of the extensive and some intensive optical properties during the year as well as during the most relevant meteorological scenarios (e.g. Pandolfi et al., 2011; Pandolfi et al., 2013; Pandolfi et al., 2014; Pandolfi et al., 2018; Ripoll et al., 2014; Ealo et al., 2016; Ealo et al., 2018; Titos et al., 2019).

These studies present a comprehensive analysis of the spatial variations between the different backgrounds over the NE of Spain. Indeed, Pandolfi et al. (2014) provided a climatology analysis of the optical extensive and intensive properties at a regional and a mountain-top background separating by seasons and the different meteorological scenarios, whereas Ripoll et al. (2014), Ripoll et al. (2015a) and Ripoll et al. (2015b) focused the analysis on the chemical composition and the different sources of aerosol particles. These studies reflected the relevance of the regional recirculation patterns and the outbreaks of mineral dust from North Africa as the main drivers of increasing PM concentrations and consequently of the extensive optical properties. Moreover, Ealo et al. (2018) analysed the contribution of the different aerosol sources to the absorption and scattering coefficients and cross-sections through a positive matrix factorization approach, and thereafter reconstructed the scattering and absorption by using the long dataset available with the aerosol sources to perform a trend analysis of the evolution of these variables. In addition, Ealo et al. (2016), successfully performed the approach proposed by Collaud Coen et al. (2004) for the detection of Saharan dust outbreaks over Europe, as well as the aethalometer model proposed by

Sandradewi et al. (2008) for biomass burning detection, and measured for these type of events the optical parameters over the area of study. These previous studies have focused on the study of the aerosol particles on the surface, and for the first time this thesis presents the vertical profiles via instrumented flights of the physico-chemical properties over the NE of Spain. In addition, this thesis presents the first analysis on the effects that absorbing OA particles, i.e. BrC, and other organic and inorganic aerosols have upon mixing with BC on the absorption enhancement of BC particles. This analysis is of special interest given the large regional heterogeneity of aerosol particles properties reported in previous studies in NE Spain, and the ability to characterize the specific aerosol optical variables at backgrounds with distinct aerosol particles properties.

3

Objectives and Structure

The main objective of this thesis is to improve the knowledge about the optical properties of atmospheric aerosols as a function of the multiple aerosol sources, the ageing state of particles, and the transport and recirculation patterns that particles undergo in NE Spain. This objective is addressed through the integration of several studies that present: i) methodological improvements for the acquisition of crucial measurements of the aerosol optical properties, ii) the horizontal and vertical variations of aerosols optical properties under different atmospheric scenarios both through continuous measurements in different environments and intensive campaigns with aircrafts, iii) the influence on the absorption enhancement of the BC particles due to its mixing with other particles under different environments with aerosols with different physico-chemical properties, and iv) the characterization of the optical properties of mineral dust particles for the most relevant source of dust particles in the Mediterranean, the Sahara.

3.1 Specific research objectives

To achieve the objective mentioned above, the following specific objectives have been set:

1. To improve the determination of the absorption coefficients from filter-based measurements by determining the spectral dependence and the cross-sensitivity to scattering of the most crucial parameter for deriving the absorption coefficients from the Aethalometer AE33.

2. To study the horizontal and vertical distribution and variability of the physico-chemical properties of atmospheric particles over the NE of Spain in the Western Mediterranean Basin. Especially for high aerosol-loaded episodes caused by meteorological recirculation patterns and Saharan dust outbreaks scenarios during summer.

3. To characterize the effect that the mixing of BC with other light absorbing carbonaceous aerosols and non-refractory material has on the enhancement of the absorption from the BC particles at an urban and a regional background sites in NE Spain.

4. To analyze the optical and physical properties of mineral dust particles over the Saharan desert, the most important emission source areas for the Mediterranean, Europe and the Earth. This objective was achieved by means of an intensive measurement campaign performed in these dust source regions.

3.2 Structure of the thesis

This doctoral thesis is presented in the form of a compendium of three publications. These publications appear in two high-impact open access journals in the scientific field of atmospheric physics from the *European Geoscience Union*, namely *Atmospheric Chemistry and Physics* and *Atmospheric Measurement Techniques*.

The thesis manuscript is structured in four parts, as follows:

Part I: Introduction. It is structured in 3 chapters: an *Introduction* chapter (**Chapter 1**) that establishes the fundamentals of the atmospheric aerosol particles research; then **Chapter 2** shows a *State of the Art Review*, where the current knowledge gaps and the approaches proposed by the academia with regards to the description of the aerosol particles optical properties, and in particular in highly heterogeneous atmospheres, are briefly reviewed. Finally, the current chapter– *Objectives and Structure*, **Chapter 3**), where the main objectives of the thesis and its structure are well-defined.

Part II: Methodology. The methodology part is presented in **Chapter 4**, and it reports the main characteristics of the areas of study, as well as the instrumentation, the data analysis and data treatment used in this thesis. In addition, a more in-depth description of the methodology for each publication can be found in its corresponding section.

Part III: Results. This section is divided into four chapters that tackle the specific objectives of this thesis. **Chapter 5** presents the characterization and relationships of a sensitive parameter, the multiple scattering, for accurately measuring the absorption coefficient and BC concentration values with a filter-based instrument at different background sites that present varying aerosol composition and are subject to different scenarios. **Chapter 6** tackles the second objective by characterizing the horizontal and vertical variability of the aerosol particles and its physico-chemical and optical properties over the NE of Spain by means of air-borne instrumentation and in-situ measurements in monitoring stations, as well as the impact of Saharan mineral dust outbreaks. Then, **Chapter 7** studies the absorption enhancement on the main area of study at an urban and a regional site produced by the mixing of the BC particles with other LACs and non-refractory materials. It explores the absorption enhancement seasonal variations and trends at the different sites and performs a sensitivity study that establishes the potential contributions by the different mixing states; additionally, it analyzes the dependency with the amount of material available for mixing, the different sources, and the ageing state of the particles. Finally, **Chapter 8** describes the optical properties at a mineral dust source emission area and studies the dependencies of these properties with the strength of the emission processes, the impact of other sources of aerosols,

and the differences associated to varying soil compositions. **Chapter 5**, **6**, and **7** results correspond to three publications in peer-reviewed journals (Yus-Díez et al., 2021; Yus-Díez et al., 2020; Yus-díez et al., 2022), whereas **Chapter 8** is an adaptation of a publication currently in preparation.

Part IV: Discussion and conclusion. This part is organized into a *Discussion* chapter (**Chapter 9**) that presents a summary and discussion of the results, and a *Conclusion* chapter **Chapter 10** which outlines the main results from this thesis and expands on further research to be explored to resolve some gaps of knowledge presented in this work.

Part II
Methodology

4

METHODOLOGY

This chapter provides an overview of the different areas of study, the instrumentation deployed therein, the most important algorithms and software used, as well as a description of the variables derived from the measurements. A more thorough description of the specific methodology used on each study presented in this thesis can be found in its corresponding publication methodology section.

4.1 Areas of study

The measurements have been performed at two distinct areas of study: i) at different background scenarios in the western corner of the Mediterranean basin, specifically in the northeastern part of Iberian Peninsula, and ii) at a mineral dust emission source, namely the northern part of the Saharan desert.

4.1.1 Western Mediterranean Basin

As briefly stated in **Chapters 1** and **2**, the Mediterranean basin presents a heterogeneous spatial and temporal distribution of aerosol particles, with multiple sources and aerosol species, as well as a large array of complex processes resulting in a large variability of the optical properties of these particles. With the aim of characterizing the aerosol particles properties over this region, the measurements were performed over an area in the Western Mediterranean Basin (WMB), on the northeastern corner of the Iberian Peninsula (Fig. 4.1).

The northeastern corner of the Iberian Peninsula is characterized by a complex topography, with the most relevant features being the Pyrenees to the North, the Mediterranean coast going from North-East to South-West, and two consecutive mountain ranges parallel to the coast, the Litoral and Pre-Litoral mountain ranges. Three main river basins cross these mountain ranges, namely the Bessòs, the Llobregat, and the Ebro/Ebre river, which given the position of the mountain ranges, result in the presence of numerous depressions (cf. Fig. 4.2). Under the adequate meteorological conditions, this arrangement of valleys and mountain ranges favours the advection of pollutants from the major urban areas near the coast upstream towards the inner depressions, favouring the accumulation, recirculation and physico-chemical transformation of aerosol particles.

Figure 4.1: Topographic map of Southern Europe, the Mediterranean Basin and North Africa. The dots represent the location of the measurement sites from the monitoring network operated by the EGAR group (IDAEA-CSIC) in northeastern Spain, and the intensive measurement campaign in the Saharan outskirts. *Topographic map adapted from the online geoportal tool from the French national geographic institute (IGN).*

The climatology of the WMB region is characterized by warm summers and temperate winters with irregular and scarce precipitation rates, especially in summer. In particular, the Azores high pressure system modulates the overall synoptic meteorology of the Iberian Peninsula (IP): in winter it is located at lower latitude, which allows low-pressure systems and its associated fronts coming from the N Atlantic to pass over the IP; whereas in summer the anticyclonic system intensifies and moves toward higher latitudes inducing strong atmospheric stagnant conditions over the IP. As aforementioned, these conditions result in an accumulation and ageing of pollutants and aerosol particles (e.g. Millán et al., 1997; Gangoiti et al., 2001; Millán et al., 2002; Rodrıguez et al., 2002; Pérez et al., 2004; Yus-Díez et al., 2020). In addition, Saharan dust outbreaks frequently affect the Iberian Peninsula, mostly in spring/summer, with the main meteorological patterns causing the outbreaks varying with the seasons, as described by Rodrıguez et al. (2001) and Escudero et al. (2005). Furthermore, the WMB is also heavily impacted by wildfire aerosol particles, both from local wildfires or from the advection of plumes from other parts of the IP and even North America. These wildfires have the ability to persist for several days and emit large amounts of BC, BrC, primary organic aerosols and precursors of secondary aerosols (Faustini et al., 2015). Finally, the complex atmospheric patterns, scarce precipitation and high exposure to solar radiation enhance photo-chemical reactions that promote high levels of secondary aerosols and ozone at background and rural areas with high levels of precursors (Rodrıguez et al., 2002; Pérez et al., 2004; Querol et al., 2016; Querol et al., 2017).

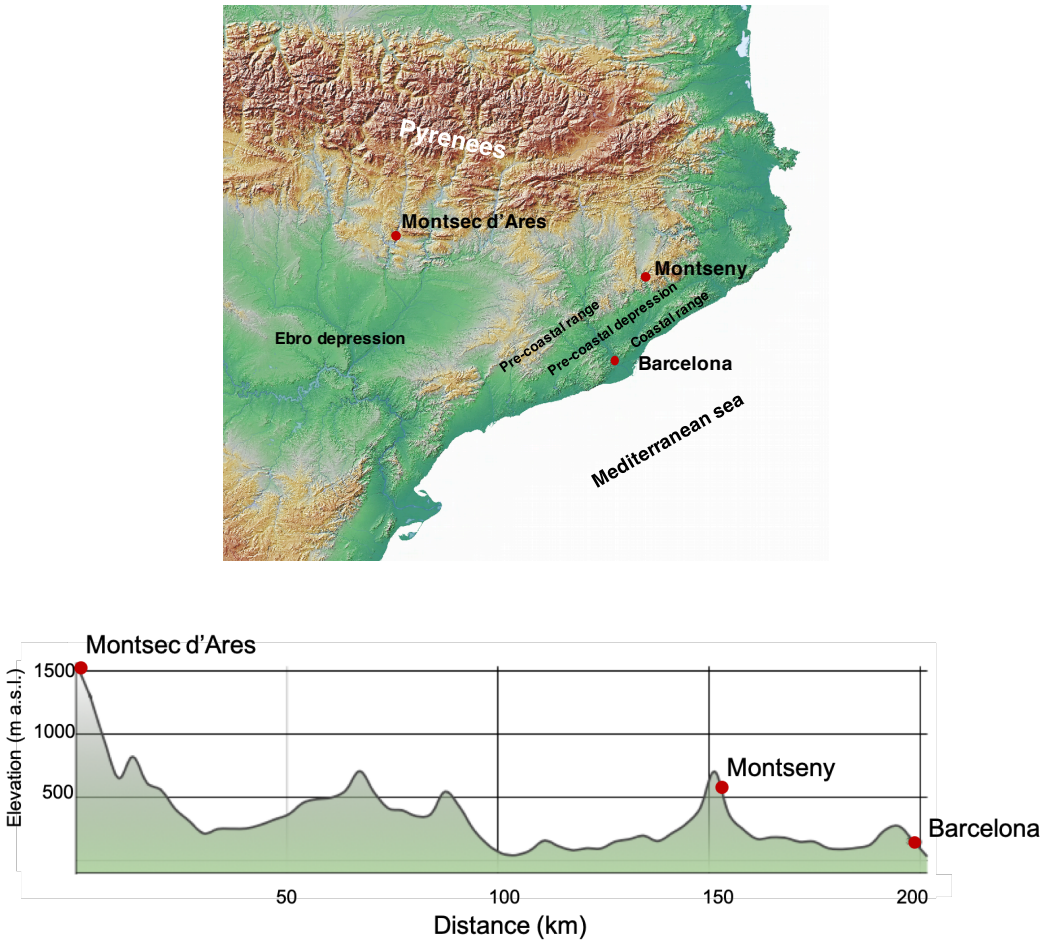

Figure 4.2: Topographic map of a) the main area of study in the NE of Spain, and b) a profile of the vertical disposition of the monitoring station and the main geographical features. *Source: Topographic map adapted from the Cartography Service of the Autonomous University of Madrid (UAM).*

Two distinct methodological approaches were used for obtaining the required measurements for the characterization of the aerosol particles over this area: longer datasets from monitoring stations, and an intensive measurement campaign during 2015 within the PRISMA project (CGL2012-39623-C02/00).

Monitoring stations

The network of monitoring station is operated in Catalunya, in the northeastern part of the Iberian Peninsula, by the EGAR group (IDAEA-CSIC) in collaboration with the Direcció General de Qualitat de Ambiental (DGQA) from the Generalitat de Catalunya, and provides continuous measurements of atmospheric aerosols and gaseous precursors. The measurement network captures the principal background scenarios most relevant among the atmospheric aerosol community: an urban background station, in Barcelona; a regional background station, in Montseny; and a mountain site, in Montsec d'Ares (Fig. 4.2).

i) **Barcelona - Palau Reial** urban background station (**BCN**) is located at the Institute of Environmental Assessment and Water Research (IDAEA-CSIC) within the Barcelona metropolitan area of nearly 4.5 million inhabitants (Fig. 4.2). It is placed around 200 m from one of the most traffic concurred avenues of the city, and at an altitude of 80 m a.s.l. at a distance of about 5 km from the coast. The main aerosol particles affecting the site are those related to the traffic emissions, as well as the industries, the Barcelona harbour, and some biomass burning from nearby agriculture fields in the Llobregat valley.

ii) **Montseny** regional background station (**MSY**) is located in a rural area in the Montseny Natural Park. MSY station is located in a hilly and densely forested area, at an altitude of around 720 m a.s.l., 50 km away to the N–NE of the Barcelona metropolitan area, and 25 km from the coastline (Fig. 4.2). Due to the isolated location of the station on a rural forested area, local biogenic and biomass burning are the main sources of aerosol particles. In addition, the atmospherics dynamics under the common high pressure system produce a breeze pattern that advects the pollutants from the coast, and more densely populated areas, up-valley to the station, that favours aerosol particles to become more oxidized, and given the availability of precursors and the high levels of insolation, the formation of secondary aerosol particles is enhanced.

iii) **Montsec d'Ares** continental/mountain-top background station (**MSA**) is located in a remote high-altitude emplacement in the southern side of the Pre-Pyrenees at the Montsec d'Ares Mountain Range (Fig. 4.2). It is at an altitude of 1570 m a.s.l. and at a distance of around 140 km to the NW of Barcelona and 140 km to the WNW of MSY. The site is characterized by an overall aerosol depleted atmosphere, with the station frequently located in the free atmosphere over the planetary boundary layer (PBL), and exposed to North Atlantic advections during large parts of the year, especially during winter. During the warmer months of the year, a daily cycle with the mountain katabatic/anabatic winds and a higher PBL favours the advection of aerosols from the valley below during midday. Furthermore, given its exposed location, it is highly influenced by the regular Saharan mineral dust outbreaks, as well as by close-by and long-range transport of wildfires smoke plumes.

Intensive measurement campaign

An intensive measurement campaign was performed during the summers of 2015 with the aim of measuring the vertical and horizontal distribution of the aerosol particles, with special interest in their physical and optical properties to, ultimately, assess the regional radiative forcing caused by the tropospheric aerosols in the WMB. This campaign was performed by the EGAR group within the PRISMA project (PRISMA: Aerosol optical properties and radiative forcing in the western Mediterranean as a function of chemical composition and sources), with remote and in-situ surface measurements performed at MSY and MSA monitoring stations, and additional airborne measurements performed with an aircraft between around 0.5 and 3.5 km a.s.l.

The objective was to characterize stacked vertical layers of aerosol particles that formed as a consequence of the recirculation pattern that takes place in the area of study during summer under the presence of high pressure systems. As aforementioned, recirculation pattern is a combination of atmospheric process, where initially the sea breeze transports the aerosol particles from the coast up-valley, up to the mountain tops, where aerosol particles are injected into the general circulation with westerly winds. Then, when this aerosol particles arrive over the coast, a combination of subsidence processes and surface winds carry these aerosols downwards and south towards until the recirculation process starts again (Gangoiti et al., 2001). In addition, during this period of the year, it is frequent the outbreaks of mineral dust aerosol masses from the Sahara. As a consequence, multiple layers of aerosols particles with different composition, ageing stages, and thus optical properties can be found in the troposphere.

4.1.2 Mineral dust emission area

As commented in **Chapters 1** and **2**, the North African arid and semi-arid regions represent the main sources of emission of mineral dust into the atmosphere, with around a 50% of the global emission load. Given its wide spatial distribution, not negligible differences in the mineralogical composition of dust particles can be found between the different emission areas in North Africa. Of these regions, the ones which affect the Western Mediterranean Basin the most are those located in the western part of the Sahara (Escudero et al., 2005).

In-situ dust measurements were performed in a mineral dust emission area in SE Morocco, at the border between the southern foothills of the Atlas mountain range and the Saharan desert in the Drâa basin. This area records very low precipitation rates (below 250 mm yr^{-1}) and very high temperatures during summer and autumn (median values between 25 and 38 $^{\circ}$C). In addition to the scarce precipitation, the Drâa river in the area of study was dried as a consequence of the construction upstream of El Mansour Eddahbi dam. However, the mountain range to the north, the Jbel Hassan Brahim range, enables the formation of strong convective storms, which create flash floods over the basin and transport high loads of sediments through the torrents or *wadis*, with the ability to also flood larger parts of the flooding plain.

The measurement site is located in the L'Bour area, which is characterized by a small terminal depression close to the the Drâa dry-river bed (see Fig. 4.3). L'Bour site is characterized by a hard packed surface with crusts as a result of aeolian erosion and paleo-sediments, as well as a surrounding of shallow sand dunes (a height < 1 m). Moreover, small depressions such as the dry-lake Iriki or *erg* Smar present large sediment concentrations. Dunes are concentrated in flat areas near the depressions where dust erosion transports the sand and sediments to, where they can be entrapped by the sporadic vegetation, mostly shrub, such a Erg Chigaga (cf. Fig. 4.3). The location of the measurement was chosen due to the prevalence of south-westerly winds over the area. This wind direction maximizes the probability of measuring processes that emit dust particles and minimizes the potential influence of anthropogenic aerosols from the nearby villages upstream to the E (cf. Fig. 4.3).

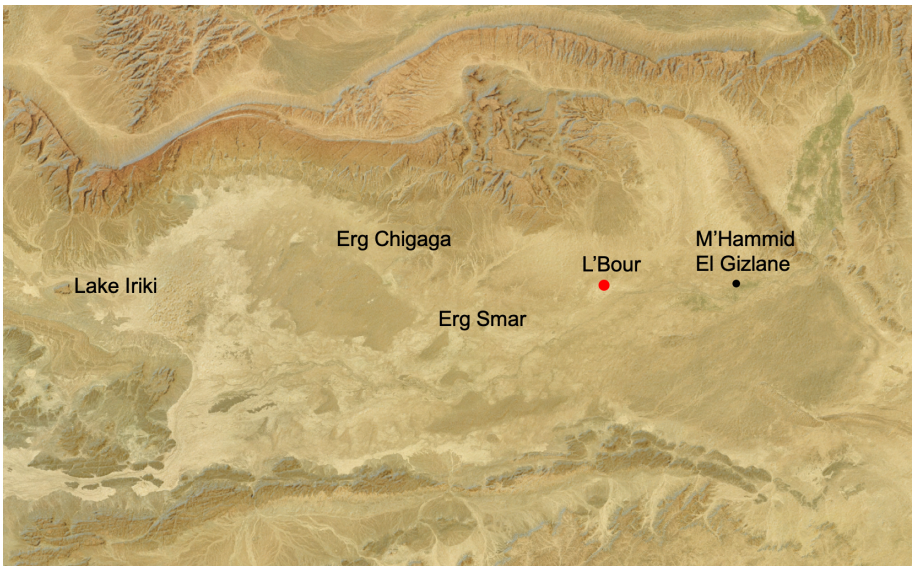

Figure 4.3: Area of study around the L'Bour measurement site in the Sahara desert, SE Morocco. The main geographic features area marked for clarification purposes: the dry-lake Iriki, the dune areas of Erg Chigaga and Smar, and the town of M'Hammid el Gizlane. *Source: Topographic map adapted from the Cartography Service of the Autonomous University of Madrid (UAM).*

4.2 Instrumentation

Throughout this thesis several instruments deployed at long-term monitoring supersites and during intensive measurement campaigns have collected the data needed for performing the required analysis. This section provides an overall description of the instruments and their working principles arranged by the variables and parameters that they provide. An overview of the instruments for obtaining the required variables is shown in Table 4.1.

4.2.1 Meteorological measurements

During this study, several meteorological parameters were used with the aim of improving the characterization of the aerosol particles in the atmosphere, such as: temperature, potential temperature, relative humidity, wind speed and direction, etc.

In **Chapter 6**, vertical profiles of the temperature (T) and relative humidity (RH) inlet sample air were measured with a Rotronic HL-RC-B - Wireless logger (ROTRONIC AG, Switzerland). In addition, a Vaisala DRYCAP dew-point transmitter (model DMT143, Vaisala, Finland) was used to measure dew point and water volume concentration of outdoor ambient air. Ambient pressure (P) data was obtained by means of a Kestrel 4000 anemometer (Kestrel Meters, USA). Potential temperature (θ) was obtained by combining the temperature (T) and pressure (P), from the Rotronic and Krestel measurements, respectively,

$$\theta = \mathrm{T} \cdot \left(\frac{\mathrm{P}_0}{\mathrm{P}}\right)^{R/c_p},$$

Table 4.1: Summary of the multiple instrumentation used throughout this thesis, both at continuous monitoring stations and intensive measurement campaigns in NE of Spain and the Sahara desert.

Parameters	Instrument	Manufacturer and model	Specifications
Meteorological	Meteorological data	Rotronic HL-RC-B	T, RH; wireless logger
	Dew-point transmitter	Vaisala Drycap DMT143	
	Anemometer	Kestrel 4000	P
	Aspirated shield temperature sensors	Campbell Scientific, 43347 RTD	high-res. T
	2-D sonic anemometers	Campbell Scientific, WINDSONIC4-L	high-res. wd, ws
Particle number concentration	Water condensation particle counter	TSI WCPC-3783	N_x
		TSI NWCPC-3788	N_x
Particle mass concentration	Optical particle counter	GRIMM 1.108.8.80	PM_x
		GRIMM 1.129-Sky-OPC	PM_x
		Digitel DH-808	PM_x
	Offline gravimetry	MCV-CAV-A	PM_x
		MCV-CAV-A/M-S	PM_x
Particle size distribution	Optical particle counter	Palas, FIDAS 200S	N_x, $0.2 < x < 18.8\mu m$
On-line chemical composition	OC-EC analyzer	Sunset Semi-Continuous OC-EC field analyzer	OC and EC conc.
	Aerosol chemical speciation monitor	Aerodyne, Q-ACSM	OA and SIA conc.
Absorption and BC concentration	Multi-Angle absorption photometer	Thermo Scientific, MAAP 5012	637 nm
		Università degli studi de Milano, PP_UniMI	405, 532, 635, 780 nm
	Multi-wavelength aethalometer	Magee Scientific, AE33	370, 470, 520, 590, 660, 880, 950 nm
Scattering	Integrating nephelometer	Ecotech, Aurora 3000	450, 525, 635 nm; 2 angles: 0 and 180 °
		Ecotech, Aurora 4000	450, 525, 635 nm; up to 17 angles (0-180 °)
Remote sensing	Ceilometer	Lufft, CHM15k-Nimbus	0.5-15 km range
	Sun-sky photometer	Cimel electronique, Aeronet CE-318	370, 380, 440, 500, 675, 870, 940, 1020 nm

where P_0 is the pressure at the surface level, R is the ideal gas constant of air, and and c_p is the specific heat capacity of air.

In addition, in **Chapter 8** the temperature (T), the wind speed (ws) and the wind direction (wd) were used for the classification of different events. The temperature was measured with aspirated shield temperature sensors (fan-aspirated shield model and a temperature probe model 43347 RTD, Campbell Scientific). The wind speed was measured with 2-D sonic anemometers (model WINDSONIC4-L, Campbell Scientifics, USA). By combining both the

wind and temperature measurements at several heights, it was possible to obtain the friction velocity (u^*) using the law of the wall methodology.

4.2.2 Particle number size distribution and total concentration

Total particle number concentration of submicrometric aerosols was measured for **Chapter 6** with a laminar flow water-based condensation particle counter (TSI WCPC, model 3783; Hakala et al., 2013), and a nano version which was used for the airborne measurements (TSI N-WCPC, model 3788; Kupc et al., 2013).

The operation principle of both WCPC models (3783 and 3788) is based on the activation of the sampled particles by condensation of a supersaturated working fluid vapor (water) on the surface of the aerosol particles so that the they are grown to optically detectable diameters (Hering and Stolzenburg, 2005). The aerosol particles reach a supersaturation region, which is produced by the disposal of two consecutive sections, a conditioner tube where the air sample is cooled, and a heated growth section where, as the mass diffusivity of water is faster than the thermal diffusivity of air, the particles size grows as water vapours condenses on the particle surface. The particles grow to the the desired diameter and are focused through a nozzle into an optical chamber where a laser beam focuses light onto the particles, and the resulting signal corresponding to the count of a particle is measured by a photodetector (Hakala et al., 2013).The 3783 WCPC model was operated at a flow mode of $3\ \mathrm{L\ min^{-1}}$ and a time resolution of 5 min, whereas the airborne 3788 N-WCPC model measured at 1 s resolution with flow rate of $0.6\ \mathrm{L\ min^{-1}}$. The 3783 WCPC instrument provides size range with a lower limit down to $7\ \mathrm{nm}$ and measured concentration range up to $2.5 \cdot 10^5\ \mathrm{cm^{-3}}$, whereas the 3788 N-WCPC lower size limit was down to $2.5\ \mathrm{nm}$ and measured concentration up to $4 \cdot 10^5\ \mathrm{cm^{-3}}$.

Particle number size distribution (PNSD) measurements for particles with particles diameters between 0.2 and 17.8 $\mu\mathrm{m}$ were obtained for **Chapter 8** with a fine dust aerosol spectrometer (FIDAS 200S, Palas Gmbh).

The FIDAS 200S has incorporated an in-house meteorology station, an inlet system composed of a specific sampling head (Sigma-2) and a sampling tube with an Intelligent Aerosol Drying System (IADS). The dried air sampled is introduced into an optical chamber equipped with a LED light source where the light scattering of the particles enables the measurement of the number of particles for different particle diameter size ranges. During **Chapter 8**, the FIDAS PNSD measurements were performed for 61 bins in an optical diameter range of 0.2-17.8 $\mu\mathrm{m}$, a time resolution of 120 s, and an inlet flow rate of around 0.3 $\mathrm{m^3\ h^{-1}}$.

Dust total particle number concentration was determined from the FIDAS PNSD by integrating all the measured particles for all the bins up to the the desired size cut-off, x,

$$\mathrm{N_x} = \int_{0.2}^{\mathrm{r_x}} \mathrm{N(r)dr}, \tag{4.1}$$

where $\mathrm{N(r)}$ is the number of particles for each given diameter size bin, and $\mathrm{r_x}$ is the upper limit of the desired size range.

4.2.3 Particle mass concentration

The particle mass concentration measurement used in **Chapters 6**, **7** and **8** were obtained through a combination of gravimetric measurements of offline filters and/or a real time monitors. Both methods report the mass concentration of aerosol particles below a given size cut-off in micrograms per cubic meter ($\mu\mathrm{g\ m^{-3}}$), commonly referred to as $\mathrm{PM_x}$, where x is the size cut-off of the measured particles.

Gravimetric particle mass concentration measurements

For **Chapters 6** and **7**, offline levels of $\mathrm{PM_{2.5}}$ and $\mathrm{PM_{10}}$ were measured via 24-hour filter samples at Barcelona, Montseny and Montsec d'Ares monitoring stations. The instrumentation used consisted of automatized sequential high-volume samplers with different cut-off inlets ($\mathrm{PM_{2.5}}$ and $\mathrm{PM_{10}}$) sampling one filter during 24 hours, every 4 days. The models deployed at the monitoring stations were: a MCV CAV-A model, at Barcelona and Montseny for $\mathrm{PM_{2.5}}$, a DIGITEL DH-80 (DIGITEL inc., Switzerland) at Barcelona and Montseny for $\mathrm{PM_{10}}$, and a MCV CAV-A/M-S model at Montsec d'Ares for $\mathrm{PM_{2.5}}$.

These instruments sample the air particles for the different sizes with a flow-rate of $30\ \mathrm{m^3 h^{-1}}$. The sample is collected on quartz microfiber filters (150 mm diameter, Pallflex 2500 QAT-UP), which are pre-treated to eliminate volatile compounds impurities, and weighted following the EN 12341 standard (CEN, 1999). After sampling, the weight of the filters is obtained following the same procedure, and the PM mass concentration is derived as the difference in weight between the filters before and after sampling.

Real time particle mass concentration

Real time PM mass concentrations measurements have been obtained by comparing and adjusting measurements from optical particle counter (OPC) with offline gravimetric measurements (Gebhart, 1993; McMurry, 2000). For **Chapter 6** two OPC models of the brand GRIMM were used, namely, models GRIMM 1.108.8.80 and GRIMM 1.129-Sky-OPC, hereafter referred to as 1.108 and 1.129 (Grimm, 2000), whereas in **Chapter 8**, PM values of mineral dust were derived from the mineral dust focused OPC from the brand Palas, model FIDAS 200S (Sect. 4.2.2).

These OPC measure the number volume concentrations at different size bins and convert the results to PM mass concentrations via an internal instrument software. The aerosol particles are sampled at a constant flow and led into a cell that is designed to allocate just one particle per measurement, where a laser diode beam is focused onto and a photodetector measures the scattered light by the particles. The photodetector associates each scattered light pulse to a single particle, and its intensity to the particle size.

The GRIMM 1.108.8.80 and GRIMM 1.129-Sky-OPC models sample aerosol particles at a flow of $1.2\ \mathrm{L\ min^{-1}}$. The particle size is accurately determined by the modulation of the light intensity of the laser diode through a so-called Multiplex Mode. Since the particle size and concentration is measured at each size bin, an internal software calculates the total PM mass concentration at three different particle sizes, PM_1, $PM_{2.5}$ and PM_{10} by integrating the measurements from all the size bins. Differences between the OPC models are given by the wavelength of the laser diode (780 nm for 1.108 and 655 nm for 1129), the modulation range of the intensity, which determines the number of channel bins (15 vs 31 bins) and its range ($0.3 - 20$ and $0.25 - 32\ \mu\mathrm{m}$).

For the FIDAS 200S model (instrument details commented in Sect. 4.2.2), the $PM_{2.5}$ and PM_{10} mass concentrations of mineral dust were derived by applying the third moment from the particle size distribution obtained with the FIDAS optical particle counter,

$$\mathrm{m_3 = PM_x} = \rho \cdot \frac{\pi}{6} \cdot \int_{0.2}^{\mathrm{r_x}} \mathrm{r^3 N(r) dr}, \tag{4.2}$$

where ρ represents the mineral dust particle density, r_x is the upper diameter size bin limit of the desired size cut-off, r is the mean particle radius, and $N(r)$ is the number of particles measured for each size bin.

4.2.4 Scattering coefficients

Aerosol particle scattering coefficients were measured on-line with multi-wavelength integrating nephelometers. The scattering measurements used through-out the thesis were performed with a multi-wavelength integrating nephelometer Aurora 3000 instruments installed at the three EGAR monitoring station (**Chapters 5** and **6**). The Aurora 3000 was also used during the aircraft measurement campaign performed within the PRISMA project (**Chapter 6**). Moreover, a multi-wavelength integrating polar nephelometer Aurora 4000 (**Chapter 8**) was deployed during the measurement campaigns performed within the FRAGMENT project.

Multi-wavelength Aurora 3000 integrating nephelometer

The Aurora 3000 is a LED-based integrating nephelometer (Ecotech Pty Ltd, Australia) that measures total scattering ($b_{scat,\lambda}$) and hemispheric backscattering ($b_{bscat,\lambda}$) at three wavelengths in the visible spectrum (450, 525 and 635 nm). The working principle of the integrating nephelometer is such that aerosol particles enter a cell where an optical glass light source emits light following a Lambertian illumination function, and the scattering of light produced by the light source interaction with the particles follows a geometrical path formed by mirrors inside the cell, which leads to a photodetector. Due to the truncation errors produced by the geometric limitations of the cell, the angular integration ranges between 10° and 171° cell. To measure the hemispheric backscatter, a shutter attached to the light source moves periodically between two set positions: i) a total scattering position in which the backscatter does not influence the measurements, and ii) a backscatter position, in which

the shutter blocks the light emitted in the forward position, and therefore the measured scattered light by the photodetector corresponds to the hemispheric backscattering.

Calibration and maintenance of the nephelometers was performed following GAW (GAW, 2016) and ACTRIS (ECAC-CAIS, 2022) guidelines. A full calibration using CO_2 as span gas was performed three times per year, while zero adjusts were performed more frequently using internally filtered particle-free air. To avoid the enhancement of light scattering by the condensation of water vapour on the particles surface, the RH threshold was set to less than $40\ \%$ by using a processor-controlled automatic heater inside the Aurora 3000 nephelometer (Fierz-Schmidhauser et al., 2010). Forward scattering coefficients were corrected for the non-ideal illumination of the light source and for the truncation of the sensing volumes following the procedure described in Müller et al. (2011a).

Multi-wavelength Aurora 4000 integrating polar nephelometer

The Aurora 4000 is a LED-based polar integrating nephelometer (Ecotech Pty Ltd, Australia) that measures the total scattering at multiple angles for three wavelengths (450, 525 and 635 nm). The Aurora 4000 working principle is based on the Aurora 3000 with the main difference due to the shutter ability to be set at a larger range of positions. The larger number of possible positions from the shutter (with a maximum of 17), allows for a larger range of angular integrated particle light scattering measurements. In **Chapter 8**, the number of angles was set to 7: 0, 10, 25, 40, 55, 70, 90, 180°.

Due to its use in an intensive measurement campaign, full calibrations with CO_2 as span gas were performed before and after the field measurement campaigns. The RH threshold was also set by using a processor-controlled automatic heater inside the cell to ensure a sampling RH of less than $40\ \%$. Forward (0°) and backward (180°) scattering coefficients were corrected for non-ideal illumination of the light source and for truncation of the cell following the procedure described in Müller et al. (2011a).

4.2.5 Absorption coefficients and Black Carbon concentration

Absorption coefficients and Black Carbon (BC), or equivalent Black Carbon (eBC), measurements were performed using different instruments depending on the necessities of each study. The deployed instruments were: a Dual-Spot Multi-Wavelength Aethalometer, AE33, a Multi-Angle Absorption Photometer, MAAP, and an offline Multi-Angle Photometer, PP_UniMI.

Multi-Wavelength Dual Spot Aethalometer (AE33)

The AE33 aethalometer was used for all the studies included in this thesis: **Chapters 5**, **6**, **7**, and **8**, with a comprehensive and full characterization of this instrument presented in **Chapter 5**. **Chapter 5** reports on the behaviour of an important parameter of the AE33 instrument, the multiple scattering correction factor. A thorough analysis of this correction factor is

fundamental in order to calculate the absorption coefficients from the AE33 aethalometers. Moreover, during the measurements performed with the aircraft, shown in **Chapter 6**, a more compact non-commercial dual-spot Aethalometer (model AE43) was used. This aethalometer was designed and manufactured specifically for aircraft measurements and it is based on the same working principle as the commercial AE33.

The AE33 multi-wavelength aethalometer (model AE33, Magee Scientific, Aerosol d.o.o.; Drinovec et al., 2015) measures the attenuation of light, b_{atn}, passing true an aerosol loaded filter-tape at 7 different wavelengths (370, 470, 520, 590, 660, 880, and 950 nm). Specifically, the new AE33 model is based on the measurement of the transmission of light through two sample spots with different flows and particle loading relative to the reference spot. It then derives the eBC concentration and the attenuation coefficients by applying eqs. (4.3) and (4.4), respectively, following Drinovec et al. (2015):

$$eBC = \frac{S \cdot (\Delta \mathrm{ATN}_1/100)}{F_1(1-\zeta) \cdot \sigma_{abs} \cdot C(1 - k\Delta \mathrm{ATN}_1) \cdot \Delta t}, \tag{4.3}$$

$$b_{atn} = \frac{S \cdot (\Delta \mathrm{ATN}_1/100)}{F_1(1-\zeta) \cdot (1 - k\Delta \mathrm{ATN}_1) \cdot \Delta t}, \tag{4.4}$$

where S is the filter surface area loaded with the sample, F_1 the volumetric flow of the spot 1, ζ the lateral airflow leakage, σ_{abs} the mass-absorption cross-section (also known as MAC), k the loading factor parameter, and $\Delta \mathrm{ATN}_1$ the variation of attenuation of light of the filter tape loaded with the sample of the spot 1, ATN_1, during the measurement timestamp Δt.

The Aethalometer absorption coefficient can be derived by dividing the attenuation coefficient (eq. 4.4) by the multiple scattering parameter C of the filter tape

$$b_{abs} = \frac{b_{atn}}{C} = \frac{1}{C} \cdot \frac{S \cdot (\Delta \mathrm{ATN}_1/100)}{F_1(1-\zeta) \cdot (1 - k\Delta \mathrm{ATN}_1) \cdot \Delta t}. \tag{4.5}$$

In most AE33 applications, it is generally assumed that the measured light attenuation is only due to the absorption of light by the collected particles (eqs. 4.3-4.4), and the cross-sensitivity to scattering of the multiple scattering factor C is neglected, and it is assumed to be constant (Drinovec et al., 2015). However, as we have shown in **Chapter 5**, these assumptions are a first approximation since the attenuation of transmitted light is also influenced by the multiple scattering of light by the collected particles (Bond et al., 1999; Arnott et al., 2005). Introducing this dependence, and following Arnott et al. (2005), eq. (4.4) and (4.5) can be reformulated as

$$b_{atn} = \frac{S}{F}\frac{\Delta \mathrm{ATN}}{\Delta t} \cdot f(ATN) + m_s \cdot b_{sp}, \tag{4.6}$$

$$b_{abs} = \frac{b_{atn}}{C_f} - m \cdot b_{sp}, \tag{4.7}$$

where m_s is the cross-sensitivity to scattering, and is related to m through $m = m_s/C_f$. C_f refers to the filter multiple scattering parameter, that depends solely on the filter tape properties. The absorption coefficient (b_{abs}) can be expressed as a function of the single-scattering albedo ($SSA = b_{scat}/b_{ext}$), similar to the approach by Schmid et al. (2006),

$$b_{abs} = \frac{b_{atn}}{C_f} \cdot \frac{1}{1 + m \cdot \frac{SSA}{1-SSA}} \tag{4.8}$$

from which measured multiple parameter, C, affected by the cross-sensitivity to scattering can be expressed as

$$C = C_f \left(1 + m \cdot \frac{SSA}{1 - SSA}\right) = C_f + m_s \cdot \frac{SSA}{1 - SSA} \tag{4.9}$$

Therefore, eq. (4.9) shows that the effective multiple scattering parameter, C, depends on the physical properties of collected particles and that the actual AE33 cross-sensitivity to scattering is more pronounced when the measured aerosol particles have higher SSA. The analysis of the dependency of the effective multiple scattering parameter C with the SSA yields the experimental fit constants (C_f and m_s) that describe the relationship between C and SSA. Therefore, the factor C to be used at measurements sites or experiments under high SSA is recommended to be obtained either by measuring the absorption coefficient with an independent reference instrument, or by applying an iterative approach to the SSA and C values, assuming a parametrized m_s and C_f values.

Multi-Angle Absorption Photometer (MAAP)

The MAAP photometer was deployed at the three EGAR monitoring stations: Barcelona, Montseny and Montsec d'Ares and was used in **Chapters 5**, **6** and **7**.

The Multi-Angle Absorption Photometer model 5012 (MAAP, discontinued; Thermo Fisher Scientific, USA) measurement principles are described in Petzold and Schönlinner (2004). The MAAP absorption coefficient at a single wavelength (637 nm) is derived by an internal software using a radiative transfer model from the measurements of transmission of light through the filter tape and backscattering of light at two different angles. The measurements of backscattered light allows the instrument to correct on-line for the artifacts due to the presence of the filter tape. MAAP measurements for this thesis were obtained with either a 1 or 5 min time resolution at a flow rate of 5 L min^{-1}, and with a PM_{10} inlet cut-off.

The MAAP focuses a radiation beam over a spot where the aerosol particles from the sampled air are accumulated over a plane membrane filter made of quartz. The incident radiation is emitted by a laser diode with an estimated wavelength of 670 nm, that was actually found to be of 637 nm, and for this reason the absorption coefficient needs to be reported at 637 nm after a correction factor of 1.05 is applied (Müller et al., 2011b). Sensors are placed at multiple angles to measure the forward scattering and attenuation at $\theta_0 = 0°$, and backscatter radiation at $\theta_1 = 130°$ and $\theta_2 = 165°$. The absorption coefficient

is then derived applying a radiative transfer scheme based on Hänel (1987), where the values for the back-scatter fraction by the filter and the asymmetry factor are fixed. Then, the BC concentration is derived by applying a mass absorption cross-section (MAC) of $6.6\ \mathrm{m^2\ g^{-1}}$ to the absorption coefficient. As opposed to the Aethalometer that derives the absorption coefficient from attenuation measurements and has to resolve measuring artifacts (e.g. multiple scattering, filter loading, cross-sensitivity to scattering, etc.), the MAAP obtains directly the absorption coefficient and, as a consequence, it is considered a reference instrument for the absorption coefficient (Collaud Coen et al., 2010; Saturno et al., 2017).

Offline Multi-Wavelength Polar Photometer (PP_UniMI)

A benchtop PP_UniMI polar photometer measurements of absorption at several wavelengths was used as a reference for absorption coefficients at **Chapter 5**.

The polar photometer PP_UniMI working principle is based on the experimental set-up proposed by Hänel (1987; 1994) and Kopp et al. (1999). It was first described in Vecchi et al. (2014), with a later evolution described in Bernardoni et al. (2017). The PP_UniMI measures the transmitted and scattered radiation at 4 wavelengths (405, 532, 635 and 780 nm) in a range of scattering angles from $0°$ to $173°$ with a resolution down to $0.4°$, and then derives the absorption coefficient by applying a radiative transfer model.

Although the same working principle applies for both MAAP and PP_UniMI, i.e. the measurement of transmitted and scattered light radiation and deriving the absorption coefficients by applying a radiative transfer scheme, some crucial differences separate them. Fundamentally, the PP_UniMI is capable of measuring at several wavelengths between the short-UV and the near-infrared, hence covering a larger part of the spectrum compared to the single wavelength of the MAAP (637 nm). More importantly, the higher number of angles used by the PP_UniMI as well as the more sophisticated radiative transfer model allow for a more precise characterization of the absorption. However, the PP_UniMI measurements are performed off-line, whereas the MAAP is able to perform online measurements and allows for continuous measurements, thus presenting a better applicability at monitoring stations in comparison with the PP_UniMI. Furthermore, an inter-comparison between the MAAP and PP_UniMI for different measurement sites, including Barcelona and Montseny, was reported in Valentini et al. (2020). In this study, the MAAP absorption measurements were found to be around 14% lower than the PP_UniMI, which was mainly associated to the improved radiative transfer scheme and larger number of measuring angles for the PP_UniMI, since no differences were observed between MAAP and PP_UniMI when the latter was used as a MAAP (PaM), i.e. using a data inversion with similar assumptions as those performed in the MAAP. Hence, when data from both instruments is available, since they are comparable, the MAAP can be adjusted to the PP_UniMI measurements.

4.2.6 Offline aerosol chemical composition analysis

In addition to the particle mass concentration levels obtained from the gravimetric analysis of the offline filters (Sect. 4.2.3), a complete chemical speciation can be obtained following the procedures proposed by Querol et al. (2001). The chemical composition obtained by offline filters was used for **Chapters 6** and **7**.

Bulk chemical analysis

The bulk chemical composition is obtained by performing different techniques over different sections of the quartz filters. Each filter section corresponds to a piece representing a quarter of the original filter.

The first quarter of the filter was used for the determination and characterization of major elements (Al, Fe, K, Ca, Na, Mg, S, P, Ba, Cr, Cu, Mn, Ni, Sr, Pb, Ti, V, Zn) and the trace elements (Li, Be, B, Sc, Ti, V, Cr, Mn, Co, Ni, Cu, Zn, Ga, Ge, As, Rb, Y, Zr, Nb, Mo, Cd, Sn, Sb, Cs, La, Ce, Pr, Nd, Sm, Eu, Gd, Tb, Dy, Ho, Er, Tm, Yb, Lu, Hf, Ta, W, Tl, Pb, Th and U). With this aim, it undergoes an acid digestion procedure. The acids are then evaporated via heating of the sample at 230 °C. The remaining dry sample is mixed into a solution which is then used to determine the major elements through Inductively Coupled Plasma Atomic Emission Spectrometry (ICP-AES, IRIS Advantage TJA Solutions, THERMO), and the trace elements through Inductively Coupled Plasma Mass Spectrometry (ICP-MS, X series II, THERMO).

The second quarter of the filter was used for the determination of the concentrations of SO_4^{2-}, NO_3^-, Cl^-, and NH_4^+. With this aim the filter portion was leached with ultra-pure water to dissolve ions. The SO_4^{2-}, NO_3^- and Cl^- ions concentration was measured through a ion chromatography system (Dionex Aquion Ion Chromatography, Thermo Fisher Scientific Inc., USA), and the NH_4^+ concentrations with ammonia selective electrode (MODEL 710 A+, THERMO Orion).

Two rectangular punches of around 1.5 cm^{-2} are used for the OC-EC analysis through a Thermal-optical method (cf. Subsect. 4.2.7) using the Sunset Laboratory OCEC analyzer following the EUSAAR 2 thermal-optical transmittance (TOT) protocol (Cavalli et al., 2010). The sampled punches are placed inside a sample oven which is heated up step-wise to remove the organic carbon and catalytically oxidize it to carbon dioxide; then, this carbon dioxide is reduced to methane which is measured with a Flame Ionizatoin Detector (FID). The concentration levels of methane are used to calibrate the measurement to a known quantity of carbon. The char formed during the catalytic process is corrected via the transmittance of light of a pulsed diode laser. Thus, from both the response of the FID and the char correction, the concentrations of organic carbon (OC) and elemental carbon (EC) from the sample can be obtained.

Finally, the remaining filer is stored for possible future analysis of the filter sample.

In addition, in order to obtain the complete chemical mass balance, additional components were indirectly obtained following different empirical equations. These additional components were: i) CO_3^{2-}, calculated as $CO_3^{2-} = 1.5 \cdot Ca$ (Querol et al., 2001); ii) SiO_2, calculated as $SiO_2 = 2.5 \cdot Al_2O_3$ (Querol et al., 2001); and iii) the organic matter (OM), which was determined from the OC measurements by applying a factor to correct for the addition of heteroatoms of the organic matter (H,N, O) missing in the OC, $OM = X \cdot OC$ (Takahama et al., 2011). The applied X factor at Barcelona and Montseny stations used in **Chapter 7** was 1.6 at Barcelona and 2.1 at Montseny station (Minguillón et al., 2015)

4.2.7 Real-time aerosol chemical composition analysis

A real-time online analysis with a high time resolution was needed for the correct analysis of the different aerosol sources and chemical species affecting the measurements when analysing sub-diurnal cycles. This was the case during the flights intensive measurements in **Chapter 6** and during the absorption enhancement analysis due to the mixing of organic and inorganic aerosols with the BC particles in **Chapter 7**. With this objective, a pair of instruments were used: i) a Semi-Continuous OC-EC analyzer to measure the amount of organic and elemental carbon of the measured carbonaceous particles, and ii) an Aerosol Chemical Speciation Monitor (ACSM) which measures mass concentration and chemical species of non-refractory aerosol particles in real-time.

Semi-Continuous OC-EC Field Analyzer

The field-deployable Sunset Semi-Continuous OC-EC Field Analyzer (Sunset Laboratory Inc., Forest Grove, Oregon, USA) provides semi real-time measurements of OC and EC. The measurements were obtained using the EUSAAR2 thermal-optical transmittance (TOT) protocol (Cavalli et al., 2010; Karanasiou et al., 2020) following the recommendations provided by the CEN standard - EN 16909:2017 for $PM_{2.5}$ (CEN, 2017). This protocol provides thermal OC and thermal EC, with their sum representing Total Carbon, TC.

The Semi-Continuous OC-EC analyzer follows the same working principle as the Thermal-optical OC-EC analyzer for offline filters by Sunset (Sect. 4.2.6). The only difference between the two OC-EC analyzers is that the measured quartz-filter samples are manually changed for the offline version, whereas the Semi-Continuous model collects the sampled particles into a quartz filter that after each measuring procedure has a 25 min period where the oven is filled with methane and heated so that all the EC sample is vaporized (Turpin et al., 1990; Bae et al., 2004).

Quadrupole Aerosol Chemical Speciation Monitor (Q-ACSM)

The Quadrupole Aerosol Chemical Speciation Monitor (Q-ACSM; Aerodyne Research Inc., Billerica, Massachusetts, USA) provides real-time characterization and monitoring of the mass and chemical composition of non-refractory submicron particles (e.g. organic aerosols, sulphate, nitrate, ammonium and chloride). The Q-ACSM follows the same working principle as the Aerodyne Aerosol Mass Spectrometer (AMS; Jayne et al., 2000; Canagaratna et al.,

2007), but is designed to be smaller and simpler to use, with the only main difference being that the AMS also reports the particle size distribution. The Q-ACSM presents a detection limit for non-refractory particles below $0.2\ \mu\mathrm{g\ m^{-3}}$ for 30 min of signal averaging at ambient conditions (Ng et al., 2011).

The Q-ACSM samples submicrometric air particles at a flow rate of $0.1\ \mathrm{L\ min^{-1}}$ through a critical orifice ($100\ \mu\mathrm{m}$ diameter) into an aerodynamic lens that is used to transport and focus the submicron particles into a set of vacuum chambers. The focused aerosol particles beam is transmitted through the first two chambers into the final detection chamber, where the particles are flash-vaporized on a hot oven at $600°\mathrm{C}$, so that non-refractory material is detected and chemically characterized via a hard electron impact ($70\mathrm{eV}$) residual gas analyzer (RGA) quadrupole mass spectrometry. An internal calibration system, composed of a naphthalene source that provides a characteristic ion mass to charge fraction spectra used for calibrating the measured ions, is collocated inside the detection chamber. The ion signal correction has to be corrected for contributions both from the ambient background and the naphthalene source inside the detection chamber. This correction is carried out by an automated filter-valve system, where the resulting signal is obtained as the difference between the sample mode and filter signals. To transform the ion spectra signals into chemical species concentrations (organics and inorganics), a set composed by a fragmentation table (Allan et al., 2004), the ion transmission correction, and response factor are used. The instrument was operated with 24 scans per measurement with a 30 min resolution. Data acquisition software (v. 1.1.4.5, 1.5.2.1 and 1.6.0.0) and analysis (v. 1.6.1.1) software were implemented in Igor Pro (Wavemetrics, Inc.) and provided by Aerodyne Research Inc. Data corrections and calibrations were performed as described in Via et al. (2021).

4.2.8 Remote sensing measurements

Remote sensing measurements, both active and passive, allows for the analysis of columnar vertical profiles of both aerosol physical and optical properties. The main difference between passive and active remote sensing measurements is based on the instrument working principle: active remote sensing instruments, such as ceilometers (used in **Chapter 6**), send a radiation beam into the atmosphere and then measure the radiation backscattered by the particles, thus providing vertically resolved aerosol backscatter profile, detection of cloud and fog, and planetary boundary height, among others. Passive remote sensing instrument, such as sun-sky photometers (also used in **Chapter 6**), measure the solar radiation field and then compare it with the expected radiation from a black body radiation, thus measuring vertical-integrated aerosol properties of the atmosphere at that given location such as the AOD.

CHM15k-Nimbus ceilometer

The ceilometer used for the active remote sensing measurements of attenuated backscatter was a Jenoptik (now Lufft) CHM15k-Nimbus (G. Lufft Mess- und Regeltechnik GmbH, Germany). The CHM15k uses a pulsed ND:YAG laser emitting at a wavelength of 1064 nm with a pulse energy of 8.4 μJ, a frequency of around 5-7 kHz, and a beam divergence below

0.3 mrad. The attenuated backscattered signal is collected on a telescope with a 0.45 mrad field of view. The instrument was operated continuously with a temporal resolution of 1 min and vertical resolution of 15 m, reaching a maximum height of 15.36 km a.g.l. The CHM15k-Nimbus ceilometer presents a complete overlap between the laser beam and the telescope field of view at 1.5 km and a measurement range of 15 km (Heese et al., 2010), and an overlap of around 60% at around 500 m a.g.l. (Martucci et al., 2010; Pandolfi et al., 2013). The CHM15k-Nimbus ceilometer used at **Chapter 6** is deployed in the valley below Montsec d'Ares mountain top-station at around 760 m a.s.l. and less than 2.5 km away from the cabin, thus the overlap is above a 85 %, so that the results obtained from the ceilometer are comparable with the scattering measurements of the MSA station. The instrument was subject to calibration following Bucholtz (1995) and Wiegner et al. (2014). Further details and information on the CHM15k-Nimbus ceilometer deployed at Montsec d'Ager station can be consulted in Titos et al. (2017).

AERONET CE-318 sun-sky photometer

The AERONET CE-318 sun-sky photometer (Cimel Electronique, France) is a robust automatic solar-powered radiometer tracking the sun over the sky and making sun measurements that provide the aerosol optical depth, precipitable water and multispectral Ångström exponent (Holben et al., 1998; Holben et al., 2001). The instrument has a field of view of around 1.2 ° with two detectors measuring direct sun, aureole and sky radiance. The spectral range of the measurement between the short-UV and the near-IR allow for measurements at 340, 380, 440, 500, 675, 870 940 and 1020 nm wavelengths. The instrument tracks the position of the sun with a microprocessor based on time, latitude and longitude, and points the head of the photometer to the sun with a set of azimuth and zenith motors with a precision of 0.05°. The measurements have been performed with a temporal resolution of 5 min in a sequence such as that a filter for each wavelength is positioned in front of the detector and direct sun measurements are obtained, then the aerosol optical depth is computed for all the measured wavelengths with the exception of 940 nm, which is used to retrieve the precipitable water. The AERONET CE-318 sun-sky photometer was deployed at MSA station, so that the measurements could be coupled with the CHM15k-Nimbus ceilometer to retrieve via the application of the GRASP algorithm the vertical profiles of physical parameters such as the particle number concentration, and the scattering coefficient, among others.

4.3 Atmospheric air-masses classification

For the characterization of the air masses affecting the areas under study, an array of model-based tools were used, namely backward trajectory and dust and aerosol weather forecasting models. These models are able to provide the origin of the air masses at different height levels as well as the spatial and temporal evolution of the concentration of the main relevant aerosol particles.

4.3.1 Atmospheric transport modeling system: HYSPLIT

The determination of the air mass origin was performed using backward trajectories provided by the Lagrangian trajectory model designed and developed by the NOAA Air Resources Laboratory: HYSPLIT (Draxler and Hess, 1997; Draxler and Hess, 1998; Draxler, 1999; Stein et al., 2015, `https://www.ready.noaa.gov/HYSPLIT.php`). The HYSPLIT model backward trajectories were used for the determination of the air mass origin at **Chapter 6**, as well as for the determination of mineral dust advection into the measurement area in **Chapters 5**, and **7**.

HYSPLIT (HYbrid Single-Particle Lagrangian Integrated Trajectory) model is able to compute air and particle mass trajectories, as well as complex aerosol dispersion and deposition simulations. It is based on a Lagrangian model, under the main assumption that the dispersion of an air parcel can be computed by integrating the advection of each air parcel over the three-dimensional (3-D) meteorological grid. That is, the dispersion of the air parcel results in a trajectory that only requires the 3-D velocity field. The backward trajectories calculated throughout this study were obtained at a daily basis at noon (12:00 UTC) for 3 different heights: 750, 1500, and 2500 m a.g.l. The trajectories were computed using meteorological data from the Global Data Assimilation System with a 1° resolution (GDAS-1) for the previous 120 hours, which has been set to be the most accurate time lag for determining the origin of an air mass (Su et al., 2015). The backward trajectories were visually classified upon its origin sector into: 1) Atlantic North, *AN*; 2) Atlantic North-West, *ANW*; 3) Atlantic South-West, *ASW*; 4) North African, *NAF*; 5) Mediterranean, *MED*; 6) European Continent, *EU*; 7) Winter Regional, *WREG*; and 8) Summer Regional, *SREG*.

4.3.2 Aerosol dispersion forecasting models

Forecasts from aerosol compounds dispersion and deposition models have been used along with the backward trajectories for **Chapters 5**, **6** and **7** with the aim of identifying at a synoptic scale the different aerosol particles and its composition affecting the measurements. Multiple forecasting models outputs were used and intercompared to obtain a more accurate description of the different events, namely: NAAPS, BSC-DREAM8b and NMMB/BSC-Dust, and SKIRON.

Navy Aerosol Analysis and Prediction System (NAAPS)

The Navy Aerosol Analysis and Prediction System (NAAPS) is a global 3-D aerosol forecasting model developed and maintained by the Naval Research Laboratory, Marine Meteorology Division, in Monterey, USA (Westphal et al., 2009, `https://www.nrlmry.navy.mil/aerosol/`). NAAPS is an offline model that forecasts sulphate, smoke, dust and sea salt aerosol concentration and visibility for the entire globe, as well as some specific regions such as Sahara, Sahel, Europe, etc.

BSC-DREAM8b and NMMB/BSC-Dust forecasting models

BSC-DREAM8b and NMMB/BSC-Dust are online forecasting models developed and maintained by the Earth Science Division of Barcelona Supercomputing Center (BSC) that provide short and mid-term dust weather forecasts (Pérez et al., 2006; Pérez et al., 2011; Basart et al., 2012, `https://dust.aemet.es/products/daily-dust-products`).

BSC-DREAM8b and NMMB/BSC-Dust are based on the Euler-type partial differential non-linear equations for mass continuity, and use the NCEP/Eta atmospheric model, and a dust module coupled with NMMB/NCEP atmospheric model, respectively. BSC-DREAM8b is a regional model that provides the dust cycle forecasting for large parts of Europe, North-Africa and the middle East, whereas NMMB/BSC-Dust is run globally. BSC-DREAM8b is the evolution of the previous BSC-DREAM dust forecasting mode, with the main improvements due to a more detailed size bin distribution and a dust-radiation interaction feature. At present, BSC-DREAM8b model has become obsolete and is no longer available, and has been replaced with a new model developed by the BSC, the MONARCH (Badia et al., 2017; Basart et al., 2020; Klose et al., 2021), that in addition to the NMMB/BSC-Dust dust module, has a full chemistry module scheme that includes gas-phase interactions and all the aerosol species (volcanic ash, sea-salt, sulphates, organic aerosols, black carbon, etc.). MONARCH produces daily forecasts for 72 hours of dust surface concentrations, dry and wet deposition, and the dust optical depth.

SKIRON/Eta dust forecasting model

SKIRON/Eta is an atmospheric model that incorporates a module for dust uptake from North-Africa and Eurasia main sources, and then computes its transport and deposition on the surface developed by the University of Athens, Atmospheric Modeling and Weather Forecasting Group, Greece (Kallos et al., 1997; Nickovic et al., 2001; Kallos et al., 2006, `https://forecast.uoa.gr/en/forecast-maps/dust/europe`). The SKIRON model dynamically couples the dust module with the atmospheric model (ETA), enabling for a dust cycle analysis at every step. This dynamic coupling results in a more accurate reproduction of the dust sources, particle size distribution evolution, dust transport and three-dimensional dust mass concentration. The SKIRON/ETA produces daily forecasts of the dust concentration near ground, dry and wet deposition, as well as some meteorological variables for Europe, the North Atlantic and Central Asia.

4.4 Data analysis

4.4.1 Intensive aerosol optical properties

In addition to the measurements obtained directly from the instruments, additional variables were derived throughout the different chapters of this thesis to better constrain and characterize the aerosol particles properties, independently of the concentration of particles. These variables are referred to as intensive optical properties, since are independent of the particle

number and mass concentration, and only depend on the physico-chemical properties of collected particles, such as the mineralogy, the particle size distribution, the shape of the particle, etc. These intensive optical properties were obtained by combining the measurements from the instruments described in Sect. 4.2 and by applying different fits and formulas to the available datasets.

Single Scattering Albedo: SSA

The Single Scattering Albedo (SSA) describes the amount of radiation that is either scattered or absorbed by the aerosol particles, i.e. the potential for either cooling or warming the atmosphere. Thus, the SSA is considered to be one of the most important optical parameters to describe the interaction of the aerosol particles with radiation. SSA is obtained as the ratio between the scattering and the total extinction produced by the aerosol particles (i.e. the sum of absorption and scattering), with theoretical values ranging between 0 for pure absorbing aerosol particles, and 1 for pure scattering particles.

$$SSA = \frac{b_{scat}}{b_{scat} + b_{abs}}. \tag{4.10}$$

The SSA was obtained at several wavelengths, by combining the absorption coefficients, either from the AE33 at 7-λ's or from the MAAP at 637 nm, and the scattering coefficients from the integrating nephelometer at 3-λ's. For this purpose, the scattering measurements were extrapolated to the absorption coefficient wavelengths. Thus, by measuring the SSA for different wavelengths, from the short-UV to the near-infrared, it was possible to report the spectral behaviour of the SSA for aerosol particles with different chemical composition.

Various aerosol compounds present SSA values at a wavelength of 525 nm close to 1 for purely scattering particles, like OA non-absorbing compounds and inorganic aerosols, such as ammonium sulphates. Moreover, SSA ranges between 0.75 and 0.84 for biomass burning aerosols, whereas for freshly emitted BC particles, the SSA can get as low as 0.2-0.3 (Bond and Bergstrom, 2006; Laskin et al., 2015). In particular, SSA values for mineral dust range between 0.9 and 0.96 at around 550 nm (Claquin et al., 1999; Schladitz et al., 2009), with the iron and iron-oxides concentration of the mineral dust considered to be the major responsible for this variation. Additionally, as a consequence of the spectral variation of the imaginary refractive index of these iron oxides particles, the SSA of mineral dust particles presents lower SSA values for the shorter wavelengths (0.92 at 370 nm and 0.98 at 880 nm; Di Biagio et al., 2019).

Ångström Exponent: scattering, absorption and single scattering albedo

The Ångström Exponent, α, was first proposed by Ångström (1929), as a wavelength-independent parameter to describe the dependence with the wavelength of light extinction by the aerosol particles. It is commonly used to analyze the spectral variation of any parameter

($\phi(\lambda)$) that follows, or can be approximated as, a power-law relationship with the wavelength,

$$\phi(\lambda) = \phi_0 \cdot \lambda^{-\alpha}. \tag{4.11}$$

The main approaches for obtaining α are: i) from the ratio of $\phi(\lambda)$ for a pair of wavelengths, ii) by fitting the $\phi(\lambda)$ data on a log-log space with a linear regression, and by iii) applying non-linear fits. The first two approaches were the ones used this thesis, with the second method as the preferred option given its higher sensitivity to a larger number of wavelengths.

The first approach to obtain α uses the ratio of $\phi(\lambda)$ for a pair of wavelengths, λ_1, λ_2, which can be described by

$$\frac{\phi(\lambda_1)}{\phi(\lambda_2)} = \left(\frac{\lambda_1}{\lambda_2}\right)^{-\alpha}, \tag{4.12}$$

so that, by converting it into the log space, the Ångström Exponent, α, can be expressed as

$$\alpha_{\lambda_1,\lambda_2} = -\frac{\ln\left(\phi(\lambda_1)/\phi(\lambda_2)\right)}{\ln\left(\lambda_1/\lambda_2\right)} \tag{4.13}$$

The second method to obtain α fits the desired parameter (ϕ) with a linear regression to the points of the multiple wavelengths plotted in the log-log space,

$$\ln(\phi(\lambda)) = -\alpha \ln(\lambda) + \beta \tag{4.14}$$

where the fitted slope, α, defines the Ångström Exponent.

In this thesis, the three parameters for which the Ångström Exponent have been obtained are: absorption (b_{abs}), scattering (b_{sp}), and single scattering albedo (SSA).

The absorption Ångström Exponent (AAE) was obtained following the aforementioned methods using the multi-wavelength absorption measurements derived by the AE33. In the case that the AAE was obtained using a pair of λ's (eq. 4.12), the selected wavelengths were 470 and 950 nm, as proposed by Zotter et al. (2017); otherwise the AAE was derived using the linear regression in the log-log space to the 7-λ.

The AAE depends on the internal mixing state, as well as on the chemical and mineralogical composition of the aerosol particles. Typical AAE values for freshly emitted BC particles range between 0.8 and 1.1 (Kirchstetter et al., 2004; Bergstrom et al., 2007; Petzold et al., 2013; Lack and Langridge, 2013). This variation is associated with the BC particle size, with a value of 1 associated to BC particles below 50 nm diameters, and a range between 0.8 and 1.1 for the BC particles formed by coagulation and collapse of smaller BC spherules (e.g. Gyawali et al., 2009; Zhang et al., 2008). BrC aerosol particles and mineral dust particles present higher AAE values due to the higher absorption efficiency of these particles at the short-UV region of the spectrum compared to the near-IR (Kirchstetter et al., 2004; Chen and Bond, 2010). For BrC particles, the AAE variation is introduced by the higher absorption towards the short-UV wavelengths of the organic aerosol particles, with AAE values between 1.5 and

5 (Schnaiter et al., 2003; Bergstrom et al., 2007; Cappa et al., 2019). For mineral dust, AAE values range between 2 and 6.5 (Schuster et al., 2016; Caponi et al., 2017). The variation in the AAE of the dust particles is caused by the spectral variations in the refractive index introduced by iron oxide containing particles, mainly goethite and magnetite (e.g. Müller et al., 2009; Schladitz et al., 2009; Schuster et al., 2006).

The scattering Ångström Exponent (SAE) was determined by performing a linear regression to the integrating nephelometer multi-wavelength scattering measurements in the log-log space. Additionally, the use of a SAE obtained through two sets of wavelengths was used for performing the corrections to the forward (0°) and backward scattering (180°) as proposed in Müller et al. (2011a).

SAE values lower than one are associated with the presence of coarse particles, that in the main area of study are mainly associated with Saharan mineral dust outbreaks, and in the mineral dust emission source regions are linked to stronger emission processes; whereas SAE around 1.5 indicate the predominance of fine particles (Seinfeld and Pandis, 1998; Schuster et al., 2006; Pandolfi et al., 2018). Indeed, when first proposed the use of the Ångström Exponent, it was already studied its relationship with the aerosols particle size (Ångström, 1929).

The single scattering albedo Ångström Exponent (SSAAE) was obtained by fitting a linear regression to the calculated multiple-wavelength SSA at the 7-λ of the AE33 in the log-log space. For this purpose, the 3-λ scattering coefficients obtained with the integrating nephelometer were extrapolated to the 7-λ of the AE33 using the SAE (eq. 4.11). The SSAAE was used as an indicator for the presence of mineral dust particles when values are <0 (Collaud Coen et al., 2004; Ealo et al., 2016).

Backscattering Fraction: BF

The hemispheric Backscattering Fraction (b or BF) is a simplified representation of the angular distribution of scattering and is calculated as the ratio of hemispheric backscattering and total scattering,

$$b = \mathrm{BF} = \frac{b_{bscat}}{b_{scat}}. \tag{4.15}$$

The backscatter fraction is an indicator of the particles size, with a higher relative amount of backward radiation compared to forward radiation for smaller particles, and vice-versa, a higher relative amount of forward scattering for coarser particles (Andrews et al., 2011b). Typical b values range between 0.10 and 0.15 (Andrews et al., 2011b). It is also affected by the asphericity of the particles, with less spherical particles presenting lower BF values (Doherty et al., 2005).

Asymmetry Parameter: g

The asymmetry parameter (g) describes the angular distribution of light scattering by aerosol particles. Theoretically, the g values range between -1 for completely backscattered light, and

+1 for entirely forward scattered light. For symmetric scattering with respect to the plane perpendicular to the incidence direction, the g is 0. The asymmetry parameter is defined as the intensity-weighted average cosine of the scattering angle, i.e. the angle between the incident and scattering light radiation (θ):

$$\mathrm{g} = \langle cos\theta \rangle = \frac{1}{2} \int_0^{\pi} \sin\theta P(\theta) \cos\theta d\theta, \tag{4.16}$$

where $P(\theta)$ is the phase function (i.e. the angular distribution of scattered light, cf. Sect. 1.3).

The asymmetry parameter can also be derived by applying the Henyey-Greenstein approximation, where an empirical function for g is obtained based on its relationship with the backscatter fraction, b. This relationship was first described by Andrews et al. (2006) based on Wiscombe and Grams (1976) for a wavelength of 550 nm and a refractive index of 1.55 + 0.015i for measurements below 40% RH:

$$\mathrm{g} = -7.143889 \cdot b^3 + 7.4644393 \cdot b^2 - 3.96356 \cdot b + 0.9893. \tag{4.17}$$

This empirical relationship proposed by Andrews et al. (2006) has been the main method followed in this thesis for deriving the asymmetry parameter when the scattering measurements were obtained with the integrating nephelometer Aurora 3000 (**Chapters 5**, **6** and **7**). Conversely, if the scattering measurements were performed with the multi-angle polar integrating nephelometer Aurora 4000 (**Chapter 8**), the asymmetry parameter was obtained following eq. (4.16), by calculating the phase function (eq. 1.7) from the multi-angle scattering measurements (Liou, 2002; Horvath et al., 2018).

Typical overall asymmetry parameter, g, values range between 0.5 and 0.7 with the variations associated to the particle number size distribution, shape factor and the chemical composition (e.g. Andrews et al., 2011a; Pandolfi et al., 2018). In particular, for mineral dust particles, g values between 0.6 and 0.85 are assumed in most climate models (Sokolik and Toon, 1999; Horvath et al., 2018; Ryder et al., 2018).

Mass Absorption, Scattering, and Extinction Efficiency: MAE, MSE, MEE

The mass efficiency of the extensive optical properties represents the ratio of radiation that is absorbed (MAE), scattered (MSE), and extincted (MEE), by the particles per unit of mass.

The mass absorption efficiency (MAE), also referred to as mass absorption cross-section (MAC), is obtained at a given wavelength as the ratio between the absorption coefficient at that given wavelength and the mass concentration of the absorbing particles (eq. 4.18).

$$MAE = \frac{\mathrm{b_{abs}}}{\mathrm{M_{PM,abs}}} \tag{4.18}$$

The mass scattering efficiency (MSE), also referred to as mass scattering cross-section (MSC), is obtained similarly to the MAE, as a fraction between the scattering coefficient and the mass concentration (eq. 4.18).

$$MSE = \frac{\mathrm{b_{scat}}}{\mathrm{M_{PM}}} \tag{4.19}$$

The extinction coefficient is the combination of both the absorption and scattering coefficients, and therefore the mass extinction efficiency (MEE), also referred to as mass extinction cross-section (MEC), is calculated as the ratio between the extinction coefficient and the mass fraction (eq. 4.18).

$$MEE = \frac{\mathrm{b_{ext}}}{\mathrm{M_{PM}}} \tag{4.20}$$

Absorption enhancement of BC particles

The absorption enhancement, $\mathrm{E_{abs}}$, is defined as the ratio between the measured ambient MAC, $\mathrm{MAC_{obs}}$, and the reference MAC for pure BC particles, $\mathrm{MAC_{ref}}$. For this case, the observed ambient MAC is defines as in eq. (4.18), but instead of the PM concentration, it is the specific concentration of elemental carbon, or pure BC, that is used,

$$\mathrm{MAC_{obs}} = \frac{\mathrm{b_{abs}}}{\mathrm{M_{EC}}}, \tag{4.21}$$

$$\mathrm{E_{abs}} = \frac{\mathrm{MAC_{obs}}}{\mathrm{MAC_{ref}}}. \tag{4.22}$$

The reference $\mathrm{MAC_{ref}}$ can be obtained either from the same experimental data that is used for obtaining $\mathrm{E_{abs}}$, or from the literature. A highly used literature $\mathrm{MAC_{ref}}$ for pure BC is the one provided by Bond and Bergstrom (2006) at 550 nm, $7.5 \pm 1.2\ \mathrm{m^2 g^{-1}}$. There are two main approaches for experimentally determining $\mathrm{MAC_{ref}}$: i) using a combination of instruments that evaporate the semi-volatile and inorganic species, and therefore only the absorption by pure BC is measured, and ii) by fitting the $\mathrm{MAC_{obs}}$ against the OC to EC ratio and using the intercept, i.e. when there are no organic compounds available to enhance the absorption, as $\mathrm{MAC_{ref}}$.

Since the absorption enhancement of BC is produced by both its external and internal mixing with other particles, $\mathrm{E_{abs}}$ can be expressed as

$$\mathrm{E_{abs}} = \mathrm{E_{abs,int}} + \mathrm{E_{abs,ext}}, \tag{4.23}$$

where $\mathrm{E_{abs,int}}$ and $\mathrm{E_{abs,ext}}$ refer to the absorption enhancement produced by the internal and the external mixing, respectively. If the absorption measurements are performed at several wavelengths, it is possible to determine the fraction of the absorption enhancement which is produced either by the internal or external mixing of particles with BC by assuming that the BrC particles do not absorb at 880 nm, i.e. the external mixing effect on $\mathrm{E_{abs}}$ is null, and it is only driven by the internally mixed BC particles. Some studies assume a

wavelength-independent $E_{abs,int}$ (Liu et al., 2015b; Zhang et al., 2018), however there are several studies showing the possibility of absorbing particles internally mixed with BC, which can alter its AAE (e.g. Lack and Cappa, 2010; Lack and Langridge, 2013). By taking into consideration the possible influence of this absorbing particles on the variations of E_{abs} with the wavelength, or by using the lensing effect terminology, the brown coatings (cf. Lack and Cappa, 2010), the absorption enhancement for the internally mixed BC at a given wavelength can be described as,

$$E^{\lambda}_{abs,int} = 1 + \frac{MAC^{880nm}_{BC,int} \cdot \left(\frac{880}{\lambda}\right)^{AAE}}{MAC^{\lambda}_{ref}}, \tag{4.24}$$

$$E^{\lambda}_{abs,ext} = E^{\lambda}_{abs} - E^{\lambda}_{abs,int}, \tag{4.25}$$

where AAE is the spectral dependency for pure BC particles, $MAC_{BC,int}$ is the internal mixing mass absorption cross-section, and λ is the wavelength.

4.4.2 Trend analysis

For datasets that present long measurement periods, an analysis of the trends was performed with the aim of observing whether the main variable of interest and additional variables which could be influencing it had a positive or negative evolution over the last decade, such as in **Chapter 7**.

The trend analysis was performed by applying the widely used Theil-Sen estimator method (Collaud Coen et al., 2020, and therein). This method fits a line to the data points, where the fitted slope is obtained as the median of slopes of all the pair of points, and the intercept is determined as the median of values of the dependent variable minus the fitted slope by the value of the independent variable.

This estimator is used for determining trends due to its lower sensitivity to the presence of outliers in the sample in comparison with a least squares regression. All the Theil-Sen trends performed in this study have been performed using the *Theil-Sen* function from the *Openair* package (Carslaw and Ropkins, 2012) in the programming language *R* (`www.r-project.org`; Team et al., 2013).

4.4.3 Optimized Noise-reduction Algorithm (ONA)

The post-processing Optimized Noise-reduction Algorithm (ONA) was used in **Chapter 5** for noise reduction of high-temporal resolution BC data from the AE33. The method was applied following the approach introduced by Hagler et al. (2011) for very high-time resolution of absorption measurements, then implemented for the Aethalometer in Springston and Sedlacek (2007), and afterwards by Backman et al. (2017) in remote Arctic stations. It was implemented for the three sets of stations deployed at the western Mediterranean basin: Barcelona, Montseny and Montsec d'Ares (cf. Sect. 4.1.1).

The ONA algorithm is based on averaging the data with a varying timestamp. This adaptive averaging time-step (Δt) is set by fixing the incremental light attenuation of light through the filter tape ($\Delta \mathrm{ATN}_1$, cf. 4.3) to a constant value, conversely to the internal instrument software (cf. Sect. 4.2.5), that fixes Δt and measures $lta\mathrm{ATN}_1$ for the given time-step. Since $\Delta \mathrm{ATN}_1$ determines the possible range of Δt, it needs to be high enough so that the signal-to-noise ratio is large; yet as low as possible so that the intrinsic variability of the measurements is conserved, thus a $\Delta \mathrm{ATN}_1$ was set to 0.01 as per recommendation of the AE33 manufacturer.

A direct cause of fixing the $\Delta \mathrm{ATN}_1$ step in eq. (4.3) is that the ONA recalculated BC concentration is determined by the time needed to reach the fixed attenuation value, hence: the faster $\Delta \mathrm{ATN}_1$ is reached, the smaller the Δt is, and the higher that the BC concentration are. The advantage of applying this methodology is that it filters the noise introduced into the BC values by $\Delta \mathrm{ATN}_1$ measurements close to the detection limit when a fixed Δt is used (i.e. the method used for deriving BC by the AE33 internal software), whilst maintaining the higher BC concentration measurements. This avoids the introduction of a bias to the measurements as is the case when performing a rolling average or averaging over a Δt larger than the original timestamp from the instrument.

Part III
Results

5

ABSORPTION COEFFICIENTS RETRIEVAL: CORRECTION FACTORS AND RELATIONSHIPS

Objective

Improve the measurement of the absorption coefficients from a filter-based dual-spot multi-wavelength aethalometer (AE33, Aerosol d.o.o.). Filter-base instruments derive the absorption by applying several correction factors to the measurements of light attenuation. The AE33 applies a parameter that corrects for the multiple scattering of the particles within the filter, the parameter C. This parameter is the only correction factor which is not corrected on-line by the instrument software, and provides the largest contribution to the absorption measurements uncertainty. With this aim, an accurate analysis of the average values at different backgrounds and the relationships with the physico-chemical properties of the samples aerosol particles proves crucial for a correct measurement of the absorption coefficients by the AE33.

Methodology

- Use of long-period datasets for the two most used AE33 filter tapes, previous model M8020, and currently used M8060, at an urban background station in Barcelona, a regional station in Montseny and a mountain-top station in Montsec d'Ares.
- Intercomparison via a multi-instrumental approach comparing the absorption coefficients form the AE33 with an online multi-angle photometer (MAAP, Thermo Sci.) and an offline photometer; and the use of a integrating nephelometer (Aurora 3000, Ecotech, Inc.) for deriving the single scattering albedo.
- Application of an Optimized Noise-reduction Algorithm (ONA) for noise reduction of the AE33 dataset. Applying this technique to reduce the signal noise is specially relevant at stations with values close to the detection limit such as Montsec d'Ares.

Results

- Large increase of the cross-sensitivity to the scattering of the C parameter with the single-scattering albedo (SSA) of the sampled aerosol particles for SSA values above 0.92-0.95, especially at the regional and mountain-top background stations. A higher dependency was found for the currently used filter tape model.
- Larger impact of the dependency of C with the SSA for the mountain-top station, Montsec d'Ares due to the higher SSA values measured on average and its larger exposure to Saharan dust outbreaks.
- Seasonal dependence of the C parameter highly correlated with the seasonal variation of the SSA.
- Statistically significant increase of the C with the wavelength at the mountain-top station for Saharan mineral dust outbreaks reaching the site.

Conclusions

- Sampling of aerosol particles with SSA values above 0.92-0.5 can introduce up to a 3-fold increase in the multiple scattering parameter, C, and consequently, if not token into account, a 3-fold reduction of the absorption measurement.
- The high cross-sensitivity to scattering of C proves crucial for an accurate measurement of the absorption coefficients at stations characterized by high SSA, as mountain-top stations and other remote stations.
- The spectral dependence of the C parameter for sites influenced by coarse mineral dust can introduce an increase of the AAE measurements at the mountain-top station.

Publication

- Yus-Díez, J., Bernardoni, V., Močnik, G., Alastuey, A., Ciniglia, D., Ivančič, M., Querol, X., Perez, N., Reche, C., Rigler, M., Vecchi, R., Valentini, S., and Pandolfi, M.: "Determination of the multiple-scattering correction factor and its cross-sensitivity to scattering and wavelength dependence for different AE33 Aethalometer filter tapes: A multi-instrumental approach". In: *Atmospheric Measurement Techniques Discussions*, 14, 6335–6355, `https://doi.org/10.5194/amt-14-6335-2021`, 2021.

Atmos. Meas. Tech., 14, 6335–6355, 2021
https://doi.org/10.5194/amt-14-6335-2021
© Author(s) 2021. This work is distributed under
the Creative Commons Attribution 4.0 License.

Atmospheric Measurement Techniques
Open Access
EGU

Determination of the multiple-scattering correction factor and its cross-sensitivity to scattering and wavelength dependence for different AE33 Aethalometer filter tapes: a multi-instrumental approach

Jesús Yus-Díez[1,2], Vera Bernardoni[3], Griša Močnik[4,5], Andrés Alastuey[1], Davide Ciniglia[3], Matic Ivančič[6], Xavier Querol[1], Noemí Perez[1], Cristina Reche[1], Martin Rigler[6], Roberta Vecchi[3], Sara Valentini[3], and Marco Pandolfi[1]

[1]Institute of Environmental Assessment and Water Research (IDAEA), CSIC, C/Jordi Girona 18–26, 08034, Barcelona, Spain
[2]Grup de Meteorologia, Departament de Física Aplicada, Universitat de Barcelona, C/Martí i Franquès, 1, 08028, Barcelona, Spain
[3]Dipartimento di Fisica "Aldo Pontremoli", Università degli Studi di Milano & INFN Milano, via Celoria 16, 20133 Milan, Italy
[4]Center for Atmospheric Research, University of Nova Gorica, Vipavska 11c, 5270 Ajdovščina, Slovenia
[5]Department of Condensed Matter Physics, Jožef Stefan Institute, Jamova 39, 1000 Ljubljana, Slovenia
[6]Aerosol d.o.o., Kamniška 39A, 1000 Ljubljana, Slovenia

Correspondence: Jesús Yus-Díez (jesus.yus@idaea.csic.es)

Received: 17 February 2021 – Discussion started: 29 March 2021
Revised: 19 July 2021 – Accepted: 25 August 2021 – Published: 1 October 2021

Abstract. Providing reliable observations of aerosol particles' absorption properties at spatial and temporal resolutions suited to climate models is of utter importance to better understand the effects that atmospheric particles have on climate. Nowadays, one of the instruments most widely used in international monitoring networks for in situ surface measurements of light absorption properties of atmospheric aerosol particles is the multi-wavelength dual-spot Aethalometer, AE33. The AE33 derives the absorption coefficients of aerosol particles at seven different wavelengths from the measurements of the optical attenuation of light through a filter where particles are continuously collected. An accurate determination of the absorption coefficients from the AE33 instrument relies on the quantification of the non-linear processes related to the sample collection on the filter. The multiple-scattering correction factor (C), which depends on the filter tape used and on the optical properties of the collected particles, is the parameter with both the greatest uncertainty and the greatest impact on the absorption coefficients derived from the AE33 measurements.

Here we present an in-depth analysis of the AE33 multiple-scattering correction factor C and its wavelength dependence for two different and widely used filter tapes, namely the old, and most referenced, TFE-coated glass, or M8020, filter tape and the currently, and most widely used, M8060 filter tape. For performing this analysis, we compared the attenuation measurements from AE33 with the absorption coefficients measured with different filter-based techniques. On-line co-located multi-angle absorption photometer (MAAP) measurements and off-line PP_UniMI polar photometer measurements were employed as reference absorption measurements for this work. To this aim, we used data from three different measurement stations located in the north-east of Spain, namely an urban background station (Barcelona, BCN), a regional background station (Montseny, MSY) and a mountaintop station (Montsec d'Ares, MSA). The median C values (at 637 nm) measured at the three stations ranged between 2.29 (at BCN and MSY, lowest 5th percentile of 1.97 and highest 95th percentile of 2.68) and 2.51 (at MSA, lowest 5th percentile of 2.06 and highest 95th percentile of 3.06). The analysis of the cross-sensitivity to

Published by Copernicus Publications on behalf of the European Geosciences Union.

scattering, for the two filter tapes considered here, revealed a large increase in the C factor when the single-scattering albedo (SSA) of the collected particles was above a given threshold, up to a 3-fold increase above the average C values. The SSA threshold appeared to be site dependent and ranged between 0.90 to 0.95 for the stations considered in the study. The results of the cross-sensitivity to scattering displayed a fitted constant multiple-scattering parameter, C_{f}, of 2.21 and 1.96, and a cross-sensitivity factor, m_{s}, of 1.8 % and 3.4 % for the MSY and MSA stations, respectively, for the TFE-coated glass filter tape. For the M8060 filter tape, C_{f} values of 2.50, 1.96 and 1.82 and m_{s} values of 1.6 %, 3.0 % and 4.9 % for the BCN, MSY and MSA stations, respectively, were obtained. SSA variations also influenced the spectral dependence of C, which showed an increase with wavelength when SSA was above the site-dependent threshold. Below the SSA threshold, no statistically significant dependence of C on the wavelength was observed. For the measurement stations considered here, the wavelength dependence of C was to some extent driven by the presence of dust particles during Saharan dust outbreaks that had the potential to increase the SSA above the average values. At the mountaintop station, an omission of the wavelength dependence of the C factor led to an underestimation of the absorption Ångström exponent (AAE) by up to 12 %. Differences in the absorption coefficient determined from AE33 measurements at BCN, MSY and MSA of around 35 %–40 % can be expected when using the site-dependent experimentally obtained C value instead of the nominal C value. Due to the fundamental role that the SSA of the particles collected on the filter tape has in the multiple-scattering parameter C, we present a methodology that allows the recognition of the conditions upon which the use of a constant and wavelength-independent C is feasible.

1 Introduction

Atmospheric aerosol particles play an important role in the Earth's radiative balance directly by scattering and absorbing solar and terrestrial radiation and indirectly by acting as cloud condensation nuclei. Large uncertainties still exist regarding the effects that atmospheric particles have on climate (Myhre et al., 2013). In fact, the aerosol–radiation interaction depends on aerosol properties such as aerosol size distribution, mixing state and refractive index, among others (e.g. Bond et al., 2013). Globally, aerosols have helped to reduce the warming effect from greenhouse gases because of their net cooling effect on climate (Myhre et al., 2013). However, this influence is likely to be reduced over the coming decades as air pollution measures are implemented around the world (Samset et al., 2018), as is already the case in parts of Europe and North America (Collaud Coen et al., 2020). Therefore, in order to properly constrain global models, it is necessary to better characterize the atmospheric absorption by aerosols from observations. Among the atmospheric aerosols, black carbon (BC) stands out as phenomenologically different, being the most efficient light-absorbing aerosol component and being responsible for the second-most-important contribution to positive climate forcing after carbon dioxide (Myhre et al., 2013). However, there are still large uncertainties related to the radiative forcing of BC particles. In fact, the climate forcing potential of BC is influenced by BC properties which are strongly source and site dependent (IPCC, 2001; Ramanathan et al., 2001; Kirchstetter et al., 2004a; Ramanathan and Carmichael, 2008; Myhre et al., 2013; Bond et al., 2013; Liu et al., 2015). In addition to BC, atmospheric absorption by aerosol particles is also driven by specific organic compounds (e.g. from incomplete combustion, biomass smoldering, and secondary and biogenic sources) often referred to as brown carbon (BrC) and by mineral dust (e.g. Alfaro et al., 2004). Unlike BC, which absorbs radiation in a wide range of wavelengths (from UV to infrared) with a wavelength-independent refractive index, the BrC and mineral dust refractive index increases at shorter wavelengths, close to the UV range (Kirchstetter et al., 2004a; Andreae and Gelencsér, 2006; Bergstrom et al., 2007; Laskin et al., 2015; Cappa et al., 2019). Therefore, having at one's disposal accurate absorption measurement techniques is crucial to determining particles' light absorption which can afterwards be used in climate projections (Mengis and Matthews, 2020; Wang et al., 2020). Moreover, there is also the need for standard aerosol particles to use as a reference for the quality assurance of absorption measurements, such as the recently developed flame-generated soot in Ess and Vasilatou (2019).

There are three main approaches in the literature to determining aerosol particles' light absorption: by measuring the suspended particles in a cell, e.g. with photo-thermal interferometry or photo-acoustic techniques, and by either on-line or off-line filter-based photometer methods (e.g. Lin et al., 1973; Terhune and Anderson, 1977; Hansen et al., 1984; Stephens et al., 2003; Moosmüller et al., 2009; Ajtai et al., 2010; Vecchi et al., 2014). Among the indirect methods for measuring absorption, the "subtraction method", which does not rely on a filter, calculates the absorption from the difference between extinction and scattering by suspended particles (Singh et al., 2014). However, this method can lead to large errors at large single-scattering albedo (SSA) values when the extinction is dominated by scattering (Onasch et al., 2015). On-line measurement methodologies based on particle suspension, such as photo-acoustic spectroscopy (PAS) (Ajtai et al., 2010), have the advantage of measuring directly the absorption by particles suspended in a sampling cell avoiding filter-based artefacts. However, in the case of photo-acoustic spectroscopy measurements, the heating of the sample and the evaporation of coating materials on the sample may lead to higher detection limit and artefacts impairing the measurement accuracy (Lack et al., 2006; Linke et al., 2016). The photo-thermal interferometry (PTI) is an absorption measurement technique originally developed for

measurements of trace gases that has also been applied to aerosol measurements (Lee and Moosmüller, 2020; Visser et al., 2020). However, the aforementioned techniques have so far proved difficult to deploy in a field setting, thus limiting their broader use in international measurement networks. Filter-based instruments (either on-line or off-line) rely on the sampling of aerosol particles collected in a filter matrix and on the measurement of the resulting change in light intensity with a photometer, either in the transmittance (Hansen et al., 1984; Bond et al., 1999; Drinovec et al., 2015) or in both transmittance and reflectance (Petzold and Schönlinner, 2004). This method is affected by artefacts resulting mainly from the effects that the filter has on the measurements. Off-line in-house-made filter-based polar photometers, which measure both transmittance and reflectance, are deployed at some research centres. Examples are the MWAA (multi-wavelength absorption analyser) deployed at the University of Genoa (Massabò et al., 2013) and the PP_UniMI polar photometer deployed at the University of Milan (Vecchi et al., 2014; Bernardoni et al., 2017). These methods can perform accurate absorption measurements by increasing the number of measuring angles (Massabò et al., 2013; Vecchi et al., 2014; Bernardoni et al., 2017), thus allowing an accurate determination of the filter artefacts.

The main advantage of the on-line filter-based methods is that these techniques are easy to use, allow for unattended operation, are relatively inexpensive and provide real-time data. For these reasons, these methods are widely used in international networks such as the Global Atmosphere Watch (GAW, World Meteorological Organization) and the European Aerosols, Clouds and Trace Gases Research Infrastructure (ACTRIS; https://www.actris.eu, last access: 20 September 2021). The most used filter-based instruments are the Aethalometer (Hansen et al., 1984; Drinovec et al., 2015), the particle soot absorption photometer (PSAP; Bond et al., 1999), the continuous light absorption photometer (CLAP; Ogren et al., 2017) and the multi-angle absorption photometer (MAAP; Model 5012, Thermo Fisher Scientific Inc., USA; Petzold and Schönlinner, 2004). The measured mass concentration of light-absorbing carbonaceous aerosols inferred via optical attenuation of light is referred to as equivalent BC (eBC; Petzold et al., 2013). The main artefacts affecting the light absorption measurements of these instruments are the multiple light scattering within the filter, the filter loading effect and the particle scattering correction (Liousse et al., 1993; Bond et al., 1999; Weingartner et al., 2003; Schmid et al., 2006; Collaud Coen et al., 2010; Lack et al., 2014). Algorithms for correcting these artefacts have been applied and their efficacy tested over the years (Weingartner et al., 2003; Arnott et al., 2005; Schmid et al., 2006; Virkkula et al., 2007; Collaud Coen et al., 2010; Virkkula et al., 2015). Currently, due to the described limitations of the filter-based photometers and other in situ methods, no reference technique for measuring near-real-time aerosol particles' light absorption is available (Petzold et al., 2013; Lack et al., 2014).

The filter loading effect consists in the accumulation of particles and the consequent loss of sensitivity of the instrument with an increasing particle load (Bond et al., 1999; Weingartner et al., 2003; Lack et al., 2008; Moosmüller et al., 2009). The cross-sensitivity to scattering is the consequence of the multiple light scattering within the filter fibres and between particles and fibres; thus it is largely dependent on the single-scattering albedo of the deposited aerosols. For the older Aethalometer model (AE31) the filter loading effect has been thoroughly studied, and different methods for its quantification have been suggested. These methods use for example the discontinuity between the eBC concentration measurements before and after a filter spot is changed (Weingartner et al., 2003; Virkkula et al., 2007) or the relationship between the eBC concentration and light attenuation (Park et al., 2010; Segura et al., 2014; Drinovec et al., 2015) to correct for the filter loading effect. For the AE33 model the loading effect is corrected on-line using dual-spot technology (Drinovec et al., 2015). In addition, the different physical and chemical properties of the collected particles influence particle optical properties, such as the backscatter fraction and the single-scattering albedo (SSA), thus also affecting the multiple scattering of the collected particles and the filter loading effect (Weingartner et al., 2003; Lack et al., 2008; Virkkula et al., 2015; Drinovec et al., 2017). Among the on-line filter-based instruments, the multi-angle absorption photometer (MAAP) also uses the measurements of light scattered by the blank and loaded filter in order to take into account both the loading effect and the aerosol particles' multiple scattering. Consequently, the MAAP directly provides particle absorption coefficients similar to those obtained with other types of instruments (e.g. PAS instruments; Petzold and Schönlinner, 2004; Petzold et al., 2005).

The multi-wavelength dual-spot Aethalometer software (AE33, Magee Scientific, Aerosol d.o.o. – Drinovec et al., 2015) corrects the loading effect on-line and directly implements the use of a correction factor (C) related to the multiple scattering within the filter matrix to convert the measured attenuation to an absorption coefficient. This C factor is generally assumed a priori, but it can be experimentally determined by using independent absorption measurements or by comparisons with other filter photometers (e.g. Weingartner et al., 2003; Arnott et al., 2005; Drinovec et al., 2015; Backman et al., 2017). For previous filter tapes and Aethalometer versions different values of the multiple-scattering parameter have been reported: for the AE31 quartz filter Weingartner et al. (2003) proposed a value of 2.14 which later on was recommended to be 3.5, i.e. larger by a factor of 1.64 (Müller, 2015; World Meteorological Organization, 2016); for the AE33 Drinovec et al. (2015) found a C value of 1.57 for the Pallflex Teflon-coated glass fibre (TFE-coated glass, also known as M8020), which, after re-normalization using the factor 1.64, resulted in $C = 2.57$. Moreover, differ-

ent experimental C-factor values have been obtained ranging between 2.57–4.24 (Müller et al., 2011b; Drinovec et al., 2020; Laing et al., 2020; Valentini et al., 2020a; Bernardoni et al., 2020). In addition, the quartz filter for the AE31 and the TFE-coated glass filter for the AE33 have been found to feature a cross-sensitivity to scattering, m_s, ranging between 1 % and 3 % (Müller et al., 2011a; Müller, 2015; Drinovec et al., 2015; Zhang et al., 2018; Corbin et al., 2018; Laing et al., 2020; Drinovec et al., 2020). However, to the best of our knowledge, so far, no in situ ambient measurements have been used for a detailed characterization of the new recommended M8060 filter tape. Moreover, no sensitivity studies of the cross-sensitivity to scattering of the C factor have been reported and only very few studies have dealt with the wavelength dependence of C for either the previous or the current filter tapes.

The recent comparison between the MAAP and the offline PP_UniMI polar photometer carried out by Valentini et al. (2020b) pointed to a possible measurement bias of the MAAP absorption coefficients. It is well established that the MAAP, although limited to one measuring wavelength, is the most accurate filter-based on-line method available for the determination of the absorption coefficient (Petzold et al., 2005; Sheridan et al., 2005; Andreae and Gelencsér, 2006; Müller et al., 2011a). Therefore, it is often taken as the reference in inter-comparison exercises with other instruments, such as the AE33, e.g. in Backman et al. (2017). The discrepancy between the MAAP and PP_UniMI reported by Valentini et al. (2020b) was mainly attributed to the value of the fraction of backscattered radiation set in the MAAP algorithm and directly measured by PP_UniMI due to its high angular resolution which scans the whole scattering plane (a resolution of 0.4° in the scattering angle range 0–173°). Valentini et al. (2020b) also reported no differences between the MAAP and PP_UniMI when PP_UniMI was used with the same assumptions as those used in the MAAP (PaM as defined in Valentini et al., 2020b).

The main objective of this study is to characterize the C factor for different filter tapes used in AE33 instruments including the currently used M8060. To this aim, we compared the absorption coefficient measurements from the offline PP_UniMI polar photometer with the on-line MAAP and AE33 measurements performed at three measurement stations (urban background, Barcelona, BCN; regional background, Montseny, MSY; and mountaintop, Montsec d'Ares, MSA) in the western Mediterranean Basin (WMB). The novelty of this study relies on the seasonal and diel variation analysis of the C factor and, especially, on the exploration of the cross-sensitivity to scattering of C and its relationship with the intensive optical properties of the collected particles at the three sites. This analysis allowed us to obtain both the multiple-scattering parameter, C_f, and the cross-sensitivity to scattering, m_s, constants for the M8060 filter currently used by the AE33 Aethalometers. Moreover, we compared the results for the M8060 filter tape with the previously used TFE-coated glass filter tape (T60A20, also referred to as M8020) (Weingartner et al., 2003; Arnott et al., 2005; Drinovec et al., 2015). As previously mentioned, the comparison between PP_UniMI and the MAAP was reported in Valentini et al. (2020b) where data from the BCN and MSY stations were also used to evaluate the performances of PP_UniMI vs. the MAAP. One of the main objectives of this study was to use the multi-wavelength absorption coefficient measurements from the off-line polar photometer extrapolated to the seven AE33 measurement wavelengths to study the wavelength dependence of the AE33 C factor at the three measurement sites.

2 Methodology

2.1 Measurement sites

Aerosols measurements were performed at Barcelona (BCN; urban background; 41°23′24.01″ N, 2°6′58.06″ E; 80 m. a.s.l.), Montseny (MSY; regional background; 41°46′46″ N, 2°21′29″ E; 720 m a.s.l.) and Montsec d'Ares (MSA; mountaintop; 42°3′5″ N, 0°43′46″ E; 1570 m a.s.l.) monitoring supersites (NE Spain). As shown later, these stations are characterized by aerosols with different physical and chemical properties that influenced the differences obtained in the C values. A detailed characterization of the three measurement stations can be found in previous works (e.g. Querol et al., 2001; Rodrıguez et al., 2001; Reche et al., 2011, for BCN; Pérez et al., 2008; Pey et al., 2009; Pandolfi et al., 2011, for MSY; Pandolfi et al., 2014a; Ripoll et al., 2014; Ealo et al., 2016, for MSA). Briefly, the BCN station is located within the Barcelona metropolitan area of nearly 4.5 million inhabitants at a distance of about 5 km from the coast. The MSY station is located in a hilly and densely forested area, 50 km to the N–NE of Barcelona and 25 km from the Mediterranean coast. The MSA station is located in a remote high-altitude emplacement on the southern side of the Pre-Pyrenees at the Montsec Range, 140 km to the NW of Barcelona and 140 km to the WNW of MSY. These supersites are part of the Catalonian Atmospheric Pollution Monitoring and Forecasting Network and of the ACTRIS and GAW networks. Aerosol optical properties at the three sites were measured following standard protocols (WMO/GAW, 2016).

The area of study is characterized by high concentrations of both primary and secondary aerosols, especially in summer (Rodríguez et al., 2002; Dayan et al., 2017; Rivas et al., 2020; Brean et al., 2020) from diverse emission sources. Anthropogenic emissions from road traffic, industry, agriculture and maritime shipping, among others, strongly contribute to the air quality impairment in this region (Querol et al., 2009b; Amato et al., 2009; Pandolfi et al., 2014b). Moreover, the Mediterranean Basin is also highly influenced by natural sources, such as mineral dust from African deserts and smoke

from forest fires (Bergametti et al., 1989; Querol et al., 1998; Rodrıguez et al., 2001; Lyamani et al., 2006; Mona et al., 2006; Koçak et al., 2007; Kalivitis et al., 2007; Querol et al., 2009b; Schauer et al., 2016; Ealo et al., 2016; Querol et al., 2019, among others).

2.2 Aerosol characterization

2.2.1 Aerosol absorption and eBC measurements

The on-line aerosol absorption coefficient, b_{abs}, was measured at the three sites with a multi-angle absorption photometer (MAAP; Model 5012, Thermo Fisher Scientific Inc., USA; Petzold and Schönlinner, 2004). This instrument derives the absorption coefficient at 637 nm (Müller et al., 2011a) and eBC concentration using a radiative transfer model from the measurements of transmission of light through the filter tape and backscattering of light at two different angles. Black carbon, eBC, and attenuation measurements, b_{atn}, were also performed with the AE33 multi-wavelength Aethalometer (model AE33, Magee Scientific, Aerosol d.o.o.; Drinovec et al., 2015). The AE33 is based on the measurement at seven different wavelengths (370, 470, 520, 590, 660, 880 and 950 nm) of the transmission of light through two sample spots with different flows and particle loading relative to the reference spot. It derives the eBC concentration and the attenuation coefficients by applying Eqs. (1) and (2), respectively, following Drinovec et al. (2015):

$$\mathrm{eBC} = \frac{S \cdot (\Delta \mathrm{ATN}_1/100)}{F_1(1-\zeta) \cdot \sigma_{abs} \cdot C(1-k\Delta \mathrm{ATN}_1) \cdot \Delta t}, \quad (1)$$

$$b_{atn} = \frac{S \cdot (\Delta \mathrm{ATN}_1/100)}{F_1(1-\zeta) \cdot (1-k\Delta \mathrm{ATN}_1) \cdot \Delta t}, \quad (2)$$

where S is the filter surface area loaded with the sample; F_1 the volumetric flow of spot 1; ζ the lateral airflow leakage; σ_{abs} the mass-absorption cross-section; k the loading factor parameter; and $\Delta \mathrm{ATN}_1$ the variation in attenuation of light of the filter tape loaded with the sample of spot 1, ATN_1, during the measurement timestamp Δt.

The Aethalometer absorption coefficient can be derived by dividing the attenuation coefficient (Eq. 2) by the multiple-scattering parameter C of the filter tape:

$$b_{abs} = \frac{b_{atn}}{C}. \quad (3)$$

Off-line multi-wavelength particle absorption coefficients were obtained using the PP_UniMI polar photometer (Vecchi et al., 2014; Bernardoni et al., 2017) measurements on the MAAP filter spots. A total of 85 filter spots collected at BCN in the period October 2018–June 2019, 126 filter spots collected at MSY between June and December 2018 (Valentini et al., 2020b), and 122 filter spots collected at MSA between June and November 2018 were analysed. The time elapsed between the MAAP measurements and the MAAP spots analysis with PP_UniMI in Milan varied between 1 year and 1 month. Once selected and cut, each MAAP spot was stored in a petri dish in a fridge and then sent to Milan. We assumed that there were no major particle losses affecting the measured optical properties, although some volatile compounds could have been evaporated over the period. PP_UniMI measures the transmitted and scattered radiation at four wavelengths (405, 532, 635 and 780 nm) in a range of scattering angles from 0 to 173° with a resolution down to 0.4° and applies a radiative transfer model to derive the absorption coefficients. The PP_UniMI working principle and the detailed analysis of the inter-comparison between the MAAP and PP_UniMI for different measurement sites, including BCN and MSY, were reported in Vecchi et al. (2014), Bernardoni et al. (2017) and Valentini et al. (2020b). As mentioned before, in these studies no differences were observed between the MAAP and PP_UniMI when the latter was used as a MAAP (PaM), i.e. using a data inversion with similar assumptions to those performed in the MAAP.

Here we obtain the wavelength-dependent attenuation coefficients $b_{atn}(\lambda)$ derived exclusively from the AE33 measurements by multiplying the eBC concentrations provided by the AE33 (Eq. 4) by the default wavelength-independent instrumental filter constant C_0 from the AE33 setup file (1.57 for the TFE-coated glass fibre tape T60A20, also referred to as M8020, and 1.39 for the M8060 filter tape):

$$\begin{aligned} b_{atn}(\lambda) &= \mathrm{eBC}(\lambda) \cdot \sigma_{abs}(\lambda) \cdot C_0 \\ &= \frac{S}{F}\frac{\Delta \mathrm{ATN}(\lambda)}{\Delta t} \cdot f(\mathrm{ATN}, \lambda), \end{aligned} \quad (4)$$

where $f(\mathrm{ATN}, \lambda)$ is the function which contains all the corrections, i.e. filter loading and leakage, which are performed by the AE33 for each wavelength (Drinovec et al., 2015). Note that the new filter tape M8060 structurally differs from the old filter tape M8020 in filter fibre material, thickness and density, thus leading to different C_0 values (details can be found in the following online document from Magee Scientific: https://mageesci.com/tape/Magee_Scientific_Filter_Aethalometer_AE_Tape_Replacement_discussion.pdf, last access: 20 September 2021).

Then, we determine the average and seasonal multiple-scattering factor C both as the ratio between the AE33 attenuation coefficients and the absorption coefficients $b_{abs}(\lambda)$ measured by the MAAP and PP_UniMI (Eq. 5) and also by applying a Deming regression between the AE33 attenuation coefficients and the MAAP absorption coefficients for the overall average values for each filter tape.

$$C(\lambda) = \frac{b_{atn}(\lambda)}{b_{abs}(\lambda)} \quad (5)$$

This value of the multiple-scattering parameter $C(\lambda)$ is the value derived from the experimental comparison of different instruments, contrasting the default instrumental constant

value C_0. The data at the BCN station were available from between 2016 and 2020; at MSY and MSA data were measured from 2013 to 2020. Different AE33 filter tapes were used during these periods at the three stations as shown in Fig. S1 in the Supplement.

2.2.2 Aerosol scattering measurements

On-line particle total scattering (b_{sp}) and hemispheric backscatter (b_{bsp}) coefficients were measured on-line at the three sites with LED-based integrating nephelometers (Aurora 3000, Ecotech Pty Ltd, Knoxfield, Australia) operating at three wavelengths (450, 525 and 635 nm). Calibration of the nephelometers was performed three times per year using CO_2 as the span gas, and zero adjusts were performed once per day using internally filtered particle-free air. The RH threshold was set by using a processor-controlled automatic heater inside the Aurora 3000 nephelometer to ensure a sampling RH of less than 40 % (World Meteorological Organization, 2016). σ_{sp} coefficients were corrected for non-ideal illumination of the light source and for truncation of the sensing volumes following the procedure described in Müller et al. (2011b).

2.3 Data treatment and conceptual model

The different analyses were performed considering the absorption coefficients provided by either the MAAP or PP_UniMI as reference absorption measurements depending on either time resolution and coverage or the measurement availability at several wavelengths. The AE33 and MAAP data (provided with a high temporal resolution) were used to study the seasonal variations and the cross-sensitivity to scattering of the C factor. The AE33 and PP_UniMI data (provided with a low temporal resolution but at different wavelengths) were used to determine the wavelength dependence of the C factor.

2.3.1 Average and seasonal value analysis and cross-sensitivity to scattering analysis

As previously mentioned, the seasonal analysis of the C factor, analysis of its average values and the study of its cross-sensitivity to scattering were performed using the long-term high-time-resolution dataset from the MAAP and AE33 measurements at the three measurement sites. For this, we applied Eq. (5) using the absorption coefficient from the MAAP and the AE33 attenuation coefficient extrapolated to the 637 nm wavelength of the MAAP through the Ångström exponent obtained from the AE33 measurements at seven wavelengths.

The cross-sensitivity to scattering which, as shown later, can strongly affect the C-factor values is neglected in AE33 applications where it is generally assumed that the measured light attenuation is only due to the absorption of light by the collected particles (Eqs. 1 and 2). Moreover, it is also generally assumed that the multiple scattering by particles is sample independent, or constant, and can be taken into account by introducing the multiple-scattering correction factor C (Drinovec et al., 2015). However, this assumption is a first approximation, since the attenuation of transmitted light is also due to the scattering of light by the collected particles (Bond et al., 1999; Arnott et al., 2005). Taking this dependence into account and following Arnott et al. (2005), we parameterized the light attenuation coefficient as

$$b_{atn} = \frac{S}{F}\frac{\Delta \mathrm{ATN}}{\Delta t} \cdot f(\mathrm{ATN}) + m_s \cdot b_{sp} \tag{6}$$

to obtain the relationship between the absorption, attenuation and scattering coefficients:

$$b_{abs} = \frac{b_{atn}}{C_f} - m \cdot b_{sp}\ . \tag{7}$$

The cross-sensitivity to scattering, which is denoted by the constant m_s, is related to m through $m = m_s/C_f$. Here C_f refers to the multiple-scattering filter parameter, that is a value (possibly wavelength dependent) that depends only on filter properties. If we rearrange Eq. (7) by expressing the scattering coefficient through the single-scattering albedo, we obtain the dependence of the absorption as a function of SSA (Eq. 8), similarly to Eq. (17) in Schmid et al. (2006). The measured multiple parameter, C, affected by the cross-sensitivity to scattering can be expressed as shown in Eq. (9).

$$b_{abs} = \frac{b_{atn}}{C_f} \cdot \frac{1}{1 + m \cdot \frac{\mathrm{SSA}}{1-\mathrm{SSA}}} \tag{8}$$

$$\begin{aligned} C &= C_f\left(1 + m \cdot \frac{\mathrm{SSA}}{1-\mathrm{SSA}}\right) \\ &= C_f + m_s \cdot \frac{\mathrm{SSA}}{1-\mathrm{SSA}} \end{aligned} \tag{9}$$

The effective multiple-scattering parameter, C, depends on the physical properties of collected particles. By comparing data from different instruments (AE33, MAAP and nephelometer) we were able to parameterize the cross-sensitivity of C to scattering (Eq. 8). Equation (9) shows that the actual AE33 cross-sensitivity to scattering is more pronounced when the measured aerosol particles have higher SSA, whereas for particles with lower SSA Eq. (9) converges to Eq. (5).

By analysing the dependency of the effective multiple-scattering parameter C on the SSA, we obtained the experimental-fit constants (C_f and m_s) that describe the relationship between C and SSA. Furthermore, we will present in Sect. 3.1 how the cross-sensitivity to scattering of C depended on some intensive aerosol particle optical properties that strongly depend on aerosol particle size distribution and chemical composition (Figs. S3–S5).

The AE33 data treatment applied to obtain the C seasonality and the cross-sensitivity to scattering included a pre-process filtering method following the approach suggested in

Springston and Sedlacek (2007) and Backman et al. (2017). This filtering method consists in setting a threshold value for the measured attenuation variation, ΔATN_1, that is high enough for the signal-to-noise ratio to be large; herein we have used a fixed value of 0.01. As can be deduced from Eq. (1), the faster the fixed ΔATN_1 is reached, the shorter the period Δt, implying therefore a higher eBC concentration value during the same period. The method we employed determines the period at which the ΔATN_1 step is reached and recalculates the eBC concentration for this Δt. As a consequence of this eBC recalculation, we filtered out the noise resulting from very small values close to the detection limit of the instrument while maintaining the higher eBC values measured without introducing a bias into the measurements as is the case when averaging. With the aim to study the seasonality of the C factor and its cross-sensitivity to scattering, we averaged $b_{abs,MAAP}$ and b_{sp} coefficients to match the corresponding AE33 variable timestamp, Δt, which ranged between approximately 3 and 14 min (see Fig. S2). Moreover, the time granularity of the measurements varied between 1 and 5 min, depending on the software used for data logging (see Table S1 in the Supplement). Given the length of the measurement periods, we assumed that the AE33 filter tapes considered here were characterized under a wide range of aerosol particle properties typically observed at the measurement stations and that the non-simultaneity of AE33 measurements with the two filter tapes did not prevent the comparison between the obtained C.

2.3.2 Wavelength dependence analysis

To study the wavelength dependence of the C factor we compared the absorption coefficients at several wavelengths measured with PP_UniMI with the attenuation coefficients obtained from the AE33 (Eq. 5). Since the off-line PP_UniMI measurements were performed on the MAAP spots, the measured attenuation and scattering coefficients from AE33 and the nephelometer, respectively, were averaged over the timestamp of each one of the selected MAAP spots. The absorption coefficients from PP_UniMI were interpolated and extrapolated to the seven AE33 wavelengths using the attenuation Ångström exponent, obtained through a log–log fit from the PP_UniMI absorption measurements.

Valentini et al. (2020b) reported that the MAAP overestimates the absorption coefficient compared to PP_UniMI. For BCN and MSY Valentini et al. (2020b) reported a MAAP overestimation of 18 % and 21 %, respectively. By applying the same methodology as in Valentini et al. (2020b) we obtained a difference between the MAAP and PP_UniMI for MSA of 19 % (Fig. A1), similar to the biases obtained for BCN and MSY. For this reason, Valentini et al. (2020b) also studied the comparison between the MAAP and PP_UniMI using the same assumptions for the PP_UniMI data inversion as those performed in the MAAP (PaM approach) and reported a 1 : 1 correlation between the two instruments. Given that most of the Aethalometer C values reported in the literature were obtained by comparing AE33 attenuation measurements and MAAP absorption measurements, we also report here the median C values obtained comparing the AE33 with PP_UniMI (Table S2) and with PaM (Table S3).

3 Results

3.1 Multiple-scattering parameter cross-sensitivity to scattering

The cross-sensitivity to scattering of the C factor at the three stations was obtained by analysing the relationship between the multiple-scattering parameter C (at 637 nm) and the measured SSA (Eq. 9).

The SSA was obtained independently at 637 nm using simultaneous MAAP and multiple-wavelength integrating nephelometer data. C was obtained through Eq. (5) from the AE33 attenuation coefficient, extrapolated at 637 nm using the absorption Ångström exponent (AAE) from AE33 and the MAAP absorption coefficients at 637 nm. The analysis was performed by binning the SSA data using Freedman and Diaconis (1981) criteria and then averaging the obtained C values within each SSA bin. Binned data were then fitted following Eq. (9) to obtain the experimental values of both C_f and m_s.

Figure 1 and Table 1 show the results of the fit for BCN, MSY and MSA for both M8020 and M8060 filter tapes. Moreover, Table 1 compares the C values obtained here with those reported in the literature for the M8020 filter tape. For M8020, we calculated a constant C_f of 2.21 ± 0.01 and a cross-sensitivity to scattering, m_s, of 1.8 ± 0.1 at MSY and of 1.96 ± 0.02 % and 3.4 ± 0.1 % at MSA. For the M8060 filter tape, the fit yielded a multiple-scattering constant C_f of 2.50 ± 0.02 and a cross-sensitivity to scattering of 1.6 ± 0.3 % at BCN, a C_f of 1.96 ± 0.01 and a m_s of 3.0 ± 0.1 % at MSY, and a constant C_f of 1.82 ± 0.02 and a m_s of 4.9 ± 0.1 % at MSA.

As a consequence of the cross-sensitivity to scattering, we can appreciate in Fig. 1 a clear increase in C with increasing SSA with an up-to-3-fold increase in C for SSA $>$ 0.90–0.95 depending on the station and filter tape considered. The cross-sensitivity to scattering was evident for both filter tapes at the regional (MSY) and mountain (MSA) stations where the probability of measuring SSA higher than 0.90–0.95 was high (57 %–70 % of the data in Fig. 1). Conversely, at the urban site (BCN), where the SSA was on average lower (12 % of SSA data were above 0.90), a lower cross-sensitivity to scattering was observed. This significant increase in the C factor at high SSA, if not accounted for, can lead to a large overestimation of both eBC concentrations and absorption coefficients from Aethalometer instruments. This effect can have a larger impact at sites where high SSA values are typically observed such as remote Arctic sites and mountaintop

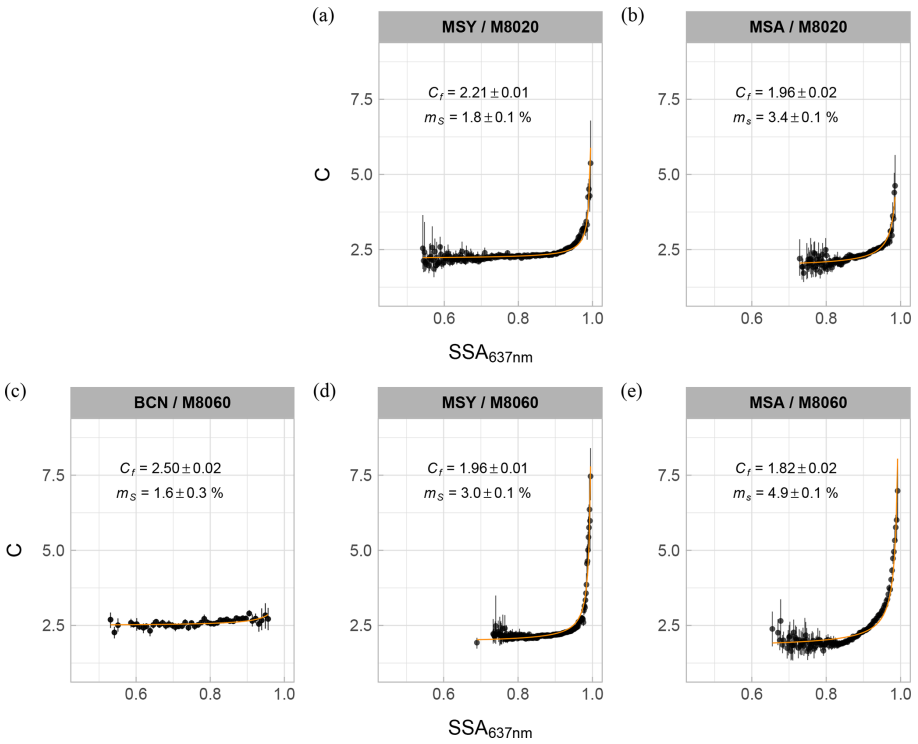

Figure 1. Cross-sensitivity to scattering analysis for TFE-coated glass tape (also known as M8020; **a**, **b**) and M8060 filter tape **(c–e)** for the BCN **(c)**, MSY **(a, d)** and MSA **(b, e)** stations obtained by attenuation coefficients from the AE33, absorption coefficients from the MAAP and scattering coefficients from the integrating nephelometer. Each data point represents the mean and the vertical bars the first and third quartile for each bin. The multiple-scattering constant, C_f, and cross-sensitivity to scattering, m_s, are determined by fitting Eq. (9) to the binned data.

Table 1. AE33 multiple-scattering parameter C for some measurement stations (including BCN, MSY and MSA, in italics) and cross-sensitivity to scattering for the BCN, MSY and MSA stations compared to literature values for AE33 TFE-coated glass (M8020). Different approaches, as mentioned in Sect. 3.2, have been used to obtain the factor C. Since the literature values are obtained through either one of the methods, we include these values in their corresponding column (C or C_{Deming}).

Site	Characteristics	Filter type	Reference	C	C_{Deming}	C_f	m_s (%)
Barcelona	Urban background	M8020	This study	*2.29 ± 0.49*	*1.99 ± 0.02*	–	–
		M8060	This study	*2.44 ± 0.57*	*2.20 ± 0.02*	*2.50 ± 0.02*	*1.6 ± 0.3*
Leipzig	Urban background	M8020	Müller (2015)	3.2			
		M8020	Bernardoni et al. (2020)		2.78		
Rome	Urban background	M8060	Valentini et al. (2020a)	2.66			
Klagenfurt	Urban background	M8020	Drinovec et al. (2020)	1.57			
Montseny	Regional background	M8020	This study	*2.29 ± 0.46*	*2.05 ± 0.02*	*2.21 ± 0.01*	*1.8 ± 0.1*
		M8060	This study	*2.23 ± 0.30*	*2.13 ± 0.01*	*1.96 ± 0.01*	*3.0 ± 0.1*
Montsec d'Ares	Mountaintop	M8020	This study	*2.36 ± 0.59*	*2.21 ± 0.03*	*1.96 ± 0.02*	*3.4 ± 0.1*
		M8060	This study	*2.51 ± 0.71*	*2.05 ± 0.02*	*1.82 ± 0.02*	*4.9 ± 0.1*
Mt Bachelor	Mountaintop	M8020	Laing et al. (2020)	4.24			

sites (Collaud Coen et al., 2004; Gyawali et al., 2009; Andrews et al., 2011; Pandolfi et al., 2014a, 2018; Schmeisser et al., 2018; Ferrero et al., 2019; Laj et al., 2020), as well as in places where increasing or decreasing trends of SSA have been observed (Collaud Coen et al., 2020). This cross-sensitivity to scattering of the filter explains the higher C factors obtained on average at these types of sites (Table 1) and suggests the need to use either a site-specific C value or a C value that takes into account the SSA measured by an independent absorption method. Given its impact on the absorption coefficient, this effect needs to be taken into account for climate studies.

In order to further characterize the observed cross-sensitivity to scattering, we explored how the variations in C with SSA depended on different intensive aerosol particle optical properties, namely the AAE (Fig. S3), backscatter fraction (BF, Fig. S4) and single-scattering albedo Ångström exponent (SSAAE, Fig. S5). We found that large C values and high SSA were often obtained when the sampled aerosol composition was dominated by mineral dust during Saharan dust outbreaks, as demonstrated by the occurrence of negative SSAAEs at high SSA (Fig. S5). In fact, Saharan dust outbreaks, which are common in the WMB (Escudero et al., 2005; Querol et al., 2004, 2009b, a, 2019; Ealo et al., 2016; Yus-Díez et al., 2020), have the potential to increase the SSA above the average values especially at the regional (MSY) and remote (MSA) stations (e.g. Pandolfi et al., 2014a). In prior studies, negative values of the SSAAE have been associated with an aerosol mixture dominated by mineral dust (Collaud Coen et al., 2004; Ealo et al., 2016; Yus-Díez et al., 2020). Moreover, we observed that high C values (for SSA > 0.95) were also associated with AAE values higher than around 1.5 (see Fig. S3), thus indicating a relatively higher absorption efficiency of the collected particles in the UV, consistent with the presence of either dust or brown carbon (BrC) particles (Kirchstetter et al., 2004a; Chen and Bond, 2010; Zotter et al., 2017; Forello et al., 2019, 2020). Furthermore, low BF values, indicative of the predominance of large particles, were also on average associated with high SSA values (see Fig. S4). Note that the dependence of C vs. SSA on the aforementioned intensive optical properties was not clearly observed in BCN, where, at least for the period under study, local pollution masked the effects of coarse dust particles on the measured intensive optical properties and on SSA which kept values lower than around 0.90–0.95. The observed dependency of C on intensive aerosol particle optical properties demonstrated that both particle size distribution and chemical composition can affect the reported C-vs.-SSA relationships.

3.2 Multiple-scattering correction factor – average values and seasonal variation

Here we present the average values and the seasonal cycle of the C factor calculated at 637 nm at BCN, MSY and MSA.

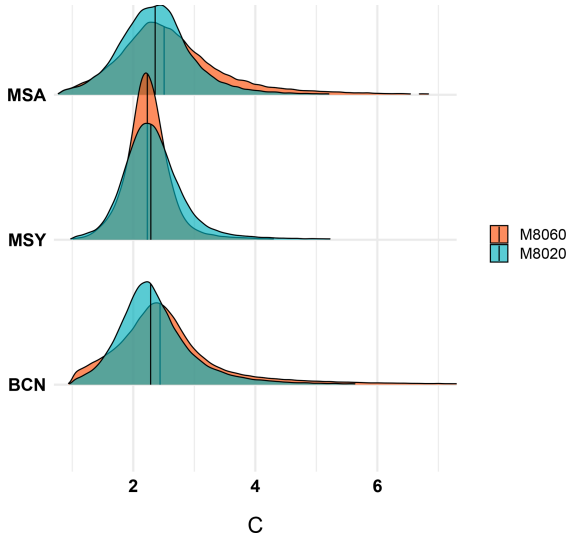

Figure 2. Density distribution of the C factor for each filter type, M8020 and M8060, as obtained through Eq. (5) using both the attenuation coefficient from the AE33 and the absorption coefficient from the MAAP. The vertical line represents the median value of each distribution.

We analysed the multiple-scattering parameter C values both through a Deming regression, taking into account the measurement error in the MAAP (12 %; Petzold and Schönlinner, 2004) and in the AE33 (15 %; Zanatta et al., 2016; Rigler et al., 2020), and by calculating the median value of the C-factor density distribution. The uncertainties in the C factor were derived as either the methodological error from the regression slope of the Deming fit or the half width at half maximum (HWHM) of the density distribution of the C factor. We present here the results from both the aforementioned methods because both methods have been reported in the literature (e.g. Backman et al., 2017; Bernardoni et al., 2020; see Table 1 in this work).

The density distribution of the C factor obtained from the ratio (with a variable time resolution, as mentioned in Sect. 2.3.1), showed a quasi-Gaussian distribution at the three measurement sites with a small tail towards higher C values (Fig. 2).

The median values of the C factor for the M8020 filter tape were 2.29 ± 0.48, 2.29 ± 0.46 and 2.36 ± 0.59 for BCN, MSY and MSA, respectively. These values were on average similar or slightly lower (with differences less than 7 %) compared to the median C values obtained for the M8060 filter tape of 2.44 ± 0.57, 2.23 ± 0.30 and 2.51 ± 0.71 (see Table 1). The Deming regression fit results (Fig. S6) showed C values of 1.99 ± 0.02, 2.05 ± 0.02 and 2.21 ± 0.03 (at BCN, MSY and MSA, respectively) for M8020 which were slightly lower (with differences < 10 %) compared to the C values of 2.20 ± 0.02, 2.13 ± 0.01 and 2.05 ± 0.02 obtained for M8060.

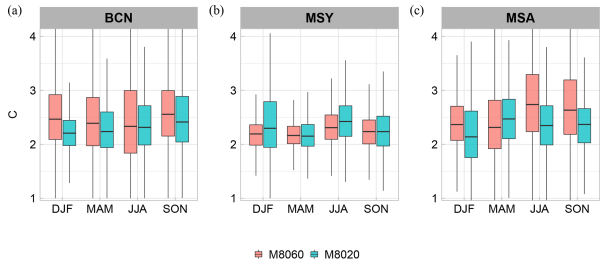

Figure 3. Seasonal evolution of the *C* factor at the **(a)** BCN, **(b)** MSY and **(c)** MSA measurement stations for both TFE-coated glass (M8020) and M8060 filter tapes. The box plot boxes show the range between the first and third quartile (IQR) with the median value for each season distribution represented by the inner line; the maximum whisker length is proportional to 1.5 times the third and first quartile difference, or inter-quartile range ($1.5 \cdot \mathrm{IQR}$).

Note that the uncertainties from the Deming regression were lower compared to the uncertainties derived as the HWHM of the distributions because the Deming regressions were performed using binned data (see Fig. S6). This also was the likely explanation for the lower *C* values on average obtained with the Deming regression compared to the median values of the density distribution. The difference in the *C* values between both methods ranged between 4 %–18 % depending on the filter tape/measurement station considered (see Table 1). However, both methods were consistent and provided a higher *C* factor for the M8060 than for the M8020 filter tape.

As reported in Table 1, overall, higher *C* values were found at MSA, where both the SSA and the cross-sensitivity of the filter tape to scattering were higher compared to at MSY and BCN (see Figs. 1 and S7). The *C* values for the AE33 M8020 and M8060 filter tapes obtained at urban background stations in Rome (Valentini et al., 2020a) and Leipzig (Müller, 2015; Bernardoni et al., 2020) were in the same range as those found in this work for BCN (Table 1).

Figure 3 shows the seasonal variability in the *C* factor for the TFE-coated glass and M8060 filter tapes at the three stations. The large variability in the obtained *C* parameters (see Fig. 3) at the three sites during all the seasons, consistent with the width of the *C*-factor density distribution (Fig. 2) and the SSA seasonal evolution variability (Fig. S7) can be appreciated.

On average, an increase in *C* was observed at MSY and MSA in summer (JJA) for both filter tapes. This increase was likely driven by a greater influence of diurnal processes and the impact of the atmospheric boundary layer (ABL) during the warm months at these two elevated stations and by changes in the chemical and physical properties of collected particles in summer compared to in winter (DJF). In fact, spring and summer seasons in the WMB are characterized by a high frequency of Saharan dust outbreaks (e.g. Pey et al., 2013; Yus-Díez et al., 2020) and the formation of high concentrations of secondary organic aerosols and secondary sulfate particles (e.g. Ripoll et al., 2015) which in turn increase the particle scattering efficiency and the SSA in summer compared to in winter (Pandolfi et al., 2011). Although dust particles can absorb radiation (e.g. Sokolik and Toon, 1999; Di Biagio et al., 2019), the effect of Saharan dust outbreaks at the measurement stations considered here was to increase the SSA (at 637 nm) over the average values. In fact, as shown by Pandolfi et al. (2014a), both scattering and absorption increased at MSY and MSA during Saharan dust outbreaks, but the resulting SSA was higher compared to other atmospheric scenarios typical of the area under study. Therefore, the higher *C* values observed during Saharan dust outbreaks were coherent with an increase in SSA over the threshold above which *C* sharply increased (see Figs. 1 and S3–S5). An increase in *C* when dust particles are deposited on the filter tape was also reported by Di Biagio et al. (2017) for the AE31 Aethalometer. Di Biagio et al. (2017) reported *C* values for dust particles by generating particles by mechanical shaking of dust samples from different desert soils using AE31 and MAAP measurements, and they reported *C* values of between 3.6 and 3.96 for Saharan soils (Table 2 of Di Biagio et al., 2017).

As shown in Sect. 3.1, high SSA increased the *C* values, and, consequently, the *C* seasonality was affected, to some degree, by the SSA seasonality. In fact, Fig. S7 shows that the seasonal evolution of the SSA at MSY and MSA mirrored quite well the seasonal evolution of *C*, with an increase in both *C* and SSA towards the warm season. In BCN, the inter-season variability in both *C* and SSA was less pronounced and *C* remained fairly constant during the different seasons. An exception was in the winter period (DJF) when both *C* (M8060) and SSA showed minima. Nevertheless, the variability within each season was the largest in BCN, due to a higher variability in the SSA values at this station within each season compared to in MSY and MSA (Fig. S7). The relationship between *C* and SSA can be also observed in Fig. S8, where the diel cycles of both *C* and SSA were reported. In BCN, both *C* and SSA showed two relative minima in the morning and in the afternoon, mirroring the traffic rush hours. At MSY, the sea-breeze-driven transport of pollutants in the afternoon caused a reduction in both SSA and *C*. Conversely, at MSA both *C* and SSA showed less variability in the diel cycles and less similarity was observed. Note that the similarities commented on above between the diel/seasonal cycles of *C* and SSA were more or less evident depending on the season/station considered. In fact, we have shown in Fig. 1 that high SSA (> 0.90–0.95) can strongly affect the *C* values, but less dependency between *C* and SSA was observed for lower SSA, thus also contributing to masking the similarities between *C* and SSA reported in Figs. 3, S7 and S8, which were obtained averaging all available data, including *C* values at lower SSA.

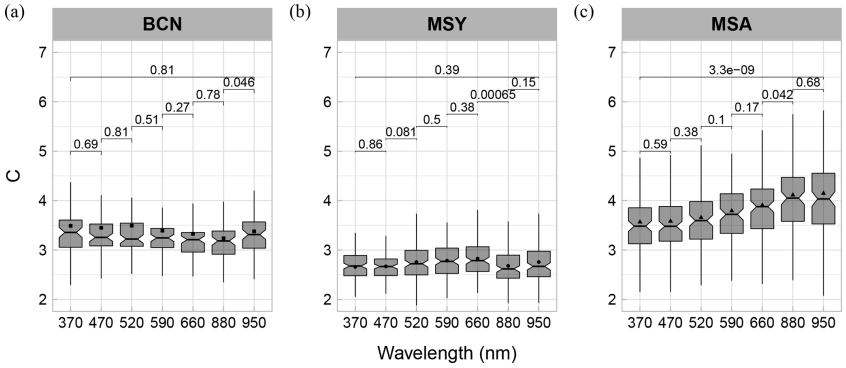

Figure 4. Wavelength dependence of C at BCN, MSY and MSA comparing b_{atn} from the AE33 measured at each wavelength and b_{abs} interpolated and extrapolated to the same wavelength from PP_UniMI. Box plots have been obtained as in Fig. 3 with the addition of the mean value of the distribution for each wavelength represented by a marker. The values above the box plots between adjacent wavelengths and between 370 and 950 nm wavelength box plots show the obtained p values, with $p < 0.05$ meaning a statistically significant difference.

3.3 Wavelength dependence analysis from the PP_UniMI-vs.-AE33 comparison

The spectral dependence of the AE33 C factor, C (λ), was studied at the three stations by comparing the attenuation coefficients, b_{atn}, from AE33 at seven different wavelengths with the absorption coefficients, b_{abs}, from PP_UniMI. To this aim, the PP_UniMI absorption coefficients were interpolated and extrapolated to the seven AE33 wavelengths using the absorption Ångström exponent (AAE) obtained from the original PP_UniMI measurements. The obtained mean AAE were 1.12 ± 0.17, 1.29 ± 0.24 and 1.35 ± 0.18 for the BCN, MSY and MSA stations, respectively, with an increase from the urban (BCN) to the regional (MSY) and remote (MSA) sites due to the increase in the relative importance of non-fossil BC sources (e.g. biomass burning) and Saharan dust at the remote sites compared to BCN.

Figure 4 shows that at the urban (BCN) and regional (MSY) stations the C factor did not present a statistically significant dependence on the wavelength. However, Fig. 4c shows that at the remote MSA station the multiple-scattering parameter C presented a statistically significant increase between 370 nm ($C = 3.47$) and 950 nm ($C = 4.03$) (see Table S2). The observed increase in the C factor with wavelength affects the absorption coefficients derived from the AE33 attenuation measurements and, consequently, can affect all the intensive optical parameters such as the AAE, SSA and SSAAE which can be derived from the multi-wavelength AE33 absorption measurements and scattering coefficient measurements. Moreover, a wavelength-dependent C factor can impair Aethalometer-based BC source apportionment analysis, such as that of the Aethalometer model, used to determine the contribution from fossil fuels vs. biomass burning emissions (Sandradewi et al., 2008). Contradictory results have been reported in the literature about the spectral dependence of C for older versions of the Aethalometer (model AE31). For example, Weingartner et al. (2003) found a strong indication of the independence of C from the wavelength, and Segura et al. (2014) did not find any wavelength dependence of the multiple-scattering parameter C. Conversely, Bernardoni et al. (2020) observed a decrease in the C factor with wavelengths, although it was not statistically significant.

As can be appreciated by comparing Figs. 2–4, the multiple-scattering correction factors obtained using the PP_UniMI reference instrument were larger than those obtained with the MAAP as a consequence of the offset in the absorption measurements between the MAAP and PP_UniMI. A detailed discussion of this offset can be found in Fig. A1 and in Fig. 2 in Valentini et al. (2020b).

Hereafter, we propose a possible explanation for the different spectral dependencies found for C at the measurement sites considered here. We have shown in Sect. 3.1 that, independently from the measurement station considered, the cross-sensitivity to scattering can strongly increase C for SSA values above an upper threshold. To explore if the SSA can also affect the C wavelength dependence, we studied the wavelength dependence of C for SSA values above and below the site-dependent SSA thresholds. Figure 5 shows the comparison between the C factor at MSY and MSA for SSA above (high SSA) and below (low SSA) the SSA thresholds of 0.95 and 0.9, respectively, for MSY and MSA (see Fig. 1). Figure 5 shows that at MSA there was a statistically significant increase in C with the wavelength for SSA > 0.90, whereas no statistically significant increase was observed for SSA < 0.90. For this specific analysis, based on the PP_UniMI off-line measurements, 86 % of SSA values at MSA (68 samples out of 79) were above the SSA threshold of 0.95. At MSY, only 1 sample out of 126 was characterized by an SSA value higher than the SSA threshold of 0.95, thus preventing a robust statistical analysis of the C wavelength dependence for high SSA at MSY. Despite this, a 17 % in-

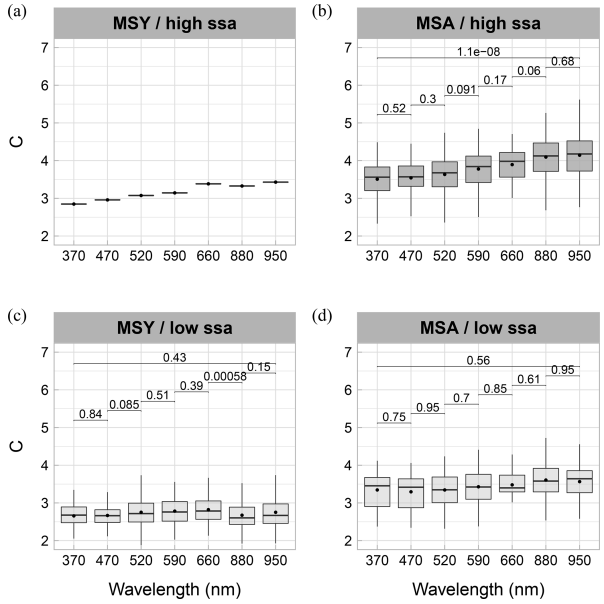

Figure 5. Wavelength dependence of C at MSY **(a, c)** and MSA **(b, d)** obtained comparing b_{atn} from the AE33 measured at each wavelength and b_{abs} interpolated and extrapolated to the same wavelength from PP_UniMI. Box plots have been obtained as in Fig. 3 and separated into two categories depending on whether the SSA was above ("high ssa"; **a**, **b**) or below ("low ssa"; **c**, **d**) the threshold at which C sharply increases. As in Fig. 3, the values above the box plots between adjacent wavelengths and between 370 and 950 nm wavelength box plots show the obtained p values, with $p < 0.05$ meaning a statistically significant difference.

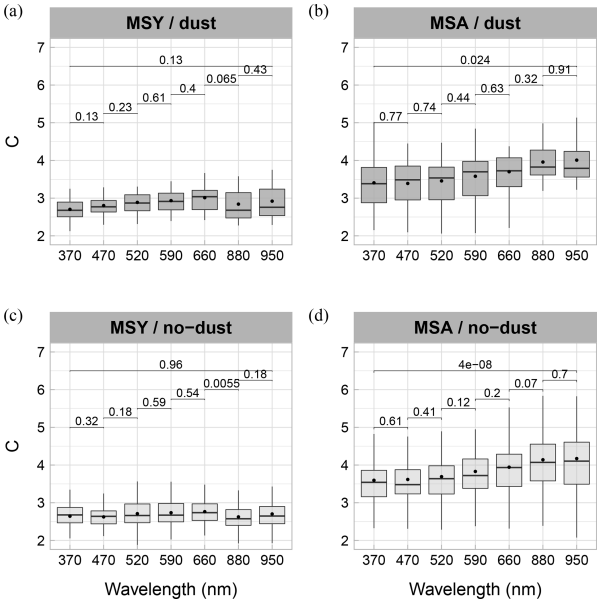

Figure 6. Wavelength dependence of C at MSY **(a, c)** and MSA **(b, d)** obtained comparing b_{atn} from the AE33 measured at each wavelength and b_{abs} interpolated and extrapolated to the same wavelength from PP_UniMI. Box plots have been obtained as in Fig. 3 and separated into two categories depending on whether Saharan dust outbreaks took place (dust) or not (no-dust). As in Fig. 3, the values above the box plots between adjacent wavelengths and between 370 and 950 nm wavelength box plots show the obtained p values, with $p < 0.05$ meaning a statistically significant difference.

crease in C with the wavelength, from 2.85 at 370 nm to 3.43 at 950 nm, for this single point was observed (see Fig. 5a). At MSY, similarly to MSA, C did not show any dependence on the wavelength for SSA < 0.95 (see Fig. 5c). Thus, this analysis demonstrated that a high SSA of the particles deposited on the filter tape can increase the C values, influencing at the same time their wavelength dependence.

We have shown in Sect. 3.1 that the sharp increase in C at high SSA at the stations herein analysed can be associated with the presence of particles dominated by dust, characterized by low SSAAEs and BFs and high AAEs and SSA (Figs. S3–S5). Therefore, we performed a similar C spectral dependence analysis to that in Fig. 5 but separating the days affected by Saharan dust (dust) from the days without dust influence (no-dust). As shown in Fig. 6, no spectral dependence of C was observed during either dust or no-dust scenarios at MSY. This lack of dependence on the dust intrusions could be due to the limited number of off-line samples at MSY characterized by high SSA (1 out of 126). Thus, due to the low temporal resolution of off-line PP_UniMI measurements, even during Saharan dust days the SSA at MSY rarely increased above the SSA threshold. Nevertheless, using high-time-resolution data (see Fig. 1) the potential effect of dust particles to increase the SSA (and consequently C) was evident at both MSY and MSA. At MSA (see Fig. 6) C showed a statistically significant increase with wavelength for both dust and no-dust samples due to the fact that the samples with high SSA at MSA (86 %) were well distributed between the two scenarios. Thus, these results confirmed that the SSA was the main parameter that influenced the spectral behaviour of the C parameter.

To further explore the possible causes that contributed to the different C spectral dependencies observed, we performed a similar analysis to that in Virkkula et al. (2015) by comparing C and its wavelength dependence with different intensive aerosol particle optical properties, namely the SSA, BF and SSAAE. Virkkula et al. (2015) and Drinovec et al. (2017) have shown that the AE33 factor loading parameter, k, increases with an increasing BF (smaller particles) and decreases with increasing SSA and that the wavelength dependence of k also depends on these two optical properties as well as on the particle mixing state. In Fig. S9 in the Supplement we present a similar analysis by studying the effects of these intensive optical properties on the multiple-scattering

parameter C instead of on k. Figure S9 shows the slope of C with the wavelength (i.e. the wavelength dependence of C) with the SSA, BF and SSAAE at the three sites. No clear relationship was observed between the C slope and the three intensive optical properties at both BCN and MSY. Moreover, the C slopes at these two sites were close to zero for the considered intensive optical properties. The observed lack of a C gradient was again likely due to the fact that at BCN and MSY the SSA did not exceed the threshold value, even when the SSAAE indicated the possible presence of Saharan dust intrusions at MSY (see Fig. S9h). However, Fig. S9c shows that at MSA there was a shift of the C slope towards large positive values when SSA was above 0.95. Below this SSA threshold value, the C slope was close to zero, confirming the reduced C wavelength dependence for low SSA values at MSA. Moreover, when the SSAAE (BF) at MSA (see Fig. S9i and f) decreased towards negative (low) values (Saharan dust intrusions), the slope of C increased, again confirming the potential of coarse Saharan dust to increase the SSA and, consequently, C especially at the remote site. Note that, as already commented on (see Fig. 6), the C slope also kept positive values at MSA for the samples not dominated by dust (SSAAE > 0), thus further indicating the predominance effect of SSA on the C wavelength dependence. Thus, the results presented in Fig. S9 confirm the effects of SSA on C presented in Figs. 5 and 6.

The lack of points for BCN (none) and MSY (1 of 126) for large SSA values, especially above the SSA threshold obtained in Fig. 1, prevented extrapolating the results to other measurement background conditions, and further studies should be performed to better characterize the spectral behaviour of C and its dependency on the cross-sensitivity to scattering under different atmospheric conditions/scenarios. This is especially important, as already commented on, in view of the contradictory results reported in the literature (e.g. Weingartner et al., 2003; Segura et al., 2014; Bernardoni et al., 2020). The results presented here clearly indicated that when the SSA exceeded a given site-dependent threshold, as determined using the method in Sect. 3.1, the C values and their wavelength dependence increased. For the measurement sites considered here, Saharan dust outbreaks were identified as a possible cause for SSA values higher than the threshold. However, from a general point of view, other factors, including the location of the measurement stations and/or absence of anthropogenic pollution, can determine the presence of a particle mixture with high or very high SSA.

Finally, we performed a sensitivity study on the effects that using a wavelength-dependent C ($C(\lambda)$) had on the AAE derived from AE33 measurements, comparing the results with those obtained using the usual approach based on the application of a constant C factor (C(const)). Figure 7 shows that the AAE values for BCN and MSY did not present any significant variation (see Table S4), with AAE mean values of 1.19 ± 0.15 and 1.27 ± 0.12 (at BCN and MSY, respectively) for C(const) and 1.17 ± 0.15 and 1.25 ± 0.12 (for BCN and MSY, respectively) for $C(\lambda)$. These results for BCN and MSY were coherent with the observed lack of spectral dependence of C at these two stations (Fig. 4). However, at MSA the observed increase in C with the wavelength introduced an increase into the AAE of around 13 %, from 1.19 ± 0.07 (C(const)) to 1.35 ± 0.07 ($C(\lambda)$). Similarly, Fig. S10a and b present the results of a sensitivity analysis performed to understand the effects that using a constant or a wavelength-dependent C had on the SSA at 470, 660 and 950 nm. As with the AAE, Fig. S10c shows no significant variation in SSA at the three considered wavelengths at BCN and MSY, again consistent with the observed lack of dependence of the C factor on the wavelength at these two sites. However, Fig. S10 shows a statistically significant increase in the SSA at the MSA station of around 1.3 % at 660 nm and 2 % at 950 nm when using $C(\lambda)$ instead of C(const). Conversely, as expected, no statistically significant change was appreciated at the lower wavelength, 470 nm. This variation introduced by $C(\lambda)$ into the AAE and SSA, although not large, is relevant since it occurs at the threshold of the SSA value for which a substantial increase in C as a function of SSA is observed, as shown in Sect. 3.1.

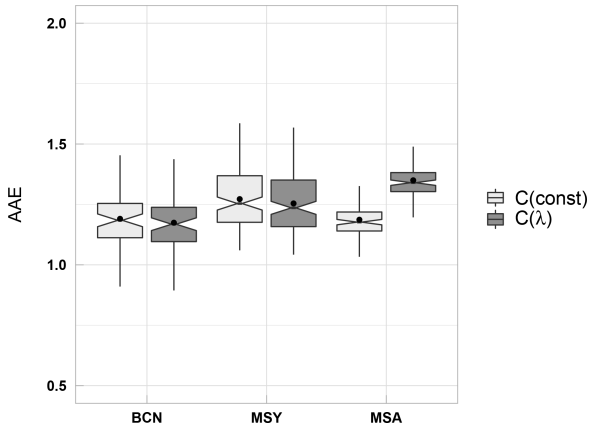

Figure 7. The absorption Ångström exponent (AAE) calculated with a constant C(const) and the wavelength-dependent $C(\lambda)$ for all stations. Box plots have been obtained as in Figs. 3 and 4, with the markers indicating the mean AAE values.

4 Conclusions

In this work we studied the multiple-scattering parameter C for two filter tapes used in AE33 dual-spot Aethalometers, i.e. the previously used M8020 and the currently used M8060 filter tapes. For this, we used data collected at three different background stations in NE Spain: an urban background station in Barcelona, BCN; a regional background station at Montseny, MSY; and a mountaintop station at Montsec

d'Ares, MSA. We obtained the C correction factor comparing the AE33 attenuation measurements with the absorption coefficients measured from MAAP instruments and used simultaneous scattering measurements from an integrating nephelometer to characterize the cross-sensitivity to scattering of C. Moreover, we studied the C wavelength dependence at the three sites comparing the AE33 attenuation coefficients with the absorption coefficients from the off-line multi-wavelength PP_UniMI.

We presented here a novel approach to characterize the cross-sensitivity to scattering of the C correction factor. This approach consisted in fitting the measurements of C versus SSA. The fits provided the constant C_f and a cross-sensitivity factor m_s. We applied the fits to the M8020 filter tape at MSY and MSA, and we obtained higher cross-sensitivity values of the C factor (1.8 ± 0.1 % and 3.4 ± 0.1 % at MSY and MSA, respectively) compared to those reported in the literature (around 1 %–1.5 %). For the first time, we also characterized here the cross-sensitivity to scattering of the new M8060 filter tape. We obtained a higher cross-sensitivity to scattering for the M8060 than for the M8020 filter tape, with values of 1.6 ± 0.3 %, 3.0 ± 0.1 % and 4.9 ± 0.1 % for BCN, MSY and MSA, respectively. The multiple-scattering parameter, C_f, for the M8020 filter tape was 2.21 ± 0.01 at MSY and 1.96 ± 0.02 at MSA. For the M8060 filter tape the fit led to C_f values of 2.50 ± 0.02 at BCN, 1.96 ± 0.01 at MSY and 1.82 ± 0.02 at MSA. The consequence of this cross-sensitivity to scattering resulted in a large increase in the C values, up to a 3-fold increase, for SSA values above 0.9–0.95. This significant increase in the C factor at high SSA, if not accounted for, can lead to a large overestimation of both eBC concentrations and absorption coefficients measured by Aethalometers. This can be especially relevant at sites typically characterized by an aerosol mixture with high SSA. In fact, the effect of this cross-sensitivity to scattering of C was the likely reason explaining the higher C values reported in the literature for mountaintop and Arctic measurement stations. Here, we observed larger C values and higher cross-sensitivity to scattering at the mountain station and much less C variability at the urban site, where the SSA rarely exceeded the SSA threshold from which changes in C can be observed.

Overall, the main difference between the two filter tapes studied here was the higher cross-sensitivity to scattering observed for the currently used M8060 filter tape compared to the previously used M8020 filter tape. Despite the different cross-sensitivity to scattering, both filter tapes showed average C values which fall within the measurement uncertainties.

We found an average multiple-scattering parameter C at 637 nm of 2.29, 2.29 and 2.36 for the M8020 filter tape and of 2.44, 2.23 and 2.51 for the M8060 filter tape for the BCN, MSY and MSA measurement stations, respectively. Due to the dominant effect of SSA on C, the obtained C factors showed seasonal and diel variability at the three sites that mirrored the variability in SSA. At MSY and MSA higher C values were on average observed in summer due to changes in the physical–chemical aerosol properties that led to SSA values being on average higher in summer than in winter. A larger fraction of dust particles and formation of secondary organic aerosols and secondary sulfates likely explained the observed increase in C in summer at these regional/remote sites. However, at the urban background station of BCN the C values remain fairly constant throughout the year.

We also analysed the wavelength dependence of the C parameter for the M8060 filter tape at BCN, MSY and MSA by comparing the AE33 attenuation data with the off-line PP_UniMI absorption measurements performed on selected MAAP spots. Overall, we found a statistically significant increase with the wavelength, from 3.47 for 370 nm to 4.03 for 950 nm at the mountaintop station (MSA), whereas at the BCN and MSY background stations no statistically significant dependence was found. The reason for the lack of wavelength dependence of C at BCN and MSY was the lack of MAAP spots characterized by high SSA. Thus, due to the low temporal resolution of off-line PP_UniMI measurements, the SSA at MSY and, especially, at BCN rarely increased above the SSA threshold. Conversely, the wavelength dependence of C at the mountain station was due to the high probability of measuring SSA values higher than the site-dependent SSA threshold, from which the C values start to increase. For this analysis, we studied the C wavelength dependence separately for samples characterized by high SSA (higher than the site-dependent threshold) and low SSA and observed that at MSA no dependence of C on the wavelength was observed for samples with low SSA, whereas a clear dependence was observed for the sample with high SSA. Thus, the analysis presented here demonstrated that a high SSA of the particles deposited on the filter tape can increase the C values, influencing at the same time their wavelength dependence. Interestingly, only 1 sample (out of 126) collected at the MSY regional station was characterized by high SSA, and for this sample the calculated C strongly increased with wavelength. The results presented here clearly indicated that when the SSA exceeded a given site-dependent threshold, the C values and their wavelength dependence increased. For the measurement sites considered here, Saharan dust outbreaks were identified as a possible cause for SSA values higher than the threshold. However, other factors, including the location of the measurement stations and/or the absence of anthropogenic pollution, can determine the presence of a particle mixture with high or very high SSA. We also investigated the effect of considering a wavelength-dependent C at the MSA station compared to using a constant C for the absorption Ångström exponent (AAE) and the single-scattering albedo (SSA) through sensitivity tests. Results revealed an increase in the AAE by 13 % and an increase in the SSA by 1.3 % when using the wavelength-dependent C factor compared to using a constant C factor (i.e. with no λ dependence). This effect may impact any source apportionment method which takes into ac-

count the multi-wavelength absorption values from the AE33 (e.g. the Aethalometer model).

In summary, based on the results herein presented, the absorption coefficients from AE33 data can be corrected with different degrees of confidence depending on the information available to estimate the multiple-scattering parameter C:

- A tailored dynamic multiple-scattering parameter can be obtained if on-line simultaneous reference absorption measurements are available. In this case, a dynamic C value with a high temporal resolution can be obtained, allowing an in situ correction of AE33 data and allowing the studying of, for example, the diel/seasonal cycles of the multiple-scattering parameter. Here we used on-line MAAP absorption measurements at one wavelength for the determination of a dynamic C value at the same MAAP wavelength.
- If independent reference multi-wavelength absorption measurements are available, then the dependence of the multiple-scattering parameter on wavelengths can be studied. Here we determined the wavelength dependence of the multiple-scattering parameter C by using the polar photometer (PP_UniMI) off-line absorption measurements performed on the MAAP filter spots and by comparing the off-line PP_UniMI measurements with AE33 attenuation data integrated over the MAAP filter spots' timestamp.
- If reference absorption measurements are not available for the experimental determination of C, then the average values of the multiple-scattering parameter provided here for three different measurement stations can be used as a reference.
- If both independent reference absorption measurements and scattering measurements are available, then the cross-sensitivity to scattering of the multiple-scattering parameter C can be determined by studying the relationship between C and single-scattering albedo (SSA). In this case, a parameterization can be obtained relating C and SSA.
- If SSA measurements are not available, this work provides parameterized formulas that allow calculating C over a wide range of SSA values.

Finally, the C values obtained in this work for different station types (urban, regional, remote) may serve as a reference for similar background measurement sites where the methodology presented here cannot be applied. Nevertheless, discrepancies may arise due to the possible differences in aerosol sources, composition and mixing state at different sites that, accordingly, will result in different aerosol particle optical properties. Similar analysis performed at other measurement sites with similar features may reduce the uncertainties around the applicability of the results presented here to other stations.

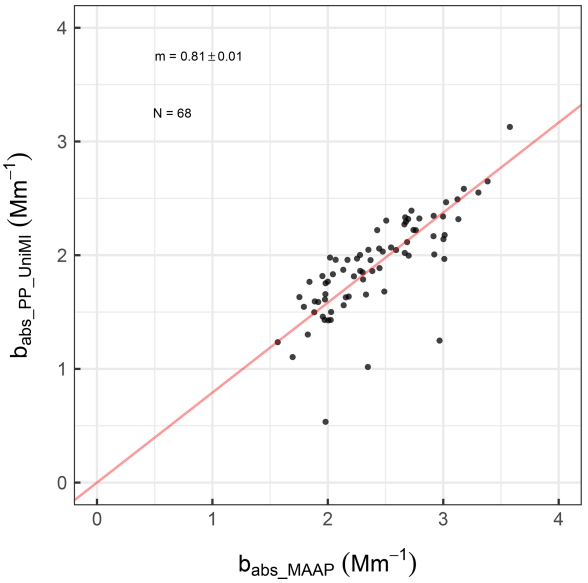

Figure A1. Comparison between the aerosol absorption coefficient measured by PP_UniMI on sample spots ($\sigma_{ap\_PP\_UniMI}$) and the MAAP (σ_{ap_MAAP}).

Appendix A: Absorption coefficient relationship between the MAAP and the PP_UniMI polar photometer for the MSA station

This appendix aims to show the result of applying the same methodology as in Sect. 3.1 of Valentini et al. (2020b) to the PP_UniMI-analysed dataset for obtaining the bias for the MSA station in the absorption coefficient measurements between the MAAP and the PP_UniMI polar photometer (Fig. A1). It consists in the application of a Deming regression fit, which results in a slope of 0.81 ± 0.01 for our dataset.

Code and data availability. The Montseny (http://ebas.nilu.no/Pages/DataSetList.aspx?key=562F658B11934EAC92BB0A2F0CD29A40, last access: 20 September 2021; EBAS, 2021b) and Montsec d'Ares (http://ebas.nilu.no/Pages/DataSetList.aspx?key=4F862F47EC324FD6AAFA5CD8CF6F8EFB, last access: 20 September 2021; EBAS, 2021a) datasets used for this publication are accessible online on the WDCA (World Data Centre for Aerosols) web page: http://ebas.nilu.no (last access: 20 September 2021). The Barcelona datasets were collected within different national and regional projects and/or agreements and are available upon request. The code used for analysis can be obtained upon request to the corresponding author.

Supplement. The supplement related to this article is available online at: https://doi.org/10.5194/amt-14-6335-2021-supplement.

Author contributions. DC, SV, RV and VB performed and analysed the measurements with the PP_UniMI polar photometer. NP, CR, MP, AA and JYD carried out the maintenance and supervision of the BCN, MSY and MSA supersites. AA, GM, MP and XQ played a crucial role in the processes of shaping the manuscript structure as well as in helping with the data analysis. JYD developed the data process, the analysis of the results, and summarized and expressed them in this paper. All authors provided advice regarding the manuscript structure and content as well as contributed to the writing of the final manuscript.

Competing interests. At the time of the research, Martin Rigler and Matic Ivančič were also employed by the manufacturer of the Aethalometer AE33.

Disclaimer. Publisher's note: Copernicus Publications remains neutral with regard to jurisdictional claims in published maps and institutional affiliations.

Acknowledgements. The authors acknowledge the support from the Spanish Ministry of Economy, Industry and Competitiveness and I+D+I "Retos Colaboración" funds, the Generalitat de Catalunya, and the European Commission. The authors also acknowledge support of the COST Action CA16109 COLOSSAL. Griša Močnik acknowledges support from the Slovenian Research Agency. IDAEA-CSIC is also acknowledged.

Financial support. This research has been supported by the Ministerio de Economía, Industria y Competitividad, Gobierno de España (CAIAC project (grant no. PID2019-108990PB-100)); the European Cooperation in Science and Technology (Action CA16109 COLOSSAL); the Agència de Gestió d'Ajuts Universitaris i de Recerca (AGAUR 2017 SGR41); and the European Commission, Horizon 2020 Framework Programme (ACTRIS IMP (grant no. 871115)).

Review statement. This paper was edited by Pierre Herckes and reviewed by two anonymous referees.

References

Ajtai, T., Filep, Á., Schnaiter, M., Linke, C., Vragel, M., Bozóki, Z. Á., Szabó, G., and Leisner, T.: A novel multi-wavelength photoacoustic spectrometer for the measurement of the UV-vis-NIR spectral absorption coefficient of atmospheric aerosols, J. Aerosol Sci., 41, 1020–1029, https://doi.org/10.1016/j.jaerosci.2010.07.008, 2010.

Alfaro, S., Lafon, S., Rajot, J., Formenti, P., Gaudichet, A., and Maille, M.: Iron oxides and light absorption by pure desert dust: An experimental study, J. Geophys. Res., 109, D08208, https://doi.org/10.1029/2003JD004374, 2004.

Amato, F., Querol, X., Alastuey, A., Pandolfi, M., Moreno, T., Gracia, J., and Rodriguez, P.: Evaluating urban PM_{10} pollution benefit induced by street cleaning activities, Atmos. Environ., 43, 4472–4480, 2009.

Andreae, M. O. and Gelencsér, A.: Black carbon or brown carbon? The nature of light-absorbing carbonaceous aerosols, Atmos. Chem. Phys., 6, 3131–3148, https://doi.org/10.5194/acp-6-3131-2006, 2006.

Andrews, E., Ogren, J. A., Bonasoni, P., Marinoni, A., Cuevas, E., Rodríguez, S., Sun, J. Y., Jaffe, D. A., Fischer, E. V., Baltensperger, U., Weingartner, E., Collaud Coen, M., Sharma, S., Macdonald, A. M., Leaitch, W. R., Lin, N.-H., Laj, P., Arsov, T., Kalapov, I., Jefferson, A., and Sheridan, P.: Climatology of aerosol radiative properties in the free troposphere, Atmos. Res., 102, 365–393, 2011.

Arnott, W. P., Hamasha, K., Moosmüller, H., Sheridan, P. J., and Ogren, J. A.: Towards aerosol light-absorption measurements with a 7-wavelength aethalometer: Evaluation with a photoacoustic instrument and 3-wavelength nephelometer, Aerosol Sci. Tech., 39, 17–29, https://doi.org/10.1080/027868290901972, 2005.

Backman, J., Schmeisser, L., Virkkula, A., Ogren, J. A., Asmi, E., Starkweather, S., Sharma, S., Eleftheriadis, K., Uttal, T., Jefferson, A., Bergin, M., Makshtas, A., Tunved, P., and Fiebig, M.: On Aethalometer measurement uncertainties and an instrument correction factor for the Arctic, Atmos. Meas. Tech., 10, 5039–5062, https://doi.org/10.5194/amt-10-5039-2017, 2017.

Bergametti, G., Dutot, A.-L., Buat-Menard, P., Losno, R., and Remoudaki, E.: Seasonal variability of the elemental composition of atmospheric aerosol particles over the northwestern Mediterranean, Tellus B, 41, 353–361, 1989.

Bergstrom, R. W., Pilewskie, P., Russell, P. B., Redemann, J., Bond, T. C., Quinn, P. K., and Sierau, B.: Spectral absorption properties of atmospheric aerosols, Atmos. Chem. Phys., 7, 5937–5943, https://doi.org/10.5194/acp-7-5937-2007, 2007.

Bernardoni, V., Valli, G., and Vecchi, R.: Set-up of a multi wavelength polar photometer for off-line absorption coefficient measurements on 1-h resolved aerosol samples, J. Aerosol Sci., 107, 84–93, https://doi.org/10.1016/j.jaerosci.2017.02.009, 2017.

Bernardoni, V., Ferrero, L., Bolzacchini, E., Forello, A. C., Gregorič, A., Massabò, D., Močnik, G., Prati, P., Rigler, M., Santagostini, L., Soldan, F., Valentini, S., Valli, G., and Vecchi, R.: Determination of Aethalometer multiple-scattering enhancement parameters and impact on source apportionment during the winter 2017/18 EMEP/ACTRIS/COLOSSAL campaign in Milan, Atmos. Meas. Tech., 14, 2919–2940, https://doi.org/10.5194/amt-14-2919-2021, 2021.

Bond, T. C., Anderson, T. L., and Campbell, D.: Calibration and Intercomparison of Filter-Based Measurements of Visible Light Absorption by Aerosols, Aerosol Sci. Tech., 30, 582–600, https://doi.org/10.1080/027868299304435, 1999.

Bond, T. C., Doherty, S. J., Fahey, D. W., Forster, P. M. Berntsen, T., DeAngelo, B. J., Flanner, M. G., Ghan, S., Kärcher, B., Koch, D., Kinne, S., Kondo, Y., Quinn, P. K., Sarofim, M. C., Schultz, M. G., Schulz, M., Venkataraman, C., Zhang, H., Zhang, S., Bellouin, N., Guttikunda, S. K., Hopke, P. K., Jacobson, M. Z., Kaiser, J. W., Klimont, Z., Lohmann, U., Schwarz, J. P., Shindell, D., Storelvmo, T., Warren, S. G., and Zender, C. S.: Bound-

ing the role of black carbon in the climate system: A scientific assessment, J. Geophys. Res.-Atmos., 118, 5380–5552, 2013.

Brean, J., Beddows, D. C. S., Shi, Z., Temime-Roussel, B., Marchand, N., Querol, X., Alastuey, A., Minguillón, M. C., and Harrison, R. M.: Molecular insights into new particle formation in Barcelona, Spain, Atmos. Chem. Phys., 20, 10029–10045, https://doi.org/10.5194/acp-20-10029-2020, 2020.

Cappa, C. D., Zhang, X., Russell, L. M., Collier, S., Lee, A. K., Chen, C. L., Betha, R., Chen, S., Liu, J., Price, D. J., Sanchez, K. J., McMeeking, G. R., Williams, L. R., Onasch, T. B., Worsnop, D. R., Abbatt, J., and Zhang, Q.: Light Absorption by Ambient Black and Brown Carbon and its Dependence on Black Carbon Coating State for Two California, USA, Cities in Winter and Summer, J. Geophys. Res.-Atmos., 124, 1550–1577, https://doi.org/10.1029/2018JD029501, 2019.

Chen, Y. and Bond, T. C.: Light absorption by organic carbon from wood combustion, Atmos. Chem. Phys., 10, 1773–1787, https://doi.org/10.5194/acp-10-1773-2010, 2010.

Collaud Coen, M., Weingartner, E., Schaub, D., Hueglin, C., Corrigan, C., Henning, S., Schwikowski, M., and Baltensperger, U.: Saharan dust events at the Jungfraujoch: detection by wavelength dependence of the single scattering albedo and first climatology analysis, Atmos. Chem. Phys., 4, 2465–2480, https://doi.org/10.5194/acp-4-2465-2004, 2004.

Collaud Coen, M., Weingartner, E., Apituley, A., Ceburnis, D., Fierz-Schmidhauser, R., Flentje, H., Henzing, J. S., Jennings, S. G., Moerman, M., Petzold, A., Schmid, O., and Baltensperger, U.: Minimizing light absorption measurement artifacts of the Aethalometer: evaluation of five correction algorithms, Atmos. Meas. Tech., 3, 457–474, https://doi.org/10.5194/amt-3-457-2010, 2010.

Collaud Coen, M., Andrews, E., Alastuey, A., Arsov, T. P., Backman, J., Brem, B. T., Bukowiecki, N., Couret, C., Eleftheriadis, K., Flentje, H., Fiebig, M., Gysel-Beer, M., Hand, J. L., Hoffer, A., Hooda, R., Hueglin, C., Joubert, W., Keywood, M., Kim, J. E., Kim, S.-W., Labuschagne, C., Lin, N.-H., Lin, Y., Lund Myhre, C., Luoma, K., Lyamani, H., Marinoni, A., Mayol-Bracero, O. L., Mihalopoulos, N., Pandolfi, M., Prats, N., Prenni, A. J., Putaud, J.-P., Ries, L., Reisen, F., Sellegri, K., Sharma, S., Sheridan, P., Sherman, J. P., Sun, J., Titos, G., Torres, E., Tuch, T., Weller, R., Wiedensohler, A., Zieger, P., and Laj, P.: Multidecadal trend analysis of in situ aerosol radiative properties around the world, Atmos. Chem. Phys., 20, 8867–8908, https://doi.org/10.5194/acp-20-8867-2020, 2020.

Corbin, J. C., Pieber, S. M., Czech, H., Zanatta, M., Jakobi, G., Massabò, D., Orasche, J., El Haddad, I., Mensah, A. A., Stengel, B., Drinovec, L., Mocnik, G., Zimmermann, R., Prévôt, A. S., and Gysel, M.: Brown and Black Carbon Emitted by a Marine Engine Operated on Heavy Fuel Oil and Distillate Fuels: Optical Properties, Size Distributions, and Emission Factors, J. Geophys. Res.-Atmos., 123, 6175–6195, https://doi.org/10.1029/2017JD027818, 2018.

Dayan, U., Ricaud, P., Zbinden, R., and Dulac, F.: Atmospheric pollution over the eastern Mediterranean during summer – a review, Atmos. Chem. Phys., 17, 13233–13263, https://doi.org/10.5194/acp-17-13233-2017, 2017.

Di Biagio, C., Formenti, P., Cazaunau, M., Pangui, E., Marchand, N., and Doussin, J.-F.: Aethalometer multiple scattering correction C_{ref} for mineral dust aerosols, Atmos. Meas. Tech., 10, 2923–2939, https://doi.org/10.5194/amt-10-2923-2017, 2017.

Di Biagio, C., Formenti, P., Balkanski, Y., Caponi, L., Cazaunau, M., Pangui, E., Journet, E., Nowak, S., Andreae, M. O., Kandler, K., Saeed, T., Piketh, S., Seibert, D., Williams, E., and Doussin, J.-F.: Complex refractive indices and single-scattering albedo of global dust aerosols in the shortwave spectrum and relationship to size and iron content, Atmos. Chem. Phys., 19, 15503–15531, https://doi.org/10.5194/acp-19-15503-2019, 2019.

Drinovec, L., Močnik, G., Zotter, P., Prévôt, A. S. H., Ruckstuhl, C., Coz, E., Rupakheti, M., Sciare, J., Müller, T., Wiedensohler, A., and Hansen, A. D. A.: The "dual-spot" Aethalometer: an improved measurement of aerosol black carbon with real-time loading compensation, Atmos. Meas. Tech., 8, 1965–1979, https://doi.org/10.5194/amt-8-1965-2015, 2015.

Drinovec, L., Gregorič, A., Zotter, P., Wolf, R., Bruns, E. A., Prévôt, A. S. H., Petit, J.-E., Favez, O., Sciare, J., Arnold, I. J., Chakrabarty, R. K., Moosmüller, H., Filep, A., and Močnik, G.: The filter-loading effect by ambient aerosols in filter absorption photometers depends on the coating of the sampled particles, Atmos. Meas. Tech., 10, 1043–1059, https://doi.org/10.5194/amt-10-1043-2017, 2017.

Drinovec, L., Sciare, J., Stavroulas, I., Bezantakos, S., Pikridas, M., Unga, F., Savvides, C., Višić, B., Remškar, M., and Močnik, G.: A new optical-based technique for real-time measurements of mineral dust concentration in PM_{10} using a virtual impactor, Atmos. Meas. Tech., 13, 3799–3813, https://doi.org/10.5194/amt-13-3799-2020, 2020.

Ealo, M., Alastuey, A., Ripoll, A., Pérez, N., Minguillón, M. C., Querol, X., and Pandolfi, M.: Detection of Saharan dust and biomass burning events using near-real-time intensive aerosol optical properties in the north-western Mediterranean, Atmos. Chem. Phys., 16, 12567–12586, https://doi.org/10.5194/acp-16-12567-2016, 2016.

EBAS: Montsec d'Ares dataset, EBAS [data set], available at: http://ebas.nilu.no/Pages/DataSetList.aspx?key=4F862F47EC324FD6AAFA5CD8CF6F8EFB, last access: 20 September 2021a.

EBAS: Montseny dataset, EBAS [data set], available at: http://ebas.nilu.no/Pages/DataSetList.aspx?key=562F658B11934EAC92BB0A2F0CD29A40, last access: 20 September 2021b.

Escudero, M., Castillo, S., Querol, X., Avila, A., Alarcón, M., Viana, M. M., Alastuey, A., Cuevas, E., and Rodríguez, S.: Wet and dry African dust episodes over eastern Spain, J. Geophys. Res., 110, D18S08, https://doi.org/10.1029/2004JD004731, 2005.

Ess, M. N. and Vasilatou, K.: Characterization of a new miniCAST with diffusion flame and premixed flame options: Generation of particles with high EC content in the size range 30 nm to 200 nm, Aerosol Sci. Tech., 53, 29–44, https://doi.org/10.1080/02786826.2018.1536818, 2019.

Ferrero, L., Ritter, C., Cappelletti, D., Moroni, B., Močnik, G., Mazzola, M., Lupi, A., Becagli, S., Traversi, R., Cataldi, M., Neuber, R., Vitale, V., and Bolzacchini, E.: Aerosol optical properties in the Arctic: The role of aerosol chemistry and dust composition in a closure experiment between Lidar and tethered balloon vertical profiles, Sci. Total Environ., 686, 452–467, https://doi.org/10.1016/j.scitotenv.2019.05.399, 2019.

Forello, A. C., Bernardoni, V., Calzolai, G., Lucarelli, F., Massabò, D., Nava, S., Pileci, R. E., Prati, P., Valentini, S., Valli, G., and Vecchi, R.: Exploiting multi-wavelength aerosol absorption coefficients in a multi-time resolution source apportionment study to retrieve source-dependent absorption parameters, Atmos. Chem. Phys., 19, 11235–11252, https://doi.org/10.5194/acp-19-11235-2019, 2019.

Forello, A. C., Amato, F., Bernardoni, V., Calzolai, G., Canepari, S., Costabile, F., Di Liberto, L., Gualtieri, M., Lucarelli, F., Nava, S., Perrino, C., Petralia, E., Valentini, S., Valli, G., and Vecchi, R.: Gaining knowledge on source contribution to aerosol optical absorption properties and organics by receptor modelling, Atmos. Environ., 243, 117 873, https://doi.org/10.1016/j.atmosenv.2020.117873, https://doi.org/10.1016/j.atmosenv.2020.117873, 2020.

Freedman, D. and Diaconis, P.: On the histogram as a density estimator: L2 theory, Z. Wahrscheinlichkeit., 57, 453–476, https://doi.org/10.1007/BF01025868, 1981.

Gyawali, M., Arnott, W. P., Lewis, K., and Moosmüller, H.: In situ aerosol optics in Reno, NV, USA during and after the summer 2008 California wildfires and the influence of absorbing and non-absorbing organic coatings on spectral light absorption, Atmos. Chem. Phys., 9, 8007–8015, https://doi.org/10.5194/acp-9-8007-2009, 2009.

Hansen, A., Rosen, H., and Novakov, T.: The aethaloemter- An instrument for the real-time measurement of optical absorption by particles, Sci. Total Environ., 36, 191–196, 1984.

IPCC; Climate Change 2001: The Scientific Basis. Contribution of Working Group I to the Third Assessment Report of the Intergovernmental Panel on Climate Change, edited by: Houghton, J. T., Ding, Y., Griggs, D. J., Noguer, M., van der Linden, P. J., Dai, X., Maskell, K., and Johnson, C. A., Cambridge University Press, Cambridge, United Kingdom and New York, NY, USA, 881 pp., 2001.

Kalivitis, N., Gerasopoulos, E., Vrekoussis, M., Kouvarakis, G., Kubilay, N., Hatzianastassiou, N., Vardavas, I., and Mihalopoulos, N.: Dust transport over the eastern Mediterranean derived from Total Ozone Mapping Spectrometer, Aerosol Robotic Network, and surface measurements, J. Geophys. Res., 112, D03202, https://doi.org/10.1029/2006JD007510, 2007.

Kirchstetter, T. W., Novakov, T., and Hobbs, P. V.: Evidence that the spectral dependence of light absorption by aerosols is affected by organic carbon, J. Geophys. Res., 109, D21208, https://doi.org/10.1029/2004JD004999, 2004.

Koçak, M., Mihalopoulos, N., and Kubilay, N.: Contributions of natural sources to high PM_{10} and $PM_{2.5}$ events in the eastern Mediterranean, Atmos. Environ., 41, 3806–3818, 2007.

Lack, D. A., Lovejoy, E. R., Baynard, T., Pettersson, A., and Ravishankara, A. R.: Aerosol Absorption Measurement using Photoacoustic Spectroscopy: Sensitivity, Calibration, and Uncertainty Developments, Aerosol Sci. Tech., 40, 697–708, https://doi.org/10.1080/02786820600803917, 2006.

Lack, D. A., Cappa, C. D., Covert, D. S., Baynard, T., Massoli, P., Sierau, B., Bates, T. S., Quinn, P. K., Lovejoy, E. R., and Ravishankara, A. R.: Bias in filter-based aerosol light absorption measurements due to organic aerosol loading: Evidence from ambient measurements, Aerosol Sci. Tech., 42, 1033–1041, https://doi.org/10.1080/02786820802389277, 2008.

Lack, D. A., Moosmüller, H., McMeeking, G. R., Chakrabarty, R. K., and Baumgardner, D.: Characterizing elemental, equivalent black, and refractory black carbon aerosol particles: A review of techniques, their limitations and uncertainties, Anal. Bioanal. Chem., 406, 99–122, https://doi.org/10.1007/s00216-013-7402-3, 2014.

Laing, J. R., Jaffe, D. A., and Sedlacek, A. J.: Comparison of filter-based absorption measurements of biomass burning aerosol and background aerosol at the Mt. Bachelor observatory, Aerosol Air Qual. Res., 20, 663–678, https://doi.org/10.4209/aaqr.2019.06.0298, 2020.

Laj, P., Bigi, A., Rose, C., Andrews, E., Lund Myhre, C., Collaud Coen, M., Lin, Y., Wiedensohler, A., Schulz, M., Ogren, J. A., Fiebig, M., Gliß, J., Mortier, A., Pandolfi, M., Petäja, T., Kim, S.-W., Aas, W., Putaud, J.-P., Mayol-Bracero, O., Keywood, M., Labrador, L., Aalto, P., Ahlberg, E., Alados Arboledas, L., Alastuey, A., Andrade, M., Artíñano, B., Ausmeel, S., Arsov, T., Asmi, E., Backman, J., Baltensperger, U., Bastian, S., Bath, O., Beukes, J. P., Brem, B. T., Bukowiecki, N., Conil, S., Couret, C., Day, D., Dayantolis, W., Degorska, A., Eleftheriadis, K., Fetfatzis, P., Favez, O., Flentje, H., Gini, M. I., Gregorič, A., Gysel-Beer, M., Hallar, A. G., Hand, J., Hoffer, A., Hueglin, C., Hooda, R. K., Hyvärinen, A., Kalapov, I., Kalivitis, N., Kasper-Giebl, A., Kim, J. E., Kouvarakis, G., Kranjc, I., Krejci, R., Kulmala, M., Labuschagne, C., Lee, H.-J., Lihavainen, H., Lin, N.-H., Löschau, G., Luoma, K., Marinoni, A., Martins Dos Santos, S., Meinhardt, F., Merkel, M., Metzger, J.-M., Mihalopoulos, N., Nguyen, N. A., Ondracek, J., Pérez, N., Perrone, M. R., Petit, J.-E., Picard, D., Pichon, J.-M., Pont, V., Prats, N., Prenni, A., Reisen, F., Romano, S., Sellegri, K., Sharma, S., Schauer, G., Sheridan, P., Sherman, J. P., Schütze, M., Schwerin, A., Sohmer, R., Sorribas, M., Steinbacher, M., Sun, J., Titos, G., Toczko, B., Tuch, T., Tulet, P., Tunved, P., Vakkari, V., Velarde, F., Velasquez, P., Villani, P., Vratolis, S., Wang, S.-H., Weinhold, K., Weller, R., Yela, M., Yus-Diez, J., Zdimal, V., Zieger, P., and Zikova, N.: A global analysis of climate-relevant aerosol properties retrieved from the network of Global Atmosphere Watch (GAW) near-surface observatories, Atmos. Meas. Tech., 13, 4353–4392, https://doi.org/10.5194/amt-13-4353-2020, 2020.

Laskin, A., Laskin, J., and Nizkorodov, S. A.: Chemistry of Atmospheric Brown Carbon, Chem. Rev., 115, 4335–4382, https://doi.org/10.1021/cr5006167, 2015.

Lee, J. and Moosmüller, H.: Measurement of light absorbing aerosols with folded-jamin photothermal interferometry, Sensors, 20, 1–13, https://doi.org/10.3390/s20092615, 2020.

Lin, C. I., Baker, M., and Charlson, R. J.: Absorption Coefficient of Atmospheric Aerosol: a Method for Measurement, Appl. Optics, 12, 1356–1363, 1973.

Linke, C., Ibrahim, I., Schleicher, N., Hitzenberger, R., Andreae, M. O., Leisner, T., and Schnaiter, M.: A novel single-cavity three-wavelength photoacoustic spectrometer for atmospheric aerosol research, Atmos. Meas. Tech., 9, 5331–5346, https://doi.org/10.5194/amt-9-5331-2016, 2016.

Liousse, C., Cachier, H., and Jennings, S. G.: Optical and thermal measurements of black carbon aerosol content in different environments: Variation of the specific attenuation cross-section, sigma (σ), Atmospheric Environment A-Gen., 27, 1203–1211, https://doi.org/10.1016/0960-1686(93)90246-U, 1993.

Liu, S., Aiken, A. C., Gorkowski, K., Dubey, M. K., Cappa, C. D., Williams, L. R., Herndon, S. C., Massoli, P., Fortner, E. C., Chhabra, P. S., Brooks, W. A., Onasch, T. B., Jayne, J. T., Worsnop, D. R., China, S., Sharma, N., Mazzoleni, C., Xu, L., Ng, N. L., Liu, D., Allan, J. D., Lee, J. D., Fleming, Z. L., Mohr, C., Zotter, P., Szidat, S., and Prévôt, A. S.: Enhanced light absorption by mixed source black and brown carbon particles in UK winter, Nat. Commun., 6, 8435, https://doi.org/10.1038/ncomms9435, 2015.

Lyamani, H., Olmo, F., Alcántara, A., and Alados-Arboledas, L.: Atmospheric aerosols during the 2003 heat wave in southeastern Spain II: Microphysical columnar properties and radiative forcing, Atmos. Environ., 40, 6465–6476, 2006.

Massabò, D., Bernardoni, V., Bove, M. C., Brunengo, A., Cuccia, E., Piazzalunga, A., Prati, P., Valli, G., and Vecchi, R.: A multi-wavelength optical set-up for the characterization of carbonaceous particulate matter, J. Aerosol Sci., 60, 34–46, https://doi.org/10.1016/j.jaerosci.2013.02.006, 2013.

Mengis, N. and Matthews, H. D.: Non-CO_2 forcing changes will likely decrease the remaining carbon budget for 1.5 °C, npj Climate and Atmospheric Science, 3, 1–7, https://doi.org/10.1038/s41612-020-0123-3, 2020.

Mona, L., Amodeo, A., Pandolfi, M., and Pappalardo, G.: Saharan dust intrusions in the Mediterranean area: Three years of Raman lidar measurements, J. Geophys. Res., 111, D16203, https://doi.org/10.1029/2005JD006569, 2006.

Moosmüller, H., Chakrabarty, R. K., and Arnott, W. P.: Aerosol light absorption and its measurement: A review, J. Quant. Spectrosc. Ra., 110, 844–878, https://doi.org/10.1016/j.jqsrt.2009.02.035, 2009.

Müller, T.: Development of correction factors for Aethalometers AE31 and AE33, ACTRIS-2 WP3 Workshop, Athens, 10–12 November 2015.

Müller, T., Henzing, J. S., de Leeuw, G., Wiedensohler, A., Alastuey, A., Angelov, H., Bizjak, M., Collaud Coen, M., Engström, J. E., Gruening, C., Hillamo, R., Hoffer, A., Imre, K., Ivanow, P., Jennings, G., Sun, J. Y., Kalivitis, N., Karlsson, H., Komppula, M., Laj, P., Li, S.-M., Lunder, C., Marinoni, A., Martins dos Santos, S., Moerman, M., Nowak, A., Ogren, J. A., Petzold, A., Pichon, J. M., Rodriquez, S., Sharma, S., Sheridan, P. J., Teinilä, K., Tuch, T., Viana, M., Virkkula, A., Weingartner, E., Wilhelm, R., and Wang, Y. Q.: Characterization and intercomparison of aerosol absorption photometers: result of two intercomparison workshops, Atmos. Meas. Tech., 4, 245–268, https://doi.org/10.5194/amt-4-245-2011, 2011a.

Müller, T., Laborde, M., Kassell, G., and Wiedensohler, A.: Design and performance of a three-wavelength LED-based total scatter and backscatter integrating nephelometer, Atmos. Meas. Tech., 4, 1291–1303, https://doi.org/10.5194/amt-4-1291-2011, 2011b.

Myhre, G., Shindell, D., Breéon, F.-M., Collins, W., Fuglestvedt, J., Huang, J., Koch, D., Lamarque, J.-F., Lee, D., Mendoza, B., Nakajima, T., Robock, A., Stephens, G., Takemura, T., and Zhang, H.: Anthropogenic and Natural Radiative Forcing, 8, 659–740, Cambridge University Press, Cambridge, United Kingdom and New York, NY, USA, https://doi.org/10.1017/CBO9781107415324.018, 2013.

Ogren, J. A., Wendell, J., Andrews, E., and Sheridan, P. J.: Continuous light absorption photometer for long-term studies, Atmos. Meas. Tech., 10, 4805–4818, https://doi.org/10.5194/amt-10-4805-2017, 2017.

Onasch, T. B., Massoli, P., Kebabian, P. L., Hills, F. B., Bacon, F. W., and Freedman, A.: Single scattering albedo monitor for airborne particulates, Aerosol Sci. Tech., 49, 267–279, https://doi.org/10.1080/02786826.2015.1022248, 2015.

Pandolfi, M., Cusack, M., Alastuey, A., and Querol, X.: Variability of aerosol optical properties in the Western Mediterranean Basin, Atmos. Chem. Phys., 11, 8189–8203, https://doi.org/10.5194/acp-11-8189-2011, 2011.

Pandolfi, M., Ripoll, A., Querol, X., and Alastuey, A.: Climatology of aerosol optical properties and black carbon mass absorption cross section at a remote high-altitude site in the western Mediterranean Basin, Atmos. Chem. Phys., 14, 6443–6460, https://doi.org/10.5194/acp-14-6443-2014, 2014a.

Pandolfi, M., Tobias, A., Alastuey, A., Sunyer, J., Schwartz, J., Lorente, J., Pey, J., and Querol, X.: Effect of atmospheric mixing layer depth variations on urban air quality and daily mortality during Saharan dust outbreaks, Sci. Total Environ., 494, 283–289, 2014b.

Pandolfi, M., Alados-Arboledas, L., Alastuey, A., Andrade, M., Angelov, C., Artiñano, B., Backman, J., Baltensperger, U., Bonasoni, P., Bukowiecki, N., Collaud Coen, M., Conil, S., Coz, E., Crenn, V., Dudoitis, V., Ealo, M., Eleftheriadis, K., Favez, O., Fetfatzis, P., Fiebig, M., Flentje, H., Ginot, P., Gysel, M., Henzing, B., Hoffer, A., Holubova Smejkalova, A., Kalapov, I., Kalivitis, N., Kouvarakis, G., Kristensson, A., Kulmala, M., Lihavainen, H., Lunder, C., Luoma, K., Lyamani, H., Marinoni, A., Mihalopoulos, N., Moerman, M., Nicolas, J., O'Dowd, C., Petäjä, T., Petit, J.-E., Pichon, J. M., Prokopciuk, N., Putaud, J.-P., Rodríguez, S., Sciare, J., Sellegri, K., Swietlicki, E., Titos, G., Tuch, T., Tunved, P., Ulevicius, V., Vaishya, A., Vana, M., Virkkula, A., Vratolis, S., Weingartner, E., Wiedensohler, A., and Laj, P.: A European aerosol phenomenology – 6: scattering properties of atmospheric aerosol particles from 28 ACTRIS sites, Atmos. Chem. Phys., 18, 7877–7911, https://doi.org/10.5194/acp-18-7877-2018, 2018.

Park, S. S., Hansen, A. D., and Cho, S. Y.: Measurement of real time black carbon for investigating spot loading effects of Aethalometer data, Atmos. Environ., 44, 1449–1455, https://doi.org/10.1016/j.atmosenv.2010.01.025, 2010.

Pérez, N., Pey, J., Castillo, S., Viana, M., Alastuey, A., and Querol, X.: Interpretation of the variability of levels of regional background aerosols in the Western Mediterranean, Sci. Total Environ., 407, 527–540, 2008.

Petzold, A. and Schönlinner, M.: Multi-angle absorption photometry–a new method for the measurement of aerosol light absorption and atmospheric black carbon, J. Aerosol Sci., 35, 421–441, 2004.

Petzold, A., Schloesser, H., Sheridan, P. J., Arnott, W. P., Ogren, J. A., and Virkkula, A.: Evaluation of multiangle absorption photometry for measuring aerosol light absorption, Aerosol Sci. Tech., 39, 40–51, https://doi.org/10.1080/027868290901945, 2005.

Petzold, A., Ogren, J. A., Fiebig, M., Laj, P., Li, S.-M., Baltensperger, U., Holzer-Popp, T., Kinne, S., Pappalardo, G., Sugimoto, N., Wehrli, C., Wiedensohler, A., and Zhang, X.-Y.: Recommendations for reporting "black carbon" measurements, At-

mos. Chem. Phys., 13, 8365–8379, https://doi.org/10.5194/acp-13-8365-2013, 2013.

Pey, J., Pérez, N., Castillo, S., Viana, M., Moreno, T., Pandolfi, M., López-Sebastián, J., Alastuey, A., and Querol, X.: Geochemistry of regional background aerosols in the Western Mediterranean, Atmos. Res., 94, 422–435, 2009.

Pey, J., Querol, X., Alastuey, A., Forastiere, F., and Stafoggia, M.: African dust outbreaks over the Mediterranean Basin during 2001–2011: PM_{10} concentrations, phenomenology and trends, and its relation with synoptic and mesoscale meteorology, Atmos. Chem. Phys., 13, 1395–1410, https://doi.org/10.5194/acp-13-1395-2013, 2013.

Querol, X., Alastuey, A., Puicercus, J. A., Mantilla, E., Miro, J. V., Lopez-Soler, A., Plana, F., and Artiñano, B.: Seasonal evolution of suspended particles around a large coal-fired power station: particulate levels and sources, Atmos. Environ., 32, 1963–1978, 1998.

Querol, X., Alastuey, A., Rodriguez, S., Plana, F., Ruiz, C. R., Cots, N., Massagué, G., and Puig, O.: PM_{10} and $PM_{2.5}$ source apportionment in the Barcelona Metropolitan area, Catalonia, Spain, Atmos. Environ., 35, 6407–6419, 2001.

Querol, X., Alastuey, A., Viana, M. M., Rodriguez, S., Artíñano, B., Salvador, P., Do Santos, S. G., Fernandez Patier, R., Ruiz, C., De la Rosa, J., Sanchez de la Campa, A., Menendez, M., and Gil, J.: Speciation and origin of PM_{10} and $PM_{2.5}$ in Spain, J. Aerosol Sci., 35, 1151–1172, 2004.

Querol, X., Alastuey, A., Pey, J., Cusack, M., Pérez, N., Mihalopoulos, N., Theodosi, C., Gerasopoulos, E., Kubilay, N., and Koçak, M.: Variability in regional background aerosols within the Mediterranean, Atmos. Chem. Phys., 9, 4575–4591, https://doi.org/10.5194/acp-9-4575-2009, 2009a.

Querol, X., Pey, J., Pandolfi, M., Alastuey, A., Cusack, M., Pérez, N., Moreno, T., Viana, M., Mihalopoulos, N., Kallos, G., and Kleanthous, S.: African dust contributions to mean ambient PM_{10} mass-levels across the Mediterranean Basin, Atmos. Environ., 43, 4266–4277, 2009b.

Querol, X., Perez, N., Reche, C., Ealo, M., Ripoll, A., Tur, J., Pandolfi, M., Pey, J., Salvador, P., Moreno, T., and Alastuey, A.: African dust and air quality over Spain: Is it only dust that matters?, Sci. Total Environ., 686, 737–752, 2019.

Ramanathan, V. and Carmichael, G.: Global and regional climate changes due to black carbon, Nat. Geosci., 1, 221–227, https://doi.org/10.1038/ngeo156, 2008.

Ramanathan, V., Crutzen, P., Kiehl, J., and Rosenfeld, D.: Aerosols, climate, and the hydrological cycle, Science, 294, 2119–2124, 2001.

Reche, C., Querol, X., Alastuey, A., Viana, M., Pey, J., Moreno, T., Rodríguez, S., González, Y., Fernández-Camacho, R., de la Rosa, J., Dall'Osto, M., Prévôt, A. S. H., Hueglin, C., Harrison, R. M., and Quincey, P.: New considerations for PM, Black Carbon and particle number concentration for air quality monitoring across different European cities, Atmos. Chem. Phys., 11, 6207–6227, https://doi.org/10.5194/acp-11-6207-2011, 2011.

Rigler, M., Drinovec, L., Lavrič, G., Vlachou, A., Prévôt, A. S. H., Jaffrezo, J. L., Stavroulas, I., Sciare, J., Burger, J., Kranjc, I., Turšič, J., Hansen, A. D. A., and Močnik, G.: The new instrument using a TC–BC (total carbon–black carbon) method for the online measurement of carbonaceous aerosols, Atmos. Meas. Tech., 13, 4333–4351, https://doi.org/10.5194/amt-13-4333-2020, 2020.

Ripoll, A., Pey, J., Minguillón, M. C., Pérez, N., Pandolfi, M., Querol, X., and Alastuey, A.: Three years of aerosol mass, black carbon and particle number concentrations at Montsec (southern Pyrenees, 1570 m a.s.l.), Atmos. Chem. Phys., 14, 4279–4295, https://doi.org/10.5194/acp-14-4279-2014, 2014.

Ripoll, A., Minguillón, M. C., Pey, J., Jimenez, J. L., Day, D. A., Sosedova, Y., Canonaco, F., Prévôt, A. S. H., Querol, X., and Alastuey, A.: Long-term real-time chemical characterization of submicron aerosols at Montsec (southern Pyrenees, 1570 m a.s.l.), Atmos. Chem. Phys., 15, 2935–2951, https://doi.org/10.5194/acp-15-2935-2015, 2015.

Rivas, I., Beddows, D. C. S., Amato, F., Green, D. C., Järvi, L., Hueglin, C., Reche, C., Timonen, H., Fuller, G. W., Niemi, J. V., Pérez, N., Aurela, M., Hopke, P. K., Alastuey, A., Kulmala, M., Harrison, R. M., Querol, X., and Kelly, F. J.: Source apportionment of particle number size distribution in urban background and traffic stations in four European cities, Environ. Int., 135, 105345, https://doi.org/10.1016/j.envint.2019.105345, 2020.

Rodrıguez, S., Querol, X., Alastuey, A., Kallos, G., and Kakaliagou, O.: Saharan dust contributions to PM_{10} and TSP levels in Southern and Eastern Spain, Atmos. Environ., 35, 2433–2447, 2001.

Rodríguez, S., Querol, X., Alastuey, A., and Plana, F.: Sources and processes affecting levels and composition of atmospheric aerosol in the western Mediterranean, J. Geophys. Res., 107, 4777, https://doi.org/10.1029/2001JD001488, 2002.

Samset, B. H., Sand, M., Smith, C. J., Bauer, S. E., Forster, P. M., Fuglestvedt, J. S., Osprey, S., and Schleussner, C. F.: Climate Impacts From a Removal of Anthropogenic Aerosol Emissions, Geophys. Res. Lett., 45, 1020–1029, https://doi.org/10.1002/2017GL076079, 2018.

Sandradewi, J., Prévôt, A. S., Szidat, S., Perron, N., Alfarra, M. R., Lanz, V. A., Weingartner, E., and Baltensperger, U. R.: Using aerosol light absorption measurements for the quantitative determination of wood burning and traffic emission contribution to particulate matter, Environ. Sci. Technol., 42, 3316–3323, https://doi.org/10.1021/es702253m, 2008.

Schauer, G., Kasper-Giebl, A., and Močnik, G.: Increased PM concentrations during a combined wildfire and saharan dust event observed at high-altitude Sonnblick observatory, Austria, Aerosol Air Qual. Res., 16, 542–554, https://doi.org/10.4209/aaqr.2015.05.0337, 2016.

Schmeisser, L., Backman, J., Ogren, J. A., Andrews, E., Asmi, E., Starkweather, S., Uttal, T., Fiebig, M., Sharma, S., Eleftheriadis, K., Vratolis, S., Bergin, M., Tunved, P., and Jefferson, A.: Seasonality of aerosol optical properties in the Arctic, Atmos. Chem. Phys., 18, 11599–11622, https://doi.org/10.5194/acp-18-11599-2018, 2018.

Schmid, O., Artaxo, P., Arnott, W. P., Chand, D., Gatti, L. V., Frank, G. P., Hoffer, A., Schnaiter, M., and Andreae, M. O.: Spectral light absorption by ambient aerosols influenced by biomass burning in the Amazon Basin. I: Comparison and field calibration of absorption measurement techniques, Atmos. Chem. Phys., 6, 3443–3462, https://doi.org/10.5194/acp-6-3443-2006, 2006.

Segura, S., Estellés, V., Titos, G., Lyamani, H., Utrillas, M. P., Zotter, P., Prévôt, A. S. H., Močnik, G., Alados-Arboledas, L., and Martínez-Lozano, J. A.: Determination and analysis of in situ spectral aerosol optical properties by a multi-

instrumental approach, Atmos. Meas. Tech., 7, 2373–2387, https://doi.org/10.5194/amt-7-2373-2014, 2014.

Sheridan, P. J., Patrick Arnott, W., Ogren, J. A., Andrews, E., Atkinson, D. B., Covert, D. S., Moosmüller, H., Petzold, A., Schmid, B., Strawa, A. W., Varma, R., and Virkkula, A.: The reno aerosol optics study: An evaluation of aerosol absorption measurement methods, Aerosol Sci. Tech., 39, 1–16, https://doi.org/10.1080/027868290901891, 2005.

Singh, S., Fiddler, M. N., Smith, D., and Bililign, S.: Error analysis and uncertainty in the determination of aerosol optical properties using cavity ring-down spectroscopy, integrating nephelometry, and the extinction-minus-scattering method, Aerosol Sci. Tech., 48, 1345–1359, https://doi.org/10.1080/02786826.2014.984062, 2014.

Sokolik, I. N. and Toon, O. B.: Incorporation of mineralogical composition into models of the radiative properties of mineral aerosol from UV to IR wavelengths, J. Geophys. Res.-Atmos., 104, 9423–9444, https://doi.org/10.1029/1998JD200048, 1999.

Springston, S. R. and Sedlacek, A. J.: Noise characteristics of an instrumental particle absorbance technique, Aerosol Sci. Tech., 41, 1110–1116, https://doi.org/10.1080/02786820701777457, 2007.

Stephens, M., Turner, N., and Sandberg, J.: Particle identification by laser-induced incandescence in a solid-state laser cavity, Appl. Optics, 42, 3726, https://doi.org/10.1364/ao.42.003726, 2003.

Terhune, R. W. and Anderson, J. E.: Spectrophone measurements of the absorption of visible light by aerosols in the atmosphere, Opt. Lett., 1, 70, https://doi.org/10.1364/ol.1.000070, 1977.

Valentini, S., Barnaba, F., Bernardoni, V., Calzolai, G., Costabile, F., Di Liberto, L., Forello, A. C., Gobbi, G. P., Gualtieri, M., Lucarelli, F., Nava, S., Petralia, E., Valli, G., Wiedensohler, A., and Vecchi, R.: Classifying aerosol particles through the combination of optical and physical-chemical properties: Results from a wintertime campaign in Rome (Italy), Atmos. Res., 235, 104 799, https://doi.org/10.1016/j.atmosres.2019.104799, 2020a.

Valentini, S., Bernardoni, V., Bolzacchini, E., Ciniglia, D., Pandolfi, M., Ferrero, L., Forello, A. C., Massabó, D., Pandolfi, M., Prati, P., Soldan, F., Valli, G., Yus-díez, J., and Vecchi, R.: Applicability of benchtop multi-wavelength polar photometers to off-line measurements of the Multi-Angle Absorption Photometer, 152, 105701, https://doi.org/10.1016/j.jaerosci.2020.105701, 2020b.

Vecchi, R., Bernardoni, V., Paganelli, C., and Valli, G.: A filter-based light-absorption measurement with polar photometer: Effects of sampling artefacts from organic carbon, J. Aerosol Sci., 70, 15–25, 2014.

Virkkula, A., Mäkelä, T., Hillamo, R., Yli-Tuomi, T., Hirsikko, A., Hämeri, K., and Koponen, I. K.: A simple procedure for correcting loading effects of aethalometer data, J. Air Waste Manage., 57, 1214–1222, https://doi.org/10.3155/1047-3289.57.10.1214, 2007.

Virkkula, A., Chi, X., Ding, A., Shen, Y., Nie, W., Qi, X., Zheng, L., Huang, X., Xie, Y., Wang, J., Petäjä, T., and Kulmala, M.: On the interpretation of the loading correction of the aethalometer, Atmos. Meas. Tech., 8, 4415–4427, https://doi.org/10.5194/amt-8-4415-2015, 2015.

Visser, B., Röhrbein, J., Steigmeier, P., Drinovec, L., Močnik, G., and Weingartner, E.: A single-beam photothermal interferometer for in situ measurements of aerosol light absorption, Atmos. Meas. Tech., 13, 7097–7111, https://doi.org/10.5194/amt-13-7097-2020, 2020.

Wang, Y., Le, T., Chen, G., Yung, Y. L., Su, H., Seinfeld, J. H., and Jiang, J. H.: Reduced European aerosol emissions suppress winter extremes over northern Eurasia, Nat. Clim. Change, 10, 225–230, https://doi.org/10.1038/s41558-020-0693-4, 2020.

Weingartner, E., Saathoff, H., Schnaiter, M., Streit, N., Bitnar, B., and Baltensperger, U.: Absorption of light by soot particles: Determination of the absorption coefficient by means of aethalometers, J. Aerosol Sci., 34, 1445–1463, https://doi.org/10.1016/S0021-8502(03)00359-8, 2003.

World Meteorological Organization: WMO/GAW Aerosol Measurement Procedures, Guidelines and Recommendations, 2nd edn., GAW Report No. 227, WMO Report No. 1177, ISBN 978-92-63-11177-7, available at: https://library.wmo.int/opac/doc_num.php?explnum_id=3073 (last access: 20 September 2021), 2016.

Yus-Díez, J., Ealo, M., Pandolfi, M., Perez, N., Titos, G., Močnik, G., Querol, X., and Alastuey, A.: Aircraft vertical profiles during summertime regional and Saharan dust scenarios over the north-western Mediterranean basin: aerosol optical and physical properties, Atmos. Chem. Phys., 21, 431–455, https://doi.org/10.5194/acp-21-431-2021, 2021.

Zanatta, M., Gysel, M., Bukowiecki, N., Müller, T., Weingartner, E., Areskoug, H., Fiebig, M., Yttri, K. E., Mihalopoulos, N., Kouvarakis, G., Beddows, D., Harrison, R. M., Cavalli, F., Putaud, J. P., Spindler, G., Wiedensohler, A., Alastuey, A., Pandolfi, M., Sellegri, K., Swietlicki, E., Jaffrezo, J. L., Baltensperger, U., and Laj, P.: A European aerosol phenomenology-5: Climatology of black carbon optical properties at 9 regional background sites across Europe, Atmos. Environ., 145, 346–364, 2016.

Zhang, Y., Favez, O., Canonaco, F., Liu, D., Močnik, G., Amodeo, T., Sciare, J., Prévôt, A. S. H., Gros, V., and Albinet, A.: Evidence of major secondary organic aerosol contribution to lensing effect black carbon absorption enhancement, npj Climate and Atmospheric Science, 1, 47, https://doi.org/10.1038/s41612-018-0056-2, 2018.

Zotter, P., Herich, H., Gysel, M., El-Haddad, I., Zhang, Y., Močnik, G., Hüglin, C., Baltensperger, U., Szidat, S., and Prévôt, A. S. H.: Evaluation of the absorption Ångström exponents for traffic and wood burning in the Aethalometer-based source apportionment using radiocarbon measurements of ambient aerosol, Atmos. Chem. Phys., 17, 4229–4249, https://doi.org/10.5194/acp-17-4229-2017, 2017.

Supplement of Atmos. Meas. Tech., 14, 6335–6355, 2021
https://doi.org/10.5194/amt-14-6335-2021-supplement
© Author(s) 2021. CC BY 4.0 License.

Atmospheric Measurement Techniques
Open Access
EGU

Supplement of

Determination of the multiple-scattering correction factor and its cross-sensitivity to scattering and wavelength dependence for different AE33 Aethalometer filter tapes: a multi-instrumental approach

Jesús Yus-Díez et al.

Correspondence to: Jesús Yus-Díez (jesus.yus@idaea.csic.es)

The copyright of individual parts of the supplement might differ from the article licence.

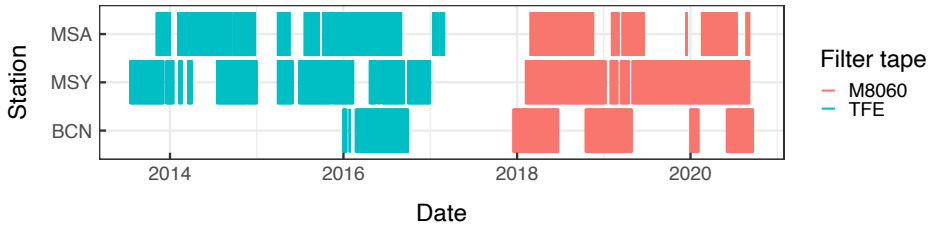

Figure S1. Multiple scattering parameter (C) availability for both M8060 and TFE filter tape at BCN, MSY and MSA measurement supersites.

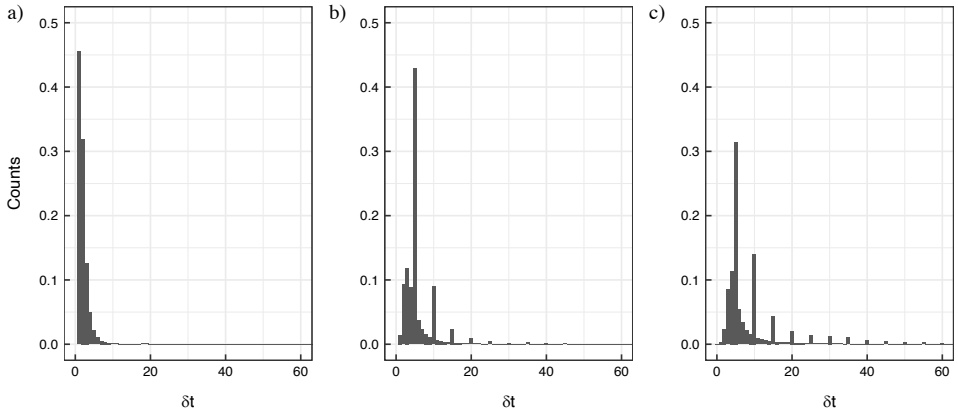

Figure S2. Normalized count distribution of the measurement timestamp, δt in minutes for a) BCN, b) MSY, and c) MSA. Time measurement resolution was set to 1 min when possible, in b) and c) the 5 min spikes are due to a measurement time resolution of 5 min during a certain period of time.

INSTRUMENT	STATION	TIMESTAMP
AE33	BCN	1 min
	MSY	1 min
	MSA	1 min
MAAP	BCN	1 min
	MSY	1 min
	MSA	1 min
NEPHELOMETER	BCN	1 min
	MSY	5 min (2013-February February 2017); 1 min (February 2017-2020)
	MSA	5 min (2013-February February 2017); 1 min (February 2017-2020)

Table S2. Timestamp of the measurement for each instrument, AE33, MAAP and nephelometer, for each station.

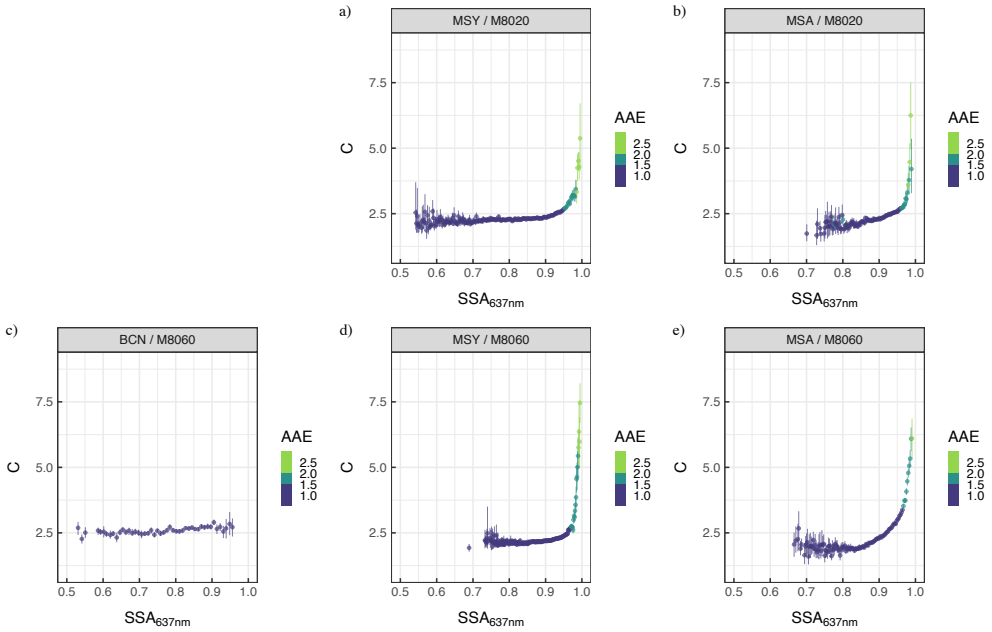

Figure S3. Multiple scattering parameter (C) dependence on the single scattering albedo (SSA) for the TFE-coated glass (upper panel) and the M8060 filter tape (lower panel) at: BCN (c), MSY (a,d) and MSA (b,e) measurement supersites as a function of the absorption Ångström exponent (AAE).

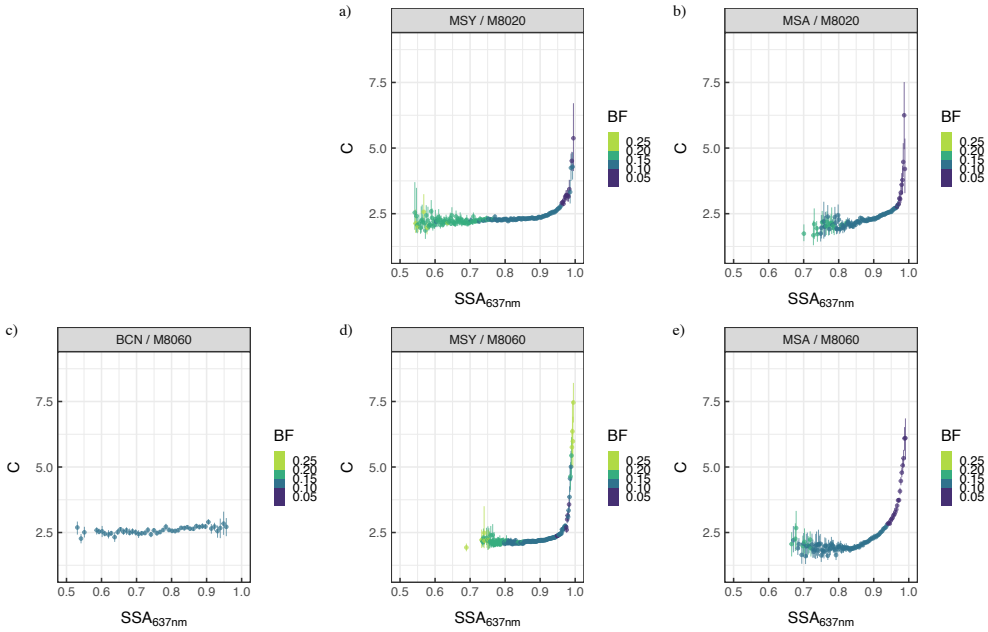

Figure S4. Multiple scattering parameter (C) dependence on the single scattering albedo (SSA) for the TFE-coated glass (upper panel) and the M8060 filter tape (lower panel) at: BCN (c), MSY (a,d) and MSA (b,e) measurement supersites as a function of the backscattered fraction at (BF).

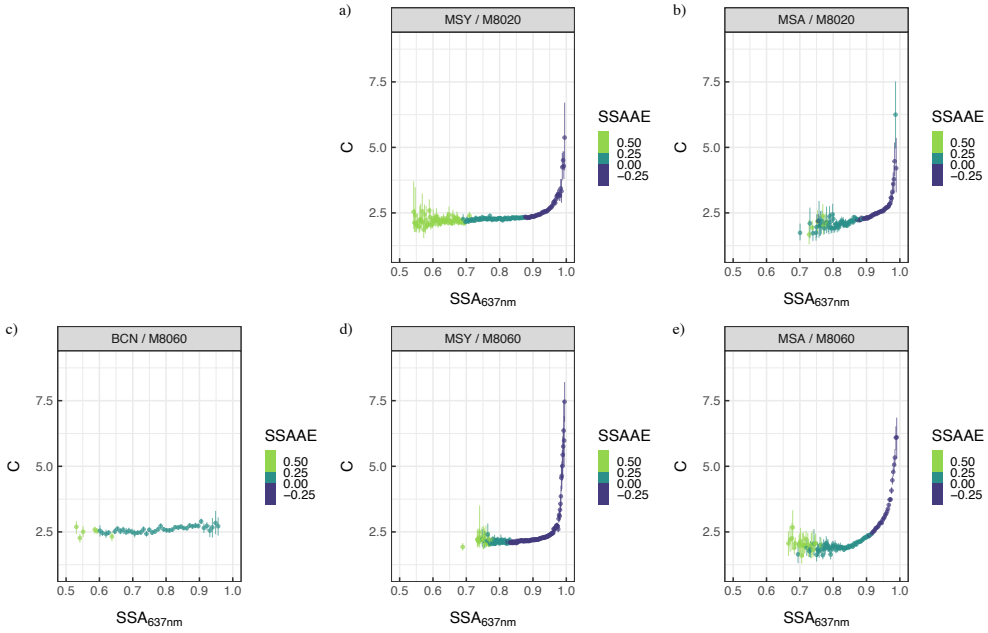

Figure S5. Multiple scattering parameter (C) dependence on the single scattering albedo (SSA) for the TFE-coated glass (upper panel) and the M8060 filter tape (lower panel) at: BCN (c), MSY (a,d) and MSA (b,e) measurement supersites as a function of the single-scattering albedo Ångström exponent (SSAAE).

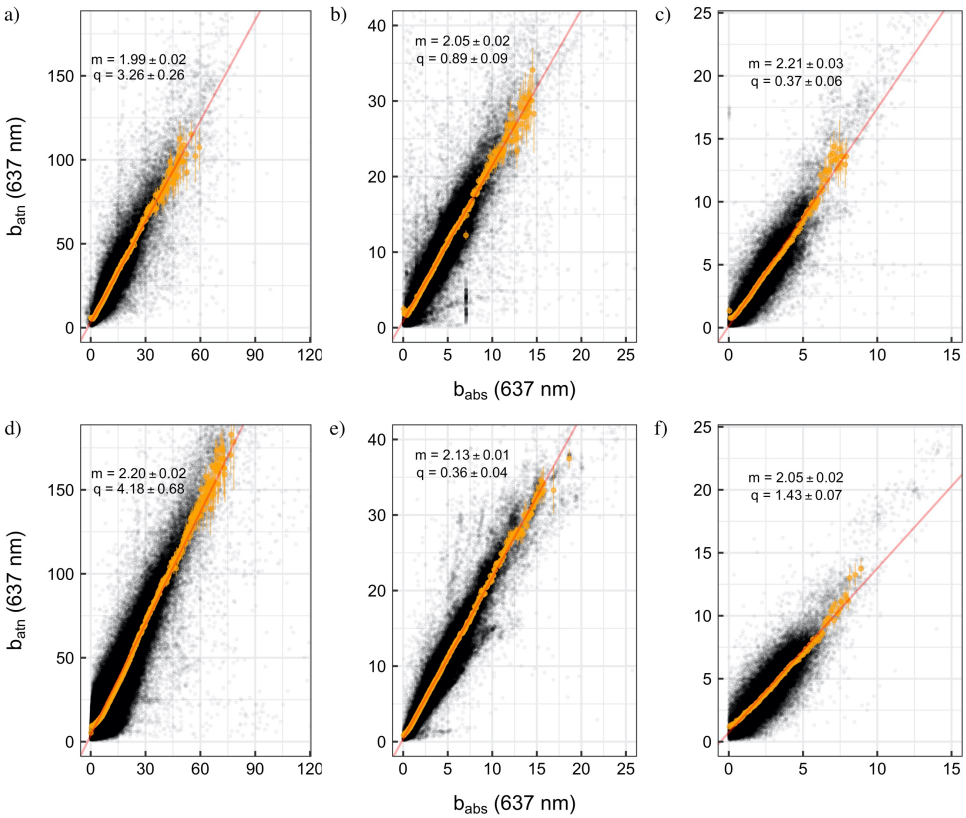

Figure S6. Scatter-plot of the binned AE33 attenuation coefficient (b_{atn} (637 nm)) vs MAAP absorption coefficient b_{abs} (637 nm)) where the slope of the Deming regression, m, represents the multiple-scattering parameter C, and q is the intercept of the regression, for the TFE-coated glass filter tape (upper panels) and M8060 filter tape (lower panels) for BCN (a,d), MSY (b,e) and MSA (c,f). The non-zero intercept, q, is indicative of the additional signal due to the cross-sensitivity to scattering of particles within the filter.

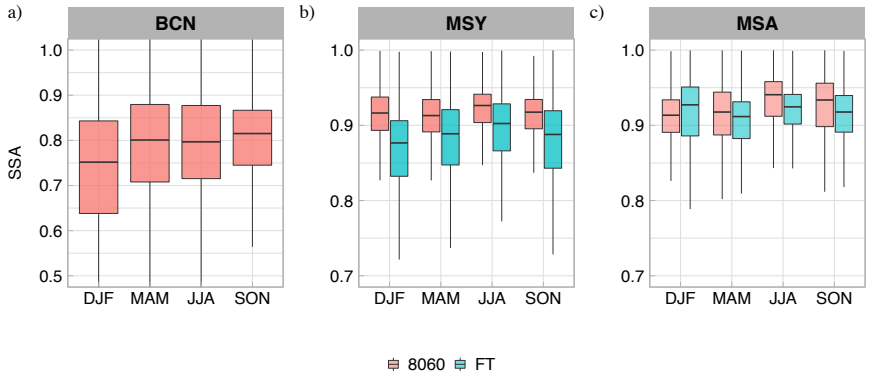

Figure S7. Seasonal evolution of the SSA at a) BCN, b) MSY and c) MSA measurement stations for both M8020 and M8060 filter tapes. The box plot boxes show the range between the first and third quartile (IQR) with the median value for each season distribution represented by the inner line; the maximum whisker length is proportional to 1.5·IQR.

a)

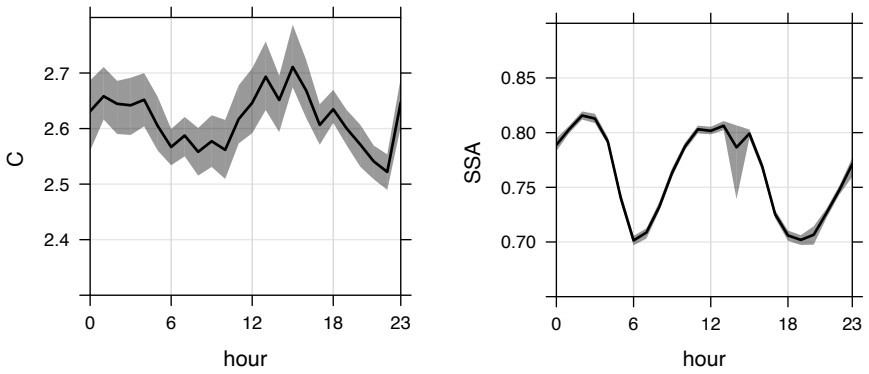

b):

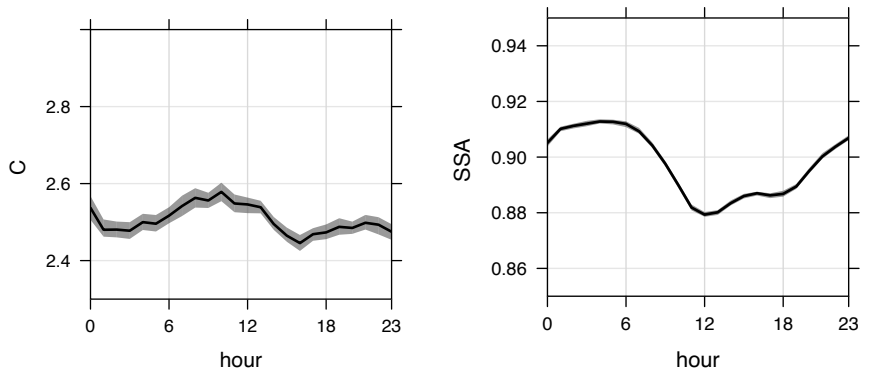

c):

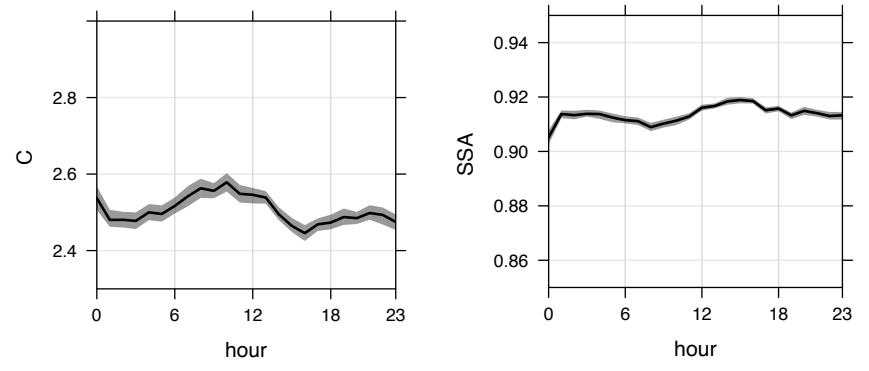

Figure S8. Diel evolution of the C and the SSA actor at a) BCN, b) MSY and c) MSA measurement stations. The measurement period of this cycles corresponds to all the available dataset for both M8020 and M8060 filter tapes (cf. Fig. S1).

	$C_{PP\_UniMI}(\lambda)$						
	370 nm	**470 nm**	**520 nm**	**590 nm**	**660 nm**	**880 nm**	**950 nm**
BCN	3.36	3.26	3.22	3.24	3.21	3.19	3.31
MSY	2.68	2.67	2.72	2.77	2.79	2.62	6.67
MSA	3.47	3.48	3.58	3.71	3.87	4.05	4.03

Table S2. Multiple scattering factor (C) at each AE33 measuring wavelength obtained using the absorption coefficient from the PP_UniMI polar photometer for BCN, MSY and MSA measurement supersites.

	$C_{PaM}(\lambda)$						
	370 nm	**470 nm**	**520 nm**	**590 nm**	**660 nm**	**880 nm**	**950 nm**
BCN	2.82	2.78	2.75	2.73	2.72	2.69	2.83
MSY	2.32	2.33	2.42	2.46	2.47	2.26	2.32
MSA	2.82	2.85	2.91	3.03	3.09	3.22	3.24

Table S3. Multiple scattering factor (C) at each AE33 measuring wavelength obtained using the absorption coefficient from the PP_UniMI polar photometer working as MAAP (PaM) for BCN, MSY and MSA measurement supersites.

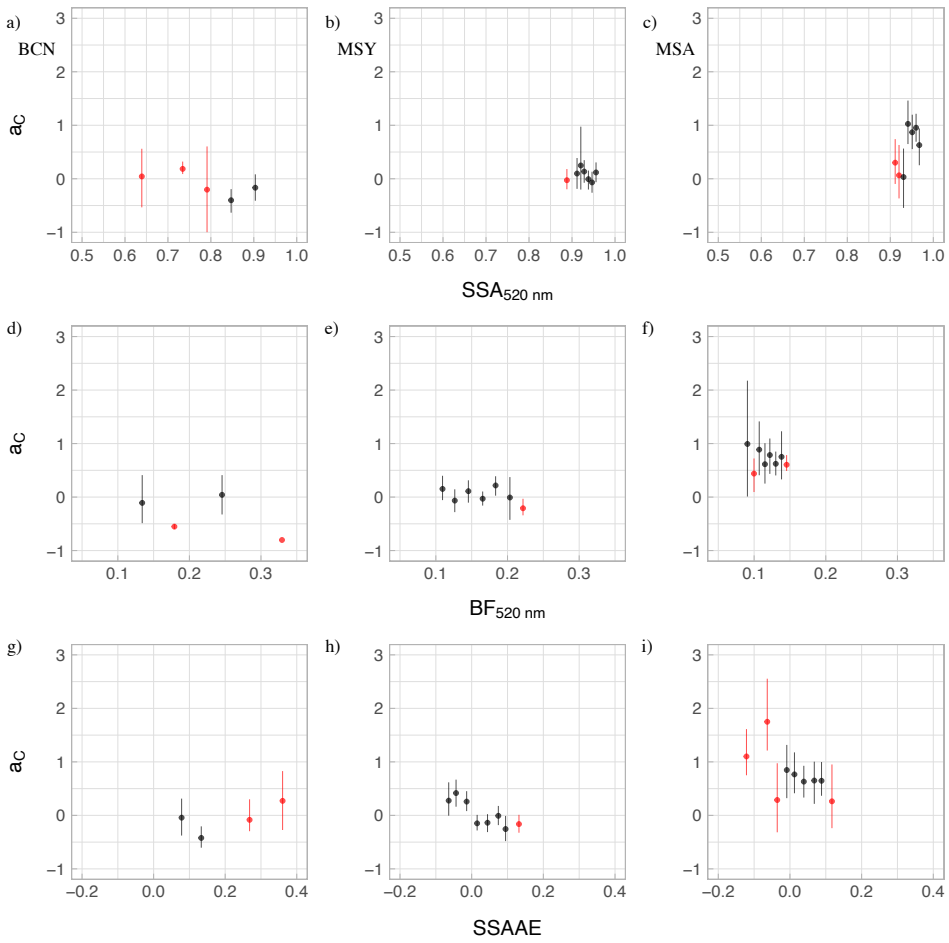

Figure S9. Relationship between the slope of the factor C and the wavelength, a_C, and the single-scattering albedo at 520 nm (SSA_{520nm}), the backscatter fraction (BF_{520nm}), and the single-scattering albedo Ångström exponent (SSAAE) at BCN (left panel), MSY (middle panel) and MSA (right panel) measurement stations. The values of a_C (y-axis) for a given station changed depending on the dependent variable (x-axis) considered due to the method employed for binning the data. Here we used the Freedman-Diaconis rule to define the bin width that can, consequently, include different data points depending on the variable considered. The red points show bins with a number of measurements which range between 2 and 5 data points.

	AAE	
	$\boldsymbol{C(const)}$	$\boldsymbol{C(\lambda)}$
BCN	1.19 ± 0.15	1.17 ± 0.15
MSY	1.27 ± 0.12	1.25 ± 0.12
MSA	1.19 ± 0.07	1.35 ± 0.07

Table S4. Mean values of the absorption Ångström exponent (AAE) for the sensitivity analysis performed in Fig. 3 on the AAE obtained using a wavelength-dependent C ($C(\lambda)$) in comparison with an AAE obtained using a constant C, C(const), parameter.

a)

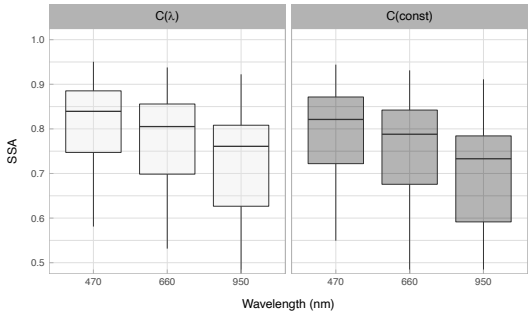

b)

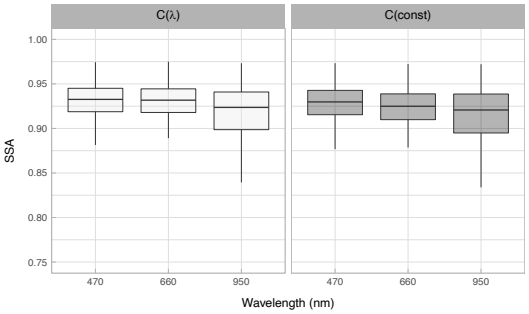

c)

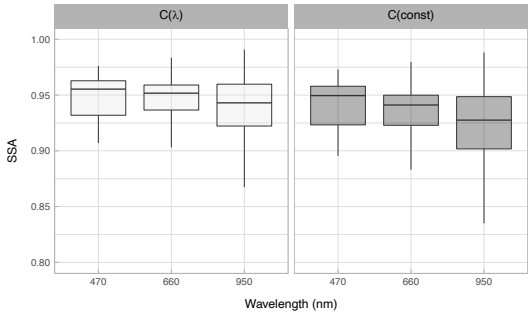

Figure S10. Sensitivity analysis of the single scattering albedo (SSA) on the wavelength-dependent C (C(λ)) in comparison with an SSA at 3 wavelengths (470, 660 and 950 nm) obtained using a constant C parameter (C(const)) for a) BCN, b) MSY and c) MSA measurement stations.

6

HORIZONTAL AND VERTICAL AEROSOL PARTICLE CHARACTERIZATION

Objective

Characterize the vertical profiles and the spatial distribution of the aerosol particles physico-chemical properties under two different typical summer scenarios in NE Spain. These scenarios, namely summer recirculation patterns and Saharan dust outbreaks, produce high aerosol particle concentration values in the area of study, not only at the surface, but also through several layers in the atmosphere. Characterizing the variations of the physico-chemical properties between the different layers is key to improve the modelization of the effects of the aerosol particles on Earth's climate.

Methodology

- Analysis of the meteorological scenarios and the air-mass back-trajectories affecting the area of study during the periods that instrumented flights were being performed.
- Coupling of surface based measurements from the regional background and mountain-top stations, Montseny and Montsec d'Ares, respectively, with airborne measurements from instrumented flights.

Results

- Higher PM concentration levels and extensive optical properties values at the measurement sites during the Saharan dust event in comparison with the averages reported in the bibliography and similar intensive optical properties. Conversely, similar overall values for the extensive and intensive optical values during the recirculation pattern for both stations, albeit slightly higher absorption and SSA at the mountain-top station.

- Multiple layers with distinct properties in comparison with their adjacent aerosol layers during the recirculation patterns, mainly characterized by the presence of BC particles within the planetary boundary layer (PBL), and both BC and BrC particles at the layers aloft. The different composition for these layers was mainly due to the ageing of the aerosol particles during the recirculation processes and the advection of biomass burning particles from wildfires.
- A more homogeneous vertical profile of the aerosol properties during the Saharan dust events. There was, however, a larger relative proportion of BC particles closer to the surface, and a higher relative proportion of mineral dust above, with multiple layers with higher mineral dust concentration.

Conclusion

- High impact of the recirculation pattern and Saharan dust events, which often take place simultaneously in summer, on the concentration values and the extensive optical properties over the NE of Spain.
- The recirculation pattern creates a very homogeneous PBL around the area of study, with additional multiple layers along the vertical profiles with similar values, although showing a larger relevance of the BrC particles due to the ageing of the aerosol particles and the advection of biomass burning particles.
- The Saharan dust events homogenize the vertical profiles of the optical properties, with values typical of those found in the Mediterranean basin during these types of events. In addition, several layers with a higher relative concentration of coarse mineral dust particles can be measured.

Publication

- Yus-Díez, J., Ealo, M., Pandolfi, M., Perez, N., Titos, G., Močnik, G., Querol, X., and Alastuey, A.: "Aircraft vertical profiles during summertime regional and Saharan dust scenarios over the north-western Mediterranean basin: aerosol optical and physical properties". In: *Atmospheric Chemistry and Physics*, 21, 431–455, `https://doi.org/10.5194/acp-21-431-2021`, 2021

Atmos. Chem. Phys., 21, 431–455, 2021
https://doi.org/10.5194/acp-21-431-2021
© Author(s) 2021. This work is distributed under
the Creative Commons Attribution 4.0 License.

Atmospheric Chemistry and Physics
Open Access
EGU

Aircraft vertical profiles during summertime regional and Saharan dust scenarios over the north-western Mediterranean basin: aerosol optical and physical properties

Jesús Yus-Díez[1,2], Marina Ealo[1,2], Marco Pandolfi[1], Noemí Perez[1], Gloria Titos[1,3,4], Griša Močnik[5,6], Xavier Querol[1], and Andrés Alastuey[1]

[1]Institute of Environmental Assessment and Water Research (IDAEA-CSIC), C/Jordi Girona 18–26, 08034, Barcelona, Spain
[2]Grup de Meteorologia, Departament de Física Aplicada, Universitat de Barcelona,
C/Martí i Franquès 1, 08028, Barcelona, Spain
[3]Andalusian Inter-University Institute for Earth System Research, University of Granada, 18006, Granada, Spain
[4]Department of Applied Physics, University of Granada, 18071, Granada, Spain
[5]Center for Atmospheric Research, University of Nova Gorica, Vipavska 11c, 5270 Ajdovščina, Slovenia
[6]Department of Condensed Matter Physics, Jožef Stefan Institute, Jamova 39, 1000 Ljubljana, Slovenia

Correspondence: Jesús Yus-Díez (jesus.yus@idaea.csic.es) and Marco Pandolfi (marco.pandolfi@idaea.csic.es)

Received: 9 August 2020 – Discussion started: 25 August 2020
Revised: 9 November 2020 – Accepted: 22 November 2020 – Published: 14 January 2021

Abstract. Accurate measurements of the horizontal and vertical distribution of atmospheric aerosol particle optical properties are key for a better understanding of their impact on the climate. Here we present the results of a measurement campaign based on instrumented flights over north-eastern Spain. We measured vertical profiles of size-segregated atmospheric particulate matter (PM) mass concentrations and multi-wavelength scattering and absorption coefficients in the western Mediterranean basin (WMB). The campaign took place during typical summer conditions, characterized by the development of a vertical multi-layer structure, under both summer regional pollution episodes (REGs) and Saharan dust events (SDEs). REG patterns in the region form under high insolation and scarce precipitation in summer, favouring layering of highly aged fine-PM strata in the lower few km a.s.l. The REG scenario prevailed during the entire measurement campaign. Additionally, African dust outbreaks and plumes from northern African wildfires influenced the study area. The vertical profiles of climate-relevant intensive optical parameters such as single-scattering albedo (SSA); the asymmetry parameter (g); scattering, absorption and SSA Ångström exponents (SAE, AAE and SSAAE); and PM mass scattering and absorption cross sections (MSC and MAC) were derived from the measurements. Moreover, we compared the aircraft measurements with those performed at two GAW–ACTRIS (Global Atmosphere Watch–Aerosol, Clouds and Trace Gases) surface measurement stations located in north-eastern Spain, namely Montseny (MSY; regional background) and Montsec d'Ares (MSA; remote site).

Airborne in situ measurements and ceilometer ground-based remote measurements identified aerosol air masses at altitudes up to more than 3.5 km a.s.l. The vertical profiles of the optical properties markedly changed according to the prevailing atmospheric scenarios. During SDE the SAE was low along the profiles, reaching values < 1.0 in the dust layers. Correspondingly, SSAAE was negative, and AAE reached values up to 2.0–2.5, as a consequence of the UV absorption increased by the presence of the coarse dust particles. During REG, the SAE increased to > 2.0, and the asymmetry parameter g was rather low (0.5–0.6) due to the prevalence of fine PM, which was characterized by an AAE close to 1.0, suggesting a fossil fuel combustion origin. During REG, some of the layers featured larger AAE (> 1.5), relatively low SSA at 525 nm (< 0.85) and high MSC ($> 9\,m^2\,g^{-1}$) and were associated with the influence of PM from wildfires. Overall, the SSA and MSC near the ground ranged around 0.85 and $3\,m^2\,g^{-1}$, respectively, and increased at higher altitudes, reaching values above 0.95 and up to $9\,m^2\,g^{-1}$. The PM,

Published by Copernicus Publications on behalf of the European Geosciences Union.

MSC and MAC were on average larger during REG compared to SDE due to the larger scattering and absorption efficiency of fine PM compared with dust. The SSA and MSC had quite similar vertical profiles and often both increased with height indicating the progressive shift toward PM with a larger scattering efficiency with altitude.

This study contributes to our understanding of regional-aerosol vertical distribution and optical properties in the WMB, and the results will be useful for improving future climate projections and remote sensing or satellite retrieval algorithms.

1 Introduction

Atmospheric aerosol particles play an important role in Earth's radiative balance directly by scattering and absorbing solar radiation and indirectly by acting as cloud condensation nuclei (Myhre et al., 2013). Globally, the aerosol particles' direct radiative effect is negative at the top of the atmosphere due to their net cooling on Earth's atmosphere system (Myhre et al., 2013). This estimation is, however, affected by a large uncertainty which reflects the large spatial and temporal variability of the optical, physical and chemical properties of optically active atmospheric aerosol particles (Myhre et al., 2013). This variability is largely due to the wide variety of aerosol sources and sinks, their intermittent nature and spatial non-uniformity together with the chemical and physical transformations that aerosol particles undergo in the atmosphere (Myhre et al., 2013). These variables affect the scattering and absorption properties of atmospheric particles and consequently their radiative properties. Thus, uncertainties remain regarding the effects that aerosol particles exert on climate from local to global scales, and a detailed characterization of their properties in the horizontal and vertical dimensions is needed (Andrews et al., 2011; Bond et al., 2013; Haywood et al., 1999; Collaud Coen et al., 2013). Accurate knowledge of their radiative forcing will improve both the climate reanalysis and forecasting models, which are needed in the current climate change context (Myhre et al., 2013). The in situ surface distribution of atmospheric particles and their physical and chemical properties is determined through an array of networks across the US and Europe and to a lesser extent in Asia and Africa (Laj et al., 2020), such as the Global Atmosphere Watch (GAW, World Meteorological Organization); the European Research Infrastructure for the observation of Aerosol, Clouds and Trace Gases (ACTRIS; http://www.actris.eu, last access: 7 January 2021); the Interagency Monitoring of Protected Visual Environments (IMPROVE; http://vista.cira.colostate.edu/Improve/, last access: 7 January 2021); the European Monitoring and Evaluation Programme (EMEP, http://www.Emep.int, last access: 7 January 2021); and the NOAA Federated Aerosol Network (NFAN; Andrews et al., 2019). These networks provide detailed optical, physical and chemical properties of atmospheric aerosol particles at the surface (Putaud et al., 2004; Putaud et al., 2010; Andrews et al., 2011; Asmi et al., 2013; Collaud Coen et al., 2013; Collaud Coen et al., 2020; Cavalli et al., 2016; Zanatta et al., 2016; Pandolfi et al., 2018; Laj et al., 2020).

Given that the radiative forcing by aerosols is produced in the whole atmospheric column, the study of the vertical distribution of aerosol particles and their properties is of great importance (Sheridan et al., 2012; Samset et al., 2013). In fact, uncertainties regarding their vertical distribution and its relationship with surface emission sources are still a subject of intensive research. For example, Sanroma et al. (2010) suggested that, during cloud-free conditions, high-altitude aerosol particles are the major contributor to variations in solar radiation flux reaching the surface, at least at the high-altitude sites they studied. Moreover, the positive radiative forcing associated with strongly absorbing particles, such as black carbon (BC), is amplified when these particles are located above clouds (Zarzycki and Bond, 2010, and references therein), and the sign and magnitude of semi-direct BC effects depend on the BC location relative to the clouds and cloud type (Bond et al., 2013), with different clouds differently impacting the atmospheric heating rate of different aerosol types (Ferrero et al., 2020).

Ground-based remote sensing measurements of aerosol particles' optical and physical properties are performed by a number of projects, such as AERONET (AErosol RObotic NETwork; https://aeronet.gsfc.nasa.gov, last access: 7 January 2021), which is the international federation of ground-based sun and sky scanning radiometers and the European Aerosol Research Lidar Network (EARLINET–ACTRIS, https://www.earlinet.org, last access: 7 January 2021), providing column-integrated and vertically resolved optical properties, respectively. Satellite and sun/sky photometer measurements provide information on the aerosol properties of the entire atmospheric column, top-down and bottom-up, respectively. Polar-orbiting satellite observations provide a wide spatial coverage yet are limited in time resolution to once or twice a day. On the other hand, laser-based active instruments such as lidars (light detection and ranging) and ceilometers provide reliable information of the vertically resolved optical properties of aerosols, such as backscattering and extinction. Lidars measure at several wavelengths (e.g. Raman-elastic lidars; Ansmann et al., 1992), whereas ceilometers are usually limited to one wavelength.

The aforementioned remote sensing methods have thus limitations for directly measuring the vertically resolved distribution of specific climate-relevant optical parameters or variables such as SSA, the asymmetry parameter (g) or absorption coefficients. Although not as frequent, airborne measurements can provide the vertical profiles and horizontal variability of these parameters, as well as of other aerosol-related patterns. Instrumented flights are usually performed for specific campaigns, with a duration ranging from multiple

weeks to a few years, allowing for determining aerosol properties up to heights of a few km a.g.l. in the free troposphere. For example, Esteve et al. (2012) performed a campaign over Bondville (Illinois) aiming at comparing AERONET remote sensing measurements with measurements of aerosol properties, such as scattering, absorption and other derived variables from instrumented flights. In Asia, Clarke et al. (2002) measured aerosol particles' microphysical, optical and chemical properties over the Indian Ocean. Recently, Singh et al. (2019) measured particle size, number (N), spectral absorption and meteorology variables in different pollution layers along a Himalayan valley in Nepal by means of instrumented flights. Vertically resolved measurement campaigns have been performed with tethered balloons, for example in the Po valley (Ferrero et al., 2014); in the Arctic (Ferrero et al., 2016); and with unmanned aerial vehicles (UAVs), such as the ones over the eastern Mediterranean by Pikridas et al. (2019). Aircraft aerosol measurements over Europe were performed for example during the EUCAARI-LONGREX (European Integrated project on Aerosol Cloud Climate and Air Quality interactions Long Range Experiment) campaign as shown by Highwood et al. (2012), who presented the results of a closure study between measured vertical aerosol particles scattering and absorption and Mie theory. In North America, Sheridan et al. (2012) performed flights between 2 and 3 times per week during 3 consecutive years, measuring more than 400 vertical profiles of aerosol particles and trace gas concentrations. The vertical profiles of total and accumulation mode N concentration, BC mass concentration, lidar measurements and the estimated radiative aerosol effect during EUCAARI-LONGREX were presented by Hamburger et al. (2010), Groß et al. (2013) and Esteve et al. (2016). In the context of the ChArMEx/ADRIMED measurement campaign (the Chemistry-Aerosol Mediterranean Experiment/Aerosol Direct Radiative Impact on the regional climate in the MEDiterranean region; e.g. Mallet et al., 2016; Denjean et al., 2016) instrumented flights measuring physical and chemical properties took place. These measurement campaigns have demonstrated the usefulness of instrumented flights providing aerosol properties which cannot be measured with conventional remote sensing techniques. These vertically resolved aerosol measurements are restricted to the time span of the campaign as well as to the regional area where these take place. However, aircraft measurements might yield very relevant information for detailed radiative forcing studies and might be extremely useful for models aiming at simulating these effects over specific regions. Moreover, the results could be extrapolated to other periods when measurements are not available in the same area or to other areas with similar meteorological patterns and pollutant emissions.

Detailed studies of the vertical profiles of climate-relevant aerosol properties are especially important in climate-sensitive areas, such as the Mediterranean basin. This is one of the regions in the world characterized by high loads of both primary and secondary aerosol particles, especially in summer (Rodríguez et al., 2002; Dayan et al., 2017), from diverse emission sources. Anthropogenic emissions from road traffic, industry, agriculture and maritime shipping, among others, negatively affect the air quality in this region (Querol et al., 2009b; Amato et al., 2009; Pandolfi et al., 2014c). Moreover, the Mediterranean basin is also highly influenced by natural sources, such as mineral dust from African deserts and smoke from forest fires (Bergametti et al., 1989; Querol et al., 1998; Rodríguez et al., 2001; Lyamani et al., 2006; Mona et al., 2006; Koçak et al., 2007; Kalivitis et al., 2007; Querol et al., 2009b; Schauer et al., 2016; Ealo et al., 2016; Querol et al., 2019, among others). In addition to this, the distribution of the different types of aerosol particles in the Mediterranean basin is largely modulated by regional and large-scale circulation (Millán et al., 1997; Gangoiti et al., 2001; Kallos et al., 2007). The complex orography surrounding the WMB (western Mediterranean basin) sea and the high insolation, scarce precipitation and low winds during summertime give rise to high rates of accumulation and formation of secondary particles (Rodríguez et al., 2002). The north-east of Spain provides a frame of study that represents well the atmospheric summer conditions of the western and central Mediterranean, characterized by frequent and severe pollution episodes with high PM, UFP (ultra-fine particle) and O_3 formation (Pey et al., 2013; Pandolfi et al., 2014a; Querol et al., 2017, among others). Typical atmospheric dynamics coupled to local orography results in local and regional vertical recirculation with a consequent accumulation of pollutants (Millán et al., 1997). Vertical recirculation and ageing of pollutants is favoured by weak gradient atmospheric conditions, scarce precipitation and continuous exposure to solar radiation driving photochemical reactions (Rodríguez et al., 2002; Pérez et al., 2004). This recirculation is very relevant in midsummer, when the solar radiation increases and the high-pressure periods last longer, so that the vertical recirculation reaches further inland and creates reservoir strata (loaded with pollutants) at 1–3 km a.s.l. (Gangoiti et al., 2001; Pérez et al., 2004). In fact, due to the geography and climatic summer meteorological patterns, the formation of strong breezes from the coast through the valleys up to the Pyrenees and pre-Pyrenees range is frequent (Ripoll et al., 2014). Additionally, and especially in spring–summer, intense Saharan dust outbreaks (Querol et al., 1998, 2009b; Querol et al., 2019; Rodríguez et al., 2001; Escudero et al., 2007; Pey et al., 2013) and forest fires (Faustini et al., 2015) influence air quality over the WMB. The above atmospheric processes might coincide in space and time in the WMB and result in summer radiative forcing above this area being among the highest in the word (Lelieveld et al., 2002, and references therein). To the best of our knowledge, only a few in situ aircraft- or balloon-borne measurement campaigns aiming at studying the optical properties of tropospheric aerosol particles were performed in the WMB such as

those performed within the ChArMEx/ADRIMED campaign (Denjean et al., 2016).

To better characterize the complex summer atmospheric scenarios of the WMB and to better understand their effect on the concentrations and optical properties of aerosols, we present here results from an aircraft measurement campaign performed in the north-western Mediterranean within the PRISMA project (aerosol optical properties and radiative forcing in the western Mediterranean as a function of chemical composition and sources). The main objective of the PRISMA project was to study the spatial and vertical distribution of the atmospheric aerosol particles with special interest in their physical and optical properties to assess the regional radiative forcing caused by the tropospheric aerosols in the WMB. To this end two measurement campaigns were performed in the summers of 2014 and 2015, combining aircraft measurements with remote and in situ surface measurements performed at the Montseny (MSY) and Montsec (MSA) stations. Herein we focus on the 2015 campaign, when vertical summer recirculation episodes, Saharan dust outbreaks and plumes from wildfires simultaneously affected air quality over the WMB. The combination of the aircraft measurements with the available surface in situ and remote measurements allowed for characterizing the summer recirculation coupled with Saharan dust outbreaks usually observed in the WMB in summer well. The results presented here provide a more exhaustive characterization of the aerosol layers than the one that can be obtained by deploying in situ surface and remote sensing techniques applied so far in the region.

In the following section (Sect. 2) we describe the methodology, with a deeper analysis of the study area, measurement stations and flight location as well as the main meteorological scenarios. In Sect. 3 we will explain the main calculations of aerosol optical properties. The main results obtained in this study are shown in Sect. 4 for the different meteorological scenarios for both surface and the vertical measurements. Finally, we discuss the obtained results in the conclusion (Sect. 5).

2 Methodology

2.1 Area of study and meteorology

Airborne aerosol measurements were performed in an area of around 3500 km^2 in the north-western Mediterranean area of Catalonia, north-eastern Spain (Fig. 1). The area is close to the Barcelona metropolitan area, where anthropogenic emissions, mostly from road traffic, industry, agriculture and maritime shipping (Barcelona is one of the major ports in the Mediterranean) negatively affect the air quality (Querol et al., 2001; Pey et al., 2013; Pérez et al., 2008; Amato et al., 2009; Amato et al., 2016; Reche et al., 2011, among others). Figure 1 shows the study area, the location of the Montseny (MSY; 720 m a.s.l.) and Montsec (MSA; 1570 m a.s.l.) measurement stations, and the location and ID codes (P1–P7) of the instrumented flights (Table 1).

This area is characterized by warm summers and temperate winters with irregular and rather scarce precipitation rates, especially in summer. The Azores high-pressure system plays an important role in the synoptic meteorology of the Iberian Peninsula (IP). In winter, the Azores anticyclone is located at lower latitudes, and so the IP is more influenced by low-pressure systems and the associated fronts coming from the North Atlantic. However, in summer, the anticyclonic system intensifies and moves toward higher latitudes inducing very weak pressure gradient conditions over the IP. These atmospheric stagnant conditions, coupled to local orography and sea breeze circulation, result in local and regional atmospheric dynamics that favour the accumulation and ageing of pollutants (Millán et al., 1997, 2002; Gangoiti et al., 2001; Rodríguez et al., 2002; Pérez et al., 2004, among others). The high surface temperatures give rise to the formation of the Iberian thermal low, which induces the convergence of surface winds from the coastal areas injecting polluted air masses into the middle troposphere (3.5–5 km height). During the daytime the sea breeze layer (up to 800 m high) is channelled into the coastal and pre-coastal valleys up to 90 km inland, transporting pollutants from the coastal area (Gangoiti et al., 2001). On the mountain and valley slopes, up-slope winds inject pollutants at higher levels. Sea breezes and up-slope winds over the coastal and pre-coastal mountains transport coastal pollutants inland, while a fraction of these pollutants is injected in their return flows aloft (2–3 km), forming high-pollution-loaded reservoir strata (Gangoiti et al., 2001). Pollutants are returned to the Mediterranean Sea owing to the prevalence of westerly winds above the mixing layer. Once in those upper layers, pollutants move back towards the sea, and compensatory subsidence creates stratified reservoir layers of aged pollutants. Then, the next morning the lowermost layers are drawn inland again by the sea breeze (Millán et al., 2002; Gangoiti et al., 2001).

Saharan dust outbreaks affect the Iberian Peninsula mostly in spring–summer, increasing the PM levels. The meteorological scenarios causing African dust transport over the study area are described in Rodríguez et al. (2001) and Escudero et al. (2005). Four main scenarios are differentiated: northern African high located at the surface level (NAH-S), Atlantic depression (AD), northern African depression (NAD) and northern African high located at upper levels (NAH-A). The WMB is mostly affected by the AD and NAD in spring and fall, by the NAH-A in summer, and by the NAH-S from January to March. Another potential significant source of PM affecting air quality in the WMB is wildfires, which might persist for several days and emit large amounts of primary PM and precursors of secondary aerosols (Faustini et al., 2015). In addition to the complex atmospheric patterns, the scarce precipitation and the high exposure to solar radiation drive photochemical reactions resulting in high

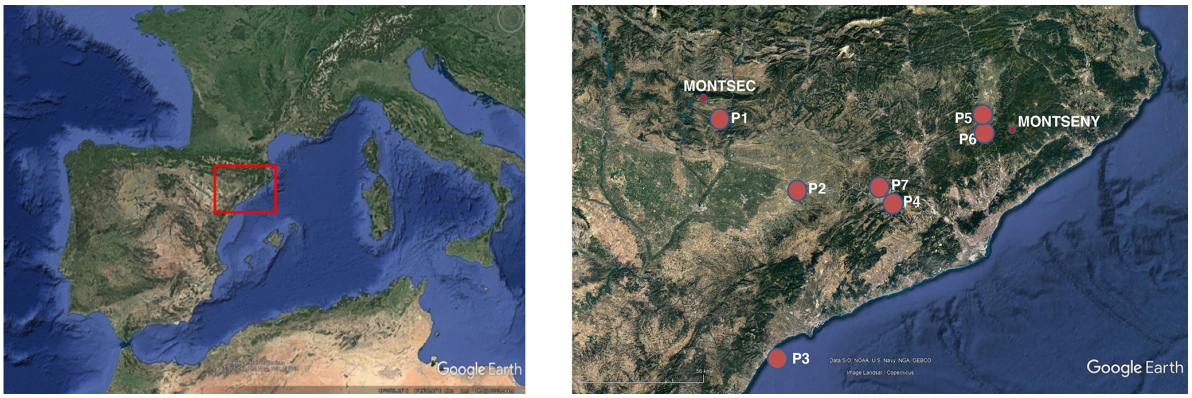

Figure 1. Western Mediterranean basin and zoom over the north-east of Spain with the MSA and MSY stations and the number ID of the instrumented flights (Table 1), with the shaded area indicating the horizontal area where measurements were taken. Satellite view from © Google Earth.

Table 1. Flight measurement location and date. Vertical profiles were performed up to heights of 3.5 km a.s.l.

Profile	Flight direction	Date	Time (UTC)	Coordinates	Area
P1	Upwards	7 Jul 2015	08:55–09:16	41.96° N, 0.75° E	MSA
P2	Upwards	7 Jul 2015	15:31–15:53	41.65° N, 1.14° E	Plain
P3	Upwards	8 Jul 2015	08:11–08:31	41.01° N, 0.94° E	Coast
P4	Downwards	14 Jul 2015	09:44–10:00	41.60° N, 1.64° E	Catalan pre-coastal mountain range
P5	Downwards	14 Jul 2015	10:56–11:12	41.85° N, 2.20° E	Catalan pre-coastal mountain range
P6	Downwards	16 Jul 2015	10:07–10:23	41.84° N, 2.24° E	Catalan pre-coastal mountain range

background levels of secondary aerosols and ozone (Rodríguez et al., 2002; Pérez et al., 2004; Querol et al., 2016; Querol et al., 2017).

2.1.1 Detailed synoptic and mesoscale meteorological scenarios during flights

Airborne measurements of tropospheric aerosol particles physical properties were conducted during 7–8 and 14–16 July 2015 during the typical summer regional pollution episodes and aerosol layering (Gangoiti et al., 2001). HYSPLIT (HYbrid Single-Particle Lagrangian Integrated Trajectory model; Draxler and Hess, 1998) back trajectories in Fig. 2 (calculated for 7 and 16 July 2015; see more trajectories for the 8 and 14 July in Fig. S2) and the potential temperature vertical profile (Fig. S3) show that both periods were characterized by atmospheric stagnation (without major synoptic flows venting the WMB). Under these summer atmospheric scenarios sea breezes, and the vertical recirculation of air masses develop. However, during the first period an African dust outbreak affected the study area (Fig. 2), probably by high-altitude transport from northern Africa and subsequent impact on surface by convective circulations over the continent. Moreover, plumes from wildfires reached also the study area in the second period as the smoke forecast from NAAPS indicated (Navy Aerosol Analysis and Prediction System; http://www.nrlmry.navy.mil/aerosol, last access: 7 January 2021; see Fig. 2).

The geopotential height at 500 hPa and surface pressure from the ERA-INTERIM reanalysis model (https://www.ecmwf.int/en/forecasts/datasets/reanalysis-datasets/era-interim, last access: 7 January 2021) show for the first day of the measurements a high-pressure system covering central Europe (Figs. 3 and S1 in the Supplement). On 7 July (coincident with the first measurements), the Azores high-pressure system and a northern European low governed the synoptic flow. This situation persisted until 16 July, with an enhancement of the Iberian and northern African thermal lows (Fig. 3).

Thus, during the campaign, the atmospheric scenario is the typical one favouring stagnation in the WMB, which leads to the recirculations of vertical air masses driven by local and regional processes (Gangoiti et al., 2001). Furthermore, the north-eastern African high pressure at high atmospheric levels (NAH-A; Escudero et al., 2005) favoured the advection of Saharan dust at high altitudes to the area of study from noon on 4 July to the afternoon of 8 July 2015. We will refer to this first period as the SDE (Saharan dust event) period, in reference to the Saharan dust event that persisted during these days. On 14 and 16 July, smoke from wildfires over northern Africa and the IP affected the study area. During this sec-

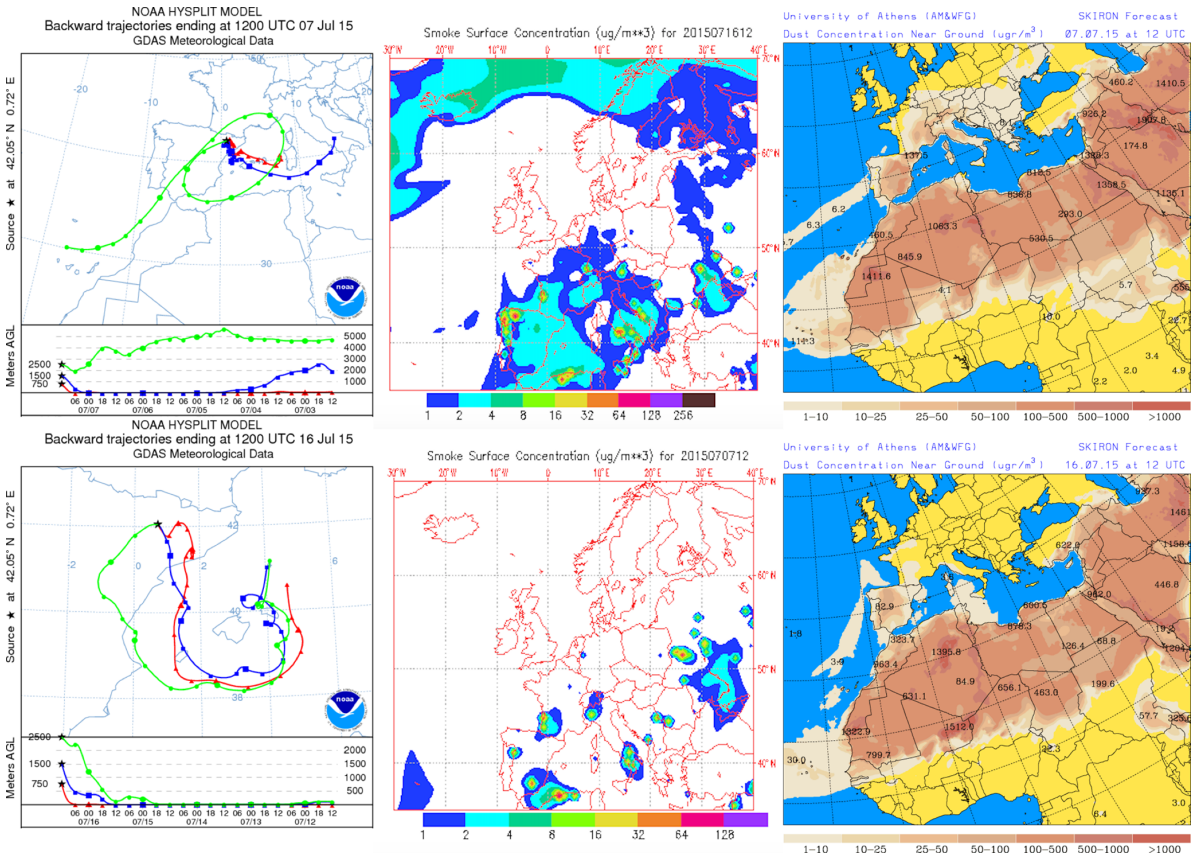

Figure 2. Upper panel shows the back trajectories at the MSA station, the dust concentration ($\mu g\,m^{-3}$) near the ground as simulated by the SKIRON forecast simulations (University of Athens) and the smoke surface concentration ($\mu g\,m^{-3}$) forecasted by the NAAPS Prediction System for 12:00 UTC of the 7 July 2015 (flights P1 and P2). The lower panels shows the same information for 12:00 UTC on 16 July 2015 (flights P6 and P7), although it should be noted that there is a smaller scale on the back-trajectory map, with a higher zoom in the study area. GDAS: Global Data Assimilation System.

ond period there was no mineral dust on 14 July, while on 16 July a light dust outbreak took place (Fig. 2). Due to the prevalence of summer regional pollution episodes with the absence of a dominant strong Saharan dust event, we will refer to this second measurement period as an REG (regional pollution episode).

2.2 Measurements and instrumentation

2.2.1 Ground supersites and measurements

Surface measurements were performed at Montseny (MSY, regional background) and Montsec (MSA, continental background) monitoring supersites (north-eastern Spain). MSY (41°46′46″ N, 02°21′29″ E, 720 m a.s.l.) is located in a densely forested area, 50 km to the north–north-east of Barcelona and 25 km from the Mediterranean coast. MSA (42°03′05″ N, 00°43′46″ E, 1570 m a.s.l.) is located in a remote high-altitude emplacement in the southern side of the pre-Pyrenees at the Montsec d'Ares mountain range, at 140 km to the north-west of Barcelona and 140 km to the west-north-west of MSY (Fig. 1). Detailed descriptions of the measurement supersites and of the measurements performed can be found for example in Pérez et al. (2008), Pey et al. (2009) and Pandolfi et al. (2011); Pandolfi et al. (2014a, 2016) for MSY and Pandolfi et al. (2014b), Ripoll et al. (2014) and Ealo et al. (2016, 2018) for MSA. These supersites are part of the Catalonian Air Quality Monitoring Network and are part of ACTRIS and GAW networks. Aerosol optical properties at the sites were measured following standard network protocols (WMO/GAW, 2016).

Similar instruments were used for in situ surface characterization of physical, chemical and optical aerosol particle properties at both MSY and MSA. Aerosol particle total scattering (σ_{sp}) and hemispheric backscattering (σ_{bsp}) coefficients were measured every 5 min at three wavelengths (450, 525 and 635 nm) with an LED-based integrating neph-

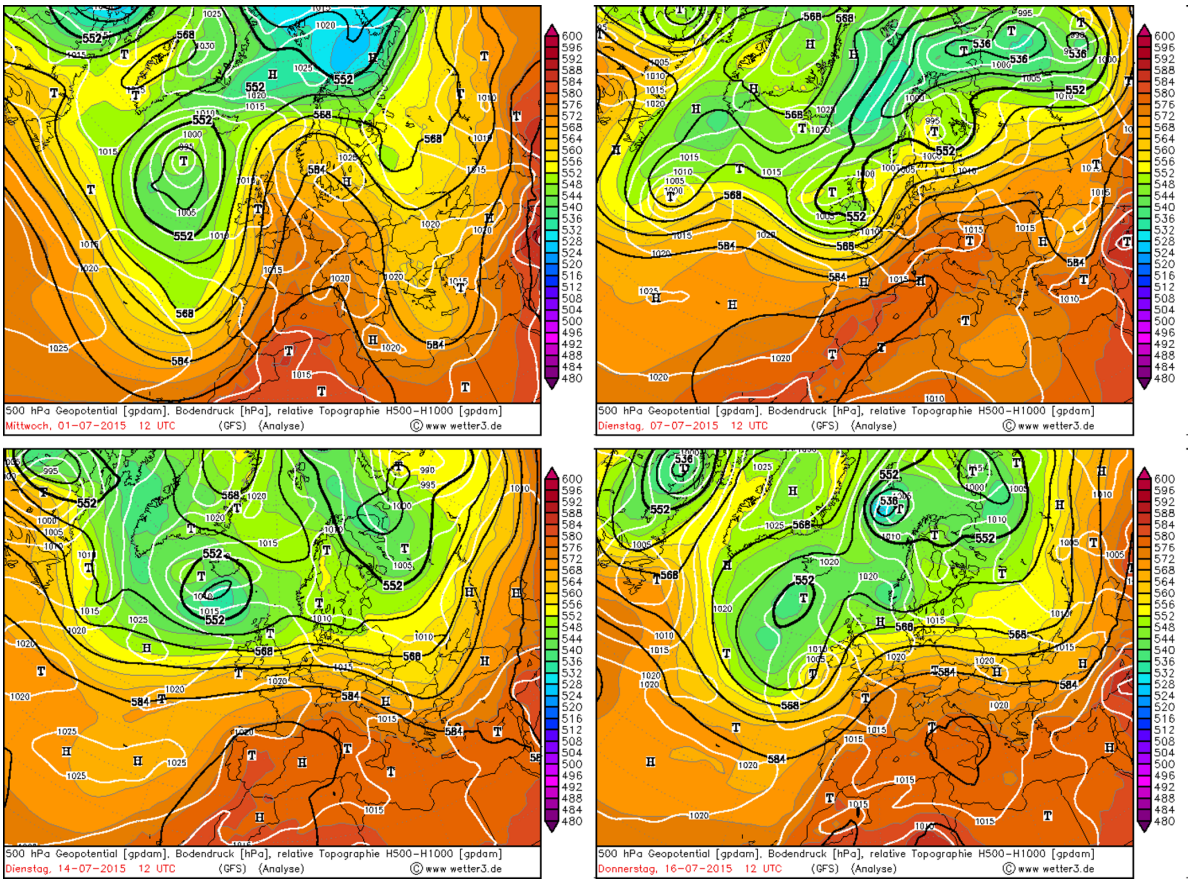

Figure 3. Synoptic meteorology with 500 hPa geopotential and surface pressure at 12:00 UTC for the 1, 7, 14 and 16 July of 2015 as modelled by the reanalysis model ERA-INTERIM, © http://www.wetter3.de last access: 7 January 2021). GFS: Global Forecast System.

elometer (Aurora 3000, Ecotech Pty, Ltd, Knoxfield, Australia). Calibration of the two nephelometers was performed four times per year using CO_2 as span gas, while zero adjusts were performed once per day using internally filtered particle-free air. The RH (relative humidity) threshold was set by using a processor-controlled automatic heater inside the Aurora 3000 nephelometer to ensure a sampling RH of less than 40 % (GAW, 2016). σ_{sp} coefficients were corrected for non-ideal illumination of the light source and for truncation of the sensing volumes following the procedure described in Müller et al. (2011b). Aerosol light absorption coefficients (σ_{ap}) at seven different wavelengths (370, 470, 520, 590, 660, 880 and 950 nm) were obtained every 1 min at both stations by means of aethalometers (Magee Scientific AE33) with filter loading being corrected online by the dual-spot manufacturer correction (Drinovec et al., 2015). At both supersites a multi-angle absorption photometer (MAAP – Multi Angle Absorption Photometer, Model 5012, Thermo, Inc., USA; Petzold and Schönlinner, 2004) was also used for obtaining the aerosol light absorption coefficient. MAAP data in this work were reported at 637 nm by multiplying the MAAP absorption data by a factor of 1.05 as suggested by Müller et al. (2011a). At both sites the instruments were connected to a PM_{10} cut-off inlet. Online surface in situ optical measurements were reported to ambient temperature (T) and pressure (P) using measurements from automatic and co-located weather stations.

PM mass concentrations were obtained with an optical particle counter (OPC) (Grimm 1108.8.80) connected to an individual inlet. Particle number volume concentrations were measured every 5 min in 15 size bins from 0.3 to 20 µm and then converted to PM mass concentration by the instrument software. PM mass concentrations were corrected by comparison with standard gravimetric PM measurements (Alastuey et al., 2011). An Aerosol Chemical Speciation Monitor (ACSM, Aerodyne Research Inc.) was used to measure real-time non-refractory submicron aerosol species (organic matter, nitrate, sulfate, ammonium and chloride). Measurements with the ACSM at MSY were available from 4 to 12 July.

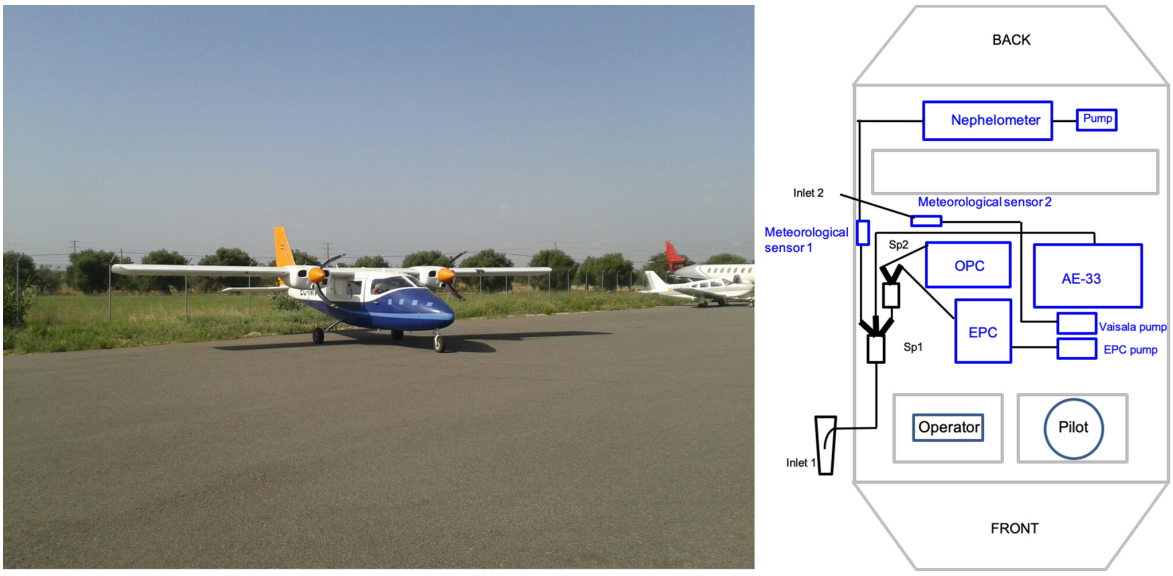

Figure 4. Piper PA 34 Seneca aircraft (left panel) and the schematic of the aerosol inlet and sampling instruments inside the aircraft (right panel). Aerosol sampling lines are shown in black, and sampling instruments are in blue. EPC: environmental particle counter.

PM_{10}, $PM_{2.5}$ and PM_1 24 h samples were daily collected on 150 mm quartz microfibre filters (Pallflex 2500 QAT-UP and Whatman QM-H) using high-volume samplers (DIGITEL DH80 and/or MCV CAV-A/MSb at 30 $m^3 h^{-1}$). The daily concentrations of major and trace elements and soluble ions (determined following the procedure by Querol et al., 2001), as well as those of organic (OC) and elemental (EC) carbon (by a thermal–optical carbon analyser, Sunset Laboratory Inc., following the EU project EUSAAR2 (European Supersites for Atmospheric Aerosol Research) protocol Cavalli et al., 2010), were measured during the whole campaign. The ratio between the fine, PM_1, and coarse, PM_{10}, mode is obtained as the fraction between these two concentration measurements, $PM_{1/10}$. The chemical analyses allowed for the determination of around 50 PM components, accounting for 75 %–85 % of the PM mass, the unexplained PM mass being mostly due to unaccounted moisture and non-analysed heteroatoms.

Active remote sensing measurements of attenuated backscatter (β_{att}) at 1064 nm were performed at MSA with a Jenoptik CHM 15k Nimbus (G. Lufft Mess- und Regeltechnik GmbH, Germany) ceilometer. The instrument operated continuously with a temporal and spatial resolution of 1 min and 15 m, respectively. The maximum height of the signal is 15.36 km a.g.l. Calibration based on the Rayleigh calibration method was applied (Bucholtz, 1995; Wiegner et al., 2014). The overlap between the laser pulse and telescope field of views of the CHM 15k is greater than 60 % at around 500 m a.g.l. (Martucci et al., 2010; Pandolfi et al., 2013). Further details of the ceilometer installed at MSA can be found in Titos et al. (2017). Passive remote sensing measurements were obtained at MSA by means of a CE-318 sun/sky photometer (Cimel Electronique, France) included in AERONET.

2.2.2 Airborne measurements

Flights were performed with a Piper PA 34 Seneca aircraft (Fig. 4) over north-eastern Spain (Fig. 1) from around 0.5 up to 3.5 km a.s.l. Both the upward and downward flights had approximately the same duration (20–30 min) (Table 1), and the ascent and descent trajectories were performed in the same area when possible. The method used to perform the vertical profiles consisted of vertical ascensions and descents following helical trajectories (Font et al., 2008), thus allowing for the measurement of the aerosol particles properties around a more constrained area. The turns during the vertical helical motions were made with a radius large enough (around 900 m) to assume that the particles entered straight into the inlet. The flights were performed at a speed of around 160 $km h^{-1}$ with a vertical speed of 152 $m min^{-1}$, slightly larger for the downwards flights. However, some losses may arise due to the perturbation of the flow by the aircraft during the sampling, the change in the pitch angle of the aircraft due to the fuel load variation and ascending vs. descending vertical motion. For most of the cases, the up and down profiles were similar, showing therefore the representativeness of the measured profiles and a minimum interference of the aircraft emissions and turbulence. Whether to present an upward or a downward vertical profile was decided based on which of the two had better data availability and vertical resolution.

During the flights, an external volume flow controller (IONER PFC-6020) was connected to the nephelometer in order to assure a constant sampling flow ($5\,L\,min^{-1}$). Similarly to the in situ surface measurements, the scattering measurements were performed at RH $< 40\,\%$ (GAW, 2016). During the SDE period the vertical profiles of scattering were collected using the Kalman filter available in the Aurora 3000 nephelometers, whereas during the REG period vertical profiles of this filter were switched off, and the raw σ_{sp} and σ_{Bsp} coefficients were collected. As shown later, the Kalman filter had the effect of smoothing the measured scattering and hemispheric backscattering coefficients.

Aerosol light absorption coefficient measurements at seven different wavelengths (370 to 950 nm) were performed with the AE33 aethalometer (Magee Scientific AE33, model AE33 AVIO). The AE33 AVIO is a modified prototype, based on the AE33 aethalometer which was re-designed for aircraft measurements. The measurement and operational principle is identical to the commercial AE33 (Drinovec et al., 2015), but the AE33 AVIO model deploys a more powerful internal pump to ensure a constant flow ($4\,L\,min^{-1}$) with changing pressure. Aethalometer measurements were performed at a 1 s resolution.

Particulate matter (PM) mass concentration was obtained using an aerosol optical particle counter (OPC) (GRIMM Spectrometer, model 1129-Sky-OPC). Particle number concentration was measured in 31 size bins at 6 s and at a flow rate of $1.2\,L\,min^{-1}$, for particles with a size diameter from 0.25 to 32 µm. The software instrument provides PM mass concentration, which is calculated assuming a constant particle density. Total particle number concentration was measured at 1 s by means of a water-base condensation particle counter (TSI EPC, model 3788) at a flow rate of $0.6\,L\,min^{-1}$. The instrument provides size range down to 5 nm and measured concentration range up to $2.5 \times 10^5\ N\ cm^{-3}$.

Temperature (T) and relative humidity (RH) inlet sample air was measured at 15 s with a Rotronic HL-RC-B wireless logger. This is a passive sensor, so no flow regulator was needed to pass the air through the sensor. A Vaisala DRYCAP® dew-point transmitter, model DMT143 was used to measure dew point and water volume concentration of outdoor ambient air at 10 s via inlet 2. Ambient air was drawn out at 10 s and at a flow rate of $2\,L\,min^{-1}$. An external pump with a flow regulator was connected to the Vaisala sensor in order to maintain a constant flow. Pressure (P) data were obtained by means of a Kestrel 4000 anemometer. All the aerosol data were converted to T and P sample air conditions.

The inlet (Fig. 4), manufactured by Aerosol d.o.o. (https://mageesci.com, last access: 7 January 2021), was designed to be close to isokinetic at a flight speed of $160\,km\,h^{-1}$, thus minimizing the inlet losses. The inlet flow was set to $10\,L\,min^{-1}$. It was mounted around 5 cm from the fuselage just where the cockpit changes its shape. It was placed around 1.5 m away in front of the leading edge of the wing and 2.5 m away from the propeller in the back of the wing. In order to determine aerosol sampling efficiency and particle transport losses we used the Particle Loss Calculator (PLC) software tool (von der Weiden et al., 2009). The results (not shown) indicated that the losses at the inlet were minimal for $PM_{2.5}$ and that the losses inside the sampling system were large for dust particles larger than around 4–5 µm. To further confirm the PLC results, we compared the PM_x measurements at the MSA station with the PM_x aircraft measurements performed at the same altitude of MSA during the closest flight to MSA at a distance of 10 km. This flight (P1; 7 July 2015; Fig. 1) was performed during a Saharan dust outbreak; thus the presence of dust particles in the atmosphere was significant. Table S1 in the Supplement shows that differences were low, around 6 % for PM_1 and 12 % for $PM_{2.5}$ with the aircraft underestimating the measurements at MSA. However, the PM_{10} aircraft measurements were around 47 % lower compared to the PM_{10} measurements performed at MSA, thus confirming the PLC results. Therefore, the inlet losses for particles other than dust were minimal. In fact, Table S1 shows that for scattering and absorption measurements (which were performed in the PM_{10} fraction at MSA) the differences were $< 9\,\%$ and $< 16\,\%$, respectively, because of the high scattering efficiency of fine particles compared to coarse particles (e.g. Malm and Hand, 2007) and because the absorbing fraction is mostly contained in the fine aerosol particle mode.

3 Determination of the intensive aerosol optical properties

The optical aerosol particle characterization was performed measuring the extensive optical properties (σ_{ap}, σ_{sp} and σ_{Bsp}) and calculating the intensive optical properties for both in situ surface and aircraft-borne measurements. The intensive optical properties (reported below) are mass-independent properties which were determined starting from the multi-wavelength measurements of extensive properties. The intensive properties strongly depend on the physicochemical aerosol properties. Hereafter there is a brief description of the calculated intensive optical properties and the equations used to derive them:

a. The scattering Ångström exponent (SAE) depends on the physical properties of aerosols and mostly on the particle size. SAE values lower than 1 are associated with the presence of coarse particles, whereas SAE values > 1.5 indicate the presence of fine particles (Seinfeld and Pandis, 1998; Schuster et al., 2006). The SAE was calculated as linear fit in a log–log space using the scattering measurements at the three wavelengths.

b. The asymmetry parameter (g) represents the probability of radiation being scattered in a given direction. The range of values is $[-1, 1]$ for backward (180°) to forward (0°) scattering, respectively. A value of around 0.7 is employed in the climate models (Ogren et al., 2006). The g was calculated from the backscatter fractions (BFs) using the semi-empirical formula provided by Andrews et al. (2006).

c. The absorption Ångström exponent (AAE) depends mostly on the chemical composition of sample particles. For pure BC, typical AAE values range from 0.9 to 1.1 (Kirchstetter et al., 2004; Petzold et al., 2013). When brown carbon (BrC) or mineral dust are sampled together with BC, the AAE increases because both BrC and dust can efficiently absorb radiation in the ultraviolet and blue region of the spectrum compared to the near-infrared (IR) (Kirchstetter et al., 2004; Chen and Bond, 2010). The AAE was calculated as a linear estimation in the log–log space using the multi-wavelength absorption measurements from AE33. For the vertical profiles reported here, the AAE was calculated using the AE33 wavelengths for which the absorption measurements were positive along the profile. For most profiles, except for P3, which had all seven wavelengths available, the AAE was calculated from 370 to 590 nm.

d. The single-scattering albedo (SSA) reported here was calculated as the ratio between the scattering and the extinction coefficients at 525 nm. SSA indicates the potential of aerosols for cooling or warming the atmosphere.

e. The single-scattering albedo Ångström exponent (SSAAE) was calculated by fitting the SSA retrieved at the same Aethalometer wavelengths used to calculate the AAE. For this, the SSA was obtained by extrapolating the total scattering to the AE33 wavelengths using the calculated SAE. SSAAE is a good indicator for the presence of coarse particles (e.g. dust) when values are < 0 (Collaud Coen et al., 2004; Ealo et al., 2016).

f. The mass scattering cross section (MSC) is the ratio between the scattering and the PM concentration. It represents the scattering efficiency of the collected particles per unit of mass.

g. The mass absorption cross section (MAC) is the ratio between the light absorption and the PM concentration. It represents the absorption efficiency of the collected particles per unit of mass.

4 Results

4.1 MSA and MSY in situ measurements

The time evolution of PM_1, PM_{10} concentrations, $PM_{1/10}$ ratios, BC, PM components (as measured by ACSM at MSY), σ_{ap}, σ_{sp}, SAE, AAE, g and SSA measured at MSY and MSA during the first 3 weeks of July 2015 is presented in Fig. 5 together with the concentrations of major species (NO_3^-, SO_4^{2-}, NH_4^+, EC, OM (organic matter; with an OM/OC ratio of 2.1), mineral matter (MM; calculated as the sum of typical mineral oxides) and sea salt (SS; $Na + Cl$)) from offline analysis of 24 h filters collected at MSY and MSA during the days of the instrumented flights. Table 2 shows the mean values of surface PM_1, PM_{10}, $PM_{1/10}$, $\sigma_{sp\ 525\,nm}$, $\sigma_{ap\ 637\,nm}$, SAE, AAE, SSA and g measured at the MSY and MSA stations on 7, 8 and 14–16 July compared to the mean values typically measured during SDE and REG pollution episodes as reported by Pandolfi et al. (2014b) and Ealo et al. (2016).

As shown in Fig. 5 an accumulation of pollutants took place from 4 to 8 July, as evidenced by the gradual increase of concentrations of SO_4^{2-}, BC, OA (organic aerosol), PM, total scattering and absorption coefficients. This accumulation was favoured by the regional stagnation and vertical recirculation of the air masses. Moreover, a Saharan dust outbreak caused a progressive increase of PM_{10} at both stations, as well as a simultaneous $PM_{1/10}$ ratio decrease (Fig. 5c and d). The dust event had a larger impact at MSA, where the PM_{10} levels increased sharply and were higher compared to MSY. As reported in Table 2 and in Fig. 5, starting from 6 July, the PM_{10} concentrations were higher compared to average PM_{10} usually measured during Saharan dust outbreaks at both stations. Then, the levels of pollutants, as well as the total scattering and absorption coefficients, decreased on 9 July due to the venting of the basin by an Atlantic north-western (ANW) advection (not shown) that cleansed the northern area of the IP (Gangoiti et al., 2006). This decrease was again sharper at MSA than at MSY due to the location of MSA at the top of a high mountain (Figs. 5c, d and S5). After this event, a new regional pollution episode occurred which favoured again the accumulation of pollutants until the end of the campaign. Furthermore, according to NAAPS modelling outputs, relatively high levels of smoke loads occurred in the air masses affecting the study area on 14–16 July 2015 (Fig. 2).

The intensive optical properties, i.e. SAE (Fig. 5g), AAE (Fig. 5h), g (525 nm; Fig. 5i) and SSA (525 nm; Fig. 5j), showed values consistent with the accumulation process and with the occurrence of the coarse Saharan dust particles, as well as the effects of the wildfires occurring in the IP. The SAE progressively decreased at both stations from values > 1.5–2.0 (indicating the predominance of fine particles) on 4 July to values < 1.0 (indicating the predominance of coarse particles) on 8 July 2015. The variability of g was less pronounced compared to the variability of the SAE, especially at MSA, likely because of the lower sensitivity of

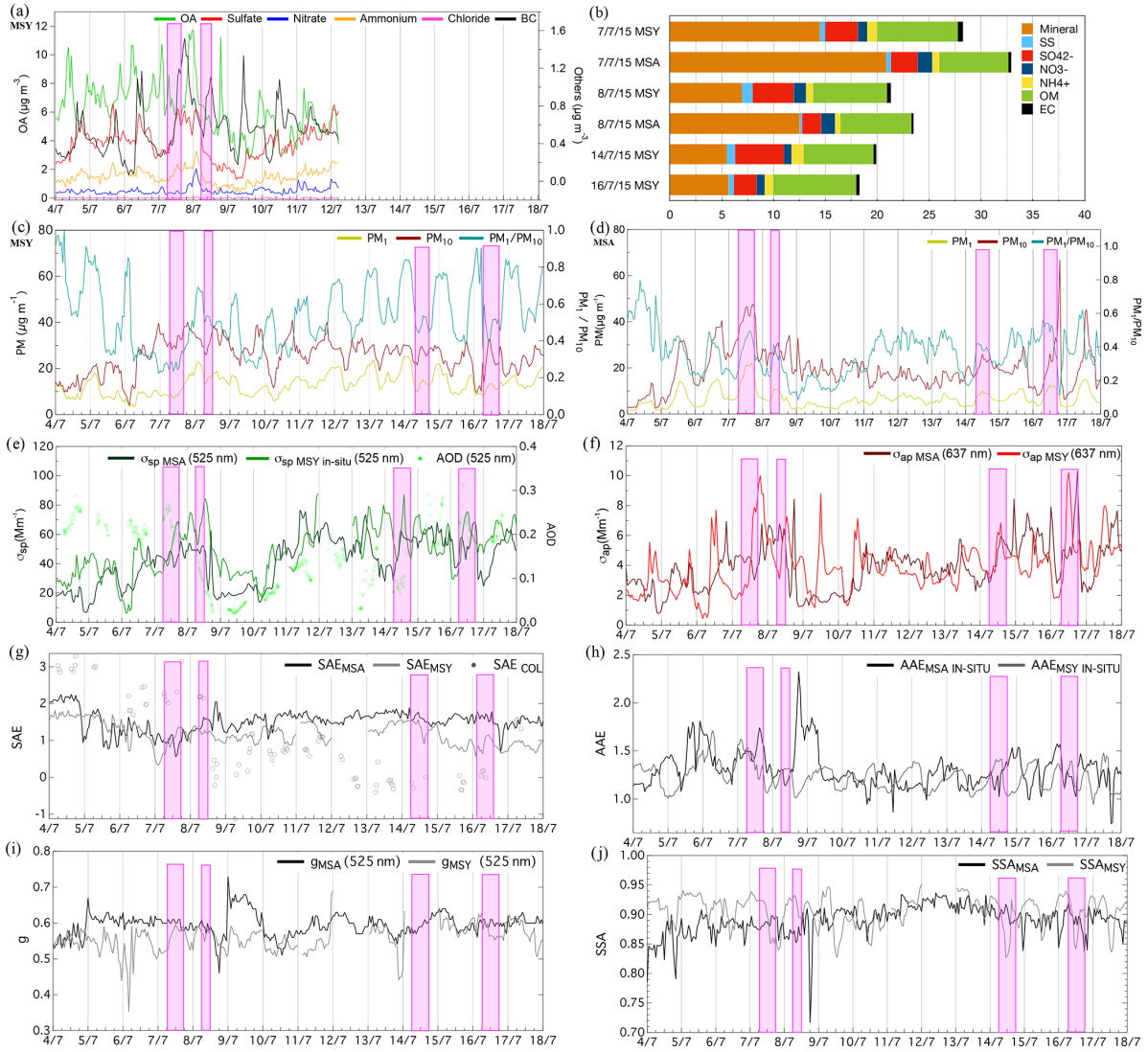

Figure 5. Ground-based physical and chemical measurements at the MSA and MSY stations: **(a)** the evolution of submicron chemical composition as measured by the ACSM and the AE33; **(b)** the offline chemical analysis of 24 h quartz filters from both the MSA and MSY stations for the instrumented flights days; and (**c, d**) the temporal evolution of PM_1, PM_{10} and the $PM_{1/10}$ ratio at MSY and MSA, respectively. The evolution during the measurement campaign of the scattering coefficient by the integrating nephelometer and the aerosol optical depth (AOD) by the ceilometer and sun/sky photometer and absorption by the MAAP are shown in **(e)** and **(f)**; the evolution of the intensive optical properties such as the scattering Ångström exponent (SAE), from both the integrating nephelometer and columnar ceilometer and sun/sky-derived scattering (COL in the figure), the absorption Ångström exponent (AAE), the asymmetry parameter (g), and the single-scattering albedo (SSA at 525 nm) are shown in **(g–j)**, respectively. The shadowed sections highlight the vertical-profile measurement periods with the aircraft.

the g parameter to coarse PM compared to SAE (Pandolfi et al., 2018). The AAE was considerably > 1.0 at both sites, reaching values > 1.5. The high AAE was due to enhanced UV absorption, which typically is observed when brown carbon (BrC) and/or mineral dust particles are present in the atmosphere (Kirchstetter et al., 2004; Fialho et al., 2005; Sandradewi et al., 2008; Alastuey et al., 2011; Chen and Bond, 2010). Interestingly, the AAE measured in the whole column with the sun photometer over MSA showed even larger values, up to 2.5, until the evening of 8 July. The cleansing effect of the ANW on 9 July caused a reduction of the PM loads and consequently of the measured scattering and absorption coefficients at both sites. During this ANW flow the SAE increased again to values of 1.5–2.0, whereas both the surface

Table 2. Mean values of in situ surface PM_1, PM_{10}, $PM_{1/10}$, $\sigma_{sp\ 525\,nm}$, $\sigma_{ap\ 637\,nm}$, SAE, AAE, SSA and g measured at the MSY and MSA stations during the SDE period of 7–8 July and the REG period of 14 and 16 July compared to the mean values typically measured (denoted by "avg") during SDE and REG episodes as reported by Pandolfi et al. (2014a) and Ealo et al. (2016).

	MSA				MSY			
	SDE_{7-8}	SDE_{avg}	REG_{7-8}	REG_{avg}	SDE_{7-8}	SDE_{avg}	REG_{7-8}	REG_{avg}
PM_1 ($\mu g\,m^{-3}$)	9.7 ± 5.6	8.4 ± 4.7	7.1 ± 3.0	7.9 ± 3.9	14.1 ± 4.6	12.3 ± 5.4	14.0 ± 4.6	11.8 ± 5.7
PM_{10} ($\mu g\,m^{-3}$)	30.8 ± 8.3	21.0 ± 17.0	19.8 ± 8.5	12.6 ± 7.0	33.2 ± 3.3	25.4 ± 17.0	23.8 ± 5.7	15.6 ± 8.0
$PM_{1/10}$ (%)	29.5 ± 10.1	39.6 ± 1.1	37.8 ± 10.8	46.2 ± 2.1	42.3 ± 13.6	–	60.0 ± 16.1	–
$\sigma_{sp\ 525\,nm}$ (Mm^{-1})	42.5 ± 11.2	53.6 ± 30.4	51.9 ± 10.9	47.0 ± 21.9	54.4 ± 14.9	60.2 ± 29.8	56.4 ± 12.8	50.6 ± 24.6
$\sigma_{ap\ 637\,nm}$ (Mm^{-1})	4.53 ± 1.66	2.84 ± 0.03	5.03 ± 1.60	2.50 ± 0.03	4.89 ± 2.19	4.04 ± 2.27	4.42 ± 1.59	4.26 ± 2.35
SAE	1.25 ± 0.31	1.33 ± 0.61	1.56 ± 0.19	1.81 ± 0.30	1.05 ± 0.28	1.50 ± 0.53	1.03 ± 0.29	1.92 ± 0.31
AAE	1.46 ± 0.25	1.41 ± 0.25	1.29 ± 0.15	1.27 ± 0.24	1.26 ± 0.17	1.27 ± 0.24	1.23 ± 0.12	1.24 ± 0.19
SSA	0.88 ± 0.03	0.93 ± 0.06	0.89 ± 0.02	0.92 ± 0.05	0.90 ± 0.03	0.91 ± 0.03	0.90 ± 0.03	0.88 ± 0.04
g	0.58 ± 0.03	0.60 ± 0.05	0.60 ± 0.02	0.57 ± 0.05	0.55 ± 0.02	0.60 ± 0.04	0.62 ± 0.08	0.58 ± 0.25

and column-integrated AAE decreased due to the removal of dust by the ANW cleansing effect. As already mentioned, after the ANW advection, another regional pollution episode developed until the end of the campaign.

In the following sections, we present a detailed description and interpretation of the evolution of pollutants and aerosol optical parameters measured at MSY and MSA during the SDE and REG period. The mean values of the considered pollutants and optical parameters during airborne measurements are reported in Table 2, together with the mean values typically registered during SDE outbreaks and REG episodes.

4.1.1 Saharan dust event period, SDE

The attenuated backscatter from the ceilometer at MSA allowed for identifying the occurrence of aerosol layers up to 5 km a.g.l. (i.e. 5.8 km a.s.l.) in this period (Fig. 6). The air masses featured significant dust concentrations which were probably further accumulated in the region by the regional vertical recirculation of air masses. Correspondingly, the PM_{10} mass concentrations measured at MSY and MSA were higher compared to the PM_{10} concentrations usually measured in dust outbreaks (Table 2). Mineral matter concentrations during these days (Fig. 5b) reached 21 and 15 $\mu g\,m^{-3}$ at MSA and MSY, respectively. The OA occurred in very similar concentrations at both sites ($\sim 7\,\mu g\,m^{-3}$). Daily concentrations of SO_4^{2-} and EC from filters were higher in the regional background (MSY) compared to the continental one (MSA) due to the larger impact of regional sources such as industries and road traffic and the emissions from maritime shipping from the Mediterranean Sea and the port of Barcelona. As expected, NO_3^- concentrations were rather low at both sites due to the thermal instability of nitrate in summer (Harrison and Pio, 1983; Querol et al., 2001, 2004, 2009a).

Figure 5a shows that the evolution of the SO_4^{2-} concentration at the MSY station, as recorded by the ACSM, was similar to that of BC, both reaching a maximum on the evening of 7 July, with two subsequent minor peaks at midnight and on the evening of 8 July (Fig. 5). The peak just after midnight, at 00:00 UTC on 8 July, was also reflected in the OA, NO_3^- and NH_4^+ concentrations. At MSA, ACSM measurements were not available; however the measured absorption showed a progressive increase on 8 July with a relative maximum being reached in the afternoon (Fig. 5d), when AAE at MSA reached values > 2.0 (Fig. 5). This sharp increase in BC was attributed to local biomass burning emissions (Fig. 2). During this first measurement period, the mean scattering and absorption coefficients at both sites (Table 2) were above the averaged values registered at the MSA and MSY stations during dust and summer regional pollution events (Pandolfi et al., 2014b). Figure 5e also shows the high AOD from the MSA sun/sky photometer during the SDE period.

Table 2 shows that during this period the intensive parameters SAE, AAE, SSA and g reached values similar to the typical coarse-PM-influenced ones recorded during dust outbreaks at both stations (Pandolfi et al., 2014b). As already pointed above, on the afternoon of 8 July a change due to local biomass burning emissions was observed in the optical aerosol properties at MSA compared to MSY. As a consequence, the SAE and AAE at MSA increased to values > 1.5 and 2.0, respectively.

4.1.2 Regional pollution episode, REG

An REG episode developed during the second aircraft measurement period leading to the accumulation of atmospheric aerosols in the area. A wildfire outbreak from northern Africa also took place (Fig. 2), as well as a light dust outbreak during 16 July (Figs. 2 and 5). The REG episode resulted in the development of aerosol layers at high altitude, as also observed with the ceilometer at MSA (Fig. 6c and d). PM_{10} concentrations were rather constant and quite similar at both MSA and MSY but on average lower than during the SDE period. Only on 16 July, PM_{10} concentrations at MSA, due

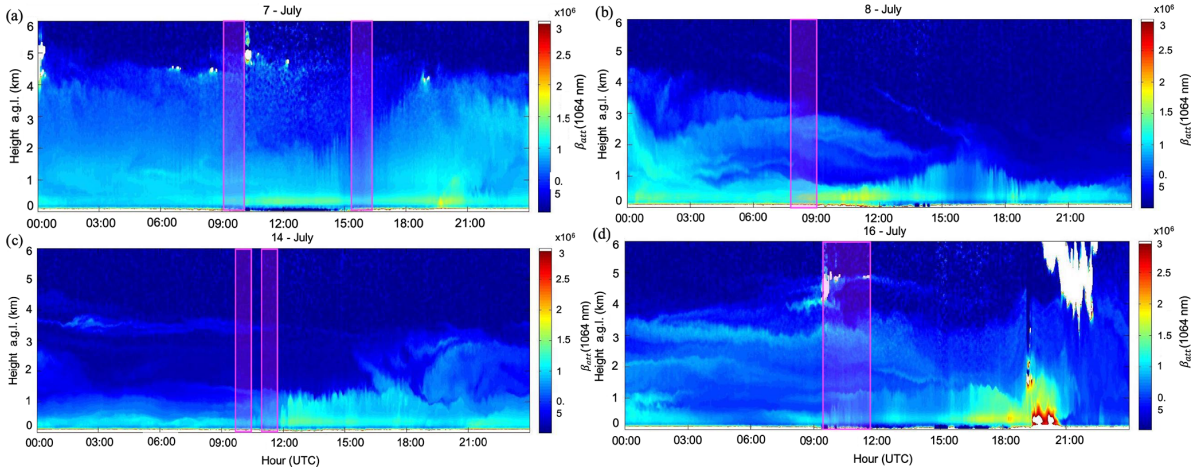

Figure 6. Time evolution of β_{att} vertical profiles as retrieved by the ceilometer deployed at the MSA station during the July 2015 measurement campaign for **(a)** 7, **(b)** 8, **(c)** 14 and **(d)** 16 July. The shadowed boxes highlight the measurements during the flights periods.

to the impact of the dust outbreak at the altitude of the MSA station, were closer to an SDE scenario rather than an REG scenario (Table 2). This pattern was also reflected in the high $PM_{1/10}$ ratio measured from 10 July with the exception of the afternoon of 16 July at MSA when the $PM_{1/10}$ ratio was lower. The lower impact of the dust outbreak during these days compared to the first period was confirmed by the markedly lower MM from PM speciation analysis (Fig. 5b). Despite the higher MM at MSA, those of the remaining PM_{10} components and BC were similar at both sites.

The scattering (Fig. 5e) and absorption coefficients (Fig. 5f) at both sites were above the average values (Table 2) presented by Pandolfi et al. (2014a) and Ealo et al. (2016) for REG episodes, due to the strong accumulation of pollutants which took place from 10 July onward for this particular REG episode. AOD (Fig. 5e) during REG was rather low when compared to the SDE period due to the absence of dust, with the exception of 16 July, when AOD increased simultaneously with the light dust outbreak and probably the influence of wildfire pollution plumes.

The asymmetry parameter g showed similar values to those observed during the SDE period at both sites and did not change much during the dust event on 16 July because, as already observed, g is less sensitive to variations of coarse-mode aerosols. Consequently, the relatively lower SAE on this day (especially visible at MSY) suggested variations in the larger end of the accumulation mode particles and above rather than in the lower end of the mode. The lower SAE at MSY compared to MSA during REG (and especially during 16 July) was then probably due to a relative reduction of PM_1 at MSY compared to the previous days, whereas PM_{10} kept similar values (Fig. 5) yet lower compared to the SDE period despite the light SDE event registered on 16 July (Table 2). Moreover, the higher relevance of fine PM at MSA compared to the MSY regional background could also explain the observed difference. This could be due to a combination of factors including a higher exposure of the MSA station to the fine PM from the wildfires, the lower impact of local and regional sources at MSA, and the larger segregation of particles during transport toward MSA due to its remote location. During REG, AAE decreased compared to the first period (especially at MSA), yet this was still > 1.0, indicating a mixing of regional aerosols with BrC and mineral dust. AAE of the whole column (sun/sky photometer data) was also close or slightly > 1.0. Finally, the SSA varied only slightly between REG and SDE at both sites.

4.2 In situ vertical profiles

Here we focus on the vertical profiles obtained by means of airborne measurements during the two distinct SDE and REG scenarios. Vertical profiles of optical extensive and intensive properties, as well as PM concentrations for upward and downward flights, are reported in Table 1. Our objective is to analyse the vertical-profile variation of these properties and their diurnal and spatial evolution and how these properties varied across layers in the troposphere. When possible, direct comparison with the surface data measured at the MSA station was made.

As reported above, the comparison of airborne measurements at 1.5 km a.s.l. with in situ surface measurements at MSA for P1 reached a good agreement (Table S1), with a relative difference $< 10\,\%$ for PM_1 and $PM_{2.5}$ concentrations and the extensive and intensive optical properties. The large underestimation of $PM_{2.5-10}$, missing $-47\,\%$ in the airborne measurements, is the reason for excluding the PM_{10} fraction from the vertical profiles. Consequently, we calculated the MSC and the MAC for $PM_{2.5}$.

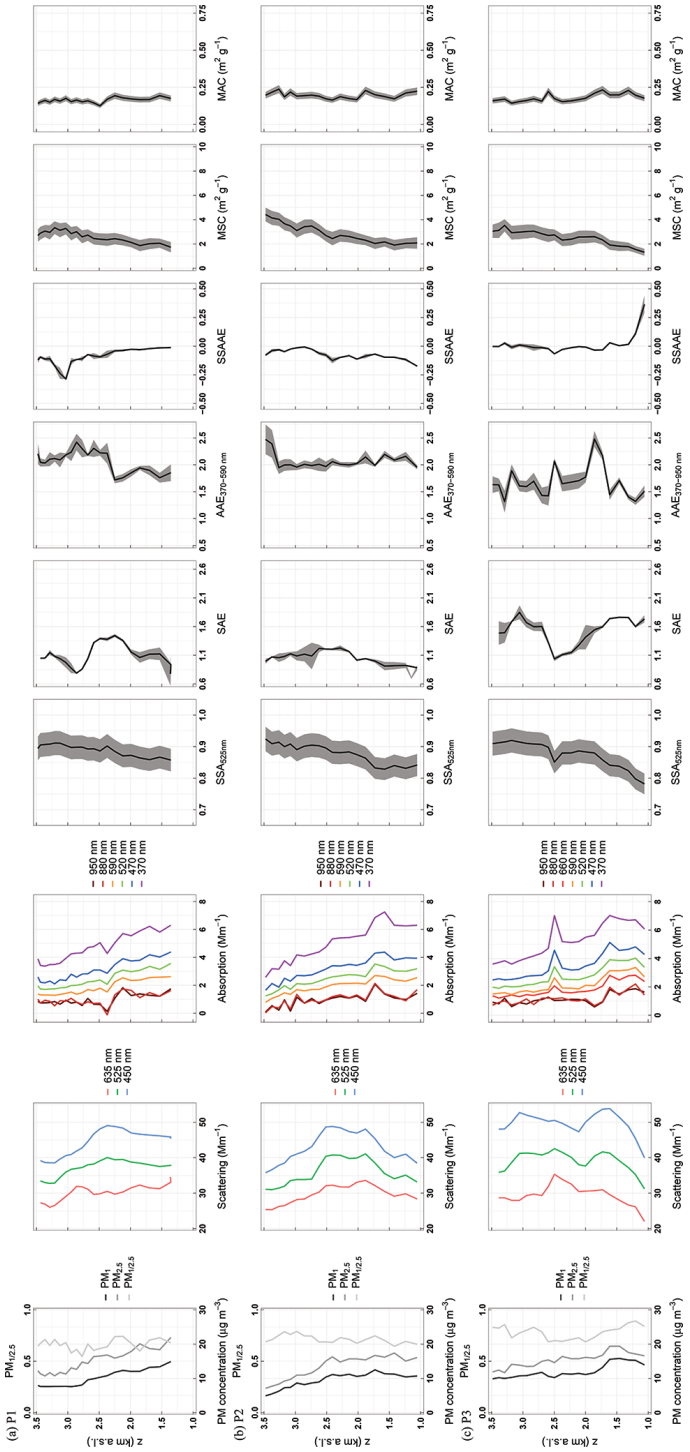

Figure 7. Vertical profiles from the extensive and intensive optical properties during the SDE period: scattering and absorption coefficients; σ_{sp} and σ_{ap}, respectively, for several wavelengths; PM_1, $PM_{2.5}$ concentration and the $PM_{1/2.5}$ ratio; single-scattering albedo (SSA); scattering Ångström exponent (SAE); absorption Ångström exponent (AAE); single-scattering albedo Ångström exponent (SSAAE); and mass scattering and absorption cross section, MSC and MAC, respectively, from left to right, for the aircraft-borne measurements for the **(a)** P1, **(b)** P2 and **(c)** P3 vertical profile. The shadowed areas around the intensive optical properties denote the standard error of the variables.

4.2.1 Saharan dust event, SDE

Figure 6a and b shows a clear atmospheric layering of pollutants from 0.8 to 5.0 km a.g.l., i.e. 1.6 to 5.8 km a.s.l. The magenta boxes in Fig. 6a and b highlight the time window when flights were performed. Figure 7 shows the three vertical profiles during the SDE period (Table 1, namely: P1 (Fig. 7a) and P2 (Fig. 7b), which were performed close to the MSA station (Fig. 1), and P3 (Fig. 7c), which was performed over the Catalan pre-coastal mountain range (Fig. 1). We can observe from Fig. 7 that during the P1 and P3 flights the PM_1 and $PM_{2.5}$ concentrations were rather high in the upper atmosphere (4–12 and 7–17 $\mu g\,m^{-3}$ for PM_1 and $PM_{2.5}$, respectively, above 2.5 km a.s.l.). At lower altitudes (< 1.5 km a.s.l.) even higher PM concentrations were measured (10–16 and 16–22 $\mu g\,m^{-3}$ for PM_1 and $PM_{2.5}$, respectively) which were on the upper range of the typical surface concentrations reported in Ealo et al. (2016) and Pandolfi et al. (2014b) for SDE scenarios in the area. The vertical profiles of PM during P1 and P2 showed a progressive upwards reduction of PM concentrations, especially evident above 2.5 km a.s.l. in P2 (Figs. 6 and 7). The vertical profiles of scattering and absorption coefficients showed similar patterns to the ones described for PM with an upward decrease. As already stated, the use of the Kalman filter in the nephelometer measurements of P1, P2 and P3 had a smoothing effect on the measured scattering coefficient, thus complicating a direct comparison with PM during these profiles.

The $PM_{1/2.5}$ ratio (Fig. 7) during P1 ranged from around 0.6 to 0.75 along the profile with a relative minimum between 2.5 and 3 km a.s.l., where the SAE reached its lowest values (< 1). Conversely, a clear increase of the $PM_{1/2.5}$ ratio above 2.5 km a.s.l. was evident for P2, when the ratio reached 0.8. The values of both SSAAE and SAE were consistent with the $PM_{1/2.5}$ ratio found for the different layers in P1 and P2. The SAE during P1 and P2 ranged between 0.8 and 1.5, and the SSAAE kept negative values along both profiles with a pronounced minimum at the 3.0 km a.s.l. layer during P1, highlighting a higher relative fraction of coarse particles attributed to the dust outbreak over the area of study. It should be noted that a direct comparison between the vertical profiles of $PM_{1/2.5}$ and SAE was difficult because of the Kalman filter, which smoothed the calculated intensive aerosol particles' scattering properties and made the comparison difficult, especially for g, which involves both the smoothed scattering and the hemispheric backscattering coefficients. For this reason, the g was not reported in Fig. 7. During P1 the AAE ranged between around 1.7 and 2.5 with the highest values measured above 2.5 km a.s.l. as a consequence of the presence of UV-absorbing dust particles in the atmosphere. During P2, the AAE showed more constant values (around 2) with altitude, mirroring the less variable SAE compared to P1. Both SSA and MSC showed increasing values with altitude during P1 and P2 ranging between 0.85–0.9 and 2–4 $m^2\,g^{-1}$, respectively, whereas the MAC (at 525 nm) kept rather constant values (around 0.2 $m^2\,g^{-1}$) with altitude with slightly lower values above 2.0–2.5 km a.s.l.

Figure 7c shows the vertical profile P3, which was consistent with P1 and P2, even if the calculated intensive optical properties suggested a reduced effect of dust particles during P3 compared to P1 and P2. PM concentrations during P3 were similar to P2 profile, although the $PM_{1/2.5}$ ratio was higher, indicating an increased importance of the fine aerosol mode during P3 compared to P2. The scattering and absorption coefficients were similar to the values measured during P1 and P2, although the scattering was higher during P3. The intensive optical properties of P3 indicated the predominance of coarse dust particles especially around 1.7 and 2.3 km a.s.l., where the SAE decreased up to values close to 1 and the SSAAE was negative. In this altitude range the AAE was on average higher compared to the rest of the profile and especially around 1.8 km a.s.l., where it reached a value of 2.5. As already noted, the observed AAE increase at these altitudes was due to the UV absorption from dust particles. Overall, during P3 the intensive properties such as SAE, AAE and SSA showed more variability with altitude compared to P1 and P2 as also reported by the ceilometer measurements, which showed a more stratified atmosphere on 8 July (P3) compared to 7 July (P1 and P2; Fig. 6a and b).

During P1, P2 and P3, the AAE varied considerably with altitude and ranged between 1.5 and 2.5 depending on the flight and altitude. These values were higher than those measured in situ at the MSA and MSY stations, as shown in Fig. 5, and were higher compared to the typical AAE values measured during SDE at these stations (Table 2). The lower AAE measured at the MSA and MSY stations compared to the AAE in the free troposphere measured during P1, P2 and P3 was due to the increased relative importance of BC particles close to the ground and within the PBL (planetary boundary layer; estimated from the observation of the pollutant concentrations, the ceilometer profiles and the meteorological conditions: potential temperature in Fig. S3), which reduced the AAE at the two measurement stations compared to the values obtained with the flights in the free troposphere. The UV absorption properties of African dust observed during P1, P2 and P3 and the corresponding increase of AAE were driven by the presence of iron oxides, such as hematite and goethite, which efficiently absorb radiation at shorter wavelengths (e.g. Alfaro et al., 2004). The obtained $PM_{2.5}$ MAC values (around 0.2–0.25 $m^2\,g^{-1}$) observed in the dust layers during P1, P2 and P3 were consistent with the MAC values, around 0.24 $m^2\,g^{-1}$, recently reported for dust particles by Drinovec et al. (2020).

For the P1, P2 and P3 profiles both SSA and MSC progressively increased with altitude (Fig. 7). SSA in P1, P2 and P3 was rather similar and ranged from 0.83 to 0.93 from 1.5 to 3.5 km a.s.l. Higher SSA at higher altitudes was due to different factors including the progressive reduction of the relative importance of BC particles with altitude and the presence of more efficient scatterers at higher altitudes, to-

gether with the presence of dust, as evidenced by the higher MSC and lower MAC. The MSC during the three flights ranged from around 2 $m^2 g^{-1}$ at 1.5 km a.s.l. to 3–4 $m^2 g^{-1}$ at 3.5 km a.s.l. Pandolfi et al. (2014b) reported an MSC of $PM_{2.5}$ at the MSA station of 3.3 ± 1.9, which was consistent with what was observed with airborne measurements at the MSA altitude (around 1.5 km a.s.l.). Pandolfi et al. (2014b) also showed that on average the highest MSC values at MSA were observed in summer, mostly because of aerosol ageing and the formation of efficient scatterers, such as secondary SO_4^{2-} particles and OA during summer regional pollution episodes. In the area under study OA is expected to be mostly secondary organic aerosols (SOAs) (e.g. Querol et al., 2017). Recently, Obiso et al. (2017) assessed the sensitivity of simulated MSC of MM, OA and SO_4^{2-} by perturbing particle microphysical properties, such as the size distribution, refractive index, mass density and shape. Perturbations were performed by changing by $\pm 20\,\%$ the widely used OPAC (optical properties of aerosols and clouds; Hess et al., 1998) reference values. (Obiso et al., 2017) compared the simulated MSC with the experimental MSC of PM and different PM components determined at the MSY station. High MSC, up to 4–5 $m^2 g^{-1}$, was simulated by Obiso et al. (2017) for OAs and SO_4^{2-}, and both were more sensitive to perturbations in the refractive index than to variations in the size distribution. Lower MSC was reported by the same study for MM (0.5–2 $m^2 g^{-1}$), and it was found to be more sensitive to perturbations of the size distribution of dust particles compared to other particle properties. Ealo et al. (2018) calculated the MSC for different pollutant sources retrieved by applying the positive matrix factorization (PMF) model on PM_{10} chemically speciated data collected at the MSA station. Ealo et al. (2018) found that the MSC changed considerably depending on the sources considered, being the highest for secondary SO_4^{2-} and the lowest for sources such as MM and SS (both mostly associated with coarse particles) and for anthropogenic sources, such as traffic or industry (also emitting less efficient scattering particles such as BC). Thus, the observed increase of MSC with altitude could be due to the relative increase of SO_4^{2-} and OA particles, causing important changes in the refractive indexes and size distributions with altitude. These changes could be related to the ageing of the particles, which is expected to be larger for particles at higher altitudes.

4.2.2 Regional pollution episode, REG

Figure 8 shows the vertical profiles P4, P5, P6 and P7 over the MSY station and the Catalan pre-coastal mountain range (Fig. 1 and Table 1). The vertical profile of the attenuated backscatter from the ceilometer (Fig. 6) showed layering of aerosol with altitude for this period. As detailed below, the observed aerosol layers probably originated mostly from the vertical recirculation of air masses during summer regional pollution episodes (Gangoiti et al., 2001). Moreover, a PM outbreak from wildfire plumes during this period and a dust outbreak on 16 July were also detected (Fig. 2).

In the P4 profiles, the PM concentrations, scattering and absorption coefficients reached higher values below the 1.5. km a.s.l. layer (i.e. within the PBL where most of the pollutants generated at ground were trapped) and decreased with altitude. The high $PM_{1/2.5}$ ratio (> 0.95) for altitudes $> 1.5.$ km a.s.l. demonstrated the prevalence of fine particles in the troposphere compared to the PBL. Accordingly, along the profile, SAE was high (1.5–2.7), indicating the predominance of fine particles, and SSAAE was positive, indicating the absence of dust particles. Correspondingly, the asymmetry parameter g decreased with altitude above 1.5. km a.s.l. down to 0.5, confirming the progressive shift toward smaller particles with altitude and an increased effect of particles in the lower end of the accumulation mode. Notable was the decrease of SAE (below 1.5) and SSAAE (close to 0) and the corresponding increase of g (up to 0.8), at around 3.3 km a.s.l., during P4, indicating the presence of coarse particles at this height. AAE kept values between 0.8 and 1.2 along the whole P4 profile, suggesting the lack of strong UV absorbers (such as BrC or mineral dust) and the prevalence of absorbing BC particles from fossil fuel combustion (e.g. Bond et al., 2004; Zotter et al., 2017). Furthermore, the MAC showed higher variability compared to P1, P2 and P3 profiles reaching values up to 0.3, suggesting a relative increasing importance of BC particles in the troposphere compared to P1, P2 and P3. As already observed during the SDE period, both SSA and $PM_{2.5}$ MSC increased with altitude, especially above 2 km a.s.l., suggesting the presence of efficient scatterers at these altitudes. Note that, as observed during the first period of measurements, the MSC at 1.5 km a.s.l. (2–3 $m^2 g^{-1}$) was consistent with the typical MSC recorded at MSA (Pandolfi et al., 2014b). At higher altitudes the MSC reached values close to 5 $m^2 g^{-1}$ with SSA around 0.95.

Profile P5 (Fig. 8b) was obtained 1 h after P4, and the distance between the two profiles was about 55 km (Table 1 and Fig. 1). The main differences between P4 and P5 were the consistently higher total scattering and absorption coefficients and PM concentrations at all heights during P5 compared to P4 and the presence of two layers at 2 and 3 km a.s.l. along P5. As in P4, PM concentrations in P5 were dominated by the fine mode (a $PM_{1/2.5} > 0.9$), as confirmed by a high SAE (> 1.75); a positive SSAAE along the profile; and rather low g values which decreased to 0.5 at 2 km a.s.l.

The absorption coefficient during P5 was dominated by BC particles from fossil fuel combustion up to 2 km a.s.l with AAE values around 1.0 or lower below 2 km a.s.l. and with SSA and MSC reaching the lowest values around 0.7 and 1, respectively, at 2 km a.s.l., indicating the predominance of absorbing BC particles at this altitude. From this layer upwards, SAE remained rather constant (1.8–2-2), whereas g, SSA, AAE and MSC progressively increased with altitude. Again, the increase of g with altitude could be indicative of variations of particle size with altitude and a progressive

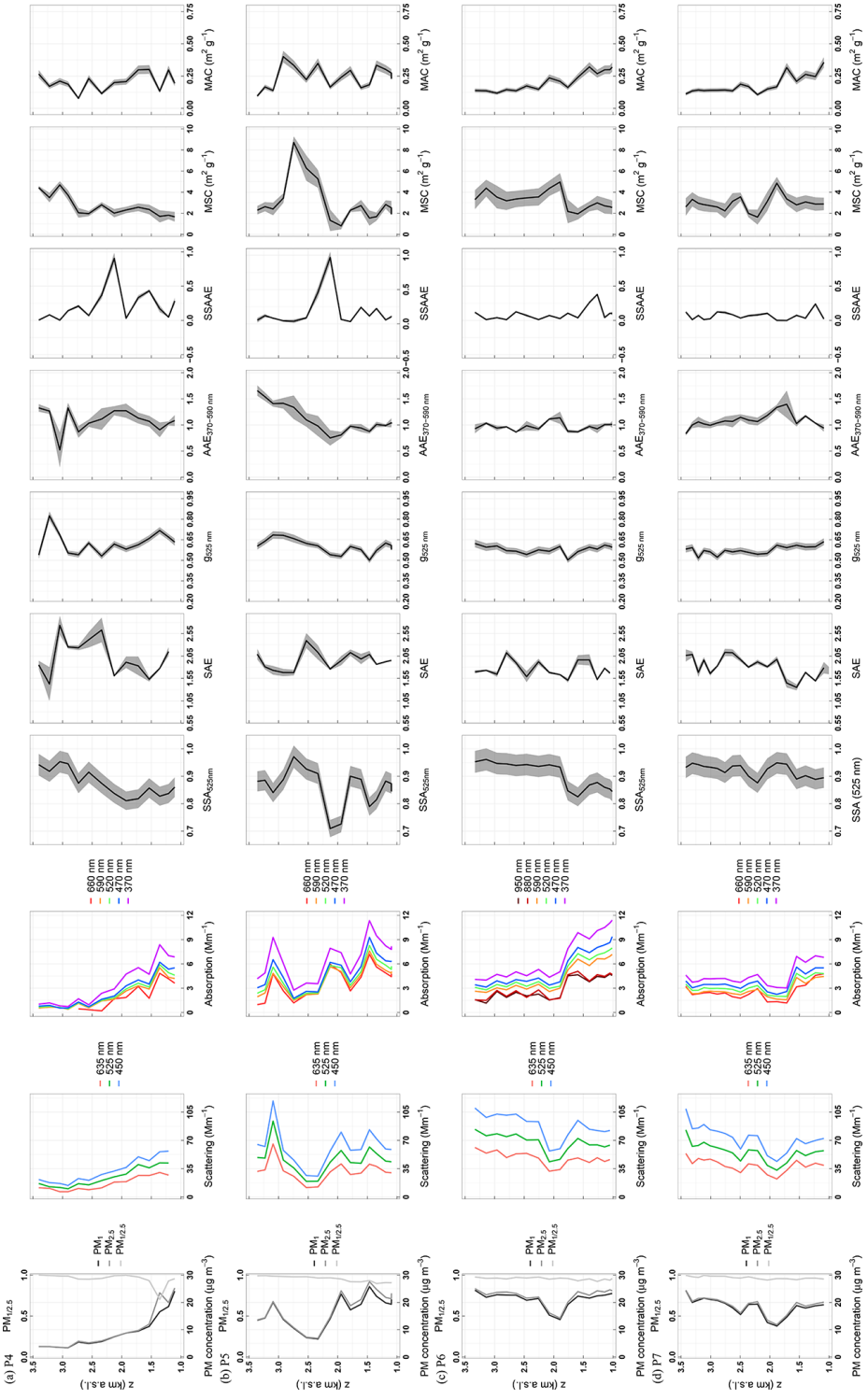

Figure 8. Vertical profiles from the extensive and intensive optical properties, as in Fig. 7 plus the asymmetry parameter (g), for the aircraft-borne measurements during the REG period for the **(a)** P4, **(b)** P5, **(c)** P6 and **(d)** P7 vertical profiles around the Catalan pre-coastal mountain range close to the MSY station. The shadowed areas around the intensive optical properties denote the standard error of the variables.

shift toward particles in the lower end of the accumulation mode. Particles in this size range are efficient scatterers at the nephelometer wavelengths, thus explaining the larger MSC. These results together with the progressive increase of AAE and positive SSAAE suggested the presence of fine BrC particles in the free troposphere probably from wildfire smoke as also shown by modelling outputs in Fig. 2. The presence of a clear separated layer at around 2.5–3 km a.s.l. was also shown by ceilometer measurements (Fig. 6c).

The P6 profile Fig. 8c was obtained close to P5 (4 km distance) on 16 July (2 d after P4 and P5; Table 1). Scattering and absorption coefficients and PM concentrations were higher compared to P5 as a consequence of the progressive accumulation of particles in the area due to the development of the regional pollution episode. This hypothesis was also supported by the higher aerosol load and layering in the troposphere compared to 14 July according the ceilometer measurements (Fig. 6). Both scattering coefficient and PM concentrations decreased above the PBL (estimated to be at 1.75 km a.s.l.), with a subsequent increase at higher altitudes where these variables kept rather constant values close to those observed within the PBL. Conversely, the absorption coefficient did not increase above the PBL, and, consequently, the SSA increased (up to 0.93–0.97) in the free troposphere compared to the SSA values obtained within the PBL. The MSC showed a similar profile to SSA reaching values around 3.5–5.0 $m^2 g^{-1}$, whereas the MAC decreased with altitude above the PBL. The relative abundance of fine particles during P6 was also supported by SAE values around 1.75 and low g values around 0.5–0.6 and a positive SSAAE along the whole profile. The AAE ranged between 0.8 and 1.2, indicating that the absorption was dominated by BC particles.

The profile P7 was obtained around 30 min after P6 and at a distance of around 60 km from P6 and about 5 km from P4. Scattering and absorption coefficients and PM concentrations from P7 were rather similar to P6. The scattering and absorption coefficients in the green spectrum and PM_1 concentrations within the PBL (below 1.75 km a.s.l.) reached 50, 5 Mm^{-1} and 20 $\mu g\,m^{-3}$, respectively. As for P6, scattering, absorption and PM decreased above the PBL and then increased again in the free troposphere, with a relative maximum at 2.0–2.5 km a.s.l., followed by a further increase with height, up to 3.5 km a.s.l.

Again, $PM_{1/2.5}$ (0.95), SAE (1.75–2.0), a positive SSAAE and g (0.5–0.6) indicated the prevalence of fine particles in the free troposphere above the PBL during P7. As observed during the previous flights, SSA and MSC had very similar profiles. In P7, two peaks were observed at 1.8 and 2.5 km a.s.l., with a marked minimum at 2.2 km a.s.l. The similarity of SSA and MSC profiles is attributed to the relative high proportion of non-absorbing particles compared to the absorbing particles (high SSA) and the high scattering efficiency of the sampled particles. These two SSA and MSC peaks were also simultaneous with a slight increase of AAE indicating an aerosol mixture with BrC particles. These AAE–SSA–MSC parallel profiles were persistent for the whole REG period. The 1.8 km a.s.l. peak was coincident with a reduction of scattering, absorption and PM concentrations just above the PBL and could be associated with the vertical diffusion along the day of a layer which, as shown in Fig. 6d, at 00:00 UTC on 16 July was at 2 km a.s.l. The lower SSA, MSC and AAE at 2.2 km a.s.l. were coincident with a relative increase of scattering, absorption and PM concentrations and indicated the presence of a layer with a larger relative proportion of BC particles. From there upwards, the subsequent observed layer can be associated with the one at 3 km a.s.l. at midnight. If we consider also the ground MSA data (Fig. 5) and those from P6, the first of these two layers can be associated with reservoir strata (a recirculating layer according to Gangoiti et al., 2001) above the PBL, which, as day progressed and the convective dynamics intensified, was then integrated into the PBL. Conversely, the largest layer can be related to an outbreak of light mineral dust and smoke from wildfire plumes affecting the PBL (and the MSA station) later in the day. This was supported by the high albedo, with SSA > 0.9 across the whole profile and increasing with height. The AAE was close to 1.0 for the whole profile, with peaks up to 1.5 where the PM concentration was at the lowest concentrations. This could be caused by a higher relative concentration of more brownish, aged and not very fine black particles, which was related to reservoir strata, produced by the vertical recirculation of air masses, with lower SAE and higher g, SSA and MSC.

5 Conclusions

We reported on the results of an aircraft measurement campaign aiming at studying the vertical profiles of physical properties (size-segregated PM mass concentration and multi-wavelength scattering and absorption coefficients) of atmospheric particles in the western Mediterranean basin (WMB). Seven vertical profiles following helical trajectories were obtained on 7–16 July 2015 over an area of 3500 km^2 in north-eastern Spain. The measurement campaign was carried out under typical summer regional pollution scenarios, with vertical recirculation of air masses that cause interlayering of polluted layers in the first few km a.s.l. (Gangoiti et al., 2001). These aged aerosol-rich layers are driven by complex atmospheric dynamics, driven by the summer atmospheric stagnation, high insolation, low precipitation and intricate orography surrounding the WMB. We measured during two regional pollution episodes, and these already complex scenarios were also affected by two African dust outbreaks and long-range transported plumes of wildfires. The summer regional pollution episodes finished by venting the polluted air masses by synoptic western and northwestern flows, a frequent occurrence in the WMB (Gangoiti et al., 2001, 2006).

We measured vertical profiles of PM_1 and PM_{10} concentrations and a set of climate-relevant aerosol optical parameters – single-scattering albedo (SSA), asymmetry parameter (g), scattering and absorption Ångström exponents (SAE and AAE), and PM mass scattering cross section (MSC). These intensive optical properties depend on the microphysical and chemical properties of atmospheric aerosol particles rather than on their mass and are key input parameters in climate models. Simultaneous in situ surface measurements performed at two monitoring supersites in the region (Montseny, MSY, regional background, 720 m a.s.l.; Montsec, MSA, remote, 1570 m a.s.l.) were also used to better characterize the aerosol particles sampled during the instrumented flights.

Ceilometer profiles indicated the occurrence of aerosol layers over the region up to more than 5 km a.s.l., and ground measurements indicated that mean PM_1 and PM_{10} mass concentrations and the scattering and absorption coefficients were similar or even higher than the typical ones obtained in the region during summer regional pollution episodes and African dust outbreaks.

During all flights, PM concentrations, scattering and absorption were high up to around 3.5 km a.s.l. (maximum altitude reached by the aircraft), detecting the regional layering of aerosol-rich strata at these altitudes. The first measurement period was affected by an African air mass outbreak with dust particles mixed with vertically recirculated regional aerosols, whereas during the second period, the typical summer regional pollution episode and the advected wildfire smoke plumes dominated over the area under study. The measured optical properties were distinctively affected by these two different scenarios. During the dust outbreaks, SAE was rather low along the profiles, < 1.0 in the high-dust loaded layers, where AAE increased up to 2.0–2.5, as a consequence of the high UV absorption enhanced by the presence of coarser dust particles. During the regional pollution dominated scenario, SAE reached higher values (> 2), and g asymmetry parameter was rather low (0.5–0.6), in this case due to the prevalence of fine primary and secondary particles, mostly from regional anthropogenic emissions and the favourable conditions for secondary aerosol formation (high insolation, relative stagnation and high biogenic emissions, among others). Furthermore, the vertical variation of AAE was not large, with values close to 1.0 (pointing to a high proportion of fossil fuel combustion aerosols), with the exception of few layers with increased AAE, probably associated with the influence of wildfire-related aerosols. MSC was on average higher during the regional pollution episodes compared to the dust outbreaks due to the higher scattering efficiency of fine particles with a diameter closer to the wavelength of the sampling visible light compared to coarse particles. Overall, MSC increased with altitude ($2\,m^2\,g^{-1}$ near the surface up to $4–5\,m^2\,g^{-1}$ in the upper levels) as the presence of more efficient scatterers increases. A previous modelling study on MSC constrained with experimental measurements performed at the MSY stations suggested that the observed high MSC at higher altitudes might be due to the predominance of fine organic (mostly secondary) and inorganic (mostly sulfate in summer) aerosols. The MSC and SSA vertical profiles were rather similar during the flights with the SSA also increasing with altitude and with a vertical variability that depended on the composition of the observed layers. Typical SSA values along the profiles ranged between 0.85 (near surface) and 0.95 (higher altitudes), with a minimum of < 0.85 in polluted layers where smoke from wildfires was probably present.

The results presented here provide a unique input for climate models aiming at studying the regional radiative and climate effects of atmospheric aerosol particles in the WMB. We presented robust vertically resolved measurements of intensive aerosol particles optical properties in the WMB troposphere where the well-known particle layering driven by the regional pollution episodes accompanied by vertical recirculation takes place especially in summer. We have shown that the distribution of aerosol particles and their optical properties vary vertically along the layers formed during several days under the typical high-PM summer regional pollution regime, as well as by the strength of the advection of aerosol particles such as dust and smoke.

Data availability. The data used in this study are available from the corresponding authors upon request.

Supplement. The supplement related to this article is available online at: https://doi.org/10.5194/acp-21-431-2021-supplement.

Author contributions. AA designed the research experiment; MP, NP, ME, GT and AA performed the instrumented flights and maintained the in situ measurement stations. GM designed the inlet and helped with the instrument settings on the aircraft. ME and GT extracted the data from the instruments as well as prepared the datasets. AA, MP and XQ played a crucial role in the processes of shaping the paper structure as well as helping with the data analysis. JYD developed the data process, analysed the results, and summarized and expressed them in this article. All authors provided advice regarding the paper structure and content and contributed to the writing of the final draft of the paper.

Competing interests. The authors declare that they have no conflict of interest. Griša Močnik was, at the time of the aircraft campaign but not during the data analysis or paper writing, employed by the manufacturer of the Aethalometer AE33.

Acknowledgements. Marco Pandolfi is funded by a Ramón y Cajal Fellowship (grant no. RYC-2013-14036) awarded by the Spanish Ministry of Economy, Industry and Competitiveness. Gloria

Titos is funded by MINECO under the Juan de la Cierva postdoctoral programme (grant nos. FJCI-2014-20819 and IJCI-2016-29838). We would also like to acknowledge Yolanda Sola for providing access to the sun/sky photometer data at the MSA station and to Aerosol d.o.o. for lending the AVIO aethalometer. The authors gratefully acknowledge the NOAA Air Resources Laboratory (ARL) for the provision of the HYSPLIT transport and dispersion model (https://www.ready.noaa.gov/HYSPLIT.php, last access: 7 January 2021) used in this publication.

Financial support. This research has been supported by the Generalitat de Catalunya, Agència de Gestió d'Ajuts Universitaris i de Recerca (grant nos. AGAUR 2014 SGR33 and AGAUR 2017 SGR41); the Ministerio de Economía, Industria y Competitividad, Gobierno de España (HOUSE; grant no. CGL2016-78594-R); and the European Commission's Horizon 2020 Framework Programme (ACTRIS-2; grant no. 654109).

We acknowledge support of the publication fee by the CSIC Open Access Publication Support Initiative through its Unit of Information Resources for Research (URICI).

Review statement. This paper was edited by Michael Schulz and reviewed by two anonymous referees.

References

Alastuey, A., Minguillón, M. C., Pérez, N., Querol, X., Viana, M., and de Leeuw, F.: PM_{10} measurement methods and correction factors: 2009 status report, ETC/ACM Technical Paper 21, ETC/ACM – The European Topic Centre on Air Pollution and Climate Change Mitigation, 34 pp., available at: https://www.eionet.europa.eu/etcs/etc-atni/products/etc-atni-reports/etcacm_tp_2011_21_pm10equivalence (last access: 7 January 2021), 2011.

Alfaro, S., Lafon, S., Rajot, J., Formenti, P., Gaudichet, A., and Maille, M.: Iron oxides and light absorption by pure desert dust: An experimental study, J. Geophys. Res.-Atmos., 109, D08208, https://doi.org/10.1029/2003JD004374, 2004.

Amato, F., Querol, X., Alastuey, A., Pandolfi, M., Moreno, T., Gracia, J., and Rodriguez, P.: Evaluating urban PM_{10} pollution benefit induced by street cleaning activities, Atmos. Environ., 43, 4472–4480, 2009.

Amato, F., Alastuey, A., Karanasiou, A., Lucarelli, F., Nava, S., Calzolai, G., Severi, M., Becagli, S., Gianelle, V. L., Colombi, C., Alves, C., Custódio, D., Nunes, T., Cerqueira, M., Pio, C., Eleftheriadis, K., Diapouli, E., Reche, C., Minguillón, M. C., Manousakas, M.-I., Maggos, T., Vratolis, S., Harrison, R. M., and Querol, X.: AIRUSE-LIFE+: a harmonized PM speciation and source apportionment in five southern European cities, Atmos. Chem. Phys., 16, 3289–3309, https://doi.org/10.5194/acp-16-3289-2016, 2016.

Andrews, E., Sheridan, P. J., Fiebig, M., McComiskey, A., Ogren, J. A., Arnott, P., Covert, D., Elleman, R., Gasparini, R., Collins, D., Jonsson, H., Schmid, B., and Wang, J.: Comparison of methods for deriving aerosol asymmetry parameter, J. Geophys. Res.-Atmos., 111, D05S04, https://doi.org/10.1029/2004JD005734, 2006.

Andrews, E., Ogren, J. A., Bonasoni, P., Marinoni, A., Cuevas, E., Rodríguez, S., Sun, J. Y., Jaffe, D. A., Fischer, E. V., Baltensperger, U., Weingartner, E., Collaud Coen, M., Sharma, S., Macdonald, A. M., Leaitch, W. R., Lin, N.-H., Laj, P., Arsov, T., Kalapov, I., Jefferson, A., and Sheridan, P.: Climatology of aerosol radiative properties in the free troposphere, Atmos. Res., 102, 365–393, 2011.

Andrews, E., Sheridan, P. J., Ogren, J. A., Hageman, D., Jefferson, A., Wendell, J., Alástuey, A., Alados-Arboledas, L., Bergin, M., Ealo, M., Gannet Hallar, A., Hoffer, A., Kalapov, I., Keywood, M., Kim, J., Kim, S. W., Kolonjari, F., Labuschagne, C., Lin, N. H., Macdonald, A., Mayol-Bracero, O. L., McCubbin, I. B., Pandolfi, M., Reisen, F., Sharma, S., Sherman, J. P., Sorribas, M., and Sun, J.: Overview of the NOAA/ESRL federated aerosol network, B. Am. Meteorol. Soc., 100, 123–135, https://doi.org/10.1175/BAMS-D-17-0175.1, 2019.

Ansmann, A., Riebesell, M., Wandinger, U., Weitkamp, C., Voss, E., Lahmann, W., and Michaelis, W.: Combined Raman elastic-backscatter lidar for vertical profiling of moisture, aerosol extinction, backscatter, and lidar ratio, Appl. Phys. B-Lasers O., 55, 18–28, 1992.

Asmi, A., Collaud Coen, M., Ogren, J. A., Andrews, E., Sheridan, P., Jefferson, A., Weingartner, E., Baltensperger, U., Bukowiecki, N., Lihavainen, H., Kivekäs, N., Asmi, E., Aalto, P. P., Kulmala, M., Wiedensohler, A., Birmili, W., Hamed, A., O'Dowd, C., G Jennings, S., Weller, R., Flentje, H., Fjaeraa, A. M., Fiebig, M., Myhre, C. L., Hallar, A. G., Swietlicki, E., Kristensson, A., and Laj, P.: Aerosol decadal trends – Part 2: In-situ aerosol particle number concentrations at GAW and ACTRIS stations, Atmos. Chem. Phys., 13, 895–916, https://doi.org/10.5194/acp-13-895-2013, 2013.

Bergametti, G., Dutot, A.-L., Buat-Menard, P., Losno, R., and Remoudaki, E.: Seasonal variability of the elemental composition of atmospheric aerosol particles over the northwestern Mediterranean, Tellus B, 41, 353–361, 1989.

Bond, T., Venkataraman, C., and Masera, O.: Global atmospheric impacts of residential fuels, Energ. Sustain. Dev., 8, 20–32, 2004.

Bond, T. C., Doherty, S. J., Fahey, D., Forster, P., Berntsen, T., DeAngelo, B., Flanner, M., Ghan, S., Kärcher, B., Koch, D., Kinne, S., Kondo, Y., Quinn, P. K., Sarofim, M. C., Schultz, M. G., Schulz, M., Venkataraman, C., Zhang, H., Zhang, S., Bellouin, N., Guttikunda, S. K., Hopke, P. K., Jacobson, M. Z., Kaiser, J. W., Klimont, Z., Lohmann, U., Schwarz, J. P., Shindell, D., Storelvmo, T., Warren, S. G., and Zender, C. S.: Bounding the role of black carbon in the climate system: A scientific assessment, J. Geophys. Res.-Atmos., 118, 5380–5552, 2013.

Bucholtz, A.: Rayleigh-scattering calculations for the terrestrial atmosphere, Appl. Optics, 34, 2765–2773, 1995.

Cavalli, F., Viana, M., Yttri, K. E., Genberg, J., and Putaud, J.-P.: Toward a standardised thermal-optical protocol for measuring atmospheric organic and elemental carbon: the EUSAAR protocol, Atmos. Meas. Tech., 3, 79–89, https://doi.org/10.5194/amt-3-79-2010, 2010.

Cavalli, F., Alastuey, A., Areskoug, H., Ceburnis, D., Čech, J., Genberg, J., Harrison, R., Jaffrezo, J., Kiss, G., Laj, P., Mihalopoulos, N., Perez, N., Quincey, P., Schwarz, J., Sellegri, K., Spindler, G., Swietlicki, E., Theodosi, C., Yttri, K. E., Aas, W., and Putaud, J.

P.: A European aerosol phenomenology-4: Harmonized concentrations of carbonaceous aerosol at 10 regional background sites across Europe, Atmos. Environ., 144, 133–145, 2016.

Chen, Y. and Bond, T. C.: Light absorption by organic carbon from wood combustion, Atmos. Chem. Phys., 10, 1773–1787, https://doi.org/10.5194/acp-10-1773-2010, 2010.

Clarke, A. D., Howell, S., Quinn, P. K., Bates, T. S., Ogren, J. A., Andrews, E., Jefferson, A., Massling, A., Mayol-Bracero, O., Maring, H., Savoie, D., and Cass, G.: INDOEX aerosol: A comparison and summary of chemical, microphysical, and optical properties observed from land, ship, and aircraft, J. Geophys. Res.-Atmos., 107, INX2 32-1–INX2 32-32, https://doi.org/10.1029/2001JD000572, 2002.

Collaud Coen, M., Weingartner, E., Schaub, D., Hueglin, C., Corrigan, C., Henning, S., Schwikowski, M., and Baltensperger, U.: Saharan dust events at the Jungfraujoch: detection by wavelength dependence of the single scattering albedo and first climatology analysis, Atmos. Chem. Phys., 4, 2465–2480, https://doi.org/10.5194/acp-4-2465-2004, 2004.

Collaud Coen, M., Andrews, E., Asmi, A., Baltensperger, U., Bukowiecki, N., Day, D., Fiebig, M., Fjaeraa, A. M., Flentje, H., Hyvärinen, A., Jefferson, A., Jennings, S. G., Kouvarakis, G., Lihavainen, H., Lund Myhre, C., Malm, W. C., Mihapopoulos, N., Molenar, J. V., O'Dowd, C., Ogren, J. A., Schichtel, B. A., Sheridan, P., Virkkula, A., Weingartner, E., Weller, R., and Laj, P.: Aerosol decadal trends – Part 1: In-situ optical measurements at GAW and IMPROVE stations, Atmos. Chem. Phys., 13, 869–894, https://doi.org/10.5194/acp-13-869-2013, 2013.

Collaud Coen, M., Andrews, E., Alastuey, A., Arsov, T. P., Backman, J., Brem, B. T., Bukowiecki, N., Couret, C., Eleftheriadis, K., Flentje, H., Fiebig, M., Gysel-Beer, M., Hand, J. L., Hoffer, A., Hooda, R., Hueglin, C., Joubert, W., Keywood, M., Kim, J. E., Kim, S.-W., Labuschagne, C., Lin, N.-H., Lin, Y., Lund Myhre, C., Luoma, K., Lyamani, H., Marinoni, A., Mayol-Bracero, O. L., Mihalopoulos, N., Pandolfi, M., Prats, N., Prenni, A. J., Putaud, J.-P., Ries, L., Reisen, F., Sellegri, K., Sharma, S., Sheridan, P., Sherman, J. P., Sun, J., Titos, G., Torres, E., Tuch, T., Weller, R., Wiedensohler, A., Zieger, P., and Laj, P.: Multidecadal trend analysis of in situ aerosol radiative properties around the world, Atmos. Chem. Phys., 20, 8867–8908, https://doi.org/10.5194/acp-20-8867-2020, 2020.

Dayan, U., Ricaud, P., Zbinden, R., and Dulac, F.: Atmospheric pollution over the eastern Mediterranean during summer – a review, Atmos. Chem. Phys., 17, 13233–13263, https://doi.org/10.5194/acp-17-13233-2017, 2017.

Denjean, C., Cassola, F., Mazzino, A., Triquet, S., Chevaillier, S., Grand, N., Bourrianne, T., Momboisse, G., Sellegri, K., Schwarzenbock, A., Freney, E., Mallet, M., and Formenti, P.: Size distribution and optical properties of mineral dust aerosols transported in the western Mediterranean, Atmos. Chem. Phys., 16, 1081–1104, https://doi.org/10.5194/acp-16-1081-2016, 2016.

Draxler, R. R. and Hess, G.: An overview of the HYSPLIT_4 modelling system for trajectories, Aust. Meteorol. Mag., 47, 295–308, 1998.

Drinovec, L., Močnik, G., Zotter, P., Prévôt, A. S. H., Ruckstuhl, C., Coz, E., Rupakheti, M., Sciare, J., Müller, T., Wiedensohler, A., and Hansen, A. D. A.: The "dual-spot" Aethalometer: an improved measurement of aerosol black carbon with real-time loading compensation, Atmos. Meas. Tech., 8, 1965–1979, https://doi.org/10.5194/amt-8-1965-2015, 2015.

Drinovec, L., Sciare, J., Stavroulas, I., Bezantakos, S., Pikridas, M., Unga, F., Savvides, C., Višić, B., Remškar, M., and Močnik, G.: A new optical-based technique for real-time measurements of mineral dust concentration in PM_{10} using a virtual impactor, Atmos. Meas. Tech., 13, 3799–3813, https://doi.org/10.5194/amt-13-3799-2020, 2020.

Ealo, M., Alastuey, A., Ripoll, A., Pérez, N., Minguillón, M. C., Querol, X., and Pandolfi, M.: Detection of Saharan dust and biomass burning events using near-real-time intensive aerosol optical properties in the north-western Mediterranean, Atmos. Chem. Phys., 16, 12567–12586, https://doi.org/10.5194/acp-16-12567-2016, 2016.

Ealo, M., Alastuey, A., Pérez, N., Ripoll, A., Querol, X., and Pandolfi, M.: Impact of aerosol particle sources on optical properties in urban, regional and remote areas in the north-western Mediterranean, Atmos. Chem. Phys., 18, 1149–1169, https://doi.org/10.5194/acp-18-1149-2018, 2018.

Escudero, M., Castillo, S., Querol, X., Avila, A., Alarcón, M., Viana, M. M., Alastuey, A., Cuevas, E., and Rodríguez, S.: Wet and dry African dust episodes over eastern Spain, J. Geophys. Res.-Atmos., 110, D18S08, https://doi.org/10.1029/2004JD004731, 2005.

Escudero, M., Querol, X., Pey, J., Alastuey, A., Pérez, N., Ferreira, F., Alonso, S., Rodríguez, S., and Cuevas, E.: A methodology for the quantification of the net African dust load in air quality monitoring networks, Atmos. Environ., 41, 5516–5524, 2007.

Esteve, A. R., Ogren, J. A., Sheridan, P. J., Andrews, E., Holben, B. N., and Utrillas, M. P.: Sources of discrepancy between aerosol optical depth obtained from AERONET and in-situ aircraft profiles, Atmos. Chem. Phys., 12, 2987–3003, https://doi.org/10.5194/acp-12-2987-2012, 2012.

Esteve, A. R., Highwood, E. J., and Ryder, C. L.: A case study of the radiative effect of aerosols over Europe: EUCAARI-LONGREX, Atmos. Chem. Phys., 16, 7639–7651, https://doi.org/10.5194/acp-16-7639-2016, 2016.

Faustini, A., Alessandrini, E. R., Pey, J., Perez, N., Samoli, E., Querol, X., Cadum, E., Perrino, C., Ostro, B., Ranzi, A., Sunyer, J., Stafoggia, M., Forastiere, F., and MED-PARTICLES study group: Short-term effects of particulate matter on mortality during forest fires in Southern Europe: results of the MED-PARTICLES Project, Occup. Environ. Med., 72, 323–329, 2015.

Ferrero, L., Castelli, M., Ferrini, B. S., Moscatelli, M., Perrone, M. G., Sangiorgi, G., D'Angelo, L., Rovelli, G., Moroni, B., Scardazza, F., Močnik, G., Bolzacchini, E., Petitta, M., and Cappelletti, D.: Impact of black carbon aerosol over Italian basin valleys: high-resolution measurements along vertical profiles, radiative forcing and heating rate, Atmos. Chem. Phys., 14, 9641–9664, https://doi.org/10.5194/acp-14-9641-2014, 2014.

Ferrero, L., Cappelletti, D., Busetto, M., Mazzola, M., Lupi, A., Lanconelli, C., Becagli, S., Traversi, R., Caiazzo, L., Giardi, F., Moroni, B., Crocchianti, S., Fierz, M., Močnik, G., Sangiorgi, G., Perrone, M. G., Maturilli, M., Vitale, V., Udisti, R., and Bolzacchini, E.: Vertical profiles of aerosol and black carbon in the Arctic: a seasonal phenomenology along 2 years (2011–2012) of field campaigns, Atmos. Chem. Phys., 16, 12601–12629, https://doi.org/10.5194/acp-16-12601-2016, 2016.

Ferrero, L., Gregorič, A., Močnik, G., Rigler, M., Cogliati, S., Barnaba, F., Di Liberto, L., Gobbi, G. P., Losi, N., and Bolzacchini, E.: The impact of cloudiness and cloud type on the atmospheric heating rate of black and brown carbon, Atmos. Chem. Phys. Discuss., https://doi.org/10.5194/acp-2020-264, in review, 2020.

Fialho, P., Hansen, A. D., and Honrath, R. E.: Absorption coefficients by aerosols in remote areas: A new approach to decouple dust and black carbon absorption coefficients using seven-wavelength Aethalometer data, J. Aerosol Sci., 36, 267–282, https://doi.org/10.1016/j.jaerosci.2004.09.004, 2005.

Font, A., Morguí, J. A., and Rodó, X.: Atmospheric CO_2 in situ measurements: Two examples of Crown Design flights in NE Spain, J. Geophys. Res.-Atmos., 113, D12308, https://doi.org/10.1029/2007JD009111, 2008.

Gangoiti, G., Millán, M. M., Salvador, R., and Mantilla, E.: Long-range transport and re-circulation of pollutants in the western Mediterranean during the project Regional Cycles of Air Pollution in the West-Central Mediterranean Area, Atmos. Environ., 35, 6267–6276, 2001.

Gangoiti, G., Alonso, L., Navazo, M., García, J. A., and Millán, M. M.: North African soil dust and European pollution transport to America during the warm season: Hidden links shown by a passive tracer simulation, J. Geophys. Res.-Atmos., 111, D10109, https://doi.org/10.1029/2005JD005941, 2006.

GAW: Coupled Chemistry-Meteorology/Climate Modelling (CCMM): status and relevance for numerical weather prediction, atmospheric pollution and climate research, GAW Report No. 226, WMO 1172, available at: https://library.wmo.int/index.php?lvl=author_see&id=12259#.X_iHdC3FRQI (last access: 7 January 2021), 2016.

Groß, S., Esselborn, M., Abicht, F., Wirth, M., Fix, A., and Minikin, A.: Airborne high spectral resolution lidar observation of pollution aerosol during EUCAARI-LONGREX, Atmos. Chem. Phys., 13, 2435–2444, https://doi.org/10.5194/acp-13-2435-2013, 2013.

Hamburger, T., McMeeking, G., Minikin, A., Birmili, W., Dall'Osto, M., O'Dowd, C., Flentje, H., Henzing, B., Junninen, H., Kristensson, A., de Leeuw, G., Stohl, A., Burkhart, J. F., Coe, H., Krejci, R., and Petzold, A.: Overview of the synoptic and pollution situation over Europe during the EUCAARI-LONGREX field campaign, Atmos. Chem. Phys., 11, 1065–1082, https://doi.org/10.5194/acp-11-1065-2011, 2011.

Harrison, R. M. and Pio, C. A.: Size-differentiated composition of inorganic atmospheric aerosols of both marine and polluted continental origin, Atmos. Environ., 17, 1733–1738, 1983.

Haywood, J., Ramaswamy, V., and Soden, B. J.: Tropospheric aerosol climate forcing in clear-sky satellite observations over the oceans, Science, 283, 1299–1303, 1999.

Hess, M., Koepke, P., and Schult, I.: Optical properties of aerosols and clouds: The software package OPAC, B. Am. Meteorol. Soc., 79, 831–844, 1998.

Highwood, E. J., Northway, M. J., McMeeking, G. R., Morgan, W. T., Liu, D., Osborne, S., Bower, K., Coe, H., Ryder, C., and Williams, P.: Aerosol scattering and absorption during the EUCAARI-LONGREX flights of the Facility for Airborne Atmospheric Measurements (FAAM) BAe-146: can measurements and models agree?, Atmos. Chem. Phys., 12, 7251–7267, https://doi.org/10.5194/acp-12-7251-2012, 2012.

Kalivitis, N., Gerasopoulos, E., Vrekoussis, M., Kouvarakis, G., Kubilay, N., Hatzianastassiou, N., Vardavas, I., and Mihalopoulos, N.: Dust transport over the eastern Mediterranean derived from Total Ozone Mapping Spectrometer, Aerosol Robotic Network, and surface measurements, J. Geophys. Res.-Atmos., 112, D03202, https://doi.org/10.1029/2006JD007510, 2007.

Kallos, G., Astitha, M., Katsafados, P., and Spyrou, C.: Long-range transport of anthropogenically and naturally produced particulate matter in the Mediterranean and North Atlantic: Current state of knowledge, J. Appl. Meteorol. Clim., 46, 1230–1251, 2007.

Kirchstetter, T. W., Novakov, T., and Hobbs, P. V.: Evidence that the spectral dependence of light absorption by aerosols is affected by organic carbon, J. Geophys. Res.-Atmos., 109, D21208, https://doi.org/10.1029/2004JD004999, 2004.

Koçak, M., Mihalopoulos, N., and Kubilay, N.: Contributions of natural sources to high PM_{10} and $PM_{2.5}$ events in the eastern Mediterranean, Atmos. Environ., 41, 3806–3818, 2007.

Laj, P., Bigi, A., Rose, C., Andrews, E., Lund Myhre, C., Collaud Coen, M., Lin, Y., Wiedensohler, A., Schulz, M., Ogren, J. A., Fiebig, M., Gliß, J., Mortier, A., Pandolfi, M., Petäja, T., Kim, S.-W., Aas, W., Putaud, J.-P., Mayol-Bracero, O., Keywood, M., Labrador, L., Aalto, P., Ahlberg, E., Alados Arboledas, L., Alastuey, A., Andrade, M., Artíñano, B., Ausmeel, S., Arsov, T., Asmi, E., Backman, J., Baltensperger, U., Bastian, S., Bath, O., Beukes, J. P., Brem, B. T., Bukowiecki, N., Conil, S., Couret, C., Day, D., Dayantolis, W., Degorska, A., Eleftheriadis, K., Fetfatzis, P., Favez, O., Flentje, H., Gini, M. I., Gregorič, A., Gysel-Beer, M., Hallar, A. G., Hand, J., Hoffer, A., Hueglin, C., Hooda, R. K., Hyvärinen, A., Kalapov, I., Kalivitis, N., Kasper-Giebl, A., Kim, J. E., Kouvarakis, G., Kranjc, I., Krejci, R., Kulmala, M., Labuschagne, C., Lee, H.-J., Lihavainen, H., Lin, N.-H., Löschau, G., Luoma, K., Marinoni, A., Martins Dos Santos, S., Meinhardt, F., Merkel, M., Metzger, J.-M., Mihalopoulos, N., Nguyen, N. A., Ondracek, J., Pérez, N., Perrone, M. R., Petit, J.-E., Picard, D., Pichon, J.-M., Pont, V., Prats, N., Prenni, A., Reisen, F., Romano, S., Sellegri, K., Sharma, S., Schauer, G., Sheridan, P., Sherman, J. P., Schütze, M., Schwerin, A., Sohmer, R., Sorribas, M., Steinbacher, M., Sun, J., Titos, G., Toczko, B., Tuch, T., Tulet, P., Tunved, P., Vakkari, V., Velarde, F., Velasquez, P., Villani, P., Vratolis, S., Wang, S.-H., Weinhold, K., Weller, R., Yela, M., Yus-Diez, J., Zdimal, V., Zieger, P., and Zikova, N.: A global analysis of climate-relevant aerosol properties retrieved from the network of Global Atmosphere Watch (GAW) near-surface observatories, Atmos. Meas. Tech., 13, 4353–4392, https://doi.org/10.5194/amt-13-4353-2020, 2020.

Lelieveld, J., Berresheim, H., Borrmann, S., Crutzen, P., Dentener, F., Fischer, H., Feichter, J., Flatau, P., Heland, J., Holzinger, R., Korrmann, R., Lawrence, M. G., Levin, Z., Markowicz, K. M., Mihalopoulos, N., Minikin, A., Ramanathan, V., de Reus, M., Roelofs, G. J., Scheeren, H. A., Sciare, J., Schlager, H., Schultz, M., Siegmund, P., Steil, B., Stephanou, E. G., Stier, P., Traub, M., Warneke, C., Williams, J., and Ziereis, H.: Global air pollution crossroads over the Mediterranean, Science, 298, 794–799, 2002.

Lyamani, H., Olmo, F., Alcántara, A., and Alados-Arboledas, L.: Atmospheric aerosols during the 2003 heat wave in southeastern Spain II: Microphysical columnar properties and radiative forcing, Atmos. Environ., 40, 6465–6476, 2006.

Mallet, M., Dulac, F., Formenti, P., Nabat, P., Sciare, J., Roberts, G., Pelon, J., Ancellet, G., Tanré, D., Parol, F., Denjean, C.,

Brogniez, G., di Sarra, A., Alados-Arboledas, L., Arndt, J., Auriol, F., Blarel, L., Bourrianne, T., Chazette, P., Chevaillier, S., Claeys, M., D'Anna, B., Derimian, Y., Desboeufs, K., Di Iorio, T., Doussin, J.-F., Durand, P., Féron, A., Freney, E., Gaimoz, C., Goloub, P., Gómez-Amo, J. L., Granados-Muñoz, M. J., Grand, N., Hamonou, E., Jankowiak, I., Jeannot, M., Léon, J.-F., Maillé, M., Mailler, S., Meloni, D., Menut, L., Momboisse, G., Nicolas, J., Podvin, T., Pont, V., Rea, G., Renard, J.-B., Roblou, L., Schepanski, K., Schwarzenboeck, A., Sellegri, K., Sicard, M., Solmon, F., Somot, S., Torres, B., Totems, J., Triquet, S., Verdier, N., Verwaerde, C., Waquet, F., Wenger, J., and Zapf, P.: Overview of the Chemistry-Aerosol Mediterranean Experiment/Aerosol Direct Radiative Forcing on the Mediterranean Climate (ChArMEx/ADRIMED) summer 2013 campaign, Atmos. Chem. Phys., 16, 455–504, https://doi.org/10.5194/acp-16-455-2016, 2016.

Malm, W. C. and Hand, J. L.: An examination of the physical and optical properties of aerosols collected in the IMPROVE program, Atmos. Environ., 41, 3407–3427, 2007.

Martucci, G., Milroy, C., and O'Dowd, C. D.: Detection of cloud-base height using Jenoptik CHM15K and Vaisala CL31 ceilometers, J. Atmos. Ocean. Tech., 27, 305–318, 2010.

Millán, M., Salvador, R., Mantilla, E., and Kallos, G.: Photooxidant dynamics in the Mediterranean basin in summer: Results from European research projects, J. Geophys. Res.-Atmos., 102, 8811–8823, 1997.

Millán, M. M., Sanz, M. J., Salvador, R., and Mantilla, E.: Atmospheric dynamics and ozone cycles related to nitrogen deposition in the western Mediterranean, Environ. Pollut., 118, 167–186, 2002.

Mona, L., Amodeo, A., Pandolfi, M., and Pappalardo, G.: Saharan dust intrusions in the Mediterranean area: Three years of Raman lidar measurements, J. Geophys. Res.-Atmos., 111, D16203, https://doi.org/10.1029/2005JD006569, 2006.

Müller, T., Henzing, J. S., de Leeuw, G., Wiedensohler, A., Alastuey, A., Angelov, H., Bizjak, M., Collaud Coen, M., Engström, J. E., Gruening, C., Hillamo, R., Hoffer, A., Imre, K., Ivanow, P., Jennings, G., Sun, J. Y., Kalivitis, N., Karlsson, H., Komppula, M., Laj, P., Li, S.-M., Lunder, C., Marinoni, A., Martins dos Santos, S., Moerman, M., Nowak, A., Ogren, J. A., Petzold, A., Pichon, J. M., Rodriquez, S., Sharma, S., Sheridan, P. J., Teinilä, K., Tuch, T., Viana, M., Virkkula, A., Weingartner, E., Wilhelm, R., and Wang, Y. Q.: Characterization and intercomparison of aerosol absorption photometers: result of two intercomparison workshops, Atmos. Meas. Tech., 4, 245–268, https://doi.org/10.5194/amt-4-245-2011, 2011a.

Müller, T., Laborde, M., Kassell, G., and Wiedensohler, A.: Design and performance of a three-wavelength LED-based total scatter and backscatter integrating nephelometer, Atmos. Meas. Tech., 4, 1291–1303, https://doi.org/10.5194/amt-4-1291-2011, 2011b.

Myhre, G., Shindell, D., Breéon, F.-M., Collins, W., Fuglestvedt, J., Huang, J., Koch, D., Lamarque, J.-F., Lee, D., Mendoza, B., Nakajima, T., Robock, A., Stephens, G., Takemura, T., and Zhang, H.: Anthropogenic and Natural Radiative Forcing, book section 8, Cambridge University Press, Cambridge, UK and New York, NY, USA, 659–740, https://doi.org/10.1017/CBO9781107415324.018, 2013.

Obiso, V., Pandolfi, M., Ealo, M., and Jorba, O.: Impact of aerosol microphysical properties on mass scattering cross sections, J. Aerosol Sci., 112, 68–82, 2017.

Ogren, J., Andrews, E., McComiskey, A., Sheridan, P., Jefferson, A., and Fiebig, M.: New insights into aerosol asymmetry parameter, in: Proceedings of the 16th ARM Science Team Meeting, Albuquerque, NM, USA, Citeseer, 27–31, available at: http://citeseerx.ist.psu.edu/viewdoc/download?doi=10.1.1.176.6111&rep=rep1&type=pdf (last access: 7 January 2021), 2006.

Pandolfi, M., Cusack, M., Alastuey, A., and Querol, X.: Variability of aerosol optical properties in the Western Mediterranean Basin, Atmos. Chem. Phys., 11, 8189–8203, https://doi.org/10.5194/acp-11-8189-2011, 2011.

Pandolfi, M., Martucci, G., Querol, X., Alastuey, A., Wilsenack, F., Frey, S., O'Dowd, C. D., and Dall'Osto, M.: Continuous atmospheric boundary layer observations in the coastal urban area of Barcelona during SAPUSS, Atmos. Chem. Phys., 13, 4983–4996, https://doi.org/10.5194/acp-13-4983-2013, 2013.

Pandolfi, M., Querol, X., Alastuey, A., Jimenez, J. L., Jorba, O., Day, D., Ortega, A., Cubison, M. J., Comerón, A., Sicard, M., Mohr, C., Prévôt, A. S. H., Minguillón, M. C., Pey, J., Baldasano, J. M., Burkhart, J. F., Seco, R., Peñuelas, J., van Drooge, B. L., Artiñano, B., DiMarco, C., Nemitz, E., Schallhart, S., Metzger, A., Hansel, A., Lorente, J., Ng, S., Jayne, J., and Szidat, S.: Effects of sources and meteorology on particulate matter in the Western Mediterranean Basin: An overview of the DAURE campaign, J. Geophys. Res.-Atmos., 119, 4978–5010, 2014a.

Pandolfi, M., Ripoll, A., Querol, X., and Alastuey, A.: Climatology of aerosol optical properties and black carbon mass absorption cross section at a remote high-altitude site in the western Mediterranean Basin, Atmos. Chem. Phys., 14, 6443–6460, https://doi.org/10.5194/acp-14-6443-2014, 2014b.

Pandolfi, M., Tobias, A., Alastuey, A., Sunyer, J., Schwartz, J., Lorente, J., Pey, J., and Querol, X.: Effect of atmospheric mixing layer depth variations on urban air quality and daily mortality during Saharan dust outbreaks, Sci. Total Environ., 494, 283–289, 2014c.

Pandolfi, M., Alastuey, A., Pérez, N., Reche, C., Castro, I., Shatalov, V., and Querol, X.: Trends analysis of PM source contributions and chemical tracers in NE Spain during 2004–2014: a multi-exponential approach, Atmos. Chem. Phys., 16, 11787–11805, https://doi.org/10.5194/acp-16-11787-2016, 2016.

Pandolfi, M., Alados-Arboledas, L., Alastuey, A., Andrade, M., Angelov, C., Artiñano, B., Backman, J., Baltensperger, U., Bonasoni, P., Bukowiecki, N., Collaud Coen, M., Conil, S., Coz, E., Crenn, V., Dudoitis, V., Ealo, M., Eleftheriadis, K., Favez, O., Fetfatzis, P., Fiebig, M., Flentje, H., Ginot, P., Gysel, M., Henzing, B., Hoffer, A., Holubova Smejkalova, A., Kalapov, I., Kalivitis, N., Kouvarakis, G., Kristensson, A., Kulmala, M., Lihavainen, H., Lunder, C., Luoma, K., Lyamani, H., Marinoni, A., Mihalopoulos, N., Moerman, M., Nicolas, J., O'Dowd, C., Petäjä, T., Petit, J.-E., Pichon, J. M., Prokopciuk, N., Putaud, J.-P., Rodríguez, S., Sciare, J., Sellegri, K., Swietlicki, E., Titos, G., Tuch, T., Tunved, P., Ulevicius, V., Vaishya, A., Vana, M., Virkkula, A., Vratolis, S., Weingartner, E., Wiedensohler, A., and Laj, P.: A European aerosol phenomenology – 6: scattering properties of atmospheric aerosol particles from 28 ACTRIS sites, At-

mos. Chem. Phys., 18, 7877–7911, https://doi.org/10.5194/acp-18-7877-2018, 2018.

Pérez, C., Sicard, M., Jorba, O., Comerón, A., and Baldasano, J. M.: Summertime re-circulations of air pollutants over the north-eastern Iberian coast observed from systematic EARLINET lidar measurements in Barcelona, Atmos. Environ., 38, 3983–4000, 2004.

Pérez, N., Pey, J., Castillo, S., Viana, M., Alastuey, A., and Querol, X.: Interpretation of the variability of levels of regional background aerosols in the Western Mediterranean, Sci. Total Environ., 407, 527–540, 2008.

Petzold, A. and Schönlinner, M.: Multi-angle absorption photometry – a new method for the measurement of aerosol light absorption and atmospheric black carbon, J. Aerosol Sci., 35, 421–441, 2004.

Petzold, A., Ogren, J. A., Fiebig, M., Laj, P., Li, S.-M., Baltensperger, U., Holzer-Popp, T., Kinne, S., Pappalardo, G., Sugimoto, N., Wehrli, C., Wiedensohler, A., and Zhang, X.-Y.: Recommendations for reporting "black carbon" measurements, Atmos. Chem. Phys., 13, 8365–8379, https://doi.org/10.5194/acp-13-8365-2013, 2013.

Pey, J., Pérez, N., Castillo, S., Viana, M., Moreno, T., Pandolfi, M., López-Sebastián, J., Alastuey, A., and Querol, X.: Geochemistry of regional background aerosols in the Western Mediterranean, Atmos. Res., 94, 422–435, 2009.

Pey, J., Querol, X., Alastuey, A., Forastiere, F., and Stafoggia, M.: African dust outbreaks over the Mediterranean Basin during 2001–2011: PM_{10} concentrations, phenomenology and trends, and its relation with synoptic and mesoscale meteorology, Atmos. Chem. Phys., 13, 1395–1410, https://doi.org/10.5194/acp-13-1395-2013, 2013.

Pikridas, M., Bezantakos, S., Močnik, G., Keleshis, C., Brechtel, F., Stavroulas, I., Demetriades, G., Antoniou, P., Vouterakos, P., Argyrides, M., Liakakou, E., Drinovec, L., Marinou, E., Amiridis, V., Vrekoussis, M., Mihalopoulos, N., and Sciare, J.: On-flight intercomparison of three miniature aerosol absorption sensors using unmanned aerial systems (UASs), Atmos. Meas. Tech., 12, 6425–6447, https://doi.org/10.5194/amt-12-6425-2019, 2019.

Putaud, J.-P., Raes, F., Van Dingenen, R., Brüggemann, E., Facchini, M.-C., Decesari, S., Fuzzi, S., Gehrig, R., Hüglin, C., Laj, P., Lorbeer, G., Maenhaut, W., Mihalopoulos, N., Müller, K., Querol, X., Rodriguez, S., Schneider, J., Spindler, G., ten Brink, H., Tørseth, K., and Wiedensohler, A.,: A European aerosol phenomenology – 2: chemical characteristics of particulate matter at kerbside, urban, rural and background sites in Europe, Atmos. Environ., 38, 2579–2595, 2004.

Putaud, J.-P., Van Dingenen, R., Alastuey, A., Bauer, H., Birmili, W., Cyrys, J., Flentje, H., Fuzzi, S., Gehrig, R., Hansson, H.-C., Harrison, R. M., Herrmann, H., Hitzenberger, R., Hüglin, C., Jones, A. M., Kasper-Giebl, A., Kiss, G., Kousa, A., Kuhlbusch, T. A. J., Löschau, G., Maenhaut, W., Molnar, A., Moreno, T., Pekkanen, J., Perrino, C., Pitz, M., Puxbaum, H., Querol, X., Rodriguez, S., Salma, I., Schwarz, J., Smolik, J., Schneider, J., Spindler, G., ten Brink, H., Tursic, J., Viana, M., Wiedensohler, A., and Raes, F.: A European aerosol phenomenology – 3: Physical and chemical characteristics of particulate matter from 60 rural, urban, and kerbside sites across Europe, Atmos. Environ., 44, 1308–1320, 2010.

Querol, X., Alastuey, A., Puicercus, J. A., Mantilla, E., Miro, J. V., Lopez-Soler, A., Plana, F., and Artiñano, B.: Seasonal evolution of suspended particles around a large coal-fired power station: particulate levels and sources, Atmos. Environ., 32, 1963–1978, 1998.

Querol, X., Alastuey, A., Rodriguez, S., Plana, F., Ruiz, C. R., Cots, N., Massagué, G., and Puig, O.: PM_{10} and $PM_{2.5}$ source apportionment in the Barcelona Metropolitan area, Catalonia, Spain, Atmos. Environ., 35, 6407–6419, 2001.

Querol, X., Alastuey, A., Viana, M. M., Rodriguez, S., Artíñano, B., Salvador, P., Garcia do Santos, S., Fernandez Patier, R., Ruiz, C. R., de la Rosa, J., Sanchez de la Campa, A., Menendez, M., and Gil, J. I.: Speciation and origin of PM_{10} and $PM_{2.5}$ in Spain, J. Aerosol Sci., 35, 1151–1172, 2004.

Querol, X., Alastuey, A., Pey, J., Cusack, M., Pérez, N., Mihalopoulos, N., Theodosi, C., Gerasopoulos, E., Kubilay, N., and Koçak, M.: Variability in regional background aerosols within the Mediterranean, Atmos. Chem. Phys., 9, 4575–4591, https://doi.org/10.5194/acp-9-4575-2009, 2009a.

Querol, X., Pey, J., Pandolfi, M., Alastuey, A., Cusack, M., Pérez, N., Moreno, T., Viana, M., Mihalopoulos, N., Kallos, G., and Kleanthous, S.: African dust contributions to mean ambient PM_{10} mass-levels across the Mediterranean Basin, Atmos. Environ., 43, 4266–4277, 2009b.

Querol, X., Alastuey, A., Reche, C., Orio, A., Pallares, M., Reina, F., Dieguez, J., Mantilla, E., Escudero, M., Alonso, L., Gangoiti, G., and Millán, M.: On the origin of the highest ozone episodes in Spain, Sci. Total Environ., 572, 379–389, 2016.

Querol, X., Gangoiti, G., Mantilla, E., Alastuey, A., Minguillón, M. C., Amato, F., Reche, C., Viana, M., Moreno, T., Karanasiou, A., Rivas, I., Pérez, N., Ripoll, A., Brines, M., Ealo, M., Pandolfi, M., Lee, H.-K., Eun, H.-R., Park, Y.-H., Escudero, M., Beddows, D., Harrison, R. M., Bertrand, A., Marchand, N., Lyasota, A., Codina, B., Olid, M., Udina, M., Jiménez-Esteve, B., Soler, M. R., Alonso, L., Millán, M., and Ahn, K.-H.: Phenomenology of high-ozone episodes in NE Spain, Atmos. Chem. Phys., 17, 2817–2838, https://doi.org/10.5194/acp-17-2817-2017, 2017.

Querol, X., Perez, N., Reche, C., Ealo, M., Ripoll, A., Tur, J., Pandolfi, M., Pey, J., Salvador, P., Moreno, T., and Alastuey, A.: African dust and air quality over Spain: Is it only dust that matters?, Sci. Total Environ., 686, 737–752, 2019.

Reche, C., Querol, X., Alastuey, A., Viana, M., Pey, J., Moreno, T., Rodríguez, S., González, Y., Fernández-Camacho, R., de la Rosa, J., Dall'Osto, M., Prévôt, A. S. H., Hueglin, C., Harrison, R. M., and Quincey, P.: New considerations for PM, Black Carbon and particle number concentration for air quality monitoring across different European cities, Atmos. Chem. Phys., 11, 6207–6227, https://doi.org/10.5194/acp-11-6207-2011, 2011.

Ripoll, A., Pey, J., Minguillón, M. C., Pérez, N., Pandolfi, M., Querol, X., and Alastuey, A.: Three years of aerosol mass, black carbon and particle number concentrations at Montsec (southern Pyrenees, 1570 m a.s.l.), Atmos. Chem. Phys., 14, 4279–4295, https://doi.org/10.5194/acp-14-4279-2014, 2014.

Rodríguez, S., Querol, X., Alastuey, A., Kallos, G., and Kakaliagou, O.: Saharan dust contributions to PM_{10} and TSP levels in Southern and Eastern Spain, Atmos. Environ., 35, 2433–2447, 2001.

Rodríguez, S., Querol, X., Alastuey, A., and Plana, F.: Sources and processes affecting levels and composition of atmospheric

aerosol in the western Mediterranean, J. Geophys. Res.-Atmos., 107, 4777, https://doi.org/10.1029/2001JD001488, 2002.

Samset, B. H., Myhre, G., Schulz, M., Balkanski, Y., Bauer, S., Berntsen, T. K., Bian, H., Bellouin, N., Diehl, T., Easter, R. C., Ghan, S. J., Iversen, T., Kinne, S., Kirkevåg, A., Lamarque, J.-F., Lin, G., Liu, X., Penner, J. E., Seland, Ø., Skeie, R. B., Stier, P., Takemura, T., Tsigaridis, K., and Zhang, K.: Black carbon vertical profiles strongly affect its radiative forcing uncertainty, Atmos. Chem. Phys., 13, 2423–2434, https://doi.org/10.5194/acp-13-2423-2013, 2013.

Sandradewi, J., Prévôt, A. S., Szidat, S., Perron, N., Alfarra, M. R., Lanz, V. A., Weingartner, E., and Baltensperger, U. R.: Using aerosol light abosrption measurements for the quantitative determination of wood burning and traffic emission contribution to particulate matter, Environ. Sci. Technol., 42, 3316–3323, https://doi.org/10.1021/es702253m, 2008.

Sanroma, E., Palle, E., and Sanchez-Lorenzo, A.: Long-term changes in insolation and temperatures at different altitudes, Environ. Res. Lett., 5, 024006, https://doi.org/10.1088/1748-9326/5/2/024006, 2010.

Schauer, G., Kasper-Giebl, A., and Močnik, G.: Increased PM concentrations during a combined wildfire and saharan dust event observed at high-altitude sonnblick observatory, Austria, Aerosol Air Qual. Res., 16, 542–554, https://doi.org/10.4209/aaqr.2015.05.0337, 2016.

Schuster, G. L., Dubovik, O., and Holben, B. N.: Angstrom exponent and bimodal aerosol size distributions, J. Geophys. Res.-Atmos., 111, D07207, https://doi.org/10.1029/2005JD006328, 2006.

Seinfeld, J. H. and Pandis, S. N.: Atmospheric Chemistry and Physics: From air pollution to climate change, John Wiley & Sons, New York, 1998.

Sheridan, P. J., Andrews, E., Ogren, J. A., Tackett, J. L., and Winker, D. M.: Vertical profiles of aerosol optical properties over central Illinois and comparison with surface and satellite measurements, Atmos. Chem. Phys., 12, 11695–11721, https://doi.org/10.5194/acp-12-11695-2012, 2012.

Singh, A., Mahata, K. S., Rupakheti, M., Junkermann, W., Panday, A. K., and Lawrence, M. G.: An overview of airborne measurement in Nepal – Part 1: Vertical profile of aerosol size, number, spectral absorption, and meteorology, Atmos. Chem. Phys., 19, 245–258, https://doi.org/10.5194/acp-19-245-2019, 2019.

Titos, G., Del Águila, A., Cazorla, A., Lyamani, H., Casquero-Vera, J., Colombi, C., Cuccia, E., Gianelle, V., Močnik, G., Alastuey, A., Olmo, F. J., and Alados-Arboledas, L.: Spatial and temporal variability of carbonaceous aerosols: assessing the impact of biomass burning in the urban environment, Sci. Total Environ., 578, 613–625, 2017.

von der Weiden, S.-L., Drewnick, F., and Borrmann, S.: Particle Loss Calculator – a new software tool for the assessment of the performance of aerosol inlet systems, Atmos. Meas. Tech., 2, 479–494, https://doi.org/10.5194/amt-2-479-2009, 2009.

Wiegner, M., Madonna, F., Binietoglou, I., Forkel, R., Gasteiger, J., Geiß, A., Pappalardo, G., Schäfer, K., and Thomas, W.: What is the benefit of ceilometers for aerosol remote sensing? An answer from EARLINET, Atmos. Meas. Tech., 7, 1979–1997, https://doi.org/10.5194/amt-7-1979-2014, 2014.

Zanatta, M., Gysel, M., Bukowiecki, N., Müller, T., Weingartner, E., Areskoug, H., Fiebig, M., Yttri, K. E., Mihalopoulos, N., Kouvarakis, G., Beddows, D., Harrison, R. M., Cavalli, F., Putaud, J. P., Spindler, G., Wiedensohler, A., Alastuey, A., Pandolfi, M., Sellegri, K., Swietlicki, E., Jaffrezo, J. L., Baltensperger, U., and Laj, P.: A European aerosol phenomenology-5: Climatology of black carbon optical properties at 9 regional background sites across Europe, Atmos. Environ., 145, 346–364, 2016.

Zarzycki, C. M. and Bond, T. C.: How much can the vertical distribution of black carbon affect its global direct radiative forcing?, Geophys. Res. Lett., 37, L20807, https://doi.org/10.1029/2010GL044555, 2010.

Zotter, P., Herich, H., Gysel, M., El-Haddad, I., Zhang, Y., Močnik, G., Hüglin, C., Baltensperger, U., Szidat, S., and Prévôt, A. S. H.: Evaluation of the absorption Ångström exponents for traffic and wood burning in the Aethalometer-based source apportionment using radiocarbon measurements of ambient aerosol, Atmos. Chem. Phys., 17, 4229–4249, https://doi.org/10.5194/acp-17-4229-2017, 2017.

Supplement of Atmos. Chem. Phys., 21, 431–455, 2021
https://doi.org/10.5194/acp-21-431-2021-supplement
© Author(s) 2021. This work is distributed under
the Creative Commons Attribution 4.0 License.

Atmospheric Chemistry and Physics Open Access

Supplement of

Aircraft vertical profiles during summertime regional and Saharan dust scenarios over the north-western Mediterranean basin: aerosol optical and physical properties

Jesús Yus-Díez et al.

Correspondence to: Jesús Yus-Díez (jesus.yus@idaea.csic.es) and Marco Pandolfi (marco.pandolfi@idaea.csic.es)

The copyright of individual parts of the supplement might differ from the CC BY 4.0 License.

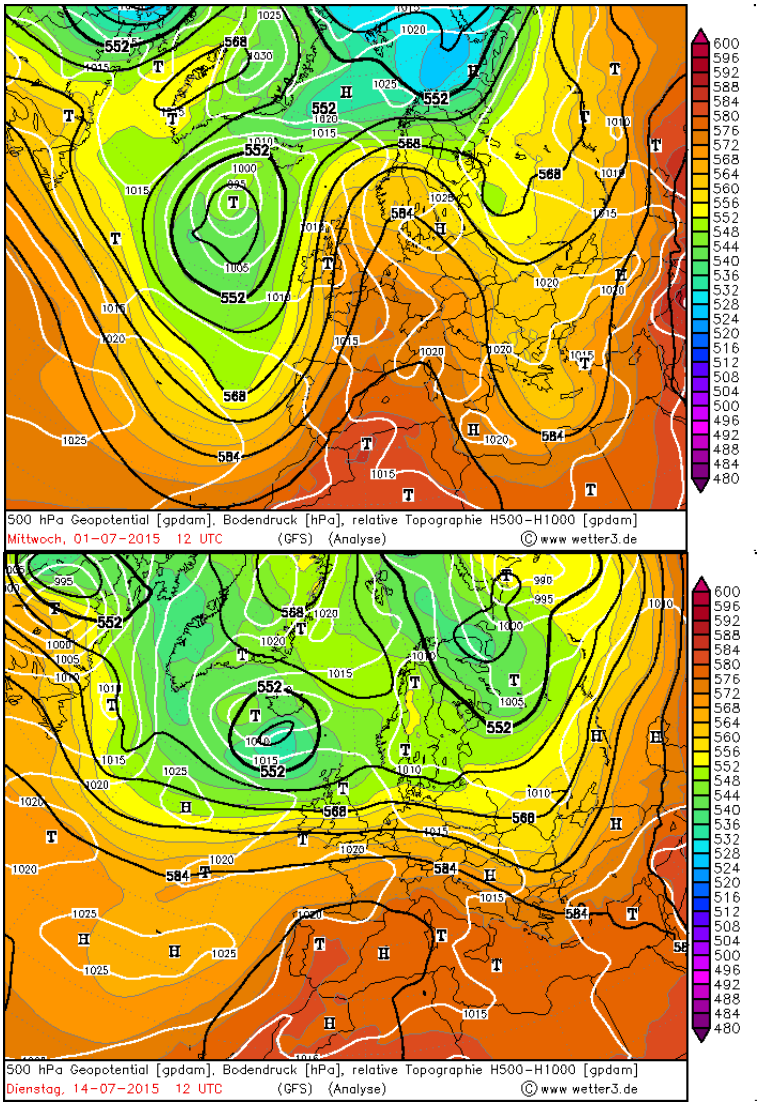

Figure S1: Synoptic mete orology with the 500 hPa Geopotential and surface pressure at 12:00 UTC for the 7th and 16th of July of 2015 as modelled by the reanalysis model ERA-INTERIM, © www.wetter3.de.

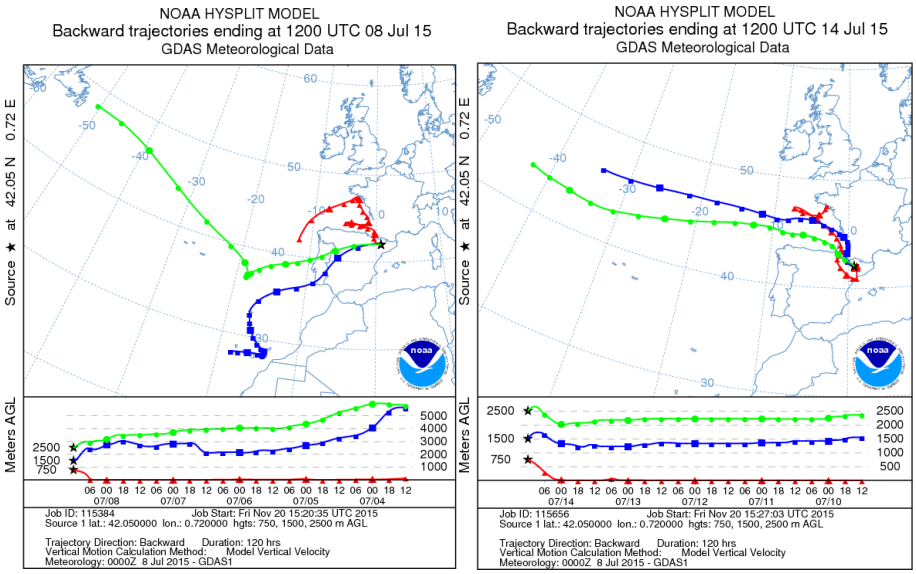

Figure S2: HYSPLIT backtrajectories for the 8th and 14th of July of 2015 at 12:00 UTC ending at MSA station.

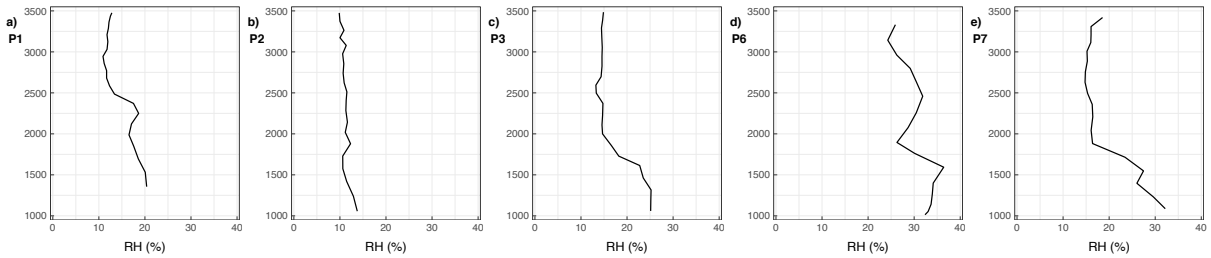

Figure S3: Vertical profiles of relative humidity (RH (%)) for a) P1, b) P2, c) P3, d) P6, and e) P7 as measured by the Kestrel unit placed in the aircraft.

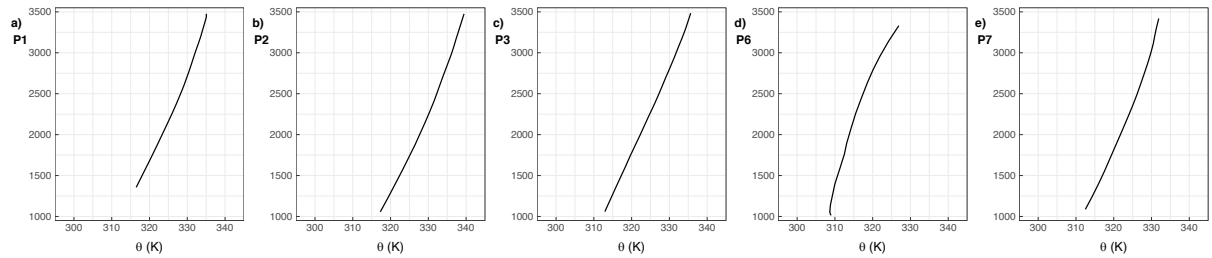

Figure S4: Vertical profiles of potential temperature (θ (K)) for a) P1, b) P2, c) P3, d) P6, and e) P7 as measured by the Kestrel unit placed in the aircraft.

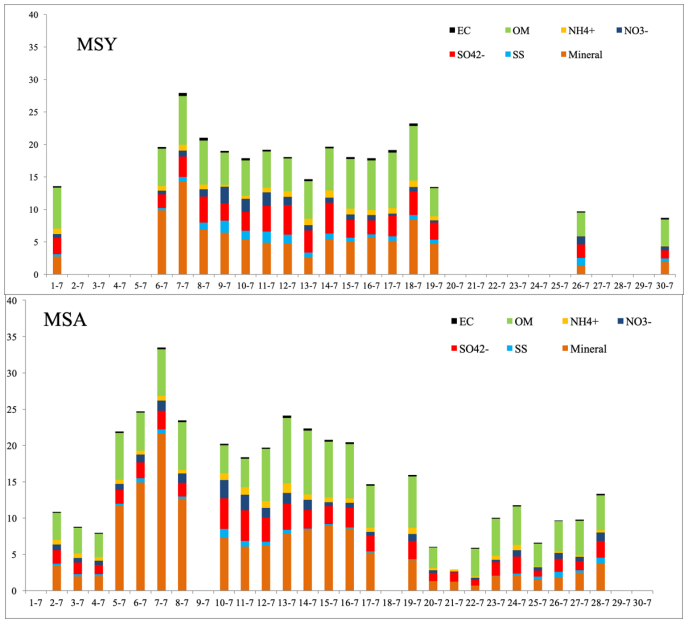

Figure S5: Daily off-line filter base chemistry analysis during the instrumented flights period of July 2015 for MSA (upper panel) and MSY (lower panel).

Table S1: Comparison between aircraft borne measurements for P1 versus the in-situ measurements of MSA station as a reference at the same time that the flight was at a height of 1500 m a.s.l. approximately.

	$PM_{10}(\mu g\ m^{-3})$	$PM_{2.5}(\mu g\ m^{-3})$	$PM_{1}(\mu g\ m^{-3})$	$PM_{1/10}$	$PM_{1/2.5}$	$\sigma_{sp\ 525\ nm}\ (Mm^{-1})$	$\sigma_{ap\ 590\ nm}(Mm^{-1})$	SAE	AAE	G	SSA
P1 – FLIGHT	**20.3**	**18.38**	**13.38**	**0.66**	**0.73**	**37.85**	**2.59**	**0.93**	**1.76**	**0.59**	**0.87**
P1 – MSA IN-SITU	**38.4**	**20.8**	**14.2**	**0.37**	**0.68**	**41.44**	**3.06**	**0.90**	**2.12**	**0.62**	**0.86**
DIFF (%)	**47.1**	**11.6**	**5.8**	**-78.2**	**-6.6**	**8. 7**	**15.36**	**-4.5**	**16.8**	**4.55**	**-0.22**

7

AEROSOL MIXING EFFECTS ON BC ABSORPTION ENHANCEMENT

Objectives

Analyze the effects that the mixing of BC particles with organic and inorganic aerosol particles have on the enhancement of the absorption efficiency of pure BC particles. The absorption enhancement of the BC particles is key to better constrain in climate models the radiative forcing of BC particles. Overall, climate models assume this enhancement to be constant, however, several studies show dependencies with the amount and the type of mixing material that the BC particles are mixed with. With this aim, an in-deep analysis of the relationships of the absorption enhancement is performed using measurements from two measurement sites with different aerosol composition, namely an urban background station (BCN) and a regional background station (MSY).

Methodology

- Merging measurements from multiple instruments that provide the aerosol absorption of BC particles, the mass concentration of pure BC, the ageing state of the aerosol particles and the main composition of species.
- Compare the site-specific mass absorption cross-sections (MAC) reference values with theoretical reference values from the literature to better represent the site-specific characteristics.
- Assess the differential contribution of the internal and external mixing to the overall absorption enhancement through a sensibility study.
- Separating the analysis of the absorption enhancement between winter and summer to better evaluate the impact that the seasonal variations of the different species have on the absorption enhancement.

- Study the contribution of the different aerosol species to the total absorption enhancement by applying a multi-lineal regression analysis.
- Perform a Theil-Sen trend analysis over decade-long measurements to analyze the evolution over time of the absorption enhancement.

Results

- Large increase of the absorption enhancement for very high concentrations of mixing material, especially at MSY regional background station. The higher amount of material available for mixing with the BC particles at MSY allowed the absorption enhancement to reach values up to 3, in comparison with the maximum of around 2 at BCN.
- More pronounced of the absorption enhancement with the ageing state of the particles and the secondary to primary organic aerosol ratio.
- Higher increase of the absorption enhancement at the shorter wavelengths during winter at BCN as a consequence of the higher relative contribution of oxidized organic aerosols particles and BrC particles that produce a higher absorption at the short-UV wavelengths in comparison with the near-IR.
- The highest contribution to the absorption enhancement at BCN was made by the traffic-related hydrocarbons OA (HOA) and the cooking-related OA (COA), with a larger contribution of biomass burning OA particles (BBOA) at the short-UV during winter, as well as from highly oxidized particles. During summer, the overall absorption enhancement values at BCN were lower, with the highest contribution from SIAs, and from OAs from COA and HOA.
- Statistically significant positive trend at MSY station during the summer season as a consequence of the positive trend for this season of the OC to EC ration and more specifically of the SOA relative contribution to the total OA concentration.

Conclusions

- Clear relationship of the absorption enhancement with the amount of material available for mixing, especially at the regional background station where the relative contribution of OAs are usually higher.
- Need for source apportionment of the different aerosol compounds and an analysis on their influence on the absorption enhancement.
- Potential positive trend of the absorption enhancement at areas with high OA concentrations and positive trends of SOA to total OA ratios.

Publication

- Yus-Díez, J., Via, M., Alastuey, A., Karanasiou, A., Minguillón, M. C., Perez, N., Querol, X., Reche, C., Ivančič, M., Rigler, M., and Pandolfi, M.: "Absorption enhancement of black carbon particles in a Mediterranean city and countryside: effect of particulate matter chemistry, ageing and trend analysis". In: *Atmospheric Chemistry and Physics*, 22, 8439–8456, https://doi.org/10.5194/acp-22-8439-2022, 2022.

Atmos. Chem. Phys., 22, 8439–8456, 2022
https://doi.org/10.5194/acp-22-8439-2022
© Author(s) 2022. This work is distributed under
the Creative Commons Attribution 4.0 License.

Atmospheric Chemistry and Physics
Open Access

Absorption enhancement of black carbon particles in a Mediterranean city and countryside: effect of particulate matter chemistry, ageing and trend analysis

Jesús Yus-Díez[1,2], Marta Via[1,2], Andrés Alastuey[1], Angeliki Karanasiou[1], María Cruz Minguillón[1], Noemí Perez[1], Xavier Querol[1], Cristina Reche[1], Matic Ivančič[3], Martin Rigler[3], and Marco Pandolfi[1]

[1]Institute of Environmental Assessment and Water Research (IDAEA-CSIC), Barcelona, 08034, Spain
[2]Grup de Meteorologia, Departament de Física Aplicada, Universitat de Barcelona, C/Martí i Franquès, 1, 08028, Barcelona, Spain
[3]Aerosol d.o.o., Ljubljana, Slovenia

Correspondence: Jesús Yus-Díez (jesus.yus@idaea.csic.es) and Marco Pandolfi (marco.pandolfi@idaea.csic.es)

Received: 21 February 2022 – Discussion started: 7 March 2022
Revised: 8 June 2022 – Accepted: 9 June 2022 – Published: 4 July 2022

Abstract. Black carbon (BC) is recognized as the most important warming agent among atmospheric aerosol particles. The absorption efficiency of pure BC is rather well-known, nevertheless the mixing of BC with other aerosol particles can enhance the BC light absorption efficiency, thus directly affecting Earth's radiative balance. The effects on climate of the BC absorption enhancement due to the mixing with these aerosols are not yet well constrained because these effects depend on the availability of material for mixing with BC, thus creating regional variations.

Here we present the mass absorption cross-section (MAC) and absorption enhancement of BC particles (E_{abs}), at different wavelengths (from 370 to 880 nm for online measurements and at 637 nm for offline measurements) measured at two sites in the western Mediterranean, namely Barcelona (BCN; urban background) and Montseny (MSY; regional background). The E_{abs} values ranged between 1.24 and 1.51 at the urban station, depending on the season and wavelength used as well as on the pure BC MAC used as a reference. The largest contribution to E_{abs} was due to the internal mixing of BC particles with other aerosol compounds, on average between a 91 % and a 100 % at 370 and 880 nm, respectively. Additionally, 14.5 % and 4.6 % of the total enhancement at the short ultraviolet (UV) wavelength (370 nm) was due to externally mixed brown carbon (BrC) particles during the cold and the warm period, respectively. On average, at the MSY station, a higher E_{abs} value was observed (1.83 at 637 nm) compared to BCN (1.37 at 637 nm), which was associated with the higher fraction of organic aerosols (OA) available for BC coating at the regional station, as denoted by the higher organic carbon to elemental carbon (OC : EC) ratio observed at MSY compared to BCN. At both BCN and MSY, E_{abs} showed an exponential increase with the amount of non-refractory (NR) material available for coating ($R_{NR\text{-}PM}$). The E_{abs} at 637 nm at the MSY regional station reached values up to 3 during episodes with high $R_{NR\text{-}PM}$, whereas in BCN, E_{abs} kept values lower than 2 due to the lower relative amount of coating materials measured at BCN compared to MSY. The main sources of OA influencing E_{abs} throughout the year were hydrocarbon OA (HOA) and cooking-related OA (COA), i.e. primary OA (POA) from traffic and cooking emissions, respectively, at both 370 and 880 nm. At the short UV wavelength (370 nm), a strong contribution to E_{abs} from biomass burning OA (BBOA) and less oxidized oxygenated OA (LO-OOA) sources was observed in the colder period. Moreover, we found an increase of E_{abs} with the ageing state of the particles, especially during the colder period. This increase of E_{abs} with particle ageing was associated with a larger relative amount of secondary OA (SOA) compared to

Published by Copernicus Publications on behalf of the European Geosciences Union.

POA. The availability of a long dataset at both stations from offline measurements enabled a decade-long trend analysis of E_{abs} at 637 nm, that showed statistically significant (s.s.) positive trends of E_{abs} during the warmer months at the MSY station. This s.s. positive trend in MSY mirrored the observed increase of the OC : EC ratio over time. Moreover, in BCN during the COVID-19 lockdown period in spring 2020 we observed a sharp increase of E_{abs} due to the observed sharp increase of the OC : EC ratio. Our results show similar values of E_{abs} to those found in the literature for similar background stations.

1 Introduction

The light-absorbing properties of atmospheric carbonaceous aerosols, i.e. black carbon (BC) and organic aerosols (OA), have been linked with a strong positive radiative forcing effect on Earth's energy budget (Liu et al., 2015; Zhang et al., 2018; Cappa et al., 2019). Recent scientific assessments (e.g. Myhre et al., 2013) on the global warming effect of anthropogenic agents have estimated that BC is the major aerosol contributing to the absorption of solar radiation from the ultraviolet (UV) to the infrared (IR) part of the spectrum, with a direct radiative forcing (DRF) of $0.71 \pm 0.17\,\mathrm{W\,m^{-2}}$ (Bond et al., 2013). However, the DRF of carbonaceous aerosols still presents large uncertainties given the limitations to constrain the spatial distribution, mixing state, and absorbing properties of these atmospheric aerosols in climate models (e.g. Myhre et al., 2013).

The BC particles can be mixed with less-absorbing and non-absorbing material through either external mixing, a heterogeneous mixture of internally homogeneous particles, or internal mixing, either a homogeneous mixture of internally homogeneous particles or a heterogeneous mixture of particle composition and population (Bond and Bergstrom, 2006). The mixing state of BC with these aerosol particles determines its mass absorption cross-section (MAC), which is a spectral quantity relating to the volumetric absorptive efficiency of a particle per unit mass, and is usually reported in square metres per gram [$\mathrm{m^2\,g^{-1}}$]. The MAC of pure BC (or elemental carbon (EC), depending on the measuring technique employed, Lack et al., 2014) is rather well constrained. However, BC aggregates are rarely emitted as pure BC as they are usually co-emitted and internally mixed with other source-dependent aerosols that can enhance the MAC of BC (e.g. Bond and Bergstrom, 2006; Knox et al., 2009; Lack and Cappa, 2010). Moreover, the absorption of radiation by less-absorbing particles externally mixed with BC, as absorbing OA, also referred to as brown carbon (BrC) (Andreae and Gelencsér, 2006), also contributes to increase the measured absorption (Lack and Cappa, 2010). Different mixing states of BC particles were the cause for the regional differences found for the MAC in different background sites in Europe (Zanatta et al., 2016). The enhancement that this mixing produces in the resulting observed MAC with respect to the theoretical pure BC MAC is defined as the absorption enhancement (E_{abs}). Understanding the relationship of E_{abs} with the BC mixing state and the different aerosol species/sources is key to better parameterize the BC impact on radiative forcing (Jacobson, 2001; Bond et al., 2013). Whilst several studies assume E_{abs} as only influenced by the internal mixing (e.g. Lack and Cappa, 2010), we used an approach similar to Liu et al. (2015) where the spectral enhancement of light absorption by BC is considered as due to both the external and internal mixing of BC particles.

Externally mixed BrC particles also contribute to the enhancement of total absorption, although the absorption efficiency of BrC significantly decreases from UV moving into the visible range (e.g. Moise et al., 2015; Laskin et al., 2015; Samset et al., 2018; Saleh et al., 2018; Saleh, 2020). BrC absorption coefficient values found in the literature display a large spatial variability (e.g. Liu et al., 2015; Saleh et al., 2018; Saleh, 2020; Zhang et al., 2020) due to the specific OA sources and composition found for each site. These differences in OA composition result in different BrC MACs, since different OAs from different sources present variations in absorption efficiencies (e.g. Saleh et al., 2018; Saleh, 2020; Zhang et al., 2020). Moreover, the MAC of different OA compounds shows different behaviour along the UV–visible (UV–VIS) range, hence the variation is found in the influence of BrC on the absorption for this spectral range (Saleh et al., 2018; Saleh, 2020). The internal mixing contribution to E_{abs} has been thoroughly studied both through core–shell models (Lack and Cappa, 2010) and by laboratory and field experiments (e.g. Cappa et al., 2019). The main differences in E_{abs} values reported in literature were associated with different diameters of both BC cores and shells in the case of model simulations, and to BC ageing in the case of laboratory and field experiments. In fact, BC particle ageing can be seen as a surrogate of the particle shell diameter since more ageing implies more coating layers (Lack and Cappa, 2010). Therefore, analysing the influence of both internal and external BC mixing states on E_{abs} is fundamental for a correct characterization of the aerosol particle light absorption, and to better constrain modelling results (Liu et al., 2015).

Several laboratory studies, field measurements, and modelling results can be found in the literature about E_{abs} values (e.g. Lack and Cappa, 2010; Cappa et al., 2012; Liu et al., 2015; Zhang et al., 2018). However, the results fail to present a ubiquitous E_{abs} value, with values ranging between almost no absorption enhancement ($E_{abs} \sim 1$, Cappa et al., 2012), to around 50 % absorption increase as assumed by some climate

models ($E_{abs} \sim 1.5$, Liu et al., 2015, and references therein) up to values of more than 100 %, especially at the shorter wavelengths, where the BrC, externally mixed, can largely contribute to the E_{abs} (e.g. Chen et al., 2017). As a consequence of the broad spectrum of values, several authors have suggested to treat E_{abs} as a region-specific parameter in climate models to account for the different sources or processes that may contribute to increase both the amount of BrC and the degree of BC internal mixing (Lack et al., 2012; Liu et al., 2015; Zhang et al., 2018).

To characterize the specific chemical species or sources that affect, and to which extent, the E_{abs}, simultaneous measurements of aerosol particle light absorption at multi-wavelengths, EC concentrations, and particulate matter (PM) chemical composition analysis are needed. Although specific instrumentation (e.g. the single particle photometer, SP2; and the soot particle aerosol mass spectrometer, SP-AMS) can be used for direct measurements of the chemical composition and internal mixing state of carbonaceous particles. Their global implementation is sparse, thus impinging a global characterization of E_{abs} values. Using more simple yet robust monitors to obtain the source-dependent chemical composition influencing the absorption enhancement is possible (e.g. Zhang et al., 2018). The applied methodology consists of obtaining each measurement, e.g. chemical speciation, EC concentrations, light absorption, and aerosol ageing through independent instruments, and merging the results to the lowest timestamp possible.

Here we present an analysis of the BC light absorption enhancement measured at an urban station (Barcelona; BCN) and a regional station (Montseny; MSY) in the western Mediterranean basin. The chemical analyses were performed using offline 24 h filter measurements at both stations (between 2010 and 2020). In BCN, online chemical composition measurements with a higher time resolution were also available (2018). In BCN, EC measurements were performed with a semi-continuous Sunset analyser (Karanasiou et al., 2020), and submicron aerosol particle chemical composition measurements were performed with an aerosol chemical speciation monitor (ACSM; Via et al., 2021). Absorption measurements were performed with a multi-wavelength Aethalometer (AE33) and multi-angle absorption photometer (MAAP) instruments. In Sect. 3.1, we present an overall analysis of both MAC and E_{abs}, showing the E_{abs} seasonal variability and the contribution of both external and internal BC mixing states to E_{abs}. In Sect. 3.2, we performed an analysis of the relationship between the absorption enhancement and the amount of non-refractory (NR) material available for coating with BC particles. Section 3.3 reports the results of a multilinear regression analysis performed to identify the main sources/species responsible for the increase of E_{abs} at both sites. Section 3.4 presents the influence of particle ageing in the E_{abs} values. Finally, we performed a trend analysis of E_{abs} using the decade-long offline filter measurements available at both stations (Sect. 3.5). To the best of our knowledge, although some studies have shown the variability of MAC in the Mediterranean basin (e.g. Pandolfi et al., 2014b; Zanatta et al., 2016), this is the first study of E_{abs} in this region and one of the few studies of its kind performed in Europe (Liu et al., 2015; Zhang et al., 2018).

2 Methodology

2.1 Aerosol sampling sites and main characteristics

Measurements were performed at the BCN (urban background, Palau Reial, Barcelona, 41°23′24.01″ N, 02°6′58.06″ E, 80 m a.s.l.), and MSY (regional background, El Brull, 41°46′46″ N, 02°21′29″ E, 720 m a.s.l.) monitoring supersites (NE Spain). These measurement stations are characterized by aerosols with different physical and chemical properties. The BCN urban station is located within the BCN metropolitan area of nearly 4.5 million inhabitants at a distance of about 5 km from the coast, and at a 200 m distance from one of the most concurred roads of the city (> 60 k vehicles per day; City council of Barcelona, 2021). The MSY regional station is located in a hilly and densely forested area within the Natural Park and Biosphere Reserve of Montseny, 50 km to the N–NE of the BCN site and 25 km from the Mediterranean coast. A detailed characterization of these measurement stations can be found in previous works for BCN (e.g. Querol et al., 2001; Rodrıguez et al., 2001; Reche et al., 2011; Brines et al., 2014, 2015; Ealo et al., 2018); and for MSY (Pérez et al., 2008; Pey et al., 2009; Pandolfi et al., 2011, 2014a, 2016). These supersites are part of the Catalonian Air Quality Monitoring Network and are part of the ACTRIS and GAW networks. Aerosol optical properties at BCN and MSY are measured following standard protocols (WMO, 2016).

Overall, the area of study is characterized by high concentrations of both primary and secondary aerosols from diverse emission sources (Rodríguez et al., 2002; Pandolfi et al., 2014a; Dayan et al., 2017; Rivas et al., 2020; Brean et al., 2020). Recently, Veld et al. (2021) presented the main aerosol sources in BCN and MSY by applying receptor modelling techniques to offline 24 h speciated $PM_{2.5}$ samples collected during the period 2009–2018. The main sources identified from OA were the secondary OA (SOA), and from the secondary inorganic aerosols (SIAs) were sulfates, nitrates and ammonia. Moreover, online ACSM measurements at the BCN station (Via et al., 2021) have also shown that the OAs are mainly dominated by secondary aerosols, also referred to as oxygenated OA (OOA), as well as by hydrocarbon and cooking-related OAs (HOA and COA). Both Via et al. (2021) and Veld et al. (2021) have shown an increasing trend in the SOA as well as a reduction in a relative contribution of the primary OA (POA) to PM at the BCN and MSY stations, mainly related to more restrictive pollutant emission policies and a larger amount of higher oxidative potential scenarios. The higher oxidative potential of the

OA is characterized by an increase in the relative proportion of the more-oxidized OOA (MO-OOA), in comparison with the less-oxidized OOA (LO-OOA) (Via et al., 2021). Finally, a common characteristic of the BCN and MSY measurement sites is that both are located in the proximity of North African deserts, thus both sites are heavily impacted by Saharan dust outbreaks (Querol et al., 2009; Yus-Díez et al., 2021a). For this reason, in order to avoid the interference due to dust absorption, we filtered out scenarios in which the sites were under the influence of dust outbreaks (following the European Commission guidelines; European Commission, 2011).

2.2 Absorption coefficients and EC measurements

At both measurement sites, aerosol particle absorption coefficients (b_{abs}) at 637 nm were obtained with MAAP instruments(Model 5012, Thermo Inc., USA, Petzold and Schönlinner, 2004). Moreover, in BCN, absorption measurements were also performed with a multi-wavelength Aethalometer (model AE33, Magee Scientific, Aerosol d.o.o., Drinovec et al., 2015) at seven different wavelengths (370, 470, 520, 590, 660, 880, and 950 nm). The MAAP absorption coefficients at 637 nm were derived by the internal MAAP software using a radiative transfer model from the measurements of transmission of light through the filter tape and backscattering of light at two different angles, and corrections were made following Müller et al. (2011). The MAAP measurements were obtained with a 1 min time resolution at a flow rate of 5 L min^{-1} and with a PM_{10} inlet cut-off. The AE33 b_{abs} coefficients in BCN were derived with the same time resolution and flow rate as that of the MAAP, and with a $PM_{2.5}$ inlet cut-off. The Aethalometer filter-loading effect was corrected online by the dual-spot manufacturer correction (Drinovec et al., 2015), and the multiple scattering correction parameter, C, was set to 2.44, as obtained for the BCN station by Yus-Díez et al. (2021b). Absorption measurement errors of 12 % and 23 % were set for MAAP and AE33, respectively (Petzold and Schönlinner, 2004; Rigler et al., 2020). For AE33, the larger uncertainty is introduced by the multiple scattering parameter, C ($\delta C = \pm 0.57$ at BCN, Yus-Díez et al., 2021b), which depends on the physical properties of the particles collected on the filter tape. In Yus-Díez et al. (2021b), the C obtained with the same instruments (i.e. MAAP and AE33) and inlet cut-offs as in the present work was found to have an average value of 2.44, and it did not present a marked dependence with the single scattering albedo (SSA) of the particles collected on the filter tape. In fact, Yus-Díez et al. (2021b) showed that the C values can increase considerably when SSA is high (> 0.95). However, these high SSAs are rarely measured in the city of BCN. Moreover, it was reported that the C is wavelength independent in BCN (cf. Fig. 1 in Yus-Díez et al., 2021b). Therefore, we used the average C value of 2.44 for deriving the absorption measurements.

The PM_{10} 24 h offline filter samples were collected at both BCN and MSY on 150 mm quartz micro-fibre filters (Pallflex 2500 QAT-UP) using high-volume samplers (MCV CAV-A and DIGITEL DH80 at 30 m^3 h^{-1}). The 24 h average concentrations of major and trace elements, and soluble ions (determined following the procedure by Querol et al., 2001), as well as those of OC and EC (by a thermal–optical carbon analyser, Sunset, following the EUSAAR2 protocol, Cavalli et al., 2010), were obtained from these offline filter samples and were estimated to have a measurement error of 10 %.

Semi-continuous EC measurements were obtained in BCN by means of a semi-continuous OC : EC aerosol analyser (Sunset Laboratory Inc.) with a $PM_{2.5}$ inlet cut-off at a flow rate of 8.0 L min^{-1}, a measuring interval of 3 h using the EUSAAR2 protocol, with a measurement error of 10 % (Karanasiou et al., 2020). The device was equipped with a C parallel-plate diffusion denuder to remove volatile organic compounds (VOCs) that can be adsorbed on quartz fibre filters and cause positive artefacts in the OC measurements (Viana et al., 2006). By comparing the EC measurements from the online and offline OC : EC measurements (Fig. S1 in the Supplement), we show that there is a good agreement between both techniques, and that on average, offline EC concentrations in the PM_{10} fraction were 26 % higher compared to online EC concentrations in the $PM_{2.5}$ fraction during the 2018 measurement period.

2.3 Submicron NR-PM chemical composition measurements and OA source apportionment

A quadrupole aerosol chemical speciation monitor (Q-ACSM, Aerodyne Research Inc.) was deployed in BCN for chemical speciation of submicrometric particles at a flow rate of 3 L min^{-1}. The incoming particles go through an aerodynamical lens, transmitting particles of aerodynamic diameters from 75 to 650 nm. Then, these particles are vaporized, ionized by hard-electron impact and fragmentated, and the resulting fragments are analysed by a quadrupole mass spectrometer. The instrument can provide the concentrations of NR PM_1 species (OA, sulfate, nitrate, ammonia and chloride) with 30 min resolution and a 12–120 Th OA spectra matrix, using a fragmentation table (Allan et al., 2004). The software used for data acquisition and treatment was provided by Aerodyne Research Inc. (versions 1.6.0.0 and 1.6.1.1, respectively) and implemented in the Igor Pro (Wavemetrics, Inc.) environment).

The retrieved OA matrices retrieved were used as input for analysis of the positive matrix factorization analysis (PMF; Paatero and Tapper, 1994), applied using a multilinear engine (ME-2; Paatero, 1999) to differentiate the different OA sources. A detailed description of the OA sources detected in BCN and used in this work can be found in Via et al. (2021). Briefly, the OA sources in BCN were: COA, HOA, biomass burning OA (BBOA), LO-OOA, and MO-OOA.

2.4 Determination of the absorption enhancement (E_{abs})

Here, similar to Zhang et al. (2018), we derived the absorption enhancement (E_{abs}) as the ratio between the measured ambient MAC calculated at the different wavelengths available from AE33 and MAAP, and the reference MAC value of pure BC.

The observed ambient MAC defines the contribution to the measured absorption coefficients from BC particles internally and externally, mixed with organic and inorganic species that can contribute positively to the measured absorption (Bond et al., 2013). The ambient MAC measurements were obtained as the ratio of the light absorption coefficients (b_{abs}) at a given wavelength, λ, and the EC concentrations obtained with the Sunset analyser, either online or offline,

$$\mathrm{MAC}^{\lambda} = \frac{\mathrm{b}^{\lambda}_{\mathrm{abs}}}{[\mathrm{EC}]}. \quad (1)$$

The E_{abs} due to both internal and external mixing of the BC particles can be quantified by normalizing the measured ambient MAC^{λ} with a reference value for pure BC, $\mathrm{MAC}^{\lambda}_{\mathrm{ref}}$. As already stated, we have applied the same methodology as in Zhang et al. (2018) and Liu et al. (2015) to determine E_{abs}, by calculating the ambient MAC through Eq. (1) applied to the 7 AE33 wavelengths. Thus, since BrC absorbs more efficiently at the shortest wavelengths (370–470 nm mostly), but not at 880 nm, the observed E_{abs} at the shortest wavelengths includes the lensing-driven enhancement and the enhancement induced by semi-volatile BrC (e.g. Liu et al., 2015), while the observed E_{abs} at 880 nm represents the lensing-driven enhancement only.

$$E^{\lambda}_{\mathrm{abs}} = \frac{\mathrm{MAC}^{\lambda}}{\mathrm{MAC}^{\lambda}_{\mathrm{ref}}}. \quad (2)$$

The reference MAC value ($\mathrm{MAC}^{\lambda}_{\mathrm{ref}}$) can be obtained either from the literature (Bond and Bergstrom, 2006), or from experimental data. There are two experimental approaches for obtaining $\mathrm{MAC}^{\lambda}_{\mathrm{ref}}$: (1) by using denuded measurements that evaporate the semi-volatile organic and inorganic species, thus allowing for a measurement of the pure BC absorption (e.g. Liu et al., 2015), and (2) by using the intercept of the relationship between the ambient MAC^{λ} and the OC : EC ratio as $\mathrm{MAC}^{\lambda}_{\mathrm{ref}}$. In this latter case, $\mathrm{MAC}^{\lambda}_{\mathrm{ref}}$ is the MAC value obtained when the OC : EC ratio is equal to 0 (Zhang et al., 2018). Here we have preferentially used the second method (intercept) to determine $\mathrm{MAC}^{\lambda}_{\mathrm{ref}}$ (Figs. S2–S4). For this purpose, we used a Deming regression fit, taking into account the propagation of errors from the absorption and OC : EC measurement errors. Additionally, we used $\mathrm{MAC}^{\lambda}_{\mathrm{ref}}$ from the literature to calculate E_{abs}, i.e. 7.5 ± 1.2 ($\mathrm{m^2\,g^{-1}}$) at 550 nm (Bond and Bergstrom, 2006), which was extrapolated to each AE33 wavelength assuming an absorption Ångström exponent (AAE) of 1.

Online MAC^{λ} and $E_{\mathrm{abs}^{\lambda}}$ values at BCN were obtained during 2018 using AE33 $b^{\lambda}_{\mathrm{abs}}$ coefficients averaged to the semi-continuous timestamp of the Sunset OC : EC measurements (3 h) when the Q-ACSM measurements were also available. Offline MAC values at both BCN and MSY were obtained by using the 24 h average b_{abs} coefficients from MAAP at 637 nm, and 24 h OC : EC concentrations from PM_{10} filters (2010–2020). Figure S6 shows the obtained $\mathrm{MAC}^{\lambda}_{\mathrm{ref}}$ for both BCN and MSY stations for all the wavelengths available from both online (BCN) and offline (BCN and MSY) measurements. Data in Fig. S6 were grouped into two periods: a cold period from December to May, and a warm period from June to October. As shown later, measurements were grouped into these two distinct periods due to the source apportionment results from Q-ACSM measurements in BCN, since the BBOA-like compounds were only detected during winter and spring (Via et al., 2021). Offline $\mathrm{MAC}^{\lambda}_{\mathrm{ref}}$ at both stations showed a good agreement with the theoretical reference value obtained in Bond and Bergstrom (2006), whereas the online measurements obtained with AE33 were higher throughout the whole spectrum. Similar values, higher than the theoretical $\mathrm{MAC}^{\lambda}_{\mathrm{ref}}$, have also been reported in other studies, such as in Zhang et al. (2018).

Furthermore, we have assumed that BrC particles do not absorb at 880 nm (Kirchstetter et al., 2004) and that the measured absorption at this wavelength was only driven by the internally mixed BC particles (i.e. the lensing effect). Moreover, although some studies assumed a lensing-driven absorption enhancement for BC particles that is wavelength independent (Liu et al., 2015; Zhang et al., 2018), other studies showed that the presence of brown coatings can produce variations in the spectral behaviour of E_{abs} with the wavelength (Lack and Cappa, 2010). Consequently, in order to take the possible influences of the brown coatings on E_{abs} into account, following Lack and Langridge (2013) we performed a sensitivity study by studying the variation of the absorption enhancement attributed to BC, the BC coating, and BrC by varying the AAE of internally mixed BC (cf. Fig. S5). For this, E_{abs} attributed to the different values of AAE for the internally mixed BC can be described as follows (Eq. 3):

$$\mathrm{E}^{\lambda}_{\mathrm{abs,int}} = 1 + \frac{\mathrm{MAC}^{880\,\mathrm{nm}}_{\mathrm{BC,int}} \times \left(\frac{880}{\lambda}\right)^{\mathrm{AAE}}}{\mathrm{MAC}^{\lambda}_{\mathrm{ref}}}, \quad (3)$$

where different AAE (0.8, 1 and 1.4) were considered for the sensitivity study presented here, following Lack and Langridge (2013).

Finally, E_{abs} due to externally mixed particles at a given wavelength ($\mathrm{E}^{\lambda}_{\mathrm{abs,ext}}$) was obtained as the difference between the measured total ambient E_{abs} and the absorption enhancement due to the internal mixing,

$$\mathrm{E}^{\lambda}_{\mathrm{abs,ext}} = \mathrm{E}^{\lambda}_{\mathrm{abs}} - \mathrm{E}^{\lambda}_{\mathrm{abs,int}}. \quad (4)$$

2.5 Chemical fractions contribution to E_{abs}

Submicron chemical composition from ACSM in BCN, and offline 24 h chemical speciated data from filter analyses at both BCN and MSY were used to determine the influence of the material available for BC coating on E_{abs}. Chemical speciated data were used to calculate the total amount of NR-PM (NR-PM_{10} for offline measurements and NR-PM_1 for online measurements) mass concentration. The NR-PM to EC concentration ratios were then calculated as follows:

$$R_{\text{NR-PM}} = \frac{\sum_i [\text{NR-PM}]_i}{[\text{EC}]}. \quad (5)$$

Thus, the calculated $R_{\text{NR-PM}}$ represents a proxy for the amount of NR material available for mixing with the BC particles (Cappa et al., 2019). The chemical species and groups of compounds taken into account using the online ACSM continuous measurements were: [HOA], [COA], [LO-OOA], [MO-OOA], [SO_4^{2-}], [NO_3^-], [NH_4^+], [Cl^-], and [BBOA] during the cold period; whereas they were [OA], [SO_4^{2-}], [NO_3^-], [NH_4^+], [Cl^-] from the 24 h filters.

Moreover, online submicron chemical composition data and OA source apportionment from ACSM in BCN were used to determine the species that mostly contributed to E_{abs}. For this, a multivariate linear regression (mlr) analysis was employed to solve the following equation:

$$E_{abs} = E_0 + m_1[q_1] + m_2[q_2] + \ldots + m_z[q_z], \quad (6)$$

where E_0 is the intercept, m_i (where $i = 1, \ldots, z$) are the regression coefficients, i.e. the relative contribution of each chemical fraction to E_{abs}, and $[q_i]$ are the dependent variables of the mlr, i.e. the ratios of each chemical fraction/-source normalized to the EC concentration. Note that E_0 should be equal to 1 (i.e. no absorption enhancement) when all the ratios are equal to 0 in Eq. (6). In order to perform a more robust mlr analysis and to reduce the effect of outliers, data points lower than the 5th and higher than the 95th percentiles were excluded from the analysis.

3 Results

3.1 Site-specific MAC and E_{abs} analysis

The median values of the ambient BC MAC and E_{abs} at different wavelengths from both online and offline measurements at BCN and MSY are reported in Tables 1 and 2, respectively. For the long-term offline measurements, the MAC at 637 nm was $9.67 \pm 2.55\ m^2\ g^{-1}$ at the BCN urban background station, and $13.10 \pm 4.47\ m^2\ g^{-1}$ at the MSY regional background station. The BC MAC at MSY showed a higher median value compared to BCN (cf. Table 1) due to the fact that BC particles reaching the regional station had more time to gather material for coating. Moreover, the frequency distribution of the MAC values at MSY was less left-skewed and more right-skewed compared to BCN (see Fig. S7). For the intensive online measurements in BCN, the MAC values range between 7.55 ± 2.06 at 950 nm and 22.74 ± 6.98 at 370 nm (Table 1). The values at 660 nm for the online measurements and 637 nm for the offline measurements were around 10.85 ± 2.98, and 9.67 ± 2.55 in BCN, and 13.10 ± 4.47 in MSY, which were within the range of MAC values reported by Zanatta et al. (2016) for similar station backgrounds. The difference between the offline and online measurements at BCN, although the mean values fall within the standard deviation of the measurements, was mainly associated with the difference in the length of the measurement periods, and the different inlet cut-off sizes, which prevent direct comparison (Fig. S1 in the Supplement). The observed increase of MAC with decreasing wavelength was expected due to both the increase of the energy radiation and the larger influence of the externally mixed BrC particles at shorter wavelengths. In fact, the effect of externally mixed BrC particles on MAC in BCN is visible in Fig. S7 where the frequency distribution of MAC at 370 nm showed a much more pronounced tile toward higher values compared to the MAC at 880 nm.

Table 1. Observed MAC ($m^2\ g^{-1}$) values obtained using online techniques via AE33 and Sunset online EC measurements at BCN for a $PM_{2.5}$ inlet cut-off, and offline at BCN and MSY via MAAP and offline EC measurements on 24 h filters for a PM_{10} inlet cut-off.

	λ (nm)	MAC
Online BCN	370	22.74 ± 6.98
	470	17.23 ± 4.80
	520	14.84 ± 4.16
	590	12.63 ± 3.50
	660	10.85 ± 3.02
	880	7.92 ± 2.16
	950	7.55 ± 2.06
Offline BCN	637	9.67 ± 2.55
Offline MSY	637	13.10 ± 4.47

The averaged multi-wavelength E_{abs} values from both online and offline measurements at BCN and MSY are shown in Table 2. The online measurements at 880 nm in BCN led to a median E_{abs} value of 1.28 ± 0.36, whereas it increased to 1.45 ± 0.51 at 370 nm. For the offline measurements, the median E_{abs} values at 637 nm were 1.42 ± 0.40 and 2.00 ± 0.75 at BCN and MSY, respectively. As reported in Table 2, the E_{abs} values from online and offline measurements in BCN were rather similar (1.31 ± 0.38 at 660 nm online and 1.42 ± 0.40 at 637 nm offline), and the observed difference was likely due to both the different periods, the inlet cut-off (Fig. S1 in the Supplement), and the different instrumentation used for the calculation of E_{abs}. As already observed for MAC, the higher E_{abs} at the regional MSY station was due to ageing of BC particles during the transport toward the regional station. The E_{abs} values reported in Table 2 were calculated

from Eq. (2) as MAC^{λ}_{ref} using the intercept values from the Deming regression fits reported in Figs. S2–S4 and S6 for online AE33 and offline BCN and MSY, respectively. If the theoretical reference MAC (Bond and Bergstrom, 2006) of uncoated BC was used, the overall median E_{abs} values were higher for the online measurements at BCN (1.59 ± 0.51 at 880 nm and 1.91 ± 0.62 for 370 nm), although within the uncertainty, and rather similar for the offline measurements at BCN and MSY, with E_{abs} values at 637 nm of 1.43 ± 0.44 and 1.92 ± 0.76, respectively (Table 2). The values found at the urban BCN area using the experimental (theoretical) reference MAC at 880 nm were similar (higher) to those observed in the literature for the same wavelength at rural/suburban areas (Liu et al., 2015; Zhang et al., 2018). The mean E_{abs} value observed at the regional background MSY station was also similar to the values reported in literature for rural areas (e.g. Cui et al., 2016).

Figure 1 shows the density distribution of E_{abs} for the cold (December–May) and warm (June–October) seasons from both online measurements at BCN and offline measurements at BCN and MSY (Fig. 1). The median values of the season-dependent frequency distributions of E_{abs} were reported in Table 2. The long-term offline measurements led, on average, to similar E_{abs} values at 637 nm in BCN during the warm (1.45 ± 0.40) and cold (1.41 ± 0.39) seasons. However, for MSY E_{abs} values they were larger during the warm season (2.24 ± 0.79) compared to the cold season (1.82 ± 0.63), mainly due to the increase in the SOA formation (Figs. S8 and S9) which was mostly driven by the increase in biogenic volatile organic compounds (BVOCs) during the warm season (Seco et al., 2013; Veld et al., 2021). Thus, as shown later in more detail, OA, and especially SOA, contributed strongly to the BC lensing-driven E_{abs}, especially at the regional station.

The online measurements performed with AE33 allowed for a multi-wavelength analysis of E^{λ}_{abs}. Figure 1a shows a seasonal decoupling of E_{abs} between the short UV and the IR wavelengths: whilst in the warm period E_{abs} remained similar for all the wavelengths, during the cold period there was an increase of E_{abs} towards the shorter wavelengths. This different amplification of E_{abs} at short UV can be associated with a larger presence of BrC-like compounds (e.g. BBOA from winter biomass burning) (Figs. S8 and S9) during the cold period (Via et al., 2021), which present larger MACs and contribution to absorption at these wavelength ranges (e.g. Lack et al., 2012; Qin et al., 2018; Saleh et al., 2018; Saleh, 2020; Kasthuriarachchi et al., 2020; Zhang et al., 2020). Figure S10 shows that by using the theoretical reference MAC, the density distribution of E_{abs} was similar, although the differences between the cold and warm periods were not that great. This was attributed to the fact that using a theoretical MAC does not take the different seasonal-dependent contributions of OA sources into account.

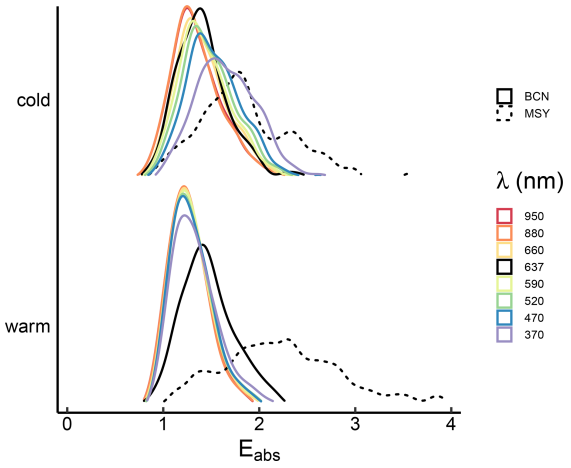

Figure 1. Seasonal frequency distributions of E_{abs} at BCN for the multi-wavelengths measured with AE33 (coloured solid lines for 370, 470, 520, 590, 660, 880 and 950 nm), and at BCN (black solid line) and MSY (black dash line) measured with MAAP for 637 nm and offline filters.

3.1.1 E_{abs} dependence on the mixing state

As already stated, ambient BC particles can be either externally or internally mixed with other aerosols (Bond and Bergstrom, 2006). In order to separate the relative contributions to E_{abs} of these two mixing states, i.e. external ($E_{abs,ext}$) and internal ($E_{abs,int}$), we used the multi-wavelength AE33 and the semi-continuous OC : EC measurements obtained in BCN (see Sect. 2.4). We assumed that E_{abs} at the near-infrared (NIR) (880 nm) was only produced by the internal mixing of BC particles, whereas at the short UV (370 nm) the E_{abs} is due to both the internal and external mixing of BC particles. Given the spectral characteristic of the BrC absorption, the contribution to E_{abs} due to external mixing was the highest at 370 nm compared to the other AE33 wavelengths. In addition, here we analysed the possible contribution of different internal mixing states of BC using different AAE for internally mixed BC, since the presence of brown coatings over the BC cores can actually produce a reduction of the enhancement of the absorption towards the shorter wavelengths (cf. Lack and Cappa, 2010).

Figure 2 shows the evolution of the contribution of the internal and external mixing states to the total E_{abs} for the three AAE values considered for the internally mixed BC. Indeed, Fig. 2 shows that an AAE of 0.8 could be related with a larger proportion of brown coatings, reducing E_{abs} due to the internally mixed BC (cf. Fig. 5 Lack and Cappa, 2010). In the case of AAE = 1, the contribution of the coating material remains fairly constant (Fig. 2). However, it presents a slight decrease with decreasing wavelengths, which is due to the fact that the MAC Ångström exponent presented here for the experimental reference MAC for pure BC particles was slightly above 1

Table 2. Overall, and cold and warm period average E_{abs} values for both multi-wavelength online measurements at BCN, and offline measurements at the near-infrared (NIR) BCN and MSY stations.

		$E_{abs,exp}$			$E_{abs,theory}$		
	λ (nm)	Overall	Cold	Warm	Overall	Cold	Warm
Online BCN	370	1.45 ± 0.51	1.67 ± 0.57	1.31 ± 0.35	1.91 ± 0.69	2.11 ± 0.79	1.79 ± 0.53
	470	1.38 ± 0.43	1.53 ± 0.50	1.27 ± 0.29	1.85 ± 0.61	2.00 ± 0.71	1.76 ± 0.45
	520	1.35 ± 0.41	1.47 ± 0.48	1.27 ± 0.30	1.76 ± 0.58	1.91 ± 0.67	1.67 ± 0.43
	590	1.33 ± 0.39	1.42 ± 0.46	1.27 ± 0.29	1.70 ± 0.55	1.83 ± 0.65	1.61 ± 0.40
	660	1.31 ± 0.38	1.39 ± 0.45	1.26 ± 0.29	1.63 ± 0.54	1.76 ± 0.63	1.55 ± 0.39
	880	1.28 ± 0.36	1.33 ± 0.43	1.25 ± 0.28	1.59 ± 0.51	1.69 ± 0.60	1.52 ± 0.37
	950	1.28 ± 0.36	1.33 ± 0.43	1.25 ± 0.28	1.59 ± 0.51	1.69 ± 0.60	1.52 ± 0.37
Offline BCN	637	1.42 ± 0.40	1.41 ± 0.39	1.45 ± 0.40	1.43 ± 0.44	1.42 ± 0.43	1.43 ± 0.44
Offline MSY	637	2.00 ± 0.75	1.82 ± 0.63	2.24 ± 0.79	1.92 ± 0.76	1.73 ± 0.66	2.02 ± 0.81

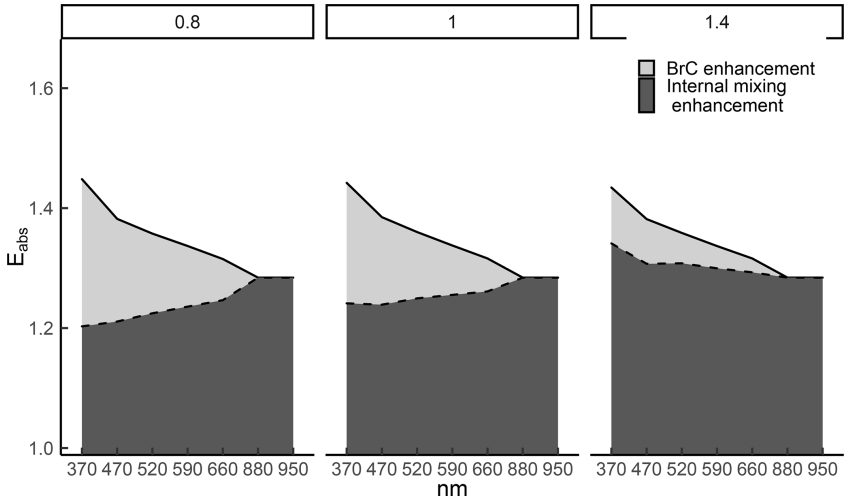

Figure 2. Absorption enhancement (E_{abs}) attribution to both internal and external mixing under different AAE conditions for the internally mixed BC (0.8, 1, 1.4) for the online measurements at the 7-AE33 wavelengths at Barcelona (BCN).

(Fig. S6). Moreover, Fig. 2 shows that for an AAE of 1.4, the internal mixing increases towards the shorter wavelengths, as observed in the simulations performed in Fig. 3 of Lack and Cappa (2010) for the case of BC core with a brown shell that does not absorb.

The overall contribution due to the internal mixing ($E_{abs,int}$) ranged between a 100 % at 880 nm, and 83 %, 86 %, and 93.5 % of the total E_{abs} at 370 for an AAE of 0.8, 1 and 1.4, respectively. Thus, the externally mixed BrC particles represented a non-negligible fraction of the total E_{abs} at short UV wavelengths (Table S1 in the Supplement), especially for the AAE = 0.8 case, for which it increased from 0.069 ± 0.066 (5.2 %) at 660 nm up to 0.17 ± 0.18 at 370 nm (16.9 %). Conversely, if an AAE = 1.4 is used, then the increase and relative contribution of E_{abs} due to the externally mixed BrC particles remains lower, from 0.023 ± 0.049 (1.7 %) at 660 nm up to 0.093 ± 0.200 at 370 nm (6.5 %).

Although BCN is an urban background station with a non-predominant contribution from biomass burning, the contribution to absorption from other potential BrC sources cannot be excluded. Since biomass burning emissions are higher during the cold season, we have found that during this season compared to the warm season, there was a small increase of the total E_{abs} due to the internal mixing (6.4 %), and a more significant increase of contribution of the external mixing E_{abs}, which increased for an AAE = 1 from 0.09 during the warm period to 0.36 during the cold season (Table S1 and Fig. S11 in the Supplement), i.e. from representing a 7 % to 22 % of the total E_{abs}, respectively. In fact, biomass burning is not the only source contributing to the presence of BrC in the atmosphere during the colder months (e.g. Zhang et al.,

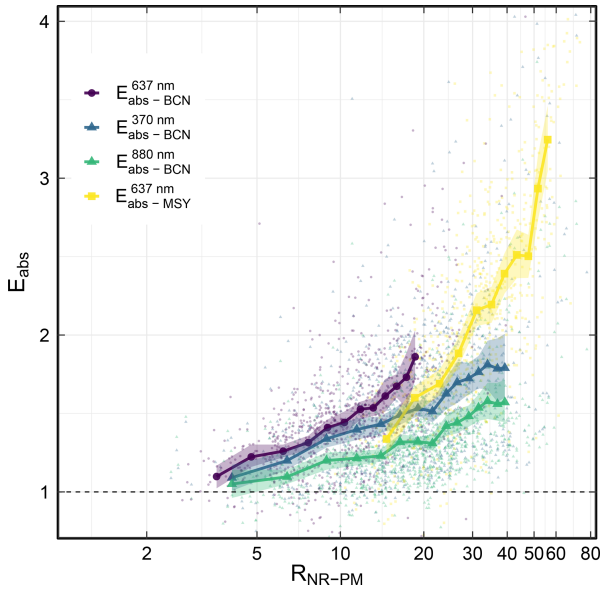

Figure 3. Absorption enhancement (E_{abs}) as a function of the NR-PM to EC ratio at the Barcelona (BCN) and Montseny (MSY) stations. The offline E_{abs} measurements with a PM_{10} inlet at 637 nm were used for both BCN and MSY. Also, at BCN, online E_{abs} measurements with a $PM_{2.5}$ inlet at the short UV (370 nm) and NIR (880 nm) wavelengths were used. The scatter points represent all the measurements, whereas the marked points show the mean of each bin, whilst the shadow of the line represents the standard deviation of each bin.

2020). As shown later, other OA sources also contribute to E_{abs}.

3.2 E_{abs} dependence on R_{NR-PM} content

Here we analysed the relationship between E_{abs} and the amount of material available for mixing with BC particles (R_{NR-PM}, cf. Sect. 2.5). As commented in Sect. 3.1, the variability of E_{abs} with the seasons can be attributed to the differences in the OA composition and concentration levels. Cappa et al. (2019) have shown the discrepancies between model, laboratory, and field studies in the behaviour of E_{abs} with R_{NR-PM}. Indeed, Fig. 1 in Cappa et al. (2019) shows that some studies reported only a slight increase of E_{abs} with the amount of the coating material (Cappa et al., 2012), whereas others measured a larger increase of E_{abs} for high concentrations of R_{NR-PM} (Liu et al., 2015; Peng et al., 2016). The authors argued that the differences could be associated with the ageing state, volatility, and amount of coating of the particles, as well as with the apportionment of external mixing to E_{abs}.

Figure 3 shows E_{abs} values as a function of R_{NR-PM} at BCN (online and offline) and MSY (offline). Overall, we observed an exponential increase of E_{abs} with the amount of NR-PM coating material available for mixing (Fig. 3), which was consistent with some of the observed behaviour found in the literature (e.g. Fig. 1 in Cappa et al., 2019).

As shown in Fig. 3, the R_{NR-PM} binned values from offline measurements at MSY spanned from around 15 up to around 55 $\mu g\,m^{-3}$, whereas R_{NR-PM} values were between around 3.5 and 20 $\mu g\,m^{-3}$ in BCN. As a consequence, E_{abs} at MSY reached values up to around 3.25, whereas E_{abs} values remained lower than 2 in BCN. Thus, the higher R_{NR-PM} at MSY implied that more material was available for BC coating at the regional site compared to BCN, thus leading to higher E_{abs} at MSY. Moreover, the lowest E_{abs} at MSY from binned data in Fig. 3 was around 1.3 indicating that on average BC particles reaching the MSY station have undergone longer ageing processes and were already coated, whereas in BCN, freshly emitted still-not-mixed BC particles were frequently measured, as denoted by E_{abs} values closer to 1. For the online measurements in BCN, R_{NR-PM} showed a larger range of values (from around 4 to 40 $\mu g\,m^{-3}$) compared to the offline measurements because of the higher time resolution of online measurements, allowing measuring events characterized by lower or higher R_{NR-PM} compared to the 24 h offline measurements. The higher E_{abs} in BCN at 637 nm compared to E_{abs} at 370 nm was mostly associated with the different inlet cut-off sizes and, to a lesser extent, with the different periods used for the online and offline measurements. In fact, as shown in Fig. S12, the mean E_{abs} calculated from offline measurements in BCN, using the same period as for the online measurements (2018), was closer, but higher nevertheless, to the E_{abs} values obtained from online measurements at 880 and 370 nm. As shown in Fig. 3, the E_{abs} values from the online and offline datasets in BCN showed similar trends for smaller concentrations of R_{NR-PM}. However, as the amount of mixing material increased, the offline method increased at a higher rate, reaching higher values for the largest R_{NR-PM} measurements. This behaviour was also observed when only the 2018 period was used for the calculation of E_{abs} from offline measurements (cf. Fig. S12). These different trends between online and offline E_{abs} versus R_{NR-PM} were probably due to two main factors: first, the offline measurements were made with a PM_{10} inlet versus the $PM_{2.5}$ inlet of the online method (Fig. S1 in the Supplement), hence coarse nitrates and other coarse particles could have influenced E_{abs}, and, second, the large annual variability observed for the offline E_{abs} measurements (see Fig. S12) could have also contributed to the observed difference.

The availability of multi-wavelength E_{abs} values at the BCN station allowed a multi-wavelength analysis of E_{abs} versus R_{NR-PM}. Since E_{abs} at 880 nm is influenced solely by the internal mixing of BC particles, the comparison of E_{abs} at 880 and 370 nm, when the external mixing influence on the absorption is the highest, showcased the influence that the mixing state had on the relationship between E_{abs} and R_{NR-PM}. Figure 3 shows similar values for both wavelengths

for the lowest amount of coating material, but as $R_{NR\text{-}PM}$ increased, the E_{abs} at 370 nm increased more rapidly than at 880 nm, mostly due to the fact that as $R_{NR\text{-}PM}$ increases, the contribution of externally mixed BrC becomes larger.

If a theoretical MAC reference was used instead, the E_{abs} values as a function of $R_{NR\text{-}PM}$ at BCN (online and offline) and MSY (offline) showed the same relationship (Fig. S13), albeit larger values were observed, especially for the AE33 measurements. These larger values were mostly due to the fact that the experimentally used MAC was higher than the theoretical ones (Fig. S6), resulting in larger E_{abs} values (Fig. S13).

3.3 Aerosol sources contribution to E_{abs}

The material available for coating on BC particles, which determines its E_{abs} properties (see Fig. 3), is formed by an array of different chemical compounds from different sources as a result of a succession of physical and chemical processes in the atmosphere. These different chemical compounds can exert different responses on E_{abs} (e.g. Zhang et al., 2018) and can increase the BC E_{abs}, depending on their relative amount compared to BC as shown in Fig. 3 and the literature (Zhang et al., 2018; Cappa et al., 2019, and therein).

Here we analysed the contribution of different OA sources and chemical species, such as sulfate and nitrate, to E_{abs} calculated in BCN from online measurements via a mlr analysis. The OA sources were obtained by means of a PMF analysis on the Q-ACSM data in BCN and were published by Via et al. (2021). Given the differences in the seasonality that the OA sources can present, as also observed in BCN (cf. Fig. S9; Minguillón et al., 2015; Via et al., 2021), and given the observed E_{abs} seasonality (Fig. 2), we applied the mlr analysis separately to the warm and cold seasons. Furthermore, in order to separate the contribution of the different BC mixing states, we performed the mlr analyses at the same wavelengths as in Sect. 3.2, namely at 370 and 880 nm.

The results of the mlr analysis were reported in Table 3. Table 3 shows that overall, regardless of the season and the wavelength considered, the main contributors to E_{abs} in BCN were HOA (associated with the emissions from traffic), and COA (emissions related to cooking). These two sources contributed 12 % and 14 %, respectively, to the measured OA mass concentration (Via et al., 2021). Thus, in BCN, HOA and COA increased E_{abs} both by contributing to the BC coating (880 nm) and by acting as BrC species externally mixed with BC (370 nm), as suggested by the higher coefficients observed for these two OA sources at 370 nm compared to 880 nm (cf. Table 3). A major source of BC in BCN was traffic (Pandolfi et al., 2016; Via et al., 2021), thus likely explaining the high potential of HOA particles that contribute to E_{abs}. Moreover, some recent studies have also shown that HOA particles in urban environments can potentially have a high absorption efficiency in the UV–VIS range (Qin et al., 2018; Chen et al., 2020; Kasthuriarachchi et al., 2020). Regarding the COA particles, some studies have shown that this OA source has a lower absorption efficiency compared to HOA particles (e.g. Qin et al., 2018; Kasthuriarachchi et al., 2020; Chen et al., 2020). This was in agreement with the lower coefficients observed for COA compared to HOA (Table 3). In addition, during the cold season, both BBOA and LO-OOA presented large positive contributions to E_{abs} at 370 nm, whereas the contribution to E_{abs} from these two sources was negative at 880 nm. For the warm season, the contribution of LO-OOA was also very low at 880 nm and negative at 370 nm, whereas BBOA did not contribute in summer, as already stated. Zhang et al. (2018) also found a negative contribution to E_{abs} for BBOA at 880 nm. The higher coefficients observed for these sources (HOA, COA, BBOA, and LO-OOA) at 370 nm compared to 880 nm highlighted the potential of these OA sources to act as BrC species externally mixed with BC. The MO-OOA particles also contributed positively to E_{abs} at both 370 and 880 nm, especially during the cold season, likely due to the higher-relative contribution of MO-OOA to OA observed in this season compared to the warm season (Via et al., 2021). Recently, Kasthuriarachchi et al. (2020) reported higher absorption efficiency in the UV–VIS range for LO-OOA particles compared to MO-OOA particles, likely due to the photodegradation chemistry (photobleaching) of BrC chromophores in this aged MO-OOA fraction. The inorganic aerosol components presented a higher variability with regards to their contribution to E_{abs}, with sulfates, and especially nitrates, becoming an important source of coating during the warm season, whilst presenting a low impact during the colder season.

Figure 4 shows the contribution to E_{abs} from the OA sources and inorganic species included in the mlr analysis as $R_{NR\text{-}PM}$ increases. The contributions to E_{abs} reported in Fig. 4 were calculated as the product between the OA sources and inorganic species mass concentrations (provided by Via et al., 2021) to EC ratios and the coefficients reported in Table 3. As shown in Fig. 4, during the cold season in BCN the absolute contribution of OA to E_{abs} was much higher compared to the contribution from inorganic aerosols (nitrates and sulfates here) at both 370 and 880 nm (Fig. 4a, c). The HOA and MO-OOA were the major sources contributing to the lensing-driven absolute BC E_{abs} at 880 nm in BCN during the cold season. Conversely, the absolute contribution of LO-OOA and COA to E_{abs} was the highest at 370 nm, suggesting their importance as a BrC source in the area under study. During the warm season, as already noted, E_{abs} was lower compared to the cold season. The major difference compared with the cold season was that the contribution of SIAs increased. The contribution of sulfates at 880 nm as BC lensing-driving species was notable. Furthermore, Fig. 4 also shows that when the contributions were negative, these did not have a large effect on the overall E_{abs}.

Table 3. Multivariate linear regression (mlr) analysis coefficients and standard deviation of the chemical fraction influence on the absorption enhancement, E_{abs}, for Barcelona at both 370 and 880 nm wavelengths using the Q-ACSM chemical sources (Via et al., 2021).

	370 nm		880 nm	
	Cold	Warm	Cold	Warm
Intercept	1.097 ± 0.062	1.112 ± 0.028	1.003 ± 0.048	1.109 ± 0.022
HOA : EC	0.195 ± 0.099	0.092 ± 0.038	0.126 ± 0.077	0.019 ± 0.029
BBOA : EC	0.175 ± 0.058		-0.062 ± 0.044	
MO-OOA : EC	0.044 ± 0.021	0.010 ± 0.007	0.040 ± 0.016	-0.009 ± 0.005
LO-OOA : EC	0.161 ± 0.064	-0.001 ± 0.006	-0.012 ± 0.049	0.006 ± 0.005
Sulfate : EC	-0.003 ± 0.017	0.010 ± 0.004	0.012 ± 0.013	0.017 ± 0.003
Nitrate : EC	-0.011 ± 0.010	0.087 ± 0.011	-0.006 ± 0.008	0.060 ± 0.009
COA : EC	0.106 ± 0.040	0.032 ± 0.022	0.035 ± 0.030	0.044 ± 0.018

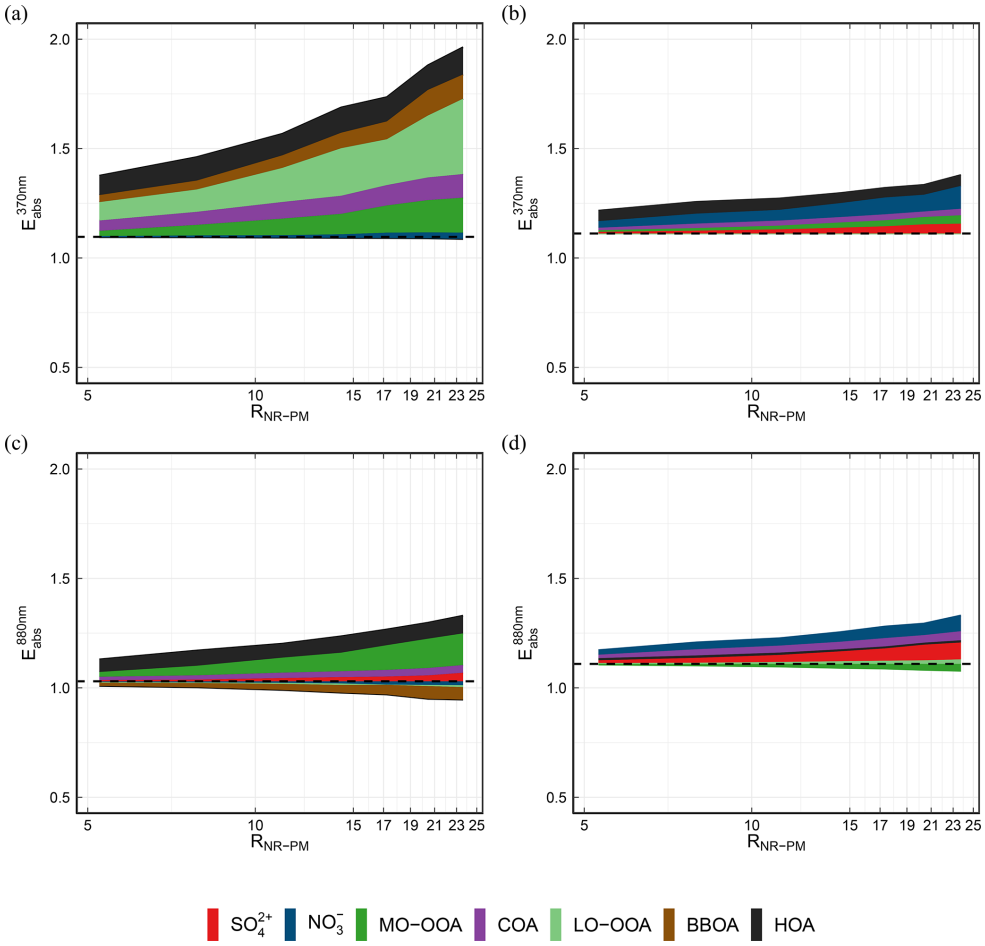

Figure 4. Contribution to the absorption enhancement, E_{abs}, as a function of the amount of coating material $R_{NR\text{-}PM}$ for the different organic and inorganic sources found in BCN during the cold season **(a, c)** and warm season **(b, d)** for 370 **(a, b)** and 880 nm **(c, d)**. The contribution for each source was computed by applying the coefficient obtained with the mlr analysis (see Table 3) to the ratio that compound-to-EC had as $R_{NR\text{-}PM}$ increased. It should be noted that for each season and wavelength, we have set the corresponding intercept of the mlr analysis as reference value above/below in which each compound presented a positive/negative influence on E_{abs}.

3.4 Atmospheric ageing influence on E_{abs}

Atmospheric ageing and oxidation of OA particles have been shown to have an important effect on the E_{abs} (e.g. Liu et al., 2015; Zhang et al., 2018; Xu et al., 2018; Wu et al., 2018). Indeed, we have shown that the SOAs (LO-OOA + MO-OOA) were the main contributors to E_{abs} during the cold season (Table 3 and Fig. 4).

Here we studied the behaviour of E_{abs} with the ageing state of the aerosols. With this aim, we followed the visual method proposed by Ng et al. (2010) to characterize the ageing state of the particles, the so-called triangular plot, where the y axis shows the f_{44} factor (m/z 44 to total concentration in the ACSM component mass spectra ratio), which is a proxy of the ageing, and the x axis is the f_{43} factor (m/z 43 to total concentration in the component mass spectra ratio), which shows the differences in the sources and chemical pathways for the OOA formation. As particles become more oxidized, they converge towards higher f_{44} values and lower f_{43} values.

As observed in Table 3 and Fig. 4, overall primary sources such as HOA, COA, and BBOA were important drivers of E_{abs}, although SOA sources, especially during the cold season and for the shorter wavelengths, were also important sources contributing to E_{abs}. Figure 5 shows the f_{44}–f_{43} relationship in BCN as a function of both E_{abs} values at 880 nm, where E_{abs} is driven by the lensing effect, and the SOA : POA ratio. Figure 5 shows a clear separation of the f_{44}–f_{43} relationship between the cold and warm seasons. In fact, during the cold season at 880 nm, as aerosols become more oxidized (higher f_{44}), the SOA : POA ratio increased altogether with an increase of E_{abs}. Conversely, during the warm season, although the SOA : POA ratio also increased with the degree of oxidation, E_{abs} did not increase significantly. Therefore, during the cold season as particles became more oxidized, BC particles internally mixed with SOA (mainly MO-OOA as shown in Fig. 4c) were the main sources responsible for the larger E_{abs} values, whereas during the warm season, since the main drivers of E_{abs} were the inorganic compounds (Fig. 4d) higher f_{44} values did not imply an increase in E_{abs}. Furthermore, E_{abs} at 370 nm (see Fig. S14) during the cold season showed a more pronounced increase as particles became more oxidized, mainly due to the role of externally mixed BrC, which, as reported in Fig. 4, were the main contributors to E_{abs}. Figure S14 showed that E_{abs} at 370 nm during the warmer period presented a slight increase as particles became oxidized, which could be attributed to the small contribution that MO-OOA particles exerted during this period (see Fig. 4b). This tendency toward higher E_{abs} values as particles become more oxidized has also been found in Paris by Zhang et al. (2018), and in London by Liu et al. (2015).

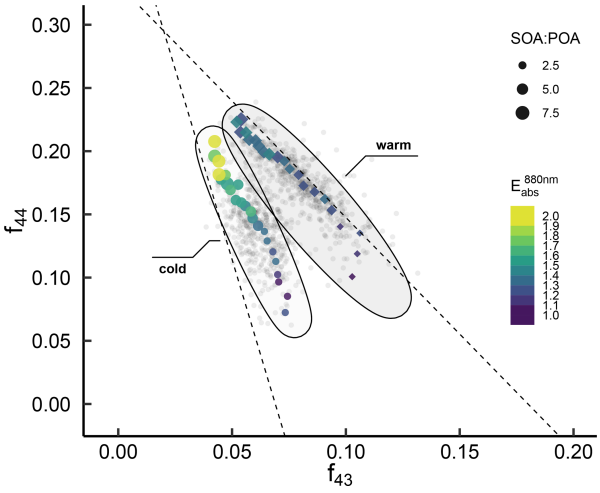

Figure 5. Absorption enhancement, E_{abs}, at 880 nm in BCN using online measurements as a function of the primary to secondary organic aerosol ratio (SOA : POA), and the atmospheric ageing (following Ng et al. (2010) proposed triangle plot, f_{44} vs f_{43}). The f_{44} and f_{43} factors used are the ones presented by Via et al. (2021) for the same time period from the Q-ACSM measurements.

3.5 E_{abs} trend analysis

As already stated, the average E_{abs} values obtained by the offline method in BCN and MSY at 637 nm were within the values found in the literature for similar urban/regional background stations. Given the impact that E_{abs} of BC particles has on climate, we performed a seasonal trend analysis of E_{abs} at both BCN (from 2011 to 2020), and MSY (from 2010 to 2020). In this trend analysis, as well as for the other results presented in this work, we excluded the days when Saharan dust outbreaks influenced the measurements to avoid UV absorption by dust in the analyses presented. Moreover, as already stated, the trend analysis was performed on E_{abs} calculated at 637 nm, where the contribution to E_{abs} from externally mixed OA was less relevant.

The method employed for the trend analysis was a Theil–Sen slope regression estimator. Previous studies performed at the MSY and BCN stations have shown statistically significant (s.s.) decreasing trends over time for the contributions from various anthropogenic sources, including traffic, industry, heavy-oil combustion, secondary sulfate and secondary nitrates mirroring the success of mitigation strategies adopted in Europe (Pandolfi et al., 2016; Veld et al., 2021). Moreover, recently Veld et al. (2021) have shown that the observed decreasing trends, in combination with the absence of a trend for OAs at both BCN and MSY stations, resulted in an increase in the relative proportion of OA in PM at these stations, and especially for SOA, which presents the higher values during the summer season.

The E_{abs} trends showed different behaviours during the spring–summer and autumn–winter seasons at the two urban and background stations considered here (Fig. 6). Figure 6 shows a s.s. increase of E_{abs} at the MSY station in summer (JJA), whereas no s.s. trends were observed in MSY during the other seasons. In BCN, the E_{abs} trends were not s.s. during all the seasons. During autumn (SON) and winter (DJF), E_{abs} showed a slight decrease at both stations although not s.s. The E_{abs} s.s. increase of a 8.16 % yr^{-1} during summer in MSY was linked to the observed increase of the OC : EC ratio (cf. Fig. S15), thus further confirming the importance of OA particles to form internal mixing with BC particles, thus increasing the E_{abs}. Conversely, the sulfate : EC ratio (Fig. S16) did not show any seasonal s.s. trend at both sites, mostly because both sulfate and EC concentrations decreased during the period under study (cf. Pandolfi et al., 2016; Veld et al., 2021). The observed OC : EC ratio increase at the MSY station in summer was mainly driven by the increase in the relative proportion of SOA particles as shown in Veld et al. (2021). We have shown here that as the aerosols become more oxidized, the SOA : POA ratio increased together with E_{abs} and the OC : EC s.s. trend observed further confirmed the importance of aged OA particles to form BC coating. In the case that the theoretical MAC was used as a reference (Bond and Bergstrom, 2006), E_{abs} showed the same behaviour with an increase at the regional station, MSY, during the summer months (Fig. S17).

During spring (MAM) of 2020, there was a notable E_{abs} increase at both stations, especially in BCN. During this period, a strict lockdown was established in Spain due to restrictions under the COVID-19 pandemic. The strict lockdown measures implied a significant decrease in the emission of BC and primary aerosols due to the orders to halt any non-essential activity (Tobías et al., 2020; Evangeliou et al., 2021; Querol et al., 2021). This decrease in the primary emissions resulted in an increase in the OC : EC ratio, as can be appreciated in Fig. S15a, which can be associated with an increase in E_{abs}.

The observed changing behaviour of E_{abs} under different SOA : POA ratios suggested that E_{abs} may undertake changes, and possibly an increase, upon new emission restrictions. In fact, as already stated and as shown in Veld et al. (2021), an increase in the relative proportion of OA in $PM_{2.5}$ was observed at both BCN and MSY stations, and this relative increase was mostly due to SOA. Thus, based on our results, future increases of the SOA : POA ratio could cause an increase in E_{abs}.

4 Conclusions

Here we have presented the results of the analysis of the absorption enhancement analysis, E_{abs}, performed in the Barcelona (BCN, urban background) and Montseny (MSY, regional background) stations in the Mediterranean basin. We studied the main characteristics of E_{abs} and its dependence on other chemical compounds using both an intensive online measurement period in BCN (2018), and a decade-long offline dataset (2010–2020) available at both the BCN and MSY stations. The online approach consisted of co-located measurements at BCN of multi-wavelength absorption coefficients with an Aethalometer (AE33), OC : EC analysis through a semi-continuous Sunset analyser, and NR fine aerosol speciation and source apportionment with Q-ACSM. The offline method consisted of comparing the MAAP absorption coefficient measurements (at 637 nm) with 24 h offline OC : EC measurements performed via a thermal–optical carbon analyser, Sunset, following the EUSAAR2 protocol.

We calculated E_{abs} as the ratio between the ambient MAC obtained from the measurements and the reference MAC value for pure BC particles. We have used two distinct reference MAC values: one based on an experimental site-specific MAC for pure BC, and a theoretical value from Bond and Bergstrom (2006). Using the site-specific reference MAC value, we reported E_{abs} values of 1.28 ± 0.36, and 1.45 ± 0.51 for the online measurements in BCN at 880 and 370 nm, respectively, and of 1.42 ± 0.40 and 1.87 ± 0.63 for the offline analysis in BCN and MSY at 637 nm, respectively. The E_{abs} values reported in this work fall within the measured values reported in the literature (Liu et al., 2015; Zhang et al., 2018; Cappa et al., 2019). Moreover, our analysis confirmed the importance of OA particles as species that can increase E_{abs} when these are both internally and externally mixed with BC particles, as also reported in Zhang et al. (2018) for the Paris area (France).

Here we showed that the seasonal behaviour of E_{abs} was a strong function of the wavelength used. In BCN we observed an increase of E_{abs} at the short UV wavelengths during the cold season and we related the observed increase to the presence of BrC particles externally mixed with BC particles. Conversely, in the red and NIR spectral range, the E_{abs} variations were smaller. The relative contribution of BrC to the E_{abs} increased from 4.6 % during the warm season up to 20.3 % during the cold season, as expected due to the increase in the biomass burning activities during winter. The E_{abs} in MSY at 637 nm showed an increase during the warm season, mainly associated with the larger contribution of SOAs affecting the regional station due to the larger emission of biogenic precursors in summer.

In this study we performed an analysis on the influence of the amount of material available for BC coating exerted on E_{abs}. We showed, in agreement with some prior studies, an exponential growth of E_{abs} with the amount of NR aerosols. Thus, at the regional site, where the amount of material available for mixing reached higher values, so did the E_{abs} values. Moreover, when evaluating the different wavelengths for the online measurements, we obtained higher values for the short UV wavelength (370 nm), in comparison with the NIR wavelengths (880 nm), which were associated with the presence of

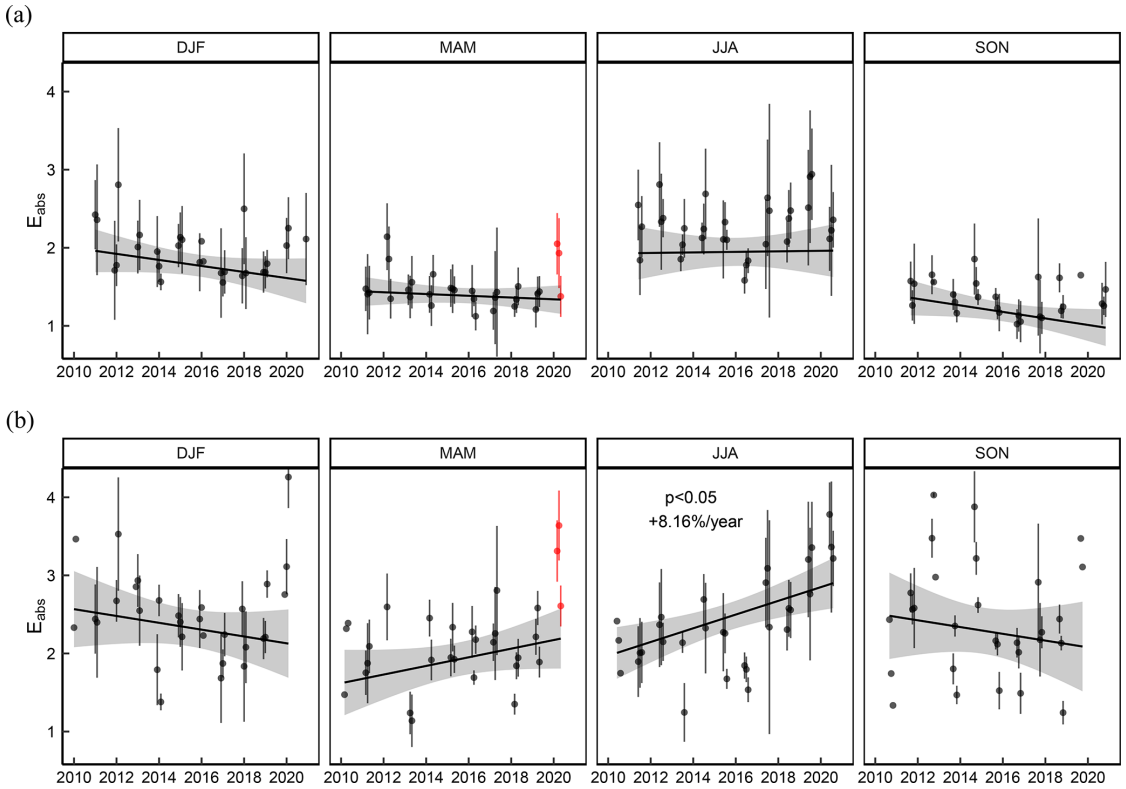

Figure 6. Absorption enhancement, E_{abs}, at 637 nm seasonal trend analysis between 2011 and 2020 at the **(a)** Barcelona and **(b)** Montseny station. The trend analysis was performed using a Theil–Sen function over the E_{abs} offline measurements.

externally mixed BrC increasing the absorption at the shorter wavelengths.

The ageing state influence on E_{abs} was examined using the triangular plot proposed by Ng et al. (2010) by means of the f_{44} and f_{43} factors derived from the Q-ACSM source analysis for online measurements at the BCN station. We observed larger E_{abs} values for more aged OAs, especially during the cold season, which was also related to a larger SOA : POA ratio.

The long database of offline filter and MAAP measurements at both the BCN and MSY stations allowed for a decade-long seasonal trend analysis of E_{abs}. Overall, no s.s. trends were observed at both stations. The exception, however, was the summer period at the MSY regional station where a s.s. increasing trend of 8.16 % yr^{-1} was observed for E_{abs}. This increase of E_{abs} in MSY in summer was mainly driven by a corresponding s.s. increase of the OC : EC ratio. A previous study recently performed in the area under study, reported an increasing trend of the relative contribution of OA to PM and of SOA to OA over time at the MSY regional station. Moreover, our analysis confirmed the importance of OA, and mostly of SOA, in contributing to the BC E_{abs}. Furthermore, at both BCN and MSY stations the forced COVID-19 lockdown in spring 2020 implied a sharp increase of E_{abs}, mainly associated with the increase in the OC : EC ratio for this period due to the large reduction of anthropogenic emissions, and especially of BC particles, in the BCN urban environment. The observed s.s. increasing trend of E_{abs} at the MSY station in summer, driven by a corresponding increase in the OC : EC ratio, suggested that E_{abs} could further increase during summer in the future due to the application of more restrictive measurements to reduce anthropogenic pollutant emissions. Thus, the higher absorption efficiency presented by the positive E_{abs} trend offsets, to some extent, the reduction of the absorption, would be associated with the decreasing trend of BC particles concentrations.

Code and data availability. The Montseny datasets used for this publication are accessible online on the WDCA (World Data Centre for Aerosols) web page (http://ebas.nilu.no, last access: 29 June 2022) and at ACTRIS (https://actris.nilu.no/Data/?key=fa6cd01674284c04bb8736bd5aca0030, Pandolfi al., 2022). The Barcelona datasets were collected within different national and regional projects and/or agreements and are available upon request. The code used for analysis can be obtained upon request to the corresponding author.

Supplement. The supplement related to this article is available online at: https://doi.org/10.5194/acp-22-8439-2022-supplement.

Author contributions. AA, MCM, AK, NP, CR, MP, MV, and JYD carried out the maintenance and supervision of the instrumentation at the BCN and MSY sites. AA, XQ, MCM, and MP helped in the processes of shaping the manuscript structure as well as with the data analysis. MV and MCM performed the analysis of the Q-ACSM data, and AK performed the measurements of OC and EC both online and offline. MI and MR provided support with the AE33 measurements. JYD processed and merged the different datasets, analysed the results, and summarized and expressed them in this article. All authors provided advice regarding the structure and content as well as contributed to the writing of the final manuscript.

Competing interests. At the time of the research, Martin Rigler and Matic Ivančič were also employed by the manufacturer of the Aethalometer AE33.

Disclaimer. Publisher's note: Copernicus Publications remains neutral with regard to jurisdictional claims in published maps and institutional affiliations.

Acknowledgements. We acknowledge support of the COST Action CA16109 COLOSSAL. IDAEA-CSIC is a Centre of Excellence Severo Ochoa (Spanish Ministry of Science and Innovation, grant no. CEX2018-000794-S). We would like to thank the Parc Natural i Reserva de la Biosfera del Montseny and the Diputació de Barcelona for the possibility of maintaining the regional background measurement station.

Financial support. This research has been supported by the Ministerio de Asuntos Económicos y Transformación Digital, Gobierno de España (CAIAC project (grant no. PID2019-108990PB-100)), FEDER funds (grant no. EQC2018-004598-P), the Agència de Gestió d'Ajuts Universitaris i de Recerca (grant no. AGAUR 2017 SGR41), the European Commission, Horizon 2020 Framework Programme (ACTRIS IMP (grant no. 871115)), and the Ministerio de Ciencia e Innovación (grant no. CEX2018-000794-S).

The article processing charges for this open-access publication were covered by the CSIC Open Access Publication Support Initiative through its Unit of Information Resources for Research (URICI).

Review statement. This paper was edited by Guangjie Zheng and reviewed by two anonymous referees.

References

Allan, J. D., Delia, A. E., Coe, H., Bower, K. N., Alfarra, M. R., Jimenez, J. L., Middlebrook, A. M., Drewnick, F., Onasch, T. B., Canagaratna, M. R., Jayne, J. T., and Worsnop, D. R.: A generalised method for the extraction of chemically resolved mass spectra from Aerodyne aerosol mass spectrometer data, J. Aerosol Sci., 35, 909–922, https://doi.org/10.1016/j.jaerosci.2004.02.007, 2004.

Andreae, M. O. and Gelencsér, A.: Black carbon or brown carbon? The nature of light-absorbing carbonaceous aerosols, Atmos. Chem. Phys., 6, 3131–3148, https://doi.org/10.5194/acp-6-3131-2006, 2006.

Bond, T. C. and Bergstrom, R. W.: Light absorption by carbonaceous particles: An investigative review, Aerosol Sci. Tech., 40, 27–67, https://doi.org/10.1080/02786820500421521, 2006.

Bond, T. C., Doherty, S. J., Fahey, D. W., Forster, P. M., Berntsen, T., Deangelo, B. J., Flanner, M. G., Ghan, S., Kärcher, B., Koch, D., Kinne, S., Kondo, Y., Quinn, P. K., Sarofim, M. C., Schultz, M. G., Schulz, M., Venkataraman, C., Zhang, H., Zhang, S., Bellouin, N., Guttikunda, S. K., Hopke, P. K., Jacobson, M. Z., Kaiser, J. W., Klimont, Z., Lohmann, U., Schwarz, J. P., Shindell, D., Storelvmo, T., Warren, S. G., and Zender, C. S.: Bounding the role of black carbon in the climate system: A scientific assessment, J. Geophys. Res.-Atmos., 118, 5380–5552, 2013.

Brean, J., Beddows, D. C. S., Shi, Z., Temime-Roussel, B., Marchand, N., Querol, X., Alastuey, A., Minguillón, M. C., and Harrison, R. M.: Molecular insights into new particle formation in Barcelona, Spain, Atmos. Chem. Phys., 20, 10029–10045, https://doi.org/10.5194/acp-20-10029-2020, 2020.

Brines, M., Dall'Osto, M., Beddows, D. C. S., Harrison, R. M., and Querol, X.: Simplifying aerosol size distributions modes simultaneously detected at four monitoring sites during SAPUSS, Atmos. Chem. Phys., 14, 2973–2986, https://doi.org/10.5194/acp-14-2973-2014, 2014.

Brines, M., Dall'Osto, M., Beddows, D. C. S., Harrison, R. M., Gómez-Moreno, F., Núñez, L., Artíñano, B., Costabile, F., Gobbi, G. P., Salimi, F., Morawska, L., Sioutas, C., and Querol, X.: Traffic and nucleation events as main sources of ultrafine particles in high-insolation developed world cities, Atmos. Chem. Phys., 15, 5929–5945, https://doi.org/10.5194/acp-15-5929-2015, 2015.

Cappa, C. D., Onasch, T. B., Massoli, P., Worsnop, D. R., Bates, T. S., Cross, E. S., Davidovits, P., Hakala, J., Hayden, K. L., Jobson, B. T., Kolesar, K. R., Lack, D. A., Lerner, B. M., Li, S. M., Mellon, D., Nuaaman, I., Olfert, J. S., Petäjä, T., Quinn, P. K., Song, C., Subramanian, R., Williams, E. J., and Zaveri, R. A.: Radiative absorption enhancements due to the mixing state of atmospheric black carbon, Science, 337, 1078–1081, https://doi.org/10.1126/science.1223447, 2012.

Cappa, C. D., Zhang, X., Russell, L. M., Collier, S., Lee, A. K., Chen, C. L., Betha, R., Chen, S., Liu, J., Price, D. J., Sanchez, K. J., McMeeking, G. R., Williams, L. R., Onasch, T. B., Worsnop, D. R., Abbatt, J., and Zhang, Q.: Light Absorption by Ambient Black and Brown Carbon and its Dependence on Black Carbon Coating State for Two California, USA, Cities in Winter and Summer, J. Geophys. Res.-Atmos., 124, 1550–1577, https://doi.org/10.1029/2018JD029501, 2019.

Cavalli, F., Viana, M., Yttri, K. E., Genberg, J., and Putaud, J.-P.: Toward a standardised thermal-optical protocol for measuring atmospheric organic and elemental carbon: the EUSAAR protocol, Atmos. Meas. Tech., 3, 79–89, https://doi.org/10.5194/amt-3-79-2010, 2010.

Chen, B., Bai, Z., Cui, X., Chen, J., Andersson, A., and Gustafsson, Ö.: Light absorption enhancement of black carbon from urban haze in Northern China winter, Environ. Pollut., 221, 418–426, https://doi.org/10.1016/j.envpol.2016.12.004, 2017.

Chen, Y., Xie, X., Shi, Z., Li, Y., Gai, X., Wang, J., Li, H., Wu, Y., Zhao, X., Chen, M., and Ge, X.: Brown carbon in atmospheric fine particles in Yangzhou, China: Light absorption properties and source apportionment, Atmos. Res., 244, 105028, https://doi.org/10.1016/j.atmosres.2020.105028, 2020.

City council of Barcelona: Volum de tràsit (Intensitat mitjana diària de vehicles en dia feiner) a les principals vies. 2014–2018, https://www.bcn.cat/estadistica/catala/dades/anuaris/anuari19/cap15/C1511010.htm, last access: 6 May 2021.

Cui, X., Wang, X., Yang, L., Chen, B., Chen, J., Andersson, A., and Gustafsson, Ö.: Radiative absorption enhancement from coatings on black carbon aerosols, Sci. Total Environ., 551–552, 51–56, https://doi.org/10.1016/j.scitotenv.2016.02.026, 2016.

Dayan, U., Ricaud, P., Zbinden, R., and Dulac, F.: Atmospheric pollution over the eastern Mediterranean during summer – a review, Atmos. Chem. Phys., 17, 13233–13263, https://doi.org/10.5194/acp-17-13233-2017, 2017.

Drinovec, L., Močnik, G., Zotter, P., Prévôt, A. S. H., Ruckstuhl, C., Coz, E., Rupakheti, M., Sciare, J., Müller, T., Wiedensohler, A., and Hansen, A. D. A.: The "dual-spot" Aethalometer: an improved measurement of aerosol black carbon with real-time loading compensation, Atmos. Meas. Tech., 8, 1965–1979, https://doi.org/10.5194/amt-8-1965-2015, 2015.

Ealo, M., Alastuey, A., Pérez, N., Ripoll, A., Querol, X., and Pandolfi, M.: Impact of aerosol particle sources on optical properties in urban, regional and remote areas in the northwestern Mediterranean, Atmos. Chem. Phys., 18, 1149–1169, https://doi.org/10.5194/acp-18-1149-2018, 2018.

European Commission: Establishing guidelines for demonstration and subtraction of exceedances attributable to natu- ral sources under the Directive 2008/50/EC on ambient air quality and cleaner air for Europe, SEC(2011) 208 final, Brussels, 15 February 2011, http://ec.europa.eu/environment/air/quality/legislation/pdf/sec_2011_0208.pdf (last access: 1 July 2022), 2011.

Evangeliou, N., Platt, S. M., Eckhardt, S., Lund Myhre, C., Laj, P., Alados-Arboledas, L., Backman, J., Brem, B. T., Fiebig, M., Flentje, H., Marinoni, A., Pandolfi, M., Yus-Dìez, J., Prats, N., Putaud, J. P., Sellegri, K., Sorribas, M., Eleftheriadis, K., Vratolis, S., Wiedensohler, A., and Stohl, A.: Changes in black carbon emissions over Europe due to COVID-19 lockdowns, Atmos. Chem. Phys., 21, 2675–2692, https://doi.org/10.5194/acp-21-2675-2021, 2021.

Jacobson, M. Z.: Global direct radiative forcing due to multicomponent anthropogenic and natural aerosols, J. Geophys. Res.-Atmos., 106, 1551–1568, 2001.

Karanasiou, A., Panteliadis, P., Perez, N., Minguillón, M. C., Pandolfi, M., Titos, G., Viana, M., Moreno, T., Querol, X., and Alastuey, A.: Evaluation of the Semi-Continuous OCEC analyzer performance with the EUSAAR2 protocol, Sci. Total Environ., 747, 141266, https://doi.org/10.1016/j.scitotenv.2020.141266, 2020.

Kasthuriarachchi, N. Y., Rivellini, L. H., Adam, M. G., and Lee, A. K.: Light Absorbing Properties of Primary and Secondary Brown Carbon in a Tropical Urban Environment, Environ. Sci. Technol., 54, 10808–10819, https://doi.org/10.1021/acs.est.0c02414, 2020.

Kirchstetter, T. W., Novakov, T., and Hobbs, P. V.: Evidence that the spectral dependence of light absorption by aerosols is affected by organic carbon, J. Geophys. Res.-Atmos., 109, 1–12, https://doi.org/10.1029/2004JD004999, 2004.

Knox, A., Evans, G. J., Brook, J. R., Yao, X., Jeong, C. H., Godri, K. J., Sabaliauskas, K., and Slowik, J. G.: Mass absorption cross-section of ambient black carbon aerosol in relation to chemical age, Aerosol Sci. Tech., 43, 522–532, https://doi.org/10.1080/02786820902777207, 2009.

Lack, D. A. and Cappa, C. D.: Impact of brown and clear carbon on light absorption enhancement, single scatter albedo and absorption wavelength dependence of black carbon, Atmos. Chem. Phys., 10, 4207–4220, https://doi.org/10.5194/acp-10-4207-2010, 2010.

Lack, D. A. and Langridge, J. M.: On the attribution of black and brown carbon light absorption using the Ångström exponent, Atmos. Chem. Phys., 13, 10535–10543, https://doi.org/10.5194/acp-13-10535-2013, 2013.

Lack, D. A., Langridge, J. M., Bahreini, R., Cappa, C. D., Middlebrook, A. M., and Schwarz, J. P.: Brown carbon and internal mixing in biomass burning particles, P. Natl. Acad. Sci. USA, 109, 14802–14807, https://doi.org/10.1073/pnas.1206575109, 2012.

Lack, D. A., Moosmüller, H., McMeeking, G. R., Chakrabarty, R. K., and Baumgardner, D.: Characterizing elemental, equivalent black, and refractory black carbon aerosol particles: A review of techniques, their limitations and uncertainties, Anal. Bioanal. Chem., 406, 99–122, https://doi.org/10.1007/s00216-013-7402-3, 2014.

Laskin, A., Laskin, J., and Nizkorodov, S. A.: Chemistry of Atmospheric Brown Carbon, Chem. Rev., 115, 4335–4382, https://doi.org/10.1021/cr5006167, 2015.

Liu, S., Aiken, A. C., Gorkowski, K., Dubey, M. K., Cappa, C. D., Williams, L. R., Herndon, S. C., Massoli, P., Fortner, E. C., Chhabra, P. S., Brooks, W. A., Onasch, T. B., Jayne, J. T., Worsnop, D. R., China, S., Sharma, N., Mazzoleni, C., Xu, L., Ng, N. L., Liu, D., Allan, J. D., Lee, J. D., Fleming, Z. L., Mohr, C., Zotter, P., Szidat, S., and Prévôt, A. S.: Enhanced light absorption by mixed source black and brown carbon particles in UK winter, Nat. Commun., 6, 8435, https://doi.org/10.1038/ncomms9435, 2015.

Minguillón, M. C., Ripoll, A., Pérez, N., Prévôt, A. S. H., Canonaco, F., Querol, X., and Alastuey, A.: Chemical characterization of submicron regional background aerosols in the western Mediterranean using an Aerosol Chemical Speciation Monitor, Atmos. Chem. Phys., 15, 6379–6391, https://doi.org/10.5194/acp-15-6379-2015, 2015.

Moise, T., Flores, J. M., and Rudich, Y.: Optical Properties of Secondary Organic Aerosols and Their Changes by Chemical Processes, Chem. Rev., 115, 4400–4439, https://doi.org/10.1021/cr5005259, 2015.

Müller, T., Henzing, J. S., de Leeuw, G., Wiedensohler, A., Alastuey, A., Angelov, H., Bizjak, M., Collaud Coen, M., En-

gström, J. E., Gruening, C., Hillamo, R., Hoffer, A., Imre, K., Ivanow, P., Jennings, G., Sun, J. Y., Kalivitis, N., Karlsson, H., Komppula, M., Laj, P., Li, S.-M., Lunder, C., Marinoni, A., Martins dos Santos, S., Moerman, M., Nowak, A., Ogren, J. A., Petzold, A., Pichon, J. M., Rodriquez, S., Sharma, S., Sheridan, P. J., Teinilä, K., Tuch, T., Viana, M., Virkkula, A., Weingartner, E., Wilhelm, R., and Wang, Y. Q.: Characterization and intercomparison of aerosol absorption photometers: result of two intercomparison workshops, Atmos. Meas. Tech., 4, 245–268, https://doi.org/10.5194/amt-4-245-2011, 2011.

Myhre, G., Shindell, D., Breéon, F.-M., Collins, W., Fuglestvedt, J., Huang, J., Koch, D., Lamarque, J.-F., Lee, D., Mendoza, B., Nakajima, T., Robock, A., Stephens, G., Takemura, T., and Zhang, H.: Anthropogenic and Natural Radiative Forcing, 8, Cambridge University Press, Cambridge, United Kingdom and New York, NY, USA, 659–740, https://doi.org/10.1017/CBO9781107415324.018, 2013.

Ng, N. L., Canagaratna, M. R., Zhang, Q., Jimenez, J. L., Tian, J., Ulbrich, I. M., Kroll, J. H., Docherty, K. S., Chhabra, P. S., Bahreini, R., Murphy, S. M., Seinfeld, J. H., Hildebrandt, L., Donahue, N. M., DeCarlo, P. F., Lanz, V. A., Prévôt, A. S. H., Dinar, E., Rudich, Y., and Worsnop, D. R.: Organic aerosol components observed in Northern Hemispheric datasets from Aerosol Mass Spectrometry, Atmos. Chem. Phys., 10, 4625–4641, https://doi.org/10.5194/acp-10-4625-2010, 2010.

Paatero, P.: The Multilinear Engine—A Table-Driven, Least Squares Program for Solving Multilinear Problems, Including the *n*-Way Parallel Factor Analysis Model, J. Comput. Graph. Stat., 8, 854–888, https://doi.org/10.1080/10618600.1999.10474853, 1999.

Paatero, P. and Tapper, U.: Positive matrix factorization: A non-negative factor model with optimal utilization of error estimates of data values, Environmetrics, 5, 111–126, https://doi.org/10.1002/env.3170050203, 1994.

Pandolfi, M., Cusack, M., Alastuey, A., and Querol, X.: Variability of aerosol optical properties in the Western Mediterranean Basin, Atmos. Chem. Phys., 11, 8189–8203, https://doi.org/10.5194/acp-11-8189-2011, 2011.

Pandolfi, M., Alastuey, A., Querol, X., González Jiménez, J. L., Jorba, O. C., Ortega, A. M., Baldasano, J. M., Minguillón, M. C., Artíñano, B., Seco, R., Peñuelas, J., Lorente, J., and Pey, J.: Effects of sources and meteorology on particulate matter in the Western Mediterranean Basin: An overview of the DAURE campaign, J. Geophys. Res.-Atmos., 119, 4978–5010, 2014a.

Pandolfi, M., Ripoll, A., Querol, X., and Alastuey, A.: Climatology of aerosol optical properties and black carbon mass absorption cross section at a remote high-altitude site in the western Mediterranean Basin, Atmos. Chem. Phys., 14, 6443–6460, https://doi.org/10.5194/acp-14-6443-2014, 2014b.

Pandolfi, M., Alastuey, A., Pérez, N., Reche, C., Castro, I., Shatalov, V., and Querol, X.: Trends analysis of PM source contributions and chemical tracers in NE Spain during 2004–2014: a multiexponential approach, Atmos. Chem. Phys., 16, 11787–11805, https://doi.org/10.5194/acp-16-11787-2016, 2016.

Peng, J., Hu, M., Guo, S., Du, Z., Zheng, J., Shang, D., Zamora, M. L., Zeng, L., Shao, M., Wu, Y. S., Zheng, J., Wang, Y., Glen, C. R., Collins, D. R., Molina, M. J., and Zhang, R.: Markedly enhanced absorption and direct radiative forcing of black carbon under polluted urban environments, P. Natl. Acad. Sci. USA, 113, 4266–4271, https://doi.org/10.1073/pnas.1602310113, 2016.

Pérez, N., Pey, J., Castillo, S., Viana, M., Alastuey, A., and Querol, X.: Interpretation of the variability of levels of regional background aerosols in the Western Mediterranean, Sci. Total Environ., 407, 527–540, 2008.

Pandolfi, M., Yus-Díez, J., Perez, N., and Alstuey, A.: Aerosol Absorption Coefficient, ACTRIS [data set], https://actris.nilu.no/Data/?key=fa6cd01674284c04bb8736bd5aca0030, last access: 29 June 2022.

Petzold, A. and Schönlinner, M.: Multi-angle absorption photometry – a new method for the measurement of aerosol light absorption and atmospheric black carbon, J. Aerosol Sci., 35, 421–441, 2004.

Pey, J., Pérez, N., Castillo, S., Viana, M., Moreno, T., Pandolfi, M., López-Sebastián, J., Alastuey, A., and Querol, X.: Geochemistry of regional background aerosols in the Western Mediterranean, Atmos. Res., 94, 422–435, 2009.

Qin, Y. M., Tan, H. B., Li, Y. J., Li, Z. J., Schurman, M. I., Liu, L., Wu, C., and Chan, C. K.: Chemical characteristics of brown carbon in atmospheric particles at a suburban site near Guangzhou, China, Atmos. Chem. Phys., 18, 16409–16418, https://doi.org/10.5194/acp-18-16409-2018, 2018.

Querol, X., Alastuey, A., Rodriguez, S., Plana, F., Ruiz, C. R., Cots, N., Massagué, G., and Puig, O.: PM_{10} and $PM_{2.5}$ source apportionment in the Barcelona Metropolitan area, Catalonia, Spain, Atmos. Environ., 35, 6407–6419, 2001.

Querol, X., Pey, J., Pandolfi, M., Alastuey, A., Cusack, M., Pérez, N., Moreno, T., Viana, M., Mihalopoulos, N., Kallos, G., and Kleanthous, S.: African dust contributions to mean ambient PM_{10} mass-levels across the Mediterranean Basin, Atmos. Environ., 43, 4266–4277, 2009.

Querol, X., Massagué, J., Alastuey, A., Moreno, T., Gangoiti, G., Mantilla, E., Duéguez, J. J., Escudero, M., Monfort, E., García-Pando, C. P., Oriol Jorba, H. P., Vázquez, V., de la Rosa Alberto Campos, J., Muñóz, M., Monge, S., Hervás, M., Javato, R., and Cornide, M. J.: Lessons from the COVID-19 air pollution decrease in Spain: Now what?, Sci. Total Environ., 779, 146380, https://doi.org/10.1016/j.scitotenv.2021.146380, 2021.

Reche, C., Querol, X., Alastuey, A., Viana, M., Pey, J., Moreno, T., Rodríguez, S., González, Y., Fernández-Camacho, R., de la Rosa, J., Dall'Osto, M., Prévôt, A. S. H., Hueglin, C., Harrison, R. M., and Quincey, P.: New considerations for PM, Black Carbon and particle number concentration for air quality monitoring across different European cities, Atmos. Chem. Phys., 11, 6207–6227, https://doi.org/10.5194/acp-11-6207-2011, 2011.

Rigler, M., Drinovec, L., Lavrič, G., Vlachou, A., Prévôt, A. S. H., Jaffrezo, J. L., Stavroulas, I., Sciare, J., Burger, J., Kranjc, I., Turšič, J., Hansen, A. D. A., and Močnik, G.: The new instrument using a TC–BC (total carbon–black carbon) method for the online measurement of carbonaceous aerosols, Atmos. Meas. Tech., 13, 4333–4351, https://doi.org/10.5194/amt-13-4333-2020, 2020.

Rivas, I., Beddows, D. C. S., Amato, F., Green, D. C., Järvi, L., Hueglin, C., Reche, C., Timonen, H., Fuller, G. W., Niemi, J. V., Pérez, N., Aurela, M., Hopke, P. K., Alastuey, A., Kulmala, M., Harrison, R. M., Querol, X., and Kelly, F. J.: Source apportionment of particle number size distribution in urban background

and traffic stations in four European cities, Environ. Int., 135, 105345, https://doi.org/10.1016/j.envint.2019.105345, 2020.

Rodrıguez, S., Querol, X., Alastuey, A., Kallos, G., and Kakaliagou, O.: Saharan dust contributions to PM_{10} and TSP levels in Southern and Eastern Spain, Atmos. Environ., 35, 2433–2447, 2001.

Rodríguez, S., Querol, X., Alastuey, A., and Plana, F.: Sources and processes affecting levels and composition of atmospheric aerosol in the western Mediterranean, J. Geophys. Res.-Atmos., 107, 4777, https://doi.org/10.1029/2001JD001488, 2002.

Saleh, R.: From Measurements to Models: Toward Accurate Representation of Brown Carbon in Climate Calculations, Curr. Pollution Rep., 6, 90–104, https://doi.org/10.1007/s40726-020-00139-3, 2020.

Saleh, R., Cheng, Z., and Atwi, K.: The Brown-Black Continuum of Light-Absorbing Combustion Aerosols, Environ. Sci. Tech. Lett., 5, 508–513, https://doi.org/10.1021/acs.estlett.8b00305, 2018.

Samset, B. H., Sand, M., Smith, C. J., Bauer, S. E., Forster, P. M., Fuglestvedt, J. S., Osprey, S., and Schleussner, C. F.: Climate Impacts From a Removal of Anthropogenic Aerosol Emissions, Geophys. Res. Lett., 45, 1020–1029, https://doi.org/10.1002/2017GL076079, 2018.

Seco, R., Peñuelas, J., Filella, I., Llusia, J., Schallhart, S., Metzger, A., Müller, M., and Hansel, A.: Volatile organic compounds in the western Mediterranean basin: urban and rural winter measurements during the DAURE campaign, Atmos. Chem. Phys., 13, 4291–4306, https://doi.org/10.5194/acp-13-4291-2013, 2013.

Tobías, A., Carnerero, C., Reche, C., Massagué, J., Via, M., Minguillón, M. C., Alastuey, A., and Querol, X.: Changes in air quality during the lockdown in Barcelona (Spain) one month into the SARS-CoV-2 epidemic, Sci. Total Environ., 726, 138540, https://doi.org/10.1016/j.scitotenv.2020.138540, 2020.

Veld, M. i. t., Alastuey, A., Pandolfi, M., Amato, F., Pérez, N., Reche, C., Via, M., Minguillón, M. C., Escudero, M., and Querol, X.: Compositional changes of $PM_{2.5}$ in NE Spain during 2009–2018: A trend analysis of the chemical composition and source apportionment, Sci. Total Environ., 795, 148728, https://doi.org/10.1016/j.scitotenv.2021.148728, 2021.

Via, M., Minguillón, M. C., Reche, C., Querol, X., and Alastuey, A.: Increase in secondary organic aerosol in an urban environment, Atmos. Chem. Phys., 21, 8323–8339, https://doi.org/10.5194/acp-21-8323-2021, 2021.

Viana, M., Chi, X., Maenhaut, W., Cafmeyer, J., Querol, X., Alastuey, A., Mikuška, P., and Večeřa, Z.: Influence of sampling artefacts on measured PM, OC, and EC levels in carbonaceous aerosols in an urban area, Aerosol Sci. Tech., 40, 107–117, https://doi.org/10.1080/02786820500484388, 2006.

WMO: WMO/GAW Aerosol Measurement Procedures, Guidelines and Recommendations, WMO-No. 1177, GAW Report-No. 227, 103, https://library.wmo.int/doc_num.php?explnum_id=3073 (last access: 1 July 2022), 2016.

Wu, Y., Cheng, T., Liu, D., Allan, J. D., Zheng, L., and Chen, H.: Light Absorption Enhancement of Black Carbon Aerosol Constrained by Particle Morphology, Environ. Sci. Technol., 52, 6912–6919, https://doi.org/10.1021/acs.est.8b00636, 2018.

Xu, X., Zhao, W., Qian, X., Wang, S., Fang, B., Zhang, Q., Zhang, W., Venables, D. S., Chen, W., Huang, Y., Deng, X., Wu, B., Lin, X., Zhao, S., and Tong, Y.: The influence of photochemical aging on light absorption of atmospheric black carbon and aerosol single-scattering albedo, Atmos. Chem. Phys., 18, 16829–16844, https://doi.org/10.5194/acp-18-16829-2018, 2018.

Yus-Díez, J., Ealo, M., Pandolfi, M., Perez, N., Titos, G., Močnik, G., Querol, X., and Alastuey, A.: Aircraft vertical profiles during summertime regional and Saharan dust scenarios over the north-western Mediterranean basin: aerosol optical and physical properties, Atmos. Chem. Phys., 21, 431–455, https://doi.org/10.5194/acp-21-431-2021, 2021a.

Yus-Díez, J., Bernardoni, V., Močnik, G., Alastuey, A., Ciniglia, D., Ivančič, M., Querol, X., Perez, N., Reche, C., Rigler, M., Vecchi, R., Valentini, S., and Pandolfi, M.: Determination of the multiple-scattering correction factor and its cross-sensitivity to scattering and wavelength dependence for different AE33 Aethalometer filter tapes: a multi-instrumental approach, Atmos. Meas. Tech., 14, 6335–6355, https://doi.org/10.5194/amt-14-6335-2021, 2021b.

Zanatta, M., Gysel, M., Bukowiecki, N., Müller, T., Weingartner, E., Areskoug, H., Fiebig, M., Yttri, K. E., Mihalopoulos, N., Kouvarakis, G., Beddows, D., Harrison, R. M., Cavalli, F., Putaud, J. P., Spindler, G., Wiedensohler, A., Alastuey, A., Pandolfi, M., Sellegri, K., Swietlicki, E., Jaffrezo, J. L., Baltensperger, U., and Laj, P: A European aerosol phenomenology-5: Climatology of black carbon optical properties at 9 regional background sites across Europe, Atmos. Environ., 145, 346–364, 2016.

Zhang, Y., Favez, O., Canonaco, F., Liu, D., Močnik, G., Amodeo, T., Sciare, J., Prévôt, A. S. H., Gros, V., and Albinet, A.: Evidence of major secondary organic aerosol contribution to lensing effect black carbon absorption enhancement, NPJ Clim. Atmos. Sci., 1, 47, https://doi.org/10.1038/s41612-018-0056-2, 2018.

Zhang, Y., Albinet, A., Petit, J. E., Jacob, V., Chevrier, F., Gille, G., Pontet, S., Chrétien, E., Dominik-Sègue, M., Levigoureux, G., Močnik, G., Gros, V., Jaffrezo, J. L., and Favez, O.: Substantial brown carbon emissions from wintertime residential wood burning over France, Sci. Total Environ., 743, 140752, https://doi.org/10.1016/j.scitotenv.2020.140752, 2020.

Supplement of Atmos. Chem. Phys., 22, 8439–8456, 2022
https://doi.org/10.5194/acp-22-8439-2022-supplement
© Author(s) 2022. CC BY 4.0 License.

Atmospheric Chemistry and Physics Open Access

Supplement of

Absorption enhancement of black carbon particles in a Mediterranean city and countryside: effect of particulate matter chemistry, ageing and trend analysis

Jesús Yus-Díez et al.

Correspondence to: Jesús Yus-Díez (jesus.yus@idaea.csic.es) and Marco Pandolfi (marco.pandolfi@idaea.csic.es)

The copyright of individual parts of the supplement might differ from the article licence.

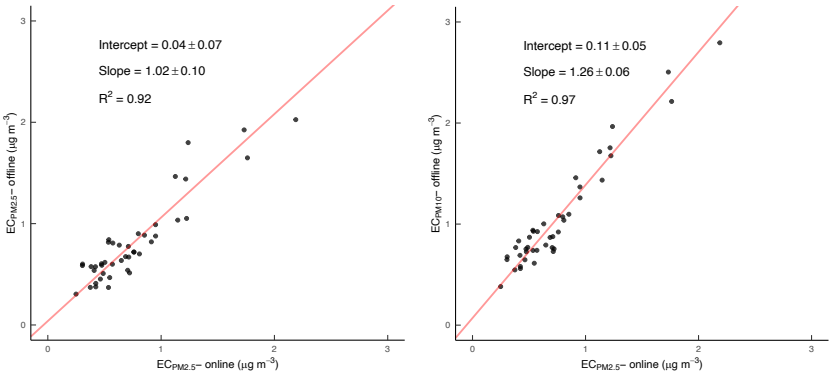

Figure S1: Relationship between the offline 24-hour filter measurements of EC with an inlet cut-off of a) PM2.5 and b) PM10, and the online retrieved measurements of EC with an inlet cut-off of PM2.5.

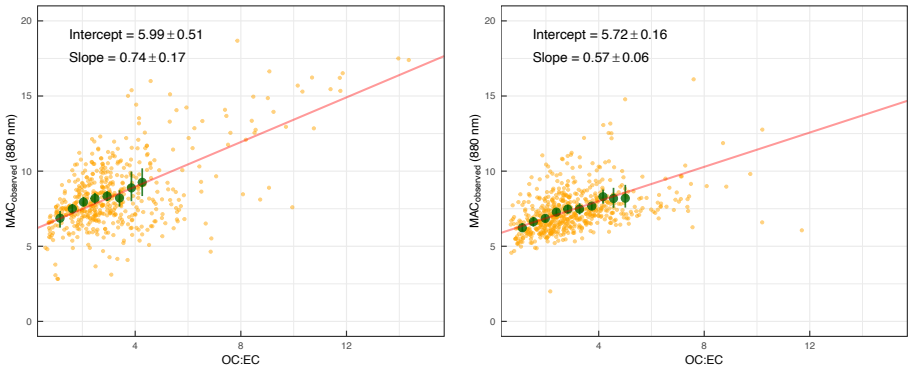

Figure S2: Mass absorption cross-section (MAC) as a function of the online OC-EC ratio at BCN for the AE33 absorption measurement at 880 nm for the a) cold and b) warm period. The intercept obtained with the Deming regression yields the experimental reference MAC of Fig. S3.

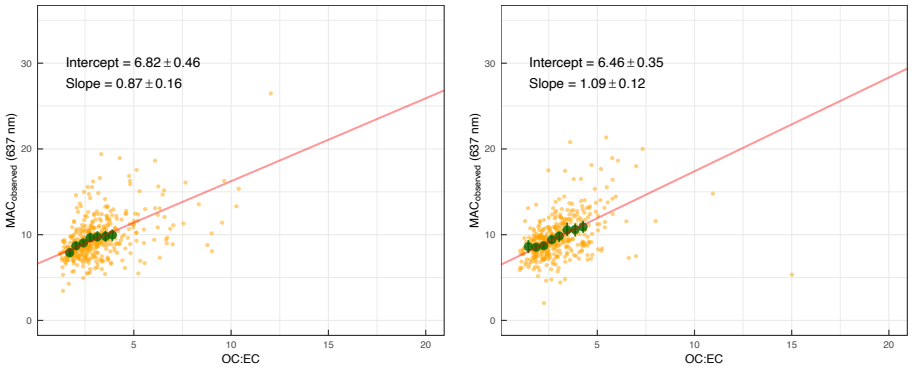

Figure S3: Mass absorption cross-section (MAC) as a function of the offline OC-EC ratio at BCN for the MAAP absorption measurement at 637 nm for the a) cold and b) warm period. The intercept obtained with the Deming regression yields the experimental reference MAC of Fig. S3.

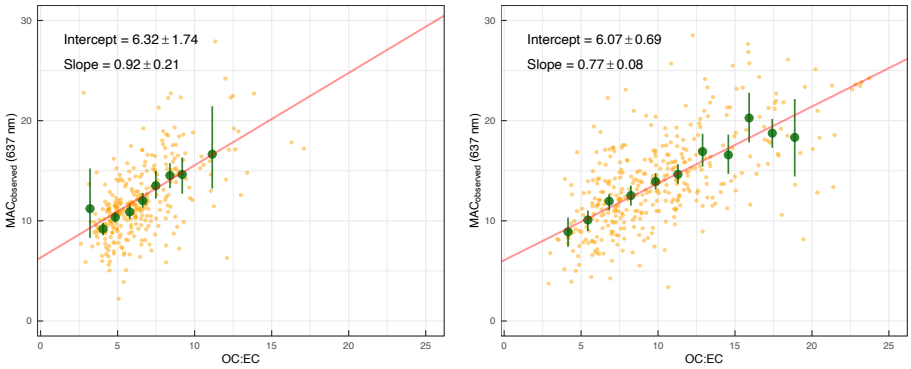

Figure S4: Mass absorption cross-section (MAC) as a function of the offline OC-EC ratio at MSY for the MAAP absorption measurement at 637 nm for the a) cold and b) warm period. The intercept obtained with the Deming regression yields the experimental reference MAC of Fig. S3.

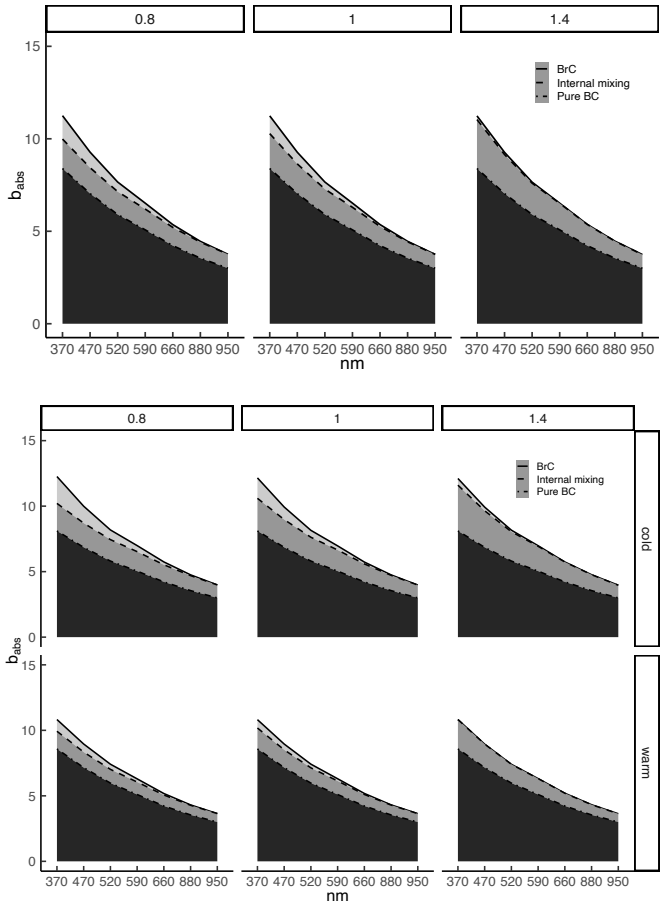

Figure S5: Absorption coefficients, b_{abs}, attribution to both internal and external mixing for the overall measurement period, as well as the cold and warm period under different AAE conditions for the internally mixed BC (0.8,1,1.4) for the online measurements at the 7-AE33 wavelengths at Barcelona (BCN).

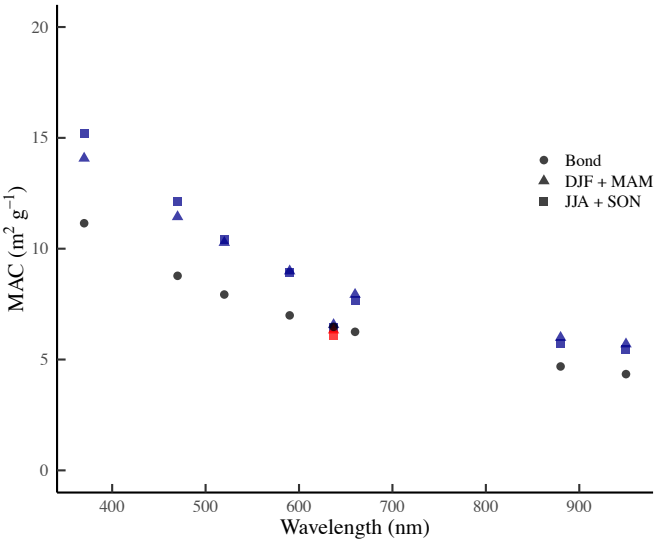

Figure S6: Pure BC MAC ($m^2 g^{-1}$) values obtained from Bond et al. (2006), and experimentally from online techniques via AE33 and Sunset online OC:EC measurements at BCN, and offline via a MAAP at 637 nm and offline OC:EC measurements. BCN station is represented by blue points and Montseny by green points.

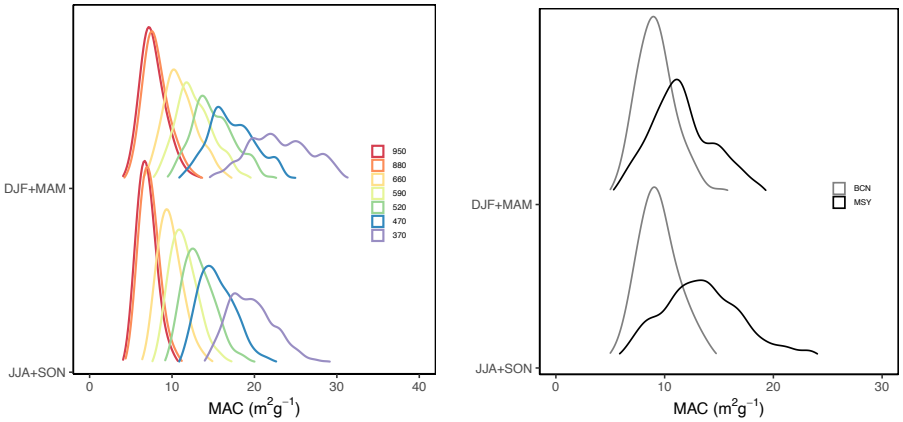

Figure S7: Seasonal frequency distributions of the mass absorption cross-section (MAC) at a) BCN station using a multi-wavelength AE33, and b) at both BCN and MSY at 637 nm using a MAAP.

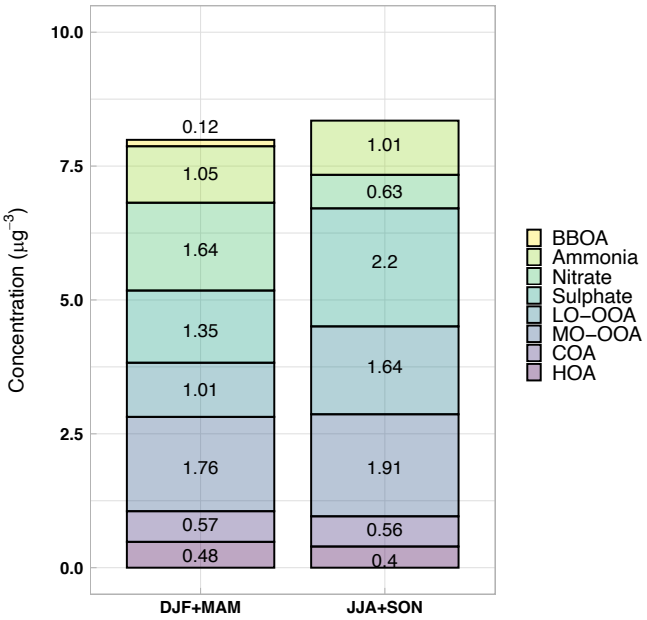

Figure S8: Proportion of the different sources of both organic and inorganic aerosols BCN through-out the seasons during the 2018-2019 period (Via et al., 2021).

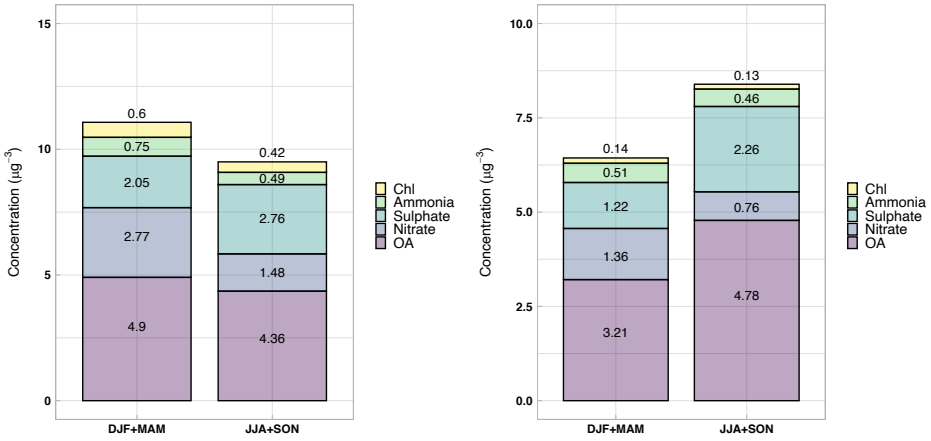

Figure S9: Proportion of the different sources of both organic and inorganic aerosols during the different seasons of the 2011-2018 measurement period at a) BCN, and b) MSY (Veld et al., 2021).

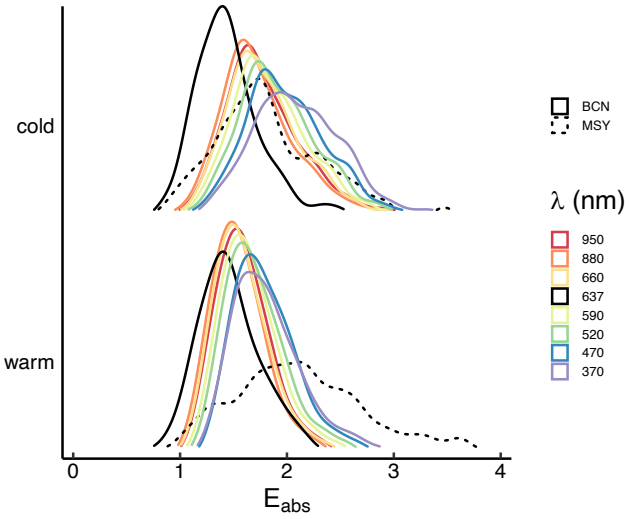

Figure S10: Seasonal frequency distributions of E_{abs} using as a reference MAC the theoretical value provided by Bond et al. (2006) extrapolated to 7 wavelengths measured AE33 wavelengths (370, 470, 520, 590,660, 880 and 950 nm) at BCN station, and to the MAAP wavelength at 637 nm at both BCN and MSY.

Table S1: Absorption enhancement for both external ($E_{abs,ext}$) and internal ($E_{abs,int}$) mixing for the overall period, and the cold and warm period using the experimental MAC ref value.

Overall

AAE	λ (nm)	$E_{abs,int}$	$E_{abs,ext}$	% $E_{abs,int}$	% $E_{abs,ext}$
0.8					
	370	1.203 ± 0.269	0.245 ± 0.272	83.06	16.94
	470	1.211 ± 0.280	0.171 ± 0.170	87.62	12.38
	520	1.225 ± 0.294	0.133 ± 0.129	90.21	9.79
	590	1.236 ± 0.309	0.101 ± 0.092	92.44	7.56
	660	1.247 ± 0.324	0.069 + 0.066	94.78	5.22
	880	1.284 ± 0.354	-	100	0
	950	1.284 ± 0.355	-	100	0
1					
	370	1.241 ± 0.320	0.201 ± 0.241	86.07	13.93
	470	1.239 ± 0.317	0.146 ± 0.146	89.47	10.53
	520	1.250 ± 0.327	0.110 ± 0.107	91.88	8.12
	590	1.255 ± 0.334	0.082 ± 0.075	93.84	6.16
	660	1.261 ± 0.343	0.055 ± 0.054	95.83	4.17
	880	1.284 ± 0.354	-	100	0
	950	1.284 ± 0.355	-	100	0
1.4					
	370	1.341 ± 0.453	0.093 ± 0.200	93.51	6.49
	470	1.307 ± 0.407	0.074 ± 0.119	94.61	5.39
	520	1.308 ± 0.403	0.051 ± 0.088	96.28	3.72
	590	1.300 ± 0.392	0.037 ± 0.064	97.23	2.77
	660	1.293 ± 0.385	0.023 ± 0.049	98.25	1.75
	880	1.284 ± 0.354	-	100	0
	950	1.284 ± 0.355	-	100	0

Cold period

AAE	λ (nm)	$E_{abs,int}$	$E_{abs,ext}$	% $E_{abs,int}$	% $E_{abs,ext}$
0.8					
	370	1.231 ± 0.324	0.420 ± 0.268	74.56	25.44
	470	1.240 ± 0.336	0.283 ± 0.165	81.40	18.60
	520	1.250 ± 0.351	0.211 ± 0.126	85.58	14.42
	590	1.262 ± 0.368	0.158 ± 0.093	88.90	11.10
	660	1.274 ± 0.385	0.112 ± 0.066	91.91	8.09
	880	1.326 ± 0.420	-	100	0
	950	1.323 ± 0.421	-	100	0
1					
	370	1.275 ± 0.385	0.363 ± 0.225	77.81	22.19
	470	1.272 ± 0.381	0.243 ± 0.128	83.98	16.02
	520	1.278 ± 0.390	0.182 ± 0.095	87.55	12.45
	590	1.284 ± 0.398	0.132 ± 0.068	90.65	9.35
	660	1.290 ± 0.407	0.093 ± 0.049	93.27	6.73
	880	1.326 ± 0.420	-	100	0
	950	1.323 ± 0.421	-	100	0
1.4					
	370	1.388 ± 0.545	0.217 ± 0.172	86.50	13.50
	470	1.349 ± 0.490	0.148 ± 0.085	90.09	9.91
	520	1.343 ± 0.481	0.106 ± 0.066	92.72	7.28
	590	1.333 ± 0.468	0.075 ± 0.050	94.65	5.35
	660	1.326 ± 0.457	0.053 ± 0.041	96.17	3.83
	880	1.326 ± 0.420	-	100	0
	950	1.323 ± 0.421	-	100	0

Warm period

AAE	λ (nm)	$E_{abs,int}$	$E_{abs,ext}$	% $E_{abs,int}$	% $E_{abs,ext}$
0.8					
	370	1.182 ± 0.202	0.120 ± 0.186	90.75	9.25
	470	1.189 ± 0.210	0.088 ± 0.109	93.08	6.92
	520	1.203 ± 0.226	0.073 ± 0.086	94.31	5.69
	590	1.214 ± 0.238	0.058 ± 0.061	95.42	4.58
	660	1.227 ± 0.253	0.037 ± 0.040	97.10	2.90
	880	1.249 ± 0.271	-	100	0
	950	1.251 ± 0.271	-	100	0
1					
	370	1.216 ± 0.240	0.088 ± 0.166	93.24	6.76
	470	1.215 ± 0.238	0.065 ± 0.095	94.93	5.07
	520	1.226 ± 0.251	0.052 ± 0.072	95.94	4.06
	590	1.232 ± 0.258	0.041 ± 0.050	96.77	3.23
	660	1.241 ± 0.268	0.026 ± 0.032	97.95	2.05

	880	1.249 ± 0.271	-	100	0
	950	1.251 ± 0.271	-	100	0
1.4					
	370	1.305 ± 0.339	0.012 ± 0.153	99.05	0.95
	470	1.276 ± 0.306	0.011 ± 0.092	99.16	0.84
	520	1.279 ± 0.310	0.004 ± 0.069	99.69	0.31
	590	1.272 ± 0.302	0.005 ± 0.051	99.65	0.35
	660	1.270 ± 0.300	-0.001 ± 0.037	100.086	-0.086
	880	1.249 ± 0.271	-	100	0
	950	1.251 ± 0.271	-	100	0

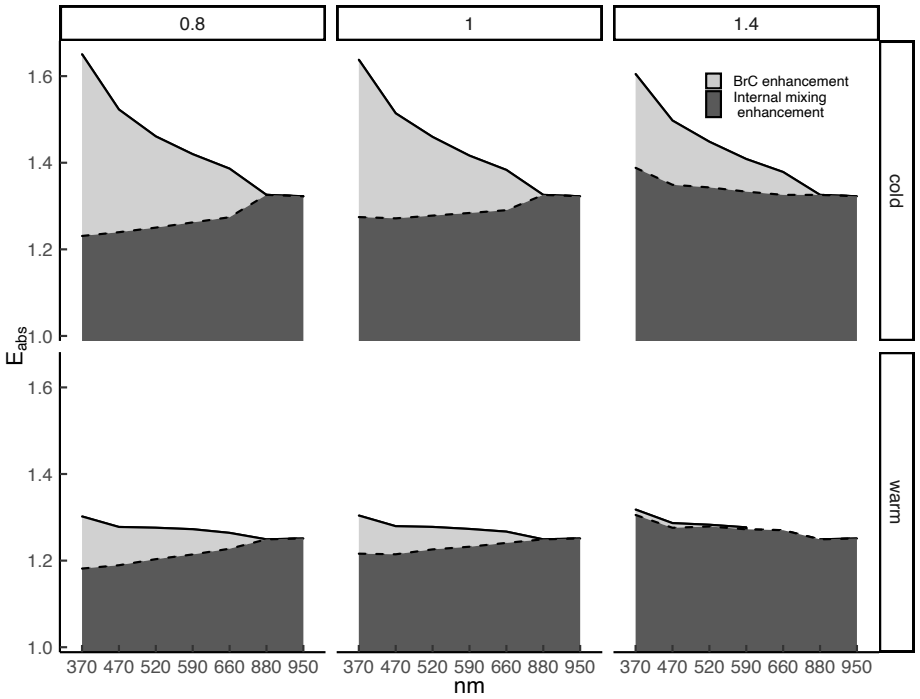

Figure S11: Absorption enhancement, E_{abs}, attribution to both internal and external mixing for both the cold and warm period under different AAE conditions for the internally mixed BC (0.8,1,1.4) for the online measurements at the 7-AE33 wavelengths at Barcelona (BCN).

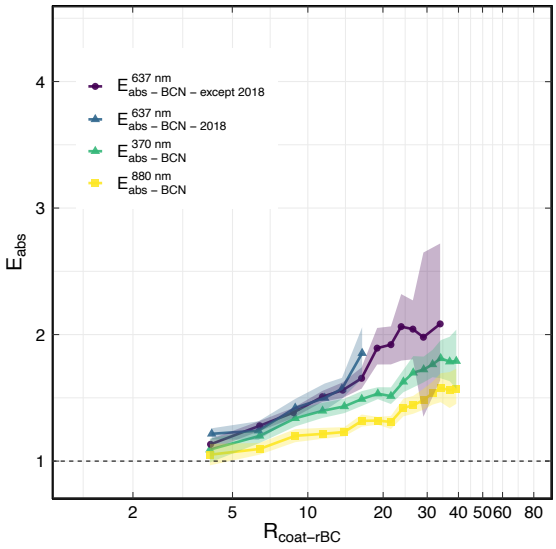

Figure S12: Absorption enhancement, E_{abs}, as a function of the non-refractory PM to EC ratio at BCN station. As in Fig. 3 but omitting the E_{abs} for MSY and showing the values of E_{abs} obtained offline for the MAAP just for 2018 and for all the years except 2018; showcasing the large inter-annual variability.

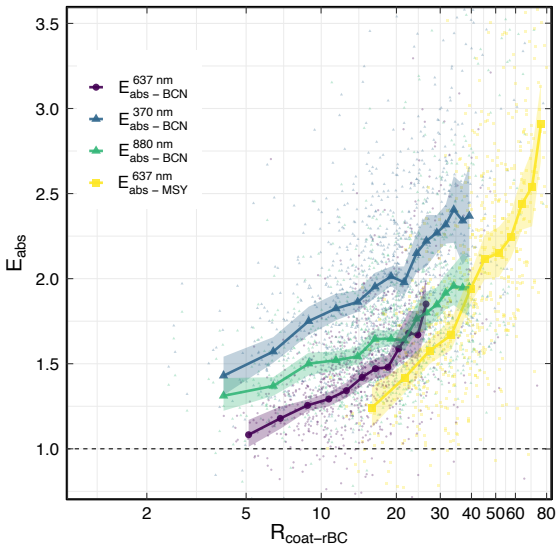

Figure S13: Absorption enhancement, E_{abs}, as a function of the non-refractory PM to EC ratio for BCN and MSY station. As in Fig. 3 but using as a reference MAC the theoretical value provided by Bond et al. (2006) and extrapolating to 370 and 880 nm for the AE33 and online OC:EC and to 637 nm for the MAAP and offline OC:EC.

Table S2: VIF (Variance Inflation Factor) between the independent variables of the multi-linear regression analysis, i.e. the chemical species obtained with the Q-ACSM, and a test of the statistical significance using the p-value of each coefficient (*: p<0.05,**<0.01,***<0.001).

	Cold period		Warm period	
	VIF	**p-value**	**VIF**	**p-value**
Intercept	-	***	-	***
HOA-to-EC	1.405	*	1.132	*
BBOA-to-EC	2.247	**	-	-
MO.OOA-to-EC	6.045	*	3.015	
LO.OOA-to-EC	1.385	*	1.827	
SO4-to-EC	2.215		1.913	*
NO3-to-EC	3.315		1.207	***
COA-to-EC	1.179	**	1.515	*

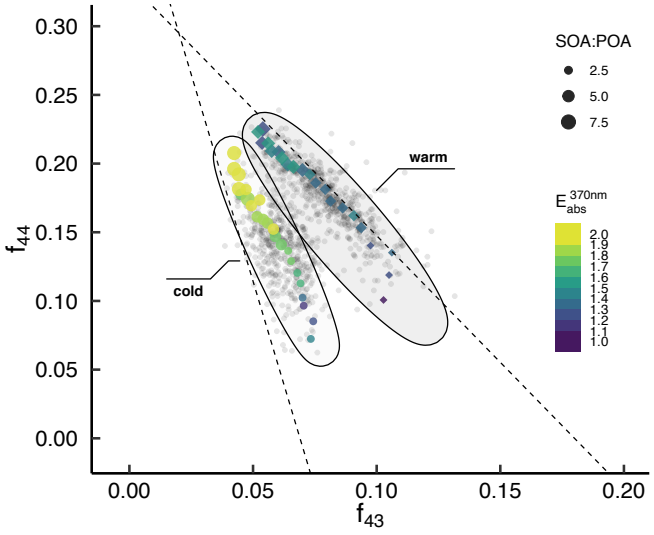

Fig. S14: Absorption enhancement, E_{abs}, at 370 nm at BCN using online measurements as a function of the primary to secondary organic aerosol ratio (POA/SOA), and the atmospheric aging (following Ng. et al., 2010 proposed triangle plot, f_{44} vs f_{43}). The $f_{44}$and f_{43} factors used are the ones presented by Via et al. (2021) for the same time period from the Q-ACSM measurements.

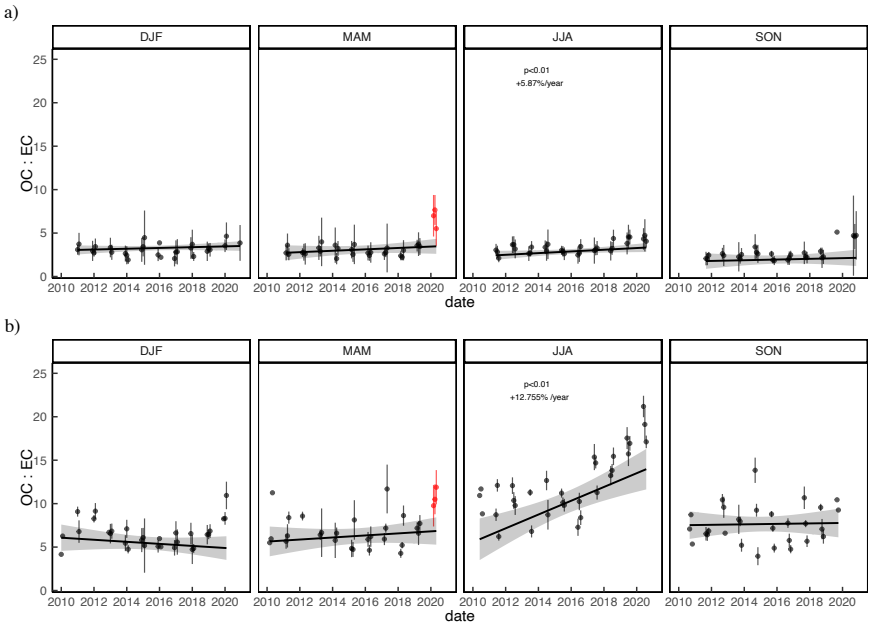

Fig. S15: Seasonal trends of the OC-EC ratio in a) BCN between 2011 and 2020, and b) MSY between 2010 and 2020. COVID-19 lockdown period is marked by the red dots.

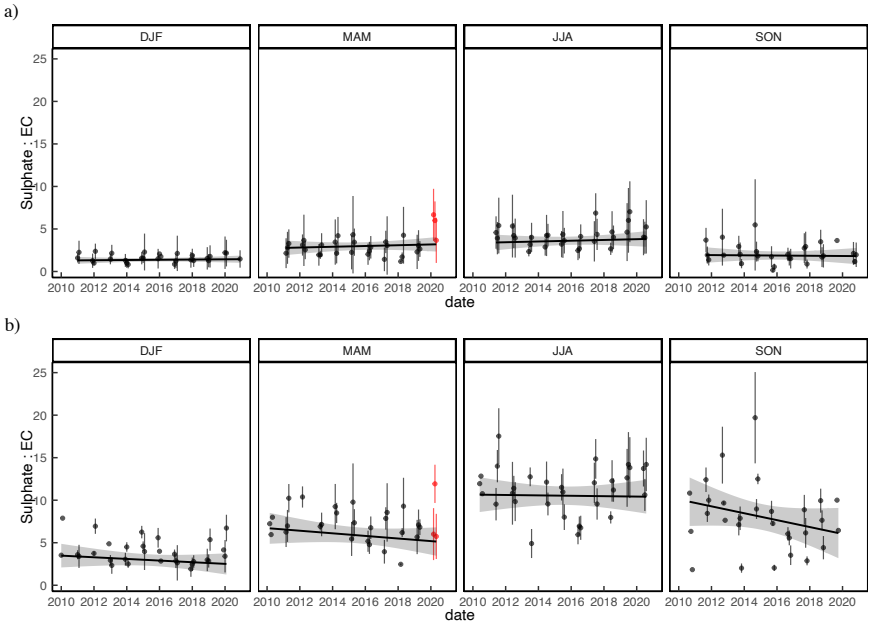

Fig. S16: Seasonal trends of the Sulphate-EC ratio in a) BCN between 2011 and 2020, and b) MSY between 2010 and 2020. COVID-19 lockdown period is marked by the red dots.

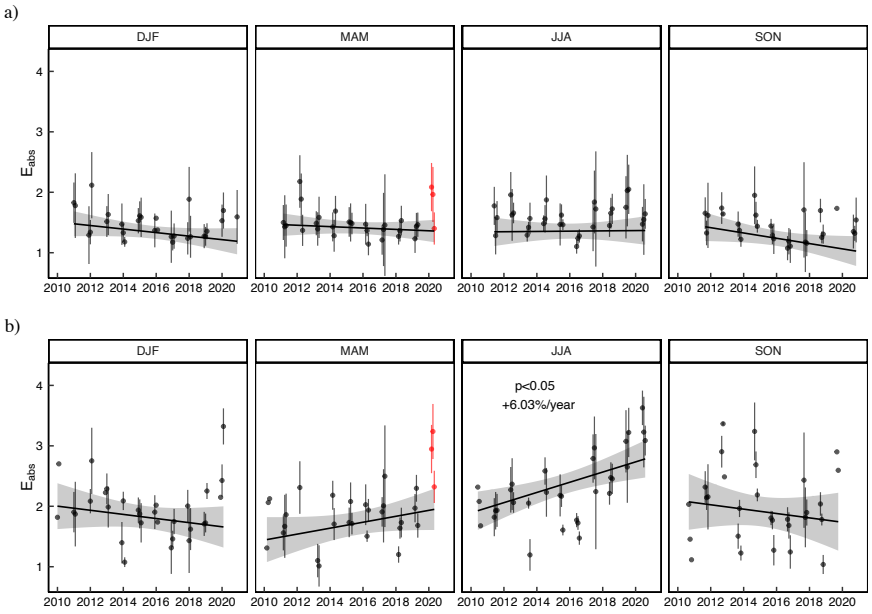

Fig. S17: Absorption enhancement, E_{abs} at 637 nm seasonal trend analysis between 2011 and 2020 at a) Barcelona and b) Montseny station. The trend analysis was performed using a Theil-Sen function over the E_{abs} offline measurements using a theoretical reference MAC (Bond et al., 2006). Dust influenced measurements were excluded. COVID-19 lockdown period is marked by the red dots.

8

MINERAL DUST PROPERTIES AT AN EMISSION AREA

Objective

Obtain the optical properties of the mineral dust particles in the most important mineral dust source region, the Sahara desert. Given the high uncertainty regarding the radiative forcing effect on climate of mineral dust, it is key to correctly characterize their optical properties, which are highly dependent on their particle size distribution, and mineralogical composition. Here, the optical properties have been analyzed upon the strength of the emission processes, which ultimately determines the particle size distribution of the emitted mineral dust particles.

Methodology

- Perform an intensive measurement campaign in a mineral dust emission area in the outskirts in the Sahara desert.
- Perform measurements with a high temporal resolution instrumentation to fully characterize the optical properties, particle size distribution and meteorological variables.
- Correct and pre-process the data from the online instrumentation to account for the peculiarities of the mineral dust particles.
- Analyze the optical properties, both extensive and intensive, for the different types of events affecting the area of study upon the particle composition and the strength of the emission processes, as determined by the friction velocity.

Results

- Overall, the extensive optical properties and the particle mass concentration showed very low background concentrations, with large increases during the mineral dust emission events.

- Similar intensive optical values to those obtained in the literature were measured during the local saltation and the regional advection of mineral dust into the measurement site, with the presence of very coarse particles and a large spectral dependency of the absorption coefficients. During periods with a higher relative contribution of local anthropogenic particles, the measured aerosol particles showed lower absorption wavelength dependence and the presence of finer particles.
- As the friction velocity increased, i.e. the emission strength, the intensive optical values converged towards typical values of mineral dust particles, with AAE around 2.5, SAEs around 0 and negative SSAAE values. Conversely, the mass absorption, scattering and extinction decreased, since the relative contribution of the more local anthropogenic aerosol particles decreased.
- The increase of the emission strength showed a clear increase in the size of the particles, as the effective radius and asymmetry parameter increased, and the backscatter fraction decreased.

Conclusions

- Mineral dust particles can present very high absorption coefficients under large emission events throughout the whole spectrum, especially at the short-UV, where the absorption presented a very high increase.
- Clear relationship between the strength of the emission processes and the relative contribution of coarse mineral dust particles to the overall aerosol particles, with intensive optical properties closer to those found in chamber studies with soil samples from the Sahara.

Publication

- The study presented in this chapter is in preparation to be submitted on a scientific peer-reviewed journal.

Quantifying variations in multi-wavelength optical properties of freshly-emitted Saharan dust from the Lower Drâa Valley, Moroccan Sahara

Jesús Yus-Díez[1,2], Marco Pandolfi[1], Andrés Alastuey[1], Cristina González-Flórez[3], Jeronimo Escribano[3], Adolfo Gonzalez-Romero[3], Matic Ivančič[4], Martin Rigler[4], Martina Klose[3,5], Konrad Kandler[6], Agnesh Panta[6], Xavier Querol[1], Cristina Reche[1], and Carlos Perez García-Pando[3,7]

[1]Institute of Environmental Assessment and Water Research (IDAEA-CSIC), Barcelona, 08034, Spain
[2]Grup de Meteorologia, Departament de Física Aplicada, Universitat de Barcelona, C/Martí i Franquès, 1, 08028, Barcelona, Spain
[3]Barcelona Supercomputing Center (BSC), Barcelona, 08034, Spain
[4]Aerosol d.o.o., Ljubljana, Slovenia
[5]Karlsruhe Institute of Technology (KIT), Institute of Meteorology and Climate Research (IMK-TRO)
[6]Technical University Darmstadt (TUDa), Darmstadt, Germany
[7]ICREA, Catalan Institution for Research and Advanced Studies, Barcelona, 08010, Spain

Abstract.

In-situ optical properties of mineral dust particles have been obtained at the Sahara desert during the FRAGMENT-Morocco field-measurement campaign (September 2019). The measurements were performed sequentially for two different size ranges, $PM_{2.5}$ and PM_{10}.

Under large dust emission scenarios, as a consequence of the larger relative proportion of mineral dust particles and the increase in the coarse fraction, as shown by the increase in the friction velocity and the effective radius of the particles, we observed that the optical values converged towards values previously measured for Moroccan mineral dust during the $PM_{2.5}$(PM_{10}) period: albedo (SSA) of around 0.95(0.87) at 370 nm, and 0.97(0.96) at 660 nm, an asymmetry parameter, g, and BF around 0.7 and 0.10 at 525 nm, respectively, an absorption ångström exponent (AAE) of 2.5, effective radius of 1.2, negative ångström exponent (SAE) and SSA ångström exponent (SSAAE).

1 Introduction

Mineral dust is one of the most abundant aerosol types by mass (Myhre et al., 2013) and impacts the Earth's climate directly by absorbing and scattering solar and terrestrial radiation, semi-directly by increasing the evaporation of cloud droplets, and indirectly through its impacts on aerosol-cloud formation, the cryosphere, and the atmospheric and biological chemistry (Engelstaedter et al., 2006; Choobari et al., 2014). The interaction of mineral dust with radiation has been subject to thorough analysis (Sokolik and Toon, 1999; Lafon et al., 2006), yet, its complexity prevents from establishing whether dust aerosols either cool or warm the atmosphere (e.g. Kok et al., 2017; Di Biagio et al., 2020; Adebiyi and Kok, 2020; Li et al., 2021). The major uncertainties on the direct radiative effect by dust particles rise from the measurement uncertainties, the sample source variability of the mineral dust particle size distribution, mass concentration, particle shape and mineralogical composition, and the vertical distribution.

Saharan dust emission areas are the major source of mid-latitude atmospheric mineral dust particles, emitting around 50 % of the global dust load with an average yearly emission of 11.5 Tg (Kok et al., 2021b). Mineral dust particles are emitted into the atmosphere following three main processes: a) direct aerodynamic entrainment when particles are loose enough so that a strong enough wind force can lift them from the ground, b) saltation bombardment from sand particles or aggregates striking the surface and producing dust emission, and c) disaggregation of mineral particles from either soil aggregates or dust coated sand particles (Shao, 2008). Saharan dust particles can undergo long-range transport, from Northern Africa to southern Europe and the Mediterranean, and

over the Atlantic into south America and the Caribbean (Engelstaedter et al., 2006). This long-range transport implies an effect by the dust particles on the radiative balance of the atmosphere not only close to the source regions, but also in much larger areas. Thus, a better understanding of the emission processes for the entrainment of mineral dust into the atmosphere is paramount for a correct quantification of the mineral dust concentration in the atmosphere. Moreover, a precise characterization of the optical properties of mineral dust is necessary for assessing the influence on the radiative balance that this particles exert.

The amount of radiation scattered and absorbed by the dust particles is determined by the real and imaginary part of the particles complex refractive index (CRI). The real part of the CRI mainly determines the scattering properties of a particle, and the imaginary part of the refractive index, mainly accounts for the absorption properties of the dust particles, although for the scattering too, since for a given extinction coefficient a larger imaginary part will imply a larger absorption and thus a smaller scattering coefficient. Both real and imaginary refractive parts of the CRI of dust particles are determined by the particle composition, i.e. mineralogical composition, their internal mixing state and geometry. Iron oxides, especially goethite and hematite, have been identified as the main absorbing compounds of the dust particles, whereas other studies have shown that the relative fraction of total iron in dust particles regulates the amount of radiation absorbed by dust (Sokolik and Toon, 1999; Lafon et al., 2006; Balkanski et al., 2007; Caponi et al., 2017; Di Biagio et al., 2019). The spectral behaviour of the imaginary refractive indexes for these iron-oxides compounds presents an increase towards the short-UV wavelengths compared to the red and near-infrared wavelengths (e.g. Sokolik and Toon, 1999; Balkanski et al., 2007). As a consequence of this higher UV refractive index for these iron-oxides compounds, the refractive index of the mineral dust particles can also present this spectral behaviour with an increased absorption efficiency towards the short-UV wavelengths (Schladitz et al., 2009; Di Biagio et al., 2019). Therefore, to constrain the mineral dust refractive index, it is needed to assess the spectral behaviour of the absorption and scattering of light radiation from the mineral dust particles, for each mineral compound and the relative proportion of each mineral for the different mineral dust sources (Choobari et al., 2014; Kok et al., 2017; Li et al., 2021).

Given the relevance of mineral dust particles in the overall particle composition of the atmosphere, it is key to provide the climate models with a proper characterization of the influence that mineral dust exerts on the atmospheric radiative balance. With this aim, many studies focused on the influence of different mineralogical compositions and particle size distributions of dust from different source regions on the mineral dust optical properties, such as the single scattering albedo, mass extinction efficiency, asymmetry parameter, etc., for obtaining the refractive index (e.g. Schladitz et al., 2009; Caponi et al., 2017; Di Biagio et al., 2019). Moreover, the processes responsible for the emission of dust particles, as well as their transport and deposition are also the topic of many analysis since these processes determine the amount of mineral dust particles, the particle number and mass size distribution, and the lifetime of mineral dust in the atmosphere. There are multiple approaches to study the mineral dust influence on the radiative balance: i) laboratory-chamber measurements of soil samples from different emission sources, ii) in-situ surface, airborne, and remote measurements, and iii) modelling simulations based on bibliographic measurements coupled with remote and in-situ observations. Numerous mineral dust soil sampling field campaigns have been carried out in main emission areas, such as the Sahara, the Sahel, the Arabian Peninsula, and some Asian and Australian areas (Claquin et al., 1999; Kandler et al., 2009; Di Biagio et al., 2019). These soils samples were subsequently re-suspended in laboratory chambers and different physic-chemical measurements were performed (e.g. Di Biagio et al., 2017, 2019). Moreover, although scarce, some in-situ surface measurements of the particles size distribution and the optical properties of dust have been carried out in the emission areas, such as during the SAMUM-1 field-campaign (Kandler et al., 2009; Müller et al., 2009; Schladitz et al., 2009). Finally, modelization studies analyze the effect of mineral dust on the Earth system by incorporating both observations of dust aerosol optical depth, measured particle size distributions, mineralogy composition and other constrains with the aim of obtaining a more accurate result and reducing the uncertainties around the effect of mineral dust on the climate radiative budget (e.g. Kok et al., 2017; Di Biagio et al., 2020; Adebiyi and Kok, 2020; Huang et al., 2020; Kok et al., 2021a; Li et al., 2021).

With the objective of closing the gap in relationship with the emission processes and better characterize the properties of the emitted dust particles, we performed a field measurement campaign in the Saharan desert in Morocco in September 2019 in the framework of the project FRontiers in dust minerAloGical coMposition and its Effects upoN climaTe (FRAGMENT; https://cordis.europa.eu/project/rcn/214076/factsheet/en). The main objectives of the FRAGMENT field campaign were to characterize the size-resolved mineralogical composition of the freshly emitted dust particles over multiple source regions of dust on Earth, the emission processes that lead to dust emission into the lower troposphere, measuring its optical properties, and the surface radiation effect of freshly emitted dust particles.

Here we present the multi-wavelength optical extensive and intensive properties of freshly emitted dust at the L'Bour area during the FRAGMENT-Morocco field-measurement campaign and its relationships with the strength of the dust emission processes. From the multi-wavelength extensive optical measurements (absorption and scattering) we obtained the intensive aerosol particles optical properties, such as the single-scattering albedo (SSA), the asymmetry param-

eter (g), the backscatter fraction (BF) and the scattering, absorption and extinction efficiencies of dust at several wavelengths (MSC, MAE and MEE). The manuscript is structured such that Sect. 2 presents the measurement area, the used instruments and briefly describes the optical properties used through-out the study and its implications for mineral dust. Sect. 3 describes an array of the main optical properties through-out the measurement campaign and its relationship with the emission strength at the site and the size of the measured particles.

2 Methodology

2.1 Measurement site

In-situ dust measurements were performed in a mineral dust emission area in SE Morocco, at the border between the southern foothills of the Atlas mountain range and the Saharan desert. The area of study is located in L'Bour, which is characterized by a small terminal depression close to the the Drâa dry-river bed west of M'Hammid El Gizlane, and east a dry-lake, Lake Iriki, and two dune fields, Erg Cheggaga and Erg Smar (see Fig. 1). L'Bour site presented mostly a hard packed surface with crusts products of wind and dust erosion, as well as a surrounding of shallow sand dunes (a height < 1 m).

2.2 Optical properties measurements

Multi-wavelength aerosol absorption coefficients, b_{abs}^{λ}, were derived using an AE33 multi-wavelength dual-spot aethalometer (Magee Scientific, Aerosol d.o.o. Drinovec et al., 2015). The AE33 measures light attenuation at 7 different wavelengths (λ) between the short-UV and the near-infrared (370, 470, 520, 590, 660, 880, and 950 nm). The AE33 software then derives the absorption coefficients by applying eq. (17) from Drinovec et al. (2015), and performs an online correction for the filter loading effects. In order to obtain the absorption coefficients from AE33 measurements, the attenuation measurements were further corrected taking into account the multiple-scattering of light within the filter-tape. In fact, this multiple-scattering parameter, C, has been shown to present higher values for aerosol particles with high SSA values, such as mineral dust particles, in comparison with the typical C value found for conventional urban and regional background sites (e.g. Di Biagio et al., 2017; Yus-Díez et al., 2021). Given that the measurements were performed in an environment mainly characterized by dust particles, we used a C value obtained by performing an iterative approach to the SSA and the C as recommended in Yus-Díez et al. (2021), using the fitted values provided therein for the mountain-top station and also its spectral dependence highly affected by mineral dust particles during Saharan dust outbreaks. This method which yield a C of 4.44 at 370 nm, 4.78 at 660 nm and 5.04 at 880 nm.

Scattering coefficients (b_{scat}) were measured with a LED-based integrating nephelometer (Aurora 4000, ECOTECH Pty Ltd, Knoxfield, Australia) operating at three wavelengths (450, 525 and 635 nm) and multiple angles (0°, 10°, 25°, 40°, 55°, 70°, 90°, and 180°). The scattering coefficients for the forward (0°) and backward (180°) scattering were corrected for non-ideal illumination of the light source and the truncation error by applying Müller et al. (2011) correction scheme for coarse particles.

The in-situ surface optical properties at the site of L'Bour were performed for $PM_{2.5}$ between the beginning of the campaign, 2019-09-04 00:00:00 UTC, and 2019-09-26 12:00:00 UTC. After that, measurements were performed with a PM_{10} cut-off.

2.3 Particle number size distribution measurements

Particle number size distribution (PNSD) measurements were performed with a fine dust aerosol spectrometer (FIDAS 200S, Palas Gmbh). The FIDAS deployed during the campaign measured the PNSD through out 61 bins in an optical diameter range of 0.20-17.8 µm, with a time resolution of 120 s and an inlet flow rate of 4.8 $\mathrm{l\,min^{-1}}$. Since the optical properties were performed using an aerodynamic inlet cut-off, and the OPC measurements report the particle size in optical diameters, we have converted the later to the former following Huang et al. (2020) by applying a factor of 1.46 to the FIDAS optical diameter. A deeper analysis of the site PNSD measurements and its implications for dust emission can be found in González-Flórez et al. (in prep.).

2.4 Meteorological measurements.

Here we have used wind measurements performed at a height of 2 m heights (roughly at the same height as the inlet head of the optical and particle size distribution measurements) through a 2-D sonic anemometer (model WINDSONIC4-L, Campbell Scientifics, USA) mounted on a 10 m meteorological tower. The anemometers were mounted pointing to the north. The wind friction velocity (u^*) was derived following an iterative procedure based on the law of the wall method. The measurements were performed with a frequency of 0.5 Hz and averaged during data processing to 15 min, so that the frequency is high enough to catch the air turbulence but not that high to mask it with noise.

2.5 Intensive aerosol optical properties

By combining the extensive optical properties obtained with the AE33 and the polar nephelometer, i.e. the absorption and scattering coefficients, with the PNSD measured with the FIDAS, we have been able to derive an array of intensive optical properties. These intensive optical properties depend on the physico-chemical properties of the dust particles as the mineralogy, the size distribution, the shape of the particle, etc (see Table 1). Hereafter we present a brief description of

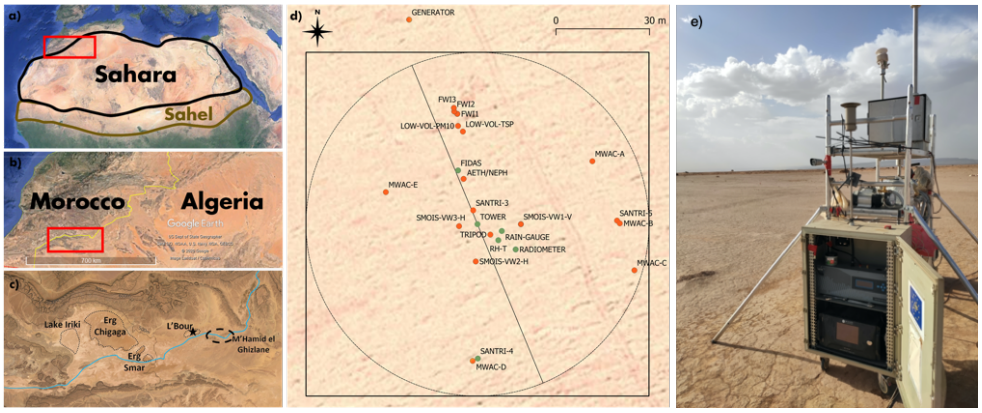

Figure 1. Area of study over a) Northern Africa, b) the instrument deployment over the L'Bour site, and c) optical instrumentation (c).

the calculated intensive optical properties and the equations used to derive them:

a. The Scattering Ångström Exponent (SAE) depends on the physical properties of aerosols, and mostly on the particle size. SAE values lower than one are associated with the presence of coarse particles, that can be associated to the emission of dust particles in L'Bour site, (Seinfeld and Pandis, 1998; Schuster et al., 2006). The SAE was calculated as linear fit in a log-log space using the scattering measurements at the three wavelengths.

b. The Absorption Ångström Exponent (AAE) depends mostly on the chemical composition of the sample particles. In highly anthropogenic backgrounds typical AAE values range between 0.9 and 1.1 (Kirchstetter et al., 2004; Petzold et al., 2013). However, under scenarios where mineral dust outbreaks affects the measurements, the AAE increases and values between 2 and 6.5 have been observed (Schuster et al., 2016; Caponi et al., 2017). This increase of AAE values is due to the higher absorption efficiency of the dust particles in the short-UV region of the spectrum compared to the near-IR (Kirchstetter et al., 2004; Chen and Bond, 2010). This disparity in the absorption efficiency of the dust particles is caused by the higher imaginary refractive index at shorter wavelengths of iron oxide containing particles as goethite (e.g. Müller et al., 2009; Schladitz et al., 2009; Schuster et al., 2006). The AAE was calculated as linear estimation in the log-log space using the multi-wavelength absorption measurements from AE33.

c. The Single Scattering Albedo (SSA) is one of the most relevant parameters for climate models since it indicates the potential of aerosols for cooling or warming the atmosphere. SSA values for Saharan dust have been found to range between 0.92 at 370 nm and 0.98 at 880 nm (Di Biagio et al., 2019), and between 0.9 and 0.96 at the green wavelengths depending on the estimated dust iron content (Claquin et al., 1999; Schladitz et al., 2009). SSA has been obtained as the ratio between the scattering and the extinction coefficients at all the AE33 wavelengths. This was achieved by extrapolating the scattering measurements at the polar nephelometer wavelengths to the AE33 wavelengths using the experimental SAE.

d. The Single Scattering Albedo Ångström Exponent (SSAAE) is used as an indicator for the presence of coarse particles (e.g. dust) when values are <0 (Collaud Coen et al., 2004; Ealo et al., 2016). SSAAE was calculated by fitting the SSA calculated at the 7 AE33 wavelengths in the log-log space.

e. The asymmetry parameter (g) represents the probability of radiation being scattered in a given direction. The range of values is $[-1, 1]$ for backward ($180°$) to forward ($0°$) scattering, respectively. Thus, for atmospheric particles positive values between 0.6-0.85 for dust particles are typically assumed in most climate models (Sokolik and Toon, 1999; Horvath et al., 2018; Ryder et al., 2018). Here we have obtained the g by calculating the phase function from the multi-angle measurements from the integrating nephelometer by assuming spherical isotropic particles (Liou, 2002; Horvath et al., 2018).

f. The Mass Absorption, Scattering, and Extinction efficiency (MAE, MSE, and MEE) represent the absorption, scattering, and extinction efficiency, respectively, of the collected particles per unit of mass and typical dust particle values around 0.32 $\mathrm{m^2\ g^{-1}}$ for the MEE have been reported (Ryder et al., 2018). The MAE, MSE and MEE were obtained as the ratio between the absorption, scattering, and extinction coefficients, respectively, and the mass concentration derived from the PNSD,

which given the location of the measurements site can be attributed exclusively to mineral dust.

3 Results

3.1 Field campaign measurements time evolution

Figure S1 shows the temporal evolution of the extensive and intensive optical properties, the mass concentration, the particles effective radius, the wind speed, and the friction velocity during the measurement campaign. As aforementioned, there were two distinct measurement periods with regards to the inlet cut-off: a first period with a $PM_{2.5}$ cut-off from the onset of the campaign up to the 26th of September, and a period with a PM_{10} cut-off period from then until the end of the campaign.

The evolution of b_{abs}, b_{scat} (Figs. S1a,b) and of the particle mass concentration (Fig. S1c), were correlated and showed a distinct behaviour, with periods characterized by very low values reflecting background conditions without dust emission and low concentration of particles, and periods with large values indicating large dust emission over the area (Fig. S1a,b,c). Similarly, the intensive optical properties (Figs. S1d,e,g) reflected the presence of either a background condition mostly dominated by few coarse dust particles (AAE between 1.5 and 2.0, SAE<1, and SSAAE<0) under calm wind conditions, and the presence of dust emission processes, with AAE values above 2, up to 3.5, negative SAE values, and a decrease in the SSAAE values. Moreover, during dust formation/resuspension g showed higher values, around 0.66-0.70, and lower BF values, around 0.10-0.12, associated to a larger relative proportion of coarser particles. In addition, there were sporadic periods with very low mineral dust particles that reflected a higher influence by anthropogenic emissions, as the period between the 7th and the 11th of September. This period was characterized by overall very low absorption and scattering values, indicating that this anthropogenic emissions were not that high, with intensive properties showing values of AAE close to 1, SAE>1, and SSAAE>0.

As aforementioned, we observed three distinct type of scenarios during the campaign that are described with more details below. These scenarios can be described as follow: local dust emission period (21st of September, Period A, Fig. 2a), regional advected dust period (also referred to as Haboob) plus the co-emitted local dust (6th of September, Period B, Fig. 2b), and anthropogenic pollution advection period mixed with some minor local dust emissions (between the 7th and the 10th of September, Period C, Fig. 2c). Fig. S2 shows that the highest mass concentrations and effective radius, indicating the presence of coarser particles, were observed during Period B (regionally advected dust in addition to local dust emission). During this period the highest wind speeds and friction velocities were recorded, thus favouring the emission of dust particles (Shao, 2008). As expected, the second most important period with regards to the mineral dust concentrations with large effective radius was during the local dust emission period (Period A). As a consequence, the absorption and scattering coefficients during Period A and B were above the average of the campaign with $PM_{2.5}$ inlet cut-off, especially during Period B (Fig. S3). During Period C, when the largest relative contribution of anthropogenic particles and the lowest dust emission were observed, the mass absorption efficiency had the largest values with values of around 0.045 at 370 nm, and of 0.014 $\mathrm{m^2\ g^{-1}}$ at 880 nm, whereas for the dust emission periods, the values were around 0.028-0.030 at 370 nm, and of 0.004 $\mathrm{m^2\ g^{-1}}$ at 880 nm, an (see Table 2). Similarly, the mass scattering efficiency (Fig. S4b) was also the highest for the Period C, with the lower values for the stronger dust emission periods (A and B). The mass extinction efficiency, mainly driven by the scattering, presented the same pattern, with a more acute difference between the different periods (Fig. S4c). With regards to the intensive optical properties, Fig. S5-S6 and Table 2 show the prevalence of coarse (SAE<0) particles during periods A and B, with an increased forward scattering (g>0.65 and BF<0.125). The g and BF increased and decreased, respectively, with increasing wavelength (see also Fig. S5) . Moreover, Figure 5a shows that dust particles during A and B were more absorbing at the short-UV (lower SSA) than for the rest of events, yet as the wavelength increased towards the near-infrared, they became the highest, whereas for Period C the SSA became the lowest for the longer wavelengths due to the presence of anthropogenic particles. This contrasting spectral behaviour of the SSA for the Periods A and B vs Period C is a consequence of the absorption decrease of the iron-oxides refractive index with the wavelength for the former, and the presence of anthropogenic particles that do not present this decrease for the latter. This spectral behaviour of the absorption with higher absorption values for the shorter wavelengths for the dust emission periods A and B was also reflected in the AAE, with values above 2, and the SSAAE, which presented negative values, whereas for period C the AAE is closer to 1 and the SSAAE if closer to 0.

The similitude of period A and the campaign average values (cf. Table 2) shows the prevalence of this type of process for the emission of dust, yet the presence of events like the one recorded during Period B are also of interest, since these events produce large entrainments of mineral dust into the troposphere and can have larger effects on the radiative budget (Bukowski and van den Heever, 2021). Moreover, Period C shows that even in remote isolated sites the measurements can also be affected by regional and local anthropogenic pollution, as also detected during SAMUM-1 (Müller et al., 2009), which should be taken into account when analyzing the optical properties and its attribution solely to mineral dust.

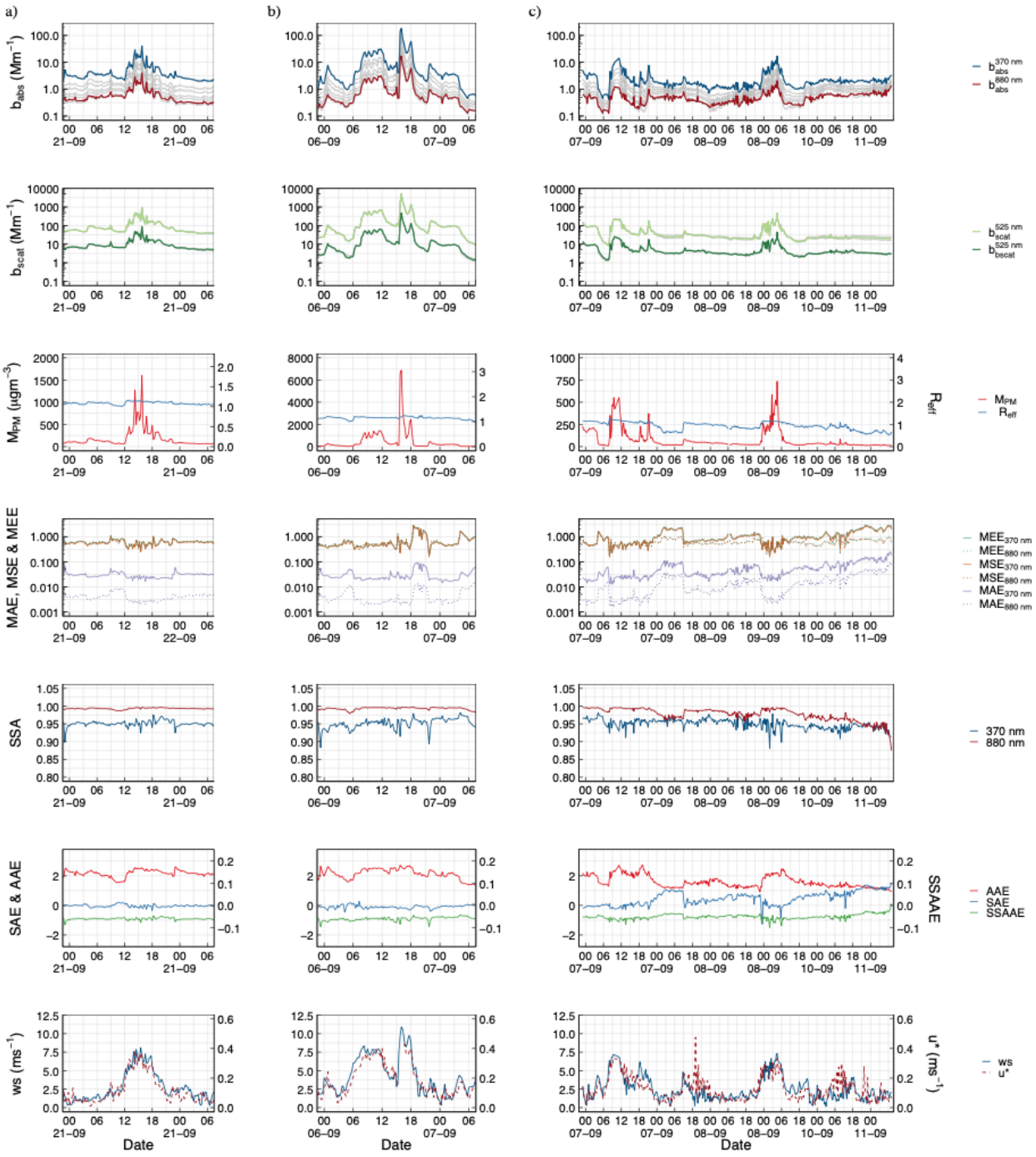

Figure 2. Time evolution during the highlighted periods of the measurement for a) Period A (between midnight 21st and morning 22nd September 2019), b) Period B (between midnight 6th and morning 7th September 2019), and c) Period C (between midnight 7th and noon 11st of September 2019) for: the absorption coefficients at 370 and 880 nm, the forward and backward scattering at 525 nm, the single scattering albedo (SSA) at both 370 and 880 nm, the scattering, absorption, mass extinction efficiency and SSA Ångström Exponent (AAE, SAE, MEEAE, SSAAE), the mass absorption, scattering and extinction efficiency (MAE, MSE, MEE), the Mass concentration and the particle effective radius extensive and intensive optical properties, as well as the mass concentration and the particles effective radius, the asymmetry parameter and the backscatter fraction (g, BF), and h) the wind speed and friction velocity (u^*).

Table 1. Parameters, instrumentation and method of derivation of the optical extensive parameters, particle number size distribution measurements and its derived moments, and the derived intensive optical properties used through-out this study for the different periods $PM_{2.5}$ and PM_{10}. In this table, r represents the particle radius and r_x the radius for both $r_{Pm2.5}$ and r_{PM10}, depending on the particle size range associated to each measurement period.

Parameters	Symbol	Range	Method
		Optical Extensive Measurements	
Absorption	b_{abs}	λ = 370, 470, 520, 590, 660, 880, 950 nm	Dual-spot multiwavelength aethalometer (AE33)
Scattering	b_{scat}	λ = 450, 525, 635 nm θ = 0, 10, 25, 40, 55, 70, 90, 180 °	Multiwavelength integrating polar nephelometer (Aurora 4000)
		Particle Size Distributions Measurements	
Particle Number Size Distribution	N(r)	$r_{PM2.5}$ = 0.2 - 2.5 μm r_{PM10} = 0.2 - 10μm	Fine dust aerosol spectrometer (FIDAS)
Particle Mass Concentration	M_{PM}	$r_{PM2.5}$ = 0.2 - 2.5 μm r_{PM10} = 0.2 - 10μm	$M_{PM} = \rho \cdot \frac{\pi}{6} \cdot \int_{0.2}^{r_x} r^3 N(r) dr$
Effective Radius	R_{eff}	$r_{PM2.5}$ = 0.2 - 2.5 μm r_{PM10} = 0.2 - 10μm	$R_{eff} = \frac{\int_{0.2}^{r_x} r^3 N(r) dr}{\int_{0.2}^{r_x} r^2 N(r) dr}$
		Optical Intensive properties	
Mass Absorption Efficiency	MAE	λ = 370, 470, 520, 590, 660, 880, 950 nm	$MAE = \frac{b_{abs}}{M_{PM}}$
Mass Scattering Efficiency	MSE	λ = 450, 525, 635 nm	$MSE = \frac{b_{scat}}{M_{PM}}$
Mass Extinction Efficiency	MAE	λ = 370, 470, 520, 590, 660, 880, 950 nm	$MEE = \frac{b_{abs} + b_{scat}}{M_{PM}}$
Single Scattering Albedo	SSA	λ = 370, 470, 520, 590, 660, 880, 950 nm	$SSA = \frac{b_{scat}}{b_{abs} + b_{scat}}$
Absorption Ångström Exponent	AAE	λ = 370-to-950 nm	Fit in the log-log scale to: $\ln(b_{abs}(\lambda)) = -AAE \cdot \ln(\lambda) + \beta$
Scattering Ångström Exponent	SAE	λ = 450-to-635 nm	Fit in the log-log scale to: $\ln(b_{scat}(\lambda)) = -SAE \cdot \ln(\lambda) + \beta$
SSA Ångström Exponent	SSAAE	λ = 370-to-950 nm	Fit in the log-log scale to: $\ln(SSA(\lambda)) = -SSAAE \cdot \ln(\lambda) + \beta$
Backscatter fraction	BF	λ = 450, 525, 635 nm	$BF = \frac{b_{scat}(\theta = 90°)}{b_{scat}(theta = 0°)}$
Asymmetry parameter	g	λ = 450, 525, 635 nm	$g = \frac{1}{2} \int_{-1}^{1} P(\cos\theta) \cos\theta d\cos\theta$, where $P(\cos\theta)$ is the phase function

3.2 Optical properties dependence with the friction velocity

Here, we have separated the analysis of the different optical parameters upon the two main dominant wind directions and the intensity of the dust emission scenarios. To be able to perform such differentiation, we used the wind direction (wd) and friction velocity (u^*). The site was characterized by a bimodal wind distribution, with a northwestern to southeastern direction sector (NE, 330-150 °) and southeastern to

Table 2. Overall campaign and different specific periods (A,B,C) mean values and standard error of the of all the obtained parameters. The result is separated upon the different inlet-cut off periods: $PM_{2.5}$ and PM_{10}. The $PM_{2.5}$ period took place between 2019-09-04 00:00:00 UTC and 2019-09-26 12:00:00 UTC; and the PM_{10} period spanned from then to the end of the measurements, the 2019-09-04 00:00:00 UTC. The number of measurements (n) refers to the 15 min. averages used for the analysis on this study.

		$PM_{2.5}$				PM_{10}
	Units	**Average (n=2156)**	**Period A (n=96)**	**Period B (n=96)**	**Period C (n=379)**	**Average (n=464)**
$b_{abs,370}$	Mm^{-1}	4.92± 0.49	5.65± 0.58	14.75± 2.65	2.30± 0.10	4.84± 0.51
$b_{abs,880}$	Mm^{-1}	0.69± 0.05	0.70± 0.06	1.54± 0.25	0.47± 0.01	0.75± 0.05
$b_{scat,525}$	Mm^{-1}	101.68± 11.74	116.28± 12.47	320.22± 62.74	41.56± 2.32	94.56± 11.08
$b_{bscat,525}$	Mm^{-1}	10.72± 1.10	12.62± 1.17	30.92± 5.91	5.02± 0.21	12.59± 1.37
N	#	50.36± 2.90	55.20± 4.14	96.60± 15.56	37.39± 0.76	32.55± 2.33
M	$\mu g\ m^{-3}$	194.63± 21.36	222.90± 24.85	631.20± 112.00	76.58± 5.46	529.43± 65.10
R_{eff}	μm	1.007± 0.007	1.095± 0.004	1.161± 0.005	0.946± 0.008	2.448± 0.010
MAE_{370}	$m^2\ g^{-1}$	0.043± 0.001	0.028± 0.001	0.031± 0.002	0.05± 0.002	0.013± 0
MAE_{880}	$m^2\ g^{-1}$	0.010± 0	0.004± 0	0.004± 0	0.014± 0.001	0.002± 0
MSE_{525}	$m^2\ g^{-1}$	0.711± 0.015	0.574± 0.013	0.653± 0.051	0.762± 0.017	0.236± 0.003
MEE_{370}	$m^2\ g^{-1}$	0.877± 0.023	0.603± 0.015	0.669± 0.052	1.002± 0.029	0.234± 0.003
MEE_{880}	$m^2\ g^{-1}$	0.622± 0.011	0.596± 0.013	0.702± 0.053	0.608± 0.01	0.255± 0.004
SSA_{370}	–	0.951± 0.001	0.952± 0.001	0.949± 0.001	0.95± 0.001	0.935± 0.003
SSA_{880}	–	0.984± 0.001	0.993± 0	0.993± 0	0.979± 0.001	0.986± 0.003
AAE	–	1.81± 0.02	2.17± 0.03	2.26± 0.03	1.61± 0.02	1.85± 0.01
SAE	–	0.26± 0.018	-0.04± 0.01	-0.12± 0.01	0.43± 0.02	-0.17± 0.01
SSAAE	–	-0.033± 0.001	-0.040± 0.001	-0.043± 0.001	-0.029± 0.001	-0.061± 0.008
MEEAE	–	0.66± 0.02	0.37± 0.01	0.28± 0.01	0.84± 0.02	-0.07± 0.01
BF_{525}	–	0.127± 0.001	0.117± 0.001	0.102± 0.001	0.135± 0.001	0.14± 0.001
g_{525}	–	0.646± 0.002	0.673± 0.002	0.694± 0.002	0.627± 0.002	0.631± 0.001

northwestern sector (SW, 150-330 °) as the main directions and with the highest wind speed and wind friction velocity values (Fig. S7). By segregating the data into different wind directions we were able to isolate the dust emission events that were possibly affected by the advection of anthropogenic particles from the upstream nearby villages at the NE sector, as well as isolate the dust coming from more local sources and also from a more regional background, SW, (see Fig. 1). Moreover, since the forces that regulate the dust emission depend on the friction velocity (Shao, 2008), the separation upon wind friction velocities was performed following González-Flórez et al. (in prep.), by defining several u^* thresholds that allowed to differentiate between various intensity levels of dust emission. A u^* below 0.1 ms^{-1} was considered to showcase scenarios with absence of emission, between 0.1 and 0.2 ms^{-1} with negligible emission and the possibility of some deposition of dust; whereas as u^* increases above 0.2 ms^{-1} so it does the dust emission González-Flórez et al. (in prep.).

3.2.1 Absorption, scattering and extinction coefficients

The extensive optical properties, namely the absorption (b_{abs}) and scattering coefficients (b_{scat}), showed an increase of the values with u^*, especially for the wind sector less influenced by anthropogenic emissions (SW) and especially at the shortest wavelengths (Figure 3). Thus, since both b_{abs} and b_{scat} values are driven by the amount of particles, the observed increase in the coefficients was related to the increase in the number concentration of dust emitted.

During the $PM_{2.5}$ period, for a given wind friction velocity, the values of the absorption and scattering for the NE sector were larger than for the SW sector, except for the 2 highest u^* for the scattering. However, during the PM_{10} period, the NE sector did not present as many events with high u^* values, with the more intense emission processes for the SW sector. By comparing between the $PM_{2.5}$ and PM_{10} period, similar absorption and scattering values were observed for the lower u^*. However, during the PM_{10} period, for the highest u^* (> 0.3 ms^{-1}), as the dust emission increased the values were twice those observed during the $PM_{2.5}$ period.

3.2.2 Absorption and scattering Ångström exponents

Figure 4 shows that as u^* increased, the AAE increased up to values around 2.25-2.5, the SAE decreased, with its lowest values when the friction velocity was the highest. The trends in the AAE and SAE with increasing friction velocities associated with an increasing relative importance of the mineral dust particles in the aerosol mix. Moreover, the reduction in the standard error presented by both Ångström exponents was mainly associated with an increasing homogeneity in the

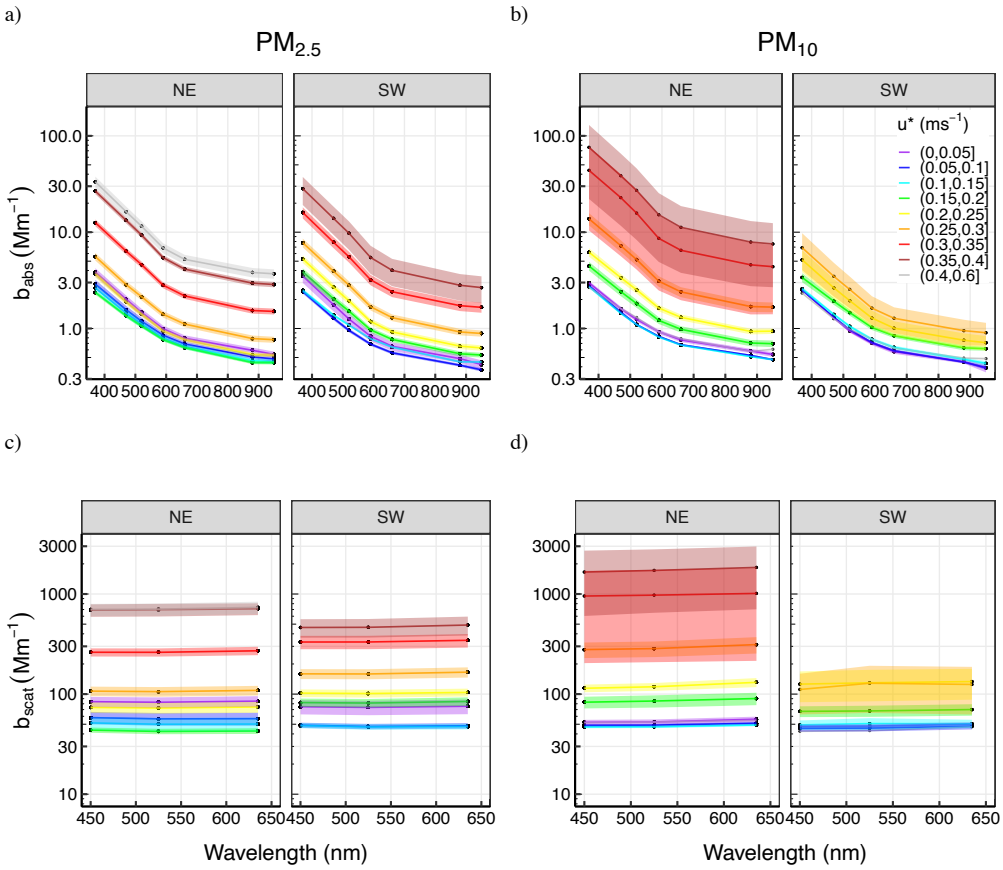

Figure 3. Multi-wavelength absorption (b_{abs}) and scattering (b_{scat}) coefficients, upper (a,b) and lower (c,d) panel, respectively, at M'Hammid separated by the two dominant wind sectors (NE and SW) and different levels of friction velocity (u^*) for both $PM_{2.5}$ (left panel) and PM_{10} (right panel) periods.

mineralogical and particle size distribution, which could also be attributed to the increasing relative importance of the mineral dust particles.

Median values separated upon wind sectors and friction velocity show as expected values associated with the presence of dust. AAE values above 1.5-2.0 implied a larger absorption efficiency at the short-UV range of wavelengths, that, in the area of study, was associated to the presence of iron oxides, within the emitted dust particles. Mineralogical analysis for the site (González-Romero et al., in prep.; Panta et al., in prep.) and nearby areas (Kandler et al., 2009) showed that a large proportion of iron oxides below 10 μm were due to iron-oxides, and could be classified as hematite-like, which have an increasing imaginary refractive index towards shorter submicrometric wavelengths (e.g. Sokolik and Toon, 1999; Lafon et al., 2006). Moreover, SAE values below 1 were found for almost all samples, reflecting a large relative proportion of coarse particles associated to the mineral dust particles, and that as u^* increased, the median SAE decreased below 0, reflecting an increase in the size of the particles (González-Flórez et al., in prep.).

Both AAE and SAE showed similar values and behaviour with the friction velocity, independently of the periods employed. The main differences between both cut-offs lays in the amount of measurements available, since the PM_{10} period lasted for fewer days (ca. 6 for PM_{10} vs 20 for PM2.5) and consequently fewer episodes with high friction velocity were recorded (see Fig. S1).

3.2.3 Mass absorption, scattering and extinction efficiency

Figure 5 shows the spectral behaviour of MAE, MSE and MEE under different u^*'s. As expected, MAE and MSE showed a similar spectral behaviour as the absorption and scattering coefficients (Figs. 3). The MAE (Figure 5a,b), independently of the used inlet cut-off, decreased with increas-

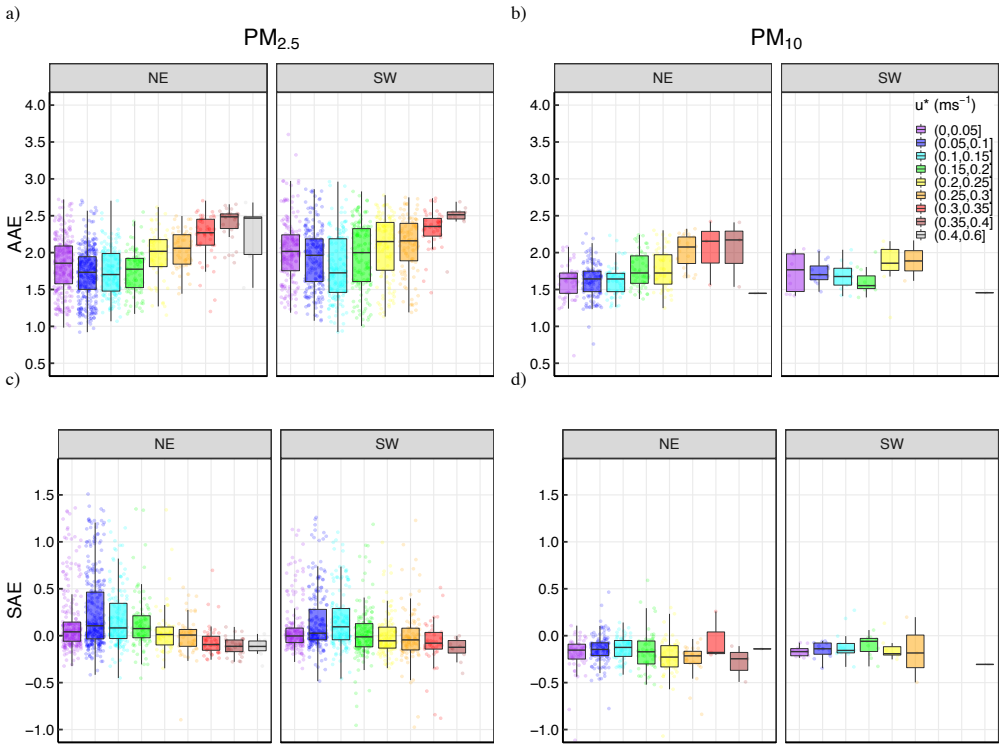

Figure 4. Boxplots of the absorption (upper panel) and scattering (lower panel) Ångström exponents at M'Hammid separated by the two dominant wind sectors (E-SW) and different levels of friction velocity (u^*) for both $PM_{2.5}$ (left panel) and PM_{10} (right panel) periods.

ing friction velocity. As already commented, Figure 3a,b shows an increase of the absorption coefficients with u^*, whereas Fig. 5a,b shows a decrease of the MAE with u^*. This behaviour can be associated to the larger absorption efficiency of the particles with an anthropogenic origin, which with a lower mass concentration can produce larger absorption coefficients. Therefore, as u^* increases, the MAE becomes closer to that of pure dust. MSE presents a similar behaviour to the MAE, although it presented larger variability. This larger variability of the MSE could be associated to the fact that the light scattering is mainly influenced by the size of the measured particles, with higher scattering efficiency for smaller particles compared to larger particles, with dust emission periods presenting both fine and coarse modes (González-Flórez et al., in prep.). The MEE (Fig. 5e,f) shows a similar pattern as the MSE one, which is to be expected given that MSE is around one order of magnitude larger than MAE.

For the scenarios with larger dust emission, the MEE values ranged between 0.5 and 0.6 for the $PM_{2.5}$, and between 0.05 and 0.2 for the PM_{10}. For the scenarios with a larger influence of the anthropogenic emissions the MEE ranged between 0.65 and 0.7, and between 0.2 and 0.3, for the $PM_{2.5}$ and PM_{10}, respectively. The MAE for PM2.5(PM10) values ranged between 0.008(0.005) and 0.02(0.008) at 880, and between 0.04(0.015) and 0.08(0.025) at 370 nm, which are slightly lower from the values of 0.015(0.016) at 880 nm and 0.107(0.099) from simulations chambers in Caponi et al. (2017).

3.2.4 Single-scattering albedo, asymmetry parameter and back-scatter fraction analysis

Here we present the single scattering albedo (SSA) and its spectral dependence (SSAAE). Overall, Figure 6 shows high values of SSA, ranging between 0.89 and 0.98, with higher values at the shorter wavelengths for the lower u^* episodes, and higher SSA values at the longest wavelengths during episodes with higher u^* values. This inversion with the u^* was mainly due to the fact that when larger dust emission takes place, the relative proportion of dust, and hence of the iron-oxides content, increased. As a consequence, the absorption at the shorter wavelengths increased, as shown in the AAE behaviour in Fig. 4. The dependency with the wavelength is distinctly shown in Fig. 6c,d, where SSAAE presented mostly negative values, especially for the highest u^* speeds, where the dispersion, and mean values were lower.

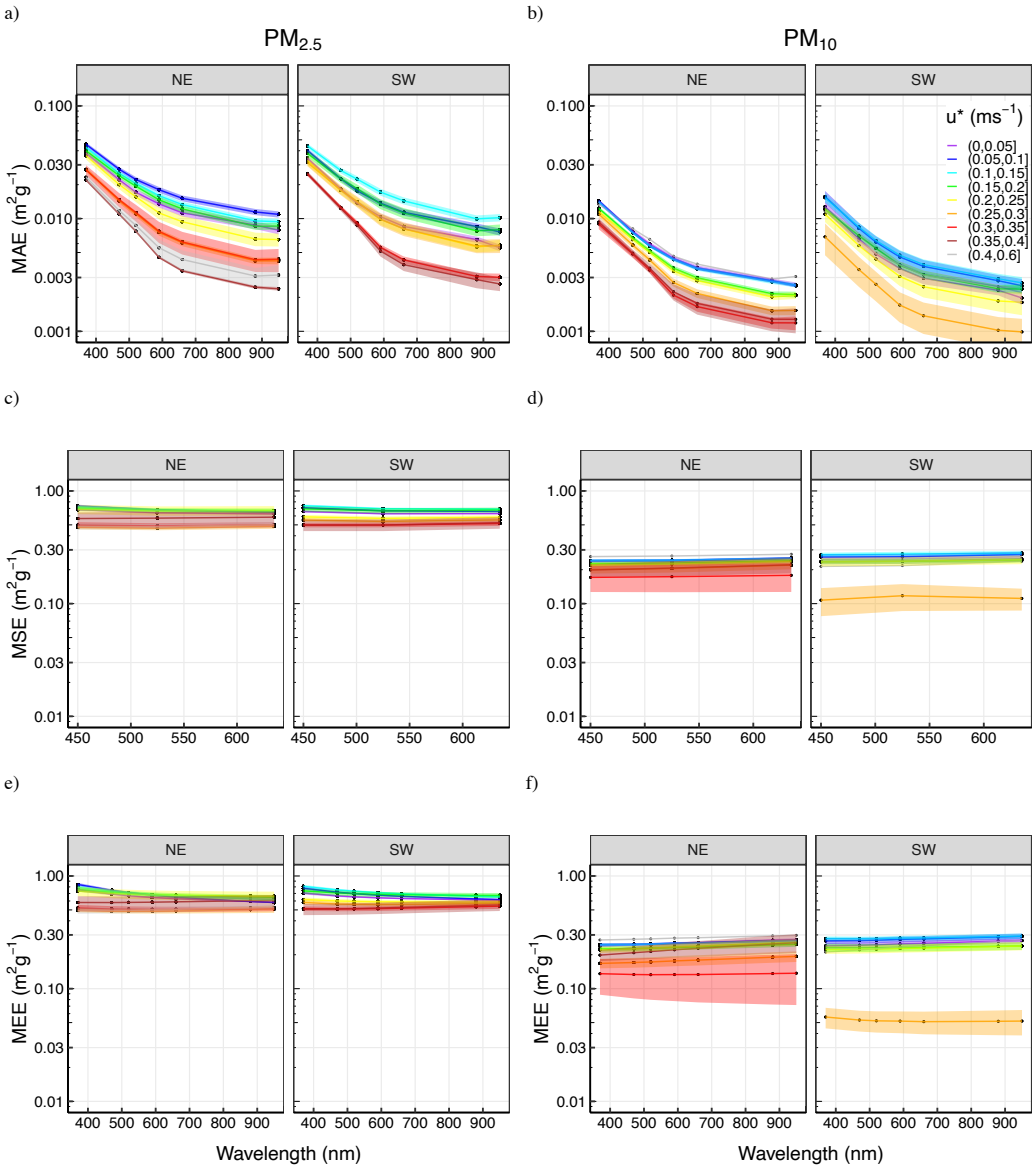

Figure 5. Mass Absorption (MAE, upper panel), Scattering (MSE, middle panel) and extinction (MEE lower panel) efficiencies at M'Hammid separated by the two dominant wind sectors (E-SW) and different levels of friction velocity (u^*) for both $PM_{2.5}$ (left panel) and PM_{10} (right panel) periods.

In addition to the SSA, the asymmetry parameter, g, and the backscatter fraction, BF, are also key parameters for the climate models, since they parametrise the relative amount of light scattered in the forward and backward directions by the particles. Here, we have analyzed the spectral behaviour of both g and BF by using the polar integrating nephelometer (see Sect. 2.5). Fig. 7a,c shows that for the $PM_{2.5}$ fraction the g(BF) increased(decreased) with the wavelength during periods with large friction velocity (u^*>0.25), whereas the opposite spectral behaviour was observed during periods with lower dust emission, i.e. less friction velocity. This behaviour reflected the larger relative proportion of coarse particles as the friction velocity increased. However, during the PM_{10} period the spectral dependency of g and BF was not observed for the periods with high u^*. The values for the g range between 0.65 and 0.72, within the range 0.6-0.85 found in the

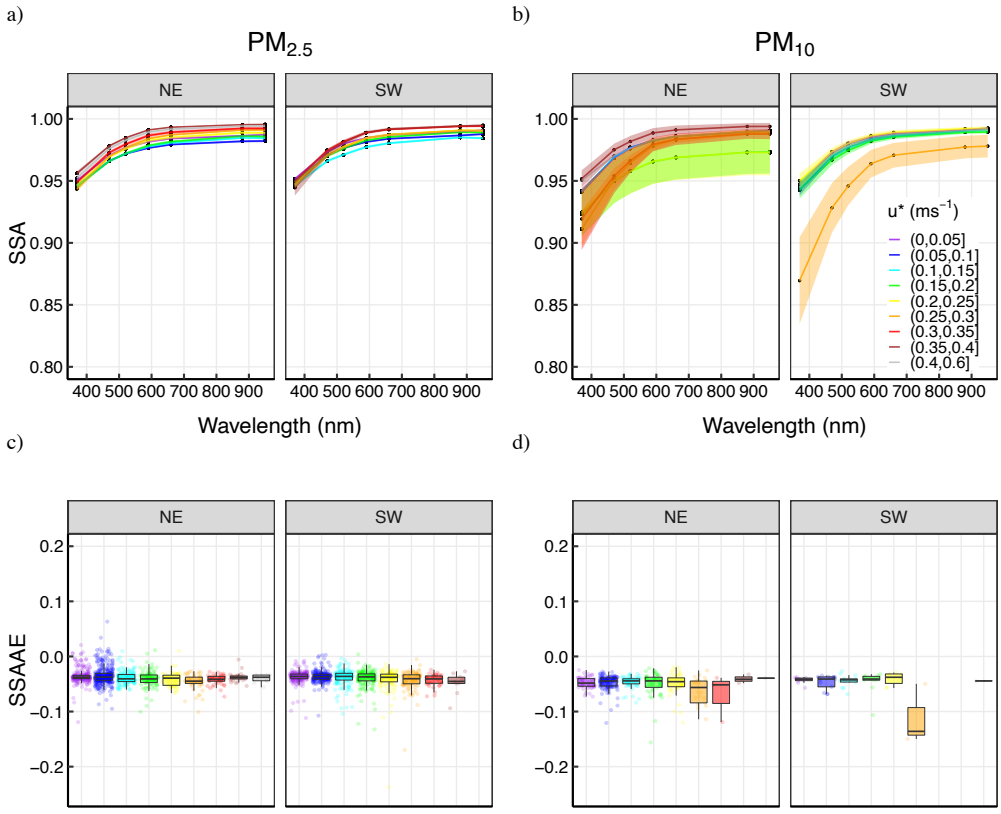

Figure 6. Multi-wavelength measurements of the Single-scattering Albedo (SSA, upper panel), and the derived SSA Ångström Exponent (SSAAE, lower panel) at M'Hammid separated by the two dominant wind sectors (E-SW) and different levels of friction velocity (u^*) for both $PM_{2.5}$ (left panel) and PM_{10} (right panel) periods.

literature (Sokolik and Toon, 1999; Horvath et al., 2018; Ryder et al., 2018).

3.3 Optical properties relationship with the effective radius

Additionally, we have analyzed the relationship between the AAE, the SAE, and the SSAAE, with the effective radius of the particles (R_{eff}) and the wind fraction velocity (u^*). It should be noted that, when comparing between the left ($PM_{2.5}$ period) and right (PM_{10} period) panels of Fig. 8, the particle size cut-off inlet change produced an expected increase in the effective radius values of the measured particles that should be taken into account.

Figure 8a shows that overall, independently of the wind sector, the relationship showed a shallow increase of AAE up to values of R_{eff} below 1 μm followed by a more pronounced increase of AAE above this values. This larger increase of the AAE as the particles became coarser could be linked with the higher relative importance of the dust emission events with larger proportion of iron content that increases the absorption at the shorter wavelengths, as denoted by both the AAE values between 2 and 2.5 for the largest R_{eff} and by the u^* increase with R_{eff}. In addition, Fig. S8, shows that when restricting the analysis for higher u^* values, the range of R_{eff} narrowed and the mean AAE values for the boxplots for this higher R_{eff} bins was higher (from around 1.2 to around 2.25), revealing an increasing relevance of the dust particles. However, Fig. S8 does not exclude the option of measuring coarse mineral dust particles for low wind friction velocities, as shown in the boxplots associated to high R_{eff} and AAE values around 2.25 for low u^*. Indeed, Fig. S8 shows that u^* could be used as a proxy to isolate the analysis just for dust emitted particles, given that the measured optical properties for u^* above a threshold (around 0.3 ms^{-1}) can be mainly associated to the emitted dust particles (AAE around 2.5 and SAE below 0). Moreover, Figs. 8c,d show the

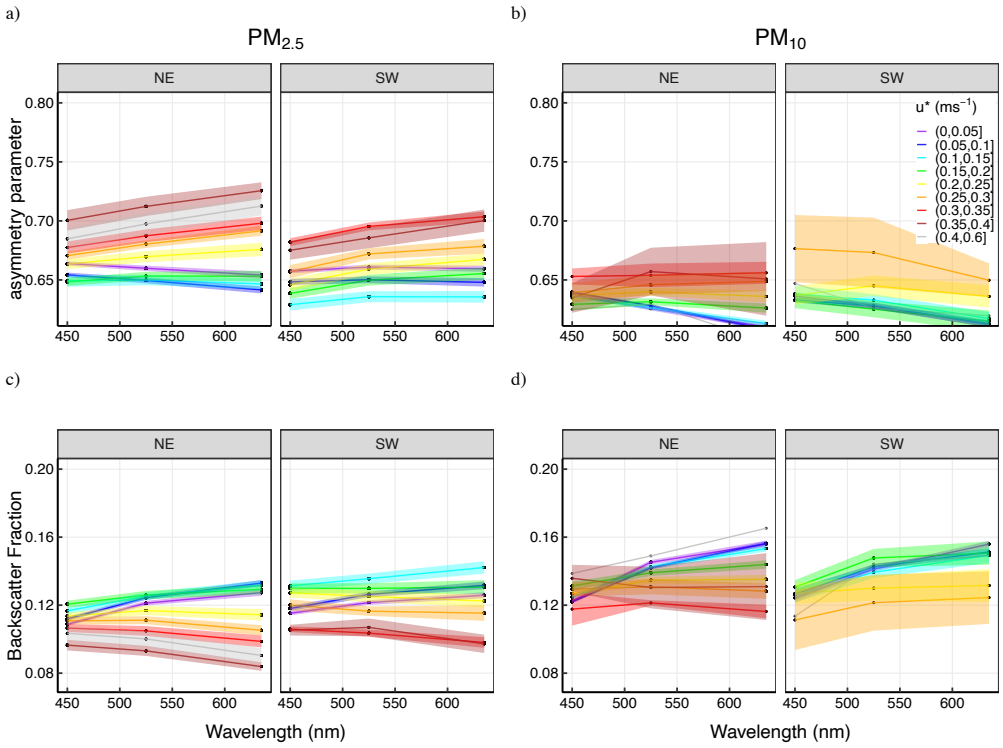

Figure 7. Multi-wavelength asymmetry parameter (g) and Backscatter Fraction (BF) at M'Hammid separated by the two dominant wind sectors (E-SW) and different levels of friction velocity (u^*) for both $PM_{2.5}$ (left panel) and PM_{10} (right panel) periods.

relationship of SSAAE with the effective radius of the particles, for the $PM_{2.5}$ inlet it shows a decrease from just positive SSAAE values with AAE close to 1 for the lowest R_{eff} (i.e. anthropogenic influenced air mass), to values around -0.07 with high AAE (above 2.2) and R_{eff} values around 1.1 μm (more heavily influenced by dust particles air mass). Regarding the behaviour of SAE with R_{eff} (colored bins points in Figs. 8 upper panel) the there are two main stand-out behaviours: first, higher SAE values were found for higher R_{eff} values, and a larger SAE values for the SW dominated sector compared to the E-NE sector, mainly due to the higher anthropogenic emissions advected from the upriver nearby towns for thie E-NE sector.

By comparing the PM_{10} with the $PM_{2.5}$, the main differences were: less pronounced increase of AAE with R_{eff}, larger AAE values for the lower R_{eff} values, and lower and more constant SSAAE and SAE values for the PM_{10}. These differences could be mainly linked to three factors: firstly, the larger inlet cut-off allows for coarser particles to be measured, which at the measurement field campaign were most probably due to mineral dust; moreover, since the inlet cut-offs measurements were not performed simultaneously, but sequentially, the measurements do not reflect the same conditions; and finally, the shorter measurement period for the PM_{10} inlet prevented the acquisition of the same variety and length of measurements as for the $PM_{2.5}$ inlet cut-off (cf. Table 2).

4 Summary and conclusions

Here we have presented the optical measurements results from the FRAGMENT-Morocco field measurement campaign that took place in L'Bour area in the Sahara during September 2019. We have derived the absorption with a dual-spot multi-wavelength aethaloemter (AE33) and the scattering with a polar multi-wavelength integrating nephelometer (Aurora 4000). From this measurements we obtained the intensive optical properties, and analyzed the behaviour of the optical parameters and its relationships with the type of event and the strength of the dust emission processes through the wind friction velocity, derived from 2-D anemometers, and the particles effective radius, obtained with a fine-dust aerosol spectrometer (FIDAS).

With regards to the optical properties the measurement campaign could be divided in two main periods in terms of the used particles inlet cut-off: a $PM_{2.5}$ period between the 4th and the 26th of September, and a PM_{10} period between

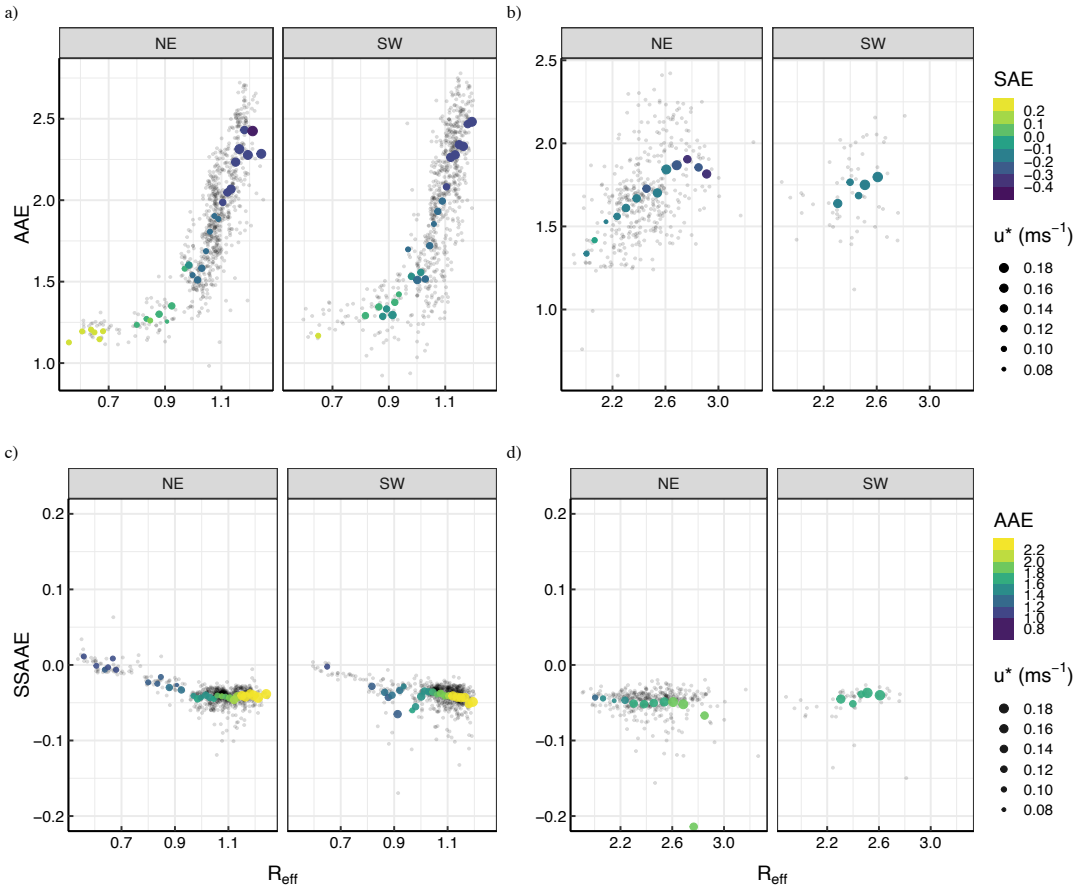

Figure 8. Scatter plot of the Absorption Ångström Exponent (AAE) as a function of the particle effective radius (R_{eff}) —x-axis— and the Scattering Ångström Exponent (SAE) —color code— at M'Hammid separated by the two dominant wind sectors (E-SW) and different levels of friction velocity (u^*) for both $PM_{2.5}$ (left panel) and PM_{10} (right panel) periods. Superimposed over each boxplot it is attached the AAE value of each measurement. The boxplots were calculated by grouping R_{eff} into different bins, with a width of 0.1 for the $PM_{2.5}$ and of 0.2 for the PM_{10} measurements.

then and the end of the campaign the 30th of September. The most recurrent form of dust emission during the campaign was local dust emission from saltation processes affecting the area of analysis with sudden and sustained increases in the wind velocity and friction velocity, although some larger-scale events with dust advection from nearby sources were also possible. Moreover, we found a period with an advection of local anthropogenic pollution on top of the local emission of dust at the site. The more local, saltation driven, processes presented values, as shown for a typical period (Period A) of around 0.919 $\pm$ 0.001 at 370 and 0.986 $\pm$ 0.001 at 880 nm for the albedo (SSA), around 0.624 $\pm$ 0.015 at 370 and 0.6 $\pm$ 0.014 at 880 nm for the mass extinction efficiency (MEE), of 2.011 $\pm$ 0.027 and -0.038 $\pm$ 0.01 for the absorption and scattering ångström exponent (AAE,SAE), respectively, and of 0.673 $\pm$ 0.002 for the asymmetry parameter (g) at 525 nm. The periods with additional regional mineral dust advection as a consequence of the influence of a Haboob storm (e.g. Period B) presented an increase in the MEE and the g values, and a decrease for the SSA, the AAE and SAE. Finally, under certain circumstances for which we were able to measure the mixing of local dust emission with anthropogenic-like particles (e.g. Period C), the optical parameters presented values indicating the presence of finer particles with a higher absorption efficiencies and a less pronounced dust-like spectral dependency.

We have analyzed the optical properties of the dust particles in an emission zone depending on the strength of the emission and how this optical properties behave under scenarios where dust particles can be assumed to be the only contributor to the total particle number concentration. In order to perform such analysis, we studied for all the relevant

optical parameters the behaviour with the friction velocity, u^*. We have found that as u^* increased, the absorption and scattering values increased, as also did the number and mass concentration of the particles, mainly due to the increase in the dust emission strength. We have found that even for low u^* values the intensive optical values are similar, as expected, to those found in the literature associated to Saharan dust, i.e. a SAE below 1, AAE above 1.5 and SSAAE below 0 (Collaud Coen et al., 2010). Moreover, as u^* increased and the local dust emission strengthened, and particles became coarser, with higher effective radius, the values drifted towards values of almost solely dust particles (AAE $\sim$ 2-2.5, SAE<0 and lower SSAAE), similar to those found in soils with a higher proportion of iron-oxides for the optical properties.

The impact of both the particle size and the different mineralogical composition of the mineral dust particles under different mineral dust emission scenarios is reflected on the SSA (and its spectral dependence) and the asymmetry parameter g. We observed that as the wind friction increases, the SSA presented two distinct trends: a decrease at the shortest wavelengths, below 520 nm, and an increase above 590 nm. This divergent behaviour is linked to the increase of AAE for the higher u^* ranges, which implies a larger amount of absorption at these shorter wavelengths, whereas at the longer wavelengths, the absorption does not present such a large increase. Under scenarios with a large emission of mineral dust particles, i.e. high u^* values, the relative proportion of coarse particles increased, and consequently there was an increase in the forward direction, as observed in the values of g and BF. Therefore, during this events, as a consequence of the scattering efficiency relationship with the size parameter, this increase was even higher for the longer wavelengths, thus causing the albedo to increase towards the longer wavelengths.

References

Adebiyi, A. A. and Kok, J. F.: Climate models miss most of the coarse dust in the atmosphere, Science Advances, 6, 1–10, https://doi.org/10.1126/sciadv.aaz9507, 2020.

Balkanski, Y., Schulz, M., Claquin, T., and Guibert, S.: Reevaluation of Mineral aerosol radiative forcings suggests a better agreement with satellite and AERONET data, Atmospheric Chemistry and Physics, 7, 81–95, https://doi.org/10.5194/acp-7-81-2007, 2007.

Bukowski, J. and van den Heever, S.: Direct radiative effects in haboobs, Journal of Geophysical Research: Atmospheres, 126, e2021JD034 814, 2021.

Caponi, L., Formenti, P., Massabó, D., Di Biagio, C., Cazaunau, M., Pangui, E., Chevaillier, S., Landrot, G., Andreae, M. O., Kandler, K., Piketh, S., Saeed, T., Seibert, D., Williams, E., Balkanski, Y., Prati, P., and Doussin, J.-F.: Spectral- and size-resolved mass absorption efficiency of mineral dust aerosols in the shortwave: a simulation chamber study, Atmospheric Chemistry and Physics Discussions, pp. 1–39, https://doi.org/10.5194/acp-2017-5, 2017.

Chen, Y. and Bond, T. C.: Light absorption by organic carbon from wood combustion., Atmospheric Chemistry & Physics, 10, 2010.

Choobari, O. A., Zawar-Reza, P., and Sturman, A.: The global distribution of mineral dust and its impacts on the climate system: A review, Atmospheric Research, 138, 152–165, https://doi.org/10.1016/j.atmosres.2013.11.007, https://www.sciencedirect.com/science/article/pii/S0169809513003281, 2014.

Claquin, T., Schulz, M., and Balkanski, Y.: Modeling the mineralogy of atmospheric dust sources, Journal of Geophysical Research: Atmospheres, 104, 22 243–22 256, 1999.

Collaud Coen, M., Weingartner, E., Schaub, D., Hueglin, C., Corrigan, C., Henning, S., Schwikowski, M., and Baltensperger, U.: Saharan dust events at the Jungfraujoch: detection by wavelength dependence of the single scattering albedo and first climatology analysis, pp. 2465–2480, 2004.

Collaud Coen, M., Weingartner, E., Apituley, A., Ceburnis, D., Fierz-Schmidhauser, R., Flentje, H., Henzing, J. S., Jennings, S. G., Moerman, M., Petzold, A., Schmid, O., and Baltensperger, U.: Minimizing light absorption measurement artifacts of the Aethalometer: Evaluation of five correction algorithms, Atmospheric Measurement Techniques, 3, 457–474, https://doi.org/10.5194/amt-3-457-2010, 2010.

Di Biagio, C., Formenti, P., Cazaunau, M., Pangui, E., Marchand, N., and Doussin, J.-F.: Corrigendum to " Aethalometer multiple scattering correction C ref for mineral dust aerosols " published in Atmos . Meas . Tech ., 10 , 2923 – 2939 , 2017, Atmospheric Measurement Techniques, 10, 2923–2939, 2017.

Di Biagio, C., Formenti, P., Balkanski, Y., Caponi, L., Cazaunau, M., Pangui, E., Journet, E., Nowak, S., Andreae, M., Kandler, K., Saeed, T., Piketh, S., Seibert, D., Williams, E., and Doussin, J.-F.: Complex refractive indices and single scattering albedo of global dust aerosols in the shortwave spectrum and relationship to iron content and size, Complex refractive indices and single scattering albedo of global dust aerosols in the shortwave spectrum and relationship to iron content and size, pp. 1–42, https://doi.org/10.5194/acp-2019-145, 2019.

Di Biagio, C., Balkanski, Y., Albani, S., Boucher, O., and Formenti, P.: Direct Radiative Effect by Mineral Dust Aerosols Constrained by New Microphysical and Spectral Optical Data, Geophysical Research Letters, 47, 1–12, https://doi.org/10.1029/2019GL086186, 2020.

Drinovec, L., Močnik, G., Zotter, P., Prévôt, A., Ruckstuhl, C., Coz, E., Rupakheti, M., Sciare, J., Müller, T., Wiedensohler, A., and Hansen, A. D. A.: The "dual-spot" Aethalometer: an improved measurement of aerosol black carbon with real-time loading compensation, Atmospheric Measurement Techniques, 8, 1965–1979, 2015.

Ealo, M., Alastuey, A., Ripoll, A., Pérez, N., Minguillón, M. C., Querol, X., and Pandolfi, M.: Detection of Saharan dust and biomass burning events using near-real-time intensive aerosol optical properties in the north-western Mediterranean, Atmospheric Chemistry and Physics, 16, 12 567–12 586, 2016.

Engelstaedter, S., Tegen, I., and Washington, R.: North African dust emissions and transport, Earth-Science Reviews, 79, 73–100, https://doi.org/10.1016/j.earscirev.2006.06.004, https://www.sciencedirect.com/science/article/pii/S001282520600081X, 2006.

González-Flórez, C., Klose, M., Alastuey, A., Dupont, S., Escribano, J., Etyemezian, V., Gonzalez-Romero, A., Huang, Y., Konrad, K., Nikolich, G., Panda, A., Querol, X., Reche, C., Yús-Díez, J., and Perez García-Pando, C.: New insights into the size-resolved dust emission from field measurements in the Moroccan Sahara, in prep.

González-Romero, A., Querol, X., Alastuey, A., González-Flórez, C., Kandler, K., Klose, M., Panta, A., Reche, C., Yús-Díez, J., and Perez García-Pando, C.: Properties of dust-source sediment and their importance on dust emission: a local example in S Morocco, in prep.

Horvath, H., Alados Arboledas, L., and José Olmo Reyes, F.: Angular scattering of the Sahara dust aerosol, Atmospheric Chemistry and Physics, 18, 17 735–17 744, https://doi.org/10.5194/acp-18-17735-2018, 2018.

Huang, Y., Kok, J. F., Kandler, K., Lindqvist, H., Nousiainen, T., Sakai, T., Adebiyi, A., and Jokinen, O.: Climate Models and Remote Sensing Retrievals Neglect Substantial Desert Dust Asphericity, Geophysical Research Letters, 47, 1–11, https://doi.org/10.1029/2019GL086592, 2020.

Kandler, K., Schütz, L., Deutscher, C., Ebert, M., Hofmann, H., Jäckel, S., Jaenicke, R., Knippertz, P., Lieke, K., Massling, A., Petzold, A., Schladitz, A., Weinzierl, B., Wiedensohler, A., Zorn, S., and Weinbruch, S.: Size distribution, mass concentration, chemical and mineralogical composition and derived optical parameters of the boundary layer aerosol at Tinfou, Morocco, during SAMUM 2006, Tellus, Series B: Chemical and Physical Meteorology, 61, 32–50, https://doi.org/10.1111/j.1600-0889.2008.00385.x, 2009.

Kirchstetter, T. W., Novakov, T., and Hobbs, P. V.: Evidence that the spectral dependence of light absorption by aerosols is affected by organic carbon, Journal of Geophysical Research: Atmospheres, 109, 2004.

Kok, J. F., Ridley, D. A., Zhou, Q., Miller, R. L., Zhao, C., Heald, C. L., Ward, D. S., Albani, S., and Haustein, K.: Smaller desert dust cooling effect estimated from analysis of dust size and abundance, Nature Geoscience, 10, 274–278, https://doi.org/10.1038/ngeo2912, 2017.

Kok, J. F., Adebiyi, A. A., Albani, S., Balkanski, Y., Checa-Garcia, R., Chin, M., Colarco, P. R., Hamilton, D. S., Huang, Y., Ito, A., Klose, M., Leung, D. M., Li, L., Mahowald, N. M., Miller, R. L., Obiso, V., Pérez García-Pando, C., Rocha-Lima, A., Wan, J. S., and Whicker, C. A.: Improved representation of the global dust cycle using observational constraints on dust properties and abundance, Atmospheric Chemistry and Physics, 21, 8127–8167, https://doi.org/10.5194/acp-21-8127-2021, 2021a.

Kok, J. F., Adebiyi, A. A., Albani, S., Balkanski, Y., Checa-Garcia, R., Chin, M., Colarco, P. R., Hamilton, D. S., Huang, Y., Ito, A., Klose, M., Li, L., Mahowald, N. M., Miller, R. L., Obiso, V., Pérez García-Pando, C., Rocha-Lima, A., and Wan, J. S.: Contribution of the world's main dust source regions to the global cycle of desert dust, Atmospheric Chemistry and Physics, 21, 8169–8193, https://doi.org/10.5194/acp-21-8169-2021, 2021b.

Lafon, S., Sokolik, I. N., Rajot, J. L., Caquincau, S., and Gaudichet, A.: Characterization of iron oxides in mineral dust aerosols: Implications for light absorption, Journal of Geophysical Research Atmospheres, 111, 1–19, https://doi.org/10.1029/2005JD007016, 2006.

Li, L., Mahowald, N. M., Miller, R. L., García-pando, C. P., Klose, M., Hamilton, D. S., Ageitos, M. G., Ginoux, P., Balkanski, Y., Green, R. O., Kalashnikova, O., Kok, J. F., Obiso, V., Paynter, D., and Thompson, D. R.: Quantifying the range of the dust direct radiative effect due to source mineralogy uncertainty, pp. 3973–4005, 2021.

Liou, K.-N.: An introduction to atmospheric radiation, vol. 84, Elsevier, 2002.

Müller, T., Schladitz, A., Massling, A., Kaaden, N., Kandler, K., and Wiedensohler, A.: Spectral absorption coefficients and imaginary parts of refractive indices of Saharan dust during SAMUM-1, Tellus, Series B: Chemical and Physical Meteorology, 61, 79–95, https://doi.org/10.1111/j.1600-0889.2008.00399.x, 2009.

Müller, T., Laborde, M., Kassell, G., and Wiedensohler, A.: Design and performance of a three-wavelength LED-based total scatter and backscatter integrating nephelometer, Atmospheric Measurement Techniques, 4, 1291–1303, 2011.

Myhre, G., Shindell, D., Breéon, F.-M., Collins, W., Fuglestvedt, J., Huang, J., Koch, D., Lamarque, J.-F., Lee, D., Mendoza, B., Nakajima, T., Robock, A., Stephens, G., Takemura, T., and Zhang, H.: Anthropogenic and Natural Radiative Forcing, book section 8, p. 659–740, Cambridge University Press, Cambridge, United Kingdom and New York, NY, USA, https://doi.org/10.1017/CBO9781107415324.018, www.climatechange2013.org, 2013.

Panta, A., Konrad, K., Alastuey, A., González-Flórez, C., Gonzalez-Romero, A., Klose, M., Querol, X., Reche, C., Yús-Díez, J., and Perez García-Pando, C.: Insights into the single particle composition, size, and shape of freshly emitted Saharan mineral dust from the Lower Drâa valley, Moroccan Sahara using electron microscopy, in prep.

Petzold, A., Ogren, J. A., Fiebig, M., Laj, P., Li, S. M., Baltensperger, U., Holzer-Popp, T., Kinne, S., Pappalardo, G., Sugimoto, N., Wehrli, C., Wiedensohler, A., and Zhang, X. Y.: Recommendations for reporting black carbon measurements, Atmospheric Chemistry and Physics, 13, 8365–8379, https://doi.org/10.5194/acp-13-8365-2013, 2013.

Ryder, C. L., Marenco, F., Brooke, J. K., Estelles, V., Cotton, R., Formenti, P., McQuaid, J. B., Price, H. C., Liu, D., Ausset, P., Rosenberg, P., Taylor, J. W., Choularton, T., Bower, K., Coe, H., Gallagher, M., Crosier, J., Lloyd, G., Highwood, E. J., and Murray, B. J.: Coarse mode mineral dust size distributions, composition and optical properties from AER-D aircraft measurements over the Tropical Eastern Atlantic, Atmospheric Chemistry and Physics Discussions, 98, 1–49, https://doi.org/10.5194/acp-2018-739, 2018.

Schladitz, A., Müller, T., Kaaden, N., Massling, A., Kandler, K., Ebert, M., Weinbruch, S., Deutscher, C., and Wiedensohler, A.: In situ measurements of optical properties at Tinfou (Morocco) during the Saharan Mineral Dust Experiment SAMUM 2006, Tellus, Series B: Chemical and Physical Meteorology, 61, 64–78, https://doi.org/10.1111/j.1600-0889.2008.00397.x, 2009.

Schuster, G. L., Dubovik, O., and Holben, B. N.: Angstrom exponent and bimodal aerosol size distributions, Journal of Geophysical Research: Atmospheres, 111, 2006.

Schuster, G. L., Dubovik, O., and Arola, A.: Remote sensing of soot carbon - Part 1: Distinguishing different absorbing aerosol species, Atmospheric Chemistry and Physics, 16, 1565–1585, https://doi.org/10.5194/acp-16-1565-2016, 2016.

Seinfeld, J. H. and Pandis, S. N.: Atmospheric Chemistry and Physics: From air pollution to climate change, John Wiley & Sons New York, 1998.

Shao, Y.: Physics and modelling of wind erosion, Springer, 2008.

Sokolik, I. N. and Toon, O. B.: Incorporation of mineralogical composition into models of the radiative properties of mineral aerosol from UV to IR wavelengths, Journal of Geophysical Research Atmospheres, 104, 9423–9444, https://doi.org/10.1029/1998JD200048, 1999.

Yus-Díez, J., Bernardoni, V., Močnik, G., Alastuey, A., Ciniglia, D., Ivančič, M., Querol, X., Perez, N., Reche, C., Rigler, M., Vecchi, R., Valentini, S., and Pandolfi, M.: Determination of the multiple-scattering correction factor and its cross-sensitivity to scattering and wavelength dependence for different AE33 Aethalometer filter tapes: A multi-instrumental approach, Atmospheric Measurement Techniques Discussions, 29, 1–30, https://doi.org/10.5194/amt-2021-46, 2021.

Optical properties of freshly emitted Saharan dust particles during FRAGMENT-Morocco

Jesús Yus-Díez [1,2], Marco Pandolfi [1], Andrés Alastuey [1], Cristina González-Flórez [3], Jeronimo Escribano [3], Adolfo Gonzalez-Romero [3], Matic Ivančič [4], Martin Rigler [4], Martina Klose [3,5], Konrad Kandler [6], Agnesh Panta [6], Xavier Querol [1], Cristina Reche [1], and Carlos Perez García-Pando [3,7]

[1]Institute of Environmental Assessment and Water Research (IDAEA-CSIC), Barcelona, 08034, Spain
[2]Grup de Meteorologia, Departament de Física Aplicada, Universitat de Barcelona, C/Martí i Franquès, 1, 08028, Barcelona, Spain
[3]Barcelona Supercomputing Center (BSC), Barcelona, 08034, Spain
[4]Aerosol d.o.o., Ljubljana, Slovenia
[5]Karlsruhe Institute of Technology (KIT), Institute of Meteorology and Climate Research (IMK-TRO)
[6]Technical University Darmstadt (TUDa), Darmstadt, Germany
[7]ICREA, Catalan Institution for Research and Advanced Studies, Barcelona, 08010, Spain

Correspondence: jesus.yus@idaea.csic.es and carlos.perez@bsc.es

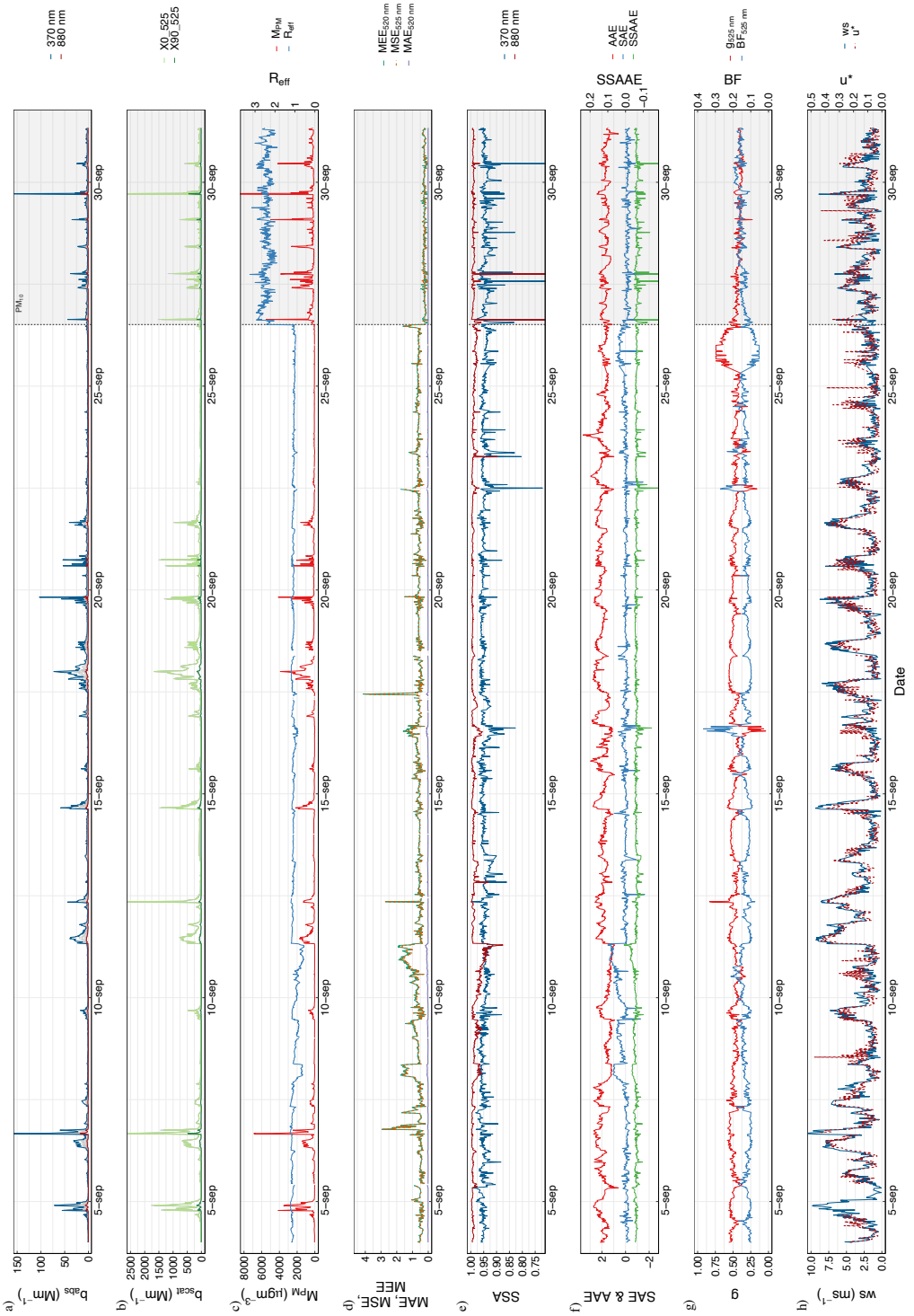

Figure S1: Time evolution during FRAGMENT-Morocco measurement campaign of hourly averages of a) the absorption coefficients at 370 and 880 nm, b) the forward and backward scattering at 525 nm, c) the single scattering albedo (SSA) at both 370 and 880 nm, d) the scattering, absorption, mass extinction efficiency and SSA Ångström Exponent (AAE, SAE, MEEAE, SSAAE), e) the mass absorption, scattering and extinction efficiency (MAE, MSE, MEE), f) the Mass concentration and the particle effective radius extensive and intensive optical properties, as well as the mass concentration and the particles effective radius, g) the asymmetry parameter and the backscatter fraction (g, BF), and h) the wind speed and fraction velocity (u*). Between the 4th and the 26th of September the inlet cut-off was of 2.5 μ, whereas from the 26th onward the inlet cut-off was of 10 µm, as denoted by both the labels and the shadowed background.

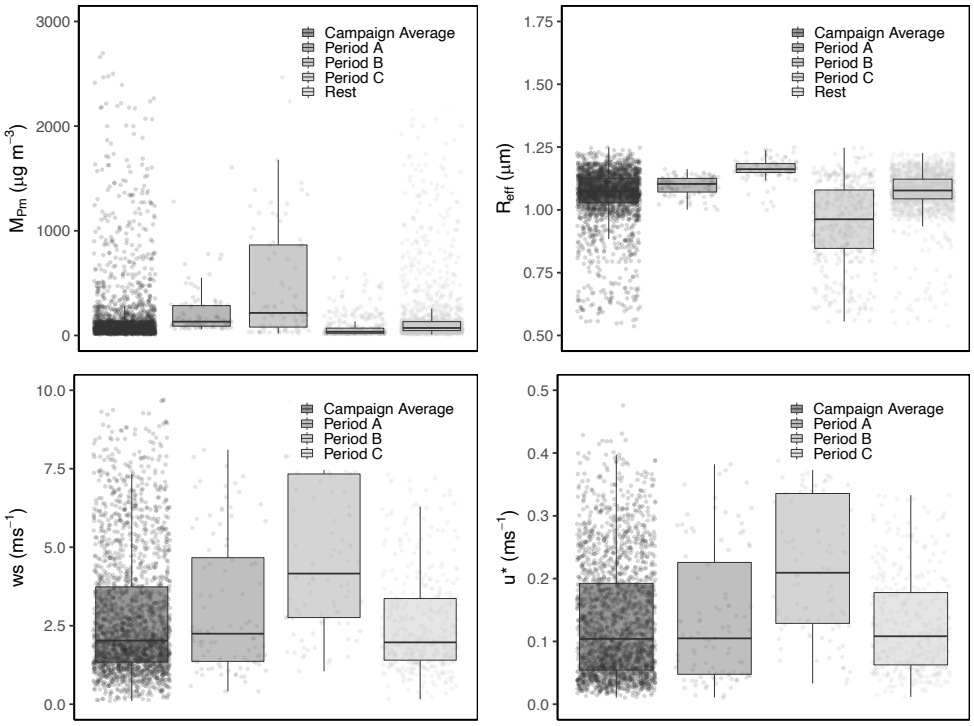

Figure S2: a) Mass concentration, b) effective radius for the selected typical event periods retrieved from the FIDAS particle number size distribution, and c) wind speed and d) u* measured with 3D wind sonics anemometers.

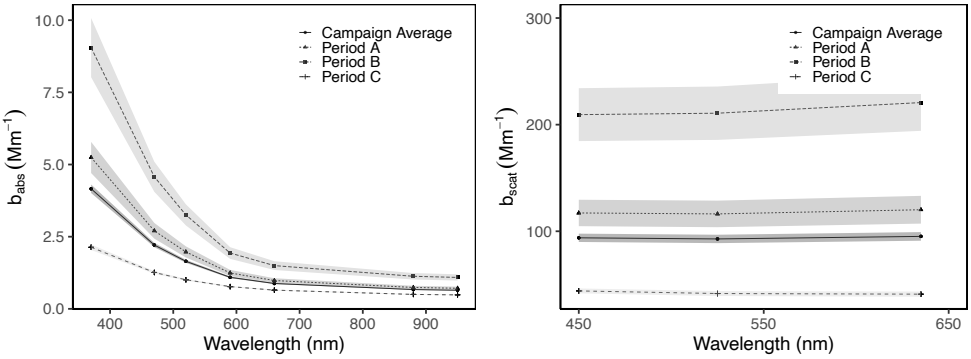

Figure S3: Extensive optical measurements for the selected typical event periods: a) absorption coefficients at the 7 AE33 measuring wavelengths (370, 470, 520, 590, 660, 880, 950 nm), b) scattering coefficients at the 3 wavelengths (450, 525, 635 nm) from the polar integrating nephelometer.

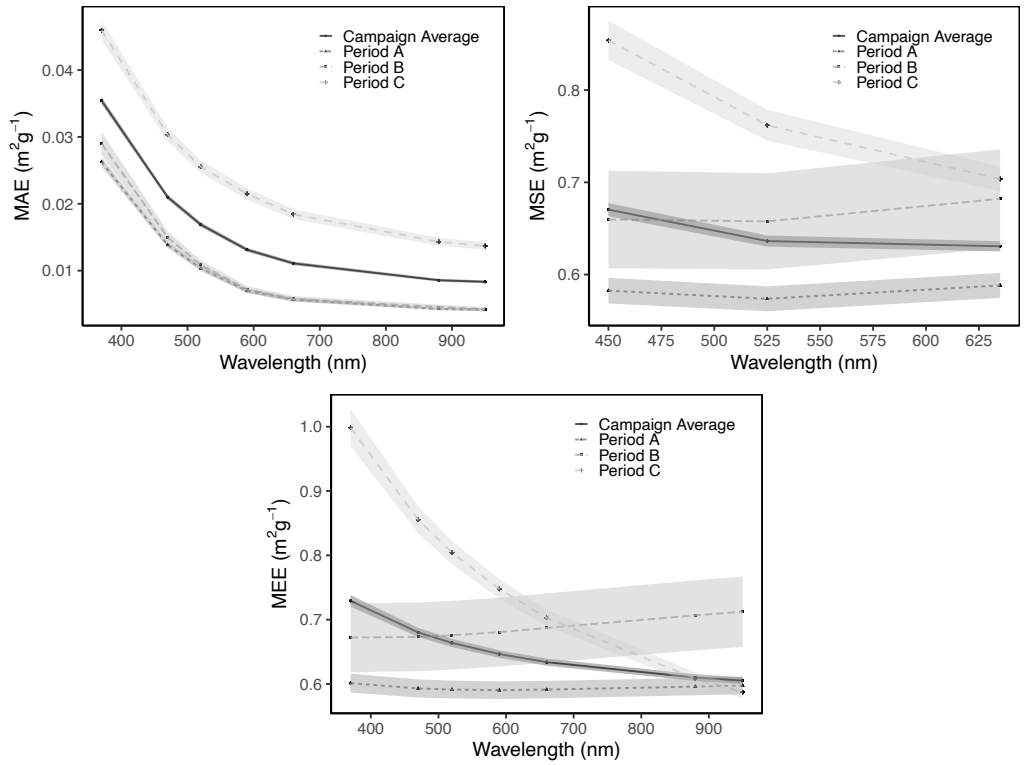

Figure S4: Absorption efficiencies for the selected typical event periods: a) absorption coefficients at the 7 AE33 measuring wavelengths (370, 470, 520, 590, 660, 880, 950 nm), b) scattering coefficients at the 3 wavelengths (450, 525, 635 nm) from the polar integrating nephelometer, and c) extinction at the 7 AE33 measuring wavelengths (370, 470, 520, 590, 660, 880, 950 nm).

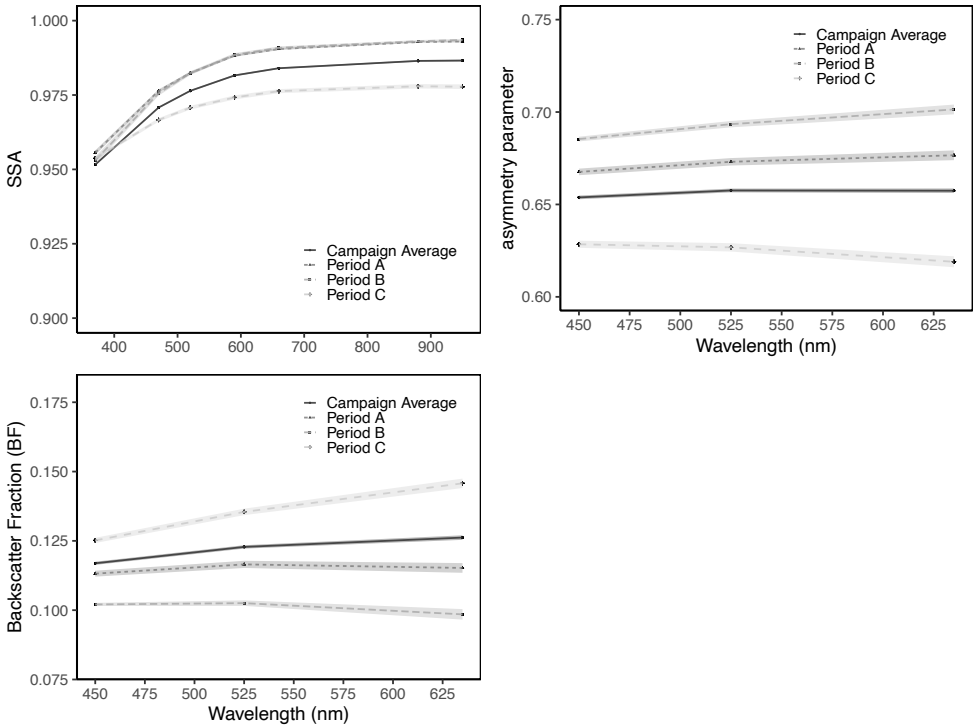

Figure S5: a) Single scattering albedo, SSA, b) asymmetry parameter, g, and c) the backscatter fraction, BF, for the selected typical event periods at the 7 AE33 measuring wavelengths (370, 470, 520, 590, 660, 880, 950 nm).

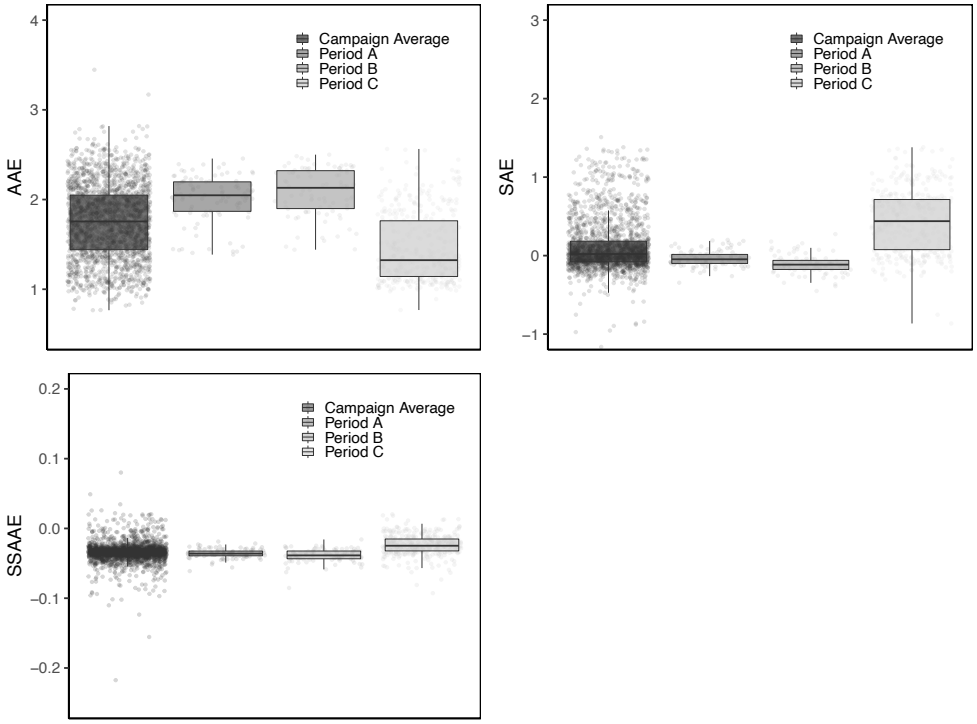

Figure S6: Ångström Exponents for the selected typical event periods for the: a) absorption, b) scattering, and c) SSA.

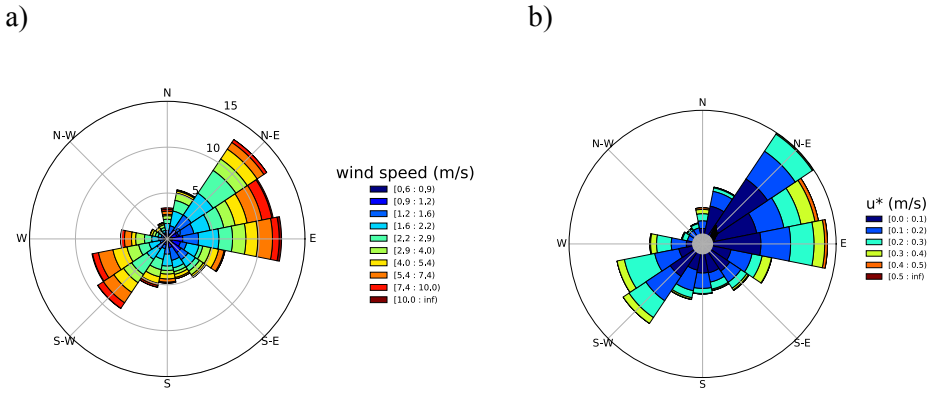

Figure S7: Windrose of the a) wind speed, and b) friction velocity (u*) at 2 m a.g.l., i.e. the same height as the head inlet of the optical and psd measurements.

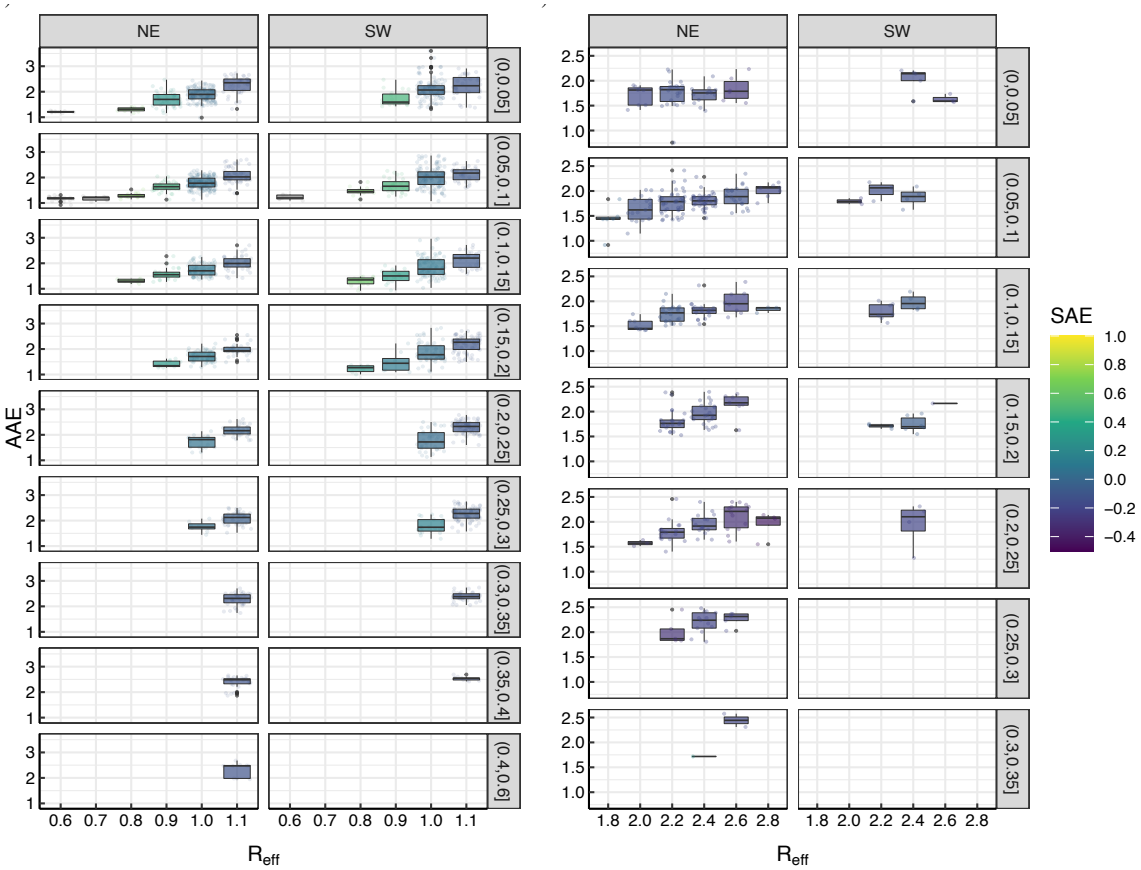

Figure S8: Boxplots of the Absorption Ångström Exponent (AAE) as a function of the particle effective radius (R_{eff}) x-axis, and the Scattering Ångström Exponent (SAE), color code, at M'Hammid separated by the two dominant wind directions (E-SW) and different levels of friction velocity (u*) for both PM2.5 (left panel) and PM10 (right panel) inlet cut-off. Superimposed over each boxplot it is attached the AAE value of each measurement. The boxplots were calculated by grouping R_{eff} into different bins, with a width of 0.1 for the PM2.5 and of 0.2 for the PM10 measurements.

Part IV
Discussion and conclusion

9

Discussion

The results obtained in this thesis provide an exhaustive analysis of the optical properties of atmospheric aerosol particles, with special focus on the role on light absorption of the main absorbing aerosols, namely, BC, BrC and mineral dust particles. The long-term continuous measurements with multiple instrumentation performed at three different background monitoring stations in NE Spain allowed to fully characterize for the first time in the literature the multiple scattering parameter C, which is the most important parameter used for deriving the multi-wavelength absorption coefficients from Aethalometer AE33 instruments. The AE33 is the most widely used instrument nowadays to derive the multi-wavelength absorption properties of atmospheric aerosol particles and it is deployed in many important international networks as ACTRIS and GAW. However, AE33 measurements must be opportunely calibrated in order to provide robust particle absorption data. This thesis describes the best procedure that can be used to derive the multi-wavelength absorption data from AE33 measurements. Moreover, the available dataset was also used to study the absorption enhancement of BC particles and how it changes depending on the mixing of BC with BrC, non absorbing OA and non-carbonaceous aerosols. The study of the BC absorption enhancement is of great relevance because the interaction of BC with electromagnetic radiations depends on the mixing state of BC particles with other chemical compounds, thus being of great importance for climate models and studies. This thesis provides for the first time in the Western Mediterranean basin a comprehensive analysis of the reasons causing the enhancement of BC absorption properties. In addition, the data collected at the three monitoring stations were coupled with data obtained during an intensive measurement campaign over the NE of Spain performed with instrumented flights. These airborne measurements enabled the study of both the horizontal and vertical distribution of the aerosol particles physico-chemical properties during periods affected by summer regional recirculation scenarios and Saharan dust outbreaks. Finally, an intensive campaign performed in the Sahara desert, in North Africa, allowed the study of the optical properties of mineral dust particles and its relationship with the dust emission strength and the dust particle size distribution for the largest emission source of mineral dust reaching the Mediterranean Basin and Europe.

The methodological approach to determine the multiple scattering correction factor C from AE33 measurements, its relationship with composition and physical properties of the aerosol particles collected on the AE33 filter tape, and its main implications for similar

monitoring stations within the ACTRIS community (Objective 1) is described in Sect. 9.1. The description of the horizontal and vertical distribution, variability and optical properties of the atmospheric aerosol particles in NE Spain (Objective 2), the absorption enhancement of the BC particles at two different background stations (Objective 3), the optical properties of mineral dust particles, both at the source and in the Western Mediterranean basin (Objective 4), and its overall implications for climate modeling are described in Sect. 9.2.

9.1 Optical instruments description and characteristics

The results of this thesis contribute strongly to our knowledge about the optical properties of atmospheric aerosol particles and remark the importance of correctly measuring the particles optical properties in order to provide valuable inputs to climate models to correctly asses their effect on the Earth's radiative budget. The measurements of the scattering coefficient are typically performed with integrating nephelometers, as in the case of this thesis (cf. **Chapter 4**). These instruments are considered as reference instruments for scattering measurements because the sampled particles are suspended in a chamber without any interference. Conversely, the measurements of the aerosol particles absorption coefficients do not have an established reference method, and a variety of instruments are deployed worldwide in many international networks. This lack of a reference technique introduces a considerable uncertainty on the absorption measurements. Given the current context of a changing and warming climate, it is especially important to reduce these sources of error to better understand how much the aerosol particles contribute to the warming of climate together with the well known greenhouse gases as CO_2 and methane. Throughout this thesis, the absorption measurements have been derived by means of filter-based photometers, namely a multi-wavelength aethalometer (AE33), a multi-angle absorption photometer (MAAP), and an offline polar photometer from the Università degli studi di Milano (PP_UniMI). Among all, the most widely used instrument for in-situ surface measurements of the absorption properties of aerosol particles is the AE33 instrument. The unique characteristic of this instrument is its ability to obtain the absorption with a high temporal resolution at multiple wavelengths from the short-UV to the near-IR. This instrument has been used in all the studies that compose this thesis as the main instrument for measuring online the multi-wavelength absorption coefficients. However, the AE33, as any other filter-based photometer, cannot be considered as a reference instrument due to the artifacts related to the presence of the filter tape where particles are collected.

As described in **Chapter 4**, the AE33 derives the aerosol particles absorption coefficients by applying a set of corrections to the measured attenuation of light through a loaded filter tape. Conversely, the MAAP and the PP_UniMI obtain the absorption coefficients by applying a radiative scheme to the measurements of transmitted and backscattered light radiation, which significantly reduces its measurement error. However, compared to the AE33, both MAAP and PP_UniMI present some disadvantage. Indeed, the MAAP provides on-line light

absorption only at one wavelength, thus limiting the comprehension of the spectral absorption properties of atmospheric particles, which is fundamental to fully understand the effects of particle absorption on climate. Whereas, the PP_UniMI, although it provides the absorption measurements at multiple wavelengths, is an off-line instrument, thus the multi-wavelength absorption properties are determined after analyzing aerosol samples previously collected on a filter tape, which reduces the time resolution of the absorption measurements. In order to reduce the uncertainties related to the AE33 instruments and especially the retrieved absorption coefficients, this thesis provides a more accurate description of the parameters that the AE33 uses to derive the absorption coefficients from the attenuation measurements. Reducing these uncertainties is fundamental for climate models. Firstly, because thousands of AE33 worldwide are providing data to the important international networks for atmospheric research as ACTRIS and GAW and, secondly, because important parameters such as the single scattering albedo (SSA) can be estimated properly only upon a correct estimation of particle absorption. In this thesis it is described how to minimize the uncertainties of the absorption measurements from AE33 using data from three different background measurement sites in NE Spain characterized by particles with different physico-chemical properties.

The AE33 derives the absorption coefficient following eq. (4.5), where the only parameter not monitored on-line by the instrument software is the multiple scattering parameter, C. Other relevant parameters affecting the measurements as the flow leakage and the more crucial filter loading effect, k, are monitored and corrected on-line by the instrument. The filter loading effect refers to the progressive reduction of the instrument sensitivity due to the increase of the aerosol load on the filter spot. This artifact produces a shadowing effect of the light radiation that is corrected on-line by the AE33 software by simultaneously measuring the attenuation of light through two filter spots with different flow rates. A comprehensive analysis of the C parameter is shown in **Chapter 5**. The C corrects for the multiple scattering within the filter tape from both the filter fibers and the sampled aerosol particles, thus it is highly sensitive to both the type of filter tape used and the physical properties of the collected particles. The analysis of this parameter was obtained using as reference instruments for the aerosol particles absorption the MAAP and the PP_UniMI. Although these instruments are not considered as reference instruments per se, it is common praxis to consider them as such as a consequence of the more complex method they use to derive the absorption that reduces the impact of the artifacts introduced by the presence of the filter tape (Backman et al., 2017).

The relationship of the multiple scattering parameter with SSA follows eq. (4.9), where the cross-sensitivity to scattering factor, m_s, determines how much the C increases with increasing SSA values. In the case that the collected particles have high scattering efficiency, i.e. high SSA values, the multiple scattering within the filter tape increases the length of the optical path of the radiation beam, thus artificially increasing the apparent absorption of the sampled particles. As a consequence of the rapid increase that the C presents for very high SSA, up to 2 or 3 times higher (see Fig. 9.1), the use of a tailored C for deriving the absorption from the AE33 attenuation coefficients becomes paramount. In fact, in **Chapter 5**, the higher overall increase of the multiple scattering parameter was observed at the mountain-top station,

Montsec d'Ares (MSA), where the SSA at 637 nm shows values often above 0.95. These high SSA values were mainly associated to the presence of mineral dust during Saharan dust outbreaks that efficiently scatter sunlight at 637 nm. At the regional background station, Montseny (MSY), although the relative importance of mineral dust on PM is lower compared to MSA, the SSA is often high due to the presence of both fine anthropogenic and biogenic sources that can increase the SSA values and, therefore, the C. At MSA, the presence of dust particles under high SSA was demonstrated by the simultaneous increase in the particle size, shown by the decrease of the backscatter fraction (BF), the increase in the short-UV absorption efficiency, causing AAE values above 2.0, and the decrease of the SSAAE to values below 0. On the other hand, at MSY the presence of high OA concentrations, causing high SSA values, was denoted by a progressive increase of the AAE with increasing SSA (cf. Figs. S3-S6 in Chapter 5). Therefore, the effects of mineral dust on SSA and on C became less crucial at the regional background station, MSY, and were not observed at the urban background station, Barcelona (BCN), mainly due to the relatively lower influence of dust particles during Saharan dust outbreaks on the overall aerosol load as a consequence of the higher relative contribution of anthropogenic sources. This higher relative contribution from anthropogenic and more absorbing sources in BCN, and to a lesser extent at MSY, compared to MSA, prevents the SSA to reach high values.

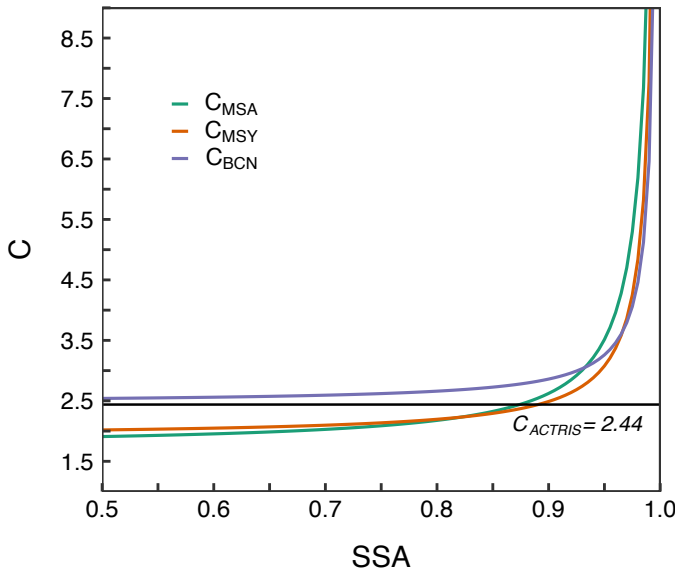

Figure 9.1: Cross-sensitivity to scattering dependency of the multiple scattering parameter, C, of the aethalometer AE33 by using the Barcelona (BCN), Montseny (MSY), and Montsec d'Ares (MSA) stations fitted values obtained in **Chapter 5**.

In addition to the dependency with the SSA, **Chapter 5** reports on the spectral dependence of the multiple scattering parameter, C(λ), at the three different background scenarios in the WMB: BCN, MSY and MSA. The analysis of the slope of the relationship between the C and the wavelength showed that the C increased with increasing wavelength at MSA under high SSA values. This progressive increase of the C with the wavelength was also associated to the presence of coarse mineral dust particles at this site. In fact, an increase in the slope

between C and wavelength was observed for negative SSAAE values (cf. Figs. 5 and S9 in **Chapter 5**). This increase of the C values towards the longer wavelengths was associated to the higher scattering efficiency of dust particles with increasing wavelength, since coarse mineral dust particles present their maximum scattering efficiency at longer wavelengths compared to fine particles (cf. **Chapter 1**). At the urban background station in BCN, no s.s. trend of the C parameter with the wavelength was found, which was associated to the absence of high SSA values that can increase the C. However, these results do not imply that the spectral dependence of C is only limited to aerosol backgrounds impacted by mineral dust particles. In fact, the results show that, given the observed increase of C with increasing SSA values, the spectral dependence of C could be observed whenever particles with high SSA dominate the sample. If the measurements are dominated by fine and highly scattering particles, such as sulphates, then the wavelength at which the scattering coefficient has its maximum will be lower, thus higher SSA values will be found at shorter wavelengths, and therefore higher C values will be obtained for the shorter wavelengths. Moreover, these fine particles can penetrate deeper into the filter, thus increasing furthermore the multiple scattering for the shorter wavelengths. Indeed, this inverse trend for the urban sites, where the C parameter decreases with increasing wavelength, is shown in Bernardoni et al. (2021), Ferrero et al. (2021) and Drinovec et al. (2022), and it can also be suggested by Fig. 5a in **Chapter 5**. In fact, Drinovec et al. (2022) has found that the scattering artifact and the C parameter increased for particles with a smaller diameter, even for soot particles with low SSA, by comparing the AE33 measurements with a photothermal interferometer (PTAAM-2λ). This becomes of great relevance, since at measurement sites where frequently fine particles are measured, a decrease of the C parameter with the wavelength could be observed.

As aforementioned, the dependencies of the C with both the SSA and the wavelength are particularly important for deriving the absorption coefficients from the AE33 aethalometer when the collected particles have high SSA. In fact, not applying a correction to the AE33 data for the increase in the cross-sensitivity to scattering hinders the accurate determination of the absorption coefficients. This relationship is of particular interest in remote areas where high SSA values are common, such as isolated Arctic stations, remote coastal sites and mountain-top monitoring sites. Previous studies have shown that the average C parameter values at these remote sites are higher than those obtained at urban background stations, even if an exhaustive analysis of the reasons causing the increase of the C parameter was not provided in these studies (Backman et al., 2017; Laing et al., 2020). In fact, as shown by Laj et al. (2020), 8 measurement sites have a higher average SSA than MSA, and around 9 had an average SSA higher than 0.925 at 550 nm, then if the absorption measurements were obtained with an AE33, around 17 out of the 30 stations analyzed would also be affected by the cross-sensitivity to scattering of the filter tape (cf. Fig. 9.1). Moreover, the spectral dependence of the C is crucial for determining the spectral dependencies of the absorption and other parameters influenced by this dependence, such as the AAE. In fact, there are numerous publications in the literature where the AAE has been derived from AE33 measurement. However, the possible spectral dependence of the C factor has been never taken into account, thus increasing the uncertainties related to the determination of the

AAE. Indeed, by using a wavelength-dependent C, an increase of the AAE up to a 13% was observed at MSA station when compared with the AAE obtained using a constant C (see Fig. 9.2).

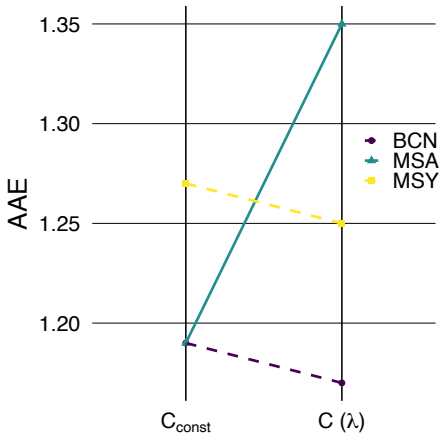

Figure 9.2: Variation of the AAE at an urban background station in Barcelona (BCN), a regional background station in Montseny (MSY) and a mountain-top station in Montsec d'Ares (MSA) depending on the use of a constant or a wavelength dependent multiple scattering parameter, C_{const} and C (λ), respectively.

Furthermore, the results presented in this thesis are also of high interest for the measurement of mineral dust particles absorption coefficients with the AE33, since SSA of mineral dust in the visible to near-IR spectral range is around the 0.9-0.95 threshold and the C is expected to increase. As proposed in **Chapter 5**, an iterative procedure should be used to obtain the site-specific C parameter in case that the AE33 absorption coefficients were not measured in parallel to a MAAP to obtain the cross-sensitivity to scattering of the C at that given location. Indeed, during the FRAGMENT campaign in the Sahara in **Chapter 8**, we derived the C value by performing a multi-step recursive algorithm that: i) assumed an initial C value that corresponded to the ACTRIS harmonized C parameter to obtain the absorption coefficient, and then calculated the average SSA, ii) thereafter it derived the new C associated to this given SSA following eq. (4.9) by assuming the cross-sensitivity fitted values from the MSA from **Chapter 5**, and iii) repeated steps i) and ii) until the C converged. In addition, it was also assumed the same spectral relationship of the C parameter as the one found in MSA, i.e. a linear increase of the C parameter with the wavelength. The C values obtained by following this iterative approach were 4.44 at 370 nm, 4.78 at 660 nm and 5.04 at 880 nm. In comparison with the SSA values obtained using the C value proposed by the ACTRIS working group on optical properties (Müller and Fiebig, 2021), the SSA from the iterative procedure showed an increase for the visible and near-IR wavelengths, from around 0.965 to 0.981 at 660 nm. Overall, the values for the C were comparable, albeit higher, with those found by Di Biagio et al. (2017) in a chamber experiment where mineral dust from different soils were resuspended, and the C for dust particles from Saharan and Sahel deserts ranged between 3.94 and 4.1 at 370 nm, and between 3.60 and 3.78 at 660 nm.

9.2 Horizontal and vertical spatial distribution of the optical properties in the NE of Spain

The characterization of the optical properties of the most relevant aerosol species with regards to their warming effect on the radiative forcing was performed at different locations in the NE of Spain that are representative of the most common background scenarios in the Mediterranean basin. The analysis of the vertical distribution of the aerosol particles physical properties in the NE of Spain was performed through airborne measurements during an intensive campaign that allowed the study of the physical properties of the multiple aerosol layers over this area under both typical summer recirculation patterns and Saharan mineral dust outbreak scenarios. In addition, it was studied the absorption enhancement of the BC particles as a consequence of its mixing with BrC particles and other aerosol species. Finally, Saharan mineral dust optical properties were characterized in an emission area of mineral dust in the Sahara desert, which is the principal contributor to mineral dust outbreaks over the Mediterranean. The mineral dust outbreaks from North Africa affecting the Mediterranean not only modify the optical properties of the aerosols, but are also associated to increasing snow melt, visibility reduction, lower air quality, and increasing human health risks, among others.

9.2.1 Optical properties of multiple aerosols layers under recirculation patterns in the Mediterranean

As commented in **Chapter 4**, the Iberian Peninsula is frequently under high pressure systems which during winter promote the stagnation of air masses with consequent accumulation of pollutants at the surface thus causing frequent excedances of the air quality limit values specified in the European Air Quality Directive (`https://www.eea.europa.eu/themes/air/air-quality-management/improving-europe-s-air-quality/policy-context`). During summer, the atmospheric conditions favour the formation of recirculation patterns, which are highly enhanced by the local orography. The temperature gradient, in the case of the Mediterranean cost between the sea and land surface, creates a pressure gradient which enables the formation of a breeze that advects the pollutants from the coast toward inland areas through the valleys (Atkinson, 1982). During summer, the larger pressure gradient creates a stronger breeze which can reach the Pyrenees mountain range where the pollutants are injected into the mid-troposphere and transported back into the Mediterranean coast where they sink through subsidence processes, creating a recirculation pattern. In addition, during this periods it is also frequent the overlap of Saharan dust outbreaks, thus further creating a more complex mixture of aerosol particles over the area of study. As a consequence, different layers of pollutants in the atmosphere that increase the aerosol optical depth and influences the radiative balance at a regional scale can be found over the Western Mediterranean coast and other regions of the Iberian Peninsula (e.g. Millán et al., 1997; Gangoiti et al., 2001; Querol et al., 2018).

The results from **Chapter 6** showed the spatial distribution of aerosol particles properties under summer regional circulation scenarios, with a period characterized by the coupling of the regional recirculation with a Saharan dust outbreak, using measurements from the regional background station of MSY and from the mountain-top station of MSA. The physico-chemical properties of the aerosol particles at these stations in the NE of Spain and the relationship between optical properties and the different sources and meteorological scenarios have been subject to thorough analysis (e.g. Ripoll et al., 2014; Pandolfi et al., 2014; Ealo et al., 2018). Ripoll et al. (2014) found that both stations had the second highest concentration values of PM, BC and particle number during summer, and especially during the recirculation pattern episodes and the Saharan dust events. Moreover, Pandolfi et al. (2014) showed that the scattering and absorption coefficients at MSA were the second highest and the highest during these summer recirculation events, and vice-versa for the Saharan dust event. Also, Pandolfi et al. (2014) reported an increase during summer of both the mass absorption and scattering cross-sections associated to the more frequent occurrence of the summer regional recirculation patterns and the Saharan dust events. This increase in the extensive optical properties in summer at MSA was associated to the increase in the amount of BC, PM and aerosol particle number concentration, the relative increase of aged organics and the advection of mineral dust particles over the area of study (Ripoll et al., 2015a). Indeed, Ealo et al. (2018) observed that at both MSY and MSA stations the main species contributing to the absorption were BC from traffic/industrial sources, which relative contribution remained similar throughout the year, aged organics, which relative contribution increased during the summer months, and secondary nitrate, which relative contribution increased in winter. Concerning the scattering, secondary sulphate and nitrates particles were identified as the most important species contributing to the measured scattering values, with the additional contribution of mineral dust particles during the Saharan dust events. Pandolfi et al. (2014) showed that these summer recirculation patterns were characterized by very fine particles, as denoted by the high concentrations of PM_1, and the SAE values around 1.8 on average, which were the highest compared with other meteorological scenarios, whereas during the Saharan dust events, although the PM_1 concentrations were also very high, the presence of very coarse mineral dust particles resulted in the lowest SAE values. Moreover, Ealo et al. (2016) showed that at MSY and MSA during the recirculation pattern the AAE ranged between 1.1 and 1.6 depending on the relative contribution to the total BC from biomass burning, and found AAE values during a Saharan dust event ranging between 1.4 and 2 at MSA.

Overall, during the recirculation episode shown in **Chapter 6** both MSY and MSA showed similar values for the PM_1 concentrations when compared with average values for this pattern reported in the literature (Pandolfi et al., 2014; Ealo et al., 2016). However, this specific recirculation episode showed higher PM_{10} concentrations with a higher fraction of coarse particles, which was clearly reflected in the intensive optical properties with lower SAE values. With regards to the extensive optical properties, the measurements showed similar scattering coefficients at both MSY and MSA stations which were also similar compared with the averages, around 50 Mm^{-1}, provided by Pandolfi et al. (2014) and Ealo et al. (2016). In contrast, the absorption values presented a larger difference, with similar absorption

coefficients at MSY to those typically registered during recirculation episodes, whereas at MSA the absorption coefficients doubled, reflecting the higher fraction of absorption particles advected to this station during this specific regional episode. Furthermore, the absorption coefficients temporal variation was highly correlated with the SSA, showing decreases of the SSA from around 0.93 to 0.85 when the absorption increased. This absorption/SSA increase/decrease was due to the advection to the site of aerosol particles with a composition of either a higher BC fraction when the AAE decreased to around 1.0, or BrC when AAE increased towards 1.5. The higher AAE values during this episode were associated to the higher ageing state of the particles, with a higher fraction of secondary organic aerosols, and to the advection of BrC particles from nearby wildfires. During the Saharan dust event higher concentrations of mineral matter were measured at the mountain-top station of MSA than at MSY, indicating that dust particles were advected at high altitude during this event, also in agreement with specific studies performed at this region (Pandolfi et al., 2014; Ealo et al., 2016), as well as by the studies over Europe characterizing the larger impact of the Saharan dust outbreaks at higher altitudes in mountain-top stations (Collaud Coen et al., 2004). With regards to the optical parameters, the AAE was similar at both stations, with average values of 1.25, and peaks up to 1.5-1.75, similar to those measured on average during the recirculation pattern episodes, .

The analysis of the vertical profiles of aerosol particles physical properties by using airborne measurements were also presented in **Chapter 6**. During the summer regional recirculation pattern, the measurements showed the accumulation of aerosol particles within the PBL, which was around 1-1.5 km a.s.l., with similar absorption and scattering values at both MSY and MSA despite the distance between the two stations and the closer proximity of MSY to the main pollutant sources compared to MSA. This similarity highlighted the highly mixed PBL over the area under these summer scenarios. During the aircraft measurements the number of layers and the vertical distribution of aerosol particles increased over time whilst the scenario kept favouring the onset of recirculation processes. The vertical profiles showed a decrease of the size of the particles with height, inferred from the slight decrease of the asymmetry parameter, from 0.65 to 0.6 and the increase in the mass scattering cross-section with height, from around 2 to 4, with some layers up to 6-8 $\mathrm{m^2 g^{-1}}$. However, some layers with coarser particles were also found up to 3.3 km a.s.l. During the flights, SSA values were around 0.75-0.85, both within the PBL and the layers with higher aerosol particles concentration, indicating the presence of very absorbing particles. Indeed, the PM mass absorption cross-sections (MAC) values were rather high and ranged between 0.3 and 0.5 $\mathrm{m^2 g^{-1}}$, and were mostly associated to the presence of BC particles, as denoted by AAE values around 1 (Fig. 9.3). However, some layers around 2 km a.s.l. showed AAE values around 1.5, indicating the presence of BrC mixed with BC in those layers. The presence of BrC particles was in some cases the consequence of the impact from wildfire smoke plumes, characterized by their large amount of absorbing organic aerosols, i.e. of BrC particles (Lack et al., 2012).

During the Saharan dust events, the vertical distribution of the optical properties showed rather constant AAE values above 1.5, with some layers at around 2 km a.s.l. showing an

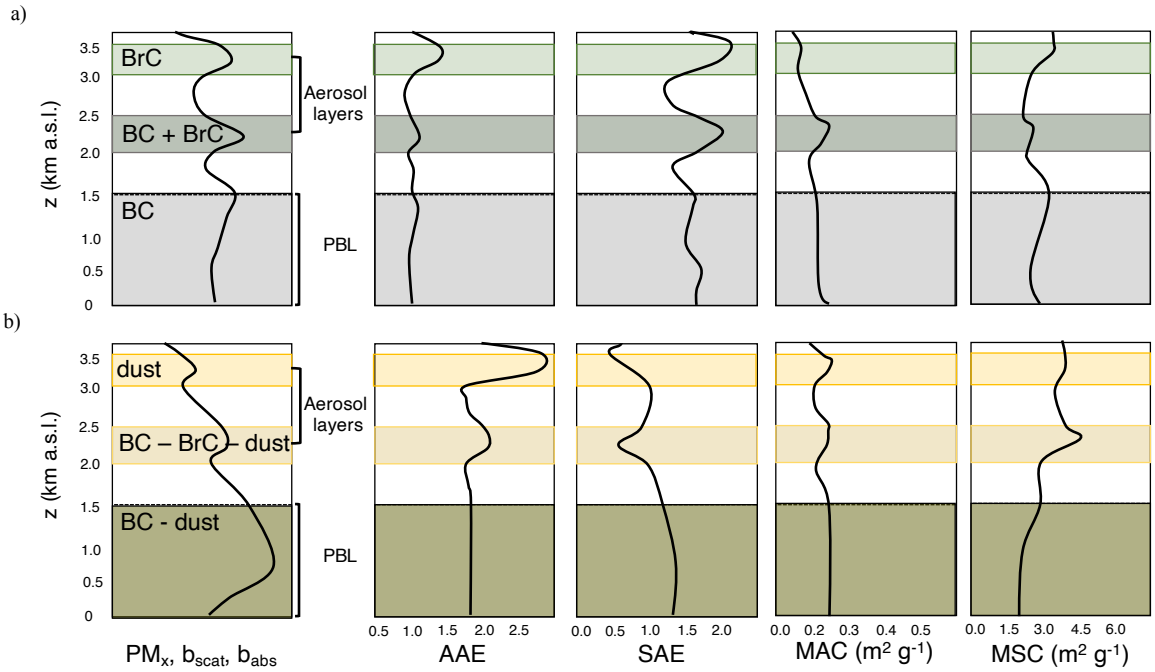

Figure 9.3: Schematic of the vertical profiles showing the variation of the PM concentration and some extensive and intensive optical properties within the PBL and at different layers during a) the regional recirculation scenario, and b) the regional recirculation scenario also affected by a Saharan dust event. The upper panel shows a PBL and a first layer with typical values and variations of a regional recirculation scenario with a mixture of BC and BrC particles, whilst the upper layer shows the possible influence of wildfire smoke affecting the area. The lower panel shows the presence of a PBL and lower layers with the influence of both the regional recirculation pattern and the mineral dust particles, with an increase with height in the relative contribution of mineral dust particles to the total aerosol load.

AAE of around 2. Through the different layers above the PBL, the SAE was mostly below 1.2 and the SSAAE was negative, confirming the presence of coarse dust particles in the whole vertical profile. Furthermore, the SSA was slightly lower within the PBL, with values around 0.85, similar to the SSA values measured at the surface stations, with a progressive increase with height toward values around 0.9 (cf. Fig. 9.3). Similarly, the MAC, calculated by taking into account the PM concentration of all the compounds, remained stable through the vertical profiles with slight decrease with height, from 0.25 to 0.2 $\mathrm{m^2 g^{-1}}$, associated to the reduction in the relative contribution of BC into the aerosol composition. In contrast, the MSC presented a more notable increase with height, from 2 to 4 $\mathrm{m^2 g^{-1}}$, as a consequence of the higher relative proportion of fine particles at higher altitudes.

In summary, the physico-chemical properties of aerosol particles during the recirculation period at both the surface and throughout the different aerosol layers formed during the recirculation scenarios showed the presence of very fine particles with a fairly homogeneous spatial distribution near the surface and within the PBL. At altitudes above the PBL there was a substantial decrease of the concentration of particles with height, with the particles becoming more fine and with a corresponding increasing mass scattering efficiency with

height. Conversely, the mass absorption efficiency of PM, mostly attributed to the presence between 1.5 and 3.5 km a.s.l. of a mixture of BC particles with OA, remained fairly stable at around 0.2-0.25 $\mathrm{m^2 g^{-1}}$. In addition, several layers with different composition were observed. Some layers presented AAE values around 1.5, suggesting the presence of aged OA particles which increase the absorption coefficients in the short-UV and visible spectra range. Conversely, other layers showed AAE values close to 1 with a large decrease of the SSA to values close to 0.7 indicating that the absorption was dominated by BC particles of anthropogenic origin. Moreover, during the dust event, the results showed a heavily aerosol loaded atmosphere with multiple layers from the ground up to 5.8 km a.s.l., and a highly homogeneous distribution of the optical properties between the layers. The homogeneous values of both extensive and intensive properties of the layers above the PBL were associated to the presence of well distributed mineral dust particles, in addition to the sporadic presence of other aerosol sources, such as biomass burning, at certain heights, and BC particles from anthropongenic sources near the surface. The presence of multiple layers above the surface increases the radiative forcing of the aerosols particles, which depends on the thickness of the layers, and the particle composition and physico-chemical properties. These layers affect the radiative forcing and are of special interest if they present high concentrations of particles with high MAE and low SSA values, associated to the presence of BC particles, and to a lesser extent of BrC.

The measurements presented in this thesis and previous studies showed the importance of continuously monitoring the physico-chemical properties of aerosol particles at sites characterized by different aerosol sources with different characteristics (e.g. Pandolfi et al., 2014; Ripoll et al., 2014; Ealo et al., 2016; Laj et al., 2020). Moreover, these long-term measurements allowed the study of the trends and seasonal variations of aerosol particles properties with large spatial coverage. In addition, performing instrumented flights, albeit presenting a more restrictive temporal resolution in comparison with remote sensing measurements via LIDARS and ceilometers, allows for a more detailed analysis of the vertical profiles of the aerosol particles properties.

9.2.2 BC and OA mixing effects on the aerosol absorption properties

The amount of organic aerosols (OA), and especially of absorbing OA, i.e. BrC, mixed with BC particles and the effects that this mixing produces in the overall absorption is highly dependent on the aerosol particles species involved in the mixing process. Moreover, in addition to the primary sources of BrC (e.g. biomass burning), the meteorological conditions can favour the ageing and formation of secondary organic aerosols from gaseous precursors. The NE of Spain is characterized by high values of BC relative to its surroundings and especially in urban and industrial areas, together with high concentrations of OA particles, both form primary and secondary anthropogenic and natural sources (Minguillón et al., 2015; Ripoll et al., 2015a; Via et al., 2021). As commented in Sect. 1.3, both BC and BrC can absorb light, with BrC particles presenting a higher absorption efficiency in the UV-VIS spectral range

compared to near-IR thus increasing the AAE, whereas if the absorption is dominated by BC of anthropogenic origin, the AAE is close to unity due to the BC particles constant complex refractive index with the wavelengths in the whole UV to IR spectrum.

Indeed, the presence of BrC particles with BC particles, in addition to the mixing with other non absorbing OA and inorganic aerosols, produces an enhancement of the absorption of BC particles (E_{abs}), which was quantified by normalizing the measured ambient MAC by a reference MAC value for pure BC. This absorption enhancement was thoroughly analyzed in **Chapter 7** at BCN and MSY measurements stations.

As commented in Sect. 1.3, the mixing of BC with other particles can be separated into two categories: external and internal, where the absorption enhancement due to the external mixing corresponds to the increase of the overall absorption from the contribution from the less absorbing OA, i.e. BrC, and internal mixing where less absorbing or non absorbing particles are tied together with BC particles. The internal mixing is usually studied through a core-shell theory approach (Lack and Cappa, 2010). Given that E_{abs} presents a high regional variability, the measurements at two different backgrounds (urban and regional) with different PM chemical composition and high seasonal and diurnal evolution of organic and inorganic aerosols enabled the analysis of the influence that this variations had on E_{abs}. Moreover, due to the availability of a decade long database, a trend analysis of E_{abs} at these different background sites was performed.

One of the most relevant results was the E_{abs} dependency with the the amount of material available for mixing, i.e. both organic (absorbing and non-absorbing) and inorganic aerosols. The material available for internal mixing with BC particles was referred to as NR-PM. On average, higher values of E_{abs} where observed at MSY than at BCN, with values at a wavelength of 637 nm of 2.0 at MSY and of 1.42 at BCN, respectively. The higher average E_{abs} observed at MSY was due to the higher ratio NR-PM/EC at the regional station compared to the urban site. Indeed, the relationship between E_{abs} and NR-PM/EC showed a progressive increase of E_{abs} with increasing NR-PM/EC ratio with values up to 3.2 at MSY and 1.9 at BCN, respectively (cf. Fig. 9.4). This result is of great relevance for climate models because it implies that for a given concentration of pure BC (or EC), the absorption coefficient of ambient BC should be corrected by a factor of E_{abs} that depends on the concentration of NR-PM/EC of in order to take into account the effect of the mixing of BC. This result further demonstrates the strong regional variability of E_{abs}. Moreover, the spectral dependence of E_{abs} was analyzed using the absorption measurements from the multi-wavelength AE33 at BCN. This analysis showed an increase of E_{abs} from 880 nm to 370 of around 13 $\%$. This increase of E_{abs} towards the UV was the consequence of the increase in the contribution to absorption from BrC particles externally mixed with BC as a consequence of the higher absorption efficiency of BrC at the short-UV wavelengths (Liu et al., 2015a; Zhang et al., 2020).

The seasonal evolution of E_{abs} was mainly linked to the evolution of the NR-PM concentrations relative to EC and the variation of the contribution from the different aerosol

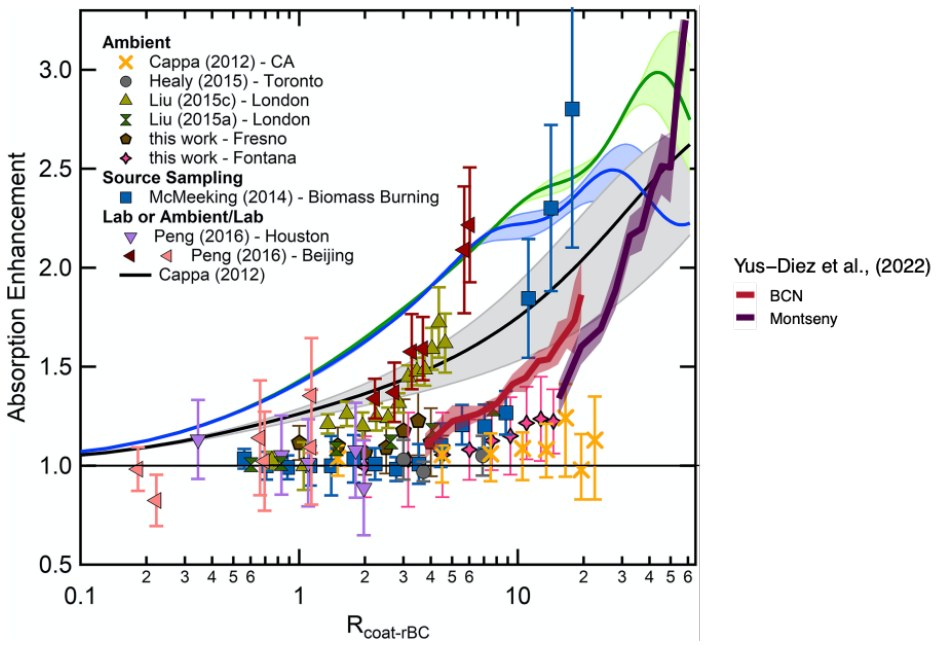

Figure 9.4: Absorption enhancement, E_{abs}, as a function of the NR-PM to EC ration obtained at Barcelona (BCN) and Montseny (MSY) station for 637 nm in **Chapter 7** and at several stations from multiple studies as shown in Fig. 1 from Cappa et al. (2019), where the wavelength is the largest wavelength available.The uncertainty error bars and the shadow of the line represent each bin standard deviation of the observations.

species. The highest E_{abs} values were measured at MSY station for the warm season as a consequence of both the higher amount of material available for BC mixing (i.e. higher NR-PM/EC ratio) and the increase in the relative proportion of SOA particles from biogenic sources and photo-chemical activity at regional level. However, at BCN, the highest E_{abs} values were measured during the cold season due to the higher accumulation of OA from traffic, cooking and biomass burning aerosols and the higher relative proportion to OA of oxidized organic aerosols. Indeed, it was found that the main sources contributing to the absorption enhancement in BCN during winter were the traffic-related hydrogen-like organic aerosols (HOA), cooking OA (COA), the highly absorbing BrC particles from biomass burning OA (BBOA) for the short-UV wavelengths, and the more oxidized and less oxidized oxygenated organic aerosols, MO-OOA and LO-OOA, respectively. BBOA has been identified as an important BrC source in numerous studies (Zhang et al., 2020), and more recently both HOA (Qin et al., 2018) and COA (Kasthuriarachchi et al., 2020) have been identified as potential sources of BrC in urban environments . Conversely, during summer, E_{abs} was lower compared to the winter period, especially at the short-UV, due to the reduction in the contribution of the externally mixed BrC. The main sources that contributed to E_{abs} during summer were HOA and COA internally mixed with BC, and secondary inorganic aerosols such as nitrates and sulphates internally mixed with BC.

Climate models assume an overall absorption enhancement of around 1.5 (e.g. Liu et al., 2015b, and references therein), which is similar to the values found in this study at BCN station and in other works reported in the literature (Cappa et al., 2019, and therein).

However, the use of a constant E_{abs} fails to describe the observed high variability of E_{abs} reported in the literature and in this thesis, and more specifically, its dependency with the concentration of BrC and other non-absorbing aerosols particles that can be mixed with BC particles. In fact, the observed high concentrations of organic and inorganic aerosols relative to EC observed in the atmosphere at many sites (e.g. Chen et al., 2017), have shown that can lead to a large increase of E_{abs} (cf. Fig. 9.4), thus potentially leading to an underestimation of the absorption enhancement of BC assumed in climate models. As an example, if the concentration of NR-PM/EC is high enough so that an E_{abs} of 3 can be expected (cf. Fig. 9.4), then the assumed E_{abs} of 1.5 can lead to an underestimation of the simulated absorption with actual absorption values two times higher that the simulated absorption values. Therefore, as an example, for an SSA of 0.8, typically observed during the recirculation episodes in NE Spain, the use of a E_{abs} of 1.5 instead of 3 would lead to an overestimation of modelled SSA of around a 16%, which ultimately will increase the positive effect of BC on the radiative forcing.

In addition to the overall NR-PM concentration levels, the effect of the different species on the absorption enhancement should also be included in the climate models, since, depending on the aerosol species, these can enhance or not the absorption by the BC particle. Indeed, the effect of the different aerosol species, along with their concentration and the oxidation state of the aerosol particles, could potentially be one of the main causes for the large observed regional differences of E_{abs}. Taking into account all these experimental evidences into climate models is paramount to accurately characterize the mass absorption cross-sections of BC and OA particles in order to reduce the current uncertainties related to their effects on radiative forcing.

The availability of a long database of both the absorption coefficients and the offline EC concentrations at both stations (urban and regional) allowed the study of the trend of E_{abs}. The E_{abs} showed no s.s. trend over time between 2010 and 2020, with the exception of the summer period at MSY, where a s.s. annual increase of 8.16 % was observed. The s.s. increase of E_{abs} observed at MSY for the summer season was associated to a corresponding positive trend of the relative contribution of OA to the NR-PM, and especially of SOA to OA (Veld et al., 2021; Via et al., 2021), that efficiently enhances the BC absorption efficiency.

In summary, the absorption enhancement of the BC particles due to the mixing of BC with other less absorbing OA, i.e. BrC, and non-absorbing OA and SIA, presents a highly regional heterogeneity due to the differences in aerosol composition and the amount of material available for mixing. Therefore, given the relevance of the BC absorption on climate radiative forcing, an accurate characterization of the regional variations of the aerosol species and their concentration is needed. Furthermore, as a consequence of the current guidelines for restricting aerosol emissions, the relative proportion of SOA to the total PM concentration has increased (e.g. Veld et al., 2021), which potentially could lead to an increase in E_{abs}, as observed in this thesis at MSY in summer. Therefore, assessing the variations over time of SOA and SIA as main drivers of E_{abs} is needed for correctly assessing the evolution over time of E_{abs}.

9.2.3 Mineral dust particles

Mineral dust particles are frequently advected over the Mediterranean basin, and a large fraction of Europe, as a consequence of the recurrent outbreaks from the North-Africa arid regions, mainly from the Saharan deserts (Collaud Coen et al., 2004; Pey et al., 2013). The impact of these events on the optical properties on the Iberian Peninsula at surface level has been characterized in the literature (e.g. Pandolfi et al., 2011; Pandolfi et al., 2014; Valenzuela et al., 2015; Ealo et al., 2016; Titos et al., 2017). This thesis also presents an exhaustive characterization of these events by studying the vertically resolved physical properties of dust particles and the physico-chemical properties of dust at an important source region in the northern outskirts of the Sahara, in L'Bour, Morocco. Once formed, dust particles undergo a large array of processes before reaching the Mediterranean Basin, mainly due to their mixing with other aerosol particles and its progressive dispersion through the atmosphere and deposition on the surface. Thus, in order to improve the characterization of the dust particles and their effects on climate, a more accurate description of pure mineral dust particles at the emission source areas are needed. With this aim, an intensive measurement campaign was performed at an arid region in the outskirts of the Sahara desert.

The observed optical properties of dust in this important dust source emission area showed a high dependency associated to the strength of the processes emitting mineral dust into the atmosphere (cf. **Chapter 8**). Essentially, during events with very high friction velocity, the emission processes increase in intensity, thus increasing the concentration of dust particles being emitted into the atmosphere. As commented in **Chapter 1**, the main processes responsible for the emission of dust are direct entrainment, saltation and disaggregation processes. Moreover, under the right atmospheric conditions, Haboobs storms can develop and lift the dust particles directly to high levels on the troposphere, as well as advect dust particles over large areas over the surface. During Haboob storms, the high wind speeds associated to the strong convective processes also favour the emission of dust at a local scale through the aforementioned emission processes. The presence of these strong dust events ultimately cause the coarse mineral dust particles to represent the only source contributing to the variation in the measured aerosol particle number concentration and optical properties at the source region. Thus, the measured physical properties under this strong emission conditions converge towards those found in chamber experiments where soil samples, previously collected in mineral dust emission areas, are resuspended and analyzed (cf. Table 9.1). We observed AAE values around 2.5, and SSA around 0.95 at 370 nm, and 0.99 at 880 nm, an asymmetry parameter a 525 nm of 0.65 and a SAE of 0.26.

The optical properties of dust particles were considerably different for many optical parameters (AAE, SAE, SSAAE, MAC, MSC, etc.) between the source region and the regional (MSY) and mountain-top (MSA) measurement sites and the vertical profiles performed over the NE of Spain during the Saharan dust outbreak. The measured MAC for $PM_{2.5}$ during the Sahara dust outbreaks over the NE of Spain ranged for a wavelength of 525 nm between 0.18 $\mathrm{m^2 g^{-1}}$ at MSY, 0.21 $\mathrm{m^2 g^{-1}}$ at MSA, and between 0.2 and 0.25 $\mathrm{m^2 g^{-1}}$ along the vertical profiles, whereas at the dust source the values were around one order of magnitude lower,

with values around 0.025 and 0.005 $\mathrm{m^2 g^{-1}}$ at 370 nm and 880 nm, respectively. The mass scattering cross-sections at 525 nm ranged between 2 and 4 $\mathrm{m^2 g^{-1}}$ during the vertical profile measurements, whereas at the source it ranged between 0.5 and 0.7 $\mathrm{m^2 g^{-1}}$ for the stronger and weaker dust emission events, respectively. The higher MAC and MSC values observed during the vertical profiles in comparison with the source area were due to the presence along the vertical of a high concentration of fine particles from local/anthropogenic origin, which increased the overall scattering, and to the mixing of dust particles with more absorbing particles, such as BC and smoke from wild fires, which increased the MAC (or MAE) of the particles in the atmosphere. Indeed, as can be seen in Table 9.1, the MAE (or MAC) of the mineral dust particles ranged around 0.02-0.06 for mineral dust particles from different emission sources in North Africa, whereas at the Mediterranean the values ranged between 0.18-0.25. This was also shown by the smaller SSA measured at the Iberian Peninsula, with values in the range of 0.88-0.90, whereas the SSA at North Africa emission areas ranged between 0.94 and 0.99. Moreover, the AAE showed lower average values at the Mediterranean due to the mixing of the mineral dust particles with particles with a weaker absorption wavelength dependence, such as BC.

Climate models simulate the temporal and the spatial (horizontal and vertical) distribution of aerosol particles and their physico-chemical properties and effects on climate by integrating the surface measurements and simulating aerosol particle emission from the different sources, which are then coupled with the meteorological forecast for the whole atmosphere in addition to the aerosol particles vertical profiles provided by the satellite. The advantage of using satellite measurements for deriving the vertical distribution of aerosol particles, and then calculating their radiative forcing, is due to the ability of satellite data to cover the entire Earth's atmosphere. However, these retrievals are still subject to large biases, such as the miss-estimation of the vertical distribution of BC, mineral dust and other relevant aerosol species (Johnson et al., 2012; Kipling et al., 2013), and the underestimation of the global load of the aerosol particles, such as mineral dust (Kok, 2011). Hence, the importance of performing more accurate and complete vertical profiles with instrumented flights to adjust the retrieved satellite-based vertical profiles and improve and portray a more accurate description of the vertical distribution of the aerosol particles physico-chemical properties and, consequently, of their effects on climate.

In summary, given the high contribution of mineral dust particles to the global aerosol load, and the uncertainties related to the sign and value of their radiative forcing, it is utterly important to correctly assess their optical properties. As already stated, North African arid and semi-arid regions are the largest source contributor of mineral dust into the atmosphere. Thus, the great relevance of correctly characterizing of the optical properties of freshly emitted mineral dust from the source areas, its relationships with the particle size distribution and the strength of emission for improving the analysis of the optical properties of dust in the climate models. It has been found that the higher the emission strength, the higher it is the relative contribution of mineral dust to the overall optical properties, thus providing values of the optical properties similar to those measured at experimental chambers using resuspended soil

Table 9.1: Average optical properties for wavelengths at various locations in emission areas of the Sahara desert and at different regions over the Mediterranean basin. The optical properties, obtained at wavelengths (λ) in the short-UV to visible spectrum range, include the Mass absorption efficiency or cross-section (MAE or MAC), single-scattering albedo (SSA), absorption Ångström exponent (AAE), scattering Ångström exponent (SAE) and the asymmetry parameter (g).

Location	λ [nm]	**MAE**	**SSA**	**AAE**	**SAE**	**g**
Sahara - Morocco[a]	525	0.02	0.97	2.2	0.26	0.65
Sahara - Morocco[b]	537		0.94-0.96			
Sahara - Egypt[c]	532	0.02	0.99	4.2		
Sahara - Morocco[c]	532	0.06	0.98	5.3		
Sahara - Tunisia[d]	532	0.01				
Sahara - Morocco[e]	532			2.25-5.13		
Sahara - Morocco[f]	532	0.03		2.6		
Sahara - Libya[f]	532	0.03		4.1		
Sahara - Algeria[f]	532	0.04		2.8		
Sahara[g]	520		0.94			
Sahara[h]	520					0.53
MSA, transported[i]	525	0.21*	0.88	1.46	1.25	0.58
MSY, transported[i]	525	0.18*	0.90	1.26	1.05	0.55
Granada, transported[j]	440		0.89	1.5	0.5	
Cape Verde, transported[k]	550		0.96			
Cyprus, transported[l]	370	0.24		1.41		
NE Spain, flights[i]	525	0.2-0.25	0.83-0.93	1.25-2.5	0.75-1.85	

[a]Yus-díez et al. (2022), [b]Schladitz et al. (2009), [c]Linke et al. (2006), [d]Alfaro et al. (2004), [e]Müller et al. (2009), [f]Caponi et al. (2017), [g]Di Biagio et al. (2019), [h]Kahnert and Nousiainen (2006), [i]Yus-Díez et al. (2020), [j]Valenzuela et al. (2015), [k]Müller et al. (2011c), [l]Drinovec et al. (2020), * New data presented in this discussion.

samples. In addition to their large contribution at a global scale, Saharan dust is the highest contributor of mineral dust particles reaching the Mediterranean basin, with an increasing contribution gradient towards the south of the basin, so that during intense dust outbreaks these particles can potentially become the most relevant species in the atmosphere. Hence continuous monitoring of these outbreaks over these regions at different backgrounds enables the analysis of the effects that they have on the physico-chemical properties of aerosols under varying aerosol particles composition regimes. Finally, since mineral dust advected into the Mediterranean basin is consequence of long-range transport, its distribution over the whole vertical layer is not restricted into a single layer, on the contrary mineral dust was found more or less homogeneously distributed with some layers presenting higher concentrations levels. The vertical profiles of the optical properties of dust particles showed higher AAEs and lower SAEs as expected given the influence of the coarse particles with heavily short-UV biased absorption efficiency.

10

CONCLUSIONS AND FUTURE RESEARCH

10.1 Conclusions

Globally, aerosol particles effects on the Earth climate are associated to a cooling effect, however there are still large uncertainties, especially related to the absorbing properties of certain species, namely BC, OA and mineral dust. The Mediterranean basin, and in particular the NE of Spain, is a region where the complex topography and meteorology coupled with the presence of multiple anthropogenic and natural sources determines the presence of aerosol particles with very different physico-chemical properties. This thesis presents a series analyses performed to improve the characterization of the effects on the optical properties of BC, BrC and mineral dust, with special focus on the absorption of light radiation.

10.1.1 Improving filter-based absorption measurements

In order to obtain the absorption coefficient, the AE33 aethaloemter uses a parameter, C, that corrects for the multiple scattering of the sampled particles on the filter tape. We analyzed the cross-sensitivity to scattering of the multiple scattering parameter, C, for the two most used AE33 filter tapes by studying their relationship with the single-scattering albedo, SSA, at three different background stations in the NE of Spain, BCN, MSY and MSA. We presented a novel approach based on the measurements of the SSA calculated from scattering measurements from integrating nephelometers and independent reference absorption measurements from MAAP. This analysis showed a large dependency of C with the SSA, with up to a 3-fold increase for SSA values above 0.95, with small variations between the two filter tapes. Indeed, this dependency dictated the diurnal and seasonal evolution of the C parameter, which mirrored the evolution of the SSA. The increase of the C was mostly associated to the presence of mineral dust particles at the mountain-top station, and to a higher concentration of OA at the regional background station (MSY), whereas at the urban background station (BCN), where the SSA is on average lower, no clear dependency of the C with SSA was observed. Given that this parameter is directly used for calculating the absorption coefficients, a 3-fold increase of this parameter implies a 3-fold reduction of the

absorption coefficient compared to the absorption calculated using the harmonized C value provided in ACTRIS.

Additionally, this thesis shows that the multiple scattering parameter at MSA presented a statistically significant (s.s.) spectral dependency, whereas no s.s. relationship with the wavelength was observed at the urban and regional background stations. The increase of the C parameter with the wavelength at the mountain-top station was associated to the higher SSA values observed at this station due to the higher relative contribution of mineral dust particles that have a higher scattering efficiency at longer wavelengths. The observed spectral dependence of the C is specially relevant at those stations where frequent Saharan dust outbreaks are observed (mainly at the Mediterranean Basin). In fact, this thesis reports an increase of the AAE by a 13% at the mountain-top station station (MSA) using a wavelength dependent C parameter instead of a constant C.

The AE33 is the most widely used instrument to measure particle absorption in international networks as GAW and ACTRIS, where guidelines to correct AE33 data have been provided, yet they still do not include the cross-sensitivity to scattering analysis provided in this thesis, nor a guideline for the possible spectral dependence of C.

10.1.2 Expanding aerosol particle characterization over the NE of Spain through vertical profiles

The NE of Spain is subject to multiple atmospheric scenarios associated with high pollution episodes at both a regional and a local scale. Among these, the most common are the winter anticyclonic episodes, summer regional recirculation periods and the mineral dust intrusions from Saharan dust outbreaks. As a result of an intensive measurement campaign performed during the summer of 2015 this thesis presents the physico-chemical properties of aerosol particles at the troposphere through a combination of surface measurements at the monitoring stations and the vertical profiles with multiple layers of aerosols in the atmosphere through instrumented flights and surface-based remote sensing ceilometers. This results provide the first study of vertical profiles of the aerosol particles in the Iberian Peninsula through instrumented flights.

The regional recirculation period showed low dispersion of aerosol particles, with concentration values similar to those found in the literature for this kind of events, with a highly homogeneous distribution of PM concentration and absorption and scattering coefficients over the area of study.

The vertical profiles showed that the PM concentration remained fairly constant within the PBL up to 1.5 km a.s.l., with very absorbing and fine particles, mostly associated to the presence of fine primary and secondary aerosols due to anthropogenic emissions and secondary aerosol formation. The AAE values were close to 1, showing that most of the absorption was driven by BC particles of anthropogenic origin. Above the PBL, the measurements showed a highly stratified atmosphere, with layer thickness ranging between 200

and 500 m, characterized by the presence of very fine particles with SAE values close to 2 and with different AAE depending on the layer and the day. Some layers showed AAE close to 1, indicating the higher relative proportion of BC particles, whilst other layers showed AAE values up to to 1.5, indicating the presence of BrC particles both from wildfires and ageing of OA during to the recirculation processes. Overall, the particles became finer and scattered more efficiently the light radiation with height, as denoted by the progressive increase/decrease of the mass scattering cross-section/asymmetry parameter. Conversely, the mass absorption cross-section showed very high values close to the ground, and then presented a progressive decrease with height, with the exception of the more BC-loaded layers where the MAC values were around 0.25-0.37 $\mathrm{m^2 g^{-1}}$, similar to those closer to the surface.

During the Saharan dust event, the ceilometer showed a high concentration of particles with multiple layers with thicknesses around 500 m up to 5 km a.s.l. as a consequence of the intrusion of mineral dust in addition to the regional recirculation of aerosols. The optical properties showed that the coarse mode particle dominated, with SAE values below 1.0 and an increase of the absorption towards the short-UV with AAE above 1.5, due to the iron-oxide content of the dust particles, especially above the PBL where the regional anthropogenic influence decreased. During this period the intensive optical properties did not show large variations since the mineral dust particles were fairly homogeneously distributed throughout,the vertical profiles. However there were several layers where the relative contribution of the coarse mineral dust particles increased, as denoted by lower SAE and AAE values up to 2-5. For comparison, during the recirculation patterns without the influence of the Saharan dust outbreak, the MAC showed fairly constant values around 0.2-0.25 $\mathrm{m^2 g^{-1}}$, and the MSC showed a progressive increase with height from around 2 to 4, $\mathrm{m^2 g^{-1}}$. This increase with MSC with height during the recirculation episode was due to increase in the relative importance of fine, more efficient scatterers with altitude.

The performed instrumented flights allowed both for the analysis of the relevant optical properties and their variation between the different layers depending on the composition of the aerosol particles, as well as for the determination of the thickness of the multiple layers observed close to the surface and aloft. These measurements reflected the importance of the regional recirculation events, often coupled with Saharan dust outbreaks, on the NE of Spain and the potential impact on climate at a regional level. Indeed, the effects on climate of aerosol particles in the area of study during summer are expected to be more complex when particles are distributed over multiple layers through the troposphere, instead of at a single layer close to the surface, i.e. the PBL. In addition to an increase in the aerosol optical depth due to the presence of the aerosol layers, the interaction with radiation has proven to be highly dependent on the composition of the aerosol particles at each given layer.

10.1.3 BC mixing with OA and SIA: effects on BC absorption

Black Carbon particles are rarely emitted in their pure state, on the contrary the combustion processes responsible for their emission simultaneously emit organic and inorganic aerosols

and precursors. Thus, shortly after emission, BC particles are mixed in the atmosphere with other compounds, which some of these, as BrC particles, can also absorb light radiation. The complexity of BC and BrC absorption of solar radiation, and its dependence on their internal and external mixing in the atmosphere, is becoming of greater interest in the scientific community. The MAC of ambient BC can present much higher values than those expected for pure BC particles. Therefore, the ratio between the measured MAC for ambient BC and the reference MAC for pure BC particles represents the absorption enhancement, E_{abs}, of the BC particles produced by its mixing with other aerosol particles. In this thesis it was found that E_{abs} was highly dependent on the composition and concentration of aerosol particles available for mixing, and therefore, presented a large regional variation. Indeed, we found an overall absorption enhancement at 637 nm of around 1.42 and 1.87 at the urban station (BCN) and at the regional station (MSY), respectively. The higher absorption enhancement at MSY was associated to the higher relative concentration of organic and inorganic particles available for BC mixing at the regional background station.

The seasonal evolution of the E_{abs} presented a strong wavelength dependence at BCN. During the cold season E_{abs} increased significantly at the short-UV wavelengths due to the increase in BrC particles externally mixed with BC, whereas in the red and the near-IR, where the relative contribution to the absorption from the BrC particles is smaller, the E_{abs} increase was smaller. Indeed, during winter the increase of biomass burning activities and the larger accumulation of pollutants increased the relative contribution of BrC particles to E_{abs} from a 4.6 % during summer up to a 20.3 %. At MSY the absorption enhancement, only analyzed at 637 nm, showed an increase during summer due to the larger contribution of SOA due to larger emissions of biogenic precursors, which at this wavelength is mostly internally mixed with BC.

A sensibility study on the variation of the relative contribution of the internal and external mixing to the overall absorption enhancement showed a large dependence on the Ångström Exponent (AE) of the MAC of pure BC particles. If the MAC was consider to have a weak wavelength dependence, then the relative contribution of the external mixing of BrC with the absorption enhancement showed a large increase towards the short-UV, whereas if the MAC had a stronger wavelength dependence, the relative contribution of the external mixing would be considerably reduced, even for the short-UV wavelengths. The contribution of the external mixing to E_{abs} is obtained as the subtraction between the total E_{abs} and that associated to the internal mixing, thus if the AE of the MAC of internally mixed BC increased, then the difference with the total obtained as the subtraction between the total E_{abs} and that associated to the internal mixing, i.e. the contribution from BrC, will decrease, and vice-versa.

The absorption enhancement showed an exponential increase at both BCN and MSY as the amount of material available for mixing increased, although, since at the regional station the relative-to-BC concentrations of mixing material were higher, the absorption enhancement reached higher values, with values up to 3 at MSY, and up to 2 at BCN. Thus, the absorption

of BC particles was significantly higher than what would be expected if it was calculated using the literature MAC values for pure BC particles and the EC concentration measurements.

The results from a multi-linear regression analysis on the contribution from the different organic and inorganic aerosol species on the absorption enhancement showed slight variations with the wavelength and very distinct results between winter and summer. During winter there was, independently from the wavelength, a large contribution to E_{abs} from primary organic aerosols from traffic and cooking related sources (HOA and COA), from the biomass burning organic aerosols at the short-UV wavelengths, and to a lesser extent, from highly oxidized organic aerosols (MO-OOA), and also from the less oxidized OOA (LO-OOA) at the short-UV wavelengths. Conversely, during summer, albeit an overall reduction of E_{abs}, the relative contribution to E_{abs} from the SIAs increased, mainly from sulphate and ammonium particles, whilst the contribution from the OA significantly decreased. Furthermore, higher absorption enhancement values were measured for the higher aged OAs particles with a higher SOA to POA ratio, especially during the winter months, when the accumulation and oxidation of aerosol particles are favoured by the longer periods with stagnant atmospheric conditions.

The trend analysis of the absorption enhancement over a decade-long dataset showed no statistically significant (s.s.) trend at both BCN or MSY. The exception was the MSY regional station during the summer months, when E_{abs} showed an s.s. increase of 8.16 $\%\ yr^{-1}$. This increase during the summer months was mainly driven by the increase of the relative contribution of the OA to the total PM and of the SOA to OA ratio. Indeed, during the COVID-19 lockdown period a sharp increase in the OC to EC ratio was observed as a consequence of the reduction of primary emissions (and consequently EC), and correspondingly the absorption enhancement also showed a sharp increase at both stations. This results suggests that the reduction of BC concentrations due to the implementation of more restrictive guidelines to improve air quality could lead to lower concentrations of ambient BC but with higher absorption efficiency.

The dependency of the absorption enhancement on the concentration relative to EC and composition of the material available for mixing as well as its trends showcases the importance of studying this parameter at a regional scale, especially at measurement sites with high OA and SIA concentrations and where the OA are prone to result in SOA. We found this to be the case at a regional measurement site with a high influence from aerosol particles from a highly populated and industrialized area. Such backgrounds are highly common along the Mediterranean and the Earth, thus extrapolating this analysis to such places will help constrain the absorption enhancement.

10.1.4 Characterizing Saharan mineral dust particles at an emission source region

An intensive campaign performed in the outskirts of the Sahara desert, the most important source of mineral dust particles in the Mediterranean, enabled the analysis of the optical

properties of the emitted dust particles. During the campaign the site showed a background with very low aerosol particle number concentration, coupled with regular local dust saltation events that emitted dust particles, with increasing strength as the friction velocity increased. In addition, the advection of dust particles from a regional scale as Haboob events was observed to also affect the area. Typical values during these events were AAE of 2.17 (2.26), SSAE of -0.04 and g of 0.67 (0.69) during local saltation (Haboob advection) events.

The measurements showed that as the friction velocity increased, i.e. the emission processes strength, the effective radius of the particles increased, reflecting a higher relative contribution of the mineral dust particles and the consequent increase in the coarse fraction mode of the aerosol particle size distribution. Following this relationship, the optical properties showed a convergence toward values closer to those found for dust measurements in chambers from soil samplings and in-situ measurement campaigns, with AAE values around 2.5, and negative SAE and SSAAE. During a period where a $PM_{2.5}$ inlet cut-off was used, the SSA showed average values around 0.97 at 525 nm, whereas the mass absorption efficiency was on average around 0.04 $\mathrm{m^2 g^{-1}}$ and decreased with increasing friction velocity. During a period with a PM_{10} inlet cut-off, the particles showed lower overall MAEs and also a lower variation with increasing friction velocity, with values around 0.005 $\mathrm{m^2 g^{-1}}$. However, the SSA showed lower values during high friction velocities events, especially for the shorter wavelengths, with values as low as 0.87 at 370 nm.

The measurements performed during the campaign showed the importance of constraining the optical properties to the strength of the emission processes, which can be of great importance in dust forecasting and climate models where the amount of emitted dust depends on the strength of the emission. Finally, the results also showcased the need for correctly characterizing the particle size distribution of mineral dust particles in the atmosphere, since the measurements performed with the different inlets, albeit representing different periods, showed lower absorption efficiencies and lower SSAs when using a PM_{10} inlet instead of a $PM_{2.5}$.

10.2 Future research

The work presented in this thesis introduces an in-depth characterization of the optical properties of the main aerosol particles (BC, BrC and mineral dust) producing an absorption of the solar and terrestrial electromagnetic radiation over the Mediterranean basin. However, some further considerations and actions are needed to expand the research here presented and address its limitations and uncertainties.

- In order to improve the acquisition of the absorption coefficients with the highly used AE33 aethalometer, it is key to expand the analysis performed in **Chapter 5** about the largest source of uncertainty, the multiple scattering parameter, C, to many other measurement stations, especially those presenting high SSA values, and those influenced by mineral dust particles. With this aim, the multi-instrumental and data processing

used in **Chapter 5** could be applied to the datasets that meet the requirements from the ACTRIS database, or if not possible due to the lack of a reference absorption measurement, then a iterative approach as the one followed in **Chapter 8** could be implemented.

- In addition to the cross-sensitivity analysis of the C with the SSA, since SSA depends on particle size and finer particles can penetrate more into the filter, it is required to expand the analysis of the dependence of the C parameter with the particle size distribution. This analysis is of special interest for determining both the variations of C with the size of the sampled particles as well as for improving the characterization of the spectral dependence of C. Currently, there are several studies analyzing the relationship of C using reference absorption measurements through multi-wavelength photothermal interferometers in controlled laboratory chambers where the albedo and the particle size distribution, composition and mixing state can be controlled.

- The integration of the vertical profiles with remote sensing measurements, both from satellites and from the surface, will improve the representativness of the aerosol vertical profiles, especially for model simulation. This proves to be of great interest both in complex regions with multiple aerosol sources as the Mediterranean, and in regions characterized by high aerosol emissions, such as biomass burning from agricultural use over the Amazon or West Africa, or Saharan mineral dust advection over the Atlantic.

- A handicap of the vertical profiles performed in **Chapter 6** was the lack of an analysis on the particle composition and the particle size distribution on the airborne measurements. Therefore, coupling such analysis with the physical and optical properties will help provide a better characterization of the aerosol particles that are found at the different layers.

- As a consequence of the large regional variability of the absorption enhancement of BC from its mixing with organic and inorganic aerosol particles found for two stations (urban, BCN, and regional, MSY, backgrounds) in NE Spain, it is also necessary to extent the analysis to the mountain-top station of MSA, as well as to other measurement sites in the Mediterranean and in Europe.

- In fact, the lack at MSY regional background station of multi-wavelength absorption measurements and online measurements of OC, EC and the chemical speciation, impaired the spectral analysis of the absorption enhancement and the attribution analysis that derived the contribution from each aerosol species. Providing these measurements will enable the analysis of the influence of the internal and external mixing and the effects of the different compounds at measurement sites with different backgrounds. Expanding this analysis to other stations at an European level using data from the ACTRIS network would greatly improve the spatial representation of the absorption enhancement.

- Moreover, an in-depth analysis of the influence of the external mixing of OA particles with BC and the chemical speciation of the OA particles can provide results on the absorption properties, most importantly the mass absorption cross-section, of the different BrC compounds and their spectral variations. This analysis would provide important results to constrain the effects of BrC, i.e. of OA, on radiative forcing. As a consequence of the regional-dependence of the aerosol species, this analysis would require a larger dataset with data from diverse backgrounds.

- One important application of AE33 aethalometers and MAAP photometers is to measure the concentration of BC particles, referred to as eBC, also relevant for air quality. Since these instruments measure the attenuation of light, the eBC concentration can be obtained by dividing the absorption coefficients provided by the instrument by the mass absorption cross-section of BC. Similarly, another approach to obtain the concentration of carbonaceous particles is through thermo-optical instruments that measure the amount of OC and EC. However, these measurements lack high temporal resolution, with the Sunset-online having a timestamp of 3h min, whereas EC and OC determined line from filters have typically time resolutions of 12-48h. With this purpose, it proves useful the use of filter-based absorption photometers as MAAP and AE33, which provide eBC with a high temporal resolution (1 min). However, a proper MAC should be determined in order to approximate the calculated concentrations of eBC to those of EC. For this, the simultaneous measurements of absorption and EC can be used. To overcome the uncertainties associated to the highly variable MAC values used by philter-based absorption photometers to obtain the eBC measurements, a rolling average MAC, calculated as the ratio between absorption and EC, can be calculated and then applied to the AE33 and MAAP measurements. This reduction in the uncertainty of the MAC enables the AE33 and MAAP eBC high temporal resolution measurements to be highly similar to those of EC.

- In order to complete the study of the optical properties of Saharan mineral dust with the emission strength and the particle size, an exploratory analysis of Lorentz-Mie simulations using the particle size distribution could be performed to obtain the complex refractive index of the mineral dust particles and also constrain the shape of the particles. These three parameters: the particle size distribution, the particle shape and the refractive index are crucial for obtaining the direct radiative effect of mineral dust in the atmosphere.

- Although North African arid and semi-arid regions are the main source of mineral dust in the atmosphere, half of the global emission load is made by other sources, thus the characterization of the optical properties and their relationships with the emission processes at these regions is also of great relevance. Due to the dependence of the absorption properties of mineral dust with the mineralogical composition, the study of this dependence is of special interest in emission regions with very distinct mineral composition. This analysis will allow an improved characterization of mineral dust particles in climate models. With this aim, currently there are several studies

in-progress within the FRAGMENT project analyzing the results from similar campaigns for high-latitude dust in Iceland, and mid-latitude dust in Jordan.

- Finally, large differences were observed when comparing the mass absorption cross-section values of mineral dust at the the source regions and in the NE of Spain after dust transport. This large difference is due to the mixing of the dust particles with more absorbing aerosols locally emitted at the receptor regions. Given the large impact that the Saharan dust outbreaks have on the Mediterranean regions, it is of great importance to correctly characterize both the amount of dust that actually reaches these regions, and the optical properties of these dust without the influence of aerosols from other sources. Since most of the highly absorbing particles at these regions are in the fine mode, and mineral dust is biased towards the coarse mode, measuring the absorption coefficients and the mass concentration of particles at these modes will enable to obtain the measurements of the dust MAC. This is the main aim of the DNAAP (Detection of non-anthropogenic air pollution) campaign being performed since 2019 up to this day in multiple backgrounds along the Mediterranean.

SCIENTIFIC CONTRIBUTION

Articles in peer-review scientific journals

Publications included in this thesis

Yus-Díez, Jesús, Bernardoni, V., Močnik, G., Alastuey, A., Ciniglia, D., Ivančič, M., Querol, X., Perez, N., Reche, C., Rigler, M., Vecchi, R., Valentini, S., and Pandolfi, M.: "Determination of the multiple-scattering correction factor and its cross-sensitivity to scattering and wavelength dependence for different AE33 Aethalometer filter tapes: A multi-instrumental approach". In: *Atmospheric Measurement Techniques*, 14, 6335–6355, https://doi.org/10.5194/amt-14-6335-2021, 2021.

Yus-Díez, Jesús, Ealo, M., Pandolfi, M., Perez, N., Titos, G., Močnik, G., Querol, X., and Alastuey, A.: "Aircraft vertical profiles during summertime regional and Saharan dust scenarios over the north-western Mediterranean basin: aerosol optical and physical properties". In: *Atmospheric Chemistry and Physics*, 21, 431–455, https://doi.org/10.5194/acp-21-431-2021, 2021

Yus-Díez, Jesús, Via, M., Alastuey, A., Karanasiou, A., Minguillón, M. C., Perez, N., Querol, X., Reche, C., Ivančič, M., Rigler, M., and Pandolfi, M.: "Absorption enhancement of black carbon particles in a Mediterranean city and countryside: effect of particulate matter chemistry, ageing and trend analysis". In: *Atmospheric Chemistry and Physics*, 22, 8439–8456, https://doi.org/10.5194/acp-22-8439-2022, 2022.

Author and co-author publications

Yus-Díez, Jesús, Udina, M., Soler, M. R., Lothon, M., Nilsson, E., Bech, J., and Sun, J.: "Nocturnal boundary layer turbulence regimes analysis during the BLLAST campaign". In: *Atmospheric Chemistry and Physics*, 19, 9495–9514, https://doi.org/10.5194/acp-19-9495-2019, 2019.

Laj, P., Bigi, A., Rose, C., Andrews, E., Lund Myhre, C., Collaud Coen, M., Lin, Y., Wiedensohler, A., Schulz, M., Ogren, J. A., Fiebig, M., Gliß, J., Mortier, A., Pandolfi, M., Petäja, T., Kim, S.-W., Aas, W., Putaud, J.-P., Mayol-Bracero, O., Keywood, M., Labrador, L., Aalto, P., Ahlberg, E., Alados Arboledas, L., Alastuey, A., Andrade, M., Artíñano, B., Ausmeel, S., Arsov, T., Asmi, E., Backman, J., Baltensperger, U., Bastian, S., Bath, O., Beukes, J. P., Brem, B. T., Bukowiecki, N., Conil, S., Couret, C., Day, D., Dayantolis, W., Degorska, A., Eleftheriadis, K., Fetfatzis, P., Favez, O., Flentje, H., Gini, M. I., Gregorič, A., Gysel-Beer, M., Hallar, A. G., Hand, J., Hoffer,

A., Hueglin, C., Hooda, R. K., Hyvärinen, A., Kalapov, I., Kalivitis, N., Kasper-Giebl, A., Kim, J. E., Kouvarakis, G., Kranjc, I., Krejci, R., Kulmala, M., Labuschagne, C., Lee, H.-J., Lihavainen, H., Lin, N.-H., Löschau, G., Luoma, K., Marinoni, A., Martins Dos Santos, S., Meinhardt, F., Merkel, M., Metzger, J.-M., Mihalopoulos, N., Nguyen, N. A., Ondracek, J., Pérez, N., Perrone, M. R., Petit, J.-E., Picard, D., Pichon, J.-M., Pont, V., Prats, N., Prenni, A., Reisen, F., Romano, S., Sellegri, K., Sharma, S., Schauer, G., Sheridan, P., Sherman, J. P., Schütze, M., Schwerin, A., Sohmer, R., Sorribas, M., Steinbacher, M., Sun, J., Titos, G., Toczko, B., Tuch, T., Tulet, P., Tunved, P., Vakkari, V., Velarde, F., Velasquez, P., Villani, P., Vratolis, S., Wang, S.-H., Weinhold, K., Weller, R., Yela, M., **Yus-Diez, J.**, Zdimal, V., Zieger, P., and Zikova, N.: "A global analysis of climate-relevant aerosol properties retrieved from the network of Global Atmosphere Watch (GAW) near-surface observatories". In *Atmospheric Measurements Techniques*, 13, 4353–4392, https://doi.org/10.5194/amt-13-4353-2020, 2020.

Evangeliou, N., Platt, S. M., Eckhardt, S., Lund Myhre, C., Laj, P., Alados-Arboledas, L., Backman, J., Brem, B. T., Fiebig, M., Flentje, H., Marinoni, A., Pandolfi, M., **Yus-Díez, J.**, Prats, N., Putaud, J. P., Sellegri, K., Sorribas, M., Eleftheriadis, K., Vratolis, S., Wiedensohler, A., and Stohl, A.: "Changes in black carbon emissions over Europe due to COVID-19 lockdowns". In: *Atmospheric Chemistry and Physics*, 21, 2675–2692, https://doi.org/10.5194/acp-21-2675-2021, 2021.

Valentini, S., Bernardoni, V., Bolzacchini, E., Ciniglia, D., Ferrero, L., Corina Forello, A., Massabó, D., Pandolfi, M., Prati, P., Soldan, F., Valli, G., **Yus-Díez, J.**, Alastuey, A., Vecchi., R. :"Applicability of benchtop multi-wavelength polar photometers to off-line measurements of the Multi-Angle Absorption Photometer". In *Journal of Aerosol Science*, 152, 10571 doi:10.1016/j.jaerosci.2020.105701., 2021.

Cuesta-Mosquera, A., Močnik, G., Drinovec, L., Müller, T., Pfeifer, S., Minguillón, M. C., Briel, B., Buckley, P., Dudoitis, V., Fernández-García, J., Fernández-Amado, M., Ferreira De Brito, J., Riffault, V., Flentje, H., Heffernan, E., Kalivitis, N., Kalogridis, A.-C., Keernik, H., Marmureanu, L., Luoma, K., Marinoni, A., Pikridas, M., Schauer, G., Serfozo, N., Servomaa, H., Titos, G., **Yus-Díez, J.**, Zioła, N., and Wiedensohler, A.: "Intercomparison and characterization of 23 Aethalometers under laboratory and ambient air conditions: procedures and unit-to-unit variabilities". In: *Atmospheric Measurements Techniques*, 14, 3195–3216, https://doi.org/10.5194/amt-14-3195-2021, 2021.

Conferences presentations

Yus-Díez, Jesús, Bernardoni, V., Pandolfi, M., Alastuey, A., Querol, X., Ciniglia, D., Močnik, G., Vecchi, R.: "On the wavelength dependence of the AE33 aethalometer multiple scattering correction factor C ". In: *European Aerosol Conference*, September, 2020.

Yus-Díez, Jesús, Pérez García-Pando, C., Alastuey, A. , Ivančič, M., González-Florez, C., Gonzalez-Romero, A., Klose, M., Querol, X., Pandolfi, M.: "Multi-wavelengths in-situ scattering and absorption measurements of Saharan dust particles during FRAGMENT ". In: *European Aerosol Conference*, September, 2020.

Yus-Díez, Jesús, Pandolfi, M., Alastuey, A., González-Flórez, C., Gonzalez-Romero, A., Ivančič, M., Kandler, K., Klose, M., Panta, A., Querol, X., Reche, C., Pérez García-Pando, C.: "Multi-wavelength scattering and absorption of freshly emitted dust during field observations in Morocco ". In: *American Geoscience Union (AGU) fall meeting*, December, A041-0006, https://agu.confex.com/agu/fm20/meetingapp.cgi/Paper/692018, 2020.

Gonzalez-Romero, A., Querol, X., Alastuey, A., González-Flórez, C., Kandler, K., Klose, M., Pandolfi, M., Panta, A., Reche, C., **Yus-Díez, J.**, Pérez García-Pando, C.: "Size-resolved mineralogy of dry- and wet-sieved surface sediment samples collected during a field campaign in Morocco ". In: *American Geoscience Union (AGU) fall meeting*, December, A019-03, https://agu.confex.com/agu/fm20/meetingapp.cgi/Paper/691794, 2020.

González-Flórez, A., Klose, M., Alastuey, A., Dupont, S., Etyemezian, D., Gonzalez-Romero, A., Kandler, K., Nikolich, G., Pandolfi, M., Panta, A., Querol, X., Reche, C., **Yus-Díez, J.**, Pérez García-Pando, C.: "Understanding size-resolved dust emission from field observations in Morocco ". In: *American Geoscience Union (AGU) fall meeting*, December, A041-0005, https://agu.confex.com/agu/fm20/meetingapp.cgi/Paper/679883, 2020.

Panta, A., Kandler, K., González-Flórez, A., Alastuey, A., Gonzalez-Romero, A., Klose, M., Pandolfi, M., Querol, X., Reche, C., **Yus-Díez, J.**, Pérez García-Pando, C.: "Physico-chemical composition of freshly emitted dust aerosol collected during field observations in Morocco ". In: *American Geoscience Union (AGU) fall meeting*, December, A041-0007, https://agu.confex.com/agu/fm20/meetingapp.cgi/Paper/697082, 2020.

Via, M., **Yus-Díez, J.**, Canonaco, F., Alastuey, A.,Petit, J.E., Hopke, P., Reche, C., Pandolfi, M., Querol, X., Minguillón, M.C.: "Insights on multi-time resolution PMF: testing different time resolutions and uncertainty weight". In: *European Aerosol Conference*, online, September, 2021.

Pérez García-Pando, C., González-Florez, C., González-Romero, A., Panta, A., **Yus-Díez, J.**, Alastuey, A., Kandler, K., Klose, M., Querol, X., Reche, C., Pandolfi, M., Dupont, S., Etyemezian, V., Nikolich, G., Escribano, J., Clark, R., Elhmann, B., Greenberger, R., Tajeddine, K., and Ivančič, M.: "Towards understanding the size distribution, composition and optical properties of freshly emitted dust and its relationship with the parent sediment". In *EGU General Assembly 2021*, online, 19–30 Apr 2021, EGU21-13606, https://doi.org/10.5194/egusphere-egu21-13606, 2021.

Perez Garcia-Pando, C., Kandler, K., Schepanski, K., Klose, M., Gonzalez-Florez, C., Gonzalez-Romero, A., Panta, A., Alastuey, A., Querol, X., Reche, C., **Yus-Diez, J.**, Pandolfi, M., Dupont, S., Irvine, M., Etyemezian, V., Nikolich, G., Clark, R., Ehlmann, B., Greenberger, R., Green, R., Brodrick, P., Dagsson-Waldhauserova, P., Dirsch, T., Meyer, H., Urbanneck, C., Umo, N.: "Comprehensive high-latitude dust field campaign in the desert of Dyngjunsandur, Iceland". In *AGU Fall Meeting 2021*, online, December 2021, A32B-01, https://agu.confex.com/agu/fm21/meetingapp.cgi/Paper/987437, 2021.

González-Flórez, C., Klose, M., Alastuey, A., Dupont, S., Etyemezian, V., González-Romero, A., Kandler, K., Nikolich, G., Pandolfi, M., Panta, A., Querol, X., Reche, C., **Yus-Díez, J.**, and

Pérez García-Pando, C.: "Size distribution of emitted dust in Morocco". In:*EGU General Assembly 2022*, Vienna, Austria, 23–27 May 2022, EGU22-11247, https://doi.org/10.5194/egusphere-egu22-11247, 2022.

Ivančič, M., Ježek, I.,Rigler, M., Alföldy, B., Gregorič, A., Drinovec, L., Podlipec, R., Sciare, J., Pikridas, M., Unga, F., Alastuey, A., Pandolfi, M., **Yus-Díez, J.**, Močnik, G.: "Size distribution of emitted dust in Morocco". In:*International Conference on Air Quality 2022*, Thessaloniki, Greece, 2022.

BIBLIOGRAPHY

Ackerman, Andy S, OB Toon, DE Stevens, AJ Heymsfield, V Ramanathan, and EJ Welton (2000). "Reduction of tropical cloudiness by soot". In: *Science* 288.5468, pp. 1042–1047.

Adebiyi, Adeyemi A. and Jasper F. Kok (2020). "Climate models miss most of the coarse dust in the atmosphere". In: *Science Advances* 6.15, pp. 1–10.

Ajtai, Tibor, Ágnes Filep, Martin Schnaiter, Claudia Linke, Marlen Vragel, Zolt Án Bozóki, GÁbor Szabó, and Thomas Leisner (2010). "A novel multi-wavelength photoacoustic spectrometer for the measurement of the UV-vis-NIR spectral absorption coefficient of atmospheric aerosols". In: *Journal of Aerosol Science* 41.11, pp. 1020–1029.

Albrecht, Bruce A (1989). "Aerosols, cloud microphysics, and fractional cloudiness". In: *Science* 245.4923, pp. 1227–1230.

Alfaro, SC, S Lafon, JL Rajot, P Formenti, A Gaudichet, and M Maille (2004). "Iron oxides and light absorption by pure desert dust: An experimental study". In: *Journal of Geophysical Research: Atmospheres* 109.D8.

Allan, James D., Alice E. Delia, Hugh Coe, Keith N. Bower, M. Rami Alfarra, Jose L. Jimenez, Ann M. Middlebrook, Frank Drewnick, Timothy B. Onasch, Manjula R. Canagaratna, John T. Jayne, and Douglas R. Worsnop (2004). "A generalised method for the extraction of chemically resolved mass spectra from Aerodyne aerosol mass spectrometer data". In: *Journal of Aerosol Science* 35.7, pp. 909–922.

Amato, Fulvio, X. Querol, Andrés Alastuey, Marco Pandolfi, Teresa Moreno, José Gracia, and Pau Rodriguez (2009). "Evaluating urban PM10 pollution benefit induced by street cleaning activities". In: *Atmospheric Environment* 43.29, pp. 4472–4480.

Andreae, M. O. and A. Gelencsér (2006). "Black carbon or brown carbon? the nature of light-absorbing carbonaceous aerosols". In: *Atmospheric Chemistry and Physics* 6.10, pp. 3131–3148.

Andreae, M. O., D. Rosenfeld, P. Artaxo, A. A. Costa, G. P. Frank, K. M. Longo, and M. A.F. Silva-Dias (2004). "Smoking Rain Clouds over the Amazon". In: *Science* 303.5662, pp. 1337–1342.

Andrews, E, PJ Sheridan, M Fiebig, A McComiskey, JA Ogren, P Arnott, D Covert, R Elleman, R Gasparini, D Collins, H Jonsson, B Shmid, and J Wang (2006). "Comparison of methods for deriving aerosol asymmetry parameter". In: *Journal of Geophysical Research: Atmospheres* 111.D5.

Andrews, E., P. J. Sheridan, and J. A. Ogren (2011a). "Seasonal differences in the vertical profiles of aerosol optical properties over rural Oklahoma". In: *Atmospheric Chemistry and Physics* 11.20, pp. 10661–10676.

Andrews, Elisabeth, J.A. Ogren, P. Bonasoni, A. Marinoni, E. Cuevas, S. Rodrıguez, J.Y. Sun, D.A. Jaffe, E.V. Fischer, U. Baltensperger, E. Weingartner, M. Collaud Coen, S. Sharna, A.M. Macdonald, W.R. Leaitch, N.-H. Lin, Laj. P., T. Arsov, and I. Kalapov (2011b). "Climatology of aerosol radiative properties in the free troposphere". In: *Atmospheric Research* 102.4, pp. 365–393.

Andrews, Elisabeth, John A. Ogren, Stefan Kinne, and Bjorn Samset (2017). "Comparison of AOD, AAOD and column single scattering albedo from AERONET retrievals and in situ profiling measurements". In: *Atmospheric Chemistry and Physics* 17.9, pp. 6041–6072.

Ångström, Anders (1929). “On the Atmospheric Transmission of Sun Radiation and on Dust in the Air”. In: *Geografiska Annaler* 11.2, pp. 156–166.

Ansmann, Albert, M Riebesell, U Wandinger, C Weitkamp, E Voss, W Lahmann, and W Michaelis (1992). “Combined Raman elastic-backscatter lidar for vertical profiling of moisture, aerosol extinction, backscatter, and lidar ratio”. In: *Applied Physics B* 55.1, pp. 18–28.

Arnott, W. Patrick, Khadeejeh Hamasha, Hans Moosmüller, Patrick J. Sheridan, and John A. Ogren (2005). “Towards aerosol light-absorption measurements with a 7-wavelength aethalometer: Evaluation with a photoacoustic instrument and 3-wavelength nephelometer”. In: *Aerosol Science and Technology* 39.1, pp. 17–29.

Asmi, E., A. Frey, A. Virkkula, M. Ehn, H. E. Manninen, H. Timonen, O. Tolonen-Kivimaki, M. Aurela, R. Hillamo, and M. Kulmala (2010). “Hygroscopicity and chemical composition of antarctic submicrometre aerosol particles and observations of new particle formation”. In: *Atmospheric Chemistry and Physics* 10.9, pp. 4253–4271.

Atkinson, B.W. (1982). “Mesoscale atmospheric circulations”. In: *Academic Press, London*.

Backman, John, Lauren Schmeisser, Aki Virkkula, John A. Ogren, Eija Asmi, Sandra Starkweather, Sangeeta Sharma, Konstantinos Eleftheriadis, Taneil Uttal, Anne Jefferson, Michael Bergin, Alexander Makshtas, Peter Tunved, and Markus Fiebig (2017). “On Aethalometer measurement uncertainties and an instrument correction factor for the Arctic”. In: *Atmospheric Measurement Techniques* 10.12, pp. 5039–5062.

Badia, Alba, Oriol Jorba, Apostolos Voulgarakis, Donald Dabdub, Carlos Pérez García-Pando, Andreas Hilboll, Gonçalves María, and Zavisa Janjic (2017). “Description and evaluation of the Multiscale Online Nonhydrostatic AtmospheRe CHemistry model (NMMB-MONARCH) version 1.0: Gas-phase chemistry at global scale”. In: *Geoscientific Model Development* 10.2, pp. 609–638.

Bae, Min Suk, James J. Schauer, Jeffrey T. DeMinter, Jay R. Turner, David Smith, and Robert A. Cary (2004). “Validation of a semi-continuous instrument for elemental carbon and organic carbon using a thermal-optical method”. In: *Atmospheric Environment* 38.18, pp. 2885–2893.

Basart, Sara, Carlos Pérez García-pando, Oriol Jorba, Francesco Benincasa, Kim Serradell, and Gilbert Montanyé (2020). “Upgrading the Monarch Operational Forecast : Bdrc-2020-001”. In: November.

Basart, Sara, Carlos PéRez, Slodoban Nickovic, Emilio Cuevas, and José MaríA Baldasano (2012). “Development and evaluation of the BSC-DREAM8b dust regional model over northern Africa, the mediterranean and the middle east”. In: *Tellus, Series B: Chemical and Physical Meteorology* 64.1.

Bergstrom, R. W., P. Pilewskie, P. B. Russell, J. Redemann, T. C. Bond, P. K. Quinn, and B. Sierau (2007). “Spectral absorption properties of atmospheric aerosols”. In: *Atmospheric Chemistry and Physics* 7.23, pp. 5937–5943.

Bernardoni, Vera, Luca Ferrero, Ezio Bolzacchini, Alice Corina Forello, Asta Gregorič, Dario Massabò, Grisa Mocnik, Paolo Prati, Martin Rigler, Luca Santagostini, Francesca Soldan, Sara Valentini, Gianluigi Valli, and Roberta Vecchi (2021). “Determination of Aethalometer multiple-scattering enhancement parameters and impact on source apportionment during the winter 2017/18 EMEP / ACTRIS / COLOSSAL campaign in Milan”. In: *Atmospheric Measurement Techniques* 14.4, pp. 2919–2940.

Bernardoni, Vera, Gianluigi Valli, and Roberta Vecchi (2017). “Set-up of a multi wavelength polar photometer for off-line absorption coefficient measurements on 1-h resolved aerosol samples”. In: *Journal of Aerosol Science* 107, pp. 84–93.

Biscaye, Pierre Eginton, Francis E Grousset, Marie Revel, Sjierk Van der Gaast, GA Zielinski, A Vaars, and G Kukla (1997). “Asian provenance of glacial dust (stage 2) in the Greenland Ice Sheet Project 2 ice core, Summit, Greenland”. In: *Journal of Geophysical Research: Oceans* 102.C12, pp. 26765–26781.

Bond, T.C. et al. (2013). “Bounding the role of black carbon in the climate system: A scientific assessment”. In: *Journal of Geophysical Research: Atmospheres* 118.11, pp. 5380–5552.

Bond, Tami, Chandra Venkataraman, and Omar Masera (2004). “Global atmospheric impacts of residential fuels”. In: *Energy for Sustainable Development* 8.3, pp. 20–32.

Bond, Tami C., Theodore L. Anderson, and Dave Campbell (1999). “Calibration and Intercomparison of Filter-Based Measurements of Visible Light Absorption by Aerosols”. In: *Aerosol Science and Technology* 30.6, pp. 582–600.

Bond, Tami C. and Robert W. Bergstrom (2006). “Light absorption by carbonaceous particles: An investigative review”. In: *Aerosol Science and Technology* 40.1, pp. 27–67.

Bressi, Michaël et al. (2021). “A European aerosol phenomenology-7: High-time resolution chemical characteristics of submicron particulate matter across Europe”. In: *Atmospheric environment: X* 10, p. 100108.

Bucholtz, Anthony (1995). “Rayleigh-scattering calculations for the terrestrial atmosphere”. In: *Applied Optics* 34.15, pp. 2765–2773.

Bukowski, J and SC van den Heever (2021). “Direct radiative effects in haboobs”. In: *Journal of Geophysical Research: Atmospheres* 126.21, e2021JD034814.

Campillo, A. J., C. J. Dodge, and H.-B. Lin (Sept. 1981). “Aerosol particle absorption spectroscopy by photothermal modulation of Mie scattered light”. In: *Appl. Opt.* 20.18, pp. 3100–3103.

Canagaratna, MR, JT Jayne, JL Jimenez, JD Allan, MR Alfarra, Qi Zhang, TB Onasch, F Drewnick, H Coe, A Middlebrook, A. Delia, L.R. Williams, A.M. Trimborn, M.J. Northway, P.F. DeCarlo, P. Kolb C.E. an Davidovits, and D.R. Worsnop (2007). “Chemical and microphysical characterization of ambient aerosols with the aerodyne aerosol mass spectrometer”. In: *Mass spectrometry reviews* 26.2, pp. 185–222.

Caponi, Lorenzo, Paola Formenti, Dario Massabó, Claudia Di Biagio, Mathieu Cazaunau, Edouard Pangui, Servanne Chevaillier, Gautier Landrot, Meinrat O. Andreae, Konrad Kandler, Stuart Piketh, Touraya Saeed, Dave Seibert, Earl Williams, Yves Balkanski, Paolo Prati, and Jean-François Doussin (2017). “Spectral- and size-resolved mass absorption efficiency of mineral dust aerosols in the shortwave: a simulation chamber study”. In: *Atmospheric Chemistry and Physics Discussions*, pp. 1–39.

Cappa, Christopher D., Xiaolu Zhang, Lynn M. Russell, Sonya Collier, Alex K.Y. Lee, Chia Li Chen, Raghu Betha, Sijie Chen, Jun Liu, Derek J. Price, Kevin J. Sanchez, Gavin R. McMeeking, Leah R. Williams, Timothy B. Onasch, Douglas R. Worsnop, Jon Abbatt, and Qi Zhang (2019). “Light Absorption by Ambient Black and Brown Carbon and its Dependence on Black Carbon Coating State for Two California, USA, Cities in Winter and Summer”. In: *Journal of Geophysical Research: Atmospheres* 124.3, pp. 1550–1577.

Carslaw, David C and Karl Ropkins (2012). “Openair—an R package for air quality data analysis”. In: *Environmental Modelling & Software* 27, pp. 52–61.

Cavalli, Fabrizia, Mar Viana, Karl Espen Yttri, Johan Genberg, and J-P Putaud (2010). “Toward a standardised thermal-optical protocol for measuring atmospheric organic and elemental carbon: the EUSAAR protocol”. In: *Atmospheric Measurement Techniques* 3.1, pp. 79–89.

CEN (1999). *Air quality – Determination of the PM10 fraction of suspended particulate matter. Reference method and field test procedure to demonstrate reference equivalence of measurement methods, EN12341:1999*.

– (2017). “CEN standard - EN 16909:2017: Ambient Air—Measurement of Elemental Carbon (EC) and Organic Carbon (OC) Collected on Filters”. In: *European Committee for Standardisation: Brussels, Belgium*.

Charron, Aurelie and Roy M. Harrison (2003). “Primary particle formation from vehicle emissions during exhaust dilution in the roadside atmosphere”. In: *Atmospheric Environment* 37.29, pp. 4109–4119.

Chen, Bing, Zhe Bai, Xinjuan Cui, Jianmin Chen, August Andersson, and Örjan Gustafsson (2017). “Light absorption enhancement of black carbon from urban haze in Northern China winter”. In: *Environmental Pollution* 221, pp. 418–426.

Chen, Yanju and Tami C Bond (2010). “Light absorption by organic carbon from wood combustion.” In: *Atmospheric Chemistry & Physics* 10.4.

Choobari, O. Alizadeh, P. Zawar-Reza, and A. Sturman (2014). “The global distribution of mineral dust and its impacts on the climate system: A review”. In: *Atmospheric Research* 138, pp. 152–165.

Claquin, T, M Schulz, and YJ Balkanski (1999). “Modeling the mineralogy of atmospheric dust sources”. In: *Journal of Geophysical Research: Atmospheres* 104.D18, pp. 22243–22256.

Colette, A., S. Solberg, W. Aas, and S.-E. Walker (2021). *Understanding Air Quality Trends in Europe*. May.

Colette, Augustin and Laurence Rouïl Ineris (2020). *Air Quality Trends in Europe : 2000-2017*. 2, pp. 2000–2017.

Collaud Coen, M, E Weingartner, D Schaub, C Hueglin, C Corrigan, S Henning, M Schwikowski, and U. Baltensperger (2004). “Saharan dust events at the Jungfraujoch: detection by wavelength dependence of the single scattering albedo and first climatology analysis”. In: 1986, pp. 2465–2480.

Collaud Coen, M., E. Weingartner, A. Apituley, D. Ceburnis, R. Fierz-Schmidhauser, H. Flentje, J. S. Henzing, S. G. Jennings, M. Moerman, A. Petzold, O. Schmid, and U. Baltensperger (2010). “Minimizing light absorption measurement artifacts of the Aethalometer: Evaluation of five correction algorithms”. In: *Atmospheric Measurement Techniques* 3.2, pp. 457–474.

Collaud Coen, M. et al. (2020). “Multidecadal trend analysis of aerosol radiative properties at a global scale”. In: *Atmospheric Chemistry and Physics Discussions* 2020, pp. 1–54.

Di Biagio, Claudia, Y. Balkanski, S. Albani, O. Boucher, and P. Formenti (2020). “Direct Radiative Effect by Mineral Dust Aerosols Constrained by New Microphysical and Spectral Optical Data”. In: *Geophysical Research Letters* 47.2, pp. 1–12.

Di Biagio, Claudia, P. Formenti, Y. Balkanski, L. Caponi, M. Cazaunau, E. Pangui, E. Journet, S. Nowak, M. Andreae, K. Kandler, T. Saeed, S. Piketh, D. Seibert, E. Williams, and J.F. Doussin (2019). “Complex refractive indices and single scattering albedo of global dust aerosols in the shortwave spectrum and relationship to iron content and size”. In: *Complex refractive indices and single scattering albedo of global dust aerosols in the shortwave spectrum and relationship to iron content and size*, pp. 1–42.

Di Biagio, Claudia, P. Formenti, M. Cazaunau, E. Pangui, N. Marchand, and J.F. Doussin (2017). “Corrigendum to “ Aethalometer multiple scattering correction C ref for mineral dust aerosols ” published in Atmos . Meas . Tech ., 10 , 2923 – 2939 , 2017”. In: *Atmospheric Measurement Techniques* 10.i, pp. 2923–2939.

Doherty, Sarah J., Patricia K. Quinn, Anne Jefferson, Christian M. Carrico, Theodore L. Anderson, and Dean Hegg (2005). “A comparison and summary of aerosol optical properties as observed in situ from aircraft, ship, and land during ACE-Asia”. In: *Journal of Geophysical Research D: Atmospheres* 110.4, pp. 1–35.

Draxler, Roland R. (1999). *HYSPLIT4 user’s guide*. NOAA Tech. Memo. ERL ARL-230. NOAA Air Resources Laboratory. Silver Spring, Maryland, USA.

Draxler, Roland R. and G. D. Hess (1997). *DESCRIPTION OF THE HYSPLIT_4 MODELING SYSTEM*. Tech. rep. December 1997.

– (1998). “An overview of the HYSPLIT_4 modelling system for trajectories, dispersion and deposition”. In: *Australian Meteorological Magazine* 47.4, pp. 295–308.

Drinovec, Luka, Uroš Jagodič, Luka Pirker, Miha Škarabot, Mario Kurtjak, Kristijan Vidović, Luca Ferrero, Bradley Visser, Jannis Röhrbein, Ernest Weingartner, Konstantina Vasilatou, Tobias Bühlmann, Celine Pascale, Thomas Müller, Alfred Wiedensohler, and Griša Močnik (2022). “A dual-wavelength photothermal aerosol absorption monitor: design, calibration and performance”. In: *Atmospheric Measurement Techniques Discussions*, pp. 3805–3825.

Drinovec, Luka, G. Močnik, P. Zotter, A.S.H. Prévôt, C. Ruckstuhl, E. Coz, M. Rupakheti, J. Sciare, T. Müller, A. Wiedensohler, and A. D. A. Hansen (2015). “The "dual-spot" Aethalometer: an improved measurement of aerosol black carbon with real-time loading compensation”. In: *Atmospheric Measurement Techniques* 8.5, pp. 1965–1979.

Drinovec, Luka, Jean Sciare, Iasonas Stavroulas, Spiros Bezantakos, Michael Pikridas, Florin Unga, Chrysanthos Savvides, Bojana Višić, Maja Remškar, and Griša Močnik (2020). "A new optical-based technique for real-time measurements of mineral dust concentration in PM10 using a virtual impactor". In: *Atmospheric Measurement Techniques Discussions* 2, pp. 1–19.

Dubovik, O, A Smirnov, B N Holben, and Y J Kaufman (2000). "Accuracy assessments of aerosol optical properties retrieved from Aerosol Robotic Network (AERONET) Sun and sky". In: 105, pp. 9791–9806.

Dubovik, Oleg and Michael D King (2000). "A flexible inversion algorithm for retrieval of aerosol optical properties from Sun and sky radiance measurements". In: 105.

Ealo, Marina, Andrés Alastuey, Noemı Pérez, Anna Ripoll, X. Querol, and Marco Pandolfi (2018). "Impact of aerosol particle sources on optical properties in urban, regional and remote areas in the north-western Mediterranean." In: *Atmospheric Chemistry & Physics* 18.2.

Ealo, Marina, Andrés Alastuey, Anna Ripoll, Noemı Pérez, Marıa Cruz Minguillón, X. Querol, and Marco Pandolfi (2016). "Detection of Saharan dust and biomass burning events using near-real-time intensive aerosol optical properties in the north-western Mediterranean". In: *Atmospheric Chemistry and Physics* 16.19, pp. 12567–12586.

ECAC-CAIS (2022). "Preliminary ACTRIS recommendations for aerosol in-situ sampling , measurements , and analyses". In: pp. 1–13.

Engelstaedter, Sebastian, Ina Tegen, and Richard Washington (2006). "North African dust emissions and transport". In: *Earth-Science Reviews* 79.1, pp. 73–100.

Escudero, M., S. Castillo, X. Querol, A. Avila, M. Alarcón, M. M. Viana, A. Alastuey, E. Cuevas, and S. Rodríguez (2005). "Wet and dry African dust episodes over eastern Spain". In: *Journal of Geophysical Research: Atmospheres* 110.D18. eprint: `https://agupubs.onlinelibrary.wiley.com/doi/pdf/10.1029/2004JD004731`.

Faustini, Annunziata, Ester R Alessandrini, Jorge Pey, Noemi Perez, Evangelia Samoli, X. Querol, Ennio Cadum, Cinzia Perrino, Bart Ostro, Andrea Ranzi, J. Sunyer, M. Stafoggia, and F Forastiere (2015). "Short-term effects of particulate matter on mortality during forest fires in Southern Europe: results of the MED-PARTICLES Project". In: *Occupational and Environmental Medicine* 72.5, pp. 323–329.

Ferrero, L., V. Bernardoni, L. Santagostini, S. Cogliati, F. Soldan, S. Valentini, D. Massabò, G. Močnik, A. Gregorič, M. Rigler, P. Prati, A. Bigogno, N. Losi, G. Valli, R. Vecchi, and E. Bolzacchini (2021). "Consistent determination of the heating rate of light-absorbing aerosol using wavelength- and time-dependent Aethalometer multiple-scattering correction". In: *Science of the Total Environment* 791.

Fierz-Schmidhauser, Rahel, Paul Zieger, Günther Wehrle, Anne Jefferson, John A Ogren, Urs Baltensperger, and Ernest Weingartner (2010). "Measurement of relative humidity dependent light scattering of aerosols". In: *Atmospheric Measurement Techniques* 3.1, pp. 39–50.

Finlayson-Pitts, Barbara J and James N Pitts Jr (1999). *Chemistry of the upper and lower atmosphere: theory, experiments, and applications*. Elsevier.

Flanner, Mark G., Charles S. Zender, James T. Randerson, and Philip J. Rasch (2007). "Present-day climate forcing and response from black carbon in snow". In: *Journal of Geophysical Research Atmospheres* 112.11, pp. 1–17.

Forster, Pierre, T. Storelvmo, K. Armour, W. Collins, J.-L. Dufresne, D. Frame, D.J. Lunt, T. Mauritsen, M.D. Palmer, M. Watanabe, M. Wild, and H. Zhang (2021). "The Earth's Energy Budget, Climate Feedbacks, and Climate Sensitivity". In: *Climate Change 2021: The Physical Science Basis. Contribution of Working Group I to the Sixth Assessment Report of the Intergovernmental Panel on Climate Change*. Ed. by V. Masson-Delmotte, P. Zhai, A. Pirani, S.L. Connors, C. Péan, S. Berger, N. Caud, Y. Chen, L. Goldfarb, M.I. Gomis, M. Huang, K. Leitzell, E. Lonnoy, J.B.R. Matthews, T.K. Maycock, T. Waterfield, O. Yelekçi, R. Yu, and B. Zhou. Cambridge, United Kingdom and New York, NY, USA: Cambridge University Press. Chap. 7, pp. 923–1054.

Gangoiti, Gotzon, Millán M Millán, Rosa Salvador, and Enrique Mantilla (2001). “Long-range transport and re-circulation of pollutants in the western Mediterranean during the project Regional Cycles of Air Pollution in the West-Central Mediterranean Area”. In: *Atmospheric Environment* 35.36, pp. 6267–6276.

GAW (2016). “GAW Report No. 226: Coupled Chemistry-Meteorology/Climate Modelling (CCMM): status and relevance for numerical weather prediction, atmospheric pollution and climate research”. In: *WMO* 1172.

Gebhart, Josef (1993). “Optical direct-reading techniques: light intensity systems”. In: *Aerosol Measurement: Principles, Techniques, and Applications*. Ed. by K. Willeke and P.A. Baron. Van Norstrand Reinhold, New York, pp. 314–344.

Gieré, Reto and Xavier Querol (2010). “Solid particulate matter in the atmosphere”. In: *Elements* 6.4, pp. 215–222.

Glaccum, Robert A and Joseph M Prospero (1980). “Saharan aerosols over the tropical North Atlantic—Mineralogy”. In: *Marine geology* 37.3-4, pp. 295–321.

Grimm (2000). *Portable Laser Aerosolspectrometer and Dust Monitor Model 1.108/1.109*.

Gyawali, M., W. P. Arnott, K. Lewis, and H. Moosmüller (2009). “In situ aerosol optics in Reno, NV, USA during and after the summer 2008 California wildfires and the influence of absorbing and non-absorbing organic coatings on spectral light absorption”. In: *Atmospheric Chemistry and Physics* 9.20, pp. 8007–8015.

Hagler, Gayle S.W., Tiffany L.B. Yelverton, Ram Vedantham, Anthony D.A. Hansen, and Jay R. Turner (2011). “Post-processing method to reduce noise while preserving high time resolution in aethalometer real-time black carbon data”. In: *Aerosol and Air Quality Research* 11.5, pp. 539–546.

Hakala, J., H. E. Manninen, T. Petäjä, and M. Sipilä (2013). “Counting efficiency of a TSI environmental particle counter monitor model 3783”. In: *Aerosol Science and Technology* 47.5, pp. 482–487.

Hand, J. L. and W. C. Malm (2007). “Review of aerosol mass scattering efficiencies from ground-based measurements since 1990”. In: *Journal of Geophysical Research Atmospheres* 112.16.

Hänel, Gottfried (1987). “Radiation budget of the boundary layer. II- Simultaneous measurement of mean solar volume absorption and extinction coefficients of particles”. In: *Beiträge zur Physik der Atmosphäre* 60, pp. 241–254.

– (1994). “Optical properties of atmospheric particles: complete parameter sets obtained through polar photometry and an improved inversion technique”. In: *Applied Optics* 33.30, p. 7187.

Hansen, A.D.A., H. Rosen, and T Novakov (1984). “The aethaloemter- An instrument for the real-time measurement of optical absorption by particles”. In: *The Science of the Total Environment* 36, pp. 191–196.

Hansen, James E and Larry D Travis (1974). “Light scattering in planetary atmospheres”. In: *Space science reviews* 16.4, pp. 527–610.

Heese, B., H. Flentje, D. Althausen, A. Ansmann, and S. Frey (2010). “Ceilometer lidar comparison: Backscatter coefficient retrieval and signal-to-noise ratio determination”. In: *Atmospheric Measurement Techniques* 3.6, pp. 1763–1770.

Hering, Susanne V. and Mark R. Stolzenburg (2005). “A method for particle size amplification by water condensation in a laminar, thermally diffusive flow”. In: *Aerosol Science and Technology* 39.5, pp. 428–436.

Holben, B. N. et al. (2001). “An emerging ground-based aerosol climatology: Aerosol optical depth from AERONET”. In: *Journal of Geophysical Research Atmospheres* 106.D11, pp. 12067–12097.

Holben, Brent N., T. F. Eck, I. Slutsker, D. Tanré, J. P. Buis, A. Setzer, E. Vermote, J. A. Reagan, Y. J. Kaufman, T. Nakajima, F. Lavenu, I. Jankowiak, and A. Smirnov (1998). “AERONET - A federated instrument network and data archive for aerosol characterization”. In: *Remote Sensing of Environment* 66.1, pp. 1–16.

Hopkins, R. J., K. Lewis, Y. Desyaterik, Z. Wang, A. V. Tivanski, W. P. Arnott, A. Laskin, and M. K. Gilles (2007). "Correlations between optical, chemical and physical properties of biomass burn aerosols". In: *Geophysical Research Letters* 34.18, pp. 1–5.

Horvath, Helmuth, Lucas Alados Arboledas, and Francisco José Olmo Reyes (2018). "Angular scattering of the Sahara dust aerosol". In: *Atmospheric Chemistry and Physics* 18.23, pp. 17735–17744.

Huang, Yue, Jasper F. Kok, Konrad Kandler, Hannakaisa Lindqvist, Timo Nousiainen, Tetsu Sakai, Adeyemi Adebiyi, and Olli Jokinen (2020). "Climate Models and Remote Sensing Retrievals Neglect Substantial Desert Dust Asphericity". In: *Geophysical Research Letters* 47.6, pp. 1–11.

IPCC, 2021 (2021). *Technical Summary. Contribution of Working Group I to the Sixth Assessment Report of the Intergovernmental Panel on Climate Change*. Ed. by V. Masson-Delmotte, P. Zhai, A. Pirani, S.L. Connors, C. Péan, S. Berger, N. Caud, Y. Chen, L. Goldfarb, M.I. Gomis, M. Huang, K. Leitzell, E. Lonnoy, J.B.R. Matthews, T.K. Maycock, T. Waterfield, O. Yelekçi, R. Yu, and B. Zhou. Cambridge, United Kingdom and New York, NY, USA: Cambridge University Press, p. 2391.

Jacobson, M. Z., D. B. Kittelson, and W. F. Watts (2005). "Enhanced coagulation due to evaporation and its effect on nanoparticle evolution". In: *Environmental Science and Technology* 39.24, pp. 9486–9492.

Jayne, John T, Danna C Leard, Xuefeng Zhang, Paul Davidovits, Kenneth A Smith, Charles E Kolb, and Douglas R Worsnop (2000). "Development of an aerosol mass spectrometer for size and composition analysis of submicron particles". In: *Aerosol Science & Technology* 33.1-2, pp. 49–70.

Jimenez, J. L. et al. (2009). "Evolution of organic aerosols in the atmosphere". In: *Science* 326.5959, pp. 1525–1529.

Johnson, Matthew S., Nicholas Meskhidze, and Velayudhan Praju Kiliyanpilakkil (2012). "A global comparison of GEOS-Chem-predicted and remotely-sensed mineral dust aerosol optical depth and extinction profiles". In: *Journal of Advances in Modeling Earth Systems* 4.7, pp. 1–15.

Kahnert, Michael and Timo Nousiainen (2006). "Uncertainties in measured and modelled asymmetry parameters of mineral dust aerosols". In: *Journal of Quantitative Spectroscopy and Radiative Transfer* 100.1-3, pp. 173–178.

Kallos, G, S Nickovic, A Papadopoulos, D Jovic, O Kakaliagou, N Misirlis, L Boukas, N Mimikou, G Sakellaridis, J Papageorgiou, E. Anadranistakis, and M. Manousakis (1997). "The regional weather forecasting system SKIRON: an overview, In: Proceedings of the International Symposium on Regional Weather Prediction on Parallel Computer Environments". In:

Kallos, George, Anastasios Papadopoulos, Petros Katsafados, and Slobodan Nickovic (2006). "Transatlantic Saharan dust transport: Model simulation and results". In: *Journal of Geophysical Research Atmospheres* 111.9, pp. 1–11.

Kandler, K., L. Schütz, C. Deutscher, M. Ebert, H. Hofmann, S. Jäckel, R. Jaenicke, P. Knippertz, K. Lieke, A. Massling, A. Petzold, A. Schladitz, B. Weinzierl, A. Wiedensohler, S. Zorn, and S. Weinbruch (2009). "Size distribution, mass concentration, chemical and mineralogical composition and derived optical parameters of the boundary layer aerosol at Tinfou, Morocco, during SAMUM 2006". In: *Tellus, Series B: Chemical and Physical Meteorology* 61.1, pp. 32–50.

Karanasiou, A., P. Panteliadis, N. Perez, M. C. Minguillón, M. Pandolfi, G. Titos, M. Viana, T. Moreno, X. Querol, and A. Alastuey (2020). "Evaluation of the Semi-Continuous OCEC analyzer performance with the EUSAAR2 protocol". In: *Science of the Total Environment* 747.

Kaspari, Susan, S McKenzie Skiles, Ian Delaney, Daniel Dixon, and Thomas H Painter (2015). "Accelerated glacier melt on Snow Dome, Mount Olympus, Washington, USA, due to deposition of black carbon and mineral dust from wildfire". In: *Journal of Geophysical Research: Atmospheres* 120.7, pp. 2793–2807.

Kasthuriarachchi, Nethmi Y., Laura Hélèna Rivellini, Max G. Adam, and Alex K.Y. Lee (2020). "Light Absorbing Properties of Primary and Secondary Brown Carbon in a Tropical Urban Environment". In: *Environmental Science and Technology* 54.17, pp. 10808–10819.

Kaufman, Yoram J, Didier Tanré, and Olivier Boucher (2002). "A satellite view of aerosols in the climate system". In: *Nature* 419.6903, pp. 215–223.

Kipling, Z., P. Stier, J. P. Schwarz, A. E. Perring, J. R. Spackman, G. W. Mann, C. E. Johnson, and P. J. Telford (2013). “Constraints on aerosol processes in climate models from vertically-resolved aircraft observations of black carbon”. In: *Atmospheric Chemistry and Physics* 13.12, pp. 5969–5986.

Kirchhoff, G. (1860). “Ueber das Verhältniss zwischen dem Emissionsvermögen und dem Absorptionsvermögen der Körper für Wärme und Licht”. In: *Annalen der Physik* 185.2, pp. 275–301. eprint: `https://onlinelibrary.wiley.com/doi/pdf/10.1002/andp.18601850205`.

Kirchstetter, Thomas W, T Novakov, and Peter V Hobbs (2004). “Evidence that the spectral dependence of light absorption by aerosols is affected by organic carbon”. In: *Journal of Geophysical Research: Atmospheres* 109.D21.

Klose, Martina, Oriol Jorba, María Gonçalves Ageitos, Jeronimo Escribano, Matthew L. Dawson, Vincenzo Obiso, Enza Di Tomaso, Sara Basart, Gilbert Montané Pinto, Francesca MacChia, Paul Ginoux, Juan Guerschman, Catherine Prigent, Yue Huang, Jasper F. Kok, Ron L. Miller, and Carlos Pérez García-Pando (2021). “Mineral dust cycle in the Multiscale Online Nonhydrostatic Atmosphere Chemistry model (MONARCH) version 2.0”. In: *Geoscientific Model Development* 14.10, pp. 6403–6444.

Köhler, Peter, Judith Hauck, Christoph Völker, Dieter A Wolf-gladrow, Martin Butzin, Joshua B Halpern, Ken Rice, and Richard E Zeebe (2018). “Comment on “ Scrutinizing the carbon cycle and CO 2 residence time in the atmosphere ” by H . Harde”. In: *Global and Planetary Change* 164.September 2017, pp. 67–71.

Kok, Jasper F. (2011). “A scaling theory for the size distribution of emitted dust aerosols suggests climate models underestimate the size of the global dust cycle”. In: *Proceedings of the National Academy of Sciences of the United States of America* 108.3, pp. 1016–1021.

Kok, Jasper F., A.A. Adebiyi, S. Albani, Y. Balkanski, R. Checa-Garcia, M. Chin, P.R. Colarco, D.S. Hamilton, Y. Huang, A. Ito, M. Klose, D.M. Leung, L. Li, N.M. Mahowald, R.L. Miller, V. Obiso, C. Pérez García-Pando, A. Rocha-Lima, J.S. Wan, and C.A. Whicker (2021a). “Improved representation of the global dust cycle using observational constraints on dust properties and abundance”. In: *Atmospheric Chemistry and Physics* 21.10, pp. 8127–8167.

Kok, Jasper F., A.A. Adebiyi, S. Albani, Y. Balkanski, R. Checa-Garcia, M. Chin, P.R. Colarco, D.S. Hamilton, Y. Huang, A. Ito, M. Klose, L. Li, N.M. Mahowald, R.L. Miller, V. Obiso, C. Pérez García-Pando, A. Rocha-Lima, and J.S. Wan (2021b). “Contribution of the world’s main dust source regions to the global cycle of desert dust”. In: *Atmospheric Chemistry and Physics* 21.10, pp. 8169–8193.

Kok, Jasper F., David A. Ridley, Qing Zhou, Ron L. Miller, Chun Zhao, Colette L. Heald, Daniel S. Ward, Samuel Albani, and Karsten Haustein (2017). “Smaller desert dust cooling effect estimated from analysis of dust size and abundance”. In: *Nature Geoscience* 10.4, pp. 274–278.

Kopp, C., A. Petzold, and R. Niessner (1999). “Investigation of the specific attenuation cross-section of aerosols deposited on fiber filters with a polar photometer to determine black carbon”. In: *Journal of Aerosol Science* 30.9, pp. 1153–1163.

Kulmala, M., H. Vehkamäki, T. Petäjä, M. Dal Maso, A. Lauri, V. M. Kerminen, W. Birmili, and P. H. McMurry (2004). “Formation and growth rates of ultrafine atmospheric particles: A review of observations”. In: *Journal of Aerosol Science* 35.2, pp. 143–176.

Kulmala, Markku et al. (2013). “Direct observations of atmospheric aerosol nucleation”. In: *Science* 339.6122, pp. 943–946.

Kupc, Agnieszka, Oliver Bischof, Torsten Tritscher, Michael Beeston, Thomas Krinke, and Paul E. Wagner (2013). “Laboratory characterization of a new nano-water-based CPC 3788 and performance comparison to an ultrafine butanol-based CPC 3776”. In: *Aerosol Science and Technology* 47.2, pp. 183–191.

Lack, D. A. and C. D. Cappa (2010). “Impact of brown and clear carbon on light absorption enhancement, single scatter albedo and absorption wavelength dependence of black carbon”. In: *Atmospheric Chemistry and Physics* 10.9, pp. 4207–4220.

Lack, D. A. and J. M. Langridge (2013). “On the attribution of black and brown carbon light absorption using the Ångström exponent”. In: *Atmospheric Chemistry and Physics* 13.20, pp. 10535–10543.

Lack, Daniel A., Justin M. Langridge, Roya Bahreini, Christopher D. Cappa, Ann M. Middlebrook, and Joshua P. Schwarz (2012). “Brown carbon and internal mixing in biomass burning particles”. In: *Proceedings of the National Academy of Sciences of the United States of America* 109.37, pp. 14802–14807.

Lack, Daniel A., Edward R. Lovejoy, Tahllee Baynard, Anders Pettersson, and A. R. Ravishankara (2006). “Aerosol Absorption Measurement using Photoacoustic Spectroscopy: Sensitivity, Calibration, and Uncertainty Developments”. In: *Aerosol Science and Technology* 40.9, pp. 697–708.

Lack, Daniel A., Hans Moosmüller, Gavin R. McMeeking, Rajan K. Chakrabarty, and Darrel Baumgardner (2014). “Characterizing elemental, equivalent black, and refractory black carbon aerosol particles: A review of techniques, their limitations and uncertainties”. In: *Analytical and Bioanalytical Chemistry* 406.1, pp. 99–122.

Lafon, Sandra, Irina N. Sokolik, Jean Louis Rajot, Sandrine Caquincau, and Annie Gaudichet (2006). “Characterization of iron oxides in mineral dust aerosols: Implications for light absorption”. In: *Journal of Geophysical Research Atmospheres* 111.21, pp. 1–19.

Laing, James R., Daniel A. Jaffe, and Arthur J. Sedlacek (2020). “Comparison of filter-based absorption measurements of biomass burning aerosol and background aerosol at the mt. Bachelor observatory”. In: *Aerosol and Air Quality Research* 20.4, pp. 663–678.

Laj, Paolo et al. (2020). “A global analysis of climate-relevant aerosol properties retrieved from the network of GAW near-surface observatories”. In: *Atmospheric Measurement Techniques*, pp. 1–70.

Laskin, Alexander, Julia Laskin, and Sergey A. Nizkorodov (2015). “Chemistry of Atmospheric Brown Carbon”. In: *Chemical Reviews* 115.10, pp. 4335–4382.

Lee, Jeonghoon and Hans Moosmüller (2020). “Measurement of light absorbing aerosols with folded-jamin photothermal interferometry”. In: *Sensors (Switzerland)* 20.9, pp. 1–13.

Lee, Shan Hu, Hamish Gordon, Huan Yu, Katrianne Lehtipalo, Ryan Haley, Yixin Li, and Renyi Zhang (2019). “New Particle Formation in the Atmosphere: From Molecular Clusters to Global Climate”. In: *Journal of Geophysical Research: Atmospheres* 124.13, pp. 7098–7146.

Lelieveld, J et al. (2002). “Global air pollution crossroads over the Mediterranean”. In: *Science* 298.5594, pp. 794–799.

Li, Longlei, N. M Mahowald, R.L. Miller, C. Pérez García-pando, M. Klose, D.S. Hamilton, M. Gonçalves Ageitos, P. Ginoux, Y. Balkanski, R. O Green, O. Kalashnikova, J. F. Kok, V. Obiso, D. Paynter, and D.R. Thompson (2021). “Quantifying the range of the dust direct radiative effect due to source mineralogy uncertainty”. In: pp. 3973–4005.

Lin, C. I., M. Baker, and R. J. Charlson (1973). “Absorption Coefficient of Atmospheric Aerosol: a Method for Measurement.” In:

Linke, C., O. Möhler, A. Veres, Á Mohácsi, Z. Bozóki, G. Szabó, and M. Schnaiter (2006). “Optical properties and mineralogical composition of different Saharan mineral dust samples: A laboratory study”. In: *Atmospheric Chemistry and Physics* 6.11, pp. 3315–3323.

Linke, Claudia, Inas Ibrahim, Nina Schleicher, Regina Hitzenberger, Meinrat O. Andreae, Thomas Leisner, and Martin Schnaiter (2016). “A novel single-cavity three-wavelength photoacoustic spectrometer for atmospheric aerosol research”. In: *Atmospheric Measurement Techniques* 9.11, pp. 5331–5346.

Liou, Kuo-Nan (2002). *An introduction to atmospheric radiation*. Vol. 84. Elsevier.

Liousse, C., H. Cachier, and S. G. Jennings (1993). “Optical and thermal measurements of black carbon aerosol content in different environments: Variation of the specific attenuation cross-section, sigma (σ)”. In: *Atmospheric Environment Part A, General Topics* 27.8, pp. 1203–1211.

Liu, P. F., N. Abdelmalki, H. M. Hung, Y. Wang, W. H. Brune, and S. T. Martin (2015a). “Ultraviolet and visible complex refractive indices of secondary organic material produced by photooxidation of the aromatic compounds toluene and m-xylene”. In: *Atmospheric Chemistry and Physics* 15.3, pp. 1435–1446.

Liu, Shang et al. (2015b). “Enhanced light absorption by mixed source black and brown carbon particles in UK winter”. In: *Nature Communications* 6.

Lord, N S, A Ridgwell, M C Thorne, and D J Lunt (2015). “Global Biogeochemical Cycles”. In:

Lorenz, Louis (1890). *Lysbevægelsen i og uden for en af plane Lysbølger belyst Kugle*. na.

Lu, Zifeng, David G. Streets, Ekbordin Winijkul, Fang Yan, Yanju Chen, Tami C. Bond, Yan Feng, Manvendra K. Dubey, Shang Liu, Joseph P. Pinto, and Gregory R. Carmichael (2015). “Light absorption properties and radiative effects of primary organic aerosol emissions”. In: *Environmental Science and Technology* 49.8, pp. 4868–4877.

Lund, Marianne Tronstad, Gunnar Myhre, Amund Søvde Haslerud, Ragnhild Bieltvedt Skeie, Jan Griesfeller, Stephen Matthew Platt, Rajesh Kumar, Cathrine Lund Myhre, and Michael Schulz (2018). “Concentrations and radiative forcing of anthropogenic aerosols from 1750 to 2014 simulated with the Oslo CTM3 and CEDS emission inventory”. In: *Geoscientific Model Development* 11.12, pp. 4909–4931.

Malm, William C, James F Sisler, Dale Huffman, Robert A Eldred, and Thomas A Cahill (1994). “Spatial and seasonal trends in particle concentration and optical extinction in the United States”. In: *Journal of Geophysical Research: Atmospheres* 99.D1, pp. 1347–1370.

Martucci, Giovanni, Conor Milroy, and Colin D O’Dowd (2010). “Detection of cloud-base height using Jenoptik CHM15K and Vaisala CL31 ceilometers”. In: *Journal of Atmospheric and Oceanic Technology* 27.2, pp. 305–318.

Massabò, D., V. Bernardoni, M. C. Bove, A. Brunengo, E. Cuccia, A. Piazzalunga, P. Prati, G. Valli, and R. Vecchi (2013). “A multi-wavelength optical set-up for the characterization of carbonaceous particulate matter”. In: *Journal of Aerosol Science* 60, pp. 34–46.

McCutcheon, Jenine, Stefanie Lutz, Christopher Williamson, Joseph M Cook, Andrew J Tedstone, Aubry Vanderstraeten, Siobhan A Wilson, Anthony Stockdale, Steeve Bonneville, Alexandre M Anesio, M.L. Yallop, J.B. McQuaid, M. Tranter, and L. Benning (2021). “Mineral phosphorus drives glacier algal blooms on the Greenland Ice Sheet”. In: *Nature communications* 12.1, pp. 1–11.

McMurry, Peter H (2000). “A review of atmospheric aerosol measurements”. In: *Atmospheric Environment* 34.12-14, pp. 1959–1999.

Meszaros, Erno (1999). *Fundamentals of atmospheric aerosol chemistry*. Akadémiai kiado.

Mie, Gustav (1908). “Beiträge zur Optik trüber Medien, speziell kolloidaler Metallösungen”. In: *Annalen der physik* 330.3, pp. 377–445.

Millán, Millán M, M Jose Sanz, Rosa Salvador, and Enrique Mantilla (2002). “Atmospheric dynamics and ozone cycles related to nitrogen deposition in the western Mediterranean”. In: *Environmental Pollution* 118.2, pp. 167–186.

Millán, MM, R Salvador, E Mantilla, and G Kallos (1997). “Photooxidant dynamics in the Mediterranean basin in summer: Results from European research projects”. In: *Journal of Geophysical Research: Atmospheres* 102.D7, pp. 8811–8823.

Minguillón, M. C., A. Ripoll, N. Pérez, A. S.H. Prévôt, F. Canonaco, X. Querol, and A. Alastuey (2015). “Chemical characterization of submicron regional background aerosols in the western Mediterranean using an Aerosol Chemical Speciation Monitor”. In: *Atmospheric Chemistry and Physics* 15.11, pp. 6379–6391.

Mishchenko, Michael I, Larry D Travis, and Andrew a Lacis (2002). “Scattering, Absorption, and Emission of Light by Small Particles”. In: *Vasa*, pp. 1–486.

Modini, Rob L., Joel C. Corbin, Benjamin T. Brem, Martin Irwin, Michele Bertò, Rosaria E. Pileci, Prodromos Fetfatzis, Kostas Eleftheriadis, Bas Henzing, Marcel M. Moerman, Fengshan Liu, Thomas Müller, and Martin Gysel-Beer (2021). “Detailed characterization of the CAPS single-scattering albedo monitor (CAPS PMssa) as a field-deployable instrument for measuring aerosol light absorption with the extinction-minus-scattering method”. In: *Atmospheric Measurement Techniques* 14.2, pp. 819–851.

Moosmüller, H., R. K. Chakrabarty, and W. P. Arnott (2009). "Aerosol light absorption and its measurement: A review". In: *Journal of Quantitative Spectroscopy and Radiative Transfer* 110.11, pp. 844–878.

Moosmüller, H. and C. M. Sorensen (2018). "Single scattering albedo of homogeneous, spherical particles in the transition regime". In: *Journal of Quantitative Spectroscopy and Radiative Transfer* 219, pp. 333–338.

Müller, T, M Laborde, G Kassell, and A Wiedensohler (2011a). "Design and performance of a three-wavelength LED-based total scatter and backscatter integrating nephelometer". In: *Atmospheric Measurement Techniques* 4.6, pp. 1291–1303.

Müller, T et al. (2011b). "Characterization and intercomparison of aerosol absorption photometers: result of two intercomparison workshops". In:

Müller, T. and M. Fiebig (2021). "ACTRIS In Situ Aerosol: Guidelines for Manual QC of AE33 absorption photometer data". In: *ACTRIS Measurement Guidelines*.

Müller, T., A. Schladitz, K. Kandler, and A. Wiedensohler (2011c). "Spectral particle absorption coefficients, single scattering albedos and imaginary parts of refractive indices from ground based in situ measurements at Cape Verde Island during SAMUM-2". In: *Tellus, Series B: Chemical and Physical Meteorology* 63.4, pp. 573–588.

Müller, Thomas, A. Schladitz, A. Massling, N. Kaaden, K. Kandler, and A. Wiedensohler (2009). "Spectral absorption coefficients and imaginary parts of refractive indices of Saharan dust during SAMUM-1". In: *Tellus, Series B: Chemical and Physical Meteorology* 61.1, pp. 79–95.

Myhre, G., D. Shindell, F.-M. Breéon, W. Collins, J. Fuglestvedt, J. Huang, D. Koch, J.-F. Lamarque, D. Lee, B. Mendoza, T. Nakajima, A. Robock, G. Stephens, T. Takemura, and H. Zhang (2013). "Anthropogenic and Natural Radiative Forcing". In: *Climate Change 2013: The Physical Science Basis. Contribution of Working Group I to the Fifth Assessment Report of the Intergovernmental Panel on Climate Change*. Ed. by T.F. Stocker, D. Qin, G.-K. Plattner, M. Tignor, S.K. Allen, J. Boschung, A. Nauels, Y. Xia, V. Bex, and P.M. Midgley. Cambridge, United Kingdom and New York, NY, USA: Cambridge University Press. Chap. 8, pp. 659–740.

Navarro, J. C.Acosta, V. Varma, I. Riipinen, Seland, A. Kirkevåg, H. Struthers, T. Iversen, H. C. Hansson, and A. M.L. Ekman (2016). "Amplification of Arctic warming by past air pollution reductions in Europe". In: *Nature Geoscience* 9.4, pp. 277–281.

Ng, N. L., S. C. Herndon, A. Trimborn, M. R. Canagaratna, P. L. Croteau, T. B. Onasch, D. Sueper, D. R. Worsnop, Q. Zhang, Y. L. Sun, and J. T. Jayne (2011). "An Aerosol Chemical Speciation Monitor (ACSM) for routine monitoring of the composition and mass concentrations of ambient aerosol". In: *Aerosol Science and Technology* 45.7, pp. 780–794.

Nickovic, Slobodan, George Kallos, Anastasios Papadopoulos, and Olga Kakaliagou (2001). "A model for prediction of desert dust cycle in the atmosphere". In: *Journal of Geophysical Research Atmospheres* 106.D16, pp. 18113–18129.

Ogren, John A., Jim Wendell, Elisabeth Andrews, and Patrick J. Sheridan (2017). "Continuous light absorption photometer for long-Term studies". In: *Atmospheric Measurement Techniques* 10.12, pp. 4805–4818.

"On the light from the sky, its polarization and colour" (1871). In: *Phil Mag* 41, p. 274.

Onasch, Timothy B., Paola Massoli, Paul L. Kebabian, Frank B. Hills, Fred W. Bacon, and Andrew Freedman (2015). "Single scattering albedo monitor for airborne particulates". In: *Aerosol Science and Technology* 49.4, pp. 267–279.

Pandolfi, M., M. Cusack, A. Alastuey, and X. Querol (2011). "Variability of aerosol optical properties in the Western Mediterranean Basin". In: *Atmospheric Chemistry and Physics* 11.15, pp. 8189–8203.

Pandolfi, M. et al. (2018). "A European aerosol phenomenology – 6: scattering properties of atmospheric aerosol particles from 28 ACTRIS sites". In: *Atmospheric Chemistry and Physics* 18.11, pp. 7877–7911.

Pandolfi, Marco, Andrés Alastuey, Noemi Pérez, Cristina Reche, Iria Castro, Victor Shatalov, and X. Querol (2016). "Trends analysis of PM source contributions and chemical tracers in NE Spain during 2004–2014: a multi-exponential approach". In: *Atmospheric Chemistry and Physics* 16.18, pp. 11787–11805.

Pandolfi, Marco, G Martucci, X. Querol, Andrés Alastuey, F Wilsenack, S Frey, CD O'Dowd, and Manuel Dall'Osto (2013). "Continuous atmospheric boundary layer observations in the coastal urban area of Barcelona during SAPUSS". In: *Atmospheric Chemistry and Physics* 13.9, pp. 4983–4996.

Pandolfi, Marco, Dennis Mooibroek, Philip Hopke, Dominik Van Pinxteren, Xavier Querol, Hartmut Herrmann, Andrés Alastuey, Olivier Favez, Christoph Hüglin, Esperanza Perdrix, Véronique Riffault, Stéphane Sauvage, Eric Van Der Swaluw, Oksana Tarasova, and Augustin Colette (2020). "Long-range and local air pollution: What can we learn from chemical speciation of particulate matter at paired sites?" In: *Atmospheric Chemistry and Physics* 20.1, pp. 409–429.

Pandolfi, Marco, Anna Ripoll, X. Querol, and Andrés Alastuey (2014). "Climatology of aerosol optical properties and black carbon mass absorption cross section at a remote high-altitude site in the western Mediterranean Basin". In: *Atmospheric Chemistry and Physics* 14.12, pp. 6443–6460.

Patterson, E. M. and C. K. McMahon (1984). "Absorption characteristics of forest fire particulate matter". In: *Atmospheric Environment (1967)* 18.11, pp. 2541–2551.

Perez, L, M Medina-Ramón, N Kunzli, Andrés Alastuey, Jorge Pey, Noemi Perez, R Garcia, Aurelio Tobıas, Xavier Querol, and Jordi Sunyer (2009). "Size fractionate particulate matter, vehicle traffic, and case-specific daily mortality in Barcelona, Spain". In: *Environmental science & technology* 43.13, pp. 4707–4714.

Pérez, C., K. Haustein, Z. Janjic, O. Jorba, N. Huneeus, J. M. Baldasano, T. Black, S. Basart, S. Nickovic, R. L. Miller, J. P. Perlwitz, M. Schulz, and M. Thomson (2011). "Atmospheric dust modeling from meso to global scales with the online NMMB/BSC-Dust model – Part 1: Model description, annual simulations and evaluation". In: *Atmospheric Chemistry and Physics* 11.24, pp. 13001–13027.

Pérez, Carlos, Slobodan Nickovic, Goran Pejanovic, José María Baldasano, and Emin Özsoy (2006). "Interactive dust-radiation modeling: A step to improve weather forecasts". In: *Journal of Geophysical Research Atmospheres* 111.16.

Pérez, Carlos, Michaël Sicard, Oriol Jorba, Adolfo Comerón, and Jose M Baldasano (2004). "Summertime re-circulations of air pollutants over the north-eastern Iberian coast observed from systematic EARLINET lidar measurements in Barcelona". In: *Atmospheric Environment* 38.24, pp. 3983–4000.

Petzold, A., J. A. Ogren, M. Fiebig, P. Laj, S. M. Li, U. Baltensperger, T. Holzer-Popp, S. Kinne, G. Pappalardo, N. Sugimoto, C. Wehrli, A. Wiedensohler, and X. Y. Zhang (2013). "Recommendations for reporting black carbon measurements". In: *Atmospheric Chemistry and Physics* 13.16, pp. 8365–8379.

Petzold, Andreas and Markus Schönlinner (2004). "Multi-angle absorption photometry—a new method for the measurement of aerosol light absorption and atmospheric black carbon". In: *Journal of Aerosol Science* 35.4, pp. 421–441.

Pey, J, N Pérez, S Castillo, M Viana, T Moreno, M Pandolfi, JM López-Sebastián, A Alastuey, and X Querol (2009). "Geochemistry of regional background aerosols in the Western Mediterranean". In: *Atmospheric Research* 94.3, pp. 422–435.

Pey, J, X Querol, A Alastuey, F Forastiere, and M Stafoggia (2013). "African dust outbreaks over the Mediterranean Basin during 2001–2011: PM 10 concentrations, phenomenology and trends, and its relation with synoptic and mesoscale meteorology". In: *Atmospheric Chemistry and Physics* 13.3, pp. 1395–1410.

Putaud, J-P et al. (2010). "A European aerosol phenomenology–3: Physical and chemical characteristics of particulate matter from 60 rural, urban, and kerbside sites across Europe". In: *Atmospheric Environment* 44.10, pp. 1308–1320.

Putaud, Jean-P et al. (2004). "A European aerosol phenomenology—2: chemical characteristics of particulate matter at kerbside, urban, rural and background sites in Europe". In: *Atmospheric environment* 38.16, pp. 2579–2595.

Qin, Yi Ming, Hao Bo Tan, Yong Jie Li, Zhu Jie Li, Misha I. Schurman, Li Liu, Cheng Wu, and Chak K. Chan (2018). “Chemical characteristics of brown carbon in atmospheric particles at a suburban site near Guangzhou, China”. In: *Atmospheric Chemistry and Physics* 18.22, pp. 16409–16418.

Querol, X, A Alastuey, C Reche, A Orio, M Pallares, F Reina, JJ Dieguez, E Mantilla, M Escudero, L Alonso, G. Gongoiti, and M. Millán (2016). “On the origin of the highest ozone episodes in Spain”. In: *Science of the Total Environment* 572, pp. 379–389.

Querol, X., Andrés Alastuey, José A Puicercus, Enrique Mantilla, José V Miro, Angel Lopez-Soler, Felicià Plana, and Begoña Artiñano (1998). “Seasonal evolution of suspended particles around a large coal-fired power station: particulate levels and sources”. In: *Atmospheric Environment* 32.11, pp. 1963–1978.

Querol, X., Andrés Alastuey, Sergio Rodriguez, Felicià Plana, Carmen R Ruiz, Nuria Cots, Guillem Massagué, and Oriol Puig (2001). “PM10 and PM2. 5 source apportionment in the Barcelona Metropolitan area, Catalonia, Spain”. In: *Atmospheric Environment* 35.36, pp. 6407–6419.

Querol, X., Andrés Alastuey, Mar M Viana, Sergio Rodriguez, Begoña Artıñano, Pedro Salvador, S Garcia Do Santos, R Fernandez Patier, CR Ruiz, J De la Rosa, A Sanchez de la Campa, M Menendez, and J.I. Gil (2004). “Speciation and origin of PM10 and PM2. 5 in Spain”. In: *Journal of Aerosol Science* 35.9, pp. 1151–1172.

Querol, X. et al. (2017). “Phenomenology of high-ozone episodes in NE Spain”. In: *Atmospheric Chemistry and Physics* 17.4, pp. 2817–2838.

Querol, Xavier, Andrés Alastuey, Gotzon Gangoiti, Noemí Perez, Hong K Lee, Heeram R Eun, Yonghee Park, Enrique Mantilla, Miguel Escudero, Gloria Titos, Lucio Alonso, Brice Temime-roussel, Nicolas Marchand, Juan R Moreta, M Arantxa Revuelta, Pedro Salvador, Begoña Artíñano, and Saúl García (2018). “Phenomenology of summer ozone episodes over the Madrid Metropolitan Area , central Spain”. In: 3, pp. 6511–6533.

Ramanathan, V, P J Crutzen, J T Kiehl, and D Rosenfeld (2020). “Aerosols , Climate , and the Hydrological Cycle”. In: 294.5549, pp. 2119–2124.

Reche, C, X. Querol, Andrés Alastuey, Mar Viana, Jorge Pey, T Moreno, S Rodrıguez, Y González, Rocıo Fernández-Camacho, J.d.l. Rosa, M. Dall’Osto, A.S.H. Prévôt, R.M. Hueglin C. ad Harrison, and P. Quincey (2011). “New considerations for PM, Black Carbon and particle number concentration for air quality monitoring across different European cities”. In: *Atmospheric Chemistry and Physics* 11.13, pp. 6207–6227.

Ripoll, A., M. C. Minguillón, J. Pey, J. L. Jimenez, D. A. Day, Y. Sosedova, F. Canonaco, A. S.H. Prévôt, X. Querol, and A. Alastuey (2015a). “Long-term real-time chemical characterization of submicron aerosols at Montsec (southern Pyrenees, 1570 m a.s.l.)” In: *Atmospheric Chemistry and Physics* 15.6, pp. 2935–2951.

Ripoll, A., M. C. Minguillón, J. Pey, N. Pérez, X. Querol, and A. Alastuey (2015b). “Joint analysis of continental and regional background environments in the western Mediterranean: PM1 and PM10 concentrations and composition”. In: *Atmospheric Chemistry and Physics* 15.2, pp. 1129–1145.

Ripoll, Anna, Jorge Pey, Marıa Cruz Minguillón, Noemı Pérez, Marco Pandolfi, X. Querol, and Andrés Alastuey (2014). “Three years of aerosol mass, black carbon and particle number concentrations at Montsec (southern Pyrenees, 1570 m asl)”. In: *Atmospheric Chemistry and Physics* 14.8, pp. 4279–4295.

Roberts, Alex and Peter Knippertz (2012). “Haboobs: Convectively generated dust storms in West Africa”. In: *Weather* 67.12, pp. 311–316.

Rodrıguez, S, X Querol, A Alastuey, G Kallos, and O Kakaliagou (2001). “Saharan dust contributions to PM10 and TSP levels in Southern and Eastern Spain”. In: *Atmospheric Environment* 35.14, pp. 2433–2447.

Rodrıguez, Sergio, X. Querol, Andrés Alastuey, and Felicia Plana (2002). “Sources and processes affecting levels and composition of atmospheric aerosol in the western Mediterranean”. In: *Journal of Geophysical Research: Atmospheres* 107.D24, AAC–12.

Román, Roberto, JA Benavent-Oltra, JA Casquero-Vera, A Lopatin, A Cazorla, H Lyamani, C Denjean, D Fuertes, Daniel Pérez-Ramırez, B Torres, C. Toledano, O. Dubovik, V.E. Cachorro, A.M. de Frutos, F.J. Olmo, and L. Alados-Arboledas (2018). "Retrieval of aerosol profiles combining sunphotometer and ceilometer measurements in GRASP code". In: *Atmospheric research* 204, pp. 161–177.

Rosenfeld, Daniel (1999). "TRMM observed first direct evidence of smoke from forest fires inhibiting rainfall". In: *Geophysical research letters* 26.20, pp. 3105–3108.

– (2000). "Suppression of rain and snow by urban and industrial air pollution". In: *science* 287.5459, pp. 1793–1796.

Ryder, Claire L., Franco Marenco, Jennifer K. Brooke, Victor Estelles, Richard Cotton, Paola Formenti, Jim B. McQuaid, Hannah C. Price, Dantong Liu, Patrick Ausset, Phil Rosenberg, Jonathan W. Taylor, Tom Choularton, Keith Bower, Hugh Coe, Martin Gallagher, Jonathan Crosier, Gary Lloyd, Eleanor J. Highwood, and Benjamin J. Murray (2018). "Coarse mode mineral dust size distributions, composition and optical properties from AER-D aircraft measurements over the Tropical Eastern Atlantic". In: *Atmospheric Chemistry and Physics Discussions* 98, pp. 1–49.

Saleh, Rawad, Zezhen Cheng, and Khairallah Atwi (2018). "The Brown-Black Continuum of Light-Absorbing Combustion Aerosols". In: *Environmental Science and Technology Letters* 5.8, pp. 508–513.

Sandradewi, Jisca, Andre S.H. Prévôt, Sönke Szidat, Nolwenn Perron, M. Rami Alfarra, Valentin A. Lanz, Ernest Weingartner, and U. R.S. Baltensperger (2008). "Using aerosol light absorption measurements for the quantitative determination of wood burning and traffic emission contribution to particulate matter". In: *Environmental Science and Technology* 42.9, pp. 3316–3323.

Sassen, Kenneth, Paul J DeMott, Joseph M Prospero, and Michael R Poellot (2003). "Saharan dust storms and indirect aerosol effects on clouds: CRYSTAL-FACE results". In: *Geophysical Research Letters* 30.12.

Saturno, Jorge, Christopher Pöhlker, Dario Massabò, Joel Brito, Samara Carbone, Yafang Cheng, Xuguang Chi, Florian Ditas, Isabella Hrab De Angelis, Daniel Morán-Zuloaga, Mira L. Pöhlker, Luciana V. Rizzo, David Walter, Qiaoqiao Wang, Paulo Artaxo, Paolo Prati, and Meinrat O. Andreae (2017). "Comparison of different Aethalometer correction schemes and a reference multi-wavelength absorption technique for ambient aerosol data". In: *Atmospheric Measurement Techniques* 10.8, pp. 2837–2850.

Schladitz, A., T. Müller, N. Kaaden, A. Massling, K. Kandler, M. Ebert, S. Weinbruch, C. Deutscher, and A. Wiedensohler (2009). "In situ measurements of optical properties at Tinfou (Morocco) during the Saharan Mineral Dust Experiment SAMUM 2006". In: *Tellus, Series B: Chemical and Physical Meteorology* 61.1, pp. 64–78.

Schmid, O., P. Artaxo, W. P. Arnott, D. Chand, L. V. Gatti, G. P. Frank, A. Hoffer, M. Schnaiter, and M. O. Andreae (2006). "Spectral light absorption by ambient aerosols influenced by biomass burning in the Amazon Basin. I: Comparison and field calibration of absorption measurement techniques". In: *Atmospheric Chemistry and Physics* 6.11, pp. 3443–3462.

Schmidt, Gavin A., Reto A. Ruedy, Ron L. Miller, and Andy A. Lacis (2010). "Attribution of the present-day total greenhouse effect". In: *Journal of Geophysical Research Atmospheres* 115.20, pp. 1–6.

Schnaiter, M., H. Horvath, O. Möhler, K. H. Naumann, H. Saathoff, and O. W. Schöck (2003). "UV-VIS-NIR spectral optical properties of soot and soot-containing aerosols". In: *Journal of Aerosol Science* 34.10, pp. 1421–1444.

Schuster, G. L., O. Dubovik, and A. Arola (2016). "Remote sensing of soot carbon - Part 1: Distinguishing different absorbing aerosol species". In: *Atmospheric Chemistry and Physics* 16.3, pp. 1565–1585.

Schuster, Gregory L, Oleg Dubovik, and Brent N Holben (2006). "Angstrom exponent and bimodal aerosol size distributions". In: *Journal of Geophysical Research: Atmospheres* 111.D7.

Seinfeld, John H and Spyros N Pandis (1998). *Atmospheric Chemistry and Physics: From air pollution to climate change*. John Wiley & Sons New York, p. 1326.

Seinfeld, John H., Spyros N. Pandis, and Kevin Noone (1998). *Atmospheric Chemistry and Physics: From Air Pollution to Climate Change*. Vol. 51. 10, pp. 88–90.

Sekiyama, TT, TY Tanaka, A Shimizu, and T Miyoshi (2010). "Data assimilation of CALIPSO aerosol observations". In: *Atmospheric Chemistry and Physics* 10.1, pp. 39–49.

Shao, Yaping (2008). *Physics and modelling of wind erosion*. Springer.

Shaw, Glenn E. (1980). "Optical, chemical and physical properties of aerosols over the antarctic ice sheet". In: *Atmospheric Environment (1967)* 14.8, pp. 911–921.

Shindell, Drew et al. (2012). "Simultaneously mitigating near-term climate change and improving human health and food security". In: *Science* 335.6065, pp. 183–189.

Shiraiwa, Manabu, Kathrin Selzle, and Ulrich Pöschl (2012). "Hazardous components and health effects of atmospheric aerosol particles: reactive oxygen species, soot, polycyclic aromatic compounds and allergenic proteins". In: *Free radical research* 46.8, pp. 927–939.

Singh, Sujeeta, Marc N. Fiddler, Damon Smith, and Solomon Bililign (2014). "Error analysis and uncertainty in the determination of aerosol optical properties using cavity ring-down spectroscopy, integrating nephelometry, and the extinction-minus-scattering method". In: *Aerosol Science and Technology* 48.12, pp. 1345–1359.

Sokolik, Irina N. and Owen B. Toon (1999). "Incorporation of mineralogical composition into models of the radiative properties of mineral aerosol from UV to IR wavelengths". In: *Journal of Geophysical Research Atmospheres* 104.D8, pp. 9423–9444.

Springston, Stephen R. and Arthur J. Sedlacek (2007). "Noise characteristics of an instrumental particle absorbance technique". In: *Aerosol Science and Technology* 41.12, pp. 1110–1116.

Stein, A. F., R. R. Draxler, G. D. Rolph, B. J.B. Stunder, M. D. Cohen, and F. Ngan (2015). "Noaa's hysplit atmospheric transport and dispersion modeling system". In: *Bulletin of the American Meteorological Society* 96.12, pp. 2059–2077.

Stephens, Michelle, Nelson Turner, and Jon Sandberg (2003). "Particle identification by laser-induced incandescence in a solid-state laser cavity". In: *Applied Optics* 42.19, p. 3726.

Stull, V Robert and Gilbert N Plass (1960). "Emissivity of dispersed carbon particles". In: *JOSA* 50.2, pp. 121–129.

Su, Lin, Zibing Yuan, Jimmy C.H. Fung, and Alexis K.H. Lau (2015). "A comparison of HYSPLIT backward trajectories generated from two GDAS datasets". In: *Science of the Total Environment* 506-507, pp. 527–537.

Szopa, S., V. Naik, B. Adhikary, P. Artaxoand, T. Berntsen, W.D. Collins, S. Fuzzi, L. Gallardo, A. Kiendler-Scharr, Z. Klimont, H. Liao, N. Unger, and P. Zanis (2021). "Short-Lived Climate Forcers". In: *Climate Change 2021: The Physical Science Basis. Contribution of Working Group I to the Sixth Assessment Report of the Intergovernmental Panel on Climate Change*. Ed. by V. Masson-Delmotte, P. Zhai, A. Pirani, S.L. Connors, C. Péan, S. Berger, N. Caud, Y. Chen, L. Goldfarb, M.I. Gomis, M. Huang, K. Leitzell, E. Lonnoy, J.B.R. Matthews, T.K. Maycock, T. Waterfield, O. Yelekçi, R. Yu, and B. Zhou. Cambridge, United Kingdom and New York, NY, USA: Cambridge University Press. Chap. 6, pp. 817–922.

Takahama, S., R. E. Schwartz, L. M. Russell, A. M. MacDonald, S. Sharma, and W. R. Leaitch (2011). "Organic functional groups in aerosol particles from burning and non-burning forest emissions at a high-elevation mountain site". In: *Atmospheric Chemistry and Physics* 11.13, pp. 6367–6386.

Tang, Weiyi, Joan Llort, Jakob Weis, Morgane MG Perron, Sara Basart, Zuchuan Li, Shubha Sathyendranath, Thomas Jackson, Estrella Sanz Rodriguez, Bernadette C Proemse, A.R. Bowie, C. Schallenberg, P.G. Strutton, R. Matear, and N. Cassar (2021). "Widespread phytoplankton blooms triggered by 2019–2020 Australian wildfires". In: *Nature* 597.7876, pp. 370–375.

Tao, Wei Kuo, Jen Ping Chen, Zhanqing Li, Chien Wang, and Chidong Zhang (2012). "Impact of aerosols on convective clouds and precipitation". In: *Reviews of Geophysics* 50.2.

Tauc, J., Radu Grigorovici, and A. Vancou (1966). "Optical Properties and Electronic Structure of Amorphous Germanium BY". In: *Physics of the state solid* 15, pp. 627–637.

Team, R Core et al. (2013). “R: A language and environment for statistical computing”. In:

Terhune, R. W. and J. E. Anderson (1977). “Spectrophone measurements of the absorption of visible light by aerosols in the atmosphere”. In: *Optics Letters* 1.2, p. 70.

Titos, G, A Del Águila, A Cazorla, H Lyamani, JA Casquero-Vera, C Colombi, E Cuccia, V Gianelle, G Močnik, A Alastuey, F.J. Olmo, and L. Alados-Arboledas (2017). “Spatial and temporal variability of carbonaceous aerosols: assessing the impact of biomass burning in the urban environment”. In: *Science of the Total Environment* 578, pp. 613–625.

Titos, G., M. Ealo, R. Román, A. Cazorla, Y. Sola, O. Dubovik, A. Alastuey, and M. Pandolfi (2019). “Retrieval of aerosol properties from ceilometer and photometer measurements: long-term evaluation with in situ data and statistical analysis at Montsec (southern Pyrenees)”. In: *Atmospheric Measurement Techniques* 12.6, pp. 3255–3267.

Turpin, B. J., R. A. Cary, and J. J. Huntzicker (1990). “An in situ, time-resolved analyzer for aerosol organic and elemental carbon”. In: *Aerosol Science and Technology* 12.1, pp. 19–161.

Twomey, Sean (1977). “The influence of pollution on the shortwave albedo of clouds”. In: *Journal of the atmospheric sciences* 34.7, pp. 1149–1152.

Twomey, Sean A, M Piepgrass, and TL Wolfe (1984). “An assessment of the impact of pollution on global cloud albedo”. In: *Tellus B* 36.5, pp. 356–366.

Twomey, SJAE (1974). “Pollution and the planetary albedo”. In: *Atmospheric Environment (1967)* 8.12, pp. 1251–1256.

Updyke, Katelyn M., Tran B. Nguyen, and Sergey A. Nizkorodov (2012). “Formation of brown carbon via reactions of ammonia with secondary organic aerosols from biogenic and anthropogenic precursors”. In: *Atmospheric Environment* 63, pp. 22–31.

Valentini, Sara, Vera Bernardoni, Ezio Bolzacchini, Davide Ciniglia, Marco Pandolfi, Luca Ferrero, Alice Corina Forello, Dario Massabó, Marco Pandolfi, Paolo Prati, Francesca Soldan, Gianluigi Valli, Jesús Yus-díez, and Roberta Vecchi (2020). “Applicability of benchtop multi-wavelength polar photometers to off-line measurements of the Multi-Angle Absorption Photometer”. In: October, pp. 1–13.

Valenzuela, A., F. J. Olmo, H. Lyamani, M. Antón, G. Titos, A. Cazorla, and L. Alados-Arboledas (2015). “Aerosol scattering and absorption Angström exponents as indicators of dust and dust-free days over Granada (Spain)”. In: *Atmospheric Research* 154, pp. 1–13.

Vecchi, R, V Bernardoni, C Paganelli, and G Valli (2014). “A filter-based light-absorption measurement with polar photometer: Effects of sampling artefacts from organic carbon”. In: *Journal of Aerosol Science* 70, pp. 15–25.

Veld, Marten in t., Andres Alastuey, Marco Pandolfi, Fulvio Amato, Noemi Pérez, Cristina Reche, Marta Via, María Cruz Minguillón, Miguel Escudero, and X. Querol (2021). “Compositional changes of PM2.5 in NE Spain during 2009–2018: A trend analysis of the chemical composition and source apportionment”. In: *Science of the Total Environment* 795.

Via, Marta, María Cruz Minguillón, Cristina Reche, X. Querol, and Andrés Alastuey (2021). “Increase in secondary organic aerosol in an urban environment”. In: *Atmospheric Chemistry and Physics* 21.10, pp. 8323–8339.

Virkkula, A., X. Chi, A. Ding, Y. Shen, W. Nie, X. Qi, L. Zheng, X. Huang, Y. Xie, J. Wang, T. Petäjä, and M. Kulmala (2015). “On the interpretation of the loading correction of the aethalometer”. In: *Atmospheric Measurement Techniques* 8.10, pp. 4415–4427.

Virkkula, Aki (2021). “Modeled source apportionment of black carbon particles coated with a light-scattering shell”. In: *Atmospheric Measurement Techniques* 14.5, pp. 3707–3719.

Virkkula, Aki, Henrik Grythe, John Backman, Tuukka Petäjä, Maurizio Busetto, Christian Lanconelli, Angelo Lupi, Silvia Becagli, Rita Traversi, Mirko Severi, Vito Vitale, Patrick Sheridan, and Elisabeth Andrews (2022). “Aerosol optical properties calculated from size distributions, filter samples and absorption photometer data at Dome C, Antarctica, and their relationships with seasonal cycles of sources”. In: *Atmospheric Chemistry and Physics* 22.7, pp. 5033–5069.

Virkkula, Aki, Timo Mäkelä, Risto Hillamo, Tarja Yli-Tuomi, Anne Hirsikko, Kaarle Hämeri, and Ismo K. Koponen (2007). “A simple procedure for correcting loading effects of aethalometer data”. In: *Journal of the Air and Waste Management Association* 57.10, pp. 1214–1222.

Visser, Bradley, Jannis Röhrbein, Peter Steigmeier, Luka Drinovec, Griša Močnik, and Ernest Weingartner (2020). “A single-beam photothermal interferometer for in-situ measurements of aerosol light absorption”. In: *Atmospheric Measurement Techniques Discussions* 2.July, pp. 1–24.

Vitols, V A L and Ntnf Stipendiat (1976). “AIRBORNE SEA SALT MEASUREMENTS A LITERATURE SURVEY BY”. In: 7.

Wang, Qiaoqiao, Daniel J. Jacob, J. Ryan Spackman, Anne E. Perring, Joshua P. Schwarz, Nobuhiro Moteki, Eloïse A. Marais, Cui Ge, Jun Wang, and Steven R.H. Barrett (2014). “Global budget and radiative forcing of black carbon aerosol: Constraints from pole-to-pole (HIPPO) observations across the Pacific”. In: *Journal of Geophysical Research* 119.1, pp. 195–206.

Weingartner, E., H. Saathoff, M. Schnaiter, N. Streit, B. Bitnar, and U. Baltensperger (2003). “Absorption of light by soot particles: Determination of the absorption coefficient by means of aethalometers”. In: *Journal of Aerosol Science* 34.10, pp. 1445–1463.

Westphal, D L, C A Curtis, M Liu, and A L Walker (2009). “Operational aerosol and dust storm forecasting”. In: *IOP Conference Series: Earth and Environmental Science* 7, p. 012007.

Whitby, KT and B Cantrell (1976). “Fine particles”. In: *International conference of environmental sensing and assessment, Las Vegas, NV, Institute of Electrical and Electronic Engineers*.

WHO (2012). *Health effects of black carbon*.

– (2016). *Health risk assessment of air pollution: general principles*. World Health Organization. Regional Office for Europe, viii + 29 p.

– (2021). *WHO global air quality guidelines: particulate matter (PM2.5 and PM10), ozone, nitrogen dioxide, sulfur dioxide and carbon monoxide*. World Health Organization, xxi, 273 p.

Wiegner, M., F. Madonna, I. Binietoglou, R. Forkel, J. Gasteiger, A. Geiß, G. Pappalardo, K. Schäfer, and W. Thomas (2014). “What is the benefit of ceilometers for aerosol remote sensing? An answer from EARLINET”. In: *Atmospheric Measurement Techniques* 7.7, pp. 1979–1997.

Wiscombe, WJ and GW Grams (1976). “The backscattered fraction in two-stream approximations”. In: *Journal of the Atmospheric Sciences* 33.12, pp. 2440–2451.

WMO (2016). *WMO/GAW Aerosol Measurement Procedures, Guidelines and Recommendations*. WMO-No. 1177; GAW Report- No. 227, p. 103.

Yus-Díez, Jesús, Vera Bernardoni, Griša Močnik, Andrés Alastuey, Davide Ciniglia, Matic Ivančič, X. Querol, Noemí Perez, Cristina Reche, Martin Rigler, Roberta Vecchi, Sara Valentini, and Marco Pandolfi (2021). “Determination of the multiple-scattering correction factor and its cross-sensitivity to scattering and wavelength dependence for different AE33 Aethalometer filter tapes: A multi-instrumental approach”. In: *Atmospheric Measurement Techniques Discussions* 29.March, pp. 1–30.

Yus-Díez, Jesús, Marina Ealo, Marco Pandolfi, Noemı Perez, Gloria Titos, Griša Močnik, X. Querol, and Andrés Alastuey (2020). “Aircraft vertical profiles during summertime regional and Saharan dust scenarios over the north-western Mediterranean Basin: aerosol optical and physical properties”. In: *Atmospheric Chemistry and Physics Discussions*, pp. 1–35.

Yus-díez, Jesús, Marta Via, Andrés Alastuey, Angeliki Karanasiou, María Cruz Minguillón, Noemí Perez, Xavier Querol, Cristina Reche, and Matic Ivan˘ (2022). “Absorption enhancement of BC particles in a Mediterranean city and countryside : effect of PM chemistry , aging and trend analysis”. In: March, pp. 1–26.

Zanatta, Marco et al. (2016). “A European aerosol phenomenology-5: Climatology of black carbon optical properties at 9 regional background sites across Europe”. In: *Atmospheric environment* 145, pp. 346–364.

Zhang, Renyi, Alexei F. Khalizov, Joakim Pagels, Dan Zhang, Huaxin Xue, and Peter H. McMurry (2008). “Variability in morphology, hygroscopicity, and optical properties of soot aerosols during atmospheric processing”. In: *Proceedings of the National Academy of Sciences of the United States of America* 105.30, pp. 10291–10296.

Zhang, Yunjiang, Alexandre Albinet, Jean Eudes Petit, Véronique Jacob, Florie Chevrier, Gregory Gille, Sabrina Pontet, Eve Chrétien, Marta Dominik-Sègue, Gilles Levigoureux, Griša Močnik, Valérie Gros, Jean Luc Jaffrezo, and Olivier Favez (2020). “Substantial brown carbon emissions from wintertime residential wood burning over France”. In: *Science of the Total Environment* 743.

Zhang, Yunjiang, Olivier Favez, Francesco Canonaco, Dantong Liu, Griša Močnik, Tanguy Amodeo, Jean Sciare, André S. H. Prévôt, Valérie Gros, and Alexandre Albinet (2018). “Evidence of major secondary organic aerosol contribution to lensing effect black carbon absorption enhancement”. In: *npj Climate and Atmospheric Science* 1.1.

Zotter, Peter, Hanna Herich, Martin Gysel, Imad El-Haddad, Yanlin Zhang, Griša Mocnik, Christoph Hüglin, Urs Baltensperger, Sönke Szidat, and André S.H. Prévôt (2017). “Evaluation of the absorption Ångström exponents for traffic and wood burning in the Aethalometer-based source apportionment using radiocarbon measurements of ambient aerosol”. In: *Atmospheric Chemistry and Physics* 17.6, pp. 4229–4249.

Colophon

Esta tesis se ha terminado e impreso entre la ciudad del aire y la del sol, entre mi tierra natal y adoptiva, con la mirada puesta, como el Ebro, en el Mediterráneo.

Barcelona, 20 de septiembre, 2022

Jesús Yus Díez